

**DEVELOPMENT OF PLANAR SOLID
OXIDE FUEL CELL USING CERMET
ANODE PREPARED BY ELECTROLESS
TECHNIQUE**

Thesis

Submitted for the degree of
Doctor of Philosophy (Science)

Jadavpur University
Kolkata – 700 032, India

by

Madhumita Mukhopadhyay (Banerjee)

Fuel Cell & Battery Division
(CSIR)-Central Glass & Ceramic Research Institute
196, Raja S.C. Mullick Road
Kolkata – 700 032, India

March 2012

Dedicated to my

“Mother”

&

“Husband”

Jadavpur University

Kolkata – 700 032, India

Index NO. 221/10/Chem/20

I. Title of the Thesis

DEVELOPMENT OF PLANAR SOLID OXIDE FUEL CELL USING
CERMET ANODE PREPARED BY ELECTROLESS TECHNIQUE

II. Name, designation & Institution of the supervisor

Dr. Rajendra Nath Basu
Chief Scientist & Head,
Fuel Cell & Battery Division
CSIR-Central Glass & Ceramic Research Institute
196, Raja S.C. Mullick Road
Kolkata – 700 032, .India
Tel: +91-33- 2473-3469/96, Ext: 3507
Fax: +91-33-24730957
E-mail: rnbasu@cgcri.res.in, rajenbasu54@gmail.com

III. List of Publications

A. Publications in SCI and other Peer-reviewed journals

Published:

1. Madhumita Mukhopadhyay, J. Mukhopadhyay, A. Das Sharma, R.N. Basu, “Engineered anode structure for enhanced electrochemical performance of anode-supported planar solid oxide fuel cell”, *International Journal of Hydrogen Energy*. **37**, 2524- 2534 (2012).

2. Madhumita Mukhopadhyay, J. Mukhopadhyay, A. Das Sharma, R.N. Basu, "In-situ patterned intra-anode triple phase boundary in SOFC electroless anode: An enhancement of electrochemical performance", *International Journal of Hydrogen Energy*, **36**, 7677-7682 (2011).
3. Madhumita Mukhopadhyay, J. Mukhopadhyay, A. Das Sharma, R.N. Basu, "High performance planar solid oxide fuel cell fabricated with Ni-yttria stabilized zirconia anode prepared by electroless technique", *International Journal of Applied Ceramic Technology*, Accepted for publication [DOI: 10.1111/j.1744-7402.2011.02646.x].
4. Madhumita Mukhopadhyay, J. Mukhopadhyay, A. Das Sharma and R.N. Basu, "Multilayered SOFC anode structure with electroless Ni-YSZ for enhancement of cell performance", *Electrochem. Soc. Transaction*, **35 (1)**, 1293-1302 (2011), The Electrochemical Society.
5. Madhumita Mukhopadhyay, J. Mukhopadhyay, A. Das Sharma and R.N. Basu, "Use of electroless anode active layer in anode-supported planer SOFC", *Electrochem. Soc. Transaction*, **25 (2)**, 2267-2274(2009), The Electrochemical Society.
6. Madhumita Mukhopadhyay, Jayanta Mukhopadhyay, Abhijit Das Sharma and Rajendra N. Basu, "Ball mill assisted synthesis of Ni-YSZ cermet anode by electroless technique and their characterization", *Material Science & Engineering B*, **163**, 120-127 (2009).
7. Jayanta Mukhopadhyay, Madhumita Banerjee and Rajendra N. Basu, "Influence of Sorption Kinetics for Zirconia Sensitization in SOFC Functional Anode Prepared by Electroless Technique", *Journal of Power Sources*, **175**, 749-759(2008).
8. J. Mukhopadhyay, M. Banerjee, A. Das Sharma, R.N. Basu and H.S. Maiti, "Development of functional SOFC anode", *Electrochem. Soc. Transaction*, **7[1]**, 1563-1572 (2007), The Electrochemical Society.

Communicated:

1. Madhumita Mukhopadhyay, J. Mukhopadhyay, A. Das Sharma, R.N. Basu, "Effect of Anode Configuration on Electrical Properties and Cell Polarization in Planar Anode Supported SOFC", Submitted to *Fuel Cells* on 24th Jan 2012.

B. Patents filed

Rajendra Nath Basu, Madhumita Mukhopadhyay, Jayanta Mukhopadhyay and Abhijit Das Sharma; "Improved process for the preparation of planar anode-supported solid oxide fuel cell", Indian patent, 1954 DEL 2010.

C. Conference Papers

1. Madhumita Mukhopadhyay, J. Mukhopadhyay, A. Das Sharma and R.N. Basu, "Electrical and Electrochemical Behavior of Novel Ni-YSZ SOFC Anode Prepared by Electroless Technique", International Symposium on Energy materials: Opportunities and challenges (ISEM -20011), CGCRI, Kolkata, 1-2nd March 2011, Page - 102.
2. Madhumita Mukhopadhyay, J. Mukhopadhyay, A. Das Sharma and R.N. Basu, "High Performance Solid Oxide Fuel Cell using Electroless Ni-YSZ Anode", International Conference on Electroceramics (ICE -2009), University of Delhi, New Delhi, 13-17th Dec. 2009, Page - 432.
3. Madhumita Mukhopadhyay, J. Mukhopadhyay, A Das Sharma and R.N. Basu, "Preparation and Application of Electroless Ni-YSZ Anode for Developing IT-SOFC", National Symposium on Advanced Ceramics and Composites, at National Metallurgical Laboratory, Jamshedpur, May 7-8th, 2009 (*Contributory talk*).
4. Madhumita Banerjee, Jayanta Mukhopadhyay, Abhijit Das Sharma and Rajendra N. Basu, "Development of planar SOFC using novel Ni-YSZ anode prepared by electroless technique",

Internal seminar – CGCRI, Kolkata, 5th -6th April 2008, Page 69-70.

5. J. Mukhopadhyay, M. Banerjee, R.N. Basu and H.S. Maiti, “A Reversible Sorption Model of Metallic Palladium on Zirconia Particulates for Solid Oxide Fuel Cell Functional Anode”, International Conference on Advanced Materials (IUMRS-ICAM 2007), Bangalore, 8-13 October 2007, Page. N-17 to N-18.
6. M. Banerjee, J. Mukhopadhyay, A. Das Sharma, A.K. Guha, R.N. Basu and H.S. Maiti, “Effect of Processing Parameters for the Development of Functional SOFC Anode”, 18th Annual General Meeting of MRSI, National Physical Laboratory, New Delhi, 10–12 February, 2007, Page - 36.

D. Courses Passed

Course work for Ph.D is successfully completed from *Jadavpur University* on the following courses/subjects:

- A) Review on research methodology
- B) Processing and Fabrication of Glass and Ceramics

CERTIFICATE

This is to certify that, the thesis entitled, "**Development of Planar Solid Oxide Fuel Cell Using Cermet Anode Prepared by Electroless Technique**" submitted by **Mrs. Madhumita Mukhopadhyay (Banerjee)** who got her name registered on 24.11.2010 for the award of Ph.D. (Science) degree of Jadavpur University, is absolutely based upon her own work under the supervision of **Dr. Rajendra Nath Basu**, Chief Scientist, Head-Fuel Cell & Battery Division, CSIR-CGCRI, Kolkata and that neither this thesis nor any part of it has been submitted for either any Degree/ Diploma or any other academic award anywhere before.



(Signature of the supervisor, date with official seal)

Dr. Rajendra Nath Basu

Chief Scientist & Head
Fuel Cell & Battery Division
CSIR-Central Glass & Ceramic Research Institute
Kolkata – 700032

Date: 16-03-2012

Place: Kolkata

डॉ० राजेन्द्र नाथ बसु
DR. RAJENDRA NATH BASU
चीफ वैज्ञानिक एवं प्रमुख
CHIEF SCIENTIST & HEAD
फ्युअल सेल एवं बैटरी प्रभाग
FUEL CELL & BATTERY DIVISION
सीएसआईआर - केन्द्रीय कांच एवं सिरामिक अनुसंधान संस्थान
CSIR - CENTRAL GLASS & CERAMIC RESEARCH INSTITUTE
196, राजा एस. सी. मल्लिक रोड/RAJA S. C. MULLICK ROAD
कोलकाता/KOLKATA-700 032

DECLARATION

I, Mrs. Madhumita Mukhopadhyay (Banerjee), hereby declare that, the thesis entitled “**Development of Planar Solid Oxide Fuel Cell Using Cermet Anode Prepared by Electroless Technique**” is submitted to Jadavpur University (registered on 24.11.2010) for the degree of Doctor of Philosophy (Science). This research work is carried out by me at CSIR- Central Glass & Ceramic Research Institute, Kolkata under the supervision of **Dr. Rajendra Nath Basu**, Chief Scientist, Head, Fuel Cell & Battery Division, CSIR-CGCRI, Kolkata. Any part of this dissertation has not been submitted either for any Degree / Diploma or for any other academic award anywhere before. Any help or source of information which has been availed in the thesis has been duly acknowledged.

Madhumita Mukhopadhyay (Banerjee)

Mrs. Madhumita Mukhopadhyay (Banerjee)

Fuel Cell & Battery Division

CSIR-Central Glass & Ceramic Research Institute
Kolkata – 700032

Date: 16.03.2012

Place: Kolkata

PREFACE

The primary rationale of the present research work is aimed at some diminutive contribution towards the development of alternate energy devices in terms of Solid Oxide Fuel Cell (SOFC). In this regard, development of SOFC anode component viz. nickel (Ni) - 8 mol % yttria stabilized zirconia (YSZ) cermet prepared by 'Electroless technique', its fabrication in the form of single cell and its application in the aforesaid electrochemical device forms the core of the present dissertation. In a number of ways, the novel electroless technique is proved to be a 'boon' for synthesizing such metal-ceramic composites with improved distinctiveness. This thesis is intended to serve a fruitful purpose to reinvestigate Ni-YSZ anode materials in a newer fashion with much superior characteristics to be used as an efficient alternate anode for IT-SOFC.

The dissertation initiates with a broad overview of the subject and provides the background necessary to appreciate the need of ceramic fuel cells and SOFC anodes in depth in 'Chapters 1, 2 and 3'. Chapter 4 is based on the experimental techniques availed during the research work. Finally, the detailed outcomes of the experiments are presented in 'Chapter 5' and concluded in 'Chapter 6' with future outlook related to such field of research activity. Ranging from the synthesis of anode by electroless technique, characterizations (physical, electrical, thermal, microstructural etc.) of the optimized Ni-YSZ cermet anodes are discussed in a comprehensive manner. Additionally, application of such functional anodes in SOFCs is also carried out to judge its applicability and competence. Furthermore, a few mathematical modeling approaches are also practised in diversified manner followed by experimental validations for some important aspects of scientific studies.

The author sincerely desires that the effort involved in the dissertation would serve some purpose towards the development of efficient anode for SOFC application which will lead to develop effective power packs in future.

Kolkata

Madhumita Mukhopadhyay (Banerjee) 16.03.2012.
Madhumita Mukhopadhyay (Banerjee)

ACKNOWLEDGEMENTS

The author wishes to express her deep sense of gratitude towards her supervisor, **Dr. R. N. Basu**, Chief Scientist and head, Fuel Cell & Battery Division, CSIR-CGCRI, Kolkata for his invaluable guidance, motivation, untiring efforts and attention at all stages of her research work.

The author is grateful to **Dr. H. S. Maiti**, former Director of CSIR-CGCRI and **Prof. I. Manna**, Director, CSIR-CGCRI, Kolkata for giving her a chance to be a part of this institute during her research period. The author sincerely acknowledges the **Council of Scientific and Industrial Research (CSIR)**, India for providing her financial support in terms of five years NET fellowship.

A special acknowledgment is expressed towards the endless mental and moral support showered by her uncle, **Prof. Arun Gangopadhyay**, ex-Professor of University of Calcutta, in every sphere of the author's life. He has always been like a mentor smoothening the path of the author throughout the years.

The author wishes to acknowledge with gratitude the endless inspiration, years of support and sacrifice that came from her mother (**Mrs. Usha Banerjee**). She also intends her gratitude towards her father (**Late Chanchal K. Banerjee**), aunty (**Late Shanti Banerjee**) and her in law parents (**Late Jaydeb Mukherjee and Late Ratna Mukherjee**) whose blessings paved her path and smoothen all the hurdles.

The greatest appreciation is expressed towards her husband (**Mr. Jayanta Mukhopadhyay**, Scientist, FCB Division, CSIR-CGCRI, Kolkata) for his selfless support and co-operation. She intends to express her sincere gratitude to her husband who has guided her immensely in her research work, article publication etc during the entire tenure. His valuable suggestions helped the author to design her experiments, data interpretation, article and thesis writing.

The author is indebted to **Dr. Abhijit Das Sharma** (Senior Scientist, FCB Division, CSIR-CGCRI, Kolkata) for the co-operation and guidance in carrying out her experimental works and article corrections at all stages of her research work.

She intends to acknowledge **Dr. S. Mahanty**, (Principle Scientist, FCB Division, CSIR-CGCRI, Kolkata), **Dr. A. Dutta** (Former Fellow Scientist, FCB Division, CSIR-CGCRI, Kolkata) and **Mr. S. Nag** (Jr. Scientist, FCB Division, CSIR-CGCRI, Kolkata) for their co-operation and many valuable discussions.

The author is acknowledged to **Mrs. M. Raut and Mr. K. V. V. Seshagiri**, Technical officers and **Mr. J. Dalui** of FCB division for their assistance and support during the course of her work. She also express her gratitude towards **Mr. S. Singh, Mr. S. Das, Mr. S. K. Ghosh, Mrs. N. Chakroborty, Mr. S. N. Barik, Mr. S. Roy, Mr. G. Dey and Mr. R. Paul** who have supported her a lot with their technical skills. She is also thankful to all concerned persons of '**Characterization Section**' for extending their fruitful co-operation during the entire research tenure. The author is thankful to her senior colleagues, **Dr. S. Ghosh, Dr. M. W. Raja, Dr. P. Ghosh**, her colleagues, **Mr. M. Kundu, Mrs. S. Patra**, and junior colleagues, **Miss. S. Dutta, Mr. S. Biswas, Mr. D. Das, Mr. Q. A. Islam, Miss. S. Bhattacharya, Mr. S. Majumdar**, and others for support and encouragement. The author also wishes to express gratitude towards few of her educators like **Mr. H. Kabir, Mr. Samir Mukherjee, Dr. T. T. Sarkar, Dr. Sasankasekhar Mahanty** and all others for their untiring efforts in teaching the author and making her capable of presenting a dissertation work before them.

Finally, any help or assistance which has been availed in the thesis is truly acknowledged.

16.03.2012.
Kolkata

Madhumita Mukhopadhyay (Banerjee)
Madhumita Mukhopadhyay (Banerjee)

CONTENTS

<i>List of Tables</i>	i-iii
<i>List of Figures</i>	v-xv
<i>Abstract</i>	xvii-xviii

Chapter –1 — Introduction **1- 47**

1.1. <i>The Rationale Behind Fuel Cell Development</i>	3
1.2. <i>Classification of Fuel Cells</i>	6
1.3. <i>Principles of SOFC</i>	15
1.4. <i>SOFC Component Materials</i>	19
1.5. <i>Broad Categories of SOFC Design</i>	26
1.6. <i>Advantages and Drawbacks of SOFC</i>	35
1.7. <i>Objective and Motivation of Present Research Work</i>	36
1.8. <i>References</i>	39

Chapter –2 — Importance & Features of ***SOFC Anode*** **49-63**

2.1. <i>Importance of Anode in Planar SOFC</i>	51
2.2. <i>SOFC Anode – The Associated Properties</i>	52
2.3. <i>Concept of TPB in SOFC – A Possibility of Extension</i>	53
2.4. <i>Influence of Various Factors on Optimization of Anode</i>	56
<i>Microstructure and Properties</i>	
2.5. <i>References</i>	60

Chapter –3 — Literature Survey 65-110

3.1.	<i>SOFC Anode Materials</i>	67
3.1.1.	<i>Ni-YSZ cermet anode material</i>	67
3.1.2.	<i>Alternate anode materials</i>	71
3.1.2.1.	Fluorite based anodes	71
3.1.2.2.	Perovskite anode materials	75
3.1.2.3.	Pyrochlore anode materials	77
3.1.2.4.	Tungsten bronze anode materials	77
3.1.2.5.	Sulfur tolerant anode materials	79
3.1.2.6.	Anodes applicable for hydrocarbon fuels	80
3.2.	<i>Anodic Reaction Mechanisms</i>	82
3.3.	<i>Ni-YSZ Anode- Applicability, Preparation, Challenges and Remedies</i>	86
3.4.	<i>Development of Anode-supported SOFCs with Structural Stability</i>	93
3.5.	<i>References</i>	98

Chapter – 4 — Experimental 111-134

4.1.	<i>Preparation of Ni-YSZ Cermet Powder</i>	113
4.1.1.	<i>Solid state technique</i>	113
4.1.2.	<i>Electroless technique</i>	114
4.1.2.1.	Ball- mill technique for YSZ sensitization	115
4.1.2.2.	High energy ultrasonification technique for YSZ sensitization	117
4.2.	<i>ICP-AES Measurements Related to Synthesis of Ni-YSZ Cermet Powder</i>	118
4.3.	<i>Ni-YSZ Powder Characterization</i>	119
4.3.1.	<i>Particle size analysis</i>	119

Contents

4.3.2. <i>X-ray diffraction technique</i>	121
4.4. <i>Preparation of Bulk Ni-YSZ Anodes</i>	121
4.4.1. <i>Uniaxial pressing</i>	121
4.4.2. <i>Tape casting and lamination</i>	121
4.5. <i>Anode Cermet Characterizations</i>	122
4.5.1. <i>Density measurements</i>	122
4.5.2. <i>Pore size distribution studies</i>	123
4.5.3. <i>Thermal expansion studies</i>	126
4.5.4. <i>Electrical conductivity studies</i>	127
4.5.5. <i>Microstructural characterizations</i>	128
4.6. <i>Fabrication of SOFC with Electroless Ni-YSZ Anode</i>	130
4.7. <i>Electrochemical Characterization of Single Cell</i>	132
4.8. <i>References</i>	134

Chapter –5 — Results & Discussion 135-318

5.1. <i>Ball Mill Assisted Ni-YSZ Electroless Anode</i>	137
5.1.1. <i>Concept of electroless technique</i>	139
5.1.2. <i>Application of ball mill theory for YSZ sensitization</i>	140
5.1.3. <i>Correlation of phase intensity ratio with milling speed</i>	145
5.1.4. <i>Effect of milling speed on anode characteristics</i>	147
5.1.4.1. <i>Densification studies</i>	147
5.1.4.2. <i>Electrical and thermal characterizations</i>	149
5.1.4.3. <i>Microstructural studies</i>	154
5.1.5. <i>Summary</i>	157
5.2. <i>High Energy Ultrasonification Assisted Ni-YSZ Electroless Anode</i>	159
5.2.1. <i>Sorption kinetic modeling for YSZ sensitization</i>	162

Contents

5.2.2. <i>Summary</i>	167
5.3. <i>Validation of Modeling Parameters with Optimized YSZ Sensitization</i>	171
5.3.1. <i>Effect of YSZ particle size on sorption kinetics</i>	173
5.3.2. <i>Effect of sonochemical agitation frequency</i>	176
5.3.3. <i>Application of external mass transfer phenomena</i>	178
5.3.4. <i>Application of intra-particle mass transfer phenomena</i>	181
5.3.5. <i>Determination of effectiveness factor and its importance</i>	183
5.3.6. <i>Summary</i>	184
5.4. <i>Electroless Cermet: Correlations with Physical Properties</i>	187
5.4.1. <i>Phase identification</i>	189
5.4.2. <i>Effect of equilibration time for YSZ sensitization on enhancement of anode functionality</i>	191
5.4.2.1. <i>Densification studies</i>	192
5.4.2.2. <i>Electrical characterizations</i>	195
5.4.2.3. <i>Microstructural studies</i>	201
5.4.2.4. <i>Study of thermal behavior</i>	202
5.4.3. <i>Summary</i>	205
5.5. <i>Patterned Intra-anode TPB Produced In-situ in Electroless Cermet: A Mathematical Approach</i>	207
5.5.1. <i>Modeling of intra-anode TPB length</i>	210
5.5.2. <i>Application of proposed model for TPB length determination</i>	213
5.5.3. <i>Manifestation of intra-anode TPB on electrical and electrochemical properties of electroless anode</i>	216
5.5.4. <i>Summary</i>	222

Contents

5.6. <i>Structure – Property Correlation of Tape cast Electroless Anode and its Application in Planar Anode – supported SOFC</i>	225
5.6.1. <i>Optimization of grain and ambipolar resistances of SOFC anode</i>	228
5.6.2. <i>Influence of anode configuration on electrical conductivity and correlation with porosity</i>	231
5.6.3. <i>Electrochemical performance evaluation of SOFC fabricated with assorted anode configuration</i>	244
5.6.4. <i>Thermal characterizations of the fabricated anodes</i>	299
5.6.5. <i>Polarization effects in anode-supported SOFC and its dependence on anode configuration</i>	301
5.6.6. <i>Summary</i>	311
5.7. <i>References</i>	315

<i>Chapter –6— <u>Conclusions & Future Outlook</u></i>	319
--	------------

<i>Reprint of Publications</i>	333
--------------------------------	------------

List of Tables

Chapter –1-- INTRODUCTION

Table 1.1 Characteristics of fuel cell systems

Table 1.2 Advantages and disadvantages of electrolyte candidates for SOFC

Table 1.3 Reactive species in SOFC anodes

Table 1.4 Characteristics of SOFC stack design

Chapter – 4 — EXPERIMENTAL

Table 4.1 Batch compositions of NiO-YSZ anode cermet prepared by Conventional solid state technique.

Table 4.2 Experimental powder examined for particle size analysis

Table 4.3 Description of anode configurations in the present research work

Chapter –5 — RESULTS & DISCUSSION

Table 5.1 I_{Ni}/I_{YSZ} of X-ray diffraction for electroless and conventional anodes

Table 5.2 Density values of anode cermet prepared by electroless and conventional solid state technique

Table 5.3 Variation of frequency factor with milling speed during YSZ sensitization for electroless technique

Table 5.4 Variation of activation energy with milling speed during YSZ sensitization for electroless technique

Table 5.5 List of symbols used in Chapter – 5. 2

Table 5.6 Determination of volumetric specific area of precursor YSZ powders

List of Tables

- Table 5.7** The calculated mass transfer coefficients at different agitation frequencies
- Table 5.8** Batch identification of Ni-YSZ cermets prepared by ultrasonic assisted electroless technique
- Table 5.9** Batch identification of Ni-YSZ cermets based on equilibration time during sensitization
- Table 5.10** Comparative electrical conductivities of SOFC anodes prepared by different techniques
- Table 5.11** Activation energies for electrical conductivities
- Table 5.12** Conductivity degradation rates of SOFC anodes upon redox and thermal cycling
- Table 5.13** List of symbols used in Chapter – 5. 5
- Table 5. 14** Fabricated anode cermets having variable configurations
- Table 5.15** Variation of activation energies for electrical conduction with variable anode configurations
- Table 5.16** Comparative electrical conductivity degradation of varied anode configurations
- Table 5.17** Effect of moisture towards electrical conductivity of SOFC anodes
- Table 5.18** Effect of NiO reduction time and sintering temperature on performance of single cells fabricated with anodes of *Configuration - I* [Anode thickness: 1250 μm]
- Table 5.19** Effect of NiO reduction time and sintering temperature on performance of single cells fabricated with anodes of *Configuration - I* [Anode thickness: 1500 μm]
- Table 5.20** Effect of NiO reduction time and sintering temperature on performance of single cells fabricated with anodes of *Configuration - II* [Anode thickness: 1250 μm]

List of Tables

- Table 5.21** Effect of NiO reduction time and sintering temperature on performance of single cells fabricated with anodes of *Configuration - II* [Anode thickness: 1500 μm]
- Table 5.22** Effect of NiO reduction time on performance of single cells fabricated with anodes of *Configuration - III*
- Table 5.23** Effect of NiO reduction time and AAL thickness on the performance of SOFC fabricated with anodes of *Configuration – IV* at 800°C
- Table 5.24** Effect of moisture in fuel on the performance of single cell fabricated with anodes of *Configuration- I and II*
- Table 5.25** Effect of moisture in fuel on the performance of single cell fabricated with anodes of *Configuration- III*
- Table 5.26** Effect of moisture in fuel on the performance of single cell fabricated with anodes of *Configuration- IV*
- Table 5.27** Effect of oxidant variation on the performances of single cell fabricated with varied anode configurations
- Table 5.28** Comparative endurance test of single cell fabricated with varied anode configurations
- Table 5.29** Effect of moisture content in the fuel on the endurance test of single cell fabricated with varied anode configurations
- Table 5.30** Dependence of Coefficient of thermal expansion (CTE) on variation of anode configuration
- Table 5.31** Variation of cell performance and limiting current density with variable anode configurations.
- Table 5.32** List of symbols used in Chapter - 5.6.

List of Figures

Chapter –1-- INTRODUCTION

Figure 1.1: Comparative system efficiencies of Carnot-dependant and independent energy conversion systems

Figure 1.2: The structure of Nafion electrolyte and influence of water content on its conductivity

Figure 1.3: Schematic of Solid Oxide Fuel Cell

Figure 1.4: Contribution of polarization factors towards cell performance and trend of power output vs. current density

Figure 1.5: Possible reaction steps at air electrode in SOFC

Figure 1.6: Oxide ion conductivity of different electrolyte material

Figure 1.7: Schematic of sealless tubular cell design

Figure 1.8: Inter-cell connections in tubular SOFC

Figure 1.9: Segmented cell in series design for a) banded and b) bell and spigot configuration

Figure 1.10: Monolithic SOFC design with a) co flow and b) cross flow configurations

Figure 1.11: Schematic of flat planar SOFC design

Figure 1.12: Different cell support architectures for SOFC planar configuration

Chapter – 2 — IMPORTANCE & FEATURES OF SOFC ANODE

Figure 2.1: A schematic representation of anode/electrolyte interface showing the possibility for existence of dual TPB by microstructural optimization

List of Figures

Chapter – 3 — LITERATURE SURVEY

- Figure 3.1:** Dependence of electrical conductivity on the Ni-YSZ phase contribution
- Figure 3.2:** Elemental distribution during co-firing of Ni-YSZ anode with Co-doped LaCrO₃ above 1400°C
- Figure 3.3:** Schematic of cubic fluorite structure
- Figure 3.4:** Effect of Ni addition to gadolinium doped ceria from AC-impedance study of the respective electrodes
- Figure 3.5:** Polarization responses of Ni-SDC anodes with and without interlayer at different temperatures
- Figure 3.6:** Schematic of Unit cell of ABO₃ perovskite structure
- Figure 3.7:** Schematic of Unit cell of A₂B₂O₇ pyrochlore structure
- Figure 3.8:** The tungsten bronze structure
- Figure 3.9:** The morphology of carbonaceous deposits on the surface of anode containing 10 wt % CeO₂ and 20 wt % Cu after long term testing in n-butane fuel at 1173 K
- Figure 3.10:** Schematic for possible reaction processes for H₂ oxidation at anode/electrolyte interface as proposed by Holtappels et al
- Figure 3.11:** Schematic of fuel oxidation steps showing the involvement of both Ni and YSZ as effective centers for reaction sites as proposed by Jian et al
- Figure 3.12:** Langmuir reaction model developed by Ihara et al regarding correlation of interfacial conductivity with anodic electrochemical reactions
- Figure 3.13:** A general processing route for Ni-YSZ cermet preparation through conventional powder mixing method

List of Figures

Figure 3.14: Micrographs of the Ni-YSZ prepared by Ni-impregnation with 13.33 vol% Ni. (a) Sintered, (b) infiltrated with NiO, (c) reduced, (d) after redox cycling

Figure 3.15: Micrographs of the Ni-YSZ reported by Koide et al with Ni-YSZ ratio: (a) 87:13, (b) 61:39 (c) 40:60

Figure 3.16: FESEM images of: (a) as spun YSZ fibres and (b) Ni-YSZ rod fibres

Figure 3.17: Cross section of reduced NiYRSZ anode -- The lighter phase is the nickel oxide or nickel and the darker phase is the zirconia

Figure 3.18: Micrograph of Ni-YSZ cermet prepared by conventional solid state technique

Chapter – 4 — EXPERIMENTAL

Figure 4.1: Schematic representation of conventional solid state synthesis.

Figure 4.2: Process flow chart for ball mill assisted electroless technique.

Figure 4.3: Basic instrumental set up of atomic absorption spectrometer along with the schematic for the basic principle of emission spectra

Figure 4.4: Pressure acting on an immersed object and schematic explanation of 'displaced fluid' by rising of fluid level- 'Buoyancy effect'

Figure 4.5: Pore types includes: a) open and b) closed pores

Figure 4.6: Nature of intrusion-extrusion curve on a porous sample by mercury porosimetry

Figure 4.7: Typical schematic of Gaussian type pore-size distribution of porous samples

Figure 4.8: Schematic of sample holder in a dilatometer along with the sample sandwiched between holders

Figure 4.9: Schematic of 4-probe sensing technique with probe positions

List of Figures

Figure 4.10: Schematic representations of: a) sample loading for 4-probe electrical measurement and b) Electrical measurement technique

Figure 4.11: Schematic of planar anode-supported single cell fabrication

Figure 4.12: Schematic of electrochemical test set up designed and fabricated at CSIR-CGCRI

Chapter –5 — RESULTS & DISCUSSION

Figure 5.1: Schematic of microstructures obtained from a) conventional solid state and b) electroless technique

Figure 5.2: Process flow chart for ball mill assisted electroless technique

Figure 5.3: Schematic for the balance of force during ball milling

Figure 5.4: Dependence of adsorption capacity on milling speed and equilibration time

Figure 5.5: XRD pattern of Ni- YSZ cermet prepared by ball mill assisted electroless and conventional solid state technique

Figure 5.6: Schematic of X-ray diffractions from Ni-YSZ cermet anodes prepared by: a) ball mill assisted electroless and b) conventional solid state technique

Figure 5.7: Electrical conductivity percolation curve of Ni-YSZ prepared by different techniques

Figure 5.8: Temperature dependent electrical conductivities of cermet anodes (33 vol % Ni) prepared by ball mill assisted electroless technique

Figure 5.9: Variation of frequency factor as a function of milling speed for YSZ sensitization during electroless technique

Figure 5.10: Variation of activation energy as a function of milling speed for YSZ sensitization during electroless technique.

List of Figures

- Figure 5.11:** a) Optical micrograph of polished Ni-YSZ cermet (33 vol% Ni) prepared by electroless technique and b) corresponding Ni mapping of the selected area.
- Figure 5.12:** FESEM image of electroless Ni-YSZ in conjunction with quantitative spot EDAX and the corresponding elemental line mapping
- Figure 5.13:** Optical micrograph of ball mill assisted electroless Ni-YSZ cermets with YSZ sensitized at: a) 25 rpm and b) 65 rpm
- Figure 5.14:** a) Optical micrograph of Ni-YSZ cermet (40 vol %) prepared by conventional solid state technique and b) corresponding Ni mapping
- Figure 5.15:** The mechanisms governing ultrasonification assisted YSZ sensitization
- Figure 5.16:** Particle size distribution of precursor YSZ powders
- Figure 5.17:** Variation of bulk densities with particle size of YSZ powder
- Figure 5.18:** Dependence of equilibrium adsorption capacity (q_e) on the characteristics of sorbent species (YSZ particulates)
- Figure 5.19:** Effect of agitation frequency on sorption frequency (q_t) of Pd^0 by a) YSZ-Tosho HT and b) YSZ-Unitec
- Figure 5.20:** Variation of external mass transfer governed sorption capacity by: a) YSZ-Tosho HT and b) YSZ-Unitec, as function of agitation frequency up to experimental time interval
- Figure 5.21:** Variation of $(q_0 - q_t) / (q_0 - q_t)$ vs. time for Pd^0 adsorption on YSZ-Tosho HT with agitation frequencies (ν) of: a) 10 kHz, b) 12 kHz, c) 14 kHz and d) 16 kHz
- Figure 5.22:** Variation of $(q_0 - q_t) / (q_0 - q_t)$ vs. time for Pd^0 adsorption on YSZ-Unitec with agitation frequencies (ν) of: a) 10 kHz, b) 12 kHz, c) 14 kHz and d) 16 kHz
- Figure 5.23:** Intra-particle mass transfer phenomena for YSZ- Pd^0 system governed by Langmuir isotherm

List of Figures

- Figure 5.24:** X-ray diffraction pattern of a) precursor YSZ powder and b) Ni-YSZ cermet prepared by electroless technique
- Figure 5.25:** X-ray diffraction pattern of Ni-YSZ cermets with variable phase compositions prepared by electroless technique
- Figure 5.26:** Schematic for dependence of Pd⁰ adsorption capacity on equilibration time
- Figure 5.27:** Variation of densities as a function of processing techniques and equilibration time for YSZ-sensitization during electroless process
- Figure 5.28:** Variation of open porosities as a function of processing techniques and equilibration time for YSZ-sensitization during electroless process
- Figure 5.29:** Comparison of electrical conductivities of Ni-YSZ cermet prepared by different techniques
- Figure 5.30:** Arrhenius plots for electrical conductivities for electroless anode as a function of Ni content, equilibrated for: a) 300 min, b) 1200 min and c) 2500 min
- Figure 5.31:** Arrhenius plots for electrical conductivities for conventionally prepared anodes as a function of Ni content
- Figure 5.32:** Optical micrographs of electroless Ni-YSZ cermet for: a) transient equilibrium adsorption (T3-series), b) non-transient equilibrium adsorption (T1-series) and c) optical micrograph of conventionally prepared cermet
- Figure 5.33:** Comparative thermal expansion behavior of fabricated anodes using different preparation techniques
- Figure 5.34:** Comparative thermal expansion plots among electroless and conventional anodes in conjugation with YSZ electrolyte
- Figure 5.35:** Schematic of anodic electrochemical reactions at dual TPB zones of Ni-YSZ electroless anode

List of Figures

- Figure 5.36:** (a-1) Zr and (a-2) Ni mapping of electroless anode, (b-1) Zr and (b-2) Ni mapping of conventional anode and sectional TPB length distribution for: (c-1) electroless and (c-2) conventional anode cermet
- Figure 5.37:** Variation of intra-anode TPB length and surface area of electroless anode as a function of Ni content
- Figure 5.38:** a) Redox profile and b) thermal profile employed during electrical conductivity measurement
- Figure 5.39:** Variation of electrical conductivity of electroless and conventional anode towards: a) redox cycling and b) thermal cycling
- Figure 5.40:** Effect of redox and thermal cycles on degradation rates of electrical conductivity for: a) electroless and b) conventional cermet
- Figure 5.41:** Effect of redox cycling on degradation rates of TPB lengths for electroless and conventional cermet
- Figure 5.42:** Comparative electrochemical performances of single cell with anodes prepared by electroless and conventional technique
- Figure 5.43:** Electrical conductivity of anode samples at different sintering temperatures
- Figure 5.44:** Conductivity percolation plots of tape cast anode samples prepared by conventional and electroless techniques as a function of Ni content
- Figure 5.45:** Temperature dependent electrical conductivities for anodes of Configuration –I and Configuration-II
- Figure 5.46:** Temperature dependent electrical conductivities for anodes of Configuration –III
- Figure 5.47:** Temperature dependent electrical conductivities for anodes of Configuration –IV.
- Figure 5.48:** Optical microstructures for layered anodes of: a) Configuration- III and b) Configuration -IV

List of Figures

- Figure 5.49:** Variation in open porosity of SOFC anode prepared through electroless and conventional techniques
- Figure 5.50:** Effect of redox cycling on electrical conductivity of: a) conventional anode (CA-series) and b) layered anode with electroless AAL [28 AAL-4 and 32 AAL-4]
- Figure 5.51:** Comparative flow pattern of gasses for: a) electrochemical reaction and b) electrical conductivity
- Figure 5.52:** Schematic of single cells fabricated with anodes of: a) Configuration-I and b) Configuration -II
- Figure 5.53:** Schematic of NiO reduction mechanism in electroless anode cermet following two distinct steps as a) non-equilibrium and b) equilibrium region
- Figure 5.54:** Electrochemical performance of SOFC with half cell sintered at 1400°C fabricated with anodes of configuration: a) CA-1 and b) CA-2
- Figure 5.55:** Electrochemical performance of SOFC with half cell sintered at 1400°C fabricated with anodes of configuration: a) 28 EL-1 and b) 28 EL-2
- Figure 5.56:** Electrochemical performance of SOFC with half cell sintered at 1400°C fabricated with anodes of configuration: a) 32 EL-1 and b) 32 EL-2
- Figure 5.57:** a) Optical micrograph [with higher magnification of anode in right side] of single cell fabricated with anodes of EL-2 series, b) corresponding line mapping of single cell after electrochemical measurement with Ni-YSZ as anode-support (EL 2 -series- Configuration-II) and c) line mapping of single cell fabricated with anodes of CA-series
- Figure 5.58:** Schematic representation of layered anode configuration (Configuration-III) with gradation in physical properties
- Figure 5.59:** Electrochemical performance of single cell fabricated with anode of 28 BLA-3

List of Figures

- Figure 5.60:** Electrochemical performance of single cell fabricated with anode of 32 BLA-3
- Figure 5.61:** Elemental Ni mapping of a) anode prepared by electroless technique and b) layered anode configuration (BLA-series, cross sectional view)
- Figure 5.62:** Electrochemical performances of single cells (measured at 800°C) as a function of electroless anode layer thickness with anodes of configuration: a) 28 BLA-series and b) 32 BLA-series
- Figure 5.63:** a) Electrochemical performance of single cell (measured at 800°C) using functional trilayer anode (TLA) along with b) FESEM micrograph for Ni mapping of TLA
- Figure 5.64:** Schematic of single cells fabricated with anodes of Configuration- IV
- Figure 5.65:** Temperature dependent electrochemical performances of single cells fabricated with anodes of Configuration-IV viz. a) 28 AAL-1, b) 28 AAL-2, c) 28 AAL-3 and d) 28 AAL-4
- Figure 5.66:** Comparative electrochemical performances of single cells at 800°C with anode configurations of: a) CA-2 with 32 AAL-1 and b) 32 AAL-2, 32 AAL-3 and 32 AAL-4
- Figure 5.67:** a) Optical micrograph and b) corresponding line mapping of single cell fabricated with anodes of Configuration –IV
- Figure 5.68:** Schematic of a layered anode (Configuration – III and IV) with gradation in properties
- Figure 5.69:** Gaussian type pore size distribution plots of anode cermet of Configuration –I
- Figure 5.70:** Gaussian type pore size distribution plots of anode cermet of Configuration –II having IDs of: a) 28 EL-series and b) 32 EL-series
- Figure 5.71:** Gaussian type pore size distribution plots of anode of Configuration – III

List of Figures

- Figure 5.72:** a) Optical microstructure and b) binerized image (at higher magnification) of single cell with anode of BLA- series after electrochemical measurement
- Figure 5.73:** Gaussian type pore size distribution plots of anode of Configuration – IV that corresponds to a) 28 AAL-series and b) 32 AAL-series
- Figure 5.74:** Dependence of measured cell ASR as a function of thickness and Ni content for anode-support of Configuration –I and II
- Figure 5.75:** Variation of the measured cell ASR for layered anodes of Configuration –III
- Figure 5.76:** Measured cell area specific resistance (ASR) at 800°C as a function of thickness for electroless AAL and Ni content of Configuration –IV
- Figure 5.77:** Comparative area specific resistance (ASR) at 800°C for single cell fabricated with anodes of various configurations
- Figure 5.78:** Correlation among type of oxidants and performances of single cell fabricated with varied anode configurations
- Figure 5.79:** Comparative endurance test on single cells with a load of 0.5 Acm^{-2} among: a) Configuration – I & II, b) Configuration – I & III and c) Configuration – I & IV
- Figure 5.80:** Degradation rates determined from durability test on single cell with varied anode configurations subjected to an electronic load of 0.5 Acm^{-2}
- Figure 5.81:** Degradation rates determined from durability test on single cell with varied anode configurations subjected to an electronic load of 0.75 Acm^{-2}
- Figure 5.82:** Degradation rates determined from durability test on single cell with varied anode configurations subjected to an electronic load of 1.0 Acm^{-2}

List of Figures

- Figure 5.83:** Optical microstructure and intensity profile for phases of: a) conventional anode, b) electroless anode after endurance test of single cell, [c) and d)] are binerized images of conventional anode and [e) and f)] are binerized images of electroless anode subjected to electronic load of 0.5 and 1.0 Acm⁻² respectively
- Figure 5.84:** Comparative coefficients of thermal expansion of YSZ electrolyte with fabricated anode configurations
- Figure 5.85:** Schematic of fundamental electrochemical processes at anode/electrolyte interface of a planar anode-supported SOFC
- Figure 5.86:** Trend of “V vs I” curve exhibiting contributions from various polarization factors and its extrapolation to obtain limiting current density
- Figure 5.87:** Variation of concentration and charge transfer polarization of single cell fabricated with anodes of Configuration – I and II
- Figure 5.88:** Variation of concentration and charge transfer polarization of single cell fabricated with anodes of a) Configuration – III and b) Configuration- IV
- Figure 5.89:** Influence of anode configuration a) Configuration -I, b) Configuration –III- 32 BLA-1, c) Configuration-III- TLA and d) Configuration –IV on electrochemical impedance spectra of SOFC

ABSTRACT

*S*olid Oxide fuel cell (SOFC) is a very promising electrical conversion device owing to its high efficiency and low gas emissions. In light of the present world scenario relating to the energy sector, research and development works on alternate energy sources viz. fuel cells, solar, hydro etc. holds special drive and attention.

Among various classifications of ceramic fuel cells (SOFCs), the present research work is based on the flat planar design owing to its ease of fabrication and potential for providing high power densities compared to other cell configurations. Till date, nickel (Ni) -8 mol % yttria stabilized zirconia (YSZ) [Ni-YSZ] cermet has been evolved out as the most widely accepted anode for SOFC application. However, such Ni-ceramic composite possesses certain shortcomings owing to which the commercialization of SOFC is limited. The endeavour of the present research is based on the development of Ni-YSZ functional anode materials by novel 'electroless technique' and its application for SOFC fabrication. Generation of unique core (YSZ)-shell (discrete Ni nanoparticulates around the YSZ core) microstructure in a patterned manner through process optimization is one of the major accomplishment of such electroless technique. Sensitization of YSZ particulates by high energy ultrasonification forms the catalytic Pd⁰ particulates in-situ in the redox reaction bath. The adsorption of such Pd⁰ onto YSZ core governs the deposition of Ni around YSZ during electroless technique and hence the microstructure. Optimization of process parameters initially involve mathematical modeling which is followed by experimental validation. The developed electroless anode is found to exhibit the required electrical conduction (~ 500 Scm⁻¹) at much lower Ni content (28 vol %) compared to other conventional cermets. The major drawbacks of thermal incompatibility and poor redox tolerance associated with such Ni-YSZ anode is rectified using

Abstract

the functional electroless anode. Efforts have been exerted to determine the length of triple phase boundary (active sites for electrochemical reactions) and reaction sequences through mathematical modeling approach.

The second phase of the present research work is focussed on the fabrication of SOFCs using such functional anodes in assorted configurations. Electroless cermet is configured as anode-support structure, multilayered anode or anode active layer (AAL). The various factors affecting electrochemical activity of single cell such as: a) thickness and sintering temperature of the half cell b) rate of NiO reduction to metallic Ni, c) effect of moisture in fuel and c) type of oxidant used at the cathode side are studied thoroughly during the course of this research work. The load bearing competence of the fabricated SOFCs with the developed anodes are also examined for a considerable period of time to determine the corresponding degradation rates. The experimental results support the superiority of electroless anodes, which showed the highest cell performance of 3.7 Acm^{-2} at 800°C without any significant degradation and lowest polarization from the associated factors. The experimental outcome of electrochemical reactions are correlated with: a) optical microstructures, b) elemental mapping, c) NiO reduction equilibrium, d) pore-size distribution in anodes, e) effect of moisture in the fuel, f) variation in oxidant type etc. The influence of polarization/resistive factors is also studied in terms of both mathematical approach and electrochemical impedance measurements.

Therefore, the entire effort of the present research work is exerted towards the development of functional Ni-YSZ anode by novel 'electroless' technique encompassing its potential to act as new-generation anode for IT-SOFC application.

****~****

C ***HAPTER- 1***

Introduction

Chapter - 1

1.1. The Rationale Behind Fuel Cell Development

Energy, being one of the nature's prime gifts to the universe, is the most valuable necessity of every single living or inert matter. Nature has blessed us with innumerable energy resources, but restricted its creation or destruction. Among the renewable (alternate) and non-renewable sources of energy, though the availability of the former resource is secured, uninterrupted usage should be ensured through modernized facilities. On the other hand, non-renewable sources of energy suffer from availability crisis. Therefore, the need of present hour is to concentrate on the conservation and recycling of alternate energy sources on which the future generation will rely on. According to thermodynamics, an energy storage/conversion system equipped with least possible intermediate energy conversion steps shows better efficiency with easy applicability. In this context, fuel cells offer competent candidature for alternate energy sources which derives electrical power from variety of fuels. Such a device bypasses the conversion of chemical energy of fuel to thermal (independent of Carnot cycling) and mechanical energy, and thus achieves significantly higher theoretical efficiency compared to other conventional sources of power generation.

The invention of fuel cells (FC) as energy conversion system was initiated in the mid of 19th century. The discovery of the underlying principle was owned by *Prof. Christian Friedrich Schonbein*¹ at the University of Basle (1829-1868), however, the invention of fuel cell as an electrical energy conversion system is attributed to *Sir William Grove*. During this tenure, the other primary energy sources (either renewable or non-renewable) were abundant, unrestricted and inexpensive, due to which development of fuel cell lacked the initial drive. However, at the beginning of 20th century, energy conversion systems became more important. Significant increase in population around the globe and the depletion of natural sources of energies have also compelled human race to

Chapter - 1

emphasize on the research and development of other alternative energy storage and conversion systems. The concept of distributed power generation plant is initiated with an intention of reducing capital cost for the installer and improving the overall efficiency due to the possibility of co-generation of heat and electricity. One of the major factors for fuel cell development as the source of alternate energy conversion has also been the increasing concern about the environmental consequences of fossil fuel based energy sector. Technologically viable fuel cell is expected to facilitate mankind to reduce dependence on non-renewable energy sources and in addition diminish poisonous emissions into atmosphere. Other renewable sources viz. water, air, wind, solar etc may also serve for compensating the world's need for the substituted electrical energy but with poor efficiencies. However, efforts are being initiated to combine some of these natural energy sources with a view to produce hydrogen (acts as the fuel) that may be coupled with fuel cells which could be a better option for future power generation.²⁻⁷

A simplistic view of fuel cell is that it is a cross between a battery (chemical energy converted directly to electrical energy) and a heat engine (a continuously fuelled, air breathing device). Therefore, it is also referred as “electrochemical engines”. The range of fuel cell applications and the size of potential markets are enormous which includes, battery replacement in small portable electronic devices, prime movers and /or auxiliary power units in vehicles, residential combined heat and power (CHP) and large-scale megawatt (MW) electrical power generation. Fuel cells share the characteristics of high efficiency, no moving parts, quiet operation and low or zero emissions during application.

Comparative system efficiency

Efficiency of internal combustion engine (ICE) is limited by ‘Carnot’s cycle’, in which chemical energy (combustion of hydrocarbon) of the exothermic reaction is accompanied by rise in temperature. The expansion of gases caused by

generated heat gets converted to mechanical work, and then finally transformed into electrical energy by means of a rotating generator. The maximum efficiency (ε_r) of ICE is given by:

$$(\varepsilon_r)_{ther} = \frac{W_r}{-\Delta H} = 1 - \frac{T_2}{T_1} \quad (1.1)$$

where, W_r , ΔH , T_1 and T_2 are reversible work, enthalpy change of the reaction and two absolute temperatures for the operation of heat engines.

Based on thermodynamics, it is known that as the number of energy conversion step is enhanced, the overall system efficiency gets reduced due to the associated energy loss during each conversion. Therefore, in general, the efficiency of ICE controlled by Carnot's cycle fails to surpass more than ~ 50 %.

The system efficiency of a fuel cell independent of Carnot's limitation can be derived from Gibb's free energy (ΔG) and the enthalpy change (ΔH) of the electrochemical reaction in terms of electrical work (W_e) as:

$$(\varepsilon_r)_{FC} = \frac{W_e}{-\Delta H} = \frac{nFV_o}{-\Delta H} = \frac{\Delta G}{\Delta H} = 1 - \frac{T\Delta S}{\Delta H} \quad (1.2)$$

The term, $T\Delta S$ represents reversible heat exchanged with external environment. Theoretically, for FC's with positive entropy change (ΔS being positive), efficiency could be more than 1 (oxidation of CO to CO₂ for FCs yields $\varepsilon_{r, FC} = 1.24$). However, practically majority of reactions are associated with negative entropy change that causes increase in temperature thereby reducing the thermodynamic efficiency of fuel cell, whilst, for an ICE, increase in temperature enhances the efficiency magnitude. Regardless of all, the polarization factors contributing towards reducing FC-efficiency, the overall system efficiencies of FCs are high in comparison to ICE as shown in [Figure 1.1](#).^{8, 9} Apart from system output, fuel cells are superior pertaining to the co-generation of heat and electricity. Efforts are being pursued over the globe to enhance the efficiency of fuel cells and coupling with devices to utilize the waste heat for energy conservation. Therefore, owing to the advantages

Chapter - 1

associated with fuel cell technology, security of electricity can be ensured in future which is also expected to induce a new era of 'hydrogen economy'.

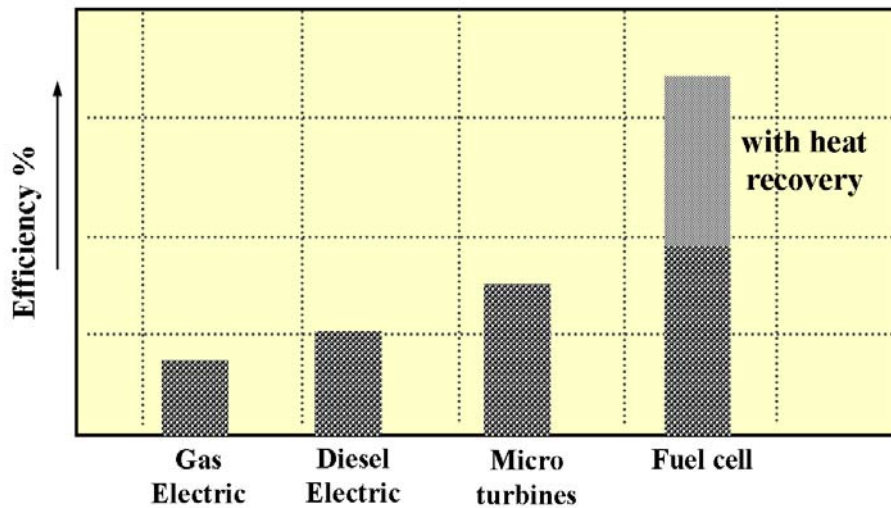


Figure 1.1: Comparative system efficiencies of Carnot-dependant and independent energy conversion systems^{8,9}

1.2. Classification of Fuel Cells

Fuel cell is usually being categorized in terms of electrolyte employed except direct methanol fuel cell (DMFC), in which classification is made with respect to the methanol fuel, fed directly to the anode. An overview of the fuel cell types is given in [Table 1.1](#).

It can be observed from the table that, depending upon the type of electrodes and electrolyte materials, operating temperature of FC is shifted from low to high temperature range (>60 -1000°C).^{7, 10-12}

Alkaline fuel cell (AFC)

AFC operates within a range of 60-90°C and has the advantage of exhibiting reasonably good efficiency. However, it intends to be operated using very pure gasses which is considered to be the major restrain in most applications. 30-45 wt

Chapter -1

% KOH is usually used as the electrolyte which accelerates the kinetics of oxygen (oxidant) reduction reaction compared to the acid fuel cells and thereby attracts attention for many specific applications.

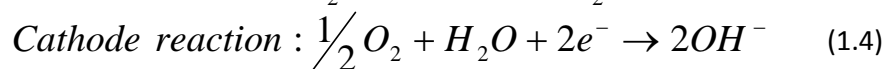
Table 1.1: Characteristics of fuel cell systems^{7, 10 - 12}

Types of fuel cell	Alkaline (AFC)	Polymer electrolyte membrane (PEMFC)	Direct methanol (DMFC)	Phosphoric acid (PAFC)	Molten carbonate (MCFC)	Solid Oxide (SOFC)
Operating Temperature (°C)	< 100	60-120	60-120	160-220	600-800	800-1000 or 500-600
Fuel	H ₂	H ₂	CH ₃ OH	H ₂	H ₂ , CO	H ₂ , CO
Oxidant	O ₂	O ₂ /Air	O ₂	O ₂	O ₂ + CO ₂	O ₂
Anode	Ni, Pt	Pt	Platinised Carbon (Pt/C)	Pt	Ni	Ni-YSZ
Cathode	Ni	Pt	Pt	Pt	Li-doped NiO	Sr-doped LaMnO ₃
Charge carrier in Electrolyte	OH ⁻	H ⁺	H ⁺	H ⁺	CO ₃ ²⁻	O ²⁻
Applications	Transportation, space, Military, Energy storage systems			Combined heat and power for decentralized stationary power systems	Combined heat and power for stationary decentralized systems and for transportation	
Realised power	Small plants, 5-150 kW modular	Small plants, 5-250 kW modular	Small plants, 5 kW	Small-medium sized plants 50kW-11 MW	Small power plants - 100kW-2 MW	Small power plants, 100-250 kW

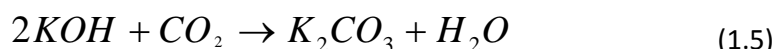
AFC electrodes used to be Ni-based catalyst, often being activated by Pt. Pt/C gas diffusion electrodes are generally used for both anode and cathode, as Pt is observed to have superior activity for oxygen reduction reaction (ORR) due to higher exchange current density. Other well known electrodes viz. Raney Ni, Pt/Pd are also used, in which the former is a very good catalyst for hydrogen oxidation, but exhibits performance decay due to wettability problem. In comparison, Pt/Pd electrode is most suited which shows very rapid decay initially but after short

Chapter - 1

instant, the performance remained constant. The basic electrochemical reaction for AFC can be written as:



AFC's suffers from serious problems relating to the management of highly corrosive liquid electrolyte and poisoning of electrolyte through the formation of carbonates in the following reaction:

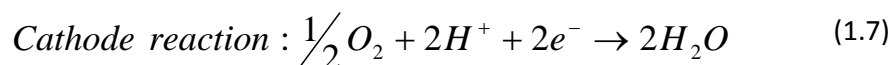
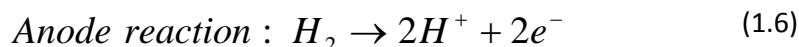


It is observed that CO_2 from air interact with the electrolyte to form carbonate crystals which can block electrolyte pathways and electrode pores.¹³ Various techniques are also cited to solve such problem, which include circulation of KOH electrolyte instead of using a stabilized matrix. It is expected that, in this way the electrolyte can be pumped out of the system which could avoid the carbonate formation. Other processes viz. usage of iron sponge system to remove CO_2 from hydrogen feed or air flow, water gas shift reactions, swing adsorption (a technique used to separate some gas species from a mixture under pressure in terms of the species molecular characteristics and affinity for an adsorbate material) etc could be used to avoid electrolyte poisoning.¹⁴⁻¹⁶

Polymer electrolyte membrane fuel cell (PEMFC)

PEM fuel cells are the first to be used in space being operated at low temperature (85-100°C) and are based on the proton exchange membrane electrolyte.¹⁷ Electrodes for PEM fuel cells are generally porous which ensures the effective diffusion of reactant gases to the active zones where noble metal catalyst is in contact with the ionic and electronic conductor. Pt - based catalyst are used as effective cathode which accelerates the rate of oxygen reduction reaction (ORR). In addition, Pt dispersed on carbon or small colloidal Pt particles are used as cathode

materials. Owing to the low operating temperature in PEMFCs, loadings for the oxygen catalyst act as significant role to compensate for slow ORR. Upon using air as the oxidant; partial pressure of available oxygen is reduced, thereby reducing the ORR further. ‘Catalyst ripening’ is an usual problem accounted in such cells which manifests itself as a decrease of active surface area of Pt due to formation of larger particles.¹⁸ Pt is also used as the anode electrode, provided pure hydrogen is used. However, CO is one of the major poisons in low temperature fuel cells where surface deactivation of Pt catalyst occurs through adsorption leading to insufficient sites available for H₂ sorption.¹⁹⁻²¹ The surface can be reactivated through oxidation of CO to CO₂. The basic electrochemical reactions can be written as:



Characteristics of proton conducting electrolyte membranes also act as a crucial role for the performance of PEMFC. Poly-tetrafluoroethylene based (PTFE) polymer termed as ‘Nafion’ is a well-known example of such membrane electrolyte which is chemically inert in both reducing and oxidizing environment (Figure 1.2).

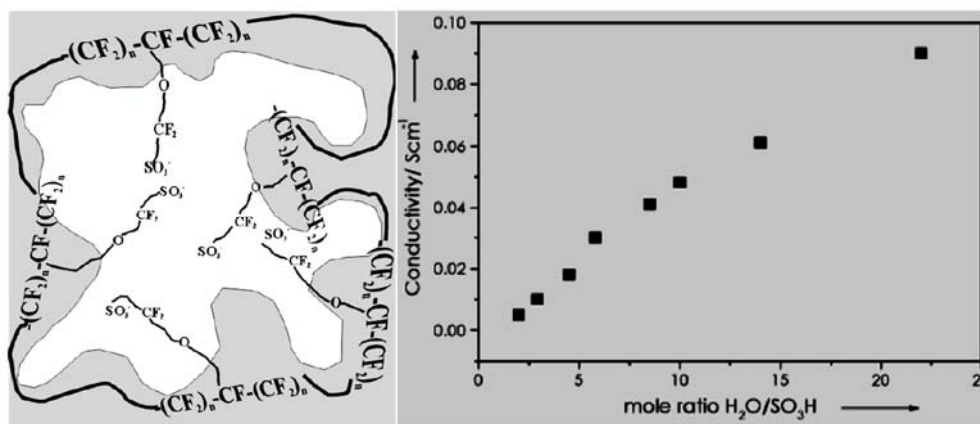


Figure 1.2: The structure of Nafion electrolyte and influence of water content on its conductivity²²⁻²³

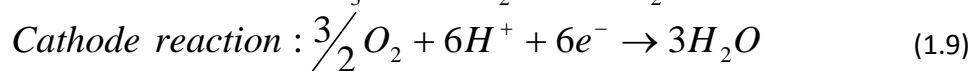
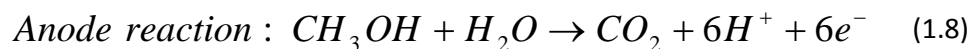
Water management of polymer electrolyte is a crucial issue, since a dried out membrane poses much lower conductivity for proton transport as shown in Figure

Chapter - 1

1.2.²²⁻²³ Factors influencing the water content in the membrane involve electro-osmotic drag through cell and back diffusion of H^+ from the cathode product (H_2O) into the membrane. Membrane water could be well managed by humidifying the reactant gasses or direct hydration of the membrane by mounting porous fibre wicks.²⁴⁻²⁵ The associated advantages for PEMFC includes high power densities compared to other low temperature FCs, small size with reasonable cost, lack of material interactions, easier fabrication of stacks etc.

Direct methanol fuel cell (DMFC)

Low temperature DMFC works primarily on the principle of PEMFC. The basic difference lies in the direct feeding of methanol as fuel without the intermediate step of alcohol reforming into hydrogen. Methanol has an advantage of being renewable energy source, and in addition possesses high specific energy density (as it is liquid at the operating temperature). The fuel mixture is composed of liquid methanol in water mixture (1-2 M); therefore, the concentration of methanol in the fuel feed should be kept constant through recycling the effluent and maintained by sensors which measures the current from electro-oxidation of methanol.²⁶⁻²⁷ Unlike hydrogen, oxidation of methanol is not very effective, therefore, metals viz. Ru, Re, Os, Rh, Mo etc are being extensively used as catalysts.²⁸⁻³⁵ Electrodes for methanol oxidation are usually bound together with Nafion to improve the ionic conductivity in the catalyst layer. The associated electrode reactions for such liquid FC is given as:

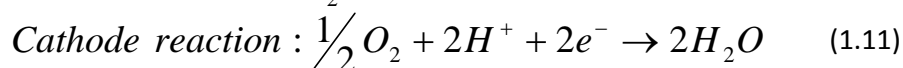
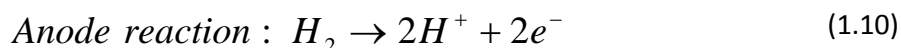


The catalysts employed for oxygen reduction for DMFC are almost equivalent to the ones used in PEMFC. The major problem encountered in DMFC is the cross-over of methanol across the electrodes. The membranes used in DMFCs are mainly

developed to be associated with PEM fuel cells whose prime criterion is to optimize the proton conductivity. As discussed earlier, the proton movement through the membrane is associated with water content. Owing to similar properties among water and methanol in terms of dipole moment, both are easily being transported by the osmotic drag and diffusion. At the cathode, methanol causes a mixed potential due to interference of methanol oxidation with oxygen reduction reaction. Therefore, such cross-over of methanol results in decrease of cell performance. To overcome such problem, alternate cathodes with selective catalyst are used which are inactive towards methanol oxidation.³⁶⁻³⁹ By this means, development of mixed potential could be avoided and relatively higher performance of cell is obtained.

Phosphoric acid fuel cell (PAFC)

PAFCs are advantageous regarding commercial developments as stationary power plants due to its simple construction, stability with respect to thermal, chemical and electrochemical and low volatility of the electrolyte at the cell operating temperature (150-200°C). In order to avoid corrosion of cell components, concentrated phosphoric acid is stabilized in a SiC based matrix. Higher concentration of the acid enhances the conductivity of the electrolyte and reduces corrosion of carbon supported electrodes. The basic cell reaction is written as:



The electrodes used in PAFCs are generally Pt-based catalyst dispersed on a carbon support (as discussed for PEM fuel cells). However, the ORR kinetics require relatively high loading of Pt compared to hydrogen oxidation reaction. Usage of liquid electrolyte in such FCs require a hydrophobic backing layer which is soaked in PTFE (Poly-tetrafluoroethylene) solution.¹¹ In addition, PTFE prevents the catalyst

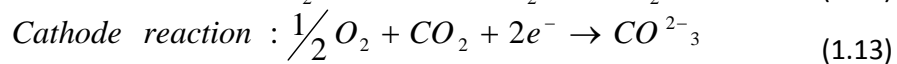
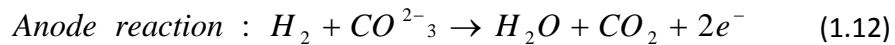
Chapter - 1

layer from being pore-flooded. A number of species has been identified as catalyst for either ORR or HOR viz. Pt-Co alloys, Pt-WO₃ etc.⁴⁰ However, Pt-Co alloy generates the problem of Co leaching out from the alloy thereby affecting the overall cell performance. In addition, 'Pt ripening'- a usual phenomenon also tend to reduce the cell performance.⁴¹ Addition of WO₃ to Pt induces an increase in electrochemically active area which accounts for the enhancement of cell performance compared to conventional Pt/C catalyst.⁴⁰ Apart from the mentioned reagents, additions of other metals e.g. Ru, W, Pd etc to Pt also showed remarkable effect in enhancing the cell performance. Pt-Ru is especially important to act as the catalyst for hydrogen oxidation when reformat hydrogen is used because the CO content present in the fuel can be easily oxidized with Ru as a secondary metal.⁴² Operating PAFCs results in significant heat loss, which needs to be cooled fast using purified coolant, else it would cause evaporation of phosphoric acid. System cost, therefore, gets enhanced upon employing such optimized coolant system. Another noted measure to be taken is to retain the PAFC above the freezing temperature of phosphoric acid (~ 42°C); otherwise, the SiC matrix may undergo cracking due to irreversible volume change during phase transformation.⁴³

Molten carbonate fuel cell (MCFC)

MCFCs operate at relatively higher temperature of 600-800°C in which the molten carbonate viz. mixture of Li₂CO₃ and K₂CO₃ or of Li₂CO₃ and Na₂CO₃, is stabilized in a matrix of LiAlO₂ supported with Al₂O₃ fibres for mechanical strength. High operating temperatures of MCFC allows the possibility of internal reforming and enhance the kinetics of ORR thereby dramatically eliminating the need for higher loading of precious metal catalyst. Upon combining the fuel cell with other power generating systems, sufficiently high efficiency of ~ 50 – 70 % can be

obtained.⁴⁴ Combined metals eg. Ni-Al or Ni-Cr is preferably used as anode materials in MCFC. Ni-metal anode cannot be used as it tends to creep out under MCFC operating conditions.^{44 - 46} Similarly, NiO based cathodes are active enough for ORR at high temperature. However, long term functioning of MCFC is interrupted by coarsening tendency of NiO particles which reduces the active surface area and ultimately causes short circuiting of the cell. The plausible solution could either be to add magnesium metal to prevent coarsening or to use alternate electrolyte which decreases the dissolution of NiO cathode. Alternate cathodes have also been used by researchers viz. doped Li₂O materials like LiFeO₂, Li₂MnO₃, LiCoO₂ or NiO/LiCoO₂ double layer cathodes which enhance the rate of ORR.⁴⁷ The electrode reactions can be written as:



The major drawback of [Li/K] based electrolytes is that, it degrades the electrode material. In comparison, [Li/Na] melt provides a slightly more alkaline system in which the rate of electrode dissolution is low. Therefore, the dendritic growth of Ni metal could be prevented with cell endurance. Though, the associated efficiency of MCFC is higher, but high operating temperature limits the material selection due to degradation, sealing and thermal expansion properties. Therefore, cost reduction still remains a major factor for fabrication of cell components in MCFC.

Solid oxide fuel cell (SOFC)

SOFC is an example of ceramic fuel cell where all the components are in solid state. Several number of excellent review articles on such type of fuel cells are available in the literature.⁴⁸⁻⁵¹ SOFC employs a solid oxide electrolyte material and is more stable with no leakage problems compared to MCFCs. Additionally, being a simple two phase gas-solid system, SOFC also does not suffer from the problems of

Chapter - 1

water management, slow ORR rate etc. It is considered to be one of the most promising power generation technologies for the future due to its high efficiency, zero or extremely low pollution level and fuel flexibility. The concept of SOFC started long before in 1911 but the perception of stationary SOFC is presented in 1937 by Baur and Preis⁵² and significant development started around 1960. A detailed review in this context is presented by Mobius.⁵³ The power and voltage of SOFC is increased by connecting individual cells in series to form a 'stack', with each cell connected to its adjacent cell using an electrically conducting interconnect which also serves to distribute reactant across the surface of the electrodes using the designed flow channels. Working temperature of SOFC is dependent on the activity and application of the associated components. SOFC can be divided into three major categories viz. a) low temperature SOFC (LT-SOFC) which operates within the working temperature of 500-650°C, b) intermediate temperature SOFC (IT-SOFC) that operates within 700-800°C and c) high temperature SOFC (HT-SOFC) which operates within 800-1000°C. Energy losses during fuel cell operation at high temperature are utilized by system integration of multiple technologies. If a high temperature fuel cell is integrated with a gas turbine in a hybrid arrangement, then, overall efficiency in excess of the individual efficiencies of the fuel cell and heat engine in isolation can be achieved. The characteristic of high temperature operating SOFC constitutes one of the toughest criteria for the dimensional and chemical stability of anode material in reducing atmosphere.⁵⁴ Similar to MCFCs, internal reforming in SOFC is possible over anode catalyst and both partial and direct oxidation of fuel have been found to occur.^{55 - 60} SOFCs offer advantages of using different fuels e.g. hydrogen, CO, natural gasses etc. But, the cell functioning is highly prone to the presence of sulfur which needs to be removed either by using an activated carbon bed or zinc adsorbent.^{48, 50} Therefore, mode of application of SOFC in multiple customs is highly dependent on material choice and flexibility.

1.3. Principles of SOFC

SOFC is a class of electrochemical cell through which free energy of a chemical reaction is converted to electrical energy. Correlation between change in Gibbs free energy (ΔG) and cell voltage is given as:¹²

$$\Delta G = -nF\Delta U_0 \quad (1.14)$$

where, n is the number of electrons involved in the reaction, F is the Faraday constant and ΔU_0 is the voltage of the cell at thermodynamic equilibrium in the absence of a current flow.

The schematic of SOFC is given in Figure 1.3, where a oxygen ion conducting solid electrolyte is sandwiched amid anode and cathode electrodes exposed to fuel (hydrogen, CO etc.) and oxidant (oxygen, air etc) respectively.

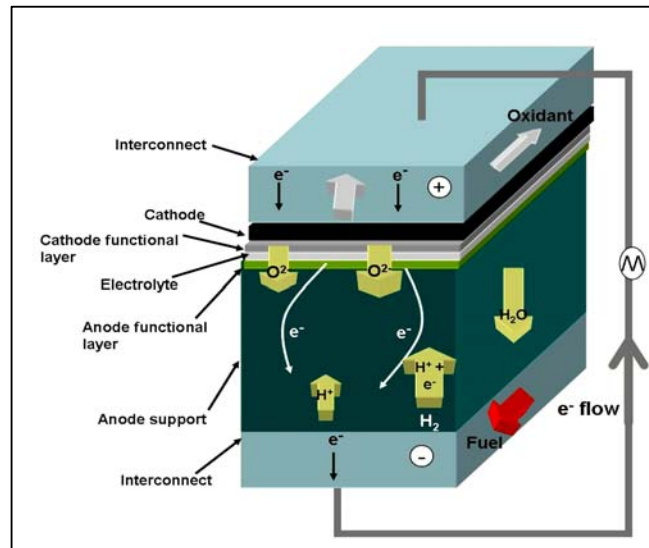


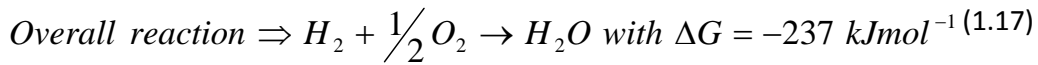
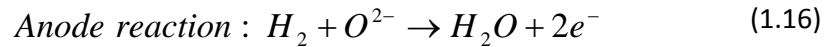
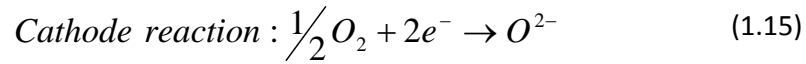
Figure 1.3: Schematic of Solid Oxide Fuel Cell⁶¹

In oxygen concentrated cells (oxygen ion conducting), the activity/concentration difference between electrodes is the prime driving force for O^{2-} movement from cathode to anode thereby yielding water at the anode. However, in proton concentrated cells, progression of H^+ ions from anode to cathode leads to the formation of water at cathode end. In order to improve the electrochemical

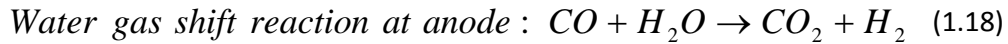
Chapter - 1

activity, incorporation of anode/cathode functional layers is a standard practice as shown in Figure 1.3.⁶¹ Such active layers tend to extend triple phase boundary (TPB), defined as the active zones where the reactant gasses coexists along with the electrode phase materials at which either fuel oxidation reaction (HOR for hydrogen fuel) or oxidant reduction reaction (ORR for oxygen oxidant) are confined.

The anode reaction in fuel cell may either be direct oxidation of hydrogen or indirect oxidation via a reforming step. The cathode reaction is based on the reduction of oxygen. The reactions can be written as:



Presence of CO along with H₂ in fuel gasses, change the reaction product as:



Equilibrium cell voltage (ΔU_0) for standard conditions for reactions 1.15 and 1.16 at 25°C is given as:

$$\Delta U_0 = \frac{-\Delta G}{nF} = 1.23 \text{ V, where, } \Delta U_0 = U_{o,C} - U_{o,A} \quad (1.19)$$

The difference between equilibrium potentials of anode ($U_{o,C}$) and cathode ($U_{o,A}$) determined through electrochemical reactions at electrodes is the theoretical magnitude of equilibrium cell voltage. Each electrochemical reaction of respective electrode is described by Nernst equation as written as Eq. 1.20 employing the above cell reactions (Eq. 1.15 and 1.16):

$$V = V_0 - \frac{RT}{nF} \ln \left(\frac{P^{\circ}_{H_2O}}{P^{\circ}_{H_2} (P^{\circ}_{O_2})^{1/2}} \right) \quad (1.20)$$

where, V, V₀, R, T, n, F and P^o are maximum theoretical current or open circuit voltage at no load condition, standard Nernst potential, the universal gas constant,

Chapter -1

reaction temperature, number of electrons associated during reaction course, Faraday's constant and partial pressures of the associated species respectively.

Even under no load condition, the open circuit voltage (OCV) can be lower than the thermodynamic Nernstian value due to mixed potential formation or other parasitic processes. Under load condition, a deviation from OCV occurs corresponding to the electrical work performed by the cell termed as 'overpotential or polarization (η)'. For a redox reaction at one electrode, the current density (I) can be written according to Butler-Volmer equation as:

$$I = I_0 \exp\left(\frac{\alpha_a \eta_a F}{RT}\right) - I_0 \exp\left(-\frac{\alpha_c \eta_c F}{RT}\right) \quad (1.21)$$

where, I_0 , α_a and α_c and T signify exchange current density, anodic and cathodic transfer coefficient and reaction temperature respectively.

The magnitude of exchange current density governs the reaction rate and is dependent on the cell configuration. Equation 1.21 is effective when charge transfer dominates at small values of current. The associated polarization is, therefore, termed as charge transfer /activation polarization (η_a) which signifies initial energy barrier required to start the electrochemical reaction. In addition to activation polarization, other limiting factors such as mass transport or diffusion, resistance / ohmic hindrance are present in real systems and are described in terms of polarization losses as shown in [Figure 1.4](#). From theoretical aspect, diffusion or concentration polarization (η_{con}) appears when electrode reaction is hindered by mass transport which is primarily diffusion controlled. The parameter that governs the diffusion rate is the limiting current density (I_{lim}). I_{lim} signifies the maximum current density that can be employed to obtain a desired electrode reaction without interference from concentration overpotentials i.e prior to the discharge of reactants.⁶² The structure and content of the gas (fuel or oxidant) diffusion electrodes is highly intricate which requires practical optimization for application purpose. The resistance or ohmic polarization (η_R) is caused by resistance to

Chapter - 1

conduction of ions (through electrolyte) and electrons (through electrodes and current collectors), and by contact resistance between cell components.⁴⁸

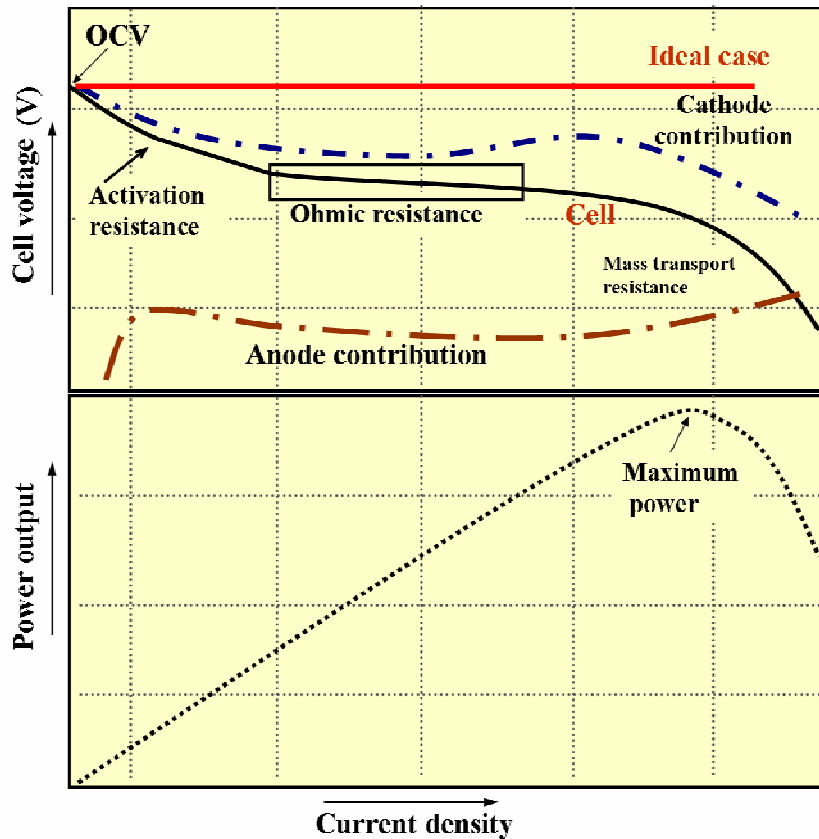


Figure 1.4: Contribution of polarization factors towards cell performance and trend of power output vs. current density^{48, 62}

The voltage loss due to ohmic polarization at intermediate current follows the relation of Ohm's law. The associated resistance also termed as 'area specific resistance (ASR)' can be obtained from the slope of 'V-I' curve of the linear portion. Depending upon the cell configuration, the ASR from the slope also correlates ohmic contribution from activation and concentration resistance. As can be viewed from Figure 1. 4, the overall cell voltage is the difference between two half cell potentials. In view of the fact that both the half cell reactions suffer from losses, the cell voltage also fails to remain constant with increasing load.

1.4. SOFC Component Materials

Solid oxide fuel cell essentially consists of two porous electrodes; cathode and anode, separated by a dense ion conducting electrolyte material. SOFC is fabricated in several designs (discussed in subsequent sections), but the basis of the material selection is based on the following criterions:

- a) Sufficient electrical conductivity values for all the components to perform their intended functions.
- b) Matching thermal expansion among the cell components.
- c) Minimal reactivity and interdiffusion among the components to avoid degradation of cell.
- d) Adequate chemical and structural stability at high temperature during both cell operation and fabrication processes.

The components for SOFC are discussed in brief below.

Cathode

The cathode or air electrode operates in an oxidizing environment of air/oxygen and functions for oxidant reduction reaction (Eq. 1.16). The air electrode in SOFCs has to meet the following requirements⁶³: (a) high electronic conductivity, (b) chemical and dimensional stability in required environments encountered during cell operation, (c) close proximity of the thermal expansion with the other cell components, (d) compatibility and minimum reactivity with the electrolyte and the interconnection with which air electrode maintains contact and (e) sufficient porosity to facilitate transport of molecular oxygen from the gas phase to the air electrode / electrolyte interface. The state-of-the-art cathode material satisfying the SOFC operating criteria is the electronically conductive ceramic oxide based perovskite, lanthanum manganite.^{49, 64} In general, substituted lanthanum manganite is used in which lanthanum is partially substituted by strontium [i.e $\text{La}_{1-x}\text{Sr}_x \text{MnO}_3$, commonly termed as LSM]. These perovskite are

Chapter - 1

electronic p-type conductors for which the electrical properties are determined by the La/Sr ratio. Formation of $\text{La}_2\text{Zr}_2\text{O}_7$ and SrO upon interaction with adjacent 8 mol % yttria stabilized zirconia (YSZ) electrolyte is inhibited by incorporating an excess of Mn (1-10 %) in the composition and keeping the sintering temperature below 1300°C .⁶⁵ The side products as mentioned above impair the cathode performance. The function of cathode in SOFC is based on the capability to reduce oxidant viz. air, oxygen etc. It is generally assumed that oxygen reduction is a multistep reaction involving adsorption and surface diffusion in a region around the triple phase boundary (TPB) as shown in Figure 1.5.

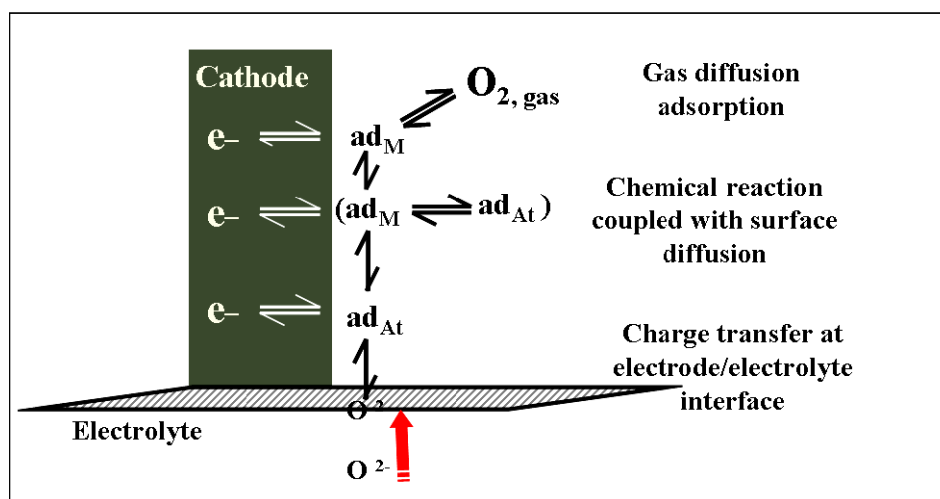


Figure 1.5: Possible reaction steps at air electrode in SOFC^{49, 64}

Mixed ionic and electronic conductor (MIEC) based perovskite cathodes such as $\text{La}_{1-x}\text{Sr}_x\text{FeO}_3$ (LSF), $\text{La}_{1-x}\text{Sr}_x\text{Fe}_{1-y}\text{Co}_y\text{O}_3$ (LSCF), $\text{Ba}_{1-x}\text{Sr}_x\text{Fe}_{1-y}\text{Co}_y\text{O}_3$ (BSCF) are also being used as SOFC cathode materials for some specific advantages over prior ones eg. the conventional LSM cathode. Significant reduction in the cost of air electrode is possible by utilizing composition that has low rare earth content.

Electrolyte

The solid electrolyte must isolate the two gas atmospheres (fuel and oxidant) from mixing and transport oxygen/hydrogen ions without considerable losses from

Chapter -1

cathode to anode. Therefore, the electrolyte for SOFC application needs to be a fast ion conductor and should simultaneously confront both reducing and oxidizing environment. In case of oxygen concentrated cells, the transport of O^{2-} ions in the electrolyte takes place via oxygen vacancies in oxygen sublattice. The concentration of vacancies and their mobility determine the ionic conductivity of the electrolyte. Among innumerable oxygen ion conductors viz. ceria, La-gallate^{66, 67}; zirconia stabilized in conductive phase with upto 10 mol% of either yttria or scandia, can be used either as tetragonal zirconia polycrystals as TZP (3YSZ: ZrO_2 doped with ~ 3 mol% Y_2O_3) or cubic stabilized zirconia viz. CSZ (8YSZ: ZrO_2 doped with ~ 8 mol% Y_2O_3)⁶⁸ are the promising candidates. Fully stabilized zirconia offers best choice of electrolyte having satisfied criterions of conductivity, chemical stability, durability etc. Although the oxide ion conductivity of TZP is relatively lower than the fully stabilized zirconia, this material is advantageous because of its outstanding mechanical stability. Significant efforts are also exerted for the study on the traditional zirconia material⁶⁹ in terms of appropriate co- dopants^{70 - 72} for improved bulk and grain boundary conductivity, aspects of mechanical stability at room and operating temperature⁷³ and fabrication technologies for thin zirconia electrolytes deposited on porous support structures.^{74, 75} Currently, theoretical and experimental work relating the studies of strain effect on oxygen migration in such zirconia based compounds is being carried out for understanding the conduction mechanism.⁷⁶ Activities for alternative electrolyte compositions are generally concentrated on doped CeO_2 or doped $LaGaO_3$ materials.^{77, 78} A comparative feature of feasible solid electrolytes used in SOFC is listed in [Table 1.2](#)⁷⁹ along with the conductivity trend as shown in [Figure 1.6](#). In the absence of suitable materials, minimizing the thickness of YSZ layer functions effectively for minimizing the polarization losses and reducing the cell operating temperature to $800^\circ C$. Apart from the usage of oxygen concentrated cells, efforts are also been made to utilize

Chapter - 1

proton conducting (H^+) ceramics derived from the family of perovskite viz. barium cerate, barium zirconates, strontium cerate ($SrCeO_2$) materials. ⁸⁰⁻⁸²

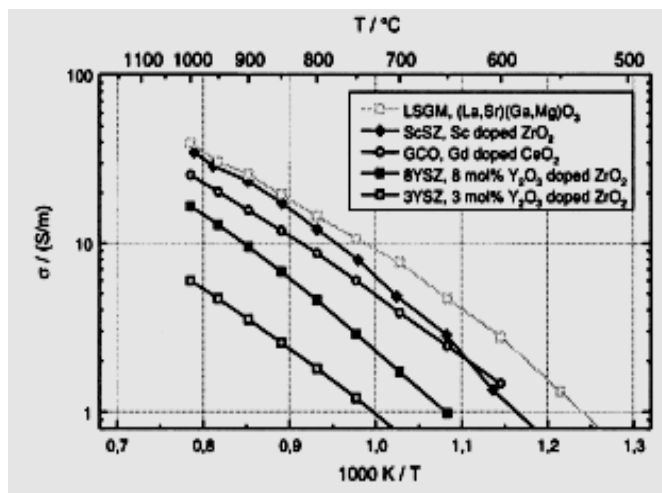


Figure 1.6: Oxide ion conductivity of different electrolyte material ^{68, 79}

Table 1.2: Advantages and disadvantages of electrolyte candidates for SOFC⁷⁹			
YSZ	CGO	LSGM	ScSZ
Advantages			
<ul style="list-style-type: none"> • Excellent stability both in oxidising and reducing environment • Mechanical stability : Moderate for 8 YSZ and excellent for 3YSZ • > 40,000 h of fuel operation possible 	<ul style="list-style-type: none"> • Good compatibility with cathode materials • Mixed electronic and ionic conductivity at low p_{O_2} (applicable for anodes) 	<ul style="list-style-type: none"> • Good compatibility with cathode materials 	<ul style="list-style-type: none"> • Excellent stability in oxidising and reducing environment • Better long term stability
Disadvantages			
<ul style="list-style-type: none"> • Low ionic conductivity (specially 3 YSZ) • Incompatible with some cathode materials 	<ul style="list-style-type: none"> • Electronic conduction at low p_{O_2} leads to lower OCV • Mechanical stability is less 	<ul style="list-style-type: none"> • Incompatible with NiO • Ga evaporation occurs at low p_{O_2} • Poor Mechanical stability 	<ul style="list-style-type: none"> • Availability of Sc is scarce with higher price

Further systematic investigation of acceptor doped oxides viz. LaAlO_3 , LaYO_3 , SrZrO_3 etc showed that these compounds could also exhibit proton conduction in hydrogen environment.^{82, 83}

Anode

SOFC anode performs the function of fuel oxidation (Eq. 1.15) thereby releasing electrons to the external circuit for utilization by cathode electrode. Therefore, the primary requirements of an anode are: a) high electronic conductivity, (b) chemical and dimensional stability in required environments encountered during cell operation, (c) close proximity of the thermal expansion with the other cell components, (d) compatibility with the adjacent electrolyte and (e) sufficient porosity to facilitate transport of molecular hydrogen from the gas phase to the fuel electrode / electrolyte interface. Under reducing atmospheres at anode, metals are stable over a wide range of operating conditions. Among various experimental metals, 'Ni' has been the choice due to high electrochemical activity for hydrogen oxidation reaction, low cost and acceptable compatibility with other cell components.^{48-51, 54, 84} However, the usual practice is to unify Ni with ceramic component, viz. YSZ (yttria stabilized zirconia), ScSZ (scandia stabilized zirconia) etc. The prime function of the ceramic phase is to prevent Ni from agglomeration, and thereby retain the porous and highly disperse microstructure of the anode. Additionally, the coefficient of thermal expansion (CTE), an indicator of thermal compatibility is adjusted by adding such ceramic phase to the anode. YSZ/ScSZ also provides oxygen ionic conduction to the anode. However, the ratio of Ni: YSZ needs to be optimized based on the requirement of conductivity and minimization of ambipolar resistance. Although Ni-YSZ has advantages as mentioned above, the high susceptibility of Ni to coking, re-oxidation in case of fuel loss and sensitivity to poisoning of the electrode by sulfur are the main concerns regarding the durability and degradation of Ni-YSZ anodes.⁴⁸ Experiments have shown that performance of

Chapter - 1

SOFC starts degrading upon increasing the sulfur content beyond ~ 5 ppm.⁸⁵ The mechanism and other factors effecting the act of sulfur containing fuels towards cell deterioration is being studied by many eminent researchers.^{86, 87} As alternate anodes, focus is on the development of fluorites, pyrochlore, perovskite, tungsten bronze –based materials.⁸⁸ With regard to the competitive performance of Ni-YSZ, only ceria based, $\text{Ce}_{0.6}\text{Gd}_{0.4}\text{O}_{1.8}$,⁸⁹ Ni-CGO and $\text{La}_{0.8}\text{Sr}_{0.2}\text{Cr}_{0.5}\text{Mn}_{0.5}\text{O}_{0.3}$ (LSCM)^{88, 89} have been developed. With respect to compatibility with YSZ electrolyte, yttria-titania modified zirconia (Y2T) is also found to be a promising mixed conducting fluoride based anode material.⁹⁰ From the aforementioned research works it can be mentioned that, SOFC has the potential of using variable fuels viz. H_2 , CO, CH_4 etc based on the possible cell component materials. An overview of the different reacting species during fuel oxidation is given in Table 1.3.⁹¹

Table 1.3: Reactive species in SOFC anodes⁹¹

Red	Ox	No. of electrons transferred in electrochemical reaction
H_2	H_2O	2
CO	CO_2	2
CH_4	$\text{CO}_2 + 2 \text{H}_2\text{O}$	8
CH_4	$\text{CO} + 2 \text{H}_2\text{O}$	6

Electrochemical reactions occurring either at anode or cathode are specified in the region of 'Triple phase boundary (TPB)'.^{92 - 100} TPB site is defined as the active sites/ centers at which pore, gas and electrode solid phase co-exist. For effective electrochemical reactions, continuity of such TPB sites is essential in order to ensure the thorough network of gas transport, electronic path and ionic migration. Existence and extension of TPB is dependent on the optimization of microstructure / phase distribution which in turn is a function of processing techniques.

Other components

Selection and fabrication of interconnect material is another important concern for fuel cell development. It connects the anode of one single cell with cathode of the other in a stack arrangement. The interconnect should fulfill the prime requirements of being electrically conductive and act as a separating component for restricting fuel /oxidant gasses to intermix at either electrodes. Additionally they should be dense, chemically and dimensionally stable in a dual oxidizing and reducing atmospheres. Material selection is highly dependant on the SOFC design and range of operating temperature. Owing to the evaporation tendency of Ni-based alloys, silver alloys are practised to work as interconnect material below 900°C. Highly conductive metal oxides are also used for the purpose.¹⁰¹ Bipolar plates based on ceramic materials viz. LaCrO_3 offer better thermal compatibility with other cell components. However, sufficient conductivity is observed upon formation of Cr_2O_3 layer on the surface of LaCrO_3 -based interconnect.^{102, 103} A new metallic-ceramic alloy is developed by *Plansee (Austria)* which shows high corrosion resistance, good thermal conductivity, high mechanical strength and low expansion coefficient. The alloy is based on a CrFe stainless steel metallic component mixed with an yttrium oxide ceramic.⁴² In addition, Fe-Cr ferritic steel alloys are also used as effective materials applicable for IT-SOFC.¹⁰⁴

Commercialization of SOFC is limited by the development of suitable sealant material capable of working at high operating temperatures. Sealants are required for preventing the intermixing of fuel and oxidant gasses in the electrode compartments.^{50,54 105, 106} Promising candidates for sealing purpose could be 'glass (SiO_2)' or 'ceramic-foams'. Normal glasses are proved to be ineffective sealants, as they often evaporate and soften with a likelihood of leakages. Pyrex seals are used and are proved to have sufficient stability at high temperatures and pressures so that leakages can be avoided.¹⁰⁷ However, upon prolonged operation, formation

Chapter - 1

of certain secondary phases are identified which may arise due to ionic diffusion or interaction of sealing glass with other cell components.^{50, 54} Ceramic foams consisting of Co-doped LSM materials have been found to have high electronic conductivity and a reasonable compressive strength, but these does not exhibit creep behaviour.¹⁰⁸ SOFC seals can be broadly classified into two major categories eg. composition specific sealants that includes compressive and rigid seals and bond specific seals (ceramic–ceramic, ceramic-metal and metal-metal). Additionally, rigid seals consist of: a) glass ceramic, b) self-healing type, c) composite and d) brazing seals.¹⁰⁹⁻¹¹³ The application of sealant type is entirely dependant on the nature of its application.

1.5. Broad Categories of SOFC Design

The design of SOFC stack is governed by restrictions offered by the selected cell components. A stack is fabricated by adjoining single cells with an intention to achieve the desired electrical and electrochemical performance, mechanical integrity, manifolding requirements etc. Broadly, four different stack configurations are designed and fabricated as:

- a) Tubular
- b) Segmented cell-in series
- c) Monolithic: Presently is an obsolete design
- d) Planar

An initial comparison based on certain primary characteristics is given in Table 1.4⁴⁸.

Features	Designs			
	Tubular	Segmented cell-in series	Monolithic	Planar
Structural support	Yes	Yes	No	No
Internal electrical resistance	High	High	Low	Medium
Gas sealing	No	Yes	No	Yes
Power density	Low	Low	High	Medium

Tubular design

Tubular SOFC is pioneered by the U.S. Westinghouse Electric Corporation (presently known as 'Siemens Westinghouse Power Corporation or SWPC') in 1970s. The design is initialized by using Ca-stabilized zirconia tube (1-2 mm thick) onto which the cylindrical anodes were deposited. Through masking, the subsequent layers viz. electrolyte, interconnect and finally the fuel electrode is deposited onto anode. During 1970's, initial attempt is made to deposit air electrode onto the central zirconia tube, where the fuel electrode is placed outside. The schematic of tubular design is shown in [Figure 1.7](#) with the descriptions of gas flow. The primary disadvantage associated with such design is the low power density which is due to the long path for electrical power for each cell and large voids within the stack structure.

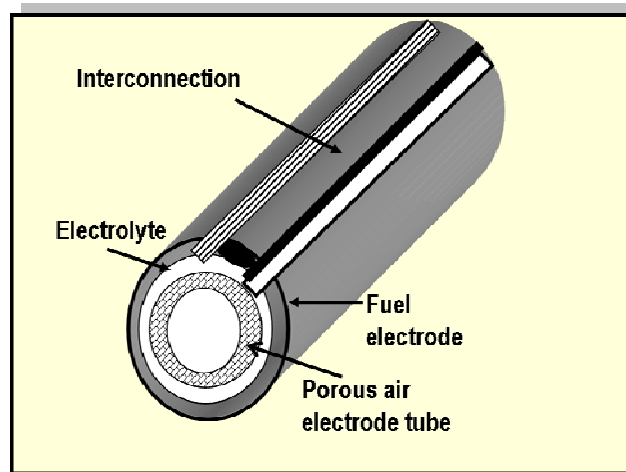


Figure 1.7: Schematic of sealless tubular cell design ⁴⁸

Recently, zirconia tubes have been eliminated and tubes of air electrode (cathode) are fabricated through extrusion. The electrolyte and cell interconnects are then deposited by means of electrochemical vapor deposition (EVD), plasma spraying etc onto the initially formed cathode which provides mechanical support to the thin cell components. The anode is sequentially formed on the electrolyte by slurry deposition technique. The advantage of this design over other designs is that

Chapter - 1

relatively large single tubular cells can be constructed onto which successive active layers can be deposited without chemical or material interference with previously deposited layers. The tubular SOFC with one end closed design almost eliminates the usage of sealants for prevention of gas mixing. The manifolding of reactant gasses for such design is also illustrated in [Figure 1.8](#). The oxidant gas is introduced via central Al_2O_3 injector tube, and fuel gas is supplied to the exterior of the closed end tube. In this arrangement, the Al_2O_3 tube extends to the proximity of the closed end of the tube, and the oxidant flows back past the cathode surface to the open end. The fuel gas flows past the anode on the exterior of the cell and in a parallel direction (co-flow) to the oxidant gas. The spent gases are exhausted into a common plenum where the remaining active gases react and the generated heat serves to preheat the incoming oxidant stream and/or drive an expander.

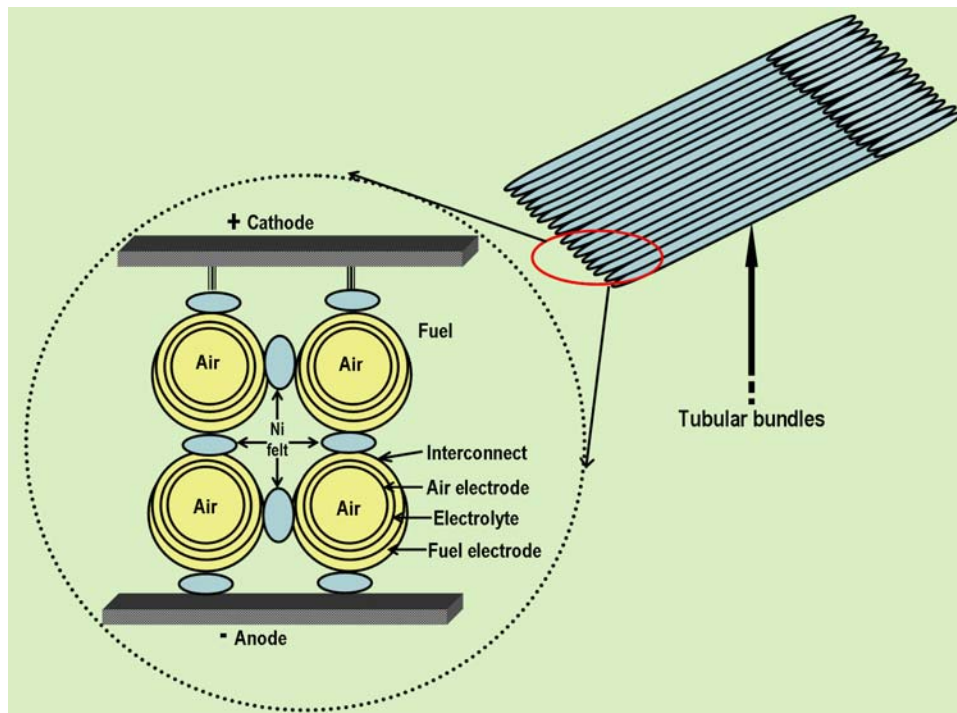


Figure 1.8: Inter-cell connections in tubular SOFC ¹¹⁴

One attractive feature of this arrangement is that it eliminates the need for leak-free gas manifolding of the fuel and oxidant streams. The electrical connections are made in the reducing anode environment in such sealless tubular design. This

arrangement allows the usage of low-cost metals for cell-to-cell contacts and current collectors. The series and parallel connection is designed to protect the tubular bundles or stack against complete failure if any individual cell fails.¹¹⁴⁻¹¹⁵

Segmented cell in series

SOFC with segmented design has been proposed in 1960's of which kilowatt size have been constructed and operated successfully. The segmented cells are arranged as a thin banded structure on porous support termed as 'banded configuration'. Another configuration of such design known as 'bell and spigot' version consists of tubular self supporting cylindrical structure (1 -1.5 cm in diameter), of the cell (0.3 to 0.4 mm thick) components.⁶⁶ Both the designs are shown in Figure 1.9. In the spigot-type structure, fuel flows from one cell to another through the tubular stacks of cells; whereas, the oxidant flows outside. The interconnect in such case, provides the compartment sealing and electrical contact between anode of one cell with the cathode of another. In the banded configuration, the support tube of 1.5-2.5 cm diameter is employed along with the cell component thickness of ~ 100-250 μm .

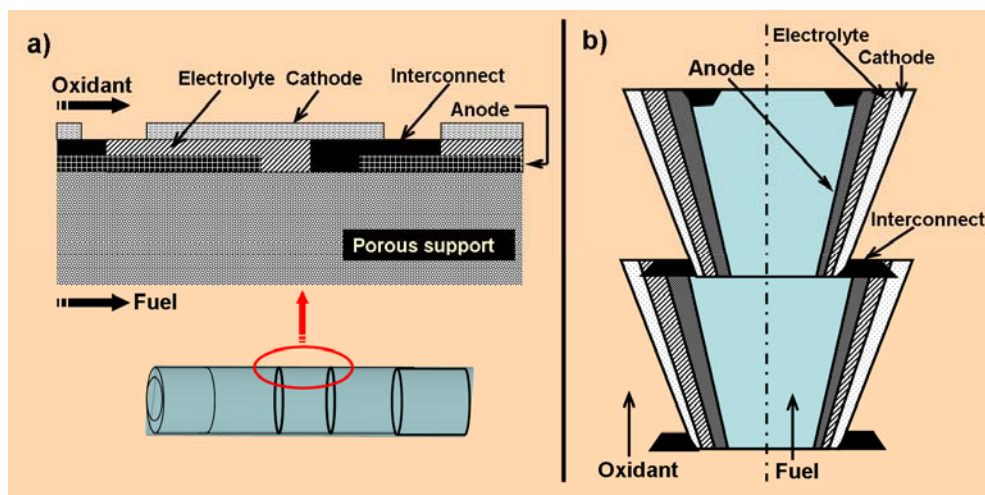


Figure 1.9: Segmented cell in series design for a) banded and b) bell and spigot configuration⁶⁶

Chapter - 1

In an operating stack, the direction of current is through the cathode of the first cell, transverses the electrolyte and travels along the anode. Alike other cell designs, the interconnect act as the medium to transfer current from one cell to another. Owing to the fact that, in such design, current travels through the plane of the electrodes, the path length of current depends on the size of the cell. Therefore, each segmented cell is made as short as possible in order to reduce the internal resistance.¹¹⁶⁻¹¹⁷ According to the experimental findings of prior arts, each tube of banded configuration (12 cells) produces ~ 35 W, whereas, that of spigot-configuration (10 cells) yields ~ 20 W.¹¹⁸

The segmented type design offers advantage of improved stack efficiency and superior structural integrity of cells. A newer design termed as 'Flatten tubular segmented-in-series (FTSS)' is being employed by Horiuchi et al. for IT-SOFC application.¹¹⁹ High temperature gas tight seals are required for the segmented cell in series design to prevent mixing of fuel and oxidant on both side of the stack, on the feed tube, and between each cell in the stack. In addition, compared to sealless tubular design, higher numbers of cells are required to yield the same power.

Monolithic design

The monolithic design consists of many cells fabricated as a single unit and exhibit potential to achieve high power density due to its compact and lightweight structure. The design posses thin cell components formed into a grooved structure of either gas 'co flow' or 'cross flow' configuration as shown in [Figure 1.10](#).^{66, 120} The structure is made up of two types of multilayer ceramics, each composed of three components: anode/electrolyte/cathode and anode/interconnect/cathode each with ~ 200 – 300 μm thickness. In the co-flow design, the FC consists of alternating layers of corrugated anode/electrolyte/cathode laminate and flat

anode/interconnect/cathode laminate. Both fuel and oxidant gases flow parallel in adjacent channels formed by the laminated layers.

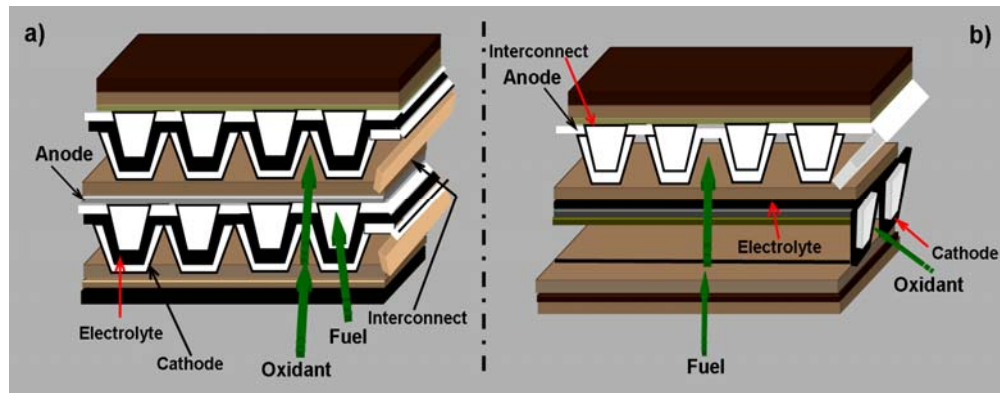


Figure 1.10: Monolithic SOFC design with a) co flow and b) cross flow configurations⁶⁶

However, in cross flow version of such design, the FC composed of alternating flat layers of both anode/electrolyte/cathode and anode/interconnect/cathode laminate, separated by corrugated anode and cathode layers oriented perpendicularly to each other. Such design offers a reduced power density with simpler means of gas diffusion when compared to the co-flow design. In co-flow design, the current path flows through the interconnect, and then travels around the circumference of the cell in the plane of the cathode. This is followed by the path through electrolyte and finally flow part way around the circumference of the cell in the plane of the anode. Monolithic design comprises of low voltage losses due to small distance between interconnect layers and thin electrolyte. The volumetric power density of the co-flow monolithic SOFC is calculated to be $\sim 4\text{kWL}^{-1}$ (FC only).¹²¹ However, the associated tribulations encountered during the cell fabrication, confines the application of such monolithic design.

Planar Cell design

The flat-planar design shown in Figure 1.11 consists of cell configuration configured as thin, planar plates and offer highest power density ($> 1 \text{ Wcm}^{-2}$)

Chapter - 1

because of shorter current path from cell to interconnect which results in less ohmic losses.

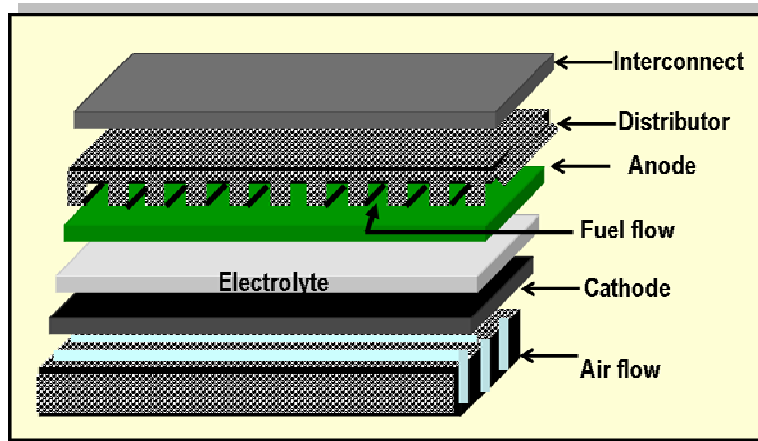


Figure 1.11: Schematic of flat planar SOFC design⁴²

A number of cell configurations exist in the planar cell design, each classified according to the layer that mechanically supports the cell as shown in Figure 1.12.^{48, 50, 54} These include individual support by each of the cell components as well as distinct structural components such as porous substrates or porous metal supports.¹²²

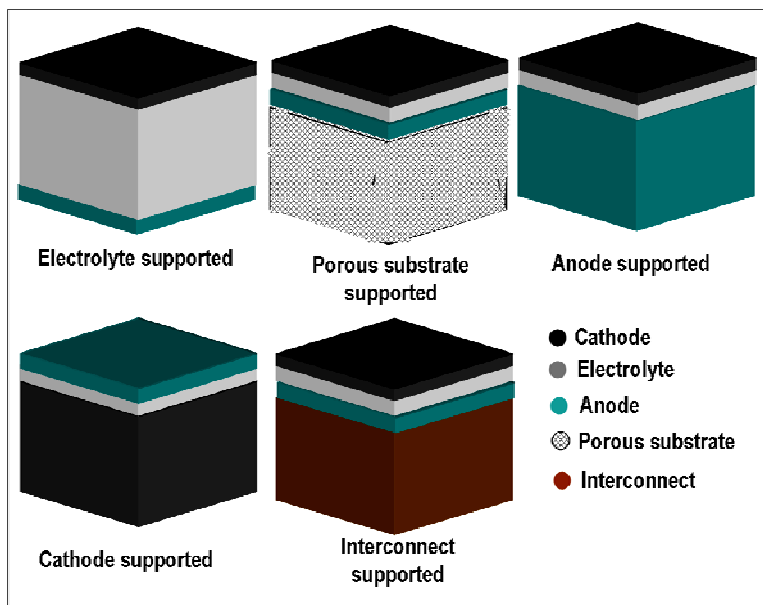


Figure 1.12: Different cell support architectures for SOFC planar configuration

Chapter -1

In order to obtain mechanically stable structure in electrolyte support cell, significantly higher electrolyte thickness ($\sim 200 \mu\text{m}$) is required. However, such high electrolyte thickness results in higher polarization losses and the operating temperature of SOFC is to be raised to $\sim 1000 \text{ }^\circ\text{C}$ for effective ionic conduction through dense electrolyte for practical application.

The commercialization of electrolyte-supported SOFC is therefore hindered because such high temperature operation demands costlier interconnect materials. These problems can be overcome if a thin electrolyte layer can be fabricated over a thick and porous electrode-support which is the basis of anode-supported design. In this design while the porous anode provides the mechanical support, the thin electrolyte helps in lowering the ohmic losses across it. As the resistance of the electrolyte is proportional to its specific resistance and thickness, the total resistance of the electrolyte layer can be lowered down by reducing its thickness to such a level so that it compensates the increase in specific resistance caused due to a lowering in operating temperature. Thus, for an anode-supported SOFC, the operating temperature can be lowered down to about 800°C or even less (depending on the thickness of the electrolyte film) without compromising with the power output. This allows the device to be made of less expensive materials. The interconnect serves as the bipolar gas separator, connecting the anode and cathode of adjoining cells. In an operating stack, the current flowing from the interconnect to the cathode at the contact point, gets distributed over the plane of cathode and over certain electrolyte area and finally travel across the plane of the electrolyte to the anode. The current then flows in the plane of the anode to the nearest interconnect contact point and finally across the plane of the interconnect to the next cell, and such process continues.

Planar SOFC design offers improved performance and high power density relative to the sealless tubular and segmented cell-in series configuration. The cross-plane conduction of planar design allows the internal resistance losses to be

Chapter - 1

independent of cell area. Therefore, the cell components can be made very thin to minimize the resistive losses. SOFC cells could have variable geometric shape viz. square, rectangular, circular, hexagonal etc in such design with simpler fabrication techniques.⁴⁸ Due to the provision of independent assembling of cell components, incorporation of different interconnect materials is feasible.¹²³ However, requirement of high temperature sealants is one of the limitations of such planar design. Compressive, glass or glass ceramic seals are often used by researchers. In addition, stacking large with too thin sintered ceramic layers is expected to be difficult which limits on the practical size for the flat plane design. Flat plane cells of large area viz. 125 cm² (active area) have shown a cell voltage of 0.7 V at 300 mAcm⁻² with humidified hydrogen as fuel and air as oxidant.¹²⁴ A 23- cm² cell (400 cm² active area) have shown a maximum power of 97 W.¹²⁴ Long term studies of such stacks [2000 h or more] exhibit a low degradation rate of only 0.3-0.5 %/1000 h.¹²⁴ Heat removal in such planar designs can be achieved by direct heat dissipation to air pre-heater coils, small sized cells enables this heat exchanger easier. Recent developments of Versa Power Systems are successful in achieving commendable performance (peak power of > 25 kW for 2000 h operation) of 20 kW-class stack with 120 number of larger cells (25 × 25 cm², active area ~ 550 cm²) over a wide temperature range.¹²⁵ The SOFC development at Topsoe Fuel Cell A/S (TOFC) and Risø DTU is also found to be significant. The said unit is focussed on the development of robust stacks with metallic interconnects, multi stack modules and Power core units for efficient integration of the manufactured integrated system with fuel processing units.¹²⁶

1.6. Advantages and Drawbacks of SOFC

The advantages and drawbacks of SOFCs are determined by their type and application. The imperative advantages and limitations are presented as follows: ^{48,}

50, 54

Advantages

- a) **High energy conversion efficiency:** Owing to the minimum intermediate switching steps viz. from chemical energy to thermal to electrical energy etc. and absence of Carnot limitation, the associated efficiency of SOFC is significantly higher. The competence can be further enhanced by complete utilization of by product heat.
- b) **Environmental compatibility:** In general, SOFC is capable of using practical renewable fuels (H₂, CO, CH₄ etc) releasing minor environmental pollutants (eg. NO_x, SO_x etc.).
- c) **Modularity:** Variable sizes of SOFC can be fabricated based upon the application purpose and the associated efficiency is relatively independent of size.
- d) **Sitting flexibility:** Due to relatively quiet operation, the fabricated stacks can be easily located near the spot of application, viz. residential complexes, hospitals etc.
- e) **Multifuel compatibility:** SOFC has the capability of utilizing a range of fuels viz. H₂, CO, CH₄ etc. In case of some HT-SOFC's, internal reforming of hydrocarbon fuels are feasible, hence the need for expensive subsystem implementation can be avoided.

Disadvantages

- a) **Material selection problem:** High temperature operation of SOFC restricts the usage of materials to be used for various cell components.

Chapter - 1

- b) **Economics:** Introduction of such fuel cells to the energy market is expected to involve a high capital cost to performance ratio.

1.7. Objective and Motivation of Present Research Work

SOFC with flat-planar design is mostly practiced throughout the globe owing to its ease of fabrication and potential for providing high power densities compared to other cell configurations. As discussed in aforementioned sections, anode-supported design has attracted researchers' attention due to higher performance, easy start up and lower polarization losses. For an anode-supported SOFC, it is possible to reduce the operating temperature to about 800°C or even less (depending upon the thickness of the electrolyte film) without compromising with the power output. This allows the device to be made of less expensive materials. The processing for anode preparation with optimized properties, phase distribution along with its related fabrication process plays important role for the operation of IT-SOFC.

Till date among several compositions, nickel – 8 mol % yttria stabilized zirconia (Ni-YSZ) is the most widely accepted anode material due to several advantages. However, such composition requires ≥ 40 vol % Ni in the cermet to fulfill the requirements of SOFC anode. Though, considerable performance is obtained using such composition, but it turn out to be ineffective during long term performance which limits the commercialization of anode-supported SOFC as energy conversion device. Usage of such a high amount of Ni in the anode is susceptible to long term degradation which can be ascribed due to the agglomeration of Ni particles at high operating temperature (800 -1000°C). In addition, such conventional anode cermet suffers from thermal incompatibility problem with other cell components due to the presence of higher Ni content (~ 40 vol % Ni). It has been observed that, agglomeration or clustering of Ni is an

outcome of dispersed distribution of Ni and YSZ phases generated through the processing techniques. Owing to the generation of such dispersed microstructure, the cermet becomes intolerable to repeated re-oxidations and therefore, its mechanical integrity and electrical continuity gets disrupted.

The main objective of the present work is based on the development of nickel (Ni) - 8 mol % yttria stabilized zirconia (YSZ) cermet by novel 'electroless technique' and its application as an anode material in the fabrication of SOFC. The process parameters involved during synthesis of such Ni-YSZ anode is optimized. Electroless technique involves an initial sensitization of YSZ which governs the final electroless deposition of metallic Ni in the as-synthesized condition. The sensitization involves surface adsorption of Pd⁰ active species onto YSZ surface which is also aimed to model kinetically. The optimized electroless process is expected to generate Ni-YSZ cermet with core (YSZ)-shell (discrete Ni nanoparticles) microstructure with uniform patterned distribution throughout the cermet. Such unique microstructure will also enable patterned interconnection of Ni, YSZ and pore phases in the matrix in contrast to conventional anodes which lacks such networking due to dispersed phase distribution. Owing to such features, electroless anode is expected to exhibit the required level of the total electrical conductivity at much lower volume percentage of Ni compared to other conventional routes. Thus, the major problem of thermal incompatibility among the cell components and coarsening of Ni during long term operation is expected to get minimized in case of electroless anode. Due to such unique core-shell microstructure, anode prepared through electroless technique is expected to extend the TPB length and enhance the performance of the SOFC single cell. Effort has also been made to determine and compare the TPB length of such developed anode cermet with that of the conventional one through mathematical modelling approach. In order to establish the functionality of electroless cermet, a number of anode configurations have been fabricated and their electrochemical performances

Chapter - 1

have been examined systematically. The various factors affecting electrochemical activity of single cell such as: a) thickness and sintering temperature of the half cell, b) rate of NiO reduction to metallic Ni, and c) type of oxidant used at the cathode side are studied thoroughly during the course of this research work. Developed anodes of all configurations are subjected to repeated redox cycling to study their endurance and are also correlated with post operated microstructural studies. The load bearing competence of the fabricated SOFCs with the developed anodes are also examined for a considerable period of time to determine the corresponding degradation rates. The Ni-YSZ cermet prepared through electroless technique is therefore expected to prevail as an 'alternate anode' for IT-SOFC application.

1.8. References

1. U. Bossel, The birth of the Fuel Cell; European Fuel Cell Forum: Oberrohrdorf, (2000).
2. F. D. Melle, *Journal of Power Sources*. **71**, 7 – 11 (1998).
3. B. M. Barnett and W. P. Teagan, *Journal of Power Sources*. **37**, 15-31 (1992).
4. D. Hart, *Journal of Power Sources*. **86**, 23 -27 (2000).
5. G. D. Callow, *Journal of Power Sources*. **80**, 17 -21 (1999).
6. A. Bauen and D. Hart, *Journal of Power Sources*. **86**, 482-494 (2000).
7. A. U. Dufour, *Journal of Power Sources*. **71**, 19-25 (1998).
8. L. J. M. J. Blomen and M. N. Mugerwa, Fuel Cell Systems; Plenum Press: New York, (1993).
9. J. Appleby and F. R. Foulkes, Fuel Cell Handbook, (1993).
10. L. Carrette, K. A. Friedrich and U. Stimming, *Chem-Phys Chem*. **1**, 162- 193 (2000).
11. S. G. Chalk, J. F. Miller and F. W. Wagner, *Journal of Power Sources*. **86**, 40 – 51 (2000).
12. L. Carrette, J. Collins, A. Dickinson and U. Stimming, *Bunsenmagazin der Deutschen Bunsengesellschaft für Physikalische Chemie*.pp. 27 (2000).
13. J. Larminie and A. Dicks, Editors, Fuel Cell Systems Explained, 2nd Edition, John Wiley, New York, (2003).
14. K. Kordesch, V. Hacker, J. Gsellmann, M. Cifrain, G. Faleschini, P. Enzinger, R. Fankhauser, M. Ortner, M. Muhr and R. R. Aronson, *Journal of Power Sources*. **86**, 162-165 (2000).
15. K. Kordesch, J. Gsellmann, M. Cifrain, S. Voss, V. Hacker, R. R. Aronson, C. Fabjan, T. Hezje and J. Daniel-Ivad, *Journal of Power Sources*. **80**, 190 - 197 (1999).

Chapter - 1

16. E. De Geeter, M. Mangan, S. Spaepen, W. Stinissen and G. Vennekens, *Journal of Power Sources*. **80**, 207 - 212 (1999).
17. P. V. Wright, *Electrochimica Acta*. **43**, 1137 - 1143 (1998).
18. M. Wilson, F. Garzon, K. Sickafus and S. Gottesfeld, *Journal of the Electrochemical Society*. **140**, 2872 -2877 (1993).
19. S. Gottesfeld and J. Pafford, *Journal of the Electrochemical Society*. **135**, 2651-2652 (1988).
20. K. Kolbrecka and J. Przyluski, *Electrochimica Acta*. **39**, 1591-1595 (1994).
21. H. F. Oetjen, V. M. Schmidt, U. Stimming and F. Trila, *Journal of the Electrochemical Society*. **143**, 3838- 3842 (1996).
22. K. Kordesch and G. Simader, *Fuel Cells and Their Applications*; 1 ed.; VCH Verlagsgesellschaft mbH: Weinheim, Germany, (1996).
23. M. Cappadonia, J. W. Erning, S. M. Saberi Niaki and U. Stimming, *Solid State Ionics*. **77**, 65-69 (1995).
24. M. S. Wilson, C. Zawodzinski and S. Gottesfeld, *Second International Symposium on Proton Conducting Membrane Fuel Cells II*, 424 (1998).
25. M. Watanabe, H. Uchida, Y. Seki and M. Emori, *Journal of the Electrochemical Society*. **143**, 3847 – 3852 (1996).
26. S. A. C. Barton, B. L. Murach, T. F. Fuller and A. C. West, *Journal of the Electrochemical Society*. **145**, 3783- 3788 (1998).
27. S. R. Narayanan, T. I. Valdez and W. Chun, *Electrochemical and Solid State Letters*. **3**, 117- 120 (2000).
28. K. L. Ley, R. Liu, C. Pu, Q. Fan, N. Leyarowska, C. Segre and E. S. Smotkin, *Journal of the Electrochemical Society*. **144**, 1543- 1548 (1997).
29. L. Liu, R. Viswanathan, R. Liu and E. S. Smotkin, *Electrochemical and Solid State Letters*. **1**, 123-125 (1998).
30. E. Reddington, A. Sapienza, B. Gurau, R. Viswanathan, S. Sarangapani, E. S. Smotkin and T. E. Mallouk, *Science*. **280**, 1735- 1737 (1998).

Chapter -1

31. N. A. Hampson, M. J. Willars and B. D. McNicol, *Journal of Power Sources*. **4**, 191- 201 (1979).
32. A. Hamnett and B. J. Kennedy, *Electrochimica Acta*. **33**, 1613-1618 (1988).
33. A. S. Arico, Z. Poltarzewski, H. Kim, A. Morana, N. Giordano and V. Antonucci, *Journal of Power Sources*, **55**, 159- 166 (1995).
34. B. D. McNicol, R. T. Short and A. G. Chapman, *Journal of Chemical Society Faraday Transaction 1*. **72**, 2735- 2743 (1976).
35. M. Götz and H. Wendt, *Electrochimica Acta*. **43**, 3637-3644 (1998).
36. N. Alonso-Vante, H. Tributsch and O. Solorza-Feria, *Electrochimica Acta*, **40**, 567- 576 (1995).
37. O. Solorza-Feria, K. Ellmer, M. Giersig and N. Alonso- Vante, *Electrochimica Acta*. **39**, 1647- 1653 (1994).
38. S. Dong and Q. Qiu, *Journal of Electroanalytical Chemistry and Interfacial Electrochemistry*. **314**, 223- 239 (1991).
39. S. Gupta, D. Tryk, S. K. Zecevic, W. Aldred, D. Guo and R. F. Savinell, *Journal of Applied Electrochemistry*. **28**, 673- 682 (1998).
40. O. Savadogo and P. Beck, *Journal of the Electrochemical Society*. **143**, 3842- 3846 (1996).
41. M. Watanabe, K. Tsurumi, T. Mizukami, T. Nakamura and P. Stonehart. *Journal of the Electrochemical Society*, **141**, 2659-2668 (1994).
42. L. Carrette, K. A. Friedrich and U. Stimming, *Fuel Cells*. **1**, 5-39 (2001).
43. W. Vielstich, A. Lamn and H.A. Gasteiger, Editors, *Handbook of Fuel Cells: Fundamentals, Technology and Applications*, Volume I, John Wiley, New York, (2003).
44. K. I. Ota, 1st Meeting of the Electrochemical Society, Fourth International Symposium on Carbonate Fuel Cell Technology, Montreal, Canada, 238 (1997).

Chapter - 1

45. B. S. Baker and H. C. Maru, 1st Meeting of the Electrochemical Society, Fourth International Symposium on Carbonate Fuel Cell Technology, Montreal, Canada, 14 (1997).
46. M. Kah, H. J. Slage and H. Wendt, 1st Meeting of the Electrochemical Society, Fourth International Symposium on Carbonate Fuel Cell Technology, Montreal, Canada, 224 (1997).
47. C. Yuh, R. Johnsen, M. Farooque and H. Maru, *Journal of Power Sources*. **56**, 1-10 (1995).
48. N.Q. Minh, T. Takahashi, *Science and Technology of Ceramic Fuel Cells*, Elsevier, New York, USA, (1995).
49. Peter Holtappels, U. Vogt and T. Graule, *Advanced Engineering Materials*. **7**, 292-302 (2005).
50. S.C Singhal, and K. Kendall, *High Temperature Solid Oxide Fuel Cells: Fundamentals, Design and Applications*. Elsevier, U. K. Editor. (2003).
51. Daniel J. L. Brett, Alan Atkinson, Nigel P. Brandon and Stephen J. Skinnerd, *Chemical Society Review*. **37**, 1568–1578 (2008).
52. A. Baur, B. Preis, *Ztschr. Electrochem*. **43**, 727- 732 (1937).
53. H.H.Mobius, *Journal of Solid State Electrochemistry*. **1**, 2- 16 (1997).
54. R.N. Basu, *Materials for Solid Oxide Fuel Cells in Recent Trends in Fuel Cell Science and Technology*. Edited by S. Basu, Jointly published by Anamaya Publishers, New Delhi (India) and Springer, p. 284, New York -USA, (2006).
55. M. Boder, R. Dittmeyer, *Journal of Power Sources*. **155**, 13–22 (2006).
56. X. Ren, M. S. Wilson and S. Gottesfeld, *Journal of the Electrochemical Society*. **143**, L12- L15 (1996).
57. S. Hamakawa, R. Shiozaki, T. Hayakawa, K. Suzuki, K. Murata, K. Takehira, M. Koizumi, J. Nakamura and T. Uchijima. *Journal of the Electrochemical Society*, **147**, 839 - 844 (2000).
58. M. Ihara, C. Yokoyama, A. Abudula, R. Kato, H. Komiyama and K. Yamada,

- Journal of the Electrochemical Society.* **146**, 2481- 2487 (1999).
59. S. Park, J. M. Vohs and R. J. Gorte, *Nature.* **404**, 265- 267 (2000).
60. S. Park, R. Craciun, J. M. Vohs and R. J. Gorte, *Journal of the Electrochemical Society.* **146**, 3603-3605 (1999).
61. Lee John H, Lee H W, et al. High Performance Anode-supported Solid Oxide Fuel Cell, US patent No. 2007/0015045 A1.
62. A. McDougall, *Fuel Cells*, MacMillan Press, London (1976).
63. S.C. Singhal, *Solid State Ionics.* **135**, 305–313 (2000).
64. Hwa Seob Song, Seungho Lee, Sang Hoon Hyun, Joosun Kim, Jooho Moon, *Journal of Power Sources.* **187**, 25-31 (2009).
65. G. Stochniol, E. Syskakis, A. Naoumidis, *Journal of American Ceramic Society.* **78**, 929- 932 (1995).
66. N. Q. Minh, *Journal of American Ceramic Society.* **76**, 563-588 (1993).
67. A. I. Ishihara, M. Honda, T. Shibayama, H. Minami, H. Nishiguchi, Y. Takita, *Journal of Electrochemical Society.* **145**, 3177- 3183 (1998).
68. R. Manner, E. Ivers-Tiffée and W. Proceedings 2nd International Symposium on SOFC. ed. P. Zegers. CEC Publ. EUR13546 EN, pp. 715–725, (1991).
69. J.P.P. Huijsmans, *Current Opinion in Solid State and Materials Science.* **5**, 317–323 (2001).
70. Y Ji, J Liu, Z Lu, X Zhao, T He, W Su, *Solid State Ionics.* **126**, 277–83 (1999).
71. M Hirano, S Watanabe, E Kato, Y Mizutani, M Kawai, Y Nakamura, *Journal of American Ceramic Society.* **82**, 2861–925 (1999).
72. R. M. Batista and E. N. S. Muccillo, *ECS Transactions, The Electrochemical Society.* **35**, 1161-1169 (2011).
73. A. Selcuk, A. Atkinson, *Am Ceram Soc.* **83**, 2029–2035 (2000).
74. J. Will, A. Mitterdorfer, C. Kleinlogel, D. Peredis, L. J. Gauckler, *Solid State Ionics.* **131**, 79–96 (2000).

Chapter - 1

75. Y. Arachi, O. Yamamoto, Y. Takeda, N. Imanishi, K. Kawate, In: SC Singhal, M Dokiya, editors. Solid oxide fuel cells VI. Proc Electrochem Soc; PV99-19:179–184 (1999).
76. W. Araki, M. Kuribara, and Y. Arai, *ECS Transactions, The Electrochemical Society*. **35**, 1117-1124 (2011).
77. BCH Steele, *Solid State Ionics*. **129**, 95–110 (2000).
78. JB Goodenough, *Nature*. **404**, 821–824 (2000).
79. Ellen Ivers-Tiffé, Andre´ Weber, Dirk Herbstritt, *Journal of the European Ceramic Society*. **21**, 1805–1811 (2001).
80. P. Ranran, W. Yan, Y. Lizhai and M. Zongqiang, *Solid State Ionics*. **177**, 389-393 (2006).
81. Simona Barison, Liudmila Doubova, Monica Fabrizio, Cecilia Mortalò, Stefano Boldrini, Lucern, Abstract [Electrolysis and proton conductors], Proceedings of 8th European SOFC Forum, (2008).
82. K.D. Kreuer, *Annual Review of Material Research*. **33**, 333-359 (2003).
83. Klaus-Dieter Kreuer, Stephen J. Paddison, Eckhart Spohr and Michael Schuster, *Chemical Review*. **104**, 4637-4678 (2004).
84. San Ping Jiang, Siew Hwa Chan, *Journal of Materials Science*. **39**, 4405 – 4439 (2004).
85. Lan Zhang, San Ping Jiang b, Hong Quan He, Xinbing Chen, Jan Ma, Xiao Chao Song, *International Journal of Hydrogen Energy*. **35**, 12359-12368 (2010).
86. Ting Shuai Li, Wei Guo Wang, *Journal of Power Sources*. **196**, 2066-2069 (2011).
87. Jens F.B. Rasmussen, Anke Hagen, *Journal of Power Sources*. **191**, 534-541 (2009).
88. S.W. Tao, J.T.S. Irvine, *The Chemical Record*. **4**, 83- 95 (2004).
89. M. Mogenson, *Journal of Electroceramics*. **5**, 141- 152 (2005).
90. M. C. Verbraeken, B. A. Boukamp, D. H. A. Blank, P. Holtappels, U. Vogt,

Chapter -1

Proceedings-9th International Symposium on Solid Oxide Fuel Cell.

91. H. H. Mobius, *Journal of Solid State Electrochemistry*. **1**, 2- 16 (1997).
92. Vinod M. Janardhanan, Vincent Heuveline, Olaf Deutschmann, *Journal of Power Sources*. **178**, 368–372 (2008).
93. Ryan O' Hayre, David M. Barnett, and Fritz B. Prinz, *Journal of the Electrochemical Society*. **152**, A439-A444 (2005).
94. Xiaohua Deng, Anthony Petric, *Journal of Power Sources*. **140**, 297-303 (2005).
95. J. Mizusaki, H. Tagawa, K. Tsuneyoshi, and A. Sawata, *Journal of The Electrochemical Society*. **138**, 1867-1873 (1991).
96. M. Kleitz and F. Petitbon, *Solid State Ionics*. **92**, 65-74 (1996).
97. J. Fleig, *Annual Review Materials Research*. **33**, 361-382 (2003).
98. A. Bieberle, L. P. Meier, and L. J. Gauckler, *Journal of The Electrochemical Society*. **148**, A646-A656 (2001).
99. V. Brichzin, J. Fleig, H. U. Habermeier, G. Cristiani, and J. Maier, *Solid State Ionics*. **152-153**, 499-507 (2002).
100. J. Fleig, *Journal of Power Sources*. **105**, 228-238 (2002).
101. W. Baukal and W. Kuhn, *Journal of Power Sources*. **1**, 91-97 (1976).
102. M. Casteel, P. Willson, T. Goren, P. O'Brien, D. Lewis, *ECS Transactions, The Electrochemical Society*. **25**, 1411-1416 (2009).
103. Saswati Ghosh, A. Das Sharma, R.N. Basu and H.S. Maiti, *Electrochemical & Solid State Letters*. **9**, A516-519(2006).
104. N. Yasuda, T. Uehara, M. Okamoto, C. Aoki, T. Ohno and A. Toji, *ECS Transactions, The Electrochemical Society*. **25**, 1447-1453 (2009).
105. B.C.H. Steele, *Journal of Material Science*. **36**, 1053-1068 (2001).
106. M. Mogensen, C. Bagger, K. A. Peterson, L.J. Christiansen, B.Sander and J. N. Paulsen, *An Introduction to Solid Oxide Fuel Cell*, Riso National Laboratory, Denmark, April (1992).

Chapter - 1

107. A. Momma, Y. Kaga, K. Fujii, K. Hohjyo, M. Kanazawa and T. Okuo, Proceedings of the 5th International Symposium on Solid Oxide Fuel Cells (SOFC-V), 311 (1997).
108. J. Will and L. J. Gauckler, Proceedings of the 5th International Symposium on Solid Oxide Fuel Cells (SOFC-V), 757 (1997).
109. J. W. Furgus, *Journal of Power Sources*. **147**, 46-57 (2005).
110. P.A. Lessing, *Journal of Material Science*. **42**, 3465-3476 (2007).
111. Raj N. Singh, *Journal of Material Engineering & Performance*. **15**, 422-426 (2006).
112. Raj N. Singh, *International Journal of Applied Ceramic Technology*. **4**, 134-144 (2007).
113. S.T. Reis and R. K. Brow, *Journal of Material Engineering & Performance*. **15**, 410-413 (2006).
114. J.H. Hirschenhofer, D.B. Stauffer, R.R. Engleman, and M.G. Klett, Fuel Cell Handbook, 4th Edition, Parsons Corporation, For U.S. Department of Energy, Morgantown, (1998).
115. S. Singhal, Recent Progress in Tubular Solid Oxide Fuel Cell Technology, in the Proceedings of the 1998 International Gas Research Conference, Madison, WI, USA, Omnipress, p. 422, (1998).
116. Y. Ohno, S. Nagata and H. Sato, in the Proceedings of the 15th IECEC, August 18-22, Seattle, WA, American Institute of Aeronautics and Astronautics, New York, p. 881, (1980).
117. E. Erdle, A. Koch, W.Schaefer, F.J.Esper and H. Friese, in Science and Technology of Zirconia II, N. Claussen, M. Ruhle and A. Heuer (eds.), American Ceramic Society, Columbus, OH , p. 685, (1984).
118. F.Umemura, H.Ota, K. Amano, S.Kaneko, T. Gengo, S. Uchida, N. Murakami and A. Notomi, in Proceedings of the International symposium of Solid Oxide Fuel Cell, November 13th -14th, 1989, Nayoga, Japan, O. Yamamoto, M. Dokia

Chapter -1

- and H. Tagawa (eds.), Science house, Tokyo, Japan, p- 25, (1989).
119. K. Horiuchi, K. Nakamura, M. Matsuzaki, S. Yamashita, T. Horita, H. Kishimoto, K. Yamaji, and H. Yokokawa, *ECS Transactions, The Electrochemical Society*. **35**, 217-223 (2011).
 120. J. P. Ackerman and J. E. young, U.S. Patent No. 4476198, October 9, (1984).
 121. C.C.McPheeters, U. Balachandran, D.W.Dees, S.E.Dorris, J.J. Heiberger, F.C.Mrazek, K.M.Myles, J.J.Picciolo and R. B. Poeppel, at the 33rd International Power Symposium, June 13, 1988, Cherry Hill, NJ, CONF-880665-4, U.S. Department of Energy, Washington, DC, (1988).
 122. N. Q. Minh, *Solid State Ionics*. **174**, 271-277 (2004).
 123. S. C. Singhal Proceedings of the 5th International Symposium on Solid Oxide Fuel Cells (SOFC-V), 37 (1997).
 124. E.R. Ray, in 1992 Fuel Cell seminar Abstracts, November 29- December 2, 1992, Tucson, AZ, Courtesy Associates, Washington, DC, p. 237, 403, 596, 603, 611 (1992).
 125. B. Borglum, E. Tang and M. Pastula, *ECS Transactions, The Electrochemical Society*. **35**, 63-69 (2011).
 126. N. Christiansen, H. Holm-Larsen, S. Primdahl, M. Wandel, S. Ramousse, A. Hagen, *ECS Transactions, The Electrochemical Society*. **35**, 71-80 (2011).

~

C *HAPTER-2*

Importance & Features of SOFC Anode

Chapter - 2

2.1. Importance of Anode in Planar SOFC

As conferred in the earlier chapter, a number of cell configurations exist in planar SOFC design, each are classified according to the layer that mechanically support the cell. ¹⁻³ Among all, the electrolyte supported cell is of limited use because of the enhanced polarizations and internal resistances that crop up due to higher thickness of the electrolyte (~ 200 μm). Additionally, the requirement of effective ionic conduction of such thick electrolyte demands a higher operating temperature of ~ 1000°C or more. The prime concern regarding the demand of costlier ceramic based interconnect material (primarily doped lanthanum chromite) and other components that could sustain such high operating temperature for considerable time period ultimately restrict the commercialization of such electrolyte supported design. These associated tribulations, give rise to the concept of 'anode-supported design' in which a thin (10 - 15 μm) dense electrolyte can be fabricated over a thick, porous anode support. Thus, for an anode-supported SOFC, the operating temperature can be lowered down to about 800°C or even less (depending on the thickness of the electrolyte film) without compromising with the overall power output. This allows the device to be made of less expensive materials particularly with metallic interconnect materials like high 'Cr' containing steel viz. Crofer 22 APU, Ebrite etc. For such anode-supported cells, the area specific resistance (ASR) of SOFCs that governs the total power output depends on the catalytic activity, microstructure and electrochemical activity of the anode component. Besides the activity of electro-oxidation of fuel, the anode should have sufficient mixed ionic and electronic conduction (MIEC) with minimum resistive losses. It should be porous enough to allow effective fuel diffusion, and in turn should optimize the amount of active triple phase boundary (TPB) where the electrochemical reactions take place in most cermets and termed as 'electrochemical reaction zone (ERZ)'. Optimization of microstructure to maximize

Chapter - 2

the effective TPB length is a major research effort in such cermets. Ideally, the anode support should have the capability to extend the TPB sites from a 1-dimensional interface to 2-dimensional area and finally to 3-dimensional contour which is of immense interest for mathematical modeling purpose of such cermets.⁴

Minimization of electrical resistance of anode is a major challenge for enhancing the life tenure of SOFC. The overall resistance comprises of internal, contact, concentration and activation polarization.⁵ The internal resistance refers to the resistance offered by transport of electrons within the anode and is therefore, determined by the magnitude of the electron resistivity and thickness of the anode. The contact resistance is caused by the poor adherence between anodes with electrolyte interface. Concentration resistance is related to the transport of gaseous species through porous electrodes and is controlled through microstructural optimization. Activation resistance is dependent on the charge transfer process and is dictated by TPB area and the electrocatalytic activity of the electrode. Elimination of all such resistive contributions of anode through system optimization, yield noteworthy improvement of electrical efficiency which eventually controls the performance of SOFC.⁵

SOFC being an example of multifuel compatible electrochemical device, capable of using gases like H₂, CO, natural gas etc, the choice and selection of anode composition is also reliant on the type of fuel utilized. Higher extent of variability induces constraint over material selection which finally limits the long term sustainability problem. Therefore, the processing for anode preparation with optimized properties and phase distribution along with its associated fabrication plays the main governing role for the operation of IT-SOFCs.⁶

2.2. SOFC Anode – The Associated Properties

The main purpose of the SOFC anode is to provide reaction sites for electrochemical oxidation of the fuel. The key requirements that must be satisfied

for anode material to be considered useful in anode-supported planar SOFC applications are mentioned below: ^{1-3, 7-10}

- a) Should have sufficient electronic conductivity
- b) Should have interconnected porosity for fuel gas transportation in high temperature under reducing environment for effective anodic electrochemical reactions.
- c) Sufficient electrochemical activity for fuel oxidation reactions
- d) Chemically stable and thermally compatible with other cell components
- e) Should have redox stability
- f) Should have extended triple phase boundary (TPB)
- g) Should be sufficiently active for oxygen surface exchange (charge transfer) reaction
- h) Should have sufficient catalytic activity, thus low polarization for electrochemical fuel oxidation
- i) If anode is used as a catalyst for internal reforming of hydrocarbons, it should also maintain its reforming effectiveness over long operating periods without significant deposit of carbon.
- j) Low material cost and simple application technology

A variety of ceramic, metallic and/or their composite materials can fulfil the aforesaid requirements of anode for SOFC application. Due to the high operating temperature of SOFC, suitable metals are limited to nickel (Ni), cobalt (Co) and noble metals. In addition, mixed conducting oxides stable in fuel reducing conditions also offers candidature for anode application.

2.3. Concept of TPB in SOFC **– A Possibility of Extension**

The concept of triple phase boundaries (TPBs) is employed extensively in SOFCs and polymer electrolyte membrane fuel cells (PEMFCs). TPBs are considered

Chapter - 2

to be the 'zones' or the 'spatial sites' at which either fuel oxidation reaction (HOR for hydrogen fuel) or oxidant reduction reaction (ORR for oxygen oxidant) are confined. The schematic is shown in [Figure 2.1a](#).¹¹ It is the interface at which the electronic and ion conducting phases co-exists with open pore containing fuel/oxidant. In anode-supported SOFC, electrochemical reactions at anodic TPB play a crucial role towards the overall cell performance as well as towards the cell degradation rate during long term operation. There are a number of instances in prior art regarding the study of such TPB in terms of geometric modelling and mathematical calculations for TPB length determination.¹²⁻¹⁷ The existence of TPB depends solely on the pattern and distribution of phases in respective to electrode and electrolyte interfaces. Usage of mixed ionic and electronic conducting (MIEC) ceramic materials are being practised in order to extend TPB from 1D – interface to 2 D- area or to 3D-contour. Microstructural control of the anode cermet also helps in the development of extension of TPBs throughout the anode matrix.¹⁸⁻²⁰ The extension of the TPBs inside the anode matrix can be visualised from [Figure 2.1 b](#). The co-existence of fuel, metallic and ceramic phases in a patterned cermet anode is expected to constitute TPB sites within anode interior. Therefore, electrochemical anodic reactions are expected to get accelerated through extension of TPB from bulk anode to anode/electrolyte interface. From scientific perspective, recent efforts have been made to more clearly delineate the nature and properties of the TPB. Maximum work related to the understanding of TPB is limited to SOFC system²¹⁻²⁶ with few relevant research works carried out for PEMFCs.²⁷⁻²⁸ Processing, preparation and fabrication of anode component is therefore aimed at maximization of these anodic TPBs at the fuel oxidising zone. Tailoring of triple phase boundaries at anodic or anode/electrolyte interface depends on:

- a) Distribution of phases i.e. microstructural control of anode¹⁸⁻²⁰

- b) Particle size of concerned species constituting anode¹⁸
- c) Maintenance of proper network among metallic phase (for electron transport), ceramic phase (for ion transport) and pore (for migration of fuel/exhaust gasses)
- d) Volume ratio among metallic and ceramic phases in cermet anode
- e) Size and distribution of pores within the anode¹⁷

Therefore, formation and extension of TPB active sites is solely a variant of processing parameters. However, determination and validation is governed through mathematical tools considering diverse assumptions based on the SOFC system.

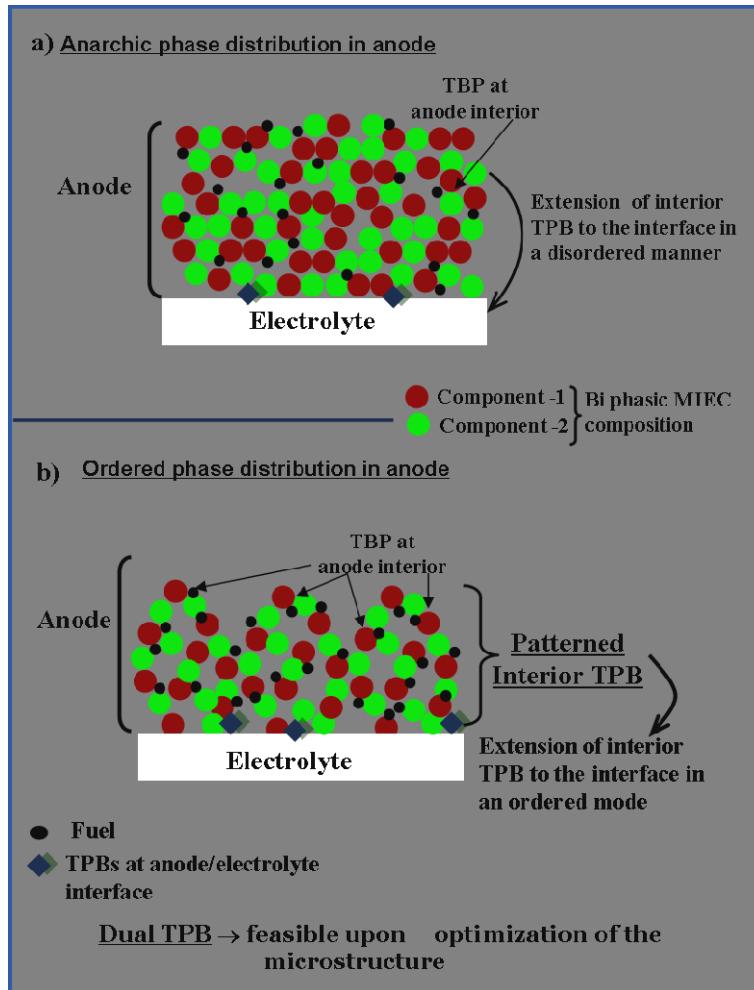


Figure 2.1: A schematic representation of anode/electrolyte interface showing the possibility for existence of dual TPB by microstructural optimization

Chapter - 2

2.4. Influence of Various Factors on Optimization of Anode Microstructure and Properties

The performance of anode for SOFC application, in terms of either electrical conductivity or electrochemical activity is exclusively dependent on the phase distribution and the related microstructure. Optimization of anode microstructure and pattern of distribution of respective phases are guided through a variety of parameters viz.

- a) Pore-size and their distribution along with the percentage of porosity
- b) Morphology and content of various phases
- c) Processing techniques
- d) Pre-treatment procedures
- e) Usage of anode active layers
- f) Employment of layered anode structure
- g) Gradation in physical properties throughout the anode cermet viz. porosity, phase content and particle size distribution etc.
- h) Sintering.

The influence of pore-size distribution of the diffusion layer on the mass transport properties is studied by Kong et al.²⁹ The extent of diffusion is studied using electrodes with hydrophobic layers applicable for proton exchange membrane fuel cells which is designed by optimization of pore-former quantity or nature followed by heat treatments. The respective loss in performance is correlated with mass transport problems and resolved by enlarging the micropore volume in the diffusion layer. Munakata et al³⁰ applied three dimensionally ordered macroporous Ni-YSZ structure upon using polystyrene beads as templates for application in IT-SOFC and enhance the power density to 374 mWcm^{-2} at 700°C . Similar research work related to the porosity of anodes for enhancement of cell performance has been carried out by many research groups.³¹⁻³²

Chapter - 2

It is established through many experiments, that most of the electrochemical reaction takes place near the anode/electrolyte interface commonly known as the anode active or functional layer.³³ Since most state-of-the-art anodes are homogeneous and monolithic in structure, a large portion of the anode is found to be non-participating in the electrochemical activity. It has been proposed by Gorte and his co-workers³⁴ that the supporting anode could be purposefully designed to have a dual microstructure. One component (a thin layer near the electrolyte) being designed to have high electrocatalytic activity (the functional layer) and the other component is meant to act as the conduction layer. This modification is expected to enhance flexibility over the microstructural design of each layer to serve a specific purpose.³⁵ In addition such exercise relaxes the need for catalytically active layer to be present in the conduction regime.

Significant efforts have also been initiated to activate SOFC by different pre-treatment methods. Jung et al³⁶ established a method of pre-treatment which includes exposure of the fabricated cells to dilute H₂/O₂ either under open circuit or close circuit conditions before their performance studies. Such experiments demonstrate that, technique via closed circuit method is observed to be more efficient than the conventional open circuit treatments. The significant changes resulted due to such closed circuit action causes an enhancement of TPB length in the anode structure. This causes an increment in the diffusivity of fuel gas and electrode conductivity as well as results in an enhancement of the anode performance.³⁶

Another alternate approach employed by many researchers is to use a layered anode structure with variation in Ni content, porosity and particle size of the constituent phases.³⁷⁻⁴¹ The researchers employed the similar techniques for fabricating various layers in such approach. Owing to the presence of higher interfacial contacts between Ni/YSZ/pore at anode-electrolyte junction, the smaller

Chapter - 2

pores effectively enhance the rate of charge transfer reaction and helps in its extension towards the bulk anode through the available TPB sites. In contrast, larger pores in the main anode support structure allow effective fuel diffusion. Similarly, the Ni content needs to be higher at the fuel inlet for higher catalytic activity. The reduction of Ni content along the thicknesses of the anode layers tends to reduce the thermal mismatch at the anode / electrolyte interface.

The influence of assorted microstructures of a similar compound through different techniques towards the cell performance is also reported by Guo et al.⁴² Ribeiro et al.⁴³ reported highly active and stable Ni-YSZ materials prepared through co-precipitation and combustion synthesis. Such developed anode is found to exhibit excellent stability towards steam reforming of methane at 900°C.⁴³ Effect of microstructure related to Ni-ScSz anode on the performance of SOFC is studied by Miyazaki et al.⁴⁴ Similar research work on optimization of anode microstructure for performance augmentation is carried out by other research groups.⁴⁵⁻⁴⁸

Agglomeration and coarsening of the associated phases within anode are considered as the major parameters responsible for degradation in contemporary SOFCs. Despite its importance, coarsening is difficult to investigate systematically because it proceeds slowly and must be examined over a long period of time. A few experiments of Ni coarsening can be found in the literature⁴⁹⁻⁵¹, but they do not examine the microstructures in three dimensions (3D), and thus it is difficult to characterize the evolution of tortuosities or connectivities of various phases.⁵² Chen et al.⁵³ have successfully simulated coarsening in three phase SOFC anodes. In the well known anode, Ni-YSZ, Ni coarsening is found to be a capillarity-driven phenomenon. Regions with high curvatures have higher chemical potentials than those with lower curvatures in accordance with the Gibbs–Thomson effect, and thus the material gets transported from these regions to lower-curvature regions when mobility is sufficiently large for the time scale of interest. This leads to lower

Chapter - 2

free energy of the system. The process can be formulated as a sharp interface free-boundary problem, but it is difficult to numerically solve in 3D since explicit tracking of the interface is required. Successful modeling based on the framework of a phase-field approach is adopted by Chen et al.⁵³ to quantitatively model the Ni coarsening in SOFC Ni-YSZ. Similar study to determine the quantification of Ni grain growth in Ni-CGO anodes is also employed by Holzer et al.⁵⁴ These experimental findings open a new horizon to optimize the microstructure of electrodes in order to restrict the rate of coarsening thereby accelerating the life cycle of SOFC.

Therefore, it can be concluded from the present section that, the property evaluation of an anode to be suited for SOFC application is a variant of a significant number of associated factors which are related towards optimization of both powder processing and cell fabrication techniques.

Chapter - 2

2.5. References

1. N.Q. Minh, T. Takahashi, *Science and Technology of Ceramic Fuel Cells*, Elsevier, New York, USA, (1995).
2. S.C Singhal, and K. Kendall, *High Temperature Solid Oxide Fuel Cells: Fundamentals, Design and Applications*. Elsevier, U. K. Editor. 2003.
3. R.N. Basu, *Materials for Solid Oxide Fuel Cells in Recent Trends in Fuel Cell Science and Technology*. Edited by S. Basu, Jointly published by Anamaya Publishers, New Delhi (India) and Springer, p. 284, New York -USA, 2006.
4. Kasra Nikooyeh, Ayodeji A. Jeje, Josephine M. Hill, *Journal of Power Sources*, **171**, 601–609 (2007).
5. W.Z. Zhu, S.C. Deevi, *Materials Science and Engineering A*. **362**, 228–239 (2003).
6. Masato Miyazaki, Kazuya Sasaki, Akihiro Suzuki and Takayuki Terai, *ECS Transactions, The Electrochemical society*. **25**, 1837-1846 (2009).
7. Peter Holtappels, U. Vogt and T. Graule, *Advanced Engineering Materials*. **7**, 292- 302 (2005).
8. Daniel J. L. Brett, Alan Atkinson, Nigel P. Brandon and Stephen J. Skinnerd, *Chemical Society Review*. **37**, 1568–1578 (2008).
9. S. C. Singhal, *Solid State Ionics*. **135**, 305-313 (2001).
10. San Ping Jiang, Siew Hwa Chan, *Journal of Materials Science*. **39**, 4405 – 4439 (2004).
11. J.W. Kim, A.V. Virkar, K.Z. Fung, K. Mehta, S.C. Singhal, *Journal of the Electrochemical Society*. **146**, 69–78 (1999).
12. Vinod M Janardhanan, Vincent Heuveline, Olaf Deutschmann, *Journal of Power Sources*, **178**, 368–372 (2008).
13. Ryan O’Hayre, David M. Barnett, and Fritz B. Prinz, *Journal of The Electrochemical Society*. **152**, A439-A444 (2005).
14. Xiaohua Deng, Anthony Petric, *Journal of Power Sources*. **140**, 297–303 (2005).

Chapter - 2

15. Kohei Miyazaki, Takeshi Abe, Koji Nishio, Haruyuki Nakanishi, Zempachi Ogumi, *Journal of Power Sources*. **195**, 6500–6503 (2010).
16. P. S. Jørgensen, K. V. Hansen, R. Larsen, J. R. Bowen, *Journal of Power Sources*. **195**, 8168–8176 (2010).
17. Ben Kenney, Mikelis Valdmanis, Craig Baker, J. G. Pharoah, Kunal Karan, *Journal of Power Sources*. **189**, 1051–1059 (2009).
18. L. Holzer, B. Münch, B. Iwanschitz, M. Cantoni, Th. Hocker, Th. Graule, *Journal of Power Sources*. **196**, 7076–7089 (2011).
19. Daifen Chen, Liu Lu, Jiayu Li, Zidong Yu, Wei Kong, Huayang Zhu, *Journal of Power Sources*. **196**, 3178–3185 (2011).
20. Abbaspour Ali, X. Wen, K. Nandakumar, Jingli Luo, Karl T. Chuang, *Journal of Power Sources*. **185**, 961–966 (2008).
21. J. Mizusaki, H. Tagawa, K. Tsuneyoshi, and A. Sawata, *Journal of The Electrochemical Society*. **138**, 1867-1873 (1991).
22. M. Kleitz and F. Petitbon, *Solid State Ionics*. **92**, 65-74 (1996).
23. J. Fleig, *Annual Review of Material Research*. **33**, 361-382 (2003).
24. A. Bieberle, L. P. Meier, and L. J. Gauckler, *Journal of The Electrochemical Society*. **148**, A646 –A656 (2001).
25. V. Brichzin, J. Fleig, H. U. Habermeier, G. Cristiani, and J. Maier, *Solid State Ionics*, **152-153**, 499-507 (2002).
26. J. Fleig, *Journal of Power Sources*, **105**, 228 -238 (2002).
27. R. O’Hayre and F. B. Prinz, *Journal of The Electrochemical Society*. **151**, A756 – A762 (2004).
28. R. P. Iczkiwski and M. B. Cutlip, *Journal of The Electrochemical Society*. **127**, 1433 -1440 (1980).
29. Chang Sun Kong, Do-Young Kim, Han-Kyu Lee, Yong –Gun Shul and Tae-Hee Lee, *Journal of Power Sources*. **108**, 185-191 (2002).
30. H. Munakata, M. Otani, Y. Katsuki, and K. Kanamura, *ECS Transaction*, The

Chapter - 2

- Electrochemical Society*, **25**, 1855-1860 (2009).
31. Andreas Bodén, Masahiro Yoshikawa, and Göran Lindbergh, *Journal of the Electrochemical Society*, **155**, B172-B179 (2008).
32. Frans van Berkel, Loek Berkeveld, Pieter Nammensma, Philipp Hofmann, Kyriakos D. Panopoulos and Jan Pieter Ouweltjes, Abstract [Anodes], Proceedings of 8th European SOFC Forum (2008).
33. M.D. Gross, J.M. Vohs, R.J. Gorte, *Electrochemical Solid-State Letters*. **10**, B65-B69 (2007).
34. M.D. Gross, J.M. Vohs, R.J. Gorte, *Journal of The Electrochemical Society*. **154**, B694 – B 699 (2007).
35. Ryan M.C. Clemmer, Stephen F. Corbin. *Solid State Ionics*, **180**, 721-730 (2009).
36. Guo-Bin Jung, Kai-Fan Lo and Shih-Hung Chan, *Journal of Solid State Electrochem.* **11**, 1435–1440 (2007).
37. M. Cassidy, G. Lindsay, K. Kendall. Proceedings of 1st Eur. SOFC Forum, pp. 205–221 (1994).
38. Z. R. Wang, J. Q. Qian, S. R. Wang, J. D. Cao and T. L. Wen, *Solid State Ionics*. **179**, 1593–1596 (2008).
39. A. C. Muller, D. Herbstritt and E. I. Tiffee, *Solid State Ionics*. **152– 153**, 537– 542 (2002).
40. M. Taillades, P. Batocchi, A. Essoumhi, G. Taillades, D. Jones and J. Roziere, *ECS Transactions, The Electrochemical Society*. **25**, 2193-2200 (2009).
41. K. Jonoa, S. Suda and M. Hattori. *ECS Transactions, The Electrochemical Society*. **7**, 1541-1546 (2007).
42. Weimin Guo, Jiang Liu, *Solid State Ionics*, **179**, 1516–1520 (2008).
43. Nielson F.P. Ribeiro, Mariana M.V.M. Souza, Octavio R. Macedo Neto, Sonia M.R. Vasconcelos, Martin Schmal, *Applied Catalysis A: General*. **353**, 305–309 (2009).
44. Masato Miyazaki, Kazuya Sasaki, Akihiro Suzuki, and Takayuki Terai, *ECS*

Chapter - 2

- Transactions, The Electrochemical Society.* **25**, 1837-1846 (2009).
45. Sun-Dong Kim, Jong-Jin Lee, Hwan Moon, Sang-Hoon Hyun,, Joocho Moon, Joosun Kim, Hae-Weon Lee, *Journal of Power Sources*, **169**, 265–270 (2007).
46. Tahereh Talebi, Mohammad Hassan Sarrafi, Mohsen Haji, Babak Raissi, Amir Maghsoudipour, *International Journal o f hydrogen energy*, **35**, 9440-9447 (2010).
47. Takehisa Fukui, Kenji Murata, Satoshi Ohara, Hiroya Abe, Makio Naito, Kiyoshi Nogi, *Journal of Power Sources.* **125**, 17–21 (2004).
48. J.-H. Lee, J.-W. Heo, D.-S. Lee, J. Kim, G.-H. Kim, H.-W. Lee, H.S. Song, J.-H. Moon, *Solid State Ionics*, **158**, 225– 232 (2003).
49. D. Simwonis, F. Tietz, D. Stover, *Solid State Ionics.* **132**, 241–251 (2000).
50. P. Tanasini, M. Cannarozzo, P. Costamagna, A. Faes, J.V. Herle, A. Hessler-Wyser, C. Comninellis, *Fuel Cells.* **9**, 740–752 (2009).
51. S. Jiang, *Journal of Material Science.* **38**, 3775-3782 (2003).
52. J. R. Wilson, W. Kobsiriphat, R. Mendoza, H. Chen, J. M. Hiller, D.J. Miller, K. Thornton, P. W. Voorhees, S. B. Adler, S. A. Barnett, *Nature Materials.* **5**, 541–544 (2006).
53. Hsun-Yi Chen, Hui-Chia Yu, J. Scott Cronin, James R. Wilson, Scott A. Barnett, Katsuyo Thornton, *Journal of Power Sources.* **196**, 1333–1337 (2011).
54. L. Holzer, B. Iwanschitz, Th. Hocker, B. Münch, M. Prestat, D. Wiedenmann, U. Vogt, P. Holtappels, J. Sfeir, A. Mai, Th. Graule, *Journal of Power Sources.* **196**, 1279–1294 (2011).

~

C *HAPTER-3*

Literature Survey

Chapter - 3

3.1. SOFC Anode Materials

The purpose of present section is to discuss an overview on the achievements and progresses related to the development of anode materials used for SOFC application. A number of ceramic and metallic materials can potentially meet the requirements (*discussed in section 2.2 of chapter 2*) of SOFC anodes. Presence of reducing environment, favour the usage of 'metals' as anode materials, but high temperature during SOFC operation, confines the choice of metals only to nickel, cobalt and noble metals. Electronically conducting ceramics and mixed conducting oxides are also found to be suitable as an anode material. In the subsequent sections on review of anode materials, conventional Ni-YSZ cermet anodes are discussed first and are followed by the review on alternate anodes for SOFC application.

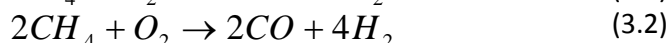
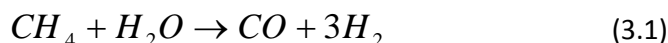
3.1.1. Ni-YSZ cermet anode material

Porous 'nickel– 8 mol % yttria stabilized zirconia (Ni-YSZ)' cermet is the most widely used anode material due to several advantages associated with it. Most importantly, the intrinsic charge transfer resistance allied with the electrocatalytic activity at Ni-YSZ interface is low. Of the two component cermet composite, Ni provides sufficient electronic conductivity and catalytic activity towards fuel oxidation process. On the other hand, YSZ functions in imparting ionic conduction to the cermet thereby extending the anodic reaction zone, provide structural support which prevents Ni coarsening and finally maintains thermal compatibility of the anode with the adjacent cell components.^{1- 4} In addition, YSZ prevents the anode layer from significant shrinkage during fabrication and also helps in retaining the interconnected micropores within the cermet anode structure. Since, Ni-YSZ cermet do not form any solid solution even at high temperature, the formed green body can be easily sintered to NiO-YSZ which can be further reduced to porous Ni-

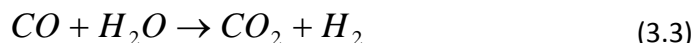
Chapter - 3

YSZ anode by controlled heat treatment under inert atmosphere.⁵ In order to fulfil the conductivity criteria, 30-50 vol % Ni is being utilized.⁶ However, the main factor that govern the requirement of Ni content is the microstructural distribution of associated phases, particle size etc.

Among innumerable advantages, certain drawbacks of Ni-YSZ cermet are its poor redox stability, low tolerance to sulphur, carbon deposition upon using hydrocarbon fuels and the tendency of nickel agglomeration after prolonged operation.⁷ In spite of being excellent catalyst for steam reforming and hydrogen cracking, it shows low tolerance for carbon deposition that makes it inappropriate for operation in hydrocarbon fuels unless excess steam is present to ensure steam reforming.^{1- 4, 8-9} Therefore, hydrogen is exclusively used as the fuel gas in the prevailing SOFC. If methane is to be used along with this anode, it has to be first converted to hydrogen via internal or external reforming as shown in Eq. 3.1 or via catalytic partial oxidation as denoted by Eq. 3.2:



The steam reforming reaction (Eq. 3.1) is associated with the following water gas shift reaction (WGS):



If the fuel contains insufficient moisture for reaction 3.1 to complete, carbon will be deposited on the anode surface by methane cracking (Eq. 3.4) or 'Boudouard reaction' (Eq. 3.5):



The feasibility of steam reforming and partial oxidation of methane over Ni-YSZ anode has been thoroughly evaluated by Cunningham and Ormerod.¹⁰ Doping of

Ni-YSZ anodes with Mo and Au have been proved to be a promising option for carbon deactivation resistance.¹¹

The electrical conductivity of Ni-YSZ cermet strongly depend upon the ratio of Ni and YSZ phases as shown by the S-shaped curve in Figure 3.1, predicted from percolation theory.^{6, 12-13} A definite Ni content is required to maintain proper metallic network throughout the cermet. Such specific magnitude of Ni is dependent on the processing technique and also related to the microstructural distribution of phases. Conventional cermet requires ~ 40 vol % of Ni to satisfy the conductivity criteria, which in turn create serious problems of coarsening at high temperature and fast degradation of performance. The percolation threshold is therefore; influenced by many variables viz. porosity, pore-size and distribution, size of constituents, contiguity of phases etc.¹⁴⁻¹⁵

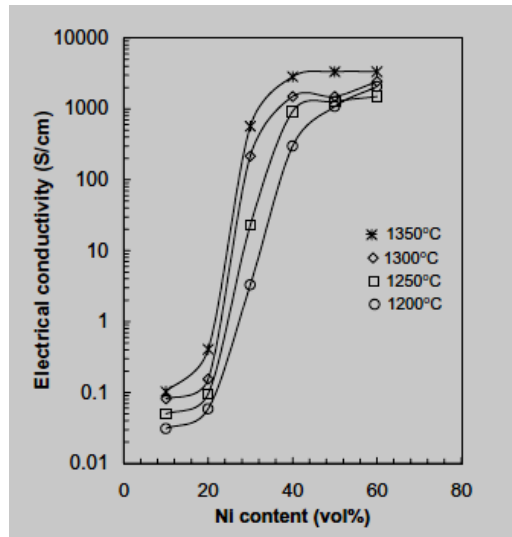


Figure 3.1: Dependence of electrical conductivity on the Ni-YSZ phase contribution¹²⁻¹³

The extent of Ni coarsening can be mathematically analyzed through transmission line analogue model.¹⁶ The anode polarization (η_A) based on the model can be written as:

$$\eta_A = \frac{1}{N_p} \left[\rho \Psi \frac{(r_o^3 + k_r t)^{1/3}}{r_o} \right]^{1/2} \coth \left[\left(\frac{\rho r_o L}{\Psi (r_o^3 + k_r t)^{1/3}} \right)^{1/2} \right] \quad (3.6)$$

Chapter - 3

where, N_p , ρ , r_0 , k_r , t , L and Ψ are number of pores per unit area, electrolyte resistivity, initial particle radius, proportionately constant, time, electrode thickness and $\Psi = rZ/2$ [r and Z are pore radius and interfacial resistance between Ni and YSZ] respectively. It has been proved from Eq. 3.6 that, the rate of coarsening increases at the beginning and continue to increase as long as the driving force for sintering/coarsening remains significant in the system.

Chemical interaction of Ni-YSZ cermets with either YSZ electrolyte or LaCrO_3 interconnect is found to be negligible below 1000°C . However, at higher temperatures, poor conducting NiCrO_4 phase form which tends to migrate into electrode forming a reaction layer at electrode/interconnect interface as shown in Figure 3.2.¹⁷ Upon co-firing anode at $\sim 1400^\circ\text{C}$ with interconnect having Co-doped LaCrO_3 , both Ca and Cr diffuse more than $100\ \mu\text{m}$ into the porous electrode thereby degrading its performance.¹⁸

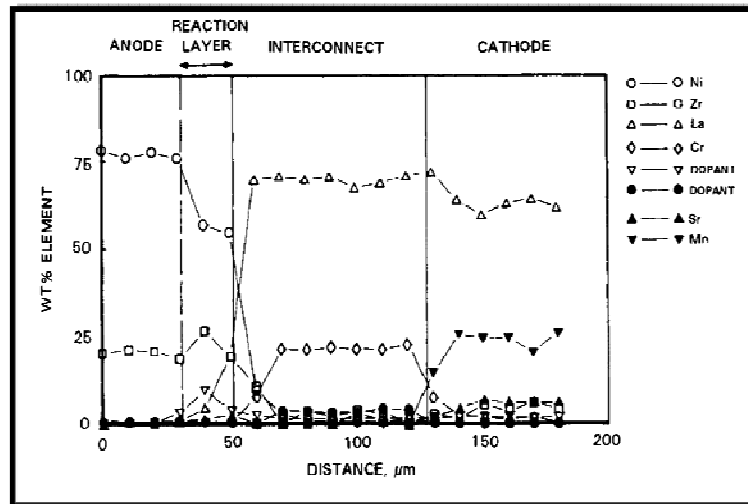


Figure 3. 2: Elemental distribution during co-firing of Ni-YSZ anode with Co-doped LaCrO_3 above 1400°C ¹⁷

In-spite of certain shortcomings, Ni-YSZ cermet being most widely used as the anode material through tailoring of properties by optimized preparation and fabrication technique which will be discussed in details in the subsequent sections.

3.1.2. Alternate anode materials

3.1.2.1. Fluorite based anodes

Fluorite-based materials such as conductive oxides have been proposed as possible anode materials for SOFC application. The structure of cubic fluorite structure is presented in Figure 3.3.

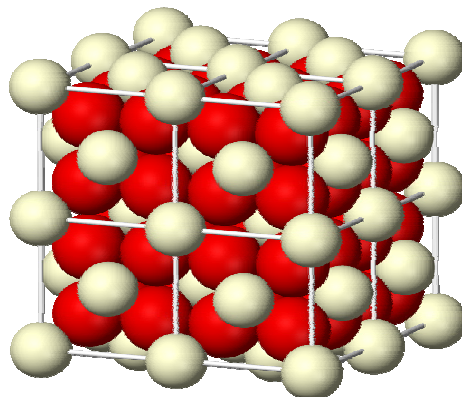


Figure 3. 3: Schematic of cubic fluorite structure¹⁹

Ceria is known to be a potential electro catalyst for methane oxidation reaction. However, a major disadvantage of ceria is the mechanical degradation of the fabricated cell due to lattice expansion due to the transition of Ce^{4+} to Ce^{3+} under the low oxygen partial pressure environment of the anode.²⁰ This causes development of crack at the electrode/electrolyte interface and subsequent delamination and degradation of the cell. Studies have shown that such dimensional change can be reduced by doping lower valent cations viz. Gd^{3+} , Sm^{3+} , Y^{3+} etc. Therefore, efforts have been made to use doped ceria as anode material for SOFCs that utilizes CH_4 as the fuel.²¹⁻²² Both doped and undoped ceria are the examples of mixed electronic and ionic conductors (MIEC) at low partial pressure of oxygen, the mechanism of which is explained in details by Steele.²³ Doping of trivalent rare earth oxides viz. Gd_2O_3 , Sm_2O_3 and Y_2O_3 in the form of solid solution with CeO_2 tend to minimize the association enthalpy of the compound thereby favouring the insertion reaction. The ability of some doped ceria to exhibit

Chapter - 3

significant ionic conduction at 500-700°C of magnitude higher than that of yttria doped zirconia enable them to act as the competent electrolyte material for application in IT-SOFC.²³ The oxygen partial pressure dependence indicates that doped ceria has a significant contribution from electronic conductivity when it is used as anode in the fuel atmosphere. Furthermore, the temperature imposes a profound effect on the electronic conductivity of doped ceria. The excellent catalytic activity of CeO₂ based materials stemmed from the oxygen-vacancy formation and migration associated with reversible CeO₂-Ce₂O₃ transition.²⁴⁻²⁵

Gadolinium doped ceria (CGO) is a well-known anode effective in suppressing carbon deposition. However, electrochemical activity of such CGO-based anodes towards methane oxidation is being questioned by Marina et al.²⁶ Primdahl et al.²⁷ found through their extensive research that addition of Ni to such MIEC anode like CGO is effective in improving the anode performance which is clearly reflected from the impedance spectra as shown in Figure 3.4.²⁷ Ahn et al.²⁸ examined the properties of Cu-ceria composite anode by replacing CeO₂ with a solid solution of Ce_{0.6}Zr_{0.4}O₂ (CZO).

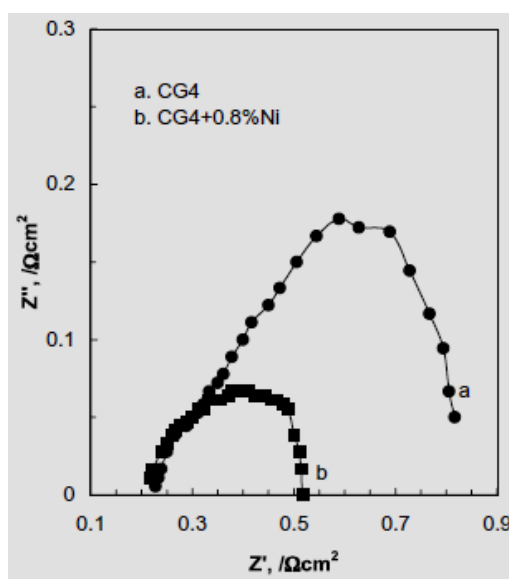


Figure 3.4: Effect of Ni addition to gadolinium doped ceria from AC-impedance study of the respective electrodes²⁵

CZO is found to improve the thermal stability of the developed anode, which is assigned to the improved reducibility of the solid solution compared to that of pure ceria. Usage of hydrocarbon fuels creates serious problems of carbon deposition on conventional Ni-YSZ anodes of SOFC, due to reaction with Ni that leads to the formation of filamentous carbon. In this context, Cu-ceria or Metal-Cu- Ceria based anodes have received special interest.^{2, 29} Copper is a relative inert metal for carbon deposition reactions and provides sufficient electrical conductivity to the anode. However, Cu is not a good catalyst for C-H bond breaking, making it necessary to add an additional catalytic component, such as ceria to oxidise hydrocarbon fuel. Many researchers have employed micro emulsion-precipitation method to synthesize Cu-CeO₂ based materials (5-25 at % Cu).³⁰ Such preparation technique allows structural control of material and introduction of a large quantity of copper into the cerium oxide (~ 21 at %), thereby obtaining a nano structured mixed oxide of high surface area. Physicochemical characterisation in reducing atmosphere has demonstrated that Cu-CeO₂ is thermally and chemically compatible with common SOFC electrolytes. On the other hand it shows an electrical behaviour suitable for its use as anode for SOFC operating at a relatively low temperature (1023 K). The catalytic activity test revealed that such anodes exhibits sufficient stability for application in direct utilisation of hydrocarbon fuels. When methane is used as fuel, the primary anode reaction is the direct methane oxidation; the lower power densities obtained under these conditions can be justified for the higher polarisation resistance associated with the slower electrochemical oxidation of methane versus hydrogen.³¹ Detailed experimental work on Cu-based cermets viz. Cu-CeO₂, Cu-YSZ etc or Cu-Metal-cermet composites viz. Cu-Ni-YSZ etc are also studied as alternate anode materials.³²⁻³⁴

Upon minor addition of Ni to CGO anode fed with hydrogen fuel, the low frequency arc in impedance spectra seems to suppress significantly.²⁵ This indicates

Chapter - 3

that electrode reaction on MIEC anode is altered because the rate-limiting step, specifically, the adsorption and/or dissociation of hydrogen is bypassed. The applicability of yttria doped ceria (YDC) and samaria doped ceria (SDC) as the potential anodes in IT-SOFC both having characteristic MIEC nature is studied by Uchida et al.³⁵ Owing to greater electronic conductivity of YDC over SDC and comparable ionic conductivity as YSZ, the anode polarization, in particular activation polarization is reduced significantly. At lower operating temperature, however, addition of trace amounts of noble metal catalyst viz. Ru, Rh etc to SDC or YDC tend to improve the anode performance.³⁶⁻³⁷ Ni-doped ceria cermet (Ni-CGO) is experimentally observed to exhibit high activity towards methane steam reforming without any appreciable deposition of carbon as studied by Livermore et al.³⁸ Since, doped ceria is considered to be electrochemically more active than doped yttria; the former is being utilized as a functional layer in between anode and electrolyte.³⁹ By placing a dense interlayer of Ni-samaria doped ceria (Ni - SDC) underneath the porous anode of same composition, the polarization resistance is observed to reduce remarkably as given in Figure 3.5.⁴⁰

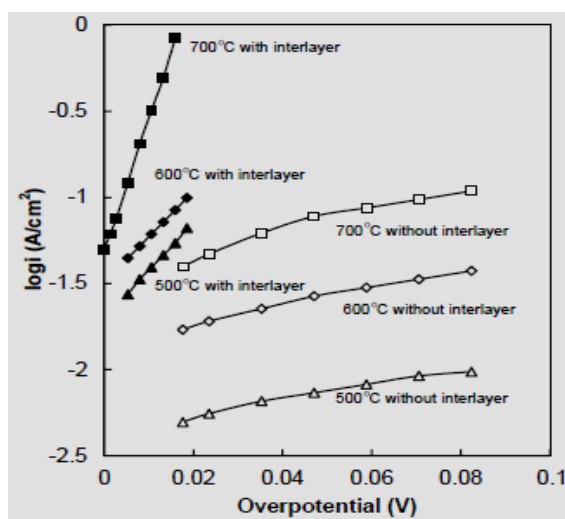


Figure 3. 5: Polarization responses of Ni-SDC anodes with and without interlayer at different temperatures^{38, 40}

3.1.2.2. Perovskite anode materials

The perovskite type oxides (ABO_3 with total charge of A and B is 6) shown in Figure 3.6 are being used as anode materials which primarily work in the environment of methane fuel.

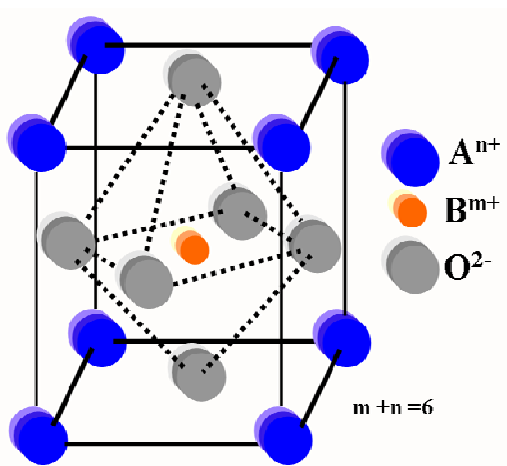


Figure 3.6: Schematic of Unit cell of ABO_3 perovskite structure ⁴¹

Ruiz-Morales et al ⁴¹ gave an excellent idea of using $La_{0.75}Sr_{0.25}Cr_{0.5}Mn_{0.5}O_{3-\delta}$ (LSCM) compound for the use of both anode and cathode thereby forming symmetrical type fuel cells (SFCs). Owing to the high performance of LSCM in both reducing and oxidising environment, promising performance of 0.5 and 0.3 Wcm^{-2} are obtained from SFCs at 950°C using H_2 and CH_4 fuels respectively. The similar composition of LSCM is also used by Tao et al ⁴² as an anode for methane oxidation at high operating temperatures. Such anode is found to have comparable electrochemical performance with Ni-YSZ cermets. However, LSCM is reported to exhibit low electronic conductivity in the reducing anodic atmosphere and unstable to sulphur impurities in the fuel. ⁴³ Impregnation of CuO however, improves the conductivity, but the associated long term performance is proven to be unsatisfactory. ⁴⁴

The aforesaid problems of LSCM-based anodes can be solved upon using oxygen deficient double perovskite ($Sr_2Mg_{1-x}Mn_xMoO_{6-\delta}$) proposed by Goodenough et al ⁴⁵ which operates in the temperature range of 650 – 1000°C. The said anode exhibit

Chapter - 3

long term stability and tolerance to sulfur. The mixed valence Mo (VI)/ Mo (V) transitions provide sufficient electronic conductivity with the ability to accept electrons from hydrocarbon thereby losing oxygen.⁴⁴ This MIEC electrode is catalytically active towards oxidation of both H₂ and hydrocarbon. A maximum power density of 438 mWcm⁻² is obtained using such anode at 800°C with dry methane as fuel.⁴⁵

Electrochemical properties of cells using other perovskites viz. La_{1-x}Sr_xCr_{1-y}Ru_yO₃ [LSCRO] and La_{1-x}Sr_xCr_{1-y}Ru_yNiO_{3-δ} [LSCRN] ($x = 0.2, 0.3, 0.4$ and $y = 0.02, 0.05$) as anode have been studied by Sauvet et al.⁴⁶ using hydrogen and methane as fuel at 750 and 850°C. Best performances are obtained by using 30 mole % of Sr doping in case of LSCRO-type anodes. At 750°C, a polarization resistance of 3.7 and 40 Ωcm² is obtained in hydrogen and methane fuel respectively upon using graded electrode viz. YSZ/CeO₂/graded La_{0.7}Sr_{0.3}Cr_{0.95}Ru_{0.5}O₃-YSZ structure. LSCRN type of anodes is found to exhibit no carbon deposition for methane steam reforming at methane: steam ratio is 1 or less. Another class of perovskite compound viz. La_{0.9}Sr_{0.1}Ga_{0.8}Mg_{0.2}O_{2.85} (LSGM) species generally used as the electrolyte material for SOFC⁴⁷⁻⁵⁰ has been combined with Ni to be used as a composite anode by Huag et al.⁵¹ The observed anodic potentials are observed to be high with significant cell degradation with time. However, anode performances can be enhanced by placing a buffer layer at the anode-electrolyte interface which prevents the formation of LaNiO₃ species. Chen et al.⁵² studied the doping of transition metal oxides into lanthanum gallates (MIEC electrodes) in order to enhance the electronic conductivity while maintaining the ionic conduction. Electrochemical measurements using an oxygen concentration cell indicate that La_{0.9}Sr_{0.1}Ga_{0.8}Mn_{0.2}O₃ is a MIEC with significant ionic conduction whereas La_{0.9}Sr_{0.1}Ga_{0.8}Co_{0.2}O₃ (also MIEC nature) shows significant electronic conduction.

3.1.2.3. Pyrochlore anode materials

The pyrochlore structure oxides $[A_2B_2O_7]$ as shown schematically in [Figure 3.7](#), are also used as anodes in SOFC; $Gd_2Ti_2O_7$ (GT) being a typical example.⁵³⁻⁵⁵ Replacement of Gd^{3+} by Ca^{2+} $[(Gd_{0.98}Ca_{0.02})_2Ti_2O_7]$ significantly increases the ionic conductivity by creating oxygen vacancies in the A_2O structure which is found to be comparable with YSZ at $1000^\circ C$.⁵⁶⁻⁵⁷ However, for application as an efficient anode material, MIEC nature is introduced by Mo doping into GT structure.⁵⁸ The solid solution of Mo doped GT $[Gd_2(Ti_{1-x}Mo_x)_2O_7]$ is found to be only stable at a specific oxygen partial pressure at high temperature. The electrical conductivity is about $70 S cm^{-1}$ and $25 S cm^{-1}$ for $x = 0.7$ and 0.5 , respectively, at $p(O_2)$ around 10^{-20} atm.

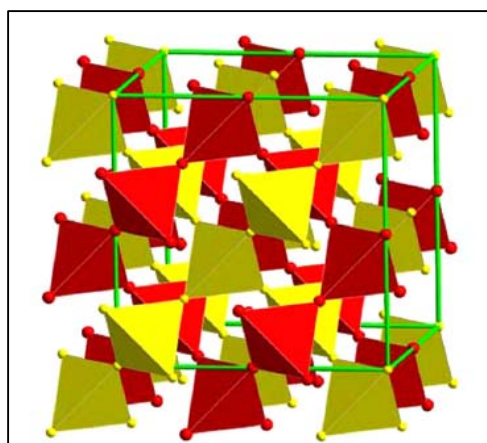


Figure 3.7: Schematic of Unit cell of $A_2B_2O_7$ pyrochlore structure⁵³⁻⁵⁵

In addition, two other pyrochlore systems viz. a) $Pr_2Zr_2O_{7\pm\delta}$ modified by the multivalent cations Mn and Ce on the Zr-site, and (b) $Pr_2Sn_2O_{7\pm\delta}$ modified by In on the Sn-site has been studied extensively by Mogensen et al.⁵⁹ Optimization of such anode composition is found to yield a stable pyrochlore structure with enhanced electronic conductivity and a wide functional range of oxygen partial pressure for application as an anode material for SOFC.

3.1.2.4. Tungsten bronze anode materials

Oxides of general formula $A_2BM_5O_{15}$ (with $M = Nb, Ta, W, Mo$ etc and A or $B = Ba, Na$) exhibit tungsten bronze structure ([Figure 3.8](#)) having two varieties viz. a)

Chapter - 3

tetragonal tungsten bronze (TTB) or b) orthorhombic tungsten bronze (OTB). Such materials have also been used as SOFC anodes by many renowned researchers.⁶⁰⁻⁶¹

Tungsten bronze (TB) oxides of composition, $(\text{Ba/Sr/Ca/La})_{0.6}\text{M}_x\text{Nb}_{1-x}\text{O}_{3-6}$ with $\text{M} = \text{Mg, Ni, Mn, Cr, Fe, In, Ti, Sn}$, is studied by Slater et al⁶²⁻⁶³ as anode for SOFC. Among the aforesaid compositions, compounds with $\text{M} = \text{Ni, Mn, Cr, Fe, Sn}$ are found to be inapplicable for anode application, either because of poor oxygen exchange kinetics due to low oxide ion conductivity or due to partial decomposition on prolonged heat treatment at 1000°C in reducing atmospheres.

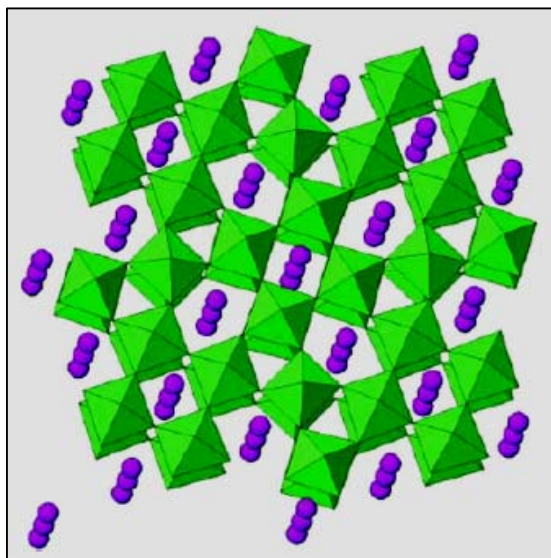


Figure 3.8: The tungsten bronze structure⁶⁰⁻⁶¹

However, compounds with $\text{M} = \text{Mg, In}$ etc are found to be stable under prolonged reduction treatment and exhibit significantly good conductivity to be applicable a potential anodes for SOFCs. A wide range of TB oxides with formula, $(\text{Ba/Sr/Ca/La})_{0.6}\text{M}_x\text{Nb}_{1-x}\text{O}_{3-6}$ ($\text{M} = \text{Mg, Ni, Mn, Cr, Fe, In, Ti, Sn}$) has been investigated by Kaiser et al.⁶⁴ Highest electronic conductivity of $\sim 10 \text{ Scm}^{-1}$ at $p(\text{O}_2) = 10\text{-}20 \text{ atm}$ is observed from the composition, $\text{Sr}_{0.2}\text{Ba}_{0.4}\text{Ti}_{0.2}\text{Nb}_{0.8}\text{O}_3$ at 930°C with the feasibility of application as SOFC anode.

3.1.2.5. Sulfur tolerant anode materials

Extensive studies has been done by Matsusaki et al ⁷ on the process variables effecting the degree of sulphur/H₂S poisoning for Ni-YSZ based anodes by electrochemical impedance spectroscopy method. Though the poisoning effect is found to be reversible at low concentrations of sulfur below ~15 ppm, but still the extent of damage is significant at lower cell operating temperature. ^{7, 65} Therefore, the requirement of newer anode arises whose functionality cannot be deactivated by sulphur containing fuels. Such anodes should however fulfil the requirements of electronic conduction, chemical and thermal stability and catalytic activity for oxidation of H₂S, H₂ and CO. Copper – ceria cermet anode (Cu-CeO₂) demonstrated by He et al. ⁶⁶ shows high sulphur tolerance upto ~ 450 ppm when operated at 800°C using hydrogen as fuel containing H₂S impurities. However, at higher H₂S concentration, considerable amount of Ce₂O₂S formed which degrade the anodic reactions thereby causing its failure. Another family of anodes viz. YSZ/La_{1-x}Sr_xBO₃ (B = Mn, Cr, Ti) is studied by Mukundan et al ⁶⁷ in moist hydrogen fuel at 1000°C. The composition Sr_{0.6}La_{0.4}TiO₃/YSZ (50/50 wt. %) successfully function as anode without any degradation upto 5000 ppm of H₂S. In addition, upon switching fuel from 1 % H₂S to hydrogen, no significant degradation is noted. ⁶⁴

A pyrochlore based anode material Gd₂Ti_{1.4}Mo_{0.6}O₇ (discussed in above section 3.1.2.3) developed by Zha et al ⁶⁸ showed remarkable tolerances towards sulphur containing fuels. Peak power density of ~ 342 mWcm² with only 0.2 Ωcm² interfacial resistance at anode/electrolyte is obtained using such anode in 10 % H₂S and 90% H₂ fuel combination for continuous 6 days without any observable degradation. Similar developmental work is also being attempted by Cheng et al ⁶⁹ which help in ruling out certain materials viz. species containing transition metal carbides, borides, nitrides, silicides etc to be used as SOFC anode.

Chapter - 3

3.1.2.6. Anodes applicable for hydrocarbon fuels

Operation of fuel cells with H₂ (as the fuel gas) is stated to be an advantage since H₂ is an example of renewable source. However, a prime fact remains ignored that the vast majority of H₂ gas is generated by external or internal reforming of hydrocarbons (described in section 3.1.1 and reactions 3.1 to 3.5).⁷⁰ Furthermore, the distribution and storage problems associated with H₂ have led to a large research effort into developing fuel-cell systems that operate on hydrocarbons. Reforming of hydrocarbons (as used for H₂ production) can be performed in a set of reactors separate from the fuel cell or, with high-temperature fuel cells such as those that use a molten-carbonate or a solid oxide electrolyte, internally at the anode.⁷¹ In either case, the requirement that the fuel first be reformed leads to significant complications as well as loss in fuel efficiency. Using such conventional Ni-based anodes, Barnett and co-workers⁷² achieved excellent power densities and stable operation for dry CH₄ fuels between 500 and 700°C because carbon formation for CH₄ is not thermodynamically favoured at this temperatures.⁷² However, carbon formation is found to prevent the cell operation with ethane.⁷³

Formation of carbon within anode upon using hydrocarbon fuel could be avoided by replacing Ni with other electronic conductors that do not catalyze carbon formation, such as Cu⁷⁴⁻⁷⁶ or conducting oxides.⁷⁷⁻⁷⁹ The research of He et al⁸⁰ is focused on the on the development of anodes made from composites of Cu, ceria, and YSZ for direct utilization hydrocarbon fuels, without initial reforming to syngas in that Cu does not catalyze the formation of carbon fibers in the presence of dry hydrocarbons in the way that Ni does. Due to the fact that Cu has a low catalytic activity for hydrocarbon oxidation, it is necessary to add ceria to the anode formulation in order to achieve reasonable power densities.⁸¹ Because CuO and Cu₂O melt at the temperatures required for processing YSZ, the fabrication of

Cu-based anodes require the development of synthetic methods that are different from those used to produce Ni-cermet composites.^{74, 75, 81, 82} Research studies have shown that exposure of Cu–ceria–YSZ anodes to *n*-butane at 973K can lead to a large increase in power density due to the formation of carbonaceous residues within the anode.^{82, 83} For the FCs with Cu contents of 20 wt.% or less, increment in power densities are observed for operation in H₂ after the anode had been exposed to *n*-butane.⁸² The degree of enhancement decreases with increasing Cu content, implying that the deposits improve the connectivity of the metallic phase in the anode. Analysis of the compounds formed by passing *n*-butane over a Cu-plated surface at 973K showed the formation of poly-aromatic compounds (e.g. anthracene and similar compounds) that were soluble in toluene but conjugated enough to provide electronic conductivity⁸⁴ as shown in Figure 3.9.⁸¹

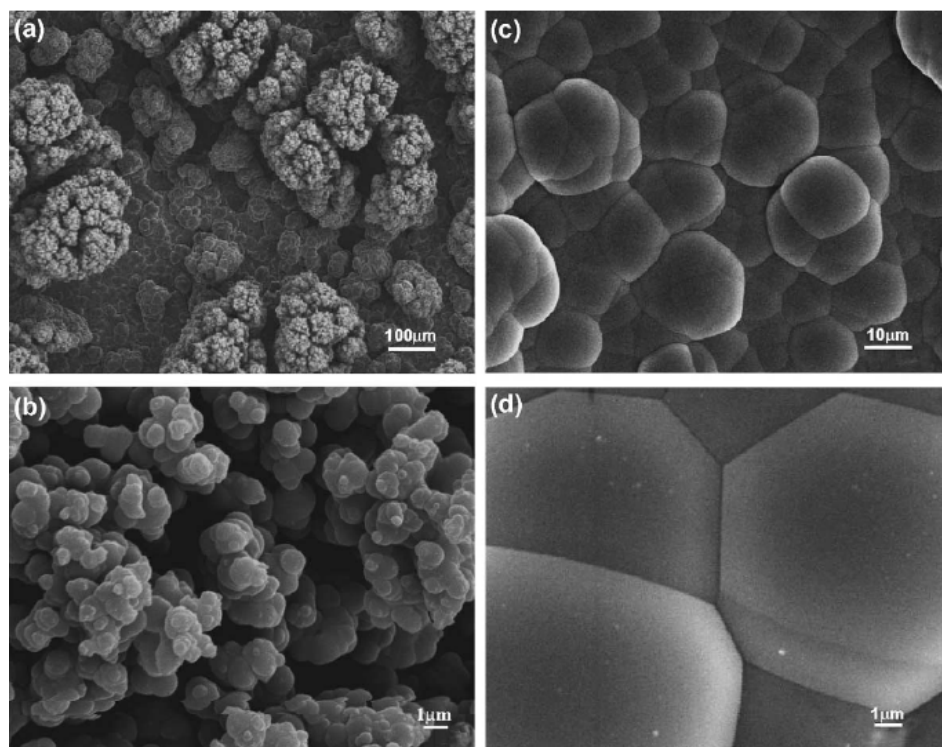


Figure 3.9: The morphology of carbonaceous deposits on the surface of anode containing 10 wt % CeO₂ and 20 wt % Cu after long term testing in *n*-butane fuel at 1173 K⁸⁰

Chapter - 3

However, it is also found that the carbonaceous deposits formed at 1073 K or higher temperature can deteriorate the performance for long-term operation. Many other researchers have also studied Cu-based anode composites for direct oxidation of hydrocarbon fuels including liquids viz. gasoline without employing external or internal reforming to H₂.^{34, 85-88} Apart from Cu-based anodes, many doped perovskite compositions like nanostructured palladium–La_{0.75}Sr_{0.25}Cr_{0.5}Mn_{0.5}O₃/Y₂O₃–ZrO₂,⁸⁹ double-perovskite, Sr₂FeMoO₆ (SFMO) synthesized with a combined citrate-EDTA complexation,⁹⁰ nonporous palladium anodes⁹¹ and Ni-based anodes modified by variable dopants eg. (Ni_{0.75}Fe_{0.25-x}MgO)/YSZ,⁹² Ni frame work coated with Sm doped ceria (SDC),⁹³ Ni-scandia stabilized zirconia (ScSZ),⁹⁴ Ni- Sm doped ceria (SDC),⁹⁵ are currently being employed as potential anode materials used for direct hydrocarbon fuels.

3.2. Anodic Reaction Mechanisms

Development and optimization of anode materials is based on the understanding of reaction mechanisms involved during fuel oxidation and interfacial electrochemical processes. Detailed knowledge on each of the reaction parameters viz. a) reaction rates, b) surface species and their extent of coverage, c) sticking coefficient – used in surface physics to describe the ratio of the number of adsorbate atoms that do adsorb or stick to the surface to the total number of atoms that impinge upon that surface during the same period of time, d) TPB patterning etc. allows to determine the limitations of fuel cell process with respect to its electrochemistry. The basic aim of developing models is to identify the rate limiting step (s) of the anodic processes. Accelerating the limiting step would lead to the progression of overall anodic reactions with enhanced efficiency.

Numerous models have been postulated to identify the rate controlling steps under various operating conditions. Some important models are identified as:⁹⁶

- 1) Surface diffusion model⁹⁷⁻⁹⁹
- 2) Charge transfer theory including species reactivity⁹⁸⁻¹⁰⁵
- 3) Adsorption model^{97, 103, 106}
- 4) Hydrogen desorption rates⁹⁸
- 5) Theories involving catalytic effects of water¹⁰⁶
- 6) Involvement of both Ni and YSZ species towards anodic reaction mechanism¹⁰⁷
- 7) Participation of oxygen can be in the form of, a) interstitial species in YSZ, b) adsorbed O^{2-} species; c) O^{2-} may form OH^- species present as interstitial, d) adsorbed OH^- on Ni surface or e) as water entity formed without any intermediate species during the reaction.¹⁰⁷

According to Haart and Mogenson^{99, 100} there are more than one limiting steps involved in the hydrogen oxidation reaction as mentioned: i) electrochemical reactions at interfacial TPB or within anode TPB (if microstructural pattern pertains), ii) transport restrictions of electrons and oxide ions through solid surfaces, iii) surface adsorption and surface diffusion of transient/ metastable species viz. H_{ad} , OH^-_{ad} , O_{ad} etc to the anode surface / reaction sites and iv) in absence of mentioned steps even concentration polarization caused by gas diffusion outside anode may emerge as one of the crucial limiting factor affecting the anode performance.

Many researchers^{98, 99, 105, 107-109} have suggested the involvement of both interstitial hydrogen and hydroxyl ion formation at the Ni-YSZ interfaces as shown in [Figure 3.10](#). This is in agreement to the study reported by Dees et al¹¹⁰ in which OH^- species is found to form as an intermediate through AC impedance. Such reaction mechanism involves an initial adsorption of hydrogen on Ni surface which further accomplish the electrochemical reaction between adsorbed hydrogen and

Chapter - 3

oxygen ions. Successive impedance measurements suggest the intermediate formation and involvement of hydroxide ion on YSZ surface. The above reaction mechanism is further improved by ascertaining the significant role of water or oxygen- containing molecules in the fuel gas.

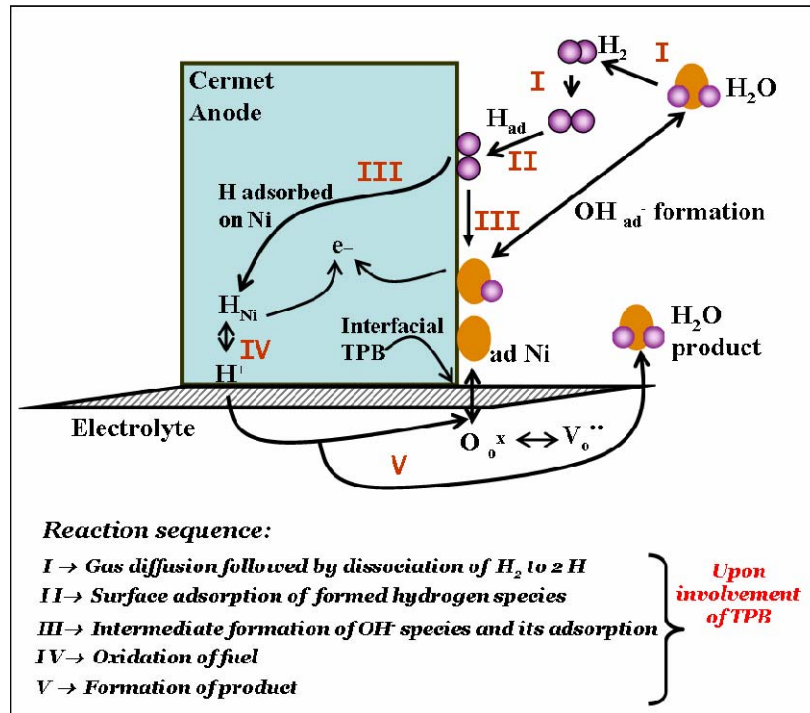


Figure 3.10: Schematic for possible reaction processes for H_2 oxidation at anode/electrolyte interface as proposed by Holtappels et al ⁹⁸⁻⁹⁹

Moisture in the fuel is found to provide adsorbed oxygen species on Ni surface and fuel oxidation is proved to be directly correlated with such oxygen activity on metal surface. However, such improved reaction mechanisms is found to be influenced by the surface contribution of both the metallic (Ni) and ceramic (YSZ) phase within the cermet anode i.e. triple contact points (Ni, YSZ and pores consisting of fuel gas) as the electrochemical active sites. Such two electrode reaction process for hydrogen oxidation is proposed by Jiang et al ^{97, 111} in which surface reactions are found to involve both Ni and YSZ species as shown in Figure 3.11. Initial adsorption of water from moist fuel occurs preferably on Ni surface which form OH-Ni as a

reaction entity. Charge transfer reactions at the active TPB sites are considered as the rate limiting steps. Microstructural optimization for enhancement of active TPB centres leads to accelerate the rate determining steps.

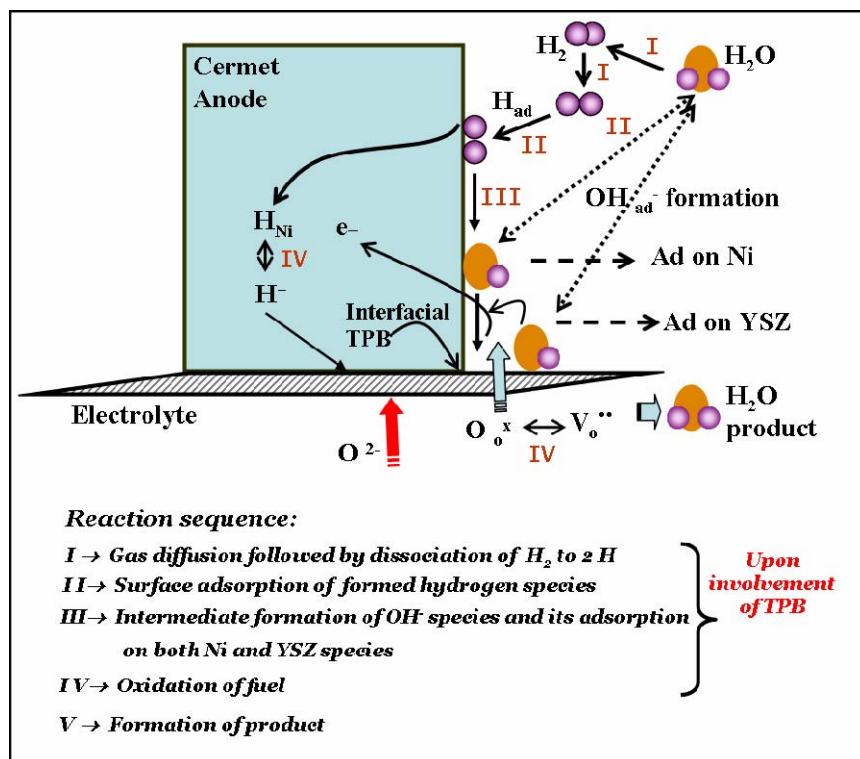


Figure 3.11: Schematic of fuel oxidation steps showing the involvement of both Ni and YSZ as effective centres for reaction sites as proposed by Jian et al^{97, 111}

A model for controlling concentration polarization is given by Williford et al.⁹⁶ Overpotentials related to concentration of active species can be controlled by means of two active phenomena, viz. competitive adsorption of reactants adjacent to TPB areas followed by slow surface diffusion to such reactive sites. Therefore, the researchers focus on the optimization of the reactive area, adsorption and surface diffusion at the anode/electrolyte interface.

Langmuir reaction model is developed by Ihara et al¹¹² as shown in Figure 3. 12 regarding the dependence of DC polarization and interfacial conductivity of Ni-YSZ cermet on partial pressure of hydrogen. The primary assumption is based on the

Chapter - 3

competitive adsorption equilibrium of H_2 , H_2O and O species on Ni surfaces at TPB and hence, the rate limiting step under such model is the Langmuir type reactions between H_{ad} with O_{ad} . In addition, adsorption of H_2 at the TPB is found to get effected by the nature anode/electrolyte interface. Therefore, from the aforementioned glimpse of research review, it can be concluded that, the principal focus towards understanding of anodic mechanisms is dependent on the rate of limiting step, acceleration of which leads to proper functioning of overall SOFC.

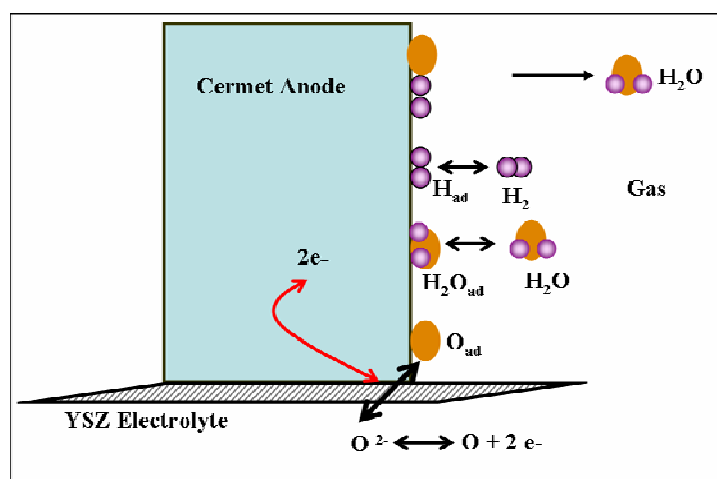


Figure 3.12: Langmuir reaction model developed by Ihara et al regarding correlation of interfacial conductivity with anodic electrochemical reactions¹¹²

3.3. Ni-YSZ Anode -- Applicability, Preparation, Challenges & Remedies

The discussions under section 3.1 and 3.2 clearly demonstrate that, Ni-YSZ cermet is currently the most preferred anode for SOFC application in which both Ni and YSZ phases are essentially immiscible and non-reactive over a very wide temperature range. This enables preparation of NiO-YSZ composite via conventional sintering followed by reduction upon exposure to fuel gases. The subsequent development of a very fine microstructure can be maintained during service for a relatively long period of time. However, the resulting high interfacial

surface area is susceptible to degradation and therefore creates a series of obstacles in achieving cells with high life cycle. The high susceptibility of Ni-YSZ to coking, re-oxidation in case of fuel loss and sensitivity to get poisoned by sulphur are the main concerns regarding the durability and degradation of such anode cermets. ¹¹³ Few weaknesses of Ni-YSZ anode are listed below: ¹¹⁴

- 1) The inability to oxidize commercial hydrocarbon fuels poses a problem for such Ni-based cermet anode. Owing to the formation of carbon as an intermediate, the structural integrity is disrupted. In recent years, modified cermets containing ceria and copper has been reported which are more tolerant to direct hydrocarbon reactions. ¹¹⁵ Trace amount of gold is also found to give Ni-catalysts tolerance to deactivation by carbon formation. ¹¹⁶⁻¹¹⁷
- 2) Intolerance of repeated oxidation is another weakness of Ni-based cermet anode. Upon exposure to fuel at high temperature, the Ni grains gradually change in morphology due to coarsening. Therefore, any subsequent re-oxidation cannot be accommodated in the available porosity of the cermet, and thereby the mechanical integrity and electrical continuity gets disrupted.
- 3) Performance of fuel cells with Ni-YSZ cells undergoes serious degradation upon subjecting to commercial natural gas or other hydrocarbon fuels. These gasses contain traces of impurities / additives which act as catalyst poisons. ¹¹⁸⁻¹¹⁹ Ni-cermets are most susceptible to sulphur (present as impurity) which cause serious deactivation and corrosion. ^{7, 120} It is observed that, practically at ~ 850°C, only ~ 5ppm of gaseous hydrogen sulphide from sulphur causes irreversible damage. ¹²¹ Therefore, commercialization of SOFC with natural gas/ hydrocarbon fuels demands a desulfuriser unit which again adds to maintenance cost.

A number of experiments have been performed to vary the fabrication of anode in terms of its preparation or configuration used in SOFC in order to minimize the

Chapter - 3

problems associated with such Ni-YSZ cermets. A two-layered anode structure for the anode-supported solid oxide fuel cell has been proposed by Virkar et al.¹²² in an attempt to minimize both the concentration and activation polarizations. Based on the requirement in SOFC, Ni-YSZ cermet is generally prepared by various techniques e.g., mixed oxide route,^{6, 123} co-precipitation route,¹²⁴ slurry coating route,¹²⁵ liquid dispersion route,^{126, 127} and heat decomposable aqueous salt solution route¹²⁸ where in almost all cases Ni is more or less uniformly distributed in YSZ matrix. A general processing route for the preparation of Ni-YSZ cermet based on conventional ceramic powder mixing process¹²⁹ is given in Figure 3.13.

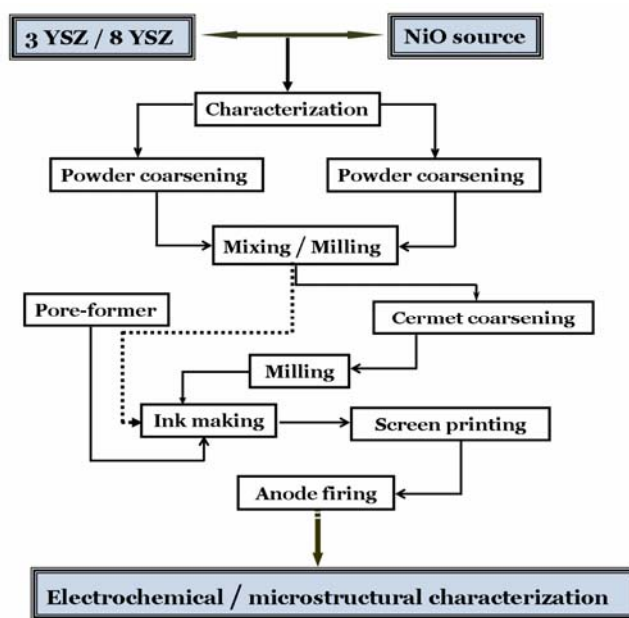


Figure 3.13: A general processing route for Ni-YSZ cermet preparation through conventional powder mixing method¹¹²

Apart from the aforementioned conventional preparation technique, a significant activity has been initiated in the recent years seeking to develop alternative fabrication routes that provide enhance catalytic activity. Towards such goal, the 'impregnation method' developed by Gorte et al. offers several significant advantages as a promising alternative for the design of new electrodes.¹³⁰ This

method involves the impregnation of liquid solutions into porous electrode scaffolds that have been preformed by co-sintering with the dense electrolyte. This enables to separate the sintering temperature of the electrolyte (YSZ) from the sintering temperature of the other electrode components. This allows a great flexibility in the choice of electrode material. The co-sintering YSZ in the electrode and in the electrolyte ensures a good connection between those two structures and limits interface resistances.¹³⁰

Corre et al. investigate SOFC anodes prepared by the infiltration of Mn containing perovskite.¹³¹ The study materials belongs to $\text{La}_{0.75}\text{Sr}_{0.25}\text{Cr}_{0.5}\text{Mn}_{0.5}\text{O}_3$ (LSCM) and $\text{La}_{0.33}\text{Sr}_{0.67}\text{Ti}_x\text{M}_{1-x}\text{O}_{3\pm\delta}$ (LSTM) family classes. Zhu et al.¹³² employed wet impregnation of $\text{La}_{0.75}\text{Sr}_{0.25}\text{Cr}_{0.5}\text{Mn}_{0.5}\text{O}_{3-\delta}$ (LSCM) based anode as well as cathodes onto dry pressed YSZ disks in order to fabricate symmetrical single cells for SOFC application. In another attempt for anode processing, Watanabe et al. used the impregnation method to incorporate metal catalysts such as Pt and Ru to Sm-doped CeO_2 anodes and Sr-doped LaMnO_3 cathodes, which lead to the significant reduction of the polarization losses of the electrodes.¹³³ Similar effect of impregnation of Pt and Pd particles on the electrode performance has also been reported by Sahibzada et al.¹³⁴ on $\text{La}_{0.6}\text{Sr}_{0.4}\text{Co}_{0.2}\text{Fe}_{0.8}\text{O}_3$ cathode and by Van Herle et al.¹³⁵ on Ni/TZ8Y cermet anodes. This implies that impregnation method could be used to deposit oxide particles into the Ni-YSZ cermet structure prior to the high-temperature sintering and reducing stages to produce a Ni-YSZ structure close to that created by the EVD and PEVD methods. Jiang et al.¹³⁶ offer manipulation of the electrode coating sintering profile and control the oxide phases by impregnating into the electrode coating. These features are found to significantly reduce the grain growth and agglomeration of the NiO and Ni phases during high-temperature sintering and reducing stages of the anode leading to significant

Chapter - 3

enhancement in the TPB areas and thus in the electrochemical activity of the electrode.¹³⁶

A promising approach of preparing interlayer anode is demonstrated by Muller et al.¹³⁷ in their innovative technique to develop multilayer anode. The process involves direct screen printing of anode paste onto electrolyte green tape followed by co-sintering. A low anode polarization resistance is recorded after relatively long-term exposure to anode-like environment which is largely attributed to the desirable anode/electrolyte adherence.

The overall electrical conductivity of Ni-YSZ cermet differs by several orders of magnitude as the fraction of coarse YSZ is raised from 0 to 100 vol %. This implies that the predominant conduction mechanism shifts from ionic to electronic as contagious phase changes gradually from YSZ to Ni. According to the requirement of anode for SOFC operation, Ni-YSZ should exhibit an electronic conductivity of $\sim 500 \text{ Scm}^{-1}$ at the operating temperature of 800°C . As electronic conductivity is governed by Ni phase, therefore a requisite vol % of Ni is necessary to fulfil the conductivity criteria. The contribution of each phase i.e Ni and YSZ is dependent on the resultant microstructure of the anode which is in turn governed by the processing technique. Klemenso et al.¹³⁸ reported the synthesis of Ni-YSZ cermet by Ni-impregnation technique as given in [Figure 3.14](#).

Ni-YSZ cermet prepared from mixtures of Ni powder ($d_{50} \sim 1 \mu\text{m}$) and YSZ powder ($d_{50} \sim 0.1 \mu\text{m}$) at volume ratios of Ni/YSZ: 31:69, 40:60, 61:39, 73:27 and 87:13 as reported by Koide et al.¹³⁹ are observed to have different microstructure as given in [Figure 3.15](#).

Li et al.¹⁴⁰ reported his work on the preparation of fibrous Ni-coated YSZ cermet with low Ni content used as SOFC anode. Uniform YSZ nano fibres are first synthesized by electro spinning of 8YSZ dispersion followed by electroless plating with a layer of Ni after sintering. The Ni-YSZ rod shaped nano fibres as shown in

Figure 3.16 are finally slurry coated onto a commercial half cell that was subsequently tested.

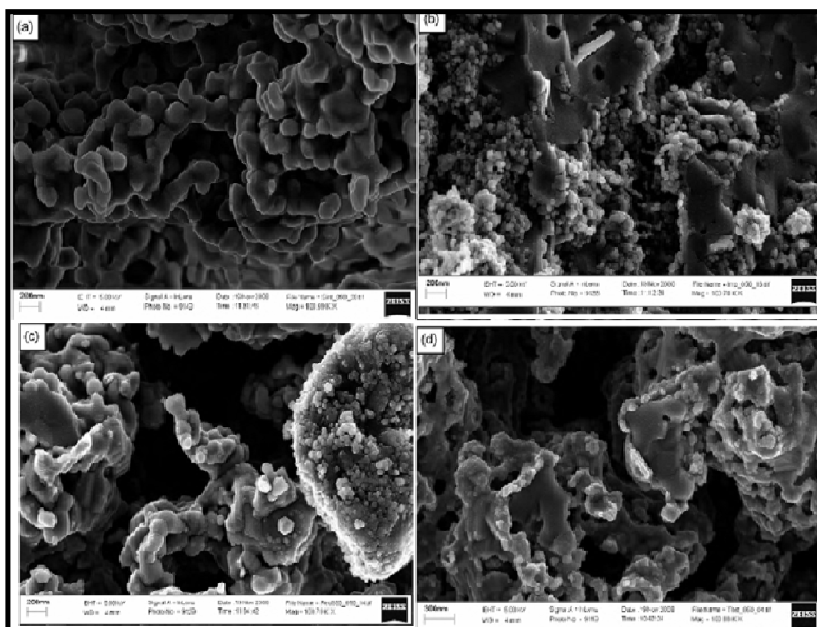


Figure 3.14: Micrographs of the Ni-YSZ prepared by Ni-impregnation with 13.33 vol% Ni. (a) Sintered, (b) infiltrated with NiO, (c) reduced, (d) after redox cycling¹³⁸

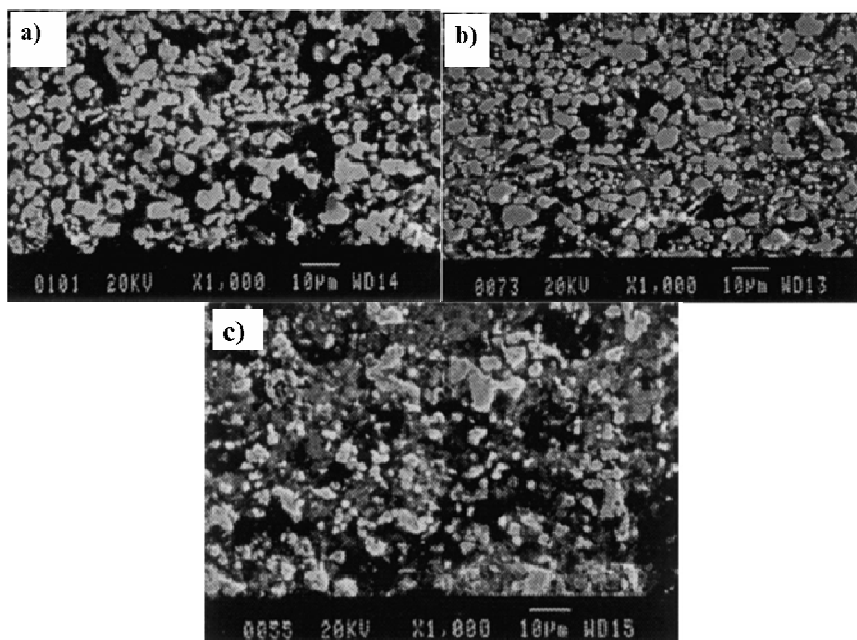


Figure 3.15: Micrographs of the Ni-YSZ reported by Koide et al. with Ni-YSZ ratio: (a) 87:13, (b) 61:39 (c) 40:60¹³⁹

Chapter - 3

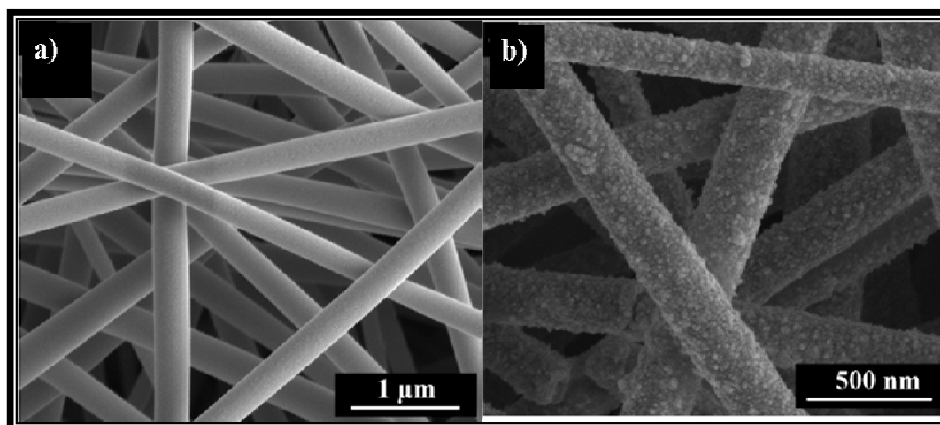


Figure 3.16: FESEM images of: (a) as spun YSZ fibres and (b) Ni-YSZ rod fibres ¹⁴⁰

A new preparation technique known as “nickel yttria reaction sintered zirconia” [NiYRSZ] is employed by Menzer et al ¹⁴¹ to form Ni-YSZ cermet anode as shown in Figure 3.17 for SOFC application. In the process, stabilization of zirconia by yttria occurs in the presence of nickel during the sintering process. Such technique is claimed to significantly reduce the cost of anode raw material thereby making the anode supported SOFC closer to commercial viability.

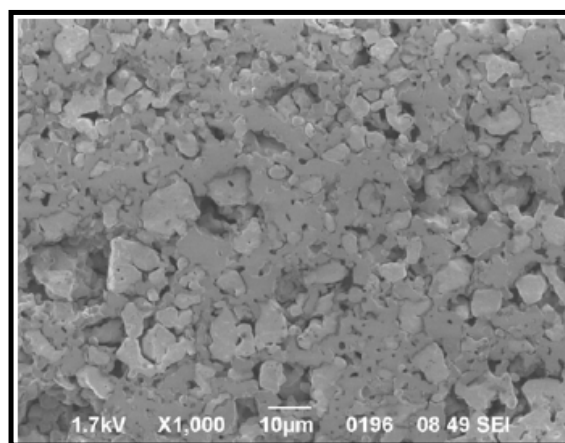


Figure 3.17: Cross-section of reduced NiYRSZ anode -- The lighter phase is the nickel oxide or nickel and the darker phase is the zirconia ¹⁴¹

Conventional solid state technique is also used by many of the research groups for synthesis of Ni-YSZ cermet anode. Such solid state processing involves

mixing of NiO and YSZ powders to prepare the anode cermet as reported by many research groups.¹⁴²⁻¹⁴⁵ The processing technique generates dispersed inhomogeneous distribution of Ni and YSZ phases throughout the matrix as given in [Figure 3.18](#). The processing technique of solid state mixing for anode preparation is simpler, cost effective, fast and up scalable. However, process optimization which includes repeatability and ordering in microstructural pattern is found to be ineffective. In recent years, high energy milling (HEM) is used instead of conventional ball milling in order to offer much better distribution of powder constituents.¹⁴⁵

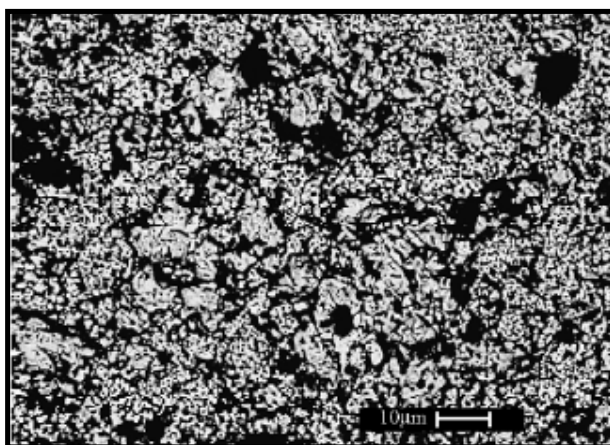


Figure 3.18: Micrograph of Ni-YSZ cermet prepared by conventional solid state technique¹⁴²

It can be said from the above discussions that, distribution of phases i.e. formation of microstructure is dependent on the involved processing techniques. The performance of Ni-YSZ cermet anodes therefore depends on the optimum phase distribution between Ni and YSZ particles that ensures the maximum electronic and ionic paths. Optimization of processing technique is the main governing factor on which performance of the anode depends.

3.4. Development of Anode-supported SOFCs with Structural Stability

From the development of commercially viable SOFC technologies, it has been possible to reduce the operating temperature from 1000°C to the range of

Chapter - 3

600-800°C. Low operating temperature not only widens the selection of components for SOFC, but also significantly reduces the risk of thermal shock and interface reactivity among cell components and thereby increases the cell performance stability and reliability. The choice of materials for the electrode supported structure is primarily related to a number of important considerations:

1. Interfacial reactions and reactivity among cell components during high temperature (in the range of 1300 to 1500°C), co-sintering should be avoided.
2. The anode support structure should have high strength as an important criterion which is needed for easy handling during the cell fabrication and stacking. Also, cell should be strong enough to withstand the thermal and mechanical stress during operation within temperature range of 700- 850°C.
3. Porosity of the associated electrodes (anode and cathode) should ensure high permeability of reactant and product gasses. Easy flow of such gases facilitates in reducing polarization losses through thicker (500 – 2000 μm) electrode support.
4. Sintering behaviour of the anode support and electrolyte must be closely matched to reduce bending and warping.
5. High electrical conductivity of anode is essential to reduce the ohmic loss of the cell and high thermal conductivity is vital for responding quickly to the temperature swing in the cell and stack.
6. Appropriate phase distribution / microstructure of anode is required to allow proper networking of TPB sites and are important for surface and shrinkage properties for easy deposition and densification of thin electrolyte layers.
7. Finally cost of the material and automation of the processing needs to be considered.

Performance of SOFCs is highly dependent on the cell components as listed above and techniques involved in the fabrication of such cells. A significantly large number of fabrication techniques are employed by various research groups in the

scientific community. Tape casting is an established industrial processing technique to make large and flat ceramic tapes, plates and laminated ceramic structure of any desired thickness based on the requirement, and thus has been employed widely for making anode-supported planar SOFC structure.^{129, 146-148} Will et al.¹⁴⁹ gave a detailed review on several techniques used for deposition / fabrication of thin and dense electrolyte layer on porous anode substrates. This includes vacuum slip casting,^{150, 151} magnetron sputtering¹⁵², spray deposition and spray pyrolysis,^{153, 154} screen printing,¹⁵⁵ electrophoretic deposition etc.¹⁵⁶⁻¹⁵⁹ For fabrication of smaller dimension cells (20-32 mm), anode-supported structures have been also prepared by powder compacting and die-pressing.^{160, 161} Dense electrolyte film as thin as 8 μm can be prepared on porous substrates by dry-pressing process.¹⁶² Yoo et al.¹⁶³ used compaction and drying of Ni-YSZ slurry to make 50 \times 50 mm size anode substrates. Anode-supported cells of 120 mm diameter are also successfully fabricated by die-pressing and coat mix technique.^{164, 165} Reports are also available on fabrication and performance of anode-supported tubular cell using extrusion technique by Song et al.¹⁶⁶

Apart from the role of Ni in the SOFC cermet anode, YSZ also renders significant contribution towards the optimization of anode as well as fabrication and stability of the developed anode-supported SOFCs.¹⁰⁷ In most of these applications, not only high ionic conductivity, but also better mechanical properties (flexural strength and fracture toughness) are required. In this group of ionic conductors, 8 mol % yttria stabilized zirconia (8YSZ) with cubic structure possesses highest ionic conductivity and good chemical stability over wide temperature and oxygen partial pressure range.¹⁶⁷ However, the low mechanical strength of such 8 YSZ hinders the fabrication of self supported electrolyte plate for use in planar SOFC systems.¹⁶⁸ Addition of second phase particles like alumina,^{168, 169}

Chapter - 3

neodymium titanate,¹⁷⁰ BaTiO₃¹⁷¹ or monoclinic zirconia¹⁷² improve mechanical strength of 8YSZ but at the same time can degrade electrical properties.^{5, 168, 169}

According to ZrO₂-Y₂O₃ phase diagram,¹⁷³ at stabilizer concentration of 3-7 mol% Y₂O₃, both cubic and tetragonal phases can be retained in the microstructure. The microstructure of these ceramics consists of a cubic phase matrix in which tetragonal phase is dispersed. This grade of ZrO₂-Y₂O₃ solid solution is termed partially stabilized zirconia (PSZ).¹⁷⁴ The presence of a significant volume fraction of metastable tetragonal phase gives good mechanical properties (strength and toughness) to the ceramic by a process known as 'transformation toughening'.¹⁷⁵

So the presence of tetragonal phase can improve mechanical properties of zirconia based solid electrolyse. As the maximum conductivity in ZrO₂-Y₂O₃ occurs at a concentration of around 8 mol% of yttria, the electrical conductivity of PSZ is lower than 8YSZ.¹⁷⁶ The addition of fine particles of PSZ enhanced the fracture toughness without significantly degrading the conductivity of 8 YSZ ceramics.¹⁷⁴ Innumerable studies have been performed on the behaviour of 3YSZ viz. induced stress by constrained sintering of PSZ,¹⁷⁷ hydrothermal ageing behaviour,¹⁷⁸ grain core and grain boundary dielectric/ electrical properties of 3YSZ¹⁷⁹ and finally fabricating 3YSZ in the form of thin film by radio frequency sputtering.¹⁸⁰

The important criteria of anode-supported SOFCs lie in the structural stability and performance reproducibility during redox (repeated reduction and oxidation) cycling processes caused due to accidental system shut down or system service requirement. According to the necessity, SOFC should able to sustain at least ~ 5 years of redox cycles without any significant performance degradation.¹⁸¹

The kinetics for reduction and re-oxidation cycle of Ni/NiO-YSZ cermet is studied by Tikekar et al.¹⁸² The reduction of NiO to Ni is found to be interface controlled, while the re-oxidation kinetics is the diffusion controlled phenomena. The volume change

Chapter - 3

associated with such cyclic redox process may either be reversible or irreversible depending upon the nature of phase distribution within the cermet which indicates its direct correlation with the processing parameters. The cermet in which the extent of irreversibility is more, rate of cell degradation is enhanced. In contrast, it is expected that if the processing parameters can be optimized in such a way that such associated volume change with redox cycling is minimum i.e. the process is reversible; it would enhance the anode life considerably.

It is therefore, apparent from above literature review that, in order to commercialize anode-supported planar SOFC, apart from erstwhile major issues, research work towards the development of anode component needs to be addressed critically. There exists innumerable specific requirements to be fulfilled by the anode in order to get accustomed for a selected fuel environment for SOFC operation. It is obvious that one particular anode composition will not likely to satisfy variable combinations of reactant gasses and other system applications. The basic aim should be therefore focussed on the optimization of certain selected anode materials which could fulfil all the necessities for a particular SOFC system and enable it to become commercially viable energy conversion device. Underneath the aforementioned background, the present research work is aimed towards the development of anode through a novel electroless technique, which is expected to resolve some of the shortcomings reported by other researchers. Additionally, effort will also be made towards the application of such developed anode for SOFC fabrication and study its operation for an extended duration.

Chapter - 3

3.5. References

1. S.C. Singhal, and K. Kendall, *High Temperature Solid Oxide Fuel Cells: Fundamentals, Design and Applications*. Elsevier, U. K. Editor. (2003).
2. A. Atkinson, S. Barnett, R.J. Gorte, J.T.S. Irvine, A.J. McEvoy, M. Mogensen, S.C. Singhal, J. Vohs, *Nature Materials*. **3**, 17–27 (2004).
3. S. McIntosh, R.J. Gorte, *Chemical Review*. **104**, 4845–4865 (2004).
4. S.P. Jiang, S.H. Chan, *Journal of Material Science*. **39**, 4405–4439 (2004).
5. N.Q. Minh, *Journal of the American Ceramic Society*. **76**, 563–588 (1993).
6. D.W. Dees, T.D. Claar, T.E. Easler, D.C. Fee, F.C. Mrazek, *Journal of the Electrochemical Society*, **134**, 2141–2146 (1987).
7. Y. Matsuzaki, I. Yasuda, *Solid State Ionics*. **132**, 261–269 (2000).
8. M. Mogensen, K. Kammer, *Annual Review of Material Research*. **33**, 321–331 (2003).
9. J.W. Fergus, *Solid State Ionics*. **177**, 1529–1541 (2006).
10. R.H. Cunningham, R.M. Ormerod, in: A.J. McEvoy (Ed.), *Proceedings of the Fourth European Solid Oxide Fuel Cells Forum*, volume 2, Lucerne, Switzerland, 10–14 July, p. 507 (2000).
11. W.Z. Zhu, S.C. Deevi, *Materials Science and Engineering A*, **362**, 228–239 (2003).
12. Jay Sanyal, Graham M. Goldin, Huayang Zhu, Robert J. Kee, *Journal of Power Sources*. **195**, 6671–6679 (2010).
13. Andrew S. Martinez, Jacob Brouwer, *Journal of Power Sources*. **195**, 7268–7277 (2010).
14. H. Itoh, T. Yamamoto, M. Mori, T. Horita, N. Sakai, H. Yokokawa, M. Dokiya, *Journal of the Electrochemical Society*. **144**, 641- 646 (1997).
15. T. Iwata, *Journal of the Electrochemical Society*. **143**, 1521- 1525 (1996).
16. S. Elangovan and A. Khandkar, in *Proceedings of the First International Symposium on ionic and mixed conducting ceramics*, October 16-17, Phoenix,

- AZ, T.A. Ramanarayanan and H. L. Tuller (eds.), Electrochemical Society, Pennington, NJ, p.122 (1991).
17. S. Murakami, Y. Akiyama, N. Ishida, T. Yasuo, T. Saito and N. Furukawa, in Proceedings of the 2nd International Symposium on Solid Oxide Fuel Cells, July 2-5, Athens, Greece, F. Grosz, P. Zegera, S. C. Singhal and O. Yamamoto (Eds.), Commission of the European Communities, Luxemburg, p-93 (1991).
18. T. Hikita, M. Hishinuma, T. Kawashima, I. Yasuda, T. Koyama and Y. Matsuzaki, in Proceedings of the 3rd International Symposium on Solid Oxide Fuel Cells, May 16-21, Honolulu, HI, S. C. Singhal and H. Iwahara (Eds.), Electrochemical Society, Pennington, NJ, p-632 (1993).
19. U. Martin, H. Boysen and F. Frey, *Acta Crystallographica Section B*. **49**, 403-413 (1993).
20. M. Mogensen, T. Lindegaard, U. R. Hansen, G. Mogensen, *Journal of Electrochemical Society*. **141**, 2122- 2128 (1994).
21. T. Takahashi, H. Iwahara, Y. Suzuki, in: Proceedings of the Third International Symposium on Fuel Cells, 16 - 20 June, Presses Academiques Europeennes, Bruxelles, p. 113 (1969).
22. B. C. H. Steele, I. Kelly, H. Middleton, R. Rudkin, *Solid State Ionics*. **28-30**, 1547-1552 (1988).
23. B. C. H. Steele, *Solid State Ionics*. **129**, 95-110 (2000).
24. Chunwen Sun, J. Sun, G. L. Xiao, H. R. Zhang, X. P. Qiu, H. Li, L. Chen, *The Journal of Physical Chemistry B*. **110**, 13445-13452 (2006).
25. N. V. Skorodumova, S. I. Simak, B. I. Lundqvist, I. A. Abrikosov, B. Johansson, *Physical Review Letter*. **89**, 166601: 1-166601: 4 (2002).
26. O. A. Marina, C. Bagger, S. Primdahl, M. Mogensen, *Solid State Ionics*. **123**, 199 - 208 (1999).
27. S. Primdahl, M. Mogensen, *Solid State Ionics*. 152-153, 597 - 608 (2002).

Chapter - 3

28. K. Ahn, H. P. He, J. M. Vohs, R. J. Gorte, *Electrochemical and Solid-State Letters*. **8**, A414–A417 (2005).
29. A. S. Aricò, D. La Rosa, M. Lo Faro, M. Minutoli, G. Monforte, V. Antonucci, A. Sin, *Electrochemical Society Transactions - The Electrochemical Society*. **25**, 2083-2090 (2009).
30. A. Fuerte, R. X. Valenzuela and L. Daza, *J. Power Sources*. **169**, 47-52 (2007).
31. A. Fuerte, R. X. Valenzuela and L. Daza, *Electrochemical Society Transactions - The Electrochemical Society*. **25**, 2173-2182 (2009).
32. Zhe Lu, Li Pei, Tian-min He, Xi-qiang Huang, Zhi-guo Liu, Yuan Ji, Xing-hai Zhao, Wen-hui Su, *Journal of Alloys and Compounds*, **334**, 299–303 (2002).
33. Zhen Xie, Changrong Xia, Mengying Zhang, Wei Zhu, Huanting Wang, *Journal of Power Sources*, **161**, 1056–1061(2006).
34. R. J. Gorte, H. Kim, J. M. Vohs, *Journal of Power Sources*. **106**, 10–15(2002).
35. H. Uchida, M. Sugimoto, M. Watanabe, in: H. Yokokawa, S.C. Singhal (Eds.), *Proceedings of the Seventh International Symposium on Solid Oxide Fuel Cells (SOFC VII)*, Tsukuba, Ibaraki, Japan, 3–8 June, p. 653 (2001).
36. Takashi Hibino, Atsuko Hashimoto, Masaya Yano, Masanori Suzuki, Mitsuru Sano, *Electrochimica Acta*. **48**, 2531-2537 (2003).
37. Steven McIntosh, John M. Vohs and Raymond J. Gorte, *Electrochemical and Solid-State Letters*. **6**, A240-A243 (2003).
38. S.J.A. Livermore, J.W. Cotton, R.M. Ormerod, in: S.C. Singhal, M. Dokiya (Eds.), *Proceedings of the Sixth International Symposium on Solid Oxide Fuel Cells (SOFC-VI)*, Honolulu, Hawaii, 17–22 October, p. 593 (1999).
39. Y. Matsuzaki, I. Yasuda, *Solid State Ionics*. **152–153**, 463 -468 (2002).
40. S. Wang, T. Kato, S. Nagata, T. Honda, T. Kaneko, N. Iwashita, M. Dokiya, in: A.J. McEvoy (Ed.), *Proceedings of the Fourth European Solid Oxide Fuel Cell Forum*, vol. 2, Lucerne, Switzerland, 10–14 July, p. 479 (2000).

41. J.C. Ruiz-Morales, J. Canales-Vázquez, J. Pena-Martínez, D.M. Lopez, P. Nunez, *Electrochimica Acta*. **52**, 278–284 (2006).
42. S.W. Tao, J.T.S. Irvine, *Nature Materials*. **2**, 320–323 (2003).
43. S. W. Zha, P. Tsang, Z. Cheng, Z. Cheng, M. L. Liu, *Journal of Solid State Chemistry*. **178** 1844–1850 (2005).
44. Y. H. Huang, R. I. Dass, J. C. Denyszyn, J. B. Goodenough, *Journal of the Electrochemical Society*. **153**, A1266–A1272 (2006).
45. Y. H. Huang, R. I. Dass, Z. L. Xing, J. B. Goodenough, *Science*. **312**, 254–257 (2006).
46. A.L. Sauvet, J. Fouletier, *Electrochimica Acta*. **47**, 987–995 (2001).
47. T. Ishihara, H. Matsuda, Y. Takita, *Journal of the American Chemical Society*. **116**, 3801–3803 (1994).
48. B. Rambabu, S. Ghosh, W. Zhao, H. Jena, *Journal of Power Sources*. **159**, 21-28 (2006).
49. K. Q. Huang, M. Feng, J. B. Goodenough, *Journal of the American Ceramic Society*. **79**, 1100–1104 (1996).
50. K. Q. Huang, M. Feng, J.B. Goodenough, M. Schmerling, *Journal of Electrochemical Society*. **143**, 3630–3636 (1996).
51. K. Huang, M. Feng, J.B. Goodenough, C. Milliken, *Journal of Electrochemical Society*. **144**, 3620–3624 (1997).
52. Fanglin Chen, Meilin Liu, *Journal of Solid State Electrochemistry*. **3**, 7–14 (1998).
53. H. L. Tuller, *Journal of Physics and Chemistry of Solids*. **55**, 1393–1404 (1994).
54. B. J. Wuensch, K. W. Eberman, C. Heremans, E. M. Ku, P. Onnerud, E. M. E. Yeo, S. M. Haile, J. K. Stalick, J. D. Jorgensen, *Solid State Ionics*. **129**, 111–133 (2000).
55. M. Pirzada, R.W. Grimes, L. Minervini, J.F. Maguire, K.E. Sickafus, *Solid State Ionics*. **140**, 201–208 (2001).
56. S. Kramer, M. Spears, H.L. Tuller, *Solid State Ionics*. **72**, 59–66 (1994).
57. S. A. Kramer, H. L. Tuller, *Solid State Ionics*. **82**, 15–23 (1995).

Chapter - 3

58. O. Porat, C. Heremans, H.L. Tuller, *Solid State Ionics*. **94**, 75–83 (1997).
59. P. Holtappels, F.W. Poulsen, M. Mogensen, *Solid State Ionics*. **135**, 675–679 (2000).
60. M. Tournoux, M. Ganne, Y. Piffard, *Journal of Solid State Chemistry*. **96**, 141–153 (1992).
61. S. W. Tao, J.T.S. Irvine, *The Chemical Record*. **4**, 83–95 (2004).
62. P. R. Slater, J.T.S. Irvine, *Solid State Ionics*. **120**, 125–134 (1999).
63. P. R. Slater, J. T. S. Irvine, *Solid State Ionics*, **124**, 61–72 (1999).
64. A. Kaiser, J. L. Bradley, P. R. Slater, J. T. S. Irvine, *Solid State Ionics*. **135**, 519–524 (2000).
65. Lan Zhang, San Ping Jiang, Hong Quan He, Xinbing Chen, Jan Ma, Xiao Chao Song, *International Journal of Hydrogen Energy*. **35**, 12359- 12368 (2010).
66. H.P. He, R.J. Gorte, J.M. Vohs, *Electrochemical and Solid-State Letters*. **8**, A279–A280 (2005).
67. R. Mukundan, E. L. Brosha, F. H. Garzon, *Electrochemical and Solid-State Letters*. **7**, A5–A7 (2004).
68. S.W. Zha, Z. Cheng, M. L. Liu, *Electrochemical and Solid-State Letters*. **8**, A406–A408 (2005).
69. Z. Cheng, S.W. Zha, M.L. Liu, *Journal of the Electrochemical Society*. **153**, A1302–A1309 (2006).
70. J. N. Armor, *Applied Catalysis A*. **176**, 159-176 (1999).
71. H. C. Maru, B. S. Baker, *Progress in Batteries and Solar Cells*. **5**, 264-272 (1984).
72. E. Perry Murray, T. Tsai, S. A. Barnett, *Nature*. **400**, 649 -651 (1999).
73. E. Perry Murray, S. A. Barnett, in SOFC VI, Proc. 6th International Symposium, Electrochemical Society, Pennington, NJ, Vol. 99-19, p. 1001 (1999).
74. S. Park, J. M. Vohs, R. J. Gorte, *Nature*. **404**, 265–267 (2000).

75. R. J. Gorte, S. Park, J. M. Vohs, C. Wang, *Advanced Materials*. **12**, 1465–1469 (2000).
76. R. J. Gorte, J. M. Vohs, *Journal of Catalysis*. **216**, 477–486 (2003).
77. H. P. He, Y. Y. Huang, J. M. Vohs, R. J. Gorte, *Solid State Ionics*. **175**, 171–176 (2004).
78. O. A. Marina, C. Bagger, S. Primdahl, M. Mogensen, *Solid State Ionics*. **123**, 199 - 208 (1999).
79. A. Sauvet, J. T. S. Irvine, *Fuel Cells*. **1**, 205 - 210 (2001).
80. Hongpeng He, John M. Vohs, Raymond J. Gorte, *Journal of Power Sources*. **144**, 135–140 (2005).
81. H. He, J. M. Vohs, R. J. Gorte, *Journal of Electrochemical Society*. **150**, A1470 - A1475 (2003).
82. S. McIntosh, H. He, S. I. Lee, O. C. Nunes, V.V. Krishnan, J.M. Vohs, R.J. Gorte, *Journal of Electrochemical Society*. **151**, A604 - A608 (2004).
83. S. McIntosh, J. M. Vohs, R. J. Gorte, *Electrochimica Acta*. **47**, 3815–3821 (2002).
84. S.-I. Lee, S. McIntosh, J.M. Vohs, R.J. Gorte, in: S.C. Singhal, M. Dokiya (Eds.), *Proceedings of the SOFC VIII, The Electrochemical Society Proceedings Series, PV 2003-07, Pennington, NJ, p. 865* (2003).
85. Z.H. Bi, J.H. Zhu, *Journal of Power Sources*. **195**, 3097–3104 (2010).
86. Zhicheng Wang, Wenjian Weng, Kui Cheng, Piyi Du, Ge Shen, Gaorong Han, *Journal of Power Sources*. **179**, 541–546 (2008).
87. A. Fuerte, R. X. Valenzuela, M. J. Escudero L. Daza, *Journal of Power Sources*, **196**, 4324–4331 (2011).
88. Xiao-Feng Ye, Bo Huang, S.R. Wang, Z.R. Wang, L. Xiong, T.L. Wen, *Journal of Power Sources*. **164**, 203–209 (2007).
89. San Ping Jiang, Yinmei Ye, Tianmin He, See Boon Ho, *Journal of Power Sources*. **185**, 179–182 (2008).

Chapter - 3

90. Zhiming Wang, Ye Tian, Yongdan Li, *Journal of Power Sources*. **196**, 6104–6109 (2011).
91. Bo-Kuai Lai, Kian Kerman, Shriram Ramanathan, *Journal of Power Sources*. **196**, 6299–6304 (2011).
92. Yan Liu, Yaohui Bai, Jiang Liu, *Journal of Power Sources*, **196**, 9965– 9969 (2011).
93. Wei Zhu, Changrong Xia, Jue Fan, Ranran Peng, Guangyao Meng, *Journal of Power Sources*. **160**, 897–902 (2006).
94. Haruo Kishimoto, Katsuhiko Yamaji, Teruhisa Horita, Yueping Xiong, Natsuko Sakai, Manuel E. Brito, Harumi Yokokawa, *Journal of Power Sources*. **172**, 67–71 (2007).
95. Jenshi B. Wang, Jiun-Ching Jang, Ta-Jen Huang, *Journal of Power Sources*. **122**, 122–131 (2003).
96. R. E. Williford, L. A. Chick, G. D. Maupin, S. P. Simner, J. W. Stevenson, *Journal of the Electrochemical Society*. **150**, A1067–A1072 (2003).
97. S. P. Jiang, S. P. S. Badwal, *Solid State Ionics*. **123**, 209–224 (1999).
98. M. Mogensen, S. Skaarup, *Solid State Ionics*. **86–88**, 1151–1160 (1996).
99. P. Holtappels, I. C. Vinke, L. G. J. de Haart, U. Stimming, *Journal of the Electrochemical Society*. **146**, 2976–2982 (1999).
100. M. Brown, S. Primdahl, M. Mogensen, *Journal of the Electrochemical Society*. **147**, 475–485 (2000).
101. J. Mizusaki, H. Takagawa, K. Isobe, M. Tajika, I. Koshiro, H. Maruyama, K. Hirano, *Journal of the Electrochemical Society*. **141**, 1674–1683 (1994).
102. D. Kek, N. Bonanos, M. Mogensen, S. Pejovnik, *Solid State Ionics*. **131**, 249–259 (2000).
103. Martin Andersson, Jinliang Yuan, Bengt Sunden, *Applied Energy*. **87**, 1461–1476 (2010).
104. B. de Boer, M. Gonzales, H. J. M. Bouwmeester, H. Verweij, *Solid State Ionics*, **127**, 269–276 (2000).

105. P. Holtappels, L.G.J. de Haart, U. Stimming, *Journal of the Electrochemical Society*. **146**, 1620–1625 (1999).
106. B. Bieberle, L. P. Meier, L. J. Gauckler, *Journal of the Electrochemical Society*. **148**, A646–A656 (2001).
107. N.Q. Minh, T. Takahashi, *Science and Technology of Ceramic Fuel Cells*, Elsevier, New York, USA, (1995).
108. R. J. Aaberg, R. Tunold, S. Tjelle, and R. Ødegård, *High Temperature Electrochemistry: Ceramics and Metals*, 17th Risø International Symposium on Materials Science, F. W. Poulsen, N. Bonanos, S. Linderoth, M. Mogensen, and B. Zachau-Christiansen, Editors, Risø National Laboratory, Roskilde, Denmark, p. 511 (1996).
109. S. Sunde, *Electrochimica Acta*, **42**, 2637-2648 (1997).
110. D.W. Dees, U. Balachandran, S.E. Dorris, J.J. Heiberger, C.C. McPheeters and J.J. Picciolo, in the Proceedings of the 1st International Symposium on Solid Oxide Fuel Cells, October 16-18, Hollywood, FL, S.C.Singhal (Eds.), Electrochemical Society, Pennington, NJ, p-317 (1989).
111. S.P. Jiang, S.P.S. Badwal, *Journal of the Electrochemical Society*. **144**, 3777–3784 (1997).
112. M. Ihara, T. Kusano, C. Yokoyama, *Journal of the Electrochemical Society*. **148**, A209–A219 (2001).
113. Peter Holtappels, U. Vogt and T. Graule, *Advanced Engineering Materials*, **7**, 292 - 302 (2007).
114. K. Ravindranathan Thampi, A. J. McEvoy, B. El-Roustop, Lucern, Abstract [Anodes], Proceedings of 8th European SOFC Forum (2008).
115. H. Kim, J. M. Vohs and R. J. Gorte, *ChemComm Communication*. 2334-2335 (2001).
116. F. Besenbacher, I. Chorkendorff, B. S. Clausen, B. Hammer, A. M. Molenbroek, J. K. Nørskov and I. Stensgaard, *Science*, **279**, 1913- 1915 (1998).

Chapter - 3

117. J. Triantafyllopoulos and S. G. Neophytides, *Journal of Catalysis*, **239**, 187-199 (2006).
118. S. Zha, Z. Cheng, and M. Liu, *Journal of the Electrochemical Society*. **154**, B201-B206 (2007).
119. K. Sasaki, K. Susuki, A. Iyoshi, M. Uchimura, N. Imamura, H. Kusaba, Y. Teraoka, H. Fuchino, K. Tsujimoto, Y. Uchida and N. Jingo, *Journal of the Electrochemical Society*. **153**, A2023 - A2029 (2006).
120. Jens F.B. Rasmussen, Anke Hagen, *Journal of Power Sources*. **191**, 534–541 (2009).
121. K. Sasaki, K. Susuki, A. Iyoshi, S. Adachi, M. Uchimura, N. Imamura, Y. Shiratori, H. Kusaba and Y. Teraoka, 7th. European SOFC Forum, Luzern, B111 (2006).
122. A. V. Virkar, J. Chen, C. W. Tanner, J. W. Kim, *Solid State Ionics*. **131**, 189-198 (2000).
123. Young Min Park, Gyeong Man Choi, *Solid State Ionics*. **120**, 265–274 (1999).
124. N. M. Sammes, M. Brown, I. W. M. Brown, *Journal of Material Science*. **31**, 6069-6072 (1996).
125. J. Macek, M. Marinsek, 2nd European SOFC Forum, Proceedings vol.1 p. 341, Osolo, (1996).
126. T. Kawada, N. Sakai, H. Yokokawa, M. Dokiya, *Solid State Ionics*. **40/41**, 402-406 (1990).
127. S. K. Pratihari, R. N. Basu, H. S. Maiti, *Transaction of Indian Ceramic Society*. **56** (1997) 85-.
128. S. K. Pratihari, R. N. Basu, S. Mazumdar, H. S. Maiti, Solid Oxide Fuel Cells (SOFC VI), Proceedings vol. 99-19, p. 513, Electrochemical Society, (1999).
129. San Ping Jiang, Siew Hwa Chan, *Journal of Materials Science*, **39**, 4405 – 4439 (2004).
130. J. M. Vohs, and R. J. Gorte, *Advance Materials*. **21**, 943-956 (2009).

131. G. Corre, G. Kim, M. Cassidy, R. J. Gorte, J. M. Vohs, and J. T. S. Irvine, *ECS Transactions The Electrochemical Society*. **25**, 2201-2211 (2009).
132. Xingbao Zhu, Zhe Lü, BoWei, Xiqiang Huang, Yaohui Zhang, Wenhui Su, *Journal of Power Sources*. **196**, 729–733 (2011).
133. M. Watanabe, H. Uchida, M. Shibata, N. Mochizuki, and K. Amikura, *Journal of the Electrochemical Society*. **141**, 342 -346 (1994).
134. M. Sahibzada, S. J. Benson, R. A. Rudkin, and J. A. Kilner, *Solid State Ionics*, **113-115**, 285-290 (1998).
135. J. van Herle, R. Ihringer, and A. J. McEvoy, in *Solid Oxide Fuel Cells V*, U. Stimming, S. C. Singhal, H. Tagawa, and W. Lehnert, Editors, PV 97-40, The Electrochemical Society Proceedings Series, Pennington, NJ. p. 565 (1997).
136. San Ping Jiang, Yvonne Y. Duan and Jonathan G. Love, *Journal of the Electrochemical Society*. **149**, A1175-A1183 (2002).
137. A.C. Muller, D. Herbstritt, E.I. Tiffée, *Solid State Ionics*. **152–153**, 537-542 (2002).
138. Trine Klemenso, Karl Thydén, Ming Chen, Hsiang-Jen Wang, *Journal of Power Sources*. **195**, 7295–7301 (2010).
139. Hideto Koide, Yoshiyuki Someya, Toshihiko Yoshida, Toshio Maruyama, *Solid State Ionics*. **132**, 253–260 (2000).
140. Luping Li, Peigen Zhang, Ranran Liu, S. M. Guo, *Journal of Power Sources*. **196**, 1242–1247 (2011).
141. Sophie Menzer, Grover Coors, Dan Storjohann, and Dustin Beeaff, Abstract [Anodes], Proceedings of 8th European SOFC Forum (2008).
142. Swadesh K. Pratihari, A. Dassharma, H.S. Maiti, *Materials Research Bulletin*. **40**, 1936–1944 (2005).
143. Xiqiang Huang, Zhiguo Liu, Zhe Lu, Li Pei, Ruibin Zhu, Yuqiang Liu, Jipeng Miao, Zhiguo Zhang, Wenhui Su, *Journal of Physics and Chemistry of Solids*. **64**, 2379–2384 (2003).

Chapter - 3

144. G. Matula, T. Jardiel, R. Jimenez, B. Levenfeld, A. Várez, *Archives of Material Science and Engineering*. **32**, 21-25 (2008).
145. Hyoup Je Cho, Gyeong Man Choi, *Journal of Power Sources*. **176**, 96–101 (2008).
146. Jung-Hoon Song, Nigel M. Sammes, Abstract [Manufacturing], section B05, Proceedings of 8th European SOFC Forum (2008).
147. R. N. Basu, A. Das Sharma, A. Dutta and J. Mukhopadhyay, *International Journal of Hydrogen Energy*. **33**, 5748-5754 (2008).
148. Shiru Le, Ke Ning Sun, Naiqing Zhang, Xiaodong Zhu, Hanxiao Sun, Yi Xing Yuan, Xiaoliang Zhou, *Journal of Power Sources*. **195**, 2644–2648 (2010).
149. J. Will, A. Mitterdorfer, C. Kleinlogel, D. Perednis and L. J. Gauckler, *Solid State Ionics*. **131**, 79- 96 (2000).
150. D. Ghosh, G. Wang, R. Brule, E. Tang and P. Huang, in SOFC-VI, edited by S. C. Singhal and M. Dokiya (Electrochemical Society, Pennington, NJ) Vol. 99–19, p. 822 (1999).
151. Rajendra N. Basu, Günter Blass, Hans Peter Buchkremer, Detlev Stöver, Frank Tietz, Egbert Wessel, Izaak C. Vinke, *Journal of the European Ceramic Society*. **25**, 463–471 (2005).
152. P. K. Srivastava, T. Quach, Y. Y. Duan, R. Donelson, S. P. Jiang, F. T. Ciacchi and S. P. S. Badwal, *Solid State Ionics*. **99**, 311-319 (1997).
153. Y. J. Leng, S. H. Chan, K. A. Khor, S. P. Jiang and P. Cheang, *Journal of Power Sources*. **117**, 26-34 (2003).
154. D. Perednis and L. J. Gauckler, *Solid State Ionics*. **166**, 229-239 (2004).
155. C. R. Xia and M. Liu, *Journal of the American Ceramic Society*. **84**, 1903-1905 (2001).
156. T. Ishihara, K. Sato, Y. Mizuhara and Y. Takita, *Chemistry Letters*. **21**, 943-946 (1992).

157. J. Will, M. K. M. Hruschka, L. Gubler and L. J. Gauckler, *Journal of the American Ceramic Society*. **84**, 328-332 (2001).
158. P. Sarkar and H. Rao, in SOFC-VIII, edited by S. C. Singhal and M. Dokiya (Electrochem. Soc., Pennington, NJ) Vol. 2003–07, p. 135 (2003).
159. Rajendra N. Basu, Clive A. Randall and Merrilea J. Mayo, *Journal of the American Ceramic Society*. **84**, 33–40 (2001).
160. J. W. Kim, A. V. Virkar, K. Z. Fung, K. Mehta and S. C. Singhal, *Journal of the Electrochemical Society*. **146**, 69-78 (1999).
161. P. Charpentier, P. Fragnaud, D. M. Schleich and E. Gehain, *Solid State Ionics*. **135**, 373- 380 (2000).
162. C. Xia and M. Liu, *ibid.*, 144 (2001) 249. change
163. Y. S. Yoo, J. H. Koh, J. W. Park and H. C. Lim, in 5th European SOFC Forum, edited by J. Huijsmans (European Fuel Cell Group, Lucerne, Switzerland) p. 191 (2002).
164. P. Holtappels, T. Graule, B. Gut, U. Vogt, L. Gauckler, M. Jorger, D. Perednis, K. Honeffer, G. Robert, S. Rambert and A. J. Mcevoy, in SOFC-VIII, edited by S. C. Singhal and M. Dokiya (Electrochem. Soc., Pennington, NJ) Vol. 2003–07, p. 1003 (2003).
165. D. Simwonis, H. Thulen, F. J. Dias, A. Naoumidis and D. Stover, *Journal of Material Processing Technology*. **92/93**, 107-111 (1999).
166. R. H. Song, K. S. Song, Y. E. Ihm and H. Yokokawa, in SOFC-VII, edited by H. Yokokawa and S. C. Singhal (Electrochem. Soc., Pennington, NJ) Vol. 2001–16, p. 1073 (2001).
167. S. P. S. Badwal, *Solid State Ionics*. **52**, 23-32 (1992).
168. A.J. Feighery, J.T.S. Irvine, *Solid State Ionics*. **121**, 209 -216 (1999).
169. M. Mori, T. Abe, H. Itoh, O. Yamamoto, Y. Takeda, T. Kawahara, *Solid State Ionics*. **74**, 157- 164 (1994).

Chapter - 3

170. X.Q. Liu, X.M. Chen, *Journal of the American Ceramic Society*. **88**, 456-458 (2005).
171. X.Q. Liu, X.M. Chen, *Ceramics International*. **30**, 2269 -2275 (2004).
172. H. Ruf, A.G. Evans, *Journal of the American Ceramic Society*. **66**, 328 -332 (1982).
173. H.G. Scott, *Journal of Material Science*. **10**, 1527- 1535 (1975).
174. E.C. Subbarao, Zirconia—an overview, in: A.H. Heuer, L.W. Hobbs (Eds.), *Advances in Ceramics, Science and Technology of Zirconia*, Vol. 3, Elsevier, Amsterdam, pp. 1–24 (1981).
175. R.H.J. Hannink, P.M. Kelly, B.C. Muddle, *Journal of the American Ceramic Society*. **83**, 461- 487 (2000).
176. V.V. Kharton, F.M.B. Marques, A. Atkinson, *Solid State Ionics*. **174**, 135-149 (2004).
177. Alan Atkinson, Jung-Sik Kim, Robert Rudkin, Samuel Taub and Xin Wang, *Journal of the American Ceramic Society*. **94**, 717–724 (2011).
178. Anish Paul, Bala Vaidhyanathan and Jon G. P. Binner, *Journal of the American Ceramic Society*. **94**, 2146–2152 (2011).
179. Nicola H. Perry, Thomas O. Mason, *Solid State Ionics*. **181**, 276–284 (2010).
180. Bor Yam Liaw, Richard E. Rocheleau, Qing-Hua Gao, *Solid State Ionics*. **92**, 85-89 (1996).
181. G. Robert, A. Kaiser, K. Honegger and E. Batawi, in 5th European SOFC Forum, edited by J. Huijsmans (European SOFC Forum, Lucerne, Switzerland) p. 116 (2002).
182. N. M. Tikekar, T. J. Armstrong and A. V. Virkar, in “SOFC-VII,” edited by S. C. Singhal and M. Dokiya (Electrochem. Soc., Pennington, NJ) Vol. 2003–07, p. 670 (2003).

~

C *HAPTER-4*

Experimental

Chapter - 4

This chapter provides details account of the experimental procedures followed in this research work. Synthesis of anode powders and the corresponding fabrication of single cell entail certain basic preparation technique. The prepared cermet anodes as well as the fabricated single cells are required to be examined in series of various characterization techniques viz. physical properties measurement, microstructural evaluation, electrical, thermal, electrochemical property evaluation and several others. The particulars of each process are depicted in the subsequent sections.

4.1. Preparation of Ni-YSZ Cermet Powder

The present research work is particularly aimed at the synthesis of nickel – 8 mol % yttria stabilized zirconia (Ni-YSZ) powder by ‘electroless technique’. However, for comparison, conventional solid state is also employed for the preparation of Ni-YSZ cermet.

4.1.1. Solid state technique

Conventional solid state technique involves mixing of 8 mol % yttria stabilized zirconia (YSZ) [Tosoh Corporation, Japan] with nickel oxide (NiO) powder [Novamet Speciality products, USA] through ball milling under methanol using zirconia (ZrO_2) as the grinding medium. The milling was continued at a fixed speed of 45 rpm for 12-14 h. The schematic of conventional solid state synthesis is shown in [Figure 4.1](#).

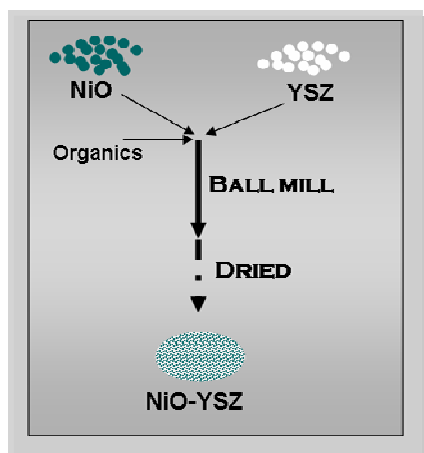


Figure 4.1: Schematic representation of conventional solid state synthesis

Chapter - 4

The slurry mixture formed after milling is allowed to dry in an oven at 50-60°C for 10-12h after which the conventional anode (NiO-YSZ) powder is obtained. Under the present investigation, the Ni content in the cermets was varied in the range of 10 to 40 vol %. The overall batch formulations for preparing conventional anode cermet are presented in Table 4.1.

Table 4.1: Batch compositions of NiO-YSZ anode cermet prepared by Conventional solid state technique

Sl. No.	Anode composition (vol %)		Amount of precursors (per 50 g batch)		Grinding media
	Nickel (Ni)	Ytria stabilized zirconia (YSZ)	NiO content (g)	YSZ content (g)	
1	10.0	90.0	9.04	42.89	ZrO ₂ balls in methanol
2	12.5	87.5	11.17	41.22	
3	15.0	85.0	13.25	39.59	
4	17.5	82.5	15.28	37.99	
5	20.0	80.0	17.30	36.40	
6	25.0	75.0	21.12	33.40	
7	30.0	70.0	24.80	30.50	
8	40.0	60.0	31.77	25.08	

4.1.2. Electroless technique

One of the primary objectives of this study is to synthesize Ni-YSZ cermet anode powder using electroless deposition technique. Preparation of such Ni-YSZ powder by electroless technique involves two important steps:

- initial sensitization of YSZ particulates by surface adsorption of metallic palladium (Pd⁰)
- in-situ reduction of Ni²⁺ from its salt solution to metallic nickel (Ni⁰) and its subsequent deposition onto sensitized YSZ powders.

The former process is an example of physical adsorption, whereas, the latter step is carried out through in-situ chemical reduction process leading to the particulate deposition. To facilitate effective sensitization, the as-received YSZ powder ($d_{50} \sim 0.2 \mu\text{m}$) is heat treated at 900°C (followed by grinding) so as to increase the d_{50}

value to $\sim 27 \mu\text{m}$. In the present investigation, the sensitization of YSZ precursor is carried out through two different techniques viz. a) ball milling and b) high energy ultrasonification.

4.1.2.1. Ball mill technique for YSZ sensitization

The YSZ sensitization was initiated by pouring the required amount of the processed YSZ powders into polypropylene jars containing redox mixture of palladium chloride [sd fine-chem Limited, India, 99.5 %] and stannous chloride [Merck, India, 99.5 %] solutions. Metallic palladium (Pd^0) was produced in-situ through the following redox reaction:



The polypropylene jars containing the redox mixture and treated YSZ was then subjected to ball milling using zirconia balls as the milling media for 15 h. During milling, the powder to milling media ratio was maintained at 0.45, and the rotating speed was varied in the range of 25 – 65 rpm. For complete reduction of Pd^{2+} in the sensitized bath, the ratio of PdCl_2 : SnCl_2 was kept at 1:3. The sensitized YSZ after milling was further equilibrated with the redox mixture for a pre-determined period of time (25 – 2000 min) in order to have effective adsorption of Pd^0 onto YSZ powder. In order to determine the time dependent concentration of adsorbed Pd^0 on YSZ surface, a certain quantity of aliquot from the supernatant solution of the sensitized bath was collected at a definite interval of time and the remnant concentration of Pd^{2+} in the supernatant solution was measured with the help of an Inductive Coupled Plasma Atomic Emission Spectrophotometer, ICP-AES (Kleve, Germany). Concentration of the adsorbed Pd^0 was calculated from the difference between initial Pd^{2+} and remnant Pd^{2+} (in the supernatant liquid) concentration. It had been taken into consideration that the total Pd^0 formed during the sensitization process was adsorbed on YSZ surface provided it was allowed to attain transient equilibrium. After the sensitization is complete, any unreduced Pd^{2+}

Chapter - 4

present in the medium was removed through siphoning of the supernatant liquid and subsequent thorough washing of the sensitized mass until it is free from Pd^{2+} ions (as evidenced by chemical analysis).

An electroless bath containing aqueous solution of nickel nitrate hexahydrate [sd fine chem, India, 99.5 %] was prepared for the deposition of Ni particulates onto sensitized YSZ particulates. A process flow chart for the synthesis of Ni-YSZ cermets by electroless technique with YSZ sensitized by ball milling is shown in Figure 4.2.

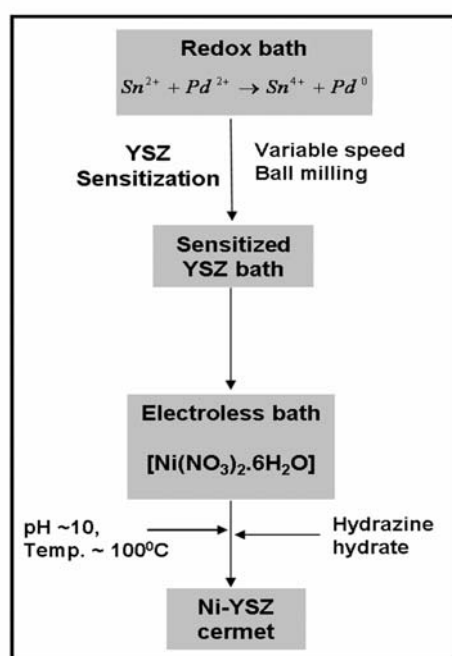


Figure 4.2: Process flow chart for ball mill assisted electroless technique

The sensitized YSZ particles were poured in the reaction bath containing Ni^{2+} salt solution for electroless deposition. The nickel concentrations in the bath were kept in such amounts so as to vary the Ni content in the ultimate cermet in the range between 5 and 40 vol%. During deposition, a pH value of ~ 10 and a bath temperature of $\sim 100^\circ\text{C}$ were maintained. The reduction of Ni^{2+} was carried out by in-situ liberation of nascent hydrogen generated by quantified addition of hydrazine hydrate. After complete reduction of Ni^{2+} to metallic Ni and precipitation of the powder ², the dissolved ammonia was completely washed with distilled

water and the clear supernatant solution was siphoned out. The precipitated black mass was finally dried in oven at $\sim 100^{\circ}\text{C}$ to obtain Ni-YSZ cermet powder in the as-synthesized condition.

4.1.2.2. High energy ultrasonification technique for YSZ sensitization

The adsorption study was carried out with the help of a high energy ultrasonifier (BRANSON, SONIFIER 450) with an adjustable agitation frequency. In this regard, experiments were performed using YSZ powder of three different particle sizes namely: a) as-received YSZ powder from Tosoh Corporation, Japan ($d_{50} \sim 0.2 \mu\text{m}$), b) heat treated YSZ from Tosoh Corporation, Japan ($d_{50} \sim 27 \mu\text{m}$ and henceforth referred to as YSZ-Tosho HT) and b) FYT from Unitech Corporation, UK ($d_{50} \sim 3 \mu\text{m}$ and henceforth referred to as YSZ-Unitec). The required amount of YSZ powder was added into a redox bath containing 0.001(M) palladium chloride solution and 0.265(M) stannous chloride solution where metallic palladium (Pd^0), produced in-situ [Reaction given in Eq. 4.1], gets adsorbed on YSZ surface upon placing the redox bath in a high energy ultrasonifier for 20 min at room temperature and at the agitation frequency range of 10-16 kHz. The sensitized bath was then kept for attaining equilibrium for effective adsorption of Pd^0 and complete precipitation of sensitized YSZ powder. As already mentioned above, concentration of the adsorbed Pd^0 is calculated with the help of ICP - AES. The YSZ particulates sensitized at different time intervals of equilibration process is subjected to an electroless bath. Electroless Ni deposition onto the ultrasonically sensitized YSZ powders is carried out in similar manner as discussed in section 4.1.2.1. The nickel concentrations in the cermets prepared by either ball milling or ultrasonic sensitization are varied in the range between 5 and 40 vol%.

Chapter - 4

4.2. ICP-AES Measurements Related to Synthesis of Ni-YSZ Cermet Powder

ICP-AES (Inductively coupled plasma – atomic emission spectroscopy) is engaged to determine the concentration of palladium (Pd) present in the supernatant solution of the YSZ sensitized bath. The amount of metallic palladium adsorbed onto YSZ surface can be determined by subtracting the Pd content of the supernatant solution from the initial concentration. The ICP measurement for finding out the adsorbed Pd concentration is very important in order to find out the attainment of the transient equilibrium state of sensitized YSZ which in turn helps in the deposition of Ni onto YSZ in an ordered fashion.

The technique comprises of initial introduction of the sample solution into plasma in the form of aerosol (mixture of fine polydisperse droplets and vapour) using nebulizer. The droplets are allowed to enter into the plasma at the rate of several millions/sec, and undergo three major phenomena viz. a) desolvation, b) volatilization and c) atomization before reaching the state of free atoms.

The instrumentation involves the formation of brilliant, tear drop shaped, high temperature plasma through the interaction of formed ionized gas with electrons under a high frequency electromagnetic field.¹⁻² The basic instrumental parts of AAS technique along with the schematic of light emission through energy state excitation is given in [Figure 4.3](#). Adding energy to the plasma via RF induced collision is known as ‘inductively coupled plasma (ICP)’. Such high temperature (7000 - 10, 000 K) plasma is the prime excitation source. Therefore, the overall ICP-AES technique comprises of three major steps: a) atom formation, b) excitation and c) emission. After atomization and excitation of concerned element by means of plasma source, the atom will emit light on coming back to the ground state, and such light is the characteristic of that element. Since, the procedure deals with the plasma state of an element, the concerned oxidation state cannot be determined

from such technique. However, the total elemental concentration of the experimental sample could be precisely determined which could even consists of a mixture of many elements.

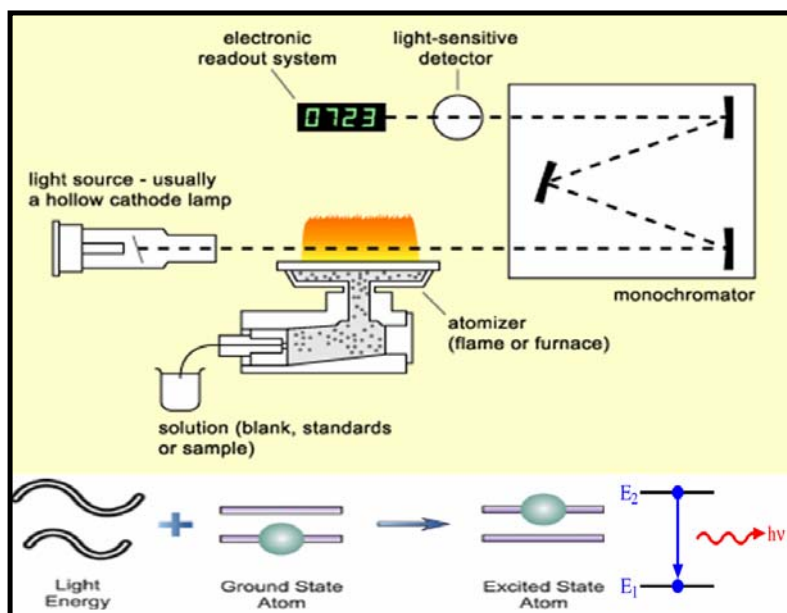


Figure 4.3: Basic instrumental set up of atomic absorption spectrometer along with the schematic for the basic principle of emission spectra ¹⁻²

Emissive light of individual elements depend on the energy difference between its excited and ground state and therefore, in order to avoid interference, the composition should comprise of elements whose energy difference is separable.

4.3. Ni-YSZ Powder Characterization

4.3.1. Particle size analysis

The particle size distributions of various experimental powders given in [Table 4.2](#) were measured by a computerized Particle Size Analyser (Sedigraph 5100, Micromeritics Corporation, USA). A single solid (porous or non-porous) sphere setting in a liquid has the terminal settling velocity which is uniquely related to its diameter. The SediGraph determines PSD using such sedimentation method. By measuring gravity induced settling velocities of different size particles in a liquid medium with known properties, the particle sizes are identified.

Chapter - 4

Table 4.2: Experimental powder examined for particle size analysis

Components		Experimental Powders
YSZ		YSZ- Unitec
		YSZ-Tosho – as received
		YSZ-Tosho-heat treated
Ni-YSZ cermet	Ball mill assisted	Ni content variation- 5-40 vol %
	Ultrasonic assisted	Ni content variation- 5-40 vol %

The instrument employs a narrow, horizontally collimated beam of X-ray to measure directly the relative mass concentration of particles dispersed in a liquid medium. The rate at which the sample powder is allowed to fall through the liquid medium is described by Stokes' law as:

$$D_{St} = \left[\frac{18 \eta V}{(\rho_{Sample} - \rho_{Medium}) \times g} \right]^{\frac{1}{2}} \quad (4.2)$$

where, D_{St} , η , V , ρ_{Sample} , ρ_{Medium} and g are Stokes' diameter, fluid viscosity, settling velocity, density of solid and liquid medium and acceleration due to gravity respectively.

The measured PSD values are a function of the particle skeletal density, which is theoretically defined as:

$$Particle\ skeletal\ density = \frac{Mass\ of\ discrete\ solid\ particles}{Volume\ of\ the\ solid\ along\ with\ the\ closed\ or\ blind\ pores} \quad (4.3)$$

However, since the Ni-YSZ samples are porous enough, the effective density will be different from the skeletal density. The effective density is a linear combination of the particle % porosity times the fluid density in combination with the (net % porosity) times the particle skeletal density as given in Eq. 4.4:

$$\rho_{Eff} = \left[\frac{P \times \rho_f + (100 - P) \rho_s}{100} \right] \quad (4.4)$$

where, ρ_{Eff} , P , ρ_f and ρ_s are effective sedimentation density for a particle with open pores, % open porosity, density of sedimentation fluid and skeletal density determined from Eq. 4.3 respectively.

4.3.2. X-ray diffraction technique

The X-ray diffraction (XRD) patterns of the synthesized Ni-YSZ powder samples prepared both by ball mill assisted and ultrasonification assisted sensitized YSZ, was recorded using an X-ray diffractometer (Philips X'pert, PANalytical, Eindhoven, Netherlands) using Cu-K α radiation ($\lambda = 1.5418 \text{ \AA}$) obtained from Cu-target using an in-built Ni filter. After the sample was irradiated with monochromatic X-rays, the reflected rays were recorded and employed for the determination of different crystalline phases present in the experimental sample. A scan rate of $10^\circ \text{ min}^{-1}$ was used to record the XRD patterns between 2θ values of 30° to 80° . The peaks of the X-rays are generally identified using standard powder diffraction files. Rietveld refinement of the obtained data was performed by PANalytical X'pert software.

4.4. Preparation of Bulk Anode Samples

4.4.1. Uniaxial pressing

The synthesized Ni-YSZ anode powders were fabricated in the form of bulk cermets and were subjected to various characterizations viz. densification, electrical, thermal etc. As synthesized powders either by electroless or solid state techniques were mixed with 1.5 wt. % polyvinyl butyral (PVB) binder and pressed uniaxially in the form of green compacts of dimension $25 \text{ mm} \times 10 \text{ mm} \times 3 \text{ mm}$ under a uniaxial pressure of 170 Mpa. The formed green compacts of anode cermets were then heat treated based on the requirements of further characterization techniques.

4.4.2. Tape casting and lamination

Apart from the bulk sample preparation of anode cermets through uniaxial pressing as stated above, the cermets were also fabricated using tape casting

Chapter - 4

technique under optimized processing parameters established by our group.³ For the preparation of NiO-YSZ tapes through conventional route, NiO and YSZ powder mixture (40:60 vol % ratio) was dispersed in a non-aqueous medium containing organic binder, plasticizer and porosifier to obtain homogenous slurry. This prepared slurry of NiO-YSZ was cast under a doctor blade of a laboratory type tape casting machine (EPH, USA). After drying, a green sheet of NiO-YSZ was obtained which is cut according to the required size. The thickness of anode tape can be varied by changing the blade gap. Several such cut green tapes of NiO-YSZ were laminated at room temperature using a uniaxial press at a pressure of ~ 200 Mpa. Similar procedure is followed to prepare Ni-YSZ tape, which were initially synthesized through electroless technique. In this regard, the as-synthesized electroless Ni-YSZ powder was mixed with other components as stated above to prepare the homogenous slurry followed by similar experimental procedure to obtain electroless Ni-YSZ anode monolith.

Tape cast monolithic blocks of NiO/Ni-YSZ anode cermets prepared through either solid state or electroless route and fabricated by either uniaxial or tape casting were sintered in air at 1400°C for 6 h after removal of organics at ~ 1000 °C. The sintered NiO-YSZ samples thus obtained are then reduced to Ni-YSZ at 1000°C under a gaseous flow of argon and hydrogen (4:1) for 10 h.

4.5. Anode Cermet Characterizations

4.5.1. Density measurements

Density measurements of all anode samples either in the sintered (NiO-YSZ) or reduced (Ni-YSZ) state prepared either by electroless or conventional solid state techniques, were carried out using 'Archimedes Principle'. According to the principle, the apparent weight of an object/sample immersed in a liquid decreases by an amount equal to the weight of the volume of the liquid that it displaces as shown in [Figure 4.4](#).

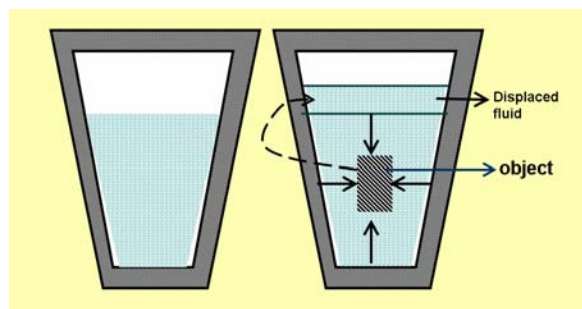


Figure 4.4: Pressure acting on an immersed object and schematic explanation of 'displaced fluid' by rising of fluid level- 'Buoyancy effect'

The density was determined by immersing the experimental Ni-YSZ samples in a liquid medium eg. Kerosene. The porous samples were allowed to get soaked in kerosene under vacuum for a considerable time period so that the internal pores were filled with the liquid medium. Prior to the immersion in the liquid medium, the dry weight of the corresponding samples were taken.

The density of the anode samples (ρ_{Anode}) are calculated using the following

Eq. 4.5:

$$\rho_{\text{Anode}} = \left[\frac{W_{\text{Dry wt.}}}{W_{\text{soaked wt.}} - W_{\text{suspended wt.}}} \right] \times \rho_{\text{Medium}} \quad (4.5)$$

where, $W_{\text{Dry wt.}}$, $W_{\text{soaked wt.}}$, $W_{\text{suspended wt.}}$, ρ_{Medium} are the dry weight of the sample in air, weight of the sample in air after soaking it in kerosene, weight of the kerosene soaked sample under kerosene and density of the medium ($\rho_{\text{kerosene}} = 0.81 \text{ gcc}^{-1}$) respectively.

4.5.2. Pore size distribution studies

The pore size distributions of both the sintered and reduced tape cast Ni/NiO-YSZ anode cermets prepared by either solid state or electroless technique were measured using mercury porosimetry (Quantachrome Poremaster 60, Version 7.01, Quantachrome Instruments, Boynton Beach, FL). Porosity refers

Chapter - 4

to the pore-space/void between particles (interparticular porosity) in a material. Pore size distribution studies could only determine the size and distribution of the 'open pores' which are the channels or cavity that communicates with the surface of the particle. Such technique fails to account for the 'closed pore' which are present in the inside the material as shown in [Figure 4.5](#).

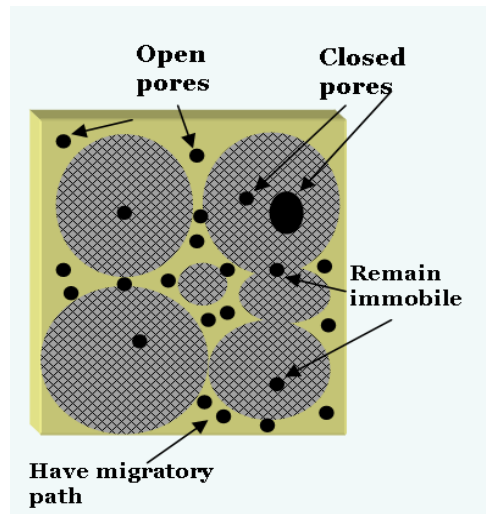


Figure 4.5: Pore types includes: a) open and b) closed pores

In mercury porosimetry, gas is initially evacuated from the sample cell and mercury is transferred into the sample cell under vacuum. A certain magnitude of pressure is applied to force the mercury into the pores of the sample. During the measurement, applied pressure (P) and intruded volume of the mercury (V) are registered. As a result, an 'intrusion-extrusion' curve is obtained as shown in [Figure 4.6](#). Mercury porosimetry is based on the 'Washburn equation' relating applied pressure (P) with intruded parameters as described in Eq. 4.6:

$$P \times r = -2\Gamma \cos \theta \quad (4.6)$$

where, r, Γ and θ are radius of the pores where mercury intrudes, surface tension of the mercury and contact angle (obtuse angle = 140°) of mercury on the surface of solid sample respectively. Therefore, the pore size distribution is studied in terms

of intruded mercury volume and referred to as 'volume pore size distribution [$D_v(d)$]' which is defined as pore volume (V) per unit interval of pore diameter (d) as:

$$D_v(d) = \frac{P}{d} \frac{dV}{dp} \quad (4.7)$$

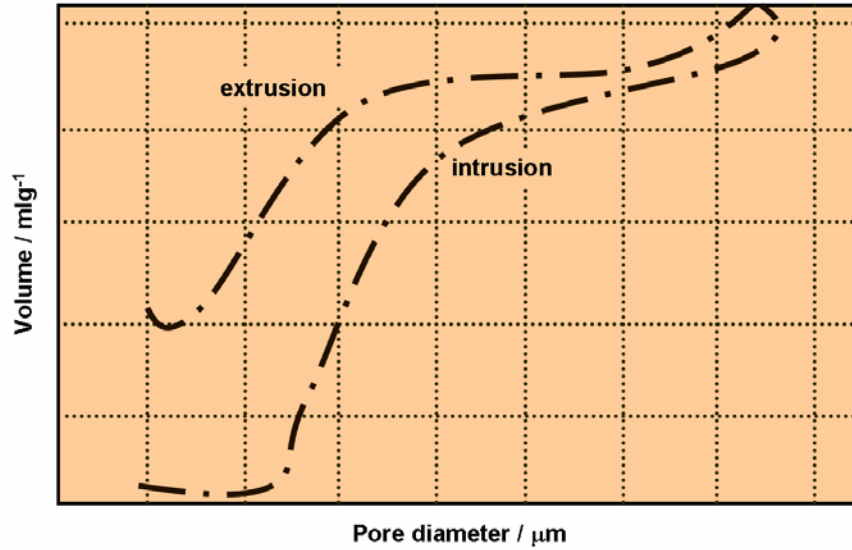


Figure 4.6: Nature of intrusion-extrusion curve on a porous sample by mercury porosimetry

In general $dV/d \log d$ vs d is plotted which results in a Gaussian type distribution as shown in Figure 4.7. In a porous sample, pores can vary in size and content based upon the preparation technique.

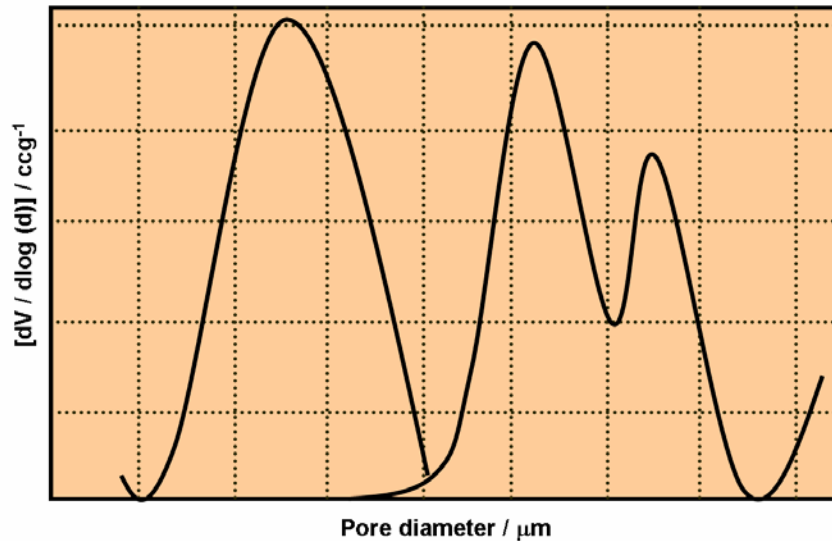


Figure 4.7: Typical schematic of Gaussian type pore-size distribution of porous samples

Chapter - 4

The Gaussian distribution may vary from unimodal to multimodal distribution depending upon the nature of pores. Therefore, study of such pore size distribution enables the identification of pores of various sizes along with their distribution.

4.5.3. Thermal expansion studies

Coefficient of thermal expansion (CTE) is a thermodynamic property of a material which relates the change in temperature to the change in materials linear dimension. CTE signifies the fractional change in length per degree of temperature change. The linear thermal expansion coefficient (α) of the experimental anode samples was determined in the temperature range of 30-1000°C using Eq. 4.8 using a horizontal push rod type dilatometer (DIL 402 C, Netzsch, Germany).

$$\begin{aligned} L_1 &= L_0 [1 + \alpha (T_2 - T_1)] \\ \Rightarrow \alpha &= \frac{1}{\Delta T} \left(\frac{L_1 - L_0}{L_0} \right) \Rightarrow \alpha = \frac{1}{\Delta T} \left(\frac{\Delta L}{L_0} \right) \end{aligned} \quad (4.8)$$

where, L_0 , L_1 , ΔL and ΔT are the lengths of the specimen at reference temperature (T_1), test temperature (T_2), net change in length and temperature respectively.

The schematic of the sample holder is given in [Figure 4.8](#), in which the experimental sample is placed between two holders. In order to prevent oxidation of the Ni-YSZ anode samples during thermal studies, inert atmosphere is maintained within the interior of the dilatometer using argon gas.

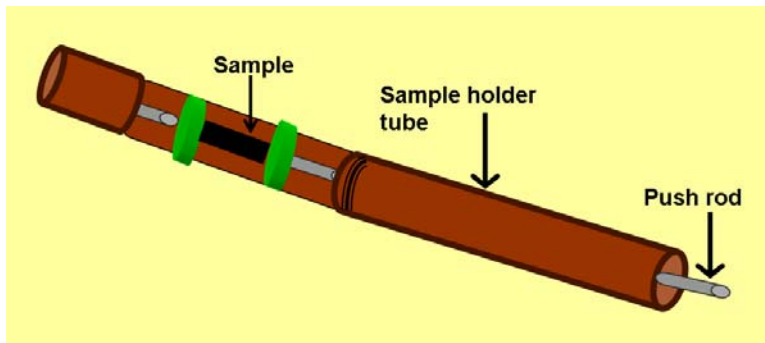


Figure 4.8: Schematic of sample holder in a dilatometer along with the sample sandwiched between holders

4.5.4. Electrical conductivity studies

Electrical conductivities of the prepared Ni-YSZ cermets of different configurations were studied through four probe or 4-terminal sensing technique. This is an example of electrical resistance measurement that uses separate pairs of current carrying and voltage sensing electrodes as shown in [Figure 4.9](#), in order to make accurate measurements compared to the 2-probe sensing techniques.

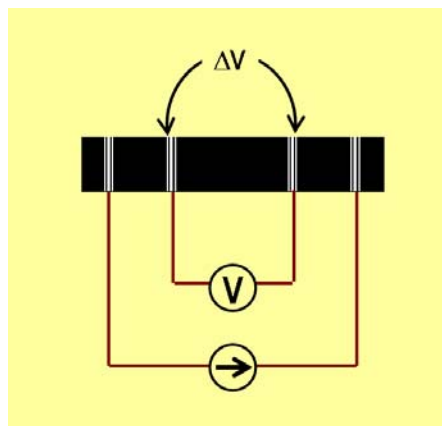


Figure 4.9: Schematic of 4-probe sensing technique with probe positions

Current was supplied at the end connections which generate a voltage drop (ΔV) across the wires. The resistance thus generated was recorded using an eight and half digit multimeter digit multimeter (Keithley, Model 2002) as a function of temperature varied in the range of 400-1000°C. The corresponding electrical conductivities in such temperature were then calculated using Eq. 4.9.

$$\sigma = \frac{L}{Rbt} \quad (4.9)$$

where, σ , R , L , b and t are the conductivity, 4-probe resistance of the sample measured, length between two voltage probes, breadth and the sample thickness respectively.

Ohmic contact of the sample with Ni wires (probes for connection) was made effective by application of Pt paste into the contact areas between the wires and the samples and cured at 1000°C. A schematic representation of sample loading and measurement technique for 4-probe electrical conductivity study is shown in

Chapter - 4

Figure 4.10. The electrical resistivity of the samples were measured in the inert atmosphere of argon and hydrogen (4: 1) with temperature variation in the range of 400-1000°C.

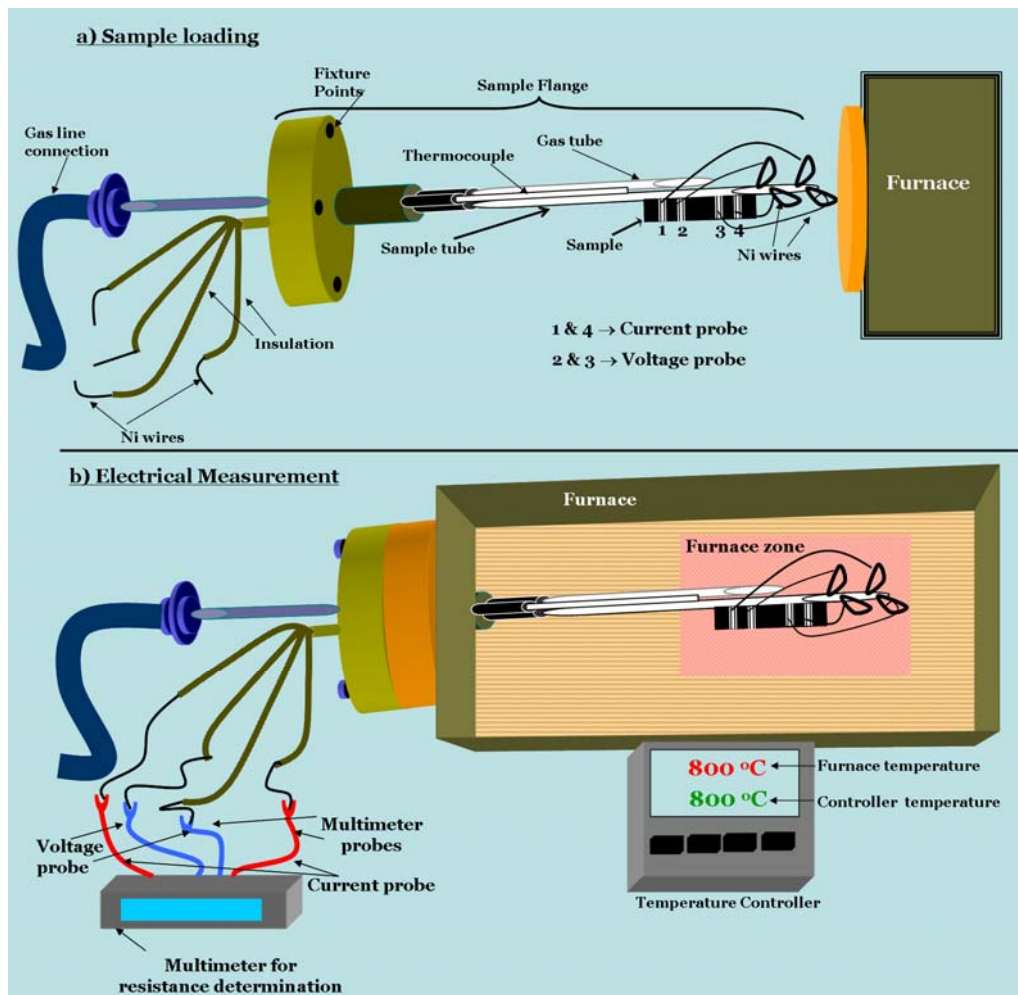


Figure 4.10: Schematic representations of: a) sample loading for 4-probe electrical measurement and b) Electrical measurement technique

4.5.5. Microstructural characterizations

4.5.5.1. Optical Microscope

The surface as well as cross-sectional features of the anodes along with the single cells having such anodes of varied configurations, were studied using optical microscope (GX71, Olympus, Japan) fitted with a computerized digital camera

(Olympus DP12, Japan). Images of the polished cross-sections / surfaces of the experimental specimen were captured through the back filtered (BF) mode.

4.5.5.2. Field Emission Scanning Electron Microscope (FESEM)

The cermet anodes as well as the single cells having anodes of different configurations prepared under the present investigations were cut into thin dimensions and were polished after mounting. These polished samples were subjected to microstructural investigations using field emission scanning electron microscope (Gemini Supra 35, Zeiss, Jena, Germany). Images were captured in either secondary electron (SE) or backscattered electron (BSE) mode depending upon the requirement. Since, the backscattered coefficient is dependent on the atomic number of the respective elements, topographic contrast of the experimental sample can be viewed through BSE mode. Unlike the optical microscope which applies optical lenses for image viewing, electron microscope utilizes the electromagnetic lenses which follows spiral path and allows variation of the focal length according to the requirement. Furthermore, focusing is done by changing current source, rather than the physical movement of lenses which is used in case of optical microscopes. Owing to such features, electron microscope renders the image capturing with enhanced resolution (4-1 nm) and higher magnification (x 50 k - x 500 k). Elemental identification at specified positions of the experimental samples was carried out through energy dispersive X-ray (EDAX) coupled with FESEM. In addition, both qualitative and quantitative estimations of the respective elements were studied. In addition to the spot identification, line and area scanning of the identified elements were also carried out to study the microstructural pattern. Prior to the sample loading into the instrument, all the samples were coated with a thin carbon paste to make the surface electronically conducting within the FESEM instrument.

Chapter - 4

4.6. Fabrication of SOFC with Electroless Ni-YSZ Anode

The schematic / flow chart for the fabrication of anode-supported single cells is shown in Figure 4.11. The first major step during the fabrication process for the development of SOFC's was the half cells (anode/electrolyte) through conventional tape casting method under processing conditions as optimized by our group.³

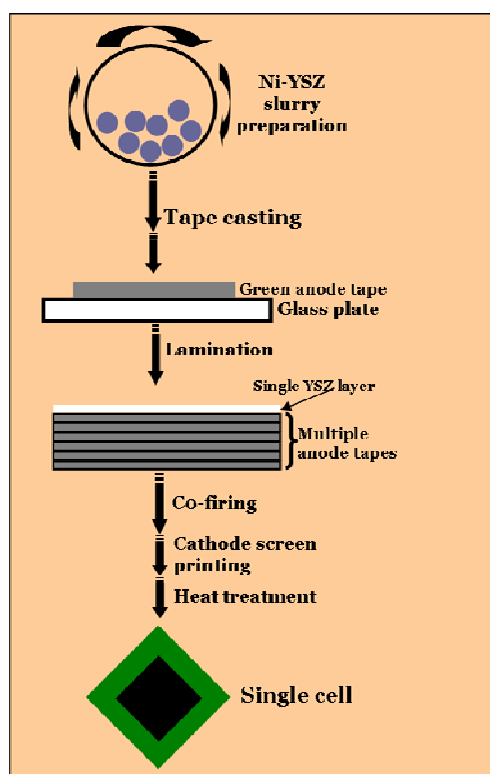
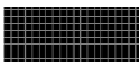
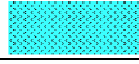

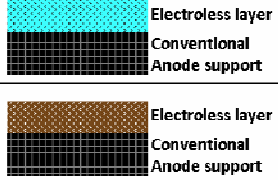
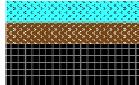
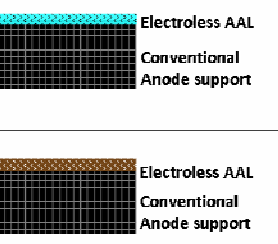





Figure 4. 11: Schematic of planar anode-supported single cell fabrication

The dried green sheets of NiO / Ni-YSZ anode as well as YSZ electrolyte, thus obtained, were cut to the required size and were laminated at room temperature together with an YSZ sheet (of same size) on top using a uniaxial press. The monolithic block thus formed, was co-fired at 1400°C for 2h with an dwell time of 3h to 6h at intermediate temperature corresponding to the decomposition points (as determined from thermogravimetric analysis) of the different organics used.

The perfectly flat half cells were then subjected to screen printing with cathode active layer [YSZ+LSM (lanthanum strontium manganite) = 1:1] and cathode current collection layer (LSM) being used in the form of viscous paste. Prior to the screen printing, the half cells were thoroughly cleaned with acetone in an ultrasonic bath followed by drying. The formed single cell was then co-fired in air at 1150°C for 2 h. A number of different anode configurations have been studied during the present research work as given in Table 4. 3.

Table 4.3: Description of anode configurations in the present research work

Anode composition		Ni content of conventional anode (vol %)	Ni content of electroless anode (vol %)	Thickness of conventional anode after sintering ($\pm 10 \mu\text{m}$)	Thickness of electroless anode after sintering ($\pm 10 \mu\text{m}$)	Sample ID	Anode Configuration
I [Conventional anode]		40	--	1250	--	CA-1	 Conventional Anode support
			--	1500	--	CA-2	
II [Electroless anode]		--	28	--	1250	28 EL-1	 Electroless Anode
				--	150	28 EL-2	
			32	--	1250	32 EL-1	 Electroless Anode
				--	1500	32 EL-2	
III [Conventional anode / Electroless anode (thick)]	Bilayer anode	40	28	1450	50	28 BLA- 1	
				1380	120	28 BLA- 2	
				1250	250	28 BLA- 3	
		40	32	1450	50	32 BLA- 1	
				1380	120	32 BLA- 2	
				1250	250	32 BLA- 3	
	Trilayer anode	40	28 + 32	1400	50 μ each	TLA	
						 Electroless layer Conventional Anode support	
IV [Conventional anode / Electroless anode (thin)]	Anode support with electroless functional layer	40	28	1485	15	28 AAL-1	
				1460	40	28 AAL-2	
				1410	90	28 AAL-3	
				1360	140	28 AAL-4	
		40	32	1485	15	32 AAL-1	
				1460	40	32 AAL-2	
				1410	90	32 AAL-3	
				1360	140	32 AAL-4	

Conventional anode-support  40 vol % Ni
 Electroless anode:  32 vol % Ni &  28 vol % Ni

Anode configurations were fabricated with the variation of constituent phases and variation in layer thicknesses. The percentage porosity were also in-situ varied in

Chapter - 4

such layered configurations owing to variation in porosities in conventional and electroless anode cermets. Single cells were fabricated using all such anode configurations to study their electrochemical performances and functionality of electroless anode. For experimental purpose, the single cells were fabricated in the form of coupon cells of dimension ~ 16 mm diameter and 1.5 mm thick.

4.7. Electrochemical Characterization of Single Cell

In order to evaluate the electrochemical performance, single cell in the form of coupon cell (~ 16 mm in diameter and 1.5 mm thick) was placed between two alumina tubes kept inside a vertical split type furnace (ATS Corporation, USA). Platinum meshes were used as current collectors at the both cathode and anode electrodes and proper electrical contact was made through platinum lead wires. The sealing of the gas compartment on the anode side was made by using a ring shaped glass kept pressed by the alumina tubes. In order to seal the electrode compartments for prevention of gas intermixing, the furnace with aforesaid arrangement was heated to about 950°C so that the glass softens and form gas-tight seal. A schematic of the electrochemical test set up for single cells is given in [Figure 4.12](#). The whole assembly was then cooled to 800°C and a flow of gaseous argon was introduced at the anode side and oxygen at the cathode side. The reduction of NiO to metallic Ni for the anode of the single cells was then achieved by gradual replacement of argon with hydrogen (saturated with ~ 3 vol% of water vapor). During testing, both fuel and oxidant flow rates are set and maintained at 100 SCCM with the help of electronic mass flow controllers (MKS Instruments, USA).

The electrochemical performance of the cell was measured between 700 and 800°C using DC methods.⁴ The various factors affecting electrochemical activity of single cell such as: a) thickness and sintering temperature of the half cell b) rate of NiO reduction to metallic Ni, c) type of oxidant used at the cathode side and d)

role of moist fuel were also studied thoroughly during the course of this research work. The role of fuel in the anodic electrochemical reactions were also studied and correlated with the associated mechanisms governing the cell reactions.

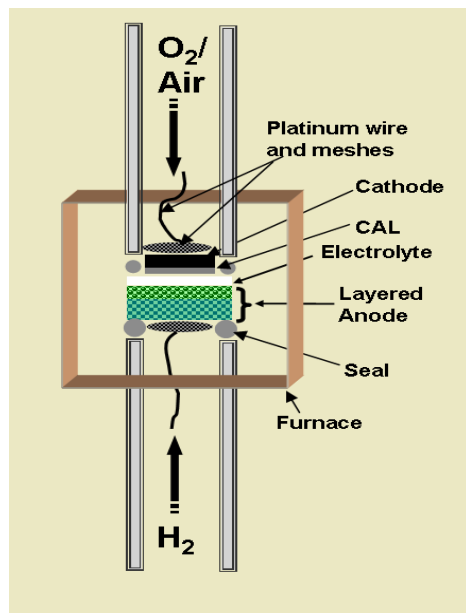


Figure 4.12: Schematic of electrochemical test set up designed and fabricated at CSIR-CGCRI

For polarization study of the cells, impedance spectroscopy measurements had been performed using an Impedance Analyzer (Solartron 1260, U.K) coupled with an Electrochemical Interface (Solartron 1260, U.K) in the frequency range 0.1 Hz to 1 MHz and measured between 700°C and 800°C. The corresponding results of the experiments highlighted in the present chapter are discussed in the subsequent sections.

Chapter - 4

4.8. References

1. Steve J. Hill (Editor), "Inductively Coupled Plasma Spectrometry and its Application", Publisher: CRC Press UK, (1999).
2. Lauri H. J. Lajunen and P. Perämäki, "Spectrochemical Analysis by Atomic Absorption and Emission", Royal Society of Chemistry (Great Britain), (2004).
3. R.N. Basu, A. Das Sharma, A. Dutta and J. Mukhopadhyay, *International Journal of Hydrogen Energy*, **33[20]**, 5748-5754 (2008).
4. V.A.C. Haanappel, J. Mertens, D. Rutenbeck, C. Tropartz, W. Herzhof, D. Sebold and F. Tietz, *Journal Power Sources*, **141**, 216 - 226 (2005).

~

C *HAPTER-5*

Results

&

Discussion

Chapter – 5.1

***5.1. Ball Mill Assisted
Ni-YSZ Electroless
Cermet***

Chapter – 5.1

5.1.1. Concept of electroless technique

In the present investigation, a novel ‘electroless’ deposition technique is employed to synthesize nickel-8 mol % yttria stabilized zirconia (Ni-YSZ) for SOFC anode application. The Ni deposition by such technique onto palladium sensitized YSZ particulates helps to generate Ni-Ni interlinking chain during high temperature sintering followed by subsequent reduction which produces a ‘core-shell’ structure with a core of YSZ being surrounded by a shell of metallic Ni particulates. Thus the functionality in the cermet is added and the flow path of electrons is made through the Ni-Ni shell deposited in an ordered fashion rather than the dispersed Ni-YSZ cermet obtained with conventional preparation technique as shown in the schematic of [Figure 5.1](#).

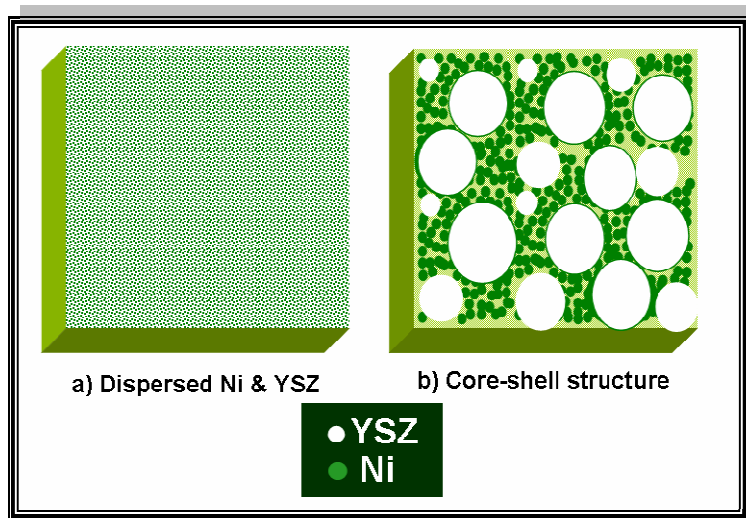


Figure 5. 1: Schematic of microstructures obtained from a) conventional solid state and b) electroless technique

Such unique core-shell microstructure is believed to prevail over certain crucial shortcomings viz. usage of higher Ni content, high temperature coarsening, thermal incompatibility, reduced triple phase boundaries (TPB), redox intolerance etc associated with Ni-YSZ cermet prepared through conventional techniques.

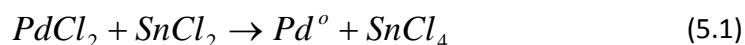
As already discussed in Chapter-4, electroless technique comprises of two major steps namely: a) initial sensitization of precursor YSZ particulates and b) in-

Chapter – 5.1

situ reduction of Ni from Ni²⁺ solution and its subsequent deposition onto the sensitized YSZ powders. The present section illustrates characteristics of electroless Ni-YSZ anode, in which the initial YSZ sensitization is carried out through ball milling technique. The prime advantage of such ball milling technique lies in the up scalability and cost effectiveness. Various milling parameters viz. rotating speed (rpm), milling time and volume ratio with respect to constituent phase have been systematically varied to study their effects on the extent of YSZ sensitization and the properties of the Ni-YSZ cermet anodes obtained by electroless Ni deposition.

5.1.2. Application of ball mill theory for YSZ sensitization

Sensitization of YSZ involves surface adsorption of in-situ produced active metallic palladium (Pd⁰) onto its surface. Metallic palladium (Pd⁰) is being reduced from its corresponding salt using stannous chloride in acidic medium which is shown in Eq. 5.1:



The active Pd⁰ particulates adsorbed onto the YSZ acts as the catalytic centres for the deposition of metallic nickel (Ni⁰) during the subsequent electroless technique. The process flow chart is given in [Figure 5.2](#). The in-situ production of active Pd⁰ sites along with its adsorption is aided by means of ball milling technique. The sensitized bath after milling at predetermined rotating speed in the range of 45-65 rpm is allowed to equilibrate for effective adsorption and complete precipitation of the sensitized YSZ powder. In this connection, a study is pertained on the basis of theoretical background regarding the optimization of milling speed for effective YSZ sensitization.

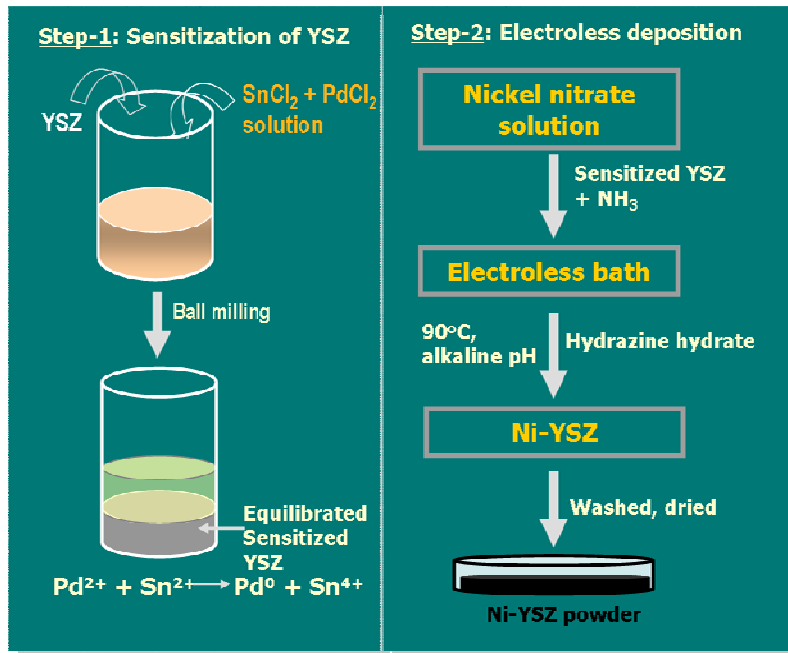


Figure 5.2: Process flow chart for ball mill assisted electroless technique

5.1.2.1. Theoretical optimization of milling speed

The sensitization of YSZ by ball technique requires a balance between mixing and grinding of the constituent particulates. While mixing helps in homogenization of the constituents, the thermal energy associated with grinding promotes the redox reaction (Eq. 5.1) towards the forward direction. However, excessive grinding beyond a certain rpm level leads to the formation of fragmented YSZ where the sensitization becomes ineffective. Alternatively, below a critical rpm level of milling, only mixing tends to predominant without any significant sensitization.

The energy input to the ball mill increase with increase in the speed of rotation. The power to the mill is transmitted from the shell lines to the first layer of grinding media and then to subsequent layers. Due to slippage of the media among the contributing layers during rotations, some power loss is significant in such process. A schematic of balanced forces in ball milling is shown in [Figure 5.3](#).

Chapter – 5.1

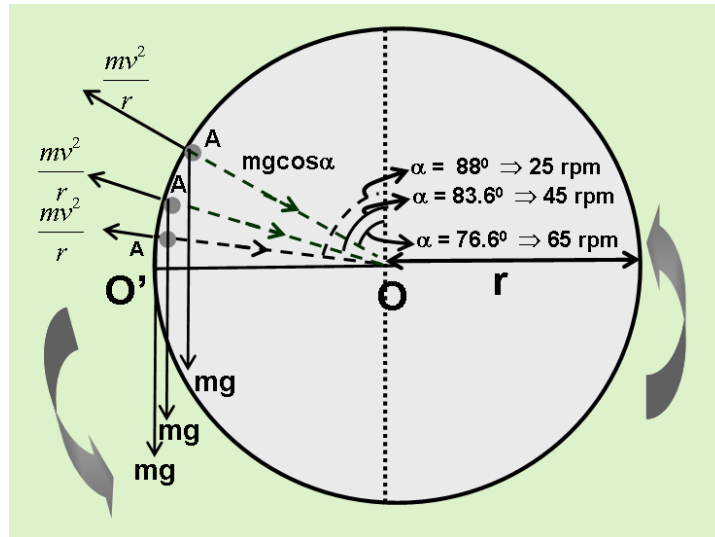


Figure 5.3: Schematic for the balance of force during ball milling

In the figure, an experimental particle is considered at position 'A' which makes angle α with the vertical axis through the centre 'O' of the mill. There are two forces acting on the particle in this condition: ¹

1. Centrifugal force (F_c) acting radially outwards
2. Gravitational force (F_g) due to mass of the particle acting vertically downwards

The centripetal component of the gravity force acts towards the centre of the mill and is given as: $F_g \cos \alpha = mg \cos \alpha$ (5.2)

The centripetal force is being balanced by centrifugal force and is given by the following equation:

$$mg \cos \alpha = \frac{mv^2}{r} \quad (5.3)$$

Substituting $v = 2\pi rn$

where, $n = \text{rpm of the mill}$

The rpm of the mill can be expressed in terms of ' α ' and radius of the container r (0.05 m) as:

$$n = \sqrt{\left(\frac{g}{4\pi^2}\right) \left(\frac{\cos \alpha}{r}\right)} \quad (5.4)$$

In the above Eq. 5.4, the radius of the grinding media (zirconia balls) has not been taken into consideration because of negligible dimension compared to the radius of

the container. Upon employing Eq. 5.4, the following correlations among milling effect and frequency of rotation (n) can be established:

- a) At $\alpha = 0$ ($\cos\alpha = 1$), the corresponding rpm is calculated to be 135.1. Below this specific rpm, the grinding action is expected to be maximum, whereas above this point the particle continues to rotate without dripping. Therefore, above this critical rpm, grinding action is absent.
- b) At $\alpha = 45^\circ$ ($\cos\alpha = 0.707$), the corresponding rpm is calculated to be ~ 113 . At this rpm, the grinding and mixing is expected to be balanced. But in the present context, excessive grinding may lead to fragmentation of the treated YSZ particulates ($d_{50} \sim 27\mu\text{m}$) which does not result in significant Pd^0 adsorption.
- c) Impact of grinding is found to be $1/4^{\text{th}}$ when rpm ~ 56 . Therefore, for optimum grinding of the YSZ particulates, the rpm must be kept ≤ 56 .
- d) Experiments were carried out at three milling speeds, 25 and 45 rpm (less than 56 rpm) and 65 rpm (above 56 rpm) in order to optimize the milling speed with respect to maximum Pd^0 adsorption capacity of YSZ.
- e) At lower rpm of 25 ($\alpha = 88^\circ$), particle mixing is predominating without significant formation of Pd^0 and its subsequent adsorption.
- f) However, at higher rpm of 65 ($\alpha = 76.6^\circ$), grinding becomes predominating which may lead to YSZ particle fragmentation which is expected to reduce the absorption capacity as will be discussed in the next section.

Therefore, an intermediate rpm of 45 is theoretically found to be most suitable for mixing as well as optimum impact of grinding which would result in favourable forward redox reaction (Eq. 5.1) followed by subsequent adsorption of Pd^0 onto YSZ.

5.1.2.2. Experimental correlation with theoretical optimization of milling speed

The aforementioned observations highlighted that, the Pd^0 adsorption (in ppm concentration level) is a variant of certain factors viz. a) milling speed (in rpm)

Chapter – 5.1

and b) equilibration time interval, as shown in Figure 5.4. Pd⁰ adsorption on YSZ being an example of reversible physisorption, the optimization of equilibration time plays the crucial for YSZ sensitization. The prime requirement is to obtain maximum coverage of YSZ particulates by Pd⁰ and limiting the backward desorption rate. It can be observed from Figure 5.4 that, irrespective of the equilibration time, the extent of Pd⁰ adsorption increases with increase in milling speed upto a maxima (corresponding to 45 rpm) and then decreases with further increase in the milling speed. The extent of Pd⁰ adsorption is ineffective with milling speed of less than 45 rpm whereas for a higher rate of frequency, the desorption rate starts dominating due to enhanced agitation in the solution phase among sorbet and sorbent species which is also evident from Figure 5.4.

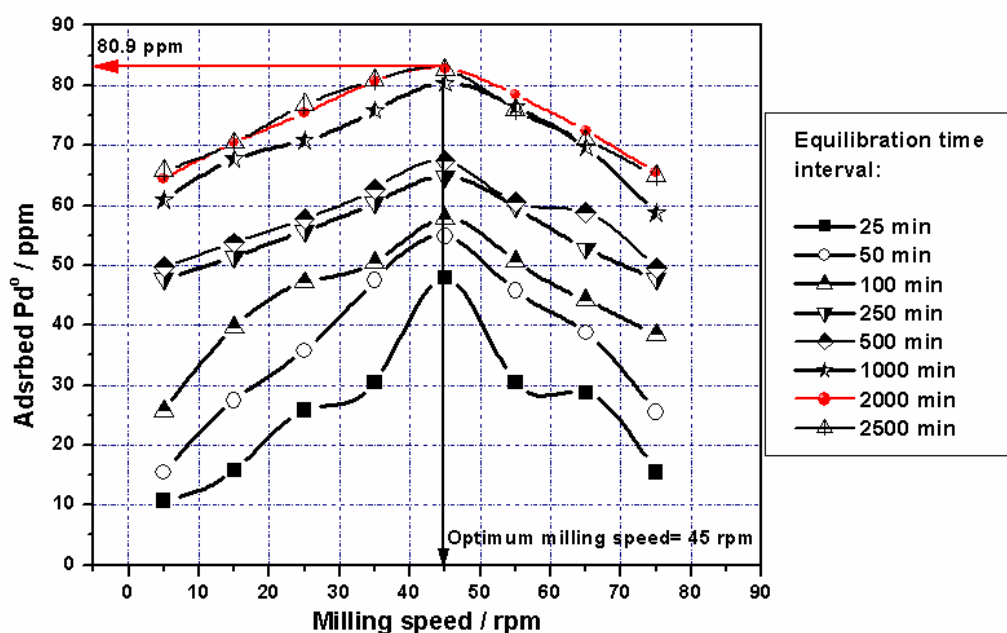


Figure 5.4: Dependence of adsorption capacity on milling speed and equilibration time

Thus, it is clear from the figure that, the amount of Pd⁰ adsorption on YSZ from the sensitized bath is found to be optimum (~ 83 ppm) at a milling speed corresponding to 45 rpm, equilibrated for about 2000 min. YSZ sensitization at such optimum milling condition promotes in-situ Ni²⁺ reduction during the subsequent

electroless Ni deposition. Beyond this equilibrium time of adsorption, the desorption rate starts predominating resulting in slight decrease in adsorbed Pd⁰ concentration as observed from Figure 5.4.

5.1.3. Correlation of phase intensity ratio with milling speed

The X-ray diffractograms of the reduced Ni-YSZ cermet prepared by either ball mill assisted electroless or conventional solid state technique is shown in Figure 5.5.

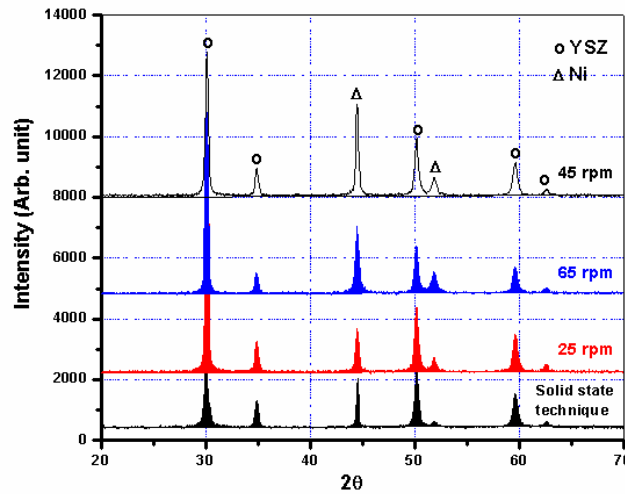


Figure 5.5: XRD pattern of Ni- YSZ cermet prepared by ball mill assisted electroless and conventional solid state technique

An interesting correlation is studied between the phase distributions within the anode prepared through either conventional or electroless technique with the ratio of relative intensities of metallic Ni and YSZ (I_{Ni} / I_{YSZ}). The I_{Ni} / I_{YSZ} values, as calculated from Figure 5.5, corresponding to the major peaks for both the batches are presented in Table 5.1.

Table 5.1: I_{Ni} / I_{YSZ} of X-ray diffraction for electroless and conventional anodes		
Ni-YSZ preparation technique	Milling speed during YSZ sensitization (rpm)	I_{Ni} / I_{YSZ}
Electroless	25	0.474
	45	0.866
	65	0.651
Conventional solid state	---	0.814

Chapter – 5.1

It is interesting to note from Table 5.1, that the value of I_{Ni} / I_{YSZ} for the powder prepared by electroless technique with YSZ sensitized at an optimum milling speed of 45 rpm is more than the intensity ratio (I_{Ni} / I_{YSZ}) of the conventionally prepared cermet. A plausible explanation for this is shown schematically in Figure 5.6. Due to the formation of core (YSZ) – shell (Ni) microstructure by electroless technique, the X-ray peak corresponding to the metallic Ni phase is found to be more intensified compared to the YSZ peak.

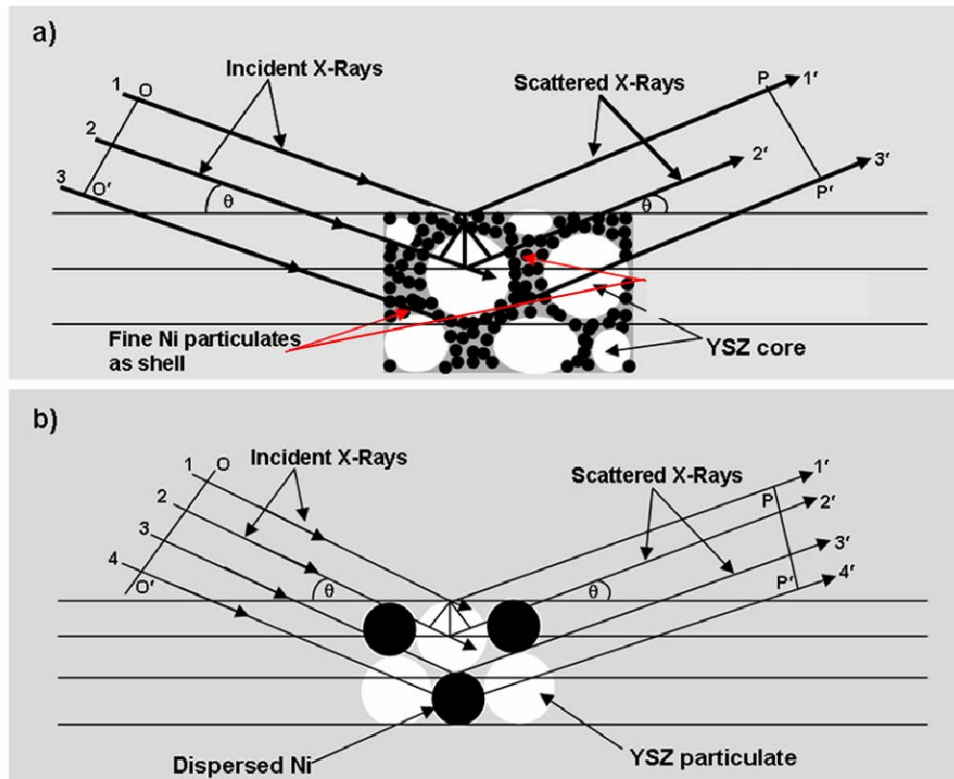


Figure 5.6: Schematic of X-ray diffractions from Ni-YSZ cermet anodes prepared by:
a) ball mill assisted electroless and b) conventional solid state technique

Accordingly, the relative intensity ratio of Ni is found to be higher compared to that of the uniformly dispersed Ni and YSZ cermet in conventional anode resulting in higher values of I_{Ni}/I_{YSZ} for such core-shell cermet. It is believed that, because of the electroless deposition of fine Ni particulates around YSZ sensitized at 45 rpm, the intensity of YSZ in the core position is found to be relatively less compared to the

intensity of Ni at the shell and therefore, I_{Ni} / I_{YSZ} is found to be higher in such electroless Ni-YSZ cermets (Figure 5.6a). On the contrary, a lower value of I_{Ni} / I_{YSZ} for conventionally prepared cermet indicates uniform scattering from both the dispersed Ni and YSZ phases (Figure 5.6 b). I_{Ni} / I_{YSZ} values for electroless anode powders prepared with YSZ sensitized at 25 and 65 rpm are even lower than the intensity ratio of conventional anode due to the insufficient YSZ sensitization as observed from the lower Pd⁰ adsorption onto YSZ at different equilibration time interval (Figure 5.3). Therefore, samples with similar phase composition exhibit variability in X-ray diffraction intensity depending upon significant microstructural variation.

5.1.4. Effect of milling speed on anode characteristics

In the above sections, significance of optimized YSZ sensitization towards the electroless technique has been discussed. The outcome of such process optimization could be further established from the experimental studies of anode characteristics as conferred in the subsequent sections.

5.1.4.1. Densification study

The anode cermets prepared through either electroless or conventional techniques are subjected to a high temperature sintering in air at 1400°C for 6h. The sintered NiO-YSZ anode samples are then reduced at 1000 °C under a gaseous flow of argon and hydrogen (4:1) for 10 h and thus Ni-YSZ cermet bulk samples are produced. The sintered and reduced densities of the synthesized Ni-YSZ cermet prepared by either electroless or conventional technique along with variable Ni content are given in Table 5.2. The table also exhibit the corresponding densities of electroless Ni-YSZ anode prepared from YSZ precursor sensitized at different milling speeds. The electroless samples prepared with YSZ sensitized at an optimum milling speed of 45 rpm (where sensitization of YSZ is found to be effective) are less dense

Chapter – 5.1

and consequently more porous compared to the cermets obtained through conventional solid state technique.

Table 5.2: Density values of anode cermet prepared by electroless and conventional solid state technique

Ni content (vol %)	Electroless technique						Solid state technique	
	Sintered density (gcc^{-1})			Reduced density (gcc^{-1})			Sintered density (gcc^{-1})	Reduced density (gcc^{-1})
	25 rpm	45 rpm	65 rpm	25 rpm	45 rpm	65 rpm		
5	6.30	6.24	6.27	5.82	5.57	5.71	--	--
10	6.07	6.02	6.05	5.67	5.37	5.58	6.09	5.53
15	6.01	5.86	5.98	5.45	5.25	5.35	6.08	5.43
20	5.99	5.79	5.84	5.04	4.89	4.95	6.02	4.99
25	5.82	5.58	5.68	5.00	4.80	4.85	5.99	4.82
30	5.73	5.49	5.57	4.87	4.68	4.72	5.97	4.69
35	5.62	5.40	5.49	4.69	4.50	4.58	5.67	4.53
40	5.70	5.67	5.69	4.57	4.49	4.50	5.77	4.51

Conversely, at the milling speed of either 25 or 65 rpm, due to ineffective adsorption (in case of milling speed of 25 rpm) or reversible desorption (in case of milling speed of 65 rpm) of Pd^0 onto YSZ surface, the catalytic sites required for the in-situ reduction of Ni^{2+} in the electroless bath turn out to be insufficient. In the absence of adequate active Pd^0 sites, quantitative addition of reducing agent in the electroless bath generates excess free Ni in the matrix. These free Ni particulates are not associated with the shell formation around the YSZ core and form isolated islands. Under the sintering conditions as applied in case of the present investigation e.g. in air at 1400°C , these uncovered YSZ particles are likely to be more sinterable resulting in a higher effective density value for electroless samples prepared from YSZ sensitized at both 25 and 65 rpm. Nevertheless, YSZ sensitization at an optimum milling speed of 45 rpm results in the formation of core-shell structure with controlled Ni deposition. During sintering in air, Ni is

converted into NiO that also covers the YSZ grains. So during sintering, direct contact between the YSZ grains are limited in such core-shell anode. As the sinterability of NiO is less than that of the YSZ, the densification of such core-shell NiO-YSZ is also found to be less than the conventional anode samples where the NiO is dispersed in YSZ.

This lower density during sintering in the electroless anode samples is also reflected in the reduced cermets. Moreover, oxygen loss during subsequent reduction of NiO to metallic Ni increases porosity of the anodes in the reduced state. On the other hand, the fully dispersed Ni particulates in the cermet matrix of conventionally prepared anodes results in relatively higher density and hence lower porosity. Densification of anode cermets is therefore, found to be a variant of microstructural pattern of the constituent phases.

5.1.4.2. Electrical and thermal characterization

The electrical conductivity value of the anode is required to be sufficiently high ($\sim 500 \text{ Scm}^{-1}$) for SOFC application which entirely depends on the distribution of Ni in the cermet matrix. Figure 5.7 shows a sigmoidal nature of the electrical conductivity (measured at 800°C) percolation of the Ni-YSZ cermets prepared through variable processing techniques. The required electrical conductivity value of the anode is found to be fulfilled at 40 vol% of Ni content when prepared by solid state technique (Figure 5. 7). However, it is interesting to note that it is possible to bring down the upper percolation threshold (corresponding to a conductivity value of 500 Scm^{-1}) of electrical conduction to ~ 33 vol% of Ni in case of the anodes prepared through electroless deposition with YSZ sensitized at an optimum milling speed of 45 rpm. Consequently, the developed electroless cermet at a milling speed of 45 rpm shows the optimum electrical conduction at a lower Ni content. Owing to disordered microstructural pattern produced through ineffective sensitization of YSZ at either 25 or 65 rpm, the upper conductivity percolation is

Chapter – 5.1

found to get shifted towards the higher Ni content. It is observed from Figure 5.7 that, irrespective of the variation of milling speeds for the period of YSZ sensitization, the onset of electrical conductivity percolation of electroless anodes starts ~ 10 vol % of Ni compared to > 25 vol % Ni required by the conventional cermet.

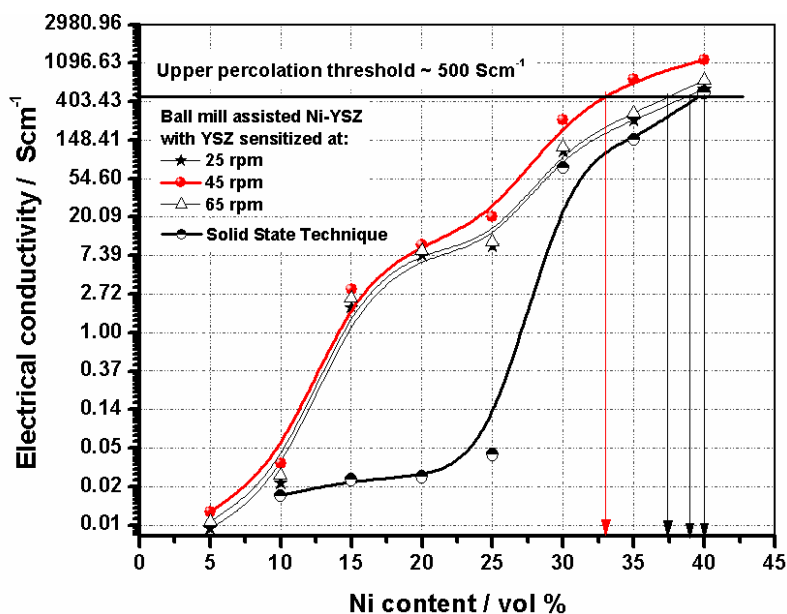


Figure 5.7: Electrical conductivity percolation curve of Ni-YSZ prepared by different techniques

Continuous metallic network is retained in the matrix of electroless cermet due to the formation of core-shell microstructure. The flow path of the electrons is thus made continuous through the Ni-Ni shell with a consequent increase in electrical conductivity at a much lower Ni content. Nevertheless, for the cermets prepared by conventional technique, the presence of randomly dispersed Ni results in the requirement of a higher metallic content for the onset of electrical conductivity percolation.

Subsequent to the study of conductivity percolation limit, the trend of temperature dependent electrical conduction for the developed electroless anode is studied in the range of 500 – 1000°C and is shown in Figure 5.8. It is envisaged

from the figure that, irrespective of the associated milling speed, the trend of conductivity vs temperature follows ‘metallic behaviour’ i.e. with temperature enhancement, the extent of electronic conduction decreases. The overall conductivities of such developed cermets are the manifestation of total ceramic and metallic components in the cermet matrix and are highly dependent on the processing condition of the materials. The temperature dependence of electrical conductivity plots (Figure 5.8) shows ‘Arrhenius type’ behaviour for the cermets prepared with sensitized YSZ at three different milling speeds (25, 45 and 65 rpm). It is evident that the electrical conduction at different temperatures is highest for the electroless Ni-YSZ cermets prepared from YSZ sensitized at optimum milling speed of 45 rpm.

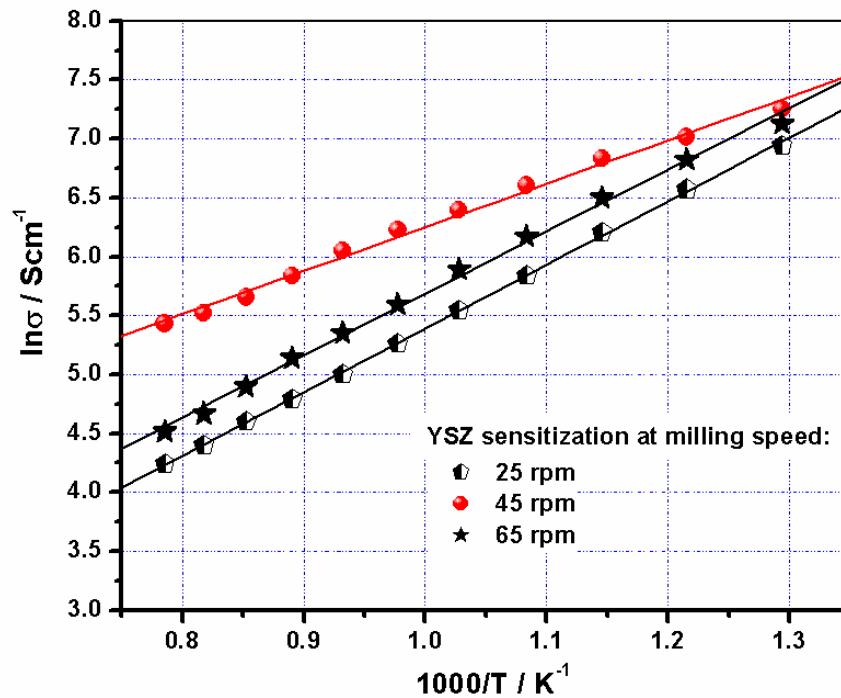


Figure 5.8: Temperature dependent electrical conductivities of cermet anodes (33 vol % Ni) prepared by ball mill assisted electroless technique

The ‘frequency factor (A)’ of the Arrhenius equation (Eq. 5.5) is obtained from the intercept of Figure 5.8.

$$\sigma = A \exp \left[-\frac{E_a}{RT} \right] \quad (5.5)$$

Chapter – 5.1

where, E_a , A , R and T are activation energy, frequency factor, universal gas constant and measurement temperature respectively.

Variation of 'A' as a function of milling speed is shown in Figure 5.9 and also tabulated in Table 5.3. The frequency factor 'A' is proportional to the number of reaction sites for adsorption of Pd^0 onto YSZ followed by in-situ reduction of Ni^{2+} to Ni^0 during electroless deposition which is found to be highest at the optimum milling speed of 45 rpm.

Table 5.3: Variation of frequency factor with milling speed during YSZ sensitization for electroless technique	
Milling speed for YSZ sensitization (rpm)	Frequency factor 'A' (scm^{-1})
25	0.986
45	12.894
65	1.537

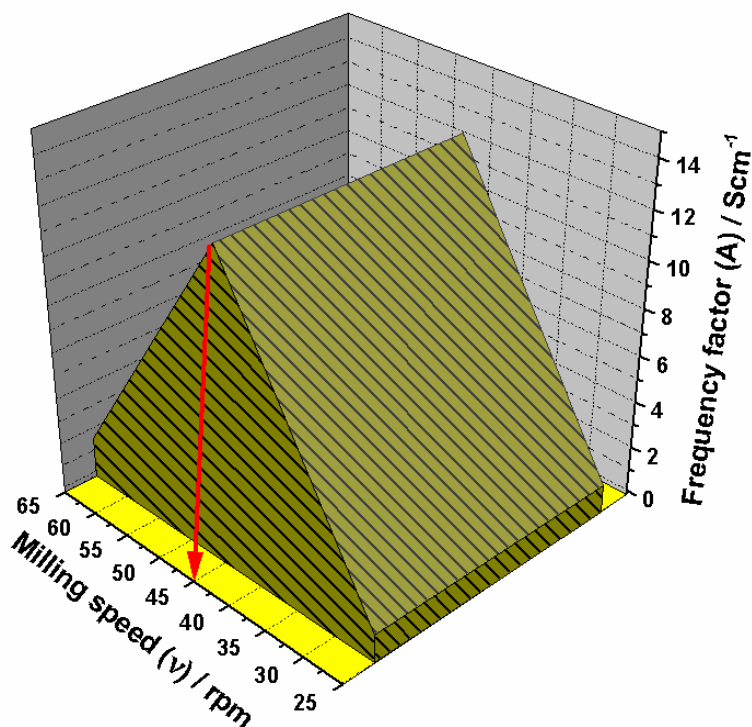


Figure 5.9: Variation of frequency factor as a function of milling speed for YSZ sensitization during electroless technique

Therefore, it is established from Figure 5.9 that, at 45 rpm, the frequency factor calculated is found to be the highest ($\sim 13 \text{ Scm}^{-1}$) and hence the milling speed of 45 rpm is the optimum milling speed that facilitates proper YSZ sensitization by surface adsorption of active Pd^0 sites ($\sim 83 \text{ ppm}$ adsorbed Pd^0 in Figure 5.3). Alleviate percolation of electronic conduction for such electroless cermet can also be correlated with the magnitude of energy barrier or ‘activation energy (E_a)’ as tabulated in Table 5.4.

Milling speed for YSZ sensitization (rpm)	Activation energy- E_a for electrical conduction (kJmol^{-1})
25	44.93
45	30.71
65	43.72

The variation of the activation energies with rotational milling speed are calculated from the corresponding slopes of Figure 5.8 and is plotted in Figure 5.10.

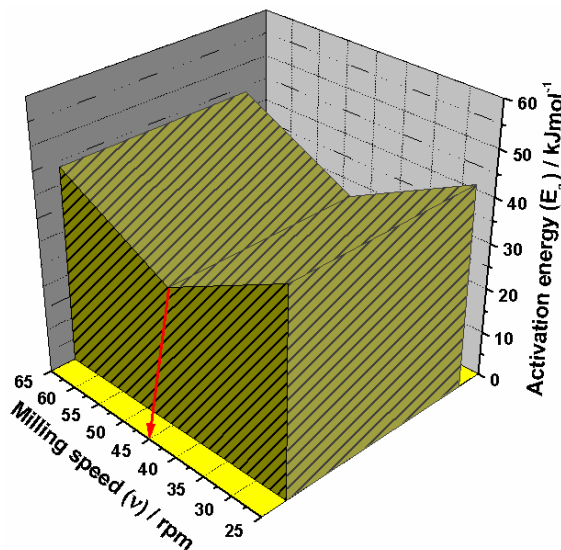


Figure 5.10: Variation of activation energy as a function of milling speed for YSZ sensitization during electroless technique

The lowest activation energy at an optimum milling speed of 45 rpm clearly indicates the presence of metallic network continuum throughout the anode

Chapter – 5.1

matrix. On the contrary, ineffective sensitization at the milling speeds of 25 or 65 rpm generates partial or wrecked Ni shell along with the formation of metallic and ceramic (YSZ) humps at various locations. The interconnection amid cohesive phases (Ni-Ni or YSZ-YSZ) are therefore hindered which results in the enhancement of energy barrier (activation energy) for electrical conduction.

The coefficient of thermal expansion (CTE) values of the electroless Ni-YSZ cermet (33 vol % Ni) prepared with YSZ sensitized at optimum milling speed of 45 rpm is found to be significantly less ($11.48 \times 10^{-6} \text{ K}^{-1}$) compared to the conventional anode ($12.79 \times 10^{-6} \text{ K}^{-1}$) consisting of ~ 40 vol % Ni. For this reason, the former is found to be thermally compatible with adjacent YSZ electrolyte ($10.85 \times 10^{-6} \text{ K}^{-1}$) which fulfils the primary criteria of an anode to be applicable for SOFC.

5.1.4.3. Microstructural study

Microstructural study enables to elucidate the significance of different processing techniques on the overall phase distribution within the cermet anode. The optical micrograph in [Figure 5.11 a](#) of electroless Ni-YSZ cermet (33 vol% Ni) prepared from sensitized YSZ under optimized milling speed of 45 rpm reveals the formation of core-shell microstructure with fine metallic Ni particulates in the grain boundary region and YSZ in the core region.

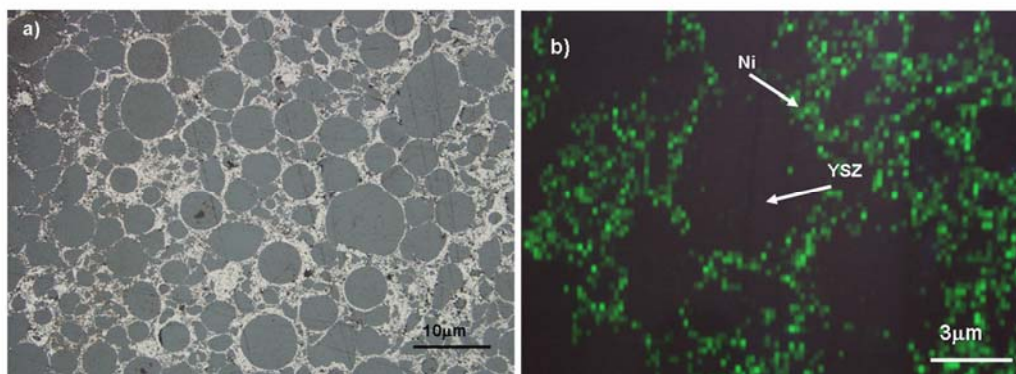


Figure 5.11: a) Optical micrograph of polished Ni-YSZ cermet (33 vol% Ni) prepared by electroless technique and b) corresponding Ni mapping of the selected area

Development of such core-shell geometry is also established through elemental Ni mapping of discreet metallic Ni shell around YSZ core for the electroless Ni-YSZ cermet prepared under the optimum conditions (Figure 5.11 b). The high resolution field emission scanning electron microscope (FESEM) image of reduced electroless Ni-YSZ cermet at an optimum milling speed (45 rpm) is shown in Figure 5.12.

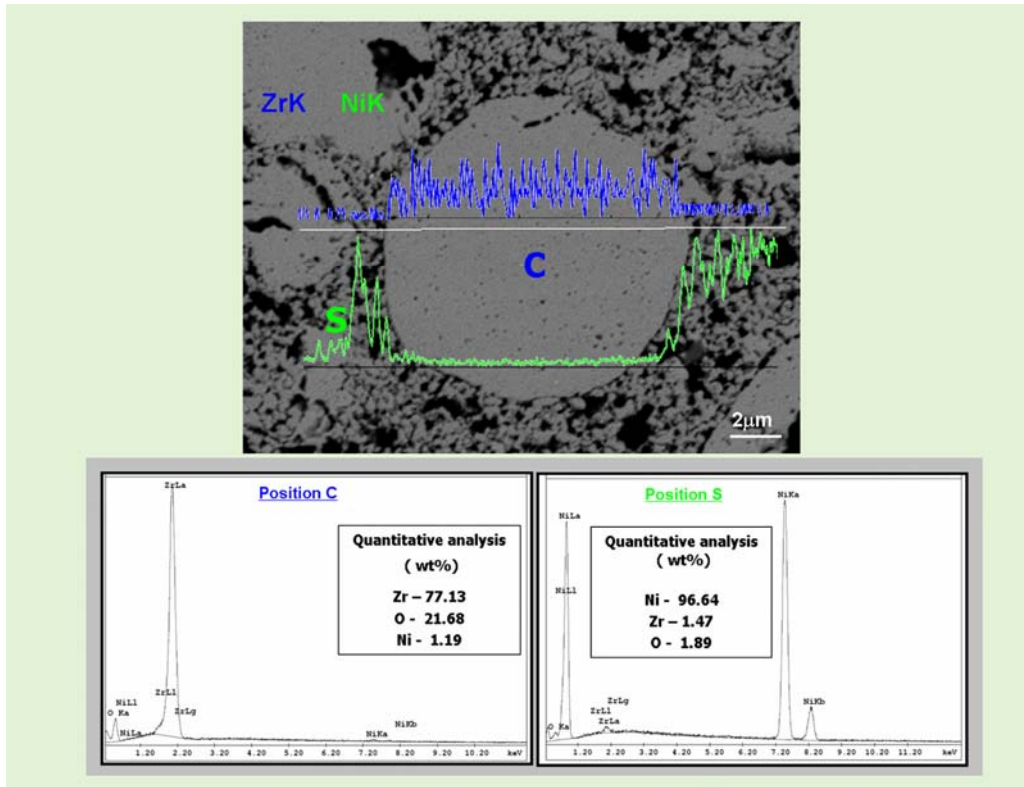


Figure 5.12: FESEM image of electroless Ni-YSZ in conjunction with quantitative spot EDAX and the corresponding elemental line mapping

The line mapping of the selected area for such electroless anode is presented in the figure by the individual colour code which clearly indicates the presence of metallic Ni in the shell and YSZ in the core. This is also supported by elemental Ni mapping as shown in Figure 5.11 b. From quantitative EDX analysis (Figure 5.12), it can be found that the core (position C) contains ~ 98 wt % zirconia whereas the shell (Position S) contains ~ 97 wt % of Ni in the reduced electroless Ni-YSZ cermets.

Chapter – 5.1

Figure 5.13 shows the optical micrographs of Ni-YSZ cermet prepared with YSZ sensitized at 25 rpm (Figure 5. 13a) and 65 rpm (Figure 5.13b). From the micrographs, it is observed that in both the cases, the Ni shell is either not formed due to ineffective sensitization of YSZ or degenerated due to excessive fragmentation of YSZ particulates because of high grinding impact. In contrast to core-shell image obtained for electroless cermet, completely different microstructure is observed in case of conventionally prepared cermet having 40 vol% Ni where a dispersed metallic nickel and YSZ matrix is observed (Figure 5.14a). Elemental mapping of the conventional cermets (Figure 5.14 b) supports the existence of randomly dispersed Ni particulates.

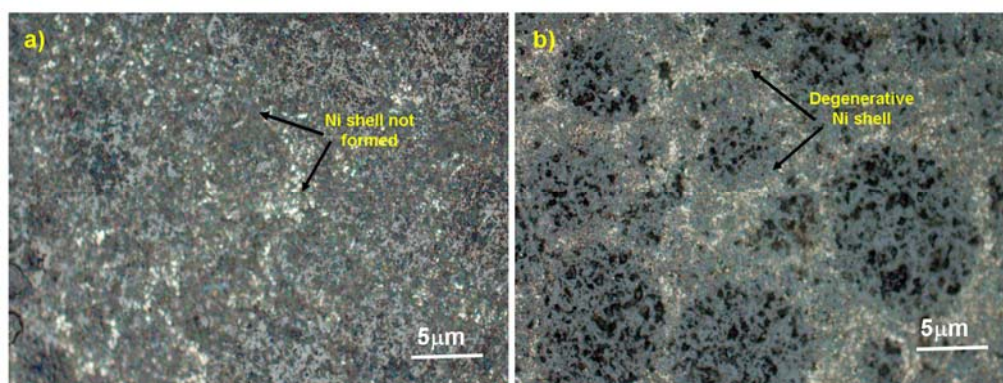


Figure 5.13: Optical micrograph of ball mill assisted electroless Ni-YSZ cermets with YSZ sensitized at: a) 25 rpm and b) 65 rpm

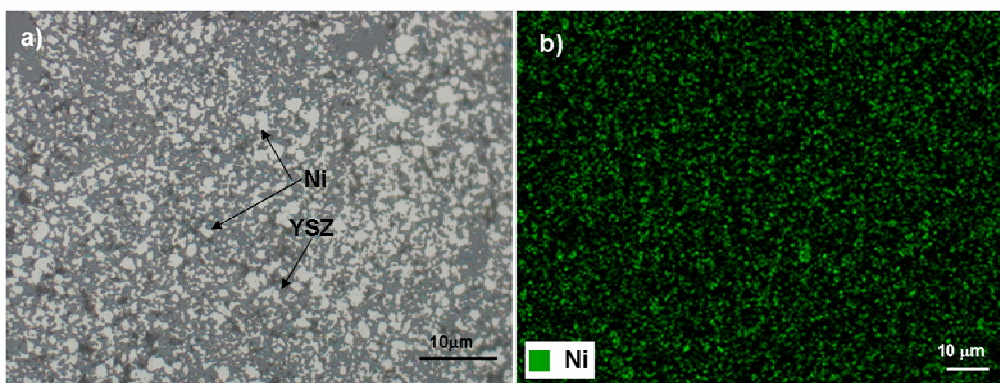


Figure 5.14: a) Optical micrograph of Ni-YSZ cermet (40 vol %) prepared by conventional solid state technique and b) corresponding Ni mapping

The particle size of Ni for the sintered and reduced electroless Ni-YSZ cermet is found to be finer than that of the Ni particles in conventional anode. From the Ni mapping of the electroless anode, it is observed that the size of electroless Ni is $\sim 0.2 - 0.3 \mu\text{m}$ (Figure 5.11 b). Conversely, from the mapping of conventional anode (Figure 5.14 b), the size range of Ni is found to be $> 1 \mu\text{m}$.

5.1.5. Summary

The experimental results obtained from the present section are based on the processing and preparation of Ni-YSZ cermet by electroless technique, which is primarily being governed by YSZ sensitization performed by ball milling. Based on the concept of ball milling theory and experimental adsorption capacity of YSZ, the milling speed is optimized as 45 rpm. Systematic studies on various parameters viz. electrical, thermal, microstructural etc of the electroless anodes prepared under different milling speed for sensitization of YSZ are correlated with the theoretical explanation of milling. Finally, the superiority of the developed electroless anode is established over conventional cermet anode which is primarily governed by process optimization during preparation of anodes applicable to SOFC.

*5.2. High Energy
Ultrasonification
Assisted Ni-YSZ
Electroless Cermet*



Chapter – 5.2

Chapter – 5.2

The electroless technique is primarily governed by the effectivity of YSZ sensitization. In the previous section, YSZ sensitization through ball milling has been extensively described along with the characteristics of the developed anode cermet. Another alternate sensitization route through ‘high energy ultrasonification’ is also pursued under the present investigation with the aim of studying its effect on the anode characteristics features. Power ultrasound has been found to have profound influence on the chemical reactions conducted in liquid phase, irrespective of whether they are homogeneous or heterogeneous in nature and can cause a number of chemical effects.²⁻⁴ This high energy sonochemical reaction is used for sensitization of zirconia by surface adsorption of Pd⁰ that forms instantaneously in the redox sensitization bath (see Eq. 5.1).

Power ultrasounds have a pronounced effect on the sensitization process. The high energy ultrasonification helps in the generation of very high temperatures and pressures at the localized position. This helps in stabilizing the reduced state of the metal (Pd⁰) quite effectively compared to the sensitization technique by ball milling. It is therefore important to study the sorption kinetics of the reduced palladium (Pd⁰) onto the sensitized YSZ precursor which ultimately governs the deposition of Ni in the electroless bath. For that reason under this present investigation, an attempt is made in order to understand the basic mechanism of Pd⁰ adsorption through a mathematically derived model based on the kinetics of sorption mechanism of Pd⁰. Pd⁰ adsorption on YSZ powder is an example of physisorption because metallic palladium is held by Vander Waal interaction with YSZ precursor powder. Therefore, Pd⁰ adsorption kinetics mainly involves two processes viz. a) the external mass transfer of Pd⁰ species from the bulk solution to the surface of YSZ and b) the intraparticle mass transfer of Pd⁰ in the pores and on the YSZ surface.⁵ An apparent kinetics takes into account the effects of both the chemical and physical rate processes and various physical process parameters, such as: a) flow conditions, b) intensity of mixing and c) heat and mass transfer of the

Chapter – 5.2

system, which can influence the kinetics rate.^{6 -9} The understanding of the physisorption process of Pd⁰ is mandatory for effective formation of the discreet Ni shell around the YSZ core that enhances the functionality by increasing the overall triple phase boundary length required for electrocatalytic oxidation of the fuel (discussed in the subsequent sections). This is reflected in attainment of ‘transient equilibrium’ during the sensitization process. Various sensitization conditions viz. agitation frequencies, equilibration time etc have a pronounced effect on the overall properties of these functional anodes which is described in the subsequent sections.

5.2.1. Sorption kinetic modeling for YSZ sensitization

The kinetics of sensitization or surface activation of YSZ precursor particulates through high energy ultrasonification engage two major processes viz. a) external mass transfer and b) intra-particle mass transfer. The schematic of these two surface active processes is shown in Figure 5.15.

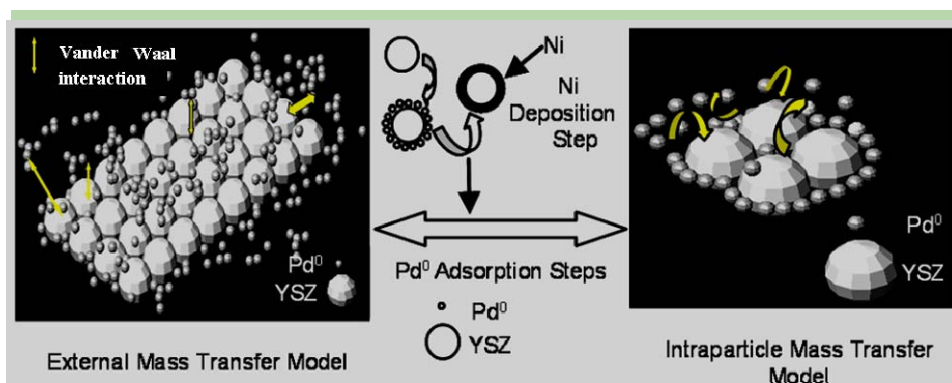


Figure 5.15: The mechanisms governing ultrasonification assisted YSZ sensitization

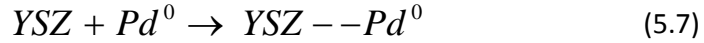
The adsorption process is mainly governed by the intraparticle mass transfer because the effect of external mass transfer gets reduced substantially by an intensive agitation (shown in the subsequent sections). Intraparticle mass transfer involves not only surface and molecular diffusion but also diffusion in the pores of the particle. These effects can be expressed by an ‘effectiveness factor (η)’ which is defined as:

$$\eta = \frac{r_p}{r_s} \quad (5.6)$$

where, r_s and r_p are the actual adsorption rate and the same evaluated at outer surface condition respectively.¹⁰

5.2.1.1. Derivation of expression for 'r_s'

YSZ sensitization process can be represented by the following equation:



where, YSZ - -Pd⁰ represents weak Vander Waal interaction between YSZ and Pd⁰.

Employing the law mass action to the reaction given in Eq. (5.7), the rate of formation of YSZ - -Pd⁰ is given as:

$$r_s = \frac{d[YSZ - -Pd^0]}{dt} = k_1 e^{-E_1/RT} [Pd^0] [YSZ] - k_2 e^{-E_2/RT} [YSZ - -Pd^0] \quad (5.8)$$

where, [] denote the concentration (ppm) of the involved species,

YSZ, Pd⁰, R, T are the adsorbent, adsorbate, universal gas constant and absolute experimental temperature respectively.

k_1 , k_2 and E_1 , E_2 are the frequency (or pre-exponential) factors and activation energies for forward and backward reactions respectively which are involved in the rate equation proposed by 'Transition State theory'.

The unoccupied surface active sites of YSZ is equal to the difference between the total active sites (YSZ_t) and the occupied surface active sites (YSZ - -Pd⁰). Hence, Eq.

(5.8) can be written as:

$$\begin{aligned} r_s &= \frac{d[YSZ - -Pd^0]}{dt} \\ &= k_1 e^{-E_1/RT} [Pd^0] [YSZ_t - YSZ - -Pd^0] - k_2 e^{-E_2/RT} [YSZ - -Pd^0] \end{aligned} \quad (5.9)$$

The above Eq. 5.9 can also be written in terms of adsorption and desorption constants as:

$$r_s = \frac{d[YSZ - -Pd^0]}{dt} = k'_{ads} [Pd^0] [YSZ_t - YSZ - -Pd^0] - k'_{des} [YSZ - -Pd^0] \quad (5.10)$$

where, $k'_{ads} = k_1 e^{-E_1/RT}$ ($ppm^{-1} \min^{-1}$) & $k'_{des} = k_2 e^{-E_2/RT}$ (\min^{-1})

The Eq. 5.10 could be further simplified as $r_s = k'_{ads} q(p_m - p) - k'_{des} p$ (5.11)

Chapter – 5.2

where, $p = [YSZ - Pd^0]$, $p_m = [YSZ_t]$, $q = [Pd^0]$

Using the Eqs. 5.7-5.11, Eq. 5.6 is written as:

$$r_p = \eta r_s = \eta [k'_{ads} q (p_m - p) - k'_{des} p] \quad (5.12)$$

5.2.1.2. External mass transport model

The external mass transfer model describes the change in adsorbate (Pd^0) concentration with time. It can be expressed as:

$$-\frac{dq}{dt} = k_f a_m (q - q_t) \quad (5.13)$$

where, ' k_f ' is the mass transfer coefficient between the bulk solution and sorbent surface ($cm \cdot min^{-1}$), ' a_m ' is the volumetric specific area of the adsorbent ($cm^2 \cdot cm^{-3}$), ' q ' and ' q_t ' are the sorbate concentrations (ppm) in the bulk solution and at the surface of YSZ respectively.

Considering the YSZ particulates to be of spherical dimension,¹¹ an equation for volumetric specific area (a_m) is given as:

$$a_m = \frac{6m}{d_p \rho_p (1 - \epsilon_p)} = \frac{6m}{d_p \rho_b} \quad (5.14)$$

where, m , d_p , ρ_p , ρ_b , ϵ_p are the concentration ($g \cdot cm^{-3}$), the average size (μm), theoretical density ($g \cdot cm^{-3}$), bulk density ($g \cdot cm^{-3}$) and porosity of YSZ respectively.

The surface concentration of metallic palladium (sorbate) is approximately taken as a constant upon considering '*external mass transfer phenomenon*' to be the controlling step. Therefore, taking the overall mass conservation into consideration, it can be written as:

$$q = q_0 - \frac{pM}{v} \quad (5.15)$$

where, q_0 , p , M and v are the initial concentration of Pd^{2+} (ppm) used (in the form of $PdCl_2$ solution), the Pd^0 uptake at equilibrium (ppm. g^{-1}), the mass quantity of YSZ powder (g) and the water volume (ml) in the sensitized bath respectively.

Substituting the value of q (from Eq. 5.15) to Eq. 5.13: $\frac{dp}{dt} = \frac{vk_f a_m (q - q_t)}{M}$ (5.16)

Chapter – 5.2

The expression for maximum adsorption capacity (q_t) can be written by using Eq. 5.10, 5.11 and 5.16 as:

$$r_s = \frac{d[YSZ - Pd^0]}{dt} = \frac{dp}{dt} = k'_{ads} q_t (p_m - p) - k'_{des} p = \frac{vk_f a_m (q - q_t)}{M}$$

$$\Rightarrow q_t = \frac{\frac{vk_f a_m q}{M} + k'_{des} p}{k'_{ads} (p_m - p) + \frac{k_f a_m v}{M}} \quad (5.17)$$

Between the external and intra particle mass transfer phenomena, when the former process becomes the prime controlling factor for Pd⁰ adsorption, two following correlations can be accounted:

$$a) \frac{k_f a_m v}{M} \ll k'_{ads} (p_m - p) \quad \text{and} \quad b) k_f a_m \rightarrow \text{small value} \quad (5.18)$$

Employing the correlations of Eq. 5.18, Eq. 5.17 is modified to:

$$q_t = \frac{k'_{des} p}{k'_{ads} (p_m - p)} \quad (5.19)$$

Considering the sorption isotherm to follow 'Langmuir equation', the expression for Pd⁰ uptake at equilibrium (p in ppm. g⁻¹) can be written as:

$$p = \frac{K_1 p_m q_s}{1 + K_1 q_s} \quad (5.20)$$

where, K_1 , p_m and q_s are the equilibrium constant (ppm⁻¹), and the total Pd⁰ concentration in the solution (ppm).

Substituting Eq. 5.20 into Eq. 5.19, expression for q_t is given as:

$$q_t = \frac{k'_{des} K_1 q_s}{k'_{ads}} \quad (5.21)$$

The above Eq. 5.21 can be reduced to: $q_t = q_s$ by taking, $K_1 = \frac{k'_{ads}}{k'_{des}}$ (5.22)

The reduced form of Eq. 5.21 i.e Eq. 5.22 is applicable on only at the condition of maximum adsorption capacity when it is considered that, the total Pd⁰ formed gets adsorbed on the sensitized YSZ surface.

As ' q_t ' is related to the equilibrium concentration, which is independent of time, Eq. 5.13 can be integrated with the following boundary conditions: at $t = 0$, $q = q_0$ (considering total reduction of Pd²⁺ to Pd⁰); and at $t = t$, $q = q$:

Chapter – 5.2

$$\ln \frac{q_0 - q_t}{q - q_t} = k_f a_m t \quad (5.23)$$

5.2.1.3. Model solution of the proposed adsorption kinetics

Employing Eqs. 5.12 and 5.15, the adsorption rates can be expressed in terms of concentration of species as:

$$\begin{aligned} r_p = \eta r_s &= \eta [k'_{ads} (q_0 - \frac{pM}{v})(p_m - p) - k'_{des} p] \\ \Rightarrow \frac{dp}{dt} &= \eta [k'_{ads} (q_0 - \frac{pM}{v})(p_m - p) - k'_{des} p] \end{aligned} \quad (5.24)$$

Integration of Eq. 5.24 yields the expression for equilibrium adsorbate uptake which is being derived below.

The above Eq. 5.24 is a function of 'p vs. t', along with other constant terms.

Therefore, the expression is transformed to integral format as:

$$\begin{aligned} \text{Eq. 5.24} \Rightarrow \frac{dp}{dt} &= \eta [k'_{ads} q_0 p_m + (-k'_{ads} p_m \frac{M}{v} - k'_{ads} q_0 - k'_{des}) p + \left(\frac{k'_{ads} M}{v} \right) p^2] \\ \Rightarrow \frac{dp}{dt} &= \eta [A + Bp + Cp^2] \end{aligned} \quad (5.25)$$

where,

$$A = k'_{ads} p_m q_0 \quad (5.26)$$

$$B = - \left(\frac{k'_{ads} p_m M}{v} + k'_{ads} q_0 + k'_{des} \right) \quad (5.27)$$

$$C = \frac{k'_{ads} M}{v} \quad (5.28)$$

$$\text{Integrating Eq. 5.25 results: } \int \frac{dp}{A + Bp + Cp^2} = \eta \int dt \Rightarrow \int \frac{dp}{A + Bp + Cp^2} = \eta t$$

$$\frac{1}{C} \int \frac{dp}{p^2 + \left(\frac{B}{C}\right)p + \left(\frac{A}{C}\right)} = \eta t \Rightarrow \frac{1}{C} \int \frac{dp}{p^2 + 2\left(\frac{B}{2C}\right)p + \frac{B^2}{4C^2} + \frac{A}{C} - \frac{B^2}{4C^2}} = \eta t$$

$$\Rightarrow \frac{1}{C} \int \frac{dp}{\left(p + \frac{B}{2C}\right)^2 - \left(\frac{\sqrt{B^2 - 4AC}}{2C}\right)^2} = \eta t \quad (5.29)$$

The left hand side (LHS) of the above Eq. 5.29 is of the standard form:

$$\int \frac{dx}{x^2 - a^2} = \frac{1}{2a} \log \left| \frac{x-a}{x+a} \right| + C$$

Therefore, solving the integral of Eq. 5.29 gives:

$$\begin{aligned} \log \left| \frac{\left(p + \frac{B}{2C}\right) - \left(\frac{\sqrt{B^2 - 4AC}}{2C}\right)}{\left(p + \frac{B}{2C}\right) + \left(\frac{\sqrt{B^2 - 4AC}}{2C}\right)} \right| &= \eta t C \left(\sqrt{\frac{B^2 - 4AC}{C^2}} \right) \\ \Rightarrow \left| \frac{\left(p + \frac{B}{2C}\right) - \left(\frac{\sqrt{B^2 - 4AC}}{2C}\right)}{\left(p + \frac{B}{2C}\right) + \left(\frac{\sqrt{B^2 - 4AC}}{2C}\right)} \right| &= e^{2.303 \eta t C \left(\sqrt{\left(\frac{B}{C}\right)^2 - \left(\frac{4A}{C}\right)} \right)} \end{aligned}$$

Finally, the expression for Pd⁰ uptake at equilibrium (p) can be written as:

$$p = \frac{\frac{B}{C} - \sqrt{\left(\frac{B}{C}\right)^2 - \left(\frac{4A}{C}\right)} - \left\{ \frac{B}{C} + \sqrt{\left(\frac{B}{C}\right)^2 - \left(\frac{4A}{C}\right)} \right\} \exp \left(2.303 \eta t C \sqrt{\left(\frac{B}{C}\right)^2 - \left(\frac{4A}{C}\right)} \right)}{2 \left[\exp \left(2.303 \eta t C \sqrt{\left(\frac{B}{C}\right)^2 - \left(\frac{4A}{C}\right)} \right) - 1 \right]} \quad (5.30)$$

Based on the above derived kinetic model, several parameters are being validated for optimization of YSZ sensitization process. The above equation provides significant correlation among kinetic parameters which in turn provides ample scope for carrying out specific experiments for authentication of the derived theory and optimization of the process constrains.

5.2.2. Summary

The present content demonstrates a newer technique for YSZ sensitization through ‘high energy ultrasonification’ during electroless process for the preparation of Ni-YSZ cermet anode for SOFC application. Such power ultrasound assisted Pd⁰ adsorption onto YSZ particulates is primarily governed by two major kinetic processes viz. a) external mass transfer and b) intraparticle mass transfer. A typical kinetic model comprising of a number of associated parameters is successfully derived based on certain rudimentary assumptions. A correlation

Chapter – 5.2

among physical adsorption (through Vander Wall interactive forces), mass transport effects, surface and molecular diffusion involving bulk and pore, equilibrium adsorption capacity etc is successfully endeavoured. Validation of the proposed theory for optimization of YSZ sensitization is presented in the next section.

Table 5.5: List of symbols used in Chapter – 5. 2		
Symbols	Word Meaning	Unit
η	Effectiveness factor	Dimensionless
r_p	Actual adsorption rate	Depend on rate equation
r_s	Adsorption rate evaluated at the outer surface condition	Depend on rate equation
YSZ -- Pd ⁰	Represents weak Vander Waal interaction between YSZ and Pd ⁰	--
R	Universal gas constant	JK ⁻¹ mol ⁻¹
T	Experimental absolute temperature	K
k_1	Frequency (or pre-exponential) factor for forward reaction	pm ⁻¹ min ⁻¹
k_2	Frequency (or pre-exponential) factor for backward reaction	min ⁻¹
E_1	Activation energy for forward reaction	Jmol ⁻¹
E_2	Activation energy for backward reaction	Jmol ⁻¹
YSZ _t	Total active YSZ sites	ppm
k'_{ads}	Forward adsorption rate constant including energy barrier term [= $k_1 \exp(E_1/RT)$]	pm ⁻¹ min ⁻¹
k'_{des}	Backward desorption rate constant including energy barrier term [= $k_2 \exp(E_2/RT)$]	min ⁻¹
p	The Pd ⁰ uptake at equilibrium [YSZ---Pd ⁰]	ppm. g ⁻¹
p_m	Maximum sorption capacity of the YSZ sorbent (YSZ _t)	
q	Pd ⁰ (sorbate) concentration in the bulk solution	ppm
q_t	Pd ⁰ (sorbate) concentration at the surface of YSZ	ppm
q_o	Initial concentration of Pd ²⁺ used (in the form of PdCl ₂ solution)	ppm
q_s	Total Pd ⁰ concentration in the solution	ppm
a_m	Volumetric specific area of the adsorbent	cm ² . cm ⁻³
k_f	Mass transfer coefficient between the bulk solution and sorbent surface	cm.min ⁻¹
m	Concentration of YSZ used	g. cm ⁻³
d_p	Average size of YSZ sorbent	μm
ρ_p	Theoretical density of YSZ	g. cm ⁻³
ρ_b	Bulk density of YSZ	g. cm ⁻³
ϵ_p	Porosity of YSZ	--
M	The mass quantity of YSZ powder	g
v	The water volume in the sensitized bath	ml
K_1	Equilibrium constant	ppm ⁻¹

*5.3. Validation of
Modeling Parameters
with Optimized YSZ
Sensitization*



Chapter – 5.3

The applicability of the proposed kinetic model for sensitization of YSZ particulates is intended to verify in terms of the associated measurable parameters. The activation energy required to overcome the initial barrier for Pd⁰ adsorption is provided to the system by specific frequency of the ultrasonifer being exposed to. The effect of prime and crucial governing factors associated with the developed theoretical model is discussed in the following sections.

5.3.1. Effect of YSZ particle size on sorption kinetics

The experiments commenced to study the effect of particle size on the sorption capacity of the sorbent is carried out at the highest sonochemical agitation frequency of 16 kHz. As already mentioned in Chapter 4 that, three different particle sizes of YSZ powder has been used to study the size effect on adsorption kinetics of Pd⁰ on YSZ powder. The particle size distribution of precursor YSZ particulates (0.2µm of YSZ-Tosho, 27µm of YSZ - Tosho HT and 3 µm of YSZ-Unitec) is shown in [Figure 5.16](#).

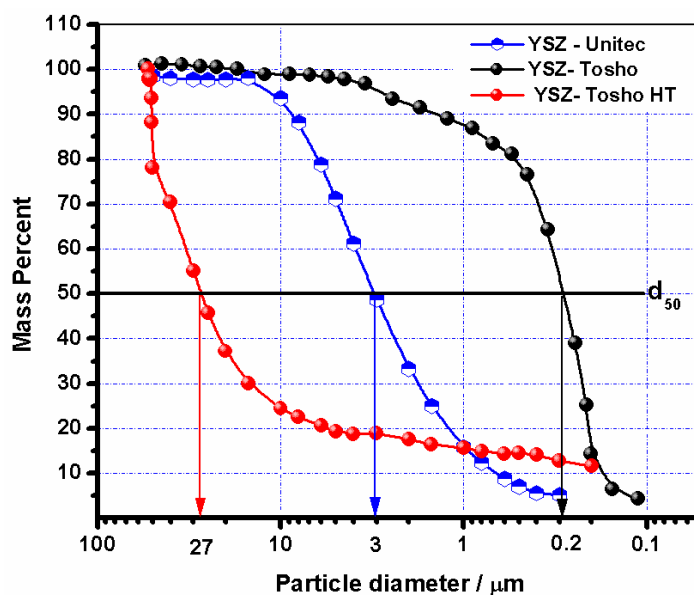


Figure 5.16: Particle size distribution of precursor YSZ powders

The volumetric specific areas (a_m) of the experimental YSZ powders can be determined using Eq. 5.14 (see section 5.2.1.2) and are summarized in [Table 5.6](#).

Chapter – 5.3

Table 5.6: Determination of volumetric specific area of precursor YSZ powders

Particle size, d_p (μm)	Bulk density, ρ_b (gcm^{-3})	Volumetric specific area, a_m ($\text{cm}^2.\text{cm}^{-3}$)
0.2	2.6	3081
3	2.3	231
27	1.3	46

The experimental details reported in Table 5.6 denote that with increase in particle size of adsorbent, bulk density decreases and thereby decreasing the volumetric specific area which is evident from Eq. 5.14. Such inverse relation among particle size and bulk density can be also observed from Figure 5.17.

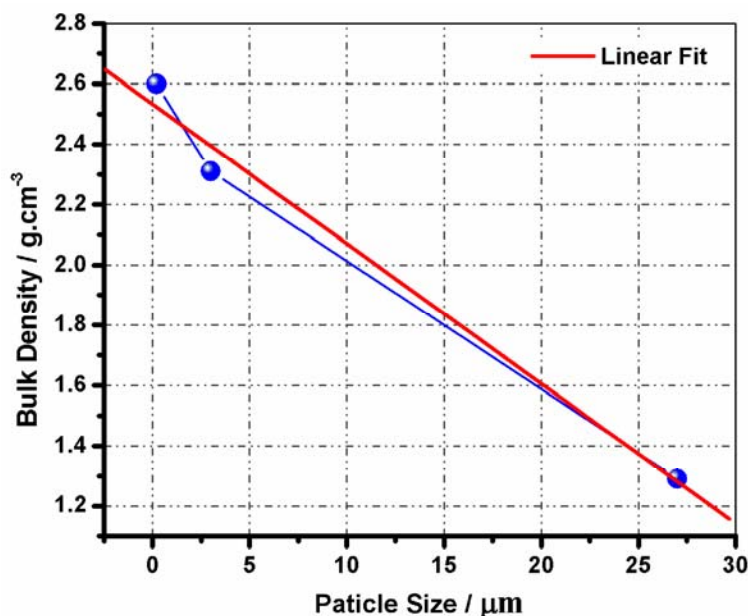


Figure 5.17: Variation of bulk densities with particle size of YSZ powder

From the theoretical concept of sorption phenomena, it is evident that, in the initial time period, physical adsorption proceeds fast due to availability of free sorbent surface. However, the forward adsorption process is limited with advancement in time due to the saturation of sorbent surface by the sorbet species. Consequently, the progression of backward desorption initiates gradually thereby leading to a reversible 'sorption' process which involves a combination of

both forward-adsorption and backward desorption reaction. The rate of either forward or backward reaction sequence is however, dependent on the type of sorbent-sorbent system dealt with and could also be optimized by controlling the reaction kinetics. The dependence of 'adsorption capacity (q_t)' on the particle size of sorbent species (YSZ) for the system of YSZ--- Pd⁰ is shown in Figure 5.18. From the figure it can be said that, adsorption of Pd⁰ onto YSZ initiates to saturate from ~ 2000 min, thereby finally achieving the 'equilibrium adsorption capacity (q_e)'. The competence of a species to act as an effective sorbent for adsorption is judged by the equilibrium adsorption capacity parameter.

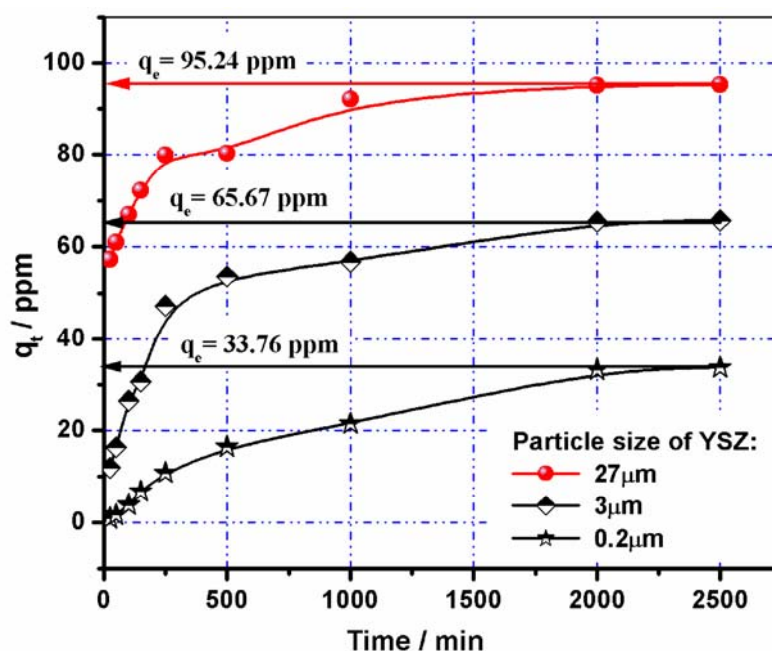


Figure 5.18: Dependence of equilibrium adsorption capacity (q_e) on the characteristics of sorbent species (YSZ particulates)

Specially treated YSZ-Tosho powder (termed as YSZ-Tosho HT) of 27 μm particle size is found to be most effective and optimum for surface adsorption of Pd⁰ which is strongly supported from the highest equilibrium Pd⁰ concentration value (q_e) of 95.24 ppm. It is observed that, with increase in particle size of the sorbent (from 0.2 μm - 27 μm), the uptake of Pd⁰ increases. At this optimum size, the extent of Vander Waal interaction among the interacting species is expected to be strong

Chapter – 5.3

enough which results in better adsorption in comparison to smaller YSZ particle sizes.

5.3.2. Effect of sonochemical agitation frequency

It is established from section 5.3.1 that, YSZ-Tosho HT powder ($d_p \sim 27 \mu\text{m}$) is most effective and optimum for surface adsorption of Pd^0 which is strongly supported from the highest equilibrium Pd^0 concentration value (q_e). Therefore, for studying the effect of sonochemical agitation frequencies viz. 10, 12, 14, 16 and 18 kHz on the sensitization process, the YSZ-Tosho HT powder is selected and the obtained results are compared with those of YSZ-Unitec powder. [Figure 5.19](#) demonstrates the optimization of specific ultrasonic frequency for effective sensitization process reported for both YSZ-Tosho HT and YSZ-Unitec. It can be said from the figure that, the extent of Pd^0 adsorption enhances steadily with increasing the agitation frequency from 10 to 16 kHz. However, the time dependant physical adsorption gets reduced with further increment in frequency to 18 kHz, thereby optimizing the ultrasonic frequency to 16 kHz as also established from the experimental results shown in [Figure 5.19](#). The equilibrium concentration value (q_e) of adsorbed Pd^0 approaches a constant value of 95.24 ppm for YSZ-Tosho HT ([Figure 5.19 a](#)) and 60.71 ppm for YSZ-Unitec ([Figure 5.19 b](#)) at the optimized frequency of 16 kHz. The highest equilibrium concentration value (q_e) clearly depicts that; the former YSZ-Tosho HT is more effective for Pd^0 sorption kinetics compared to YSZ – Unitec particulates.

It can be explained from the above figure that for the frequency range of 10-16 kHz, the equilibrium concentration value (q_e) of adsorbed Pd^0 approaches a maximum constant value of 95.24 ppm for YSZ-Tosho HT, but the equilibrium state is reached quickly at a relatively higher frequency. An increase in the adsorption rate with increase in agitation frequency can be explained by an enhanced turbulence in the solution (sensitized bath) which results in a decreased thickness of liquid boundary layer surrounding particles leading to the increment in external

mass transfer coefficient. At the optimized agitation frequency value of 16 kHz, finally the boundary layer becomes very thin and approaches to the laminar sub layer. Under these conditions, the external mass transfer resistance and coefficient values are almost constant and thus can be neglected.

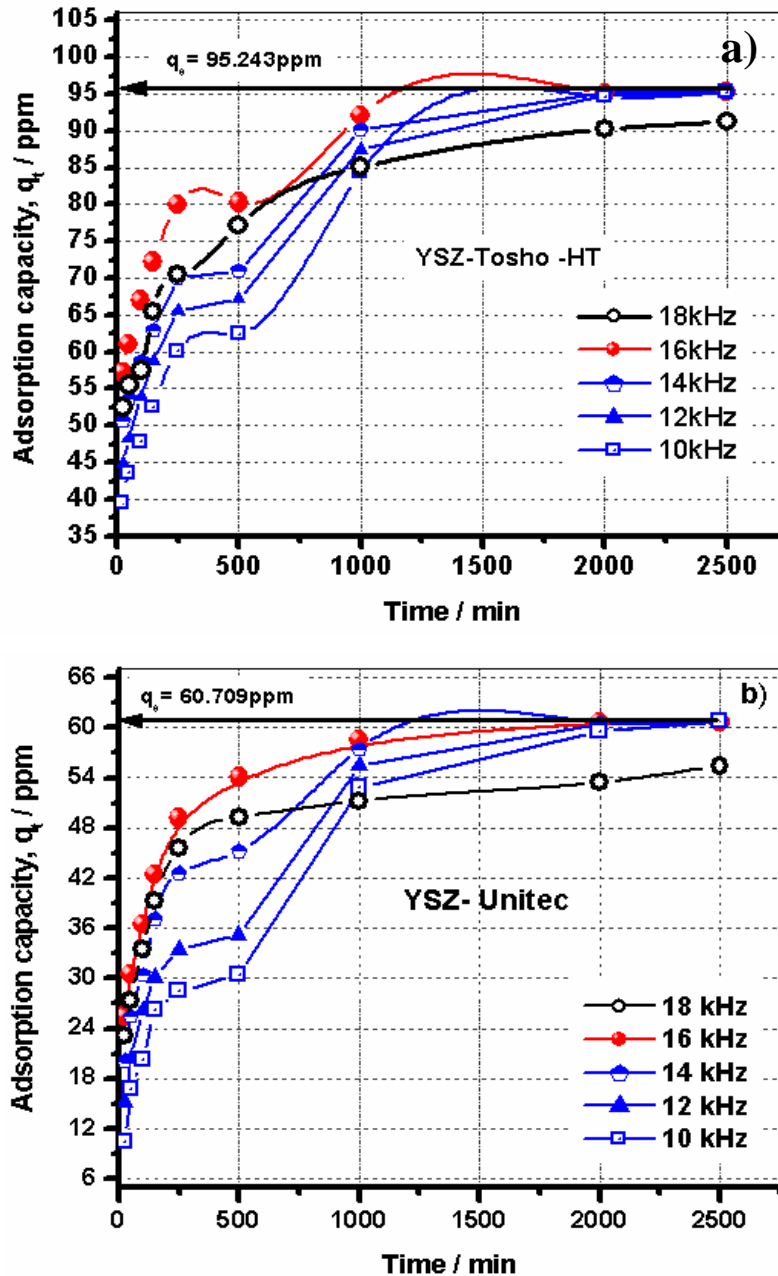


Figure 5.19: Effect of agitation frequency on sorption frequency (q_t) of Pd^0 by a) YSZ-Tosho HT and b) YSZ-Unitec

Chapter – 5.3

However, increasing the turbulence of the sensitized bath beyond a limit is believed to favor the backward desorption rate as observed from the reduced adsorption capacity at the agitation frequency of 18 kHz. At such higher frequency, rate of desorption overshadow the forward equilibration of adsorbed Pd⁰ species. The degree of adsorption, being dependent on the nature of adsorbent, varied considerably for two YSZ variants (YSZ-Tosho HT and YSZ-Unitec); however, the trend of sorption reaction with frequency variation (10-18 kHz) shows similarity for the experimental YSZ powders.

5.3.3. Application of external mass transfer phenomena

As already discussed in section 5.2, adsorption of Pd⁰ on YSZ particulate is governed mainly by 'external mass transfer' and 'intraparticle mass transfer' phenomena.

From [Figure 5.19](#) it could be visualized that, depending on time, the kinetics for Pd⁰ adsorption proceeds at two different rates.¹²⁻¹³ Initially (upto nearly 500 min) and the adsorption of Pd⁰ proceeds very fast which is indicated by a much steeper slope in the graph ([Figure 5.19](#)). The high initial rate of Pd⁰ uptake suggests that the adsorption occurs mainly at the sorbent (YSZ) surface and external mass transfer plays active role during this period of time. This is followed by a longer period of slower adsorption (plateau region in the graph) upto 2500 min. The later slower adsorption is indicative of the involvement of intraparticle mass transfer (diffusion technique) mechanism in the sorption kinetic model. The variation of external mass transfer governed sorption capacity (q_t) for two YSZ-varieties is shown in [Figure 5.20](#).

Experimental linear fit of the external mass transfer model [Eq. (5.23)] for Pd⁰ adsorption kinetics for both YSZ –Tosho HT and YSZ- Unitec, upto experimental time interval at different agitation frequencies is shown in [Figures 5.21](#) and [5.22](#). The adsorbed and bulk concentrations of Pd⁰ (q_t and q) species at different time

interval are determined from Figure 5.20 and are linearly fit as shown in Figures 5.21 and 5.22. It can be said upon comparing Figures 5.21 and 5.22 that, external mass transfer model fits upto 250 min in-case of YSZ- Tosho HT whereas, the model is valid only upto 150 min for YSZ-Unitec precursor. The values of volumetric external mass transfer coefficient (k_v), which is equal to the product of external mass transfer coefficient (k_f) and specific area of YSZ particle (a_m), are obtained from the slope of Figure 5.21 and 5.22 and are tabulated along with the corresponding ' k_f ' values in Table 5.7.

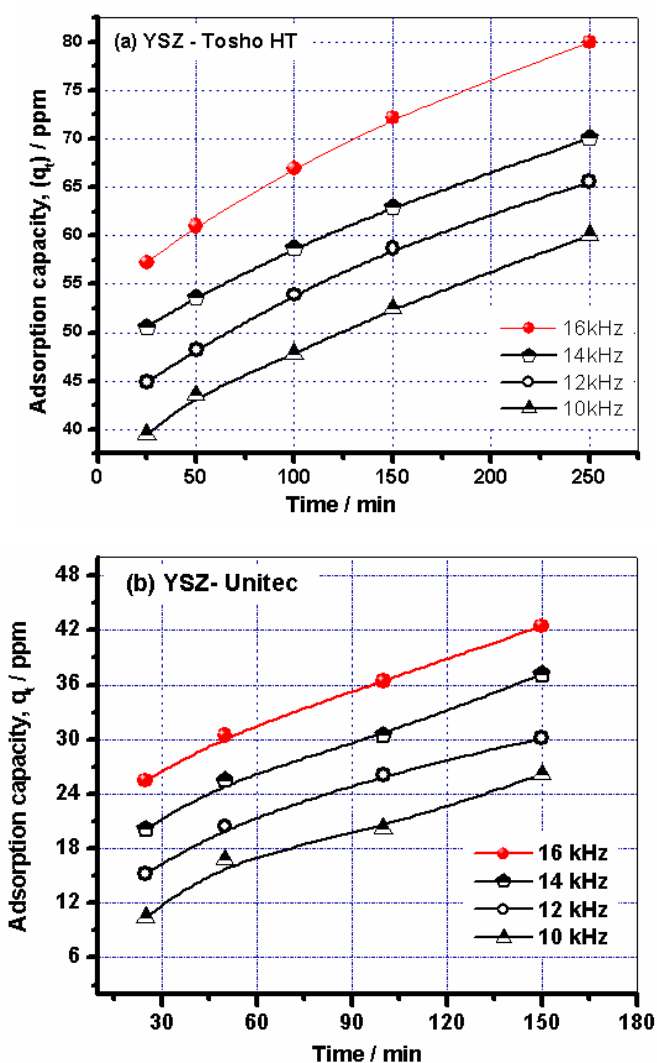


Figure 5.20: Variation of external mass transfer governed sorption capacity by: a) YSZ-Tosho HT and b) YSZ-Unitec, as function of agitation frequency upto experimental time interval

Chapter - 5.3

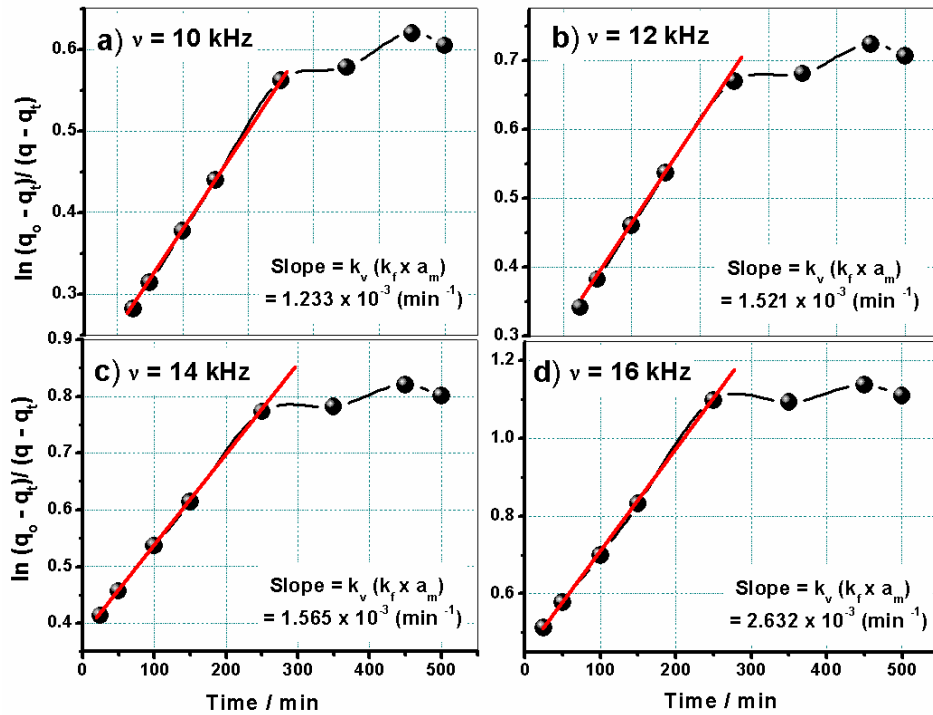


Figure 5.21: Variation of $(q_o - q_t / q - q_t)$ vs. time for Pd^0 adsorption on YSZ-Tosho HT with agitation frequencies (ν) of: a) 10 kHz, b) 12 kHz, c) 14 kHz and d) 16 kHz

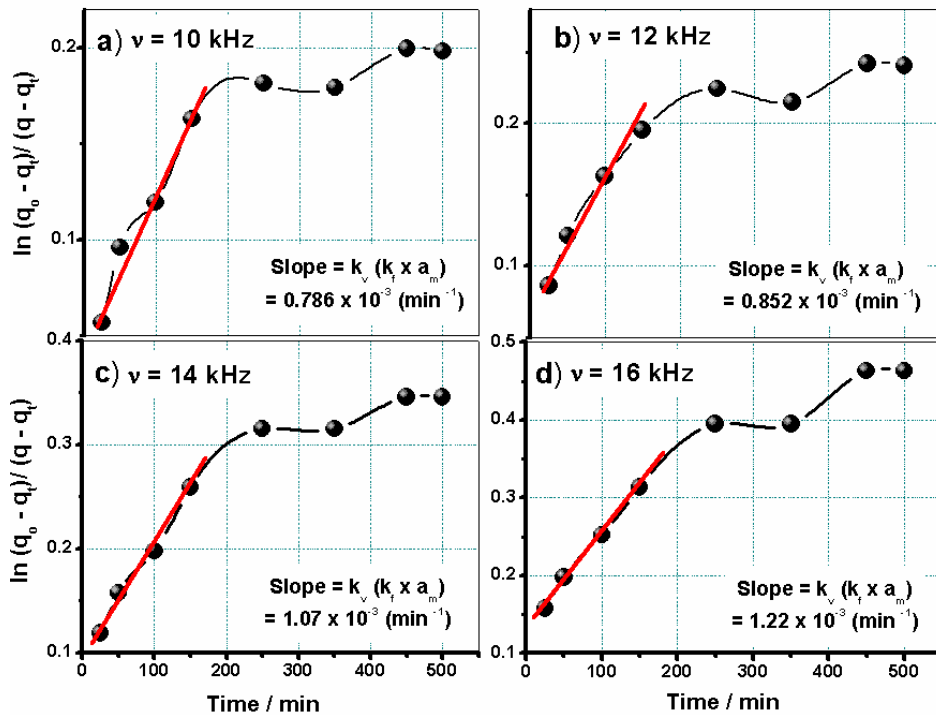


Figure 5.22: Variation of $(q_o - q_t / q - q_t)$ vs. time for Pd^0 adsorption on YSZ-Unitec with agitation frequencies (ν) of: a) 10 kHz, b) 12 kHz, c) 14 kHz and d) 16 kHz

Table 5.7: The calculated mass transfer coefficients at different agitation frequencies

Agitation Frequency (kHz)		10	12	14	16
k_f ($\times 10^{-5} \text{ cm} \cdot \text{min}^{-1}$)	YSZ-Tosho	2.68	3.31	3.40	5.72
	YSZ-Unitec	0.3402	0.369	0.463	0.528
k_v ($\times 10^{-3} \text{ min}^{-1}$)	YSZ-Tosho	1.23	1.52	1.57	2.63
	YSZ-Unitec	0.786	0.852	1.07	1.22

Irrespective of the precursors used, the mass transfer coefficients (k_f or k_v) are found to follow a linear increasing trend with ascend in agitation frequency, which supports that the adsorption regime is primary controlled by external mass transfer. However, comparison of the experimental mass transfer coefficients clearly depicts that, YSZ-Tosho HT powder is more effectively sensitized due to higher Pd^0 adsorption capacity as ascertained by the higher coefficient values at any agitation frequencies. The lesser magnitude of transfer coefficients for Pd^0 adsorption by YSZ-Unitec precursor is the direct consequence of relatively lower time interval (150 min) upto which the external mass transfer phenomenon is operative. The obtained results are therefore, indicative of the fact that, the initial external mass transfer phenomena is effectively operative for Pd^0 adsorption onto YSZ-Tosho HT at an optimized agitation frequency of 16 kHz.

5.3.4. Application of intra-particle mass transfer phenomena

It is proved from the validation of the derived kinetic model that particle size of the YSZ precursor has a pronounced effect on the sensitization mechanism. YSZ-Tosho HT, thus being optimized for external mass transfer phenomena during reversible adsorption by Pd^0 active species, it is only considered for further study of the sorption model.

Chapter – 5.3

To obtain the equilibrium constant (K_1) for Pd^0 adsorption on YSZ-Tosho HT ($d_p \sim 27 \mu\text{m}$) for the reaction given in Eq. 5.7, ‘Langmuir adsorption isotherm’ (Eq. 5.20) is used which can be linearly expressed as:

$$\frac{1}{p} = \frac{1}{p_m} + \frac{1}{K_1 p_m q_s} \quad (5.31)$$

$$\Rightarrow \frac{q_s}{p} = q_s \left(\frac{1}{p_m} \right) + \frac{1}{K_1 p_m} \quad (5.32)$$

where, p , p_m , q_s , K_1 are Pd^0 uptake at equilibrium ($\text{ppm} \cdot \text{g}^{-1}$), maximum sorption capacity of the sorbent ($\text{ppm} \cdot \text{g}^{-1}$), total Pd^0 concentration in the solution (ppm) and the equilibrium constant (ppm^{-1}) respectively.

In order to fit ‘Langmuir adsorption isotherm’ data in Figure 5.19 a, Eq. 5.32 is used and is represented in Figure 5.23.

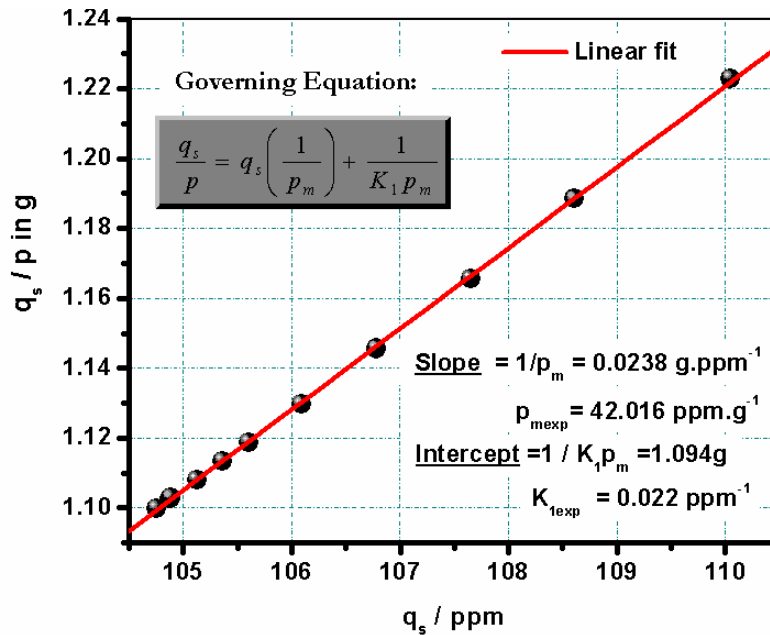


Figure 5.23: Intra-particle mass transfer phenomena for YSZ- Pd^0 system governed by Langmuir isotherm

As the parameters in the Langmuir equation are governed by the equilibrium state of a time dependent reversible process, Eq. 5.32 can only be applied in the transient equilibrium range (from 1000 min to 2500 min) shown in Figure 5.19a. It

can be observed from the linear fit of [Figure 5.23](#) that, the Langmuir adsorption isotherm is valid in the latter stage of Pd⁰ adsorption ([Figure 5.19a](#)), where the kinetics is entirely governed by intraparticle mass transfer phenomena and is responsible for slower adsorption rate.

The obtained experimental results therefore, corroborate/ validate the involvement of both external mass transfer and intraparticle mass transfer phenomena towards the overall sorption phenomena for the present adsorbent-adsorbate system viz. YSZ-Pd⁰. The effectivity of the aforementioned mechanisms is however dependent on the ‘effectiveness factor’ which governs the feasibility of an involved reaction towards forward direction.

5.3.5. Determination of effectiveness factor and its importance

For any reversible reaction as given in Eq. 5.7, the equilibrium constant (K_1) can be written in terms of forward (k'_{ads}) and backward (k'_{des}) rate constants as:

$$K_1 = \frac{k'_{ads}}{k'_{des}} \quad (5.33)$$

Therefore, using Eq. 5.33, Eqs. 5.26, 5.27 and 5.28 can be modified as:

$$\frac{B}{C} = -\left(p_m + q_0 v / M + v / MK_1\right) \quad (5.34)$$

and

$$\frac{A}{C} = \frac{p_m q_0 v}{M} \quad (5.35)$$

Considering the average equilibration time at 1750 min ([Figure 5.17](#)) and $q = q_s$ in Eq. 5.20, theoretical adsorbate uptake at equilibrium (p) can be calculated from the Langmuir isotherm (Eq. 5.20). Using Eqs. 5.33 -5.35 and calculating the value of ‘ p ’, Eq. 5.30 can be solved as:

$$\eta k'_{ads} = 7.595 \text{ ml (g min)}^{-1} \quad (5.36)$$

$$\eta k'_{des} = 3.45 \times 10^{-4} \text{ min}^{-1} \quad (5.37)$$

Chapter – 5.3

The physical significance of $\eta > 0$ is that, diffusional resistances favor the forward reaction rate (adsorption) whereas, $\eta < 0$ promote the desorption rate.⁹ Therefore, from Eqs. 5.36 and 5.37, it can be proposed that, the diffusion process (intraparticle mass transfer) not only favors the attainment of adsorption equilibrium, but at the same time, it favors the adsorption rate. However, as ' $k'_{ads} \gg k'_{des}$ ' [evident from Eqs. 5.36 and 5.37] and η has positive value in the equilibrium region of adsorption kinetics, the same is preferred over the backward desorption kinetics. Consequently, the concentration gradient of Pd^0 from the YSZ surface to the bulk is minimized, thereby reducing the Ni concentration gradient during subsequent electroless deposition from the bulk to YSZ surface which, in turn, enhances the functionality of the materials for fuel cell applications.

5.3.6. Summary

The present content is based on the validation of the proposed kinetic model presented in *Section 5.2*, applicable for adsorption of Pd^0 onto YSZ sorbent species. The kinetic parameters, viz. effectiveness factor (η), time dependent sorption capacity (q_t) and equilibrium sorption capacity (q_e) are found to be the variants of particle size of the sorbent (YSZ) species. In lieu of this fact, two varieties of sorbent such as, YSZ-Tosho HT and YSZ-Unitec are employed, between which the former is proved to be more effective for adsorption through various experimental outcomes. Although, the initial adsorption is preferably governed by external mass transfer but intraparticle mass transfer phenomena favors to attain the adsorption equilibrium. The external mass transfer coefficient is found to depend on the agitation frequency, but at the optimized ultrasonic frequency of 16 kHz, its effect can be neglected after attaining equilibration. In this particular equilibrium adsorption regime, sorption kinetics solely depends on intraparticle mass transfer since the sorption of Pd^0 on YSZ surface is an example of physical adsorption. The

Chapter – 5.3

effectiveness factor (η) for Pd⁰ adsorption is found to be positive which favors the forward adsorption rate in the equilibrium region where intraparticle mass transfer is the rate controlling step.

*5.4. Electroless Cermet:
Correlations with
Physical Properties*



Chapter – 5.4

Process optimization for sensitization/surface activation of YSZ powder precursors through high energy power ultrasonification has been studied explicitly along with the validation of modeling parameters as documented in sections 5.2 and 5.3. The result of such process optimization could further be established from the experimental studies of anode characteristics as conferred in the subsequent sections. Such detailed property correlations with the mathematical modeling could even enlighten the prospect of high energy ultrasonification as an important technique for sensitization of YSZ related to the synthesis of Ni-YSZ electroless cermets.

5.4.1. Phase identification

The X-ray diffraction pattern of as-synthesized Ni-YSZ cermet prepared by electroless technique is shown along with the XRD pattern of precursor YSZ powder in [Figure 5.24](#).

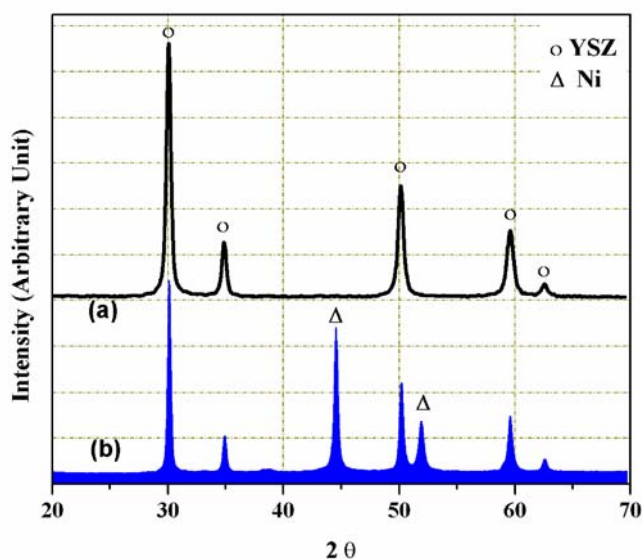


Figure 5.24: X-ray diffraction pattern of a) precursor YSZ powder and b) Ni-YSZ cermet prepared by electroless technique

Comparison of [Figure 5. 24a](#) with [Figure 5. 24b](#) clearly indicates the formation of phase pure biphasic matrix of Ni-YSZ cermet prepared by electroless technique. The overall batch formulation of the Ni-YSZ cermet prepared by electroless

Chapter – 5.4

technique is given in Table 5.8 along with the sample identification codes. Optimization of processing technique viz. ultrasonic assisted YSZ sensitization and electroless Ni deposition as discussed in sections 5. 2 and 5.3 generate such phase pure Ni-YSZ cermet even at a very low Ni content and the phase purity of such synthesized cermets covers the full range from 5-40 vol % of Ni as shown in Figure 5.25.

Table 5.8: Batch identification of Ni-YSZ cermets prepared by ultrasonic assisted electroless technique

Sl. No.	Anode composition (vol %)		Batch ID
	Nickel (Ni)	Yttria stabilized zirconia (YSZ)	
1	5	95	5- UEL
2	10	90	10-UEL
3	15	85	15-UEL
4	20	80	20-UEL
5	25	75	25- UEL
6	28	72	28-UEL
7	30	70	30- UEL
8	35	65	35-UEL
9	40	60	40- UEL

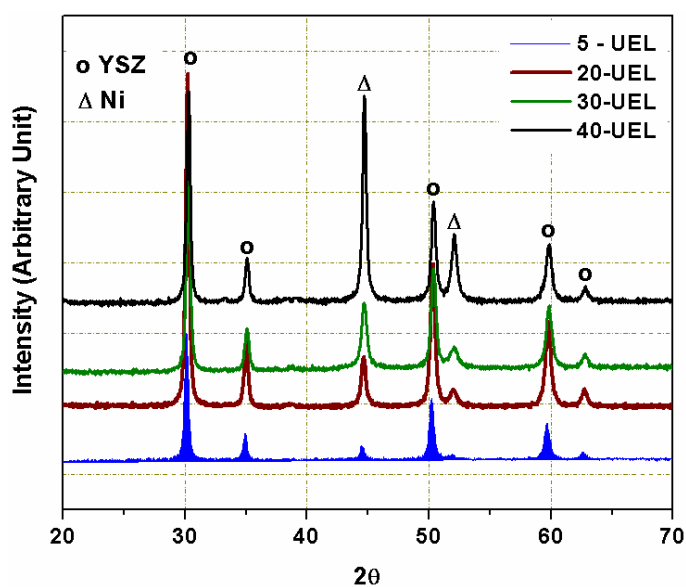


Figure 5.25: X-ray diffraction pattern of Ni-YSZ cermets with variable phase compositions prepared by electroless technique

5.4.2. Effect of equilibration time for YSZ sensitization on enhancement of anode functionality

Surface adsorption of Pd⁰ onto YSZ during sensitization is observed (Chapters 5.2 and 5.3) to be governed by two mechanisms viz. a) external mass transfer controlling the initial half of adsorption kinetics and b) intra-particle mass transfer; helps the adsorbent--adsorbate system to achieve transient equilibrium. It has been established from earlier sections that, time dependent sensitization of YSZ-Tosho HT could be alienated into distinct regimes as shown in the schematic of Figure 5.26.

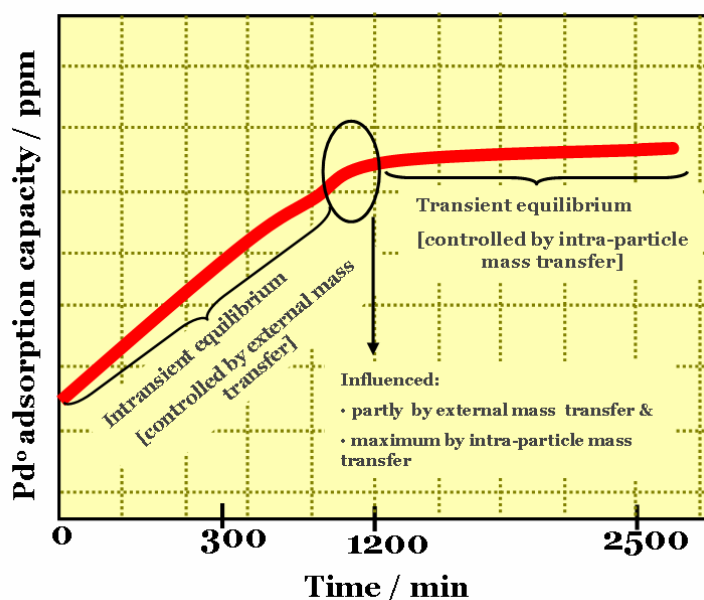


Figure 5.26: Schematic for dependence of Pd⁰ adsorption capacity on equilibration time

Based on such time dependence, three series of Ni-YSZ cermets are prepared by electroless technique (Table 5.9) with the usage of YSZ-Tosho HT as the precursor powder: i) in the first series (designated as T1-series); where the sensitized bath is equilibrated for 300 min, ii) in the second series (designated as T2-series); the sensitized bath is equilibrated for 1200 min and iii) in the third series (designated as T3 series); where the sensitized bath is equilibrated for 2500 min. In addition to the

Chapter – 5.4

batches prepared by electroless technique (T1-, T2- and T3 - series), several batches with Ni content between 10-40 vol% have also been prepared by conventional solid state technique (designated as CA-series) as tabulated in Table 5.9, using specially treated YSZ-Tosho HT for comparison.

Table 5.9: Batch identification of Ni-YSZ cermets based on equilibration time during sensitization

Ni content (vol %)	Batch ID			
	Electroless Anodes			Conventional Anodes
	Equilibration time (min)			
	300	1200	2500	
5	T1-5-UEL	T2-5-UEL	T3-5-UEL	--
10	T1-10-UEL	T2-10-UEL	T3-10-UEL	CA-10
15	T1-15-UEL	T2-15-UEL	T3-15-UEL	CA-15
20	T1-20-UEL	T2-20-UEL	T3-20-UEL	CA-20
25	T1-25-UEL	T2-25-UEL	T3-25-UEL	CA-25
28	T1-28-UEL	--	--	--
30	T1-30-UEL	T2-30-UEL	T3-30-UEL	CA-30
33	--	T2-33-UEL	--	--
35	T1-35-UEL	T2-35-UEL	T3-35-UEL	CA-35
37	--	--	T3-37-UEL	--
40	T1-40-UEL	T2-40-UEL	T3-40-UEL	CA-40

The anode cermets prepared through either electroless or conventional techniques are subjected to a high temperature sintering in air at 1400°C for 6h. The sintered NiO-YSZ anode samples are then reduced at 1000 °C under a gaseous flow of argon and hydrogen (4:1) for 10 h and thus Ni-YSZ cermet bulk samples are produced. The abovementioned anode formulations are subjected to a series of physical characterizations, discussed in the subsequent sections.

5.4.2.1. Densification study

The extent of densification of the formulated anode cermets prepared by either solid state or electroless technique is studied by measuring the densities and open porosity through standard ‘Archimedes principle’, discussed in Chapter 4. The

experimentally obtained densities and open porosities are represented as a function of Ni content in Figure 5.27 and Figure 5.28 respectively.

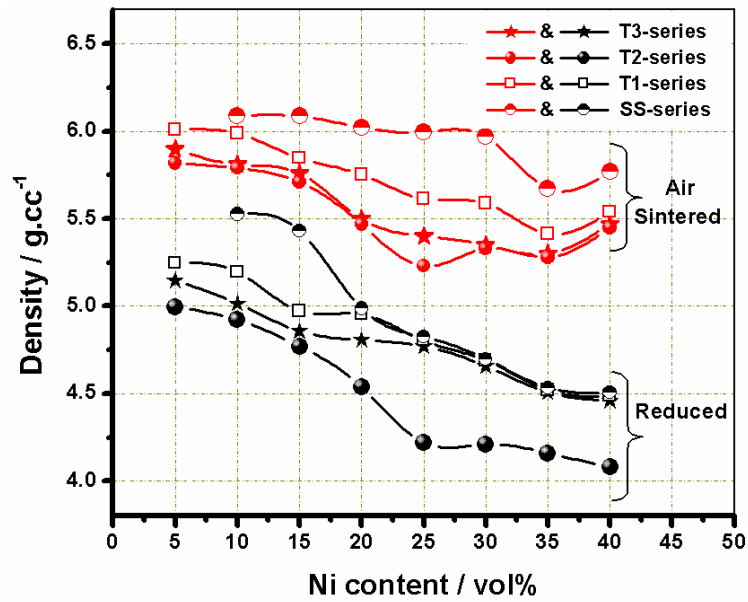


Figure 5.27: Variation of densities as a function of processing techniques and equilibration time for YSZ-sensitization during electroless process

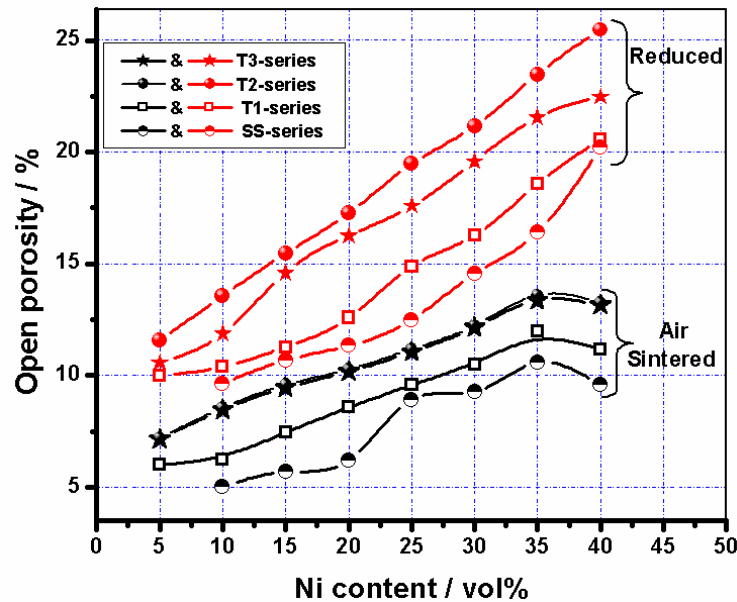


Figure 5.28: Variation of open porosities as a function of processing techniques and equilibration time for YSZ-sensitization during electroless process

Chapter – 5.4

It is observed from [Figure 5.27](#) that, irrespective of the preparation technique, with increase in Ni content, the sintered densities of NiO-YSZ varies non-linearly, whereas after reduction, change in density follows a linear decreasing trend. As expected, the corresponding porosity of all the sintered samples is found to vary non-linearly but follows an increasing trend after reduction ([Figure 5.28](#)). This can be explained on the basis that with increase in Ni content in the anode cermet, the extent of oxygen loss also increases which consequently enhances the open porosity in the matrix.¹⁴ The effect of equilibration time during the YSZ sensitization on density and porosity of electroless anode can be observed from the comparative plots of [Figure 5.27](#) and [5.28](#).

As demonstrated by the schematic in [Figure 5.26](#), Pd⁰ adsorption onto YSZ-Tosho HT in T1-series (equilibration time = 300 min) is solely controlled by external mass transfer phenomena. Such non-transient YSZ sensitization for only 300 min results in the formation of excess free Ni in the cermet during electroless deposition due to ineffective YSZ sensitization. Formation of these free Ni in the T1-series batches fails to get deposited onto sensitized YSZ effectively and thereby increases the bulk density through effective bonding between available YSZ-YSZ and Ni-Ni active surfaces. Consequently, the open porosities of T1-series samples are found to be lower in comparison to T2- and T3-series. Longer equilibration time in case of both T2- and T3-series promotes effective diffusion controlled Pd⁰ adsorption (intraparticle mass transfer) which facilitates significant sensitization of YSZ particulates. However, the number density of active Pd⁰ sensitized YSZ sites is more in T3- series due to highest equilibration time which results in the formation of prominent core-shell structure with Ni-Ni continuous network throughout the matrix. Owing to the formation of prominent interconnected microstructure due to optimized densification for T3-series anode, its effectivity is well manifested for SOFC application. Compared to T3- series, in T2-series, the presence of lesser active YSZ sites leads to the formation of relatively ineffective core-shell structure which

limits the overall densification. Consequently, the sintered or reduced matrix of T2-series acquires more porosity that restricts the mechanical strength of the resultant anode.

At length, the extent of densification is found to get influenced by the microstructural phase distribution generated through different anode preparation techniques. It can be observed from [Figure 5.27](#) and [5.28](#) that, electroless anode cermets of T1, T2 or T3-series are less dense and consequently more porous either in the sintered or reduced state compared to the conventionally prepared Ni-YSZ cermet (SS-series). Dispersed distribution of Ni and YSZ (revealed in the following sections) in the matrix of conventional anode contributes for higher density and lesser open porosity. In contrast, unique core-shell microstructure of electroless cermet results in lower density compared to the former conventional anode.

5.4.2.2. Electrical characterizations

According to the prior art theories,¹⁵ electrical conductivity of a cermet, e.g. Ni-YSZ anode, is guided by the ratio of contributing phases (Ni : YSZ) present in the matrix. The electrical conductivity of Ni-YSZ anode is strongly dependant on the corresponding Ni content. The conductivity of the cermet as a function of Ni content shows a typical 'S-shaped' curve as predicted by the 'Percolation theory'.^{15, 16} The percolation threshold for the conductivity is found to be dependant on the processing technique utilized for anode preparation. In alternate means, it could be also believed that the Ni content required for the initiation of electrical conductivity percolation is a variant of microstructural distribution.

The correlative representation among electrical conductivity and Ni content for electroless and conventional anode cermets at 800°C is given in [Figure 5.29](#). It can be observed from [Figure 5.29](#) that for the Ni-YSZ cermets prepared by electroless technique, the 'upper percolation threshold' (at which the conductivity value is sufficiently high for SOFC application) is dependent on the equilibration

Chapter – 5.4

time of the YSZ sensitization process. For T3-series batches, the upper percolation threshold is brought down to ~ 28 vol % of Ni compared to ~ 40 vol % Ni in conventionally prepared anodes. However, the similar percolation threshold is found to be shifted towards ~ 33 vol % Ni for T2 - and ~ 37 vol% Ni for T1-series batches respectively. According to Figure 5.19a (section 5.3) it can be clearly demonstrated that, equilibration of the YSZ-Tosho HT sensitized bath is optimized at ~ 2500 min which enables maximum absorption of active Pd⁰ ($q_e = 95.243$ ppm) species. However, inefficient sensitization of YSZ in T1- and T2-series equilibrated for > 2500 min, results in the formation of weaker core-shell structure.

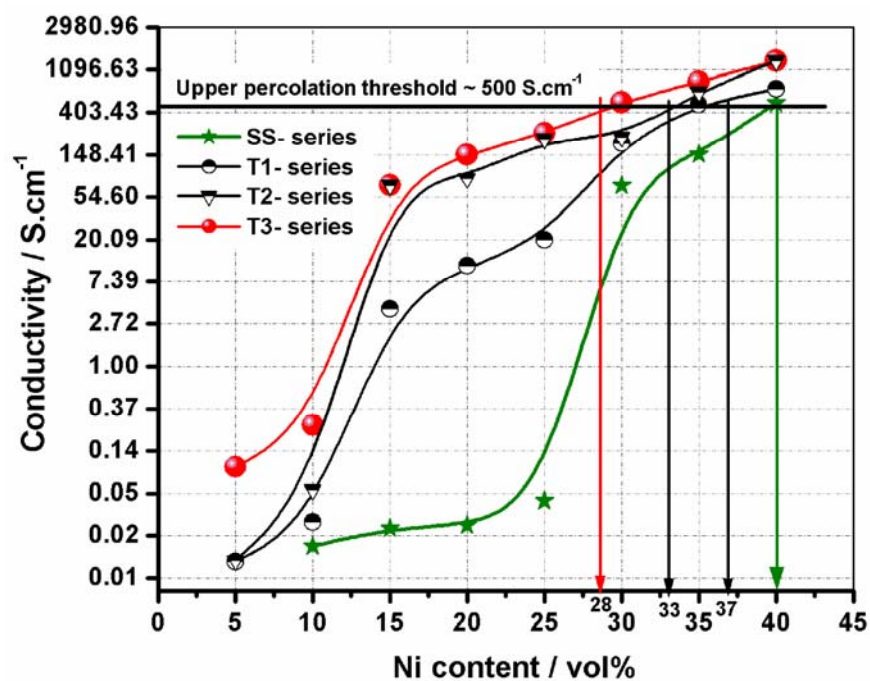


Figure 5.29: Comparison of electrical conductivities of Ni-YSZ cermet prepared by different techniques

Due to the discontinuous electronic path within the cermet matrix of T1- and T2- series batches, the upper electrical percolation threshold is found to be at a relatively higher Ni content in comparison to T3-series in which effective sensitization results in the formation of prominent core-shell structure with higher electrical conductivity at a lower Ni content. The comparative electrical

conductivities of functional and conventional anodes at the experimental temperature of 800 and 1000°C are also presented in Table 5.10. Hence, significance enhancement in the electronic conductivity can be obtained at only 28 vol % Ni for electroless Ni-YSZ, compared to 40 vol % Ni required by conventional anodes.

Table 5.10: Comparative electrical conductivities of SOFC anodes prepared by different techniques

Temperature (°C)	Electrical Conductivity, S.cm ⁻¹			
	Electroless anode			Conventional anode CA-40
	T1-37-UEL	T2-33-UEL	T3-28-UEL	
1000	206	247.4	265	149
800	486.19	488.8	489.5	505.7

The influence of anode microstructure on electrical conductivity can also be accounted from the Ni content required for the ‘lower percolation threshold’. The transition from ionic (governed predominantly by YSZ phase) to electronic (governed by Ni phase) conductivity is initiated at a considerably low Ni content (> 10 vol %) in electroless cermet, whereas, the percolation necessitates more than 30 vol % of Ni for the conventional anodes. The unique core (YSZ) –shell (Ni) microstructure of electroless cermet enables easy percolation among Ni, YSZ and pore phases throughout the matrix. This help in imparting the contribution of both Ni and YSZ phase to the overall electrical conductivity at considerably low metallic content.

It is established from the prior arts¹⁵ that the electrical conductivity of Ni-YSZ cermet anode is a variant of a) phase composition, b) microstructural distribution, c) processing technique, d) experimental temperature, etc. Beyond certain Ni content in cermet anode viz. 5 vol % for electroless and 25-30 vol % for conventional cermet, the electrical conductivity is found to be higher by three orders of magnitude. This sudden transformation is corresponding to a change in mechanism from ionic (controlled by ceramic phase) to electronic conduction

Chapter – 5.4

through the nickel phase.¹⁵ This is supported by the fact that the electrical conductivity of Ni-YSZ cermet is found to decrease with increase in temperature. Such inverse dependence of the electrical conductivity of Ni-YSZ anode on temperature follows 'Arrhenius behavior' according to Eq. 5.5.

$$\sigma = A \exp \left[-\frac{E_a}{RT} \right]; E_a = \text{Activation energy} \quad (5.5 \text{ of Section 5.1})$$

where, σ , A , R , E_a , T are the electrical conductivity, frequency factor, universal gas constant, activation energy and experimental temperature respectively.

The Arrhenius plots for the reduced Ni-YSZ cermets prepared by electroless technique for T1-, T2- and T3- series batches are shown in [Figure 5.30](#) along with the conductivities of conventionally prepared cermets ([Figure 5.31](#)). Irrespective of the preparation technique, the nature of electrical conduction in these Ni-YSZ cermets is found to follow metallic behaviour i.e. with temperature enhancement, the extent of electronic conduction decreases. In this context it is to be mentioned that the overall conductivities of such developed cermets are the manifestation of total ceramic and metallic components in the cermet matrix and are highly dependent on the processing condition of the materials. The activation energies for electrical conduction are process dependent parameter i.e. vary significantly with microstructural distribution. In case of the electroless cermets, equilibration time period during the YSZ sensitization controls the prominence of the core-shell structure in the cermet matrix that ultimately affects the activation energies of the concerned anodes.

It is observed from [Table 5.11](#) that though the activation energy for electrical conduction decreases linearly from 15 to 30 vol% of for the electroless anodes of T1-, T2- and T3-series, however, for all the series, the values of the activation energies are found to be highest for T1- and lowest for T2- series respectively. The attainment of transient equilibrium for T3-series leads to the formation of prominent core-shell structure which makes the electronic path

continuous in the cermetes thereby increasing the conductivity at lower activation energy in comparison to the functional anodes prepared at non-transient equilibrated state (T1-series).

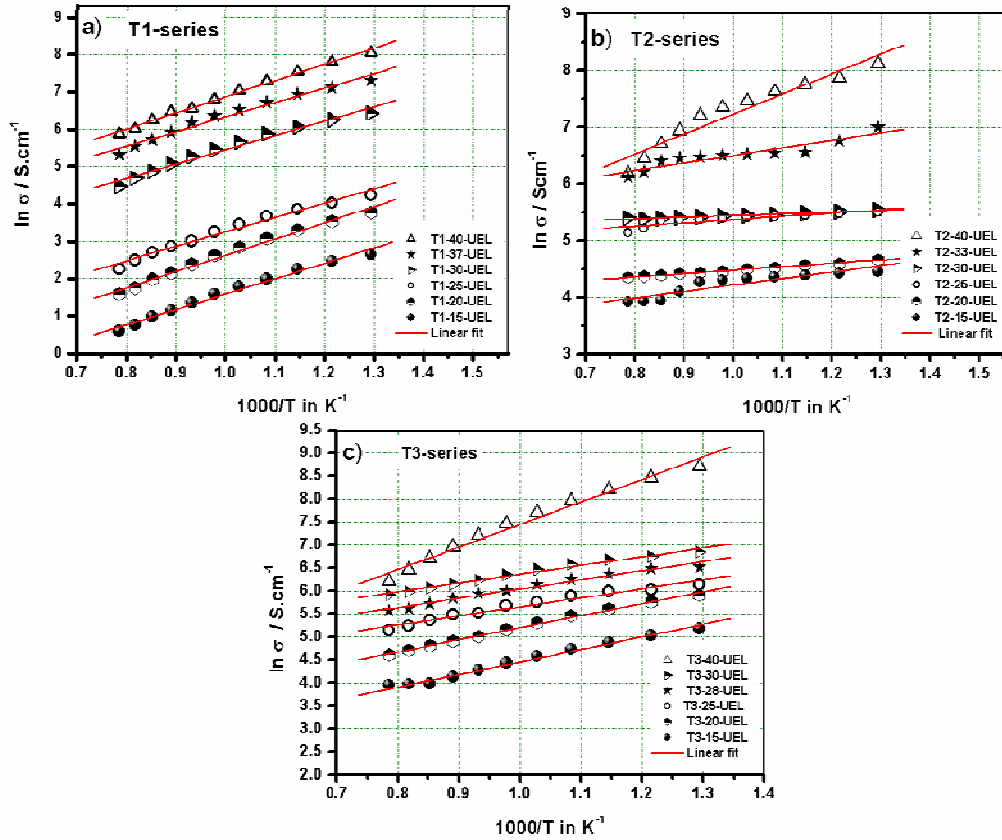


Figure 5.30: Arrhenius plots for electrical conductivities for electroless anode as a function of Ni content, equilibrated for a) 300 min, b) 1200 min and c) 2500 min

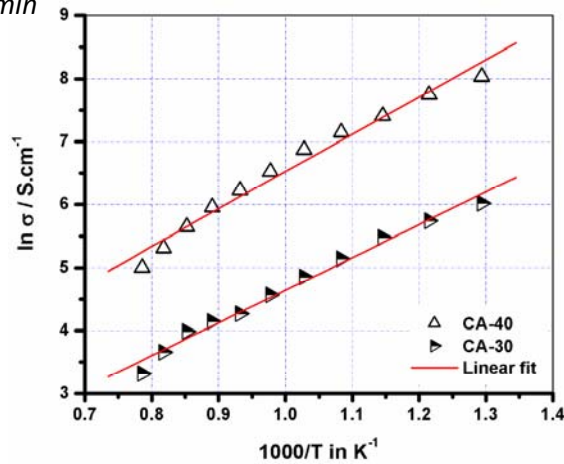


Figure 5.31: Arrhenius plots for electrical conductivities for conventionally prepared anodes as a function of Ni content

Chapter – 5.4

Ni content (vol %)	15	20	25	28	30	33	37	40	
Activation Energy, E_a (kJ.mol ⁻¹)	T1-series	38.01	36.24	33.17	--	32.96	--	32.71	36.09
	T2-series	9.44	4.99	4.79	--	2.52	11.00	--	29.35
	T3-series	23.59	21.76	16.77	16.56	16.44	--	--	40.09
	SS-series	--	--	--	--	43.18	--	--	49.31

The lowest activation energies in case of T2-series indicate that the rate of change of conductivity with temperature is lowest because of the formation much open porosity (Figure 5.28) in the cermet. The adsorption regime for this batch is primarily governed by external mass transfer but intra particle mass transfer is also initiated in this region (upto 1200 min). This allows formation of reasonably good core-shell microstructure but at the same time generates much open porosity from the structure during reduction. However, owing to insufficient YSZ sensitization in the T2-series, the electronic phase continuity is not developed that results in relatively lesser electrical conductivity in comparison to T3-series. Simultaneously the effect of Ni shell also happens to be less in this T2-series that results in lower activation energy for electrical conduction. Adsorption regime for the preparation of T3-series (equilibration time 2500min) is predominantly governed by intraparticle mass transfer that allows the surface of YSZ covered with active Pd⁰. Therefore, electroless Ni deposition in T3-series is highly optimized. The activation energies for such T3-series is found higher compared to T2-series because of the effect of denser Ni shell formation but the electrical conductivity of T3-series is found highest among the series. It is observed from Table 5.10 that a reverse trend of activation energy in the functional anodes is observed beyond 30 vol% Ni. Formation of thicker core-shell structure in 40 vol% Ni of the functional anode prepared at transient equilibrated state results in higher rate of change of conductivities with temperature. This could be attributed to the fact that with

thicker Ni shell around the YSZ core is more susceptible for phonon scattering at higher temperature and hence the effect of rate of change of electrical conductivity with temperature is found to be more prominent. It is found that a reasonable conductivity is obtained at a significantly higher vol% of Ni (≥ 40 vol% Ni) for the CA-series anode with maximum activation energy among the series.

5.4.2.3. Microstructural studies

Optical micrographs of the functional cermets prepared by electroless technique at transient (T3-28-UEL) and non-transient (T1-37-UEL) equilibration time interval are compared with that of the conventionally prepared anodes (CA-40) in [Figure 5.32](#).

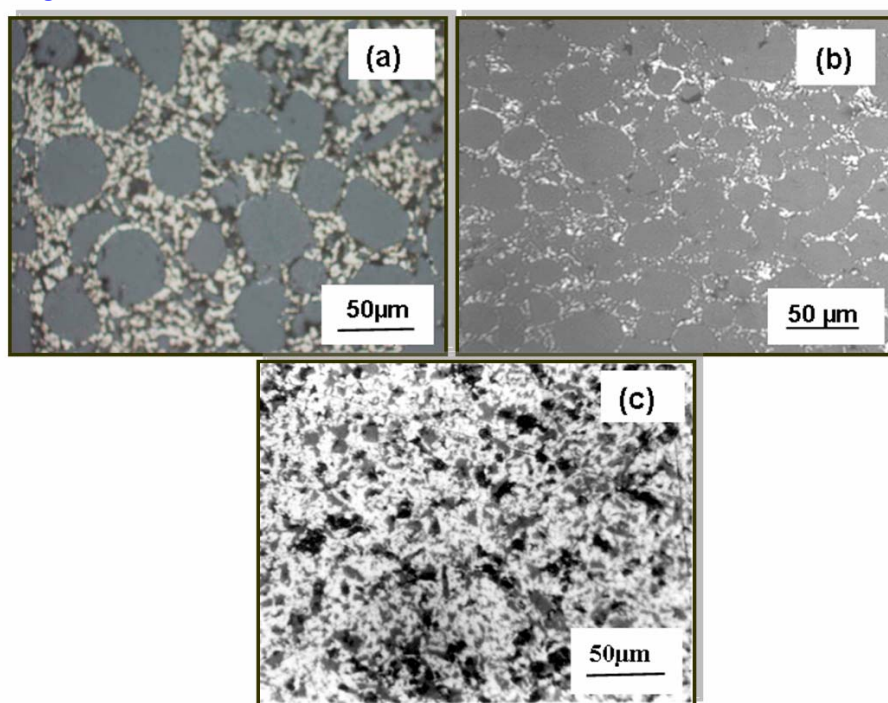


Figure 5.32: Optical micrographs of electroless Ni-YSZ cermet for: a) transient equilibrium adsorption (T3-series), b) non-transient equilibrium adsorption (T1-series) and c) conventionally prepared cermet

Completely distinct microstructures are observed in the functional anodes prepared by electroless technique that forms core-shell microstructures with Ni in grain boundary region and YSZ in the core. Core-shell microstructure is more prominent and optimized in [Figure 5.32a](#) due to better sensitization of YSZ

Chapter – 5.4

particulate in comparison to [Figure 5.32b](#). This difference in the optical micrographs can be explained by the fact that in case of [Figure 5.32 a](#), the sensitized bath is allowed to equilibrate for 2500 min which allows the formation of adequate active YSZ sites that facilitates effective Ni deposition in the electroless bath. Such transient equilibrated sensitization process helps to encapsulate YSZ with freshly adsorbed Pd⁰ which is evident from the positive value of effectiveness factor of the proposed kinetic model (section 5.3). Thus, it is expected that because of the formation of distributed Ni shell formation around the YSZ core, Ni distribution is expected to be more uniform across the thickness of the shell which, in turn, enhances the triple phase boundary length required for fuel oxidation at the anode side. Reduction in the equilibration time from 2500 min to 300 min results in ineffective sensitization of YSZ due to excess free Ni is generated in the cermet matrix with weak core-shell structure ([Figure 5.32b](#)). Compared to the microstructure of the functional anodes prepared at different equilibration time, the micrograph observed in case of the conventionally prepared cermet shown in [Figure 5.32c](#), is completely distinct where a uniformly dispersed Ni in the YSZ matrix is observed.

5.4.2.4. Study of thermal behavior

Thermal expansion – a thermodynamic property of a material, arise from the asymmetry of potential energy vs. inter atomic distance plot of ‘Condom-Morse potential energy diagram’.¹⁷ The degree of asymmetry is guided by the mode of orientation of the constituent phases or the microstructural distribution pattern within the matrix of the concerned material. The extent of expansion resulted due to thermal agitation is represented in terms of ‘coefficient of thermal expansion (CTE)’, obtained from the slope of change in length w.r.t. the initial length vs. temperature plot.

A comparative representation of the CTE values of the prepared anodes is given in Figure 5.33. The figure clearly demonstrates the dependence of thermal behaviour on the equilibration time of the YSZ sensitized bath for electroless technique. As already discussed in section 5.4.2.3 that, owing to the optimized sensitization for the corresponding T3-series anodes, unique patterned core-shell microstructure is generated which allows interconnection among Ni, YSZ and pore phases. However, ineffective sensitization in case of T1-and T2-series anodes fails to form patterned core-shell microstructure during electroless deposition. Consequently, the densification and the associated properties viz. electrical conductivity are found to be much inferior compared to the T3-series batches.

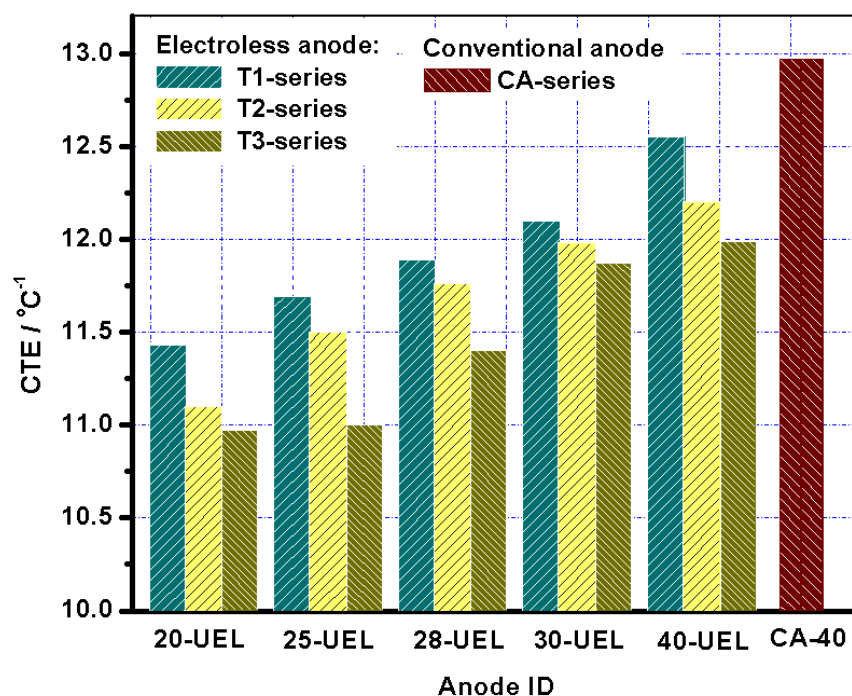


Figure 5.33: Comparative thermal expansion behavior of fabricated anodes using different preparation techniques

Unorganized microstructural distribution of Ni and YSZ in T1- and T2-series anodes contributes for the enhanced asymmetry of deposited Ni which increases the rate of thermal expansion with increment in experimental temperature compared to T3-series having least CTE values at any Ni content. It may be noted that, between

Chapter – 5.4

T1-and T2-series, the CTE values are lower for the later batches in which the sensitized YSZ is allowed to equilibrate for 1200 min with the involvement of intra particle diffusion technique.

The expansion behaviour of conventional anode with dispersed distribution of constituent phases gets highly affected with temperature change as observed from the highest CTE value among the series. Irrespective of equilibration time for YSZ sensitization as reported for the electroless cermet, the values of CTE are found to be lower compared to that of the conventional anode. This may be explained on the basis that, electroless technique in the present investigation generates unique core-shell structure; the degree of uniformity is however dependant on the extent of optimized YSZ sensitization. Therefore, in spite of the variability in equilibration time in T1 to T3-series, the primary orientation of the phases follows similar core-shell structure. In contrast, owing to the random mixing of constituent phases, even a more disorganized microstructure of Ni-YSZ cermet is generated through conventional technique having higher asymmetry in the matrix and hence the overall CTE values are found to be highest.

Finally for SOFC application, the prepared anode happen should enable similar expansion behaviour with the adjacent YSZ electrolyte. [Figure 5.34](#) describes comparative expansion plots among electroless and conventional anode in conjugation with the YSZ electrolyte.

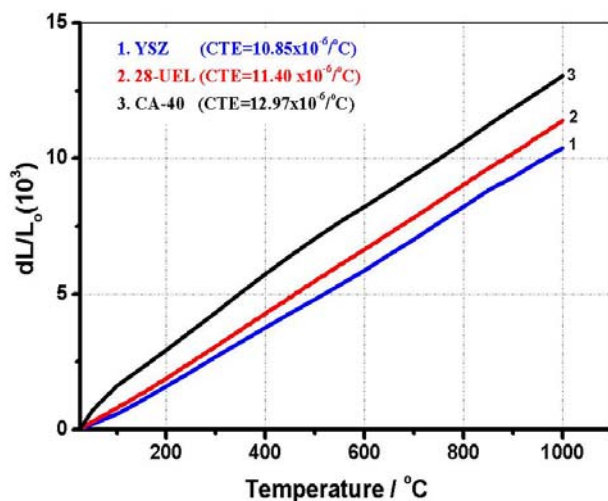


Figure 5.34: Comparative thermal expansion plots among electroless and conventional anodes in conjugation with YSZ electrolyte

It can be observed that, the transient equilibrated electroless anode having only 28 vol % is found to be thermally compatible with adjacent YSZ electrolyte ($10.85 \times 10^{-6} \text{ K}^{-1}$) which fulfils the primary criteria of an anode to be applicable for SOFC.

5.4.3. Summary

The experimental results obtained from the present section are based on the property correlation of Ni-YSZ cermet through electroless technique, which is primarily being governed by YSZ sensitization performed by high energy ultrasonification. Based on the kinetic modeling for Pd^0 adsorption onto YSZ (Section 5.3), it is established that effective sensitization is an outcome of transient equilibration for ~ 2500 min. The importance of optimized sensitization has been correlated with several experimental parameters viz. densification, electrical conductivity, thermal compatibility and microstructural distribution of the electroless Ni-YSZ anode. Conductivities with transient equilibrated sensitized YSZ shows prominence of Ni-shell formation across the YSZ-core and are correlated with the optical micrographs. Owing to the unique core-shell microstructure of electroless cermet, conductivity percolation is brought down to ~ 28 vol % Ni (for T3 series) compared to 40 vol % for the conventionally prepared cermets with lower activation barrier. Such developed electroless anodes are expected to be thermally more compatible with the adjacent YSZ electrolyte. Long term endurance and redox tolerance of such developed anode are to be discussed in details in the next section.

*5.5. Patterned Intra-
anode TPB Produced
In-situ in Electroless
Cermet: A
Mathematical Approach*



Chapter – 5.5

Chapter – 5.5

The basic reaction of solid oxide fuel cell (SOFC) involves electrochemical combination of reactants at the 'triple phase boundary (TPB)' of anode-electrolyte and electrolyte-cathode interfaces. TPBs are considered to be the 'zones' or the 'spatial sites' at which either fuel oxidation reaction (HOR for hydrogen fuel) or oxidant reduction reaction (ORR for oxygen oxidant) is confined.¹⁸ In anode-supported SOFC, electrochemical reactions at anodic TPB play a crucial role towards the overall cell performance as well as towards the cell degradation rate during long term operation. Therefore, understanding and optimizing the TPB of anodes in SOFC provides excellent opportunities for performance enhancement. The prime factor governing the TPB distribution is based on the optimization of anode microstructure through selected processing techniques.¹⁹ The details for the process optimization of electroless technique have been discussed in sections – 5.2-5.4. Optimized deposition of Ni around YSZ core by electroless technique generates a patterned core (YSZ)-shell (Ni) microstructure that developed in-situ during the synthesis of the cermet which ensures intra (Ni/Ni, YSZ/YSZ and connected pore) and inter (Ni/YSZ/pore) phase contact of YSZ, Ni and pores throughout the matrix. Such interconnection between YSZ/YSZ, Ni/Ni and YSZ/Ni with the associated pores helps in the formation of patterned intra-anode TPB [Ni/YSZ/fuel (through pores)] within the anode. Therefore, percolation of O^{2-} ions (through YSZ), electrons (through Ni) and H_2 (through interconnected pores) also follows a patterned network throughout the electroless cermet.

In the present section, a mathematical model is proposed for determining intra-anode TPB length for electroless cermets and is experimentally validated as a function of Ni content. Intra-anode TPB lengths of electroless anodes are measured and correlated with degradation in conductivity during repeated redox cycling. A brief discussion related to the parameters affecting the extension of TPB from anode interior to the interface of anode/electrolyte junction is also presented.

Chapter – 5.5

5.5.1. Modeling of intra-anode TPB length

A mathematical model is proposed for determining intra-anode TPB length of SOFC cermet anode. The electrochemical behaviour of fuel oxidation, e.g. hydrogen under this present investigation is significantly influenced by the water or oxygen containing molecules. The associated moisture/water act as the source of oxygen species which gets adsorbed on nickel surface which in turn controls the rate of hydrogen oxidation kinetics.²⁰ The proposed mechanism for fuel (moist) oxidation involves the following steps:

- a) Dissociative decomposition of water/moisture to provide adsorbed oxygen species on Ni surface ($O_{ad, Ni}$)
- b) Dissociative absorption of hydrogen ($H_{ad, YSZ}$ and $H_{ad, Ni-O}$)
- c) Charge transfer reaction ($O_{ad, YSZ}^{2-}$ to $O_{ad, Ni}^{2-}$)
- d) Water (product) formation (combination of $H_{ad, Ni-O}$ and $O_{ad, Ni}$)

Among the series of reactions mentioned above, the mechanism for charge transfer reaction from $O_{ad, YSZ}^{2-}$ to $O_{ad, Ni}^{2-}$ occurs at the conventional TPB which exists at the anode-electrolyte interface.¹⁵ This charge transfer is progressive in the bulk anode preferentially through intra-anode TPB because Ni, YSZ and pores are patterned and interlinked in a definite pattern in the electroless cermet matrix. [Figure 5.35](#) describes the anodic electrochemical reactions at dual TPB zones [conventional and intra-anode] of electroless anode.

In the proposed model, ' ν ' defines the number of closely contacted Ni with YSZ within a specified length (l) of sample and ' χ_{ν} ' denotes the length of each ν^{th} contact. In addition, ' τ ' denotes the number of core-shell particles under consideration. At the contact points, pores also co-exist with Ni and YSZ phases and thereby ensure the availability of electrons, O^{2-} ions and fuel at intra-anode TPB sites.

Summation of all contact lengths [α] can be written as:

$$\alpha = \left(\sum_1^v \chi_v \right) \quad (5.38)$$

$$\text{TPB length } [\Gamma] \text{ can be expressed as: } \Gamma \propto \alpha v \tau \Rightarrow \Gamma = k \alpha v \tau \quad (5.39)$$

where, k is proportionality constant.

Though, TPB exists in 3D contour, TPB length, a uni-dimensional parameter, is modelled based on two dimensional cross-sections.

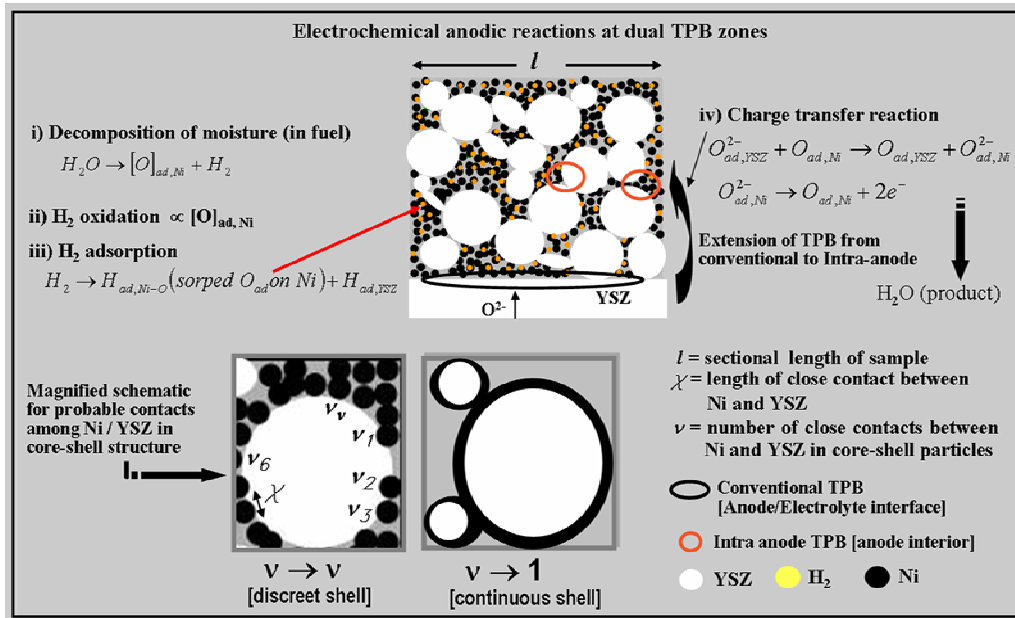


Figure 5.35: Schematic of anodic electrochemical reactions at dual TPB zones of Ni-YSZ electroless anode

Considering circular geometry of 2D plane, TPB length can be written as:

$$\Gamma_{ind} = \pi \alpha v \tau \quad , \text{ valid for continuous Ni shell } [v \rightarrow 1, \text{ Figure 5.35}] \quad (5.40)$$

where, ' Γ_{ind} ' defines TPB length in ' μm ' independent of sample sectional length (l).

Generation of continuous Ni shell as shown in Figure 5.35 (Eq. 5.40) is ineffective for maximization of TPB, as it decreases the number of contact points. In addition, formation of continuous Ni shell also restricts the YSZ contribution to functionality of such anode cermet.

Maximizing the number of contacts at, $v \rightarrow v$ (highest limit, Figure 5.35), which signifies discrete deposition of Ni particulates around YSZ core, ' Γ_{ind} ' is written as:

$$\Gamma_{ind} = \pi \alpha v \tau \quad (5.41)$$

Chapter – 5.5

Similarly, contacted surface area (ξ) expressed in ' μm^2 ' for TPB independent of *sample* sectional length (l) can be written as:

$$\xi_{ind} = \pi \left(\frac{\alpha^2}{4} \right) v_{xy}^2 \tau_{xy}^2 \text{ at } v \rightarrow v \text{ (highest limit)} \quad (5.42)$$

Eqs. 5.41 and 5.42 is applicable to theoretical determination of TPB length, although it is invariant of experimental sample sectional length. For the purpose of practical application, both the TPB length and contact surface area needs to be represented in terms of sample sectional length. Equations governing ' Γ_{dep} ' [expressed in $\mu\text{m} \cdot \mu\text{m}^{-2}$] and ' ξ_{dep} ' [expressed in $\mu\text{m}^2 \cdot \mu\text{m}^{-4}$] dependent of sample sectional length (l) are given as:

$$\begin{aligned} \Gamma_{dep} &= \pi \left(\frac{\alpha}{l} \right) \left(\frac{v}{l} \right) \left(\frac{\tau}{l} \right) \text{ and } \xi_{dep} = \pi \left(\frac{\alpha}{2l} \right)^2 \left(\frac{v}{l} \right)^2 \left(\frac{\tau}{l} \right)^2 \\ \therefore \Gamma_{dep} &= \pi A N T \text{ and } \xi_{dep} = \pi \left(\frac{A^2}{4} \right) N^2 T^2 \end{aligned} \quad (5.43)$$

where, A, N and T are total contact lengths, number of active contact interfaces and number of core-shell particles per unit sectional length respectively.

The two boundary conditions for the developed model are discussed as follows:

a) Limiting range of ' v ' varies from unity to infinity $[v]_1^\infty$. At the highest limiting range $[v \rightarrow \infty]$, both TPB and surface area are enhanced as evident from Eqs. 5.41-

$$5.43: \quad \Gamma \propto v \text{ or } N \text{ and } \xi \propto v^2 \text{ or } N^2$$

This signifies that optimized Ni deposition around YSZ core during electroless technique increases the number of active contact points enhancing both intra-anode TPB and surface area.

b) The size factor ratio (β) is defined as $\beta = \frac{d_{YSZ}}{d_{Ni}} \approx 10^n$, where d_{YSZ} and d_{Ni} are the average particle size of YSZ and Ni particulates respectively. For measurable intra-anode TPB in electroless anode, β should vary at least an order of 10. Theoretically, with increase in β , v increases but τ (number of core shell particulates) decreases. Therefore, an optimization between the size ratio of YSZ and Ni particles is necessary for enhancing the TPB. Average particle sizes of Ni and YSZ of electroless anode are ~ 70 nm and ~ 30 μm respectively. Therefore, β vary in

the range of $10^2 - 10^3$ and thereby satisfy the required boundary condition. Average particle sizes of Ni and YSZ phases of the conventional cermet are almost in the same order of magnitude ($\beta = 10^0-10^1$). In addition, due to disperse Ni and YSZ distribution in the microstructure of conventional cermets, [$\tau \rightarrow 0$ & $\nu \rightarrow$ undefined $\Rightarrow \Gamma \approx 0$] patterned intra-anode TPBs are not observed. Therefore, existence of dual TPB zones is not feasible in the matrix of conventional anode.

5.5.2. Application of proposed model for TPB length determination

Triple phase boundary (TPB) in real terms is meant for a three dimensional (3D) contour/space at which the fundamental electrochemical reactions occur. The primary motivation behind the experimental research is therefore based on the determination of such TPB in-terms of 1 D entity, with an intention of tailoring its dimension according to the system requirement. The theoretical mathematical model derived in the above section facilitates the determination of TPB length for the prepared anodes for SOFC application.

Intra-anode TPB dependent on sample sectional length is calculated from Eq. 5.43. As already mentioned, the values of interfacial contact points (ν) and their respective lengths (χ_ν) are obtained from image analysis. TPB length of Ni-YSZ anode prepared by electroless is calculated in different sections (I_1, I_2, I_3) (Figure 5.36 a, c-1) of the sample, each having a length of $\sim 43 \mu\text{m}$. The respective TPB zones are identified upon mapping the locations of Zr and Ni phases as shown in Figure 5.36 a. It can be observed from Figure 5.36 c-1 that, distribution of TPB in the electroless cermet is identical with equivalent distributions in all the sections of the anode. The experimental TPB lengths of core-shell electroless anode are therefore calculated with negligible error percentage ($\sim 0.08 \%$). This attributes towards the uniform distribution of intra-anode TPB length throughout the cermet matrix.

Chapter – 5.5

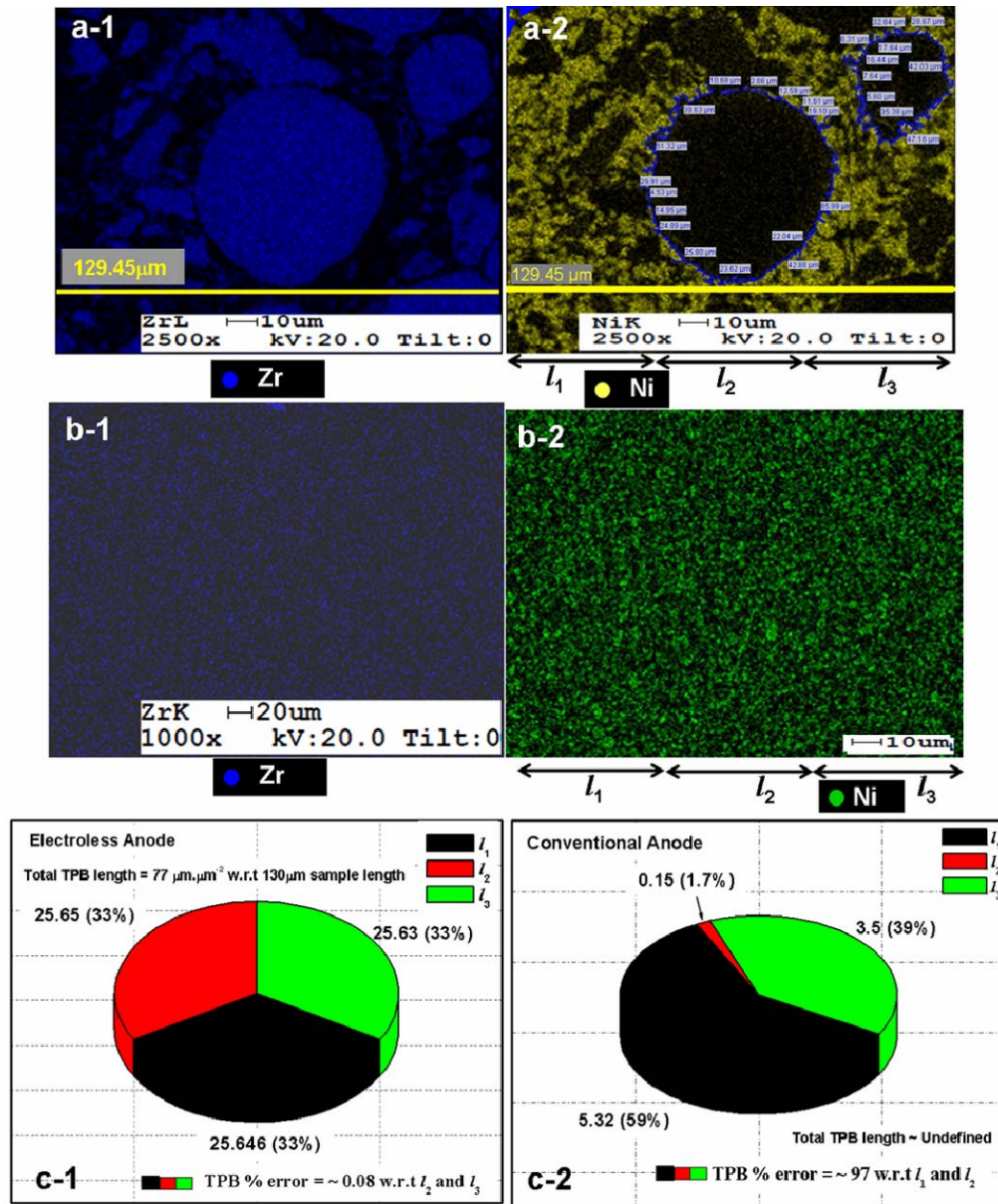


Figure 5.36: (a-1) Zr and (a-2) Ni mapping of electroless anode, (b-1) Zr and (b-2) Ni mapping of conventional anode and sectional TPB length distribution for: (c-1) electroless and (c-2) conventional anode cermet

It has been already viewed from section 5.4.2.3 that conventional anode cermet consists of disperse distribution of the constituent phases viz. Ni, YSZ and pores. Such incoherency in phase distribution also affects the distribution of TPB within the matrix. Though patterned intra-anode TPB are absent in conventional cermet, TPB lengths are measured considering probable contacts of Ni with YSZ

through elemental mapping (Figure 5.36 b). The experimental calculations support the incoherent distribution and clearly depict that only 3 % probability (as shown in Figure 5.36 c-2) exists for the presence of intra-anode TPB sites in the conventional anodes. The processing conditions for synthesizing the conventional anode by mechanical mixing generate inhomogeneous distribution of Ni, YSZ and pores. Therefore, it can not ensure the uniform three phases contact throughout the matrix. This inhomogeneous distribution does not lead to patterned intra-anode TPBs within the conventional anode which is also supported experimentally by the model.

Maximization of intra-anode TPB length is dependant on a certain governing factors viz. a) distribution of Ni, YSZ and pores within the matrix, b) amount of constituent's phases etc. It has been already established that, owing to the presence of unique core (YSZ)-shell (Ni) microstructure, formation of patterned TPB is facilitated in the electroless matrix. Furthermore, the magnitude of intra-anode TPB is found to be a variant of Ni content. It is observed from Figure 5.37 that,

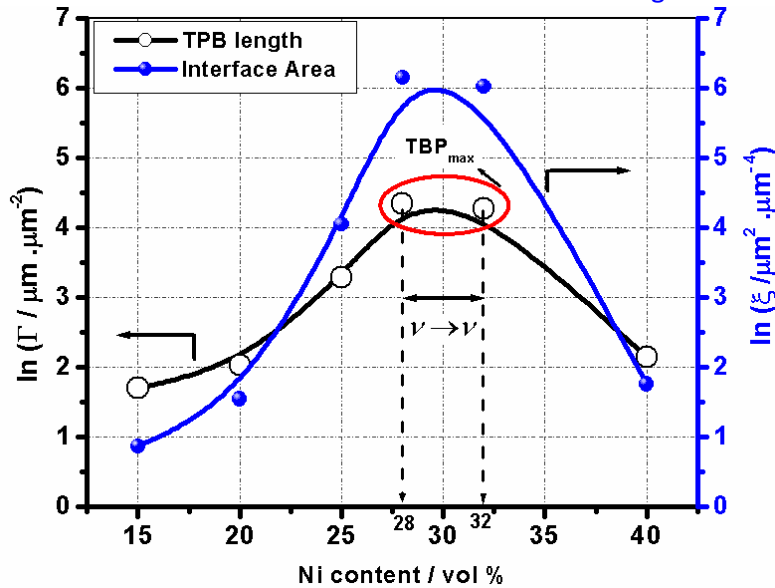


Figure 5.37: Variation of intra-anode TPB length and surface area of electroless anode as a function of Ni content

TPB length of electroless anode increases with increase in Ni content and reaches a maximum of $\sim 77 \mu\text{m} \cdot \mu\text{m}^{-2}$ in the range of 28-32 vol% of Ni in the cermet matrix.

Chapter – 5.5

At lower Ni content of this threshold (below 25 vol % Ni), active Ni-YSZ interfaces are found to be of smaller interfacial length which results in lower TPB. On the other hand, as evident from [Figure 5.37](#), the increment of shell thickness is found to be significant with increase in Ni content (> 32 vol %) thereby reducing the intra-anode TPB length.

5.5.3. Manifestation of intra-anode TPB on electrical and electrochemical properties of electroless anode

5.5.3.1. Effect of redox cycling on electrical conductivity and TPB length of electroless anode

In order to examine the durability of developed anodes, they are subjected to repeated oxidation to NiO-YSZ at 1000°C and re-reduction (at 800°C) in the same atmosphere of Ar: H₂ ([Figure 5.38 a](#)). Furthermore, the anodes are subjected to thermal cycling in the temperature range of 500 to 1000° C in the reduced condition ([Figure 5.38 b](#)). The effect of 20 such redox and thermal cycles on degradation of electrical conductivities of anode cermets are examined to correlate with the experimental intra-anode TPB lengths.

[Figure 5.39 a](#) shows the effect of redox cycling on the electrical conductivity of both electroless and conventional cermet anode. Three samples of electroless anodes having Ni content 15, 28 and 40 vol % are selected for such durability test. According to [Figure 5.37](#), it has been already observed that maximum TPB length is obtained at ~ 28 vol % Ni, whereas lowest TPB length is observed at either 15 vol % Ni in the lower metallic content and 40 vol % Ni in the higher Ni content respectively. It can be observed from [Figure 5.39a](#) that, before redox cycling, electrical conductivity (~ 500 Scm⁻¹) of electroless anode with only 28 vol % Ni is equivalent to the conductivity value of conventional cermet having much higher Ni content (40 vol %).

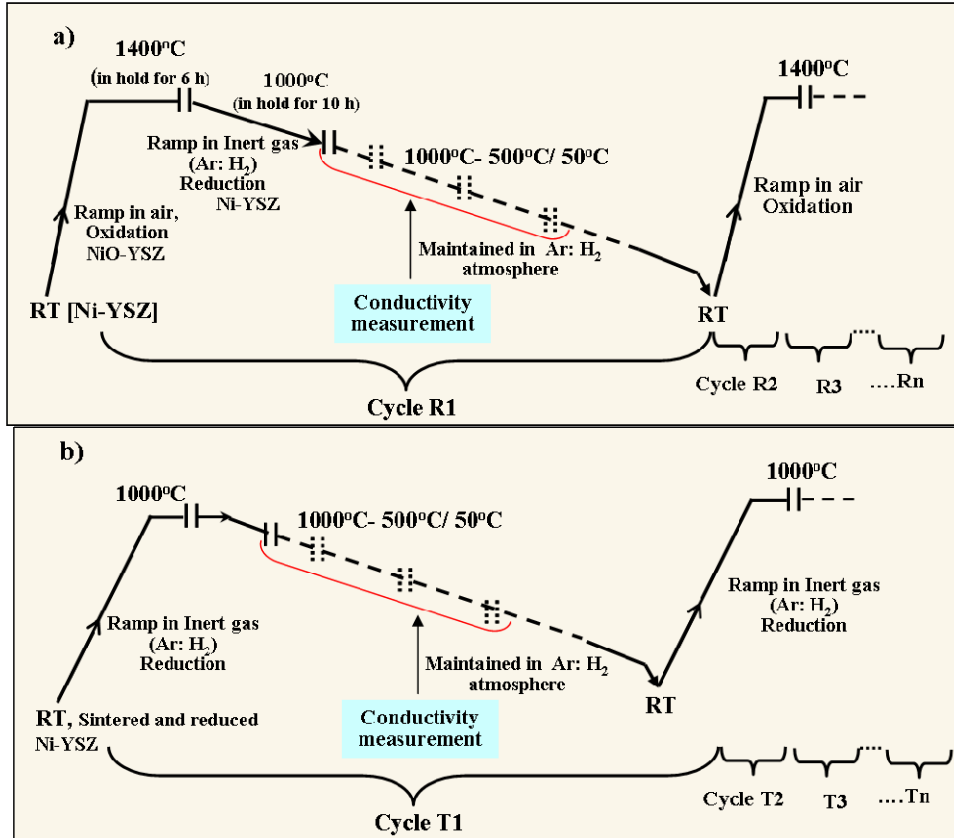


Figure 5.38: a) Redox profile and b) thermal profile employed during electrical conductivity measurement

As discussed already in the previous sections, this can be attributed to the formation of unique core (YSZ) – shell (Ni) microstructure in the electroless matrix. The optimized deposition of discrete Ni particulates enables continuous network of both metallic (Ni) and ceramic (YSZ) phases throughout the cermet thereby results in higher electrical conduction at much lower Ni content. At high operating temperature of 800°C, it is believed that Ni coarsens not only because of phonon scattering, but also due to localized joule heating (I^2R). This causes overall reduction in electrical conductivity of the anode upon repeated redox cycling as is observed in [Figure 5.39a](#). Additionally, each redox cycle results in irreversible Ni grain growth due to expanded NiO volume after oxidation. The ongoing Ni grain

Chapter – 5.5

growth decreases the intra-anode TPB by reducing the interfacial contact points

(v).

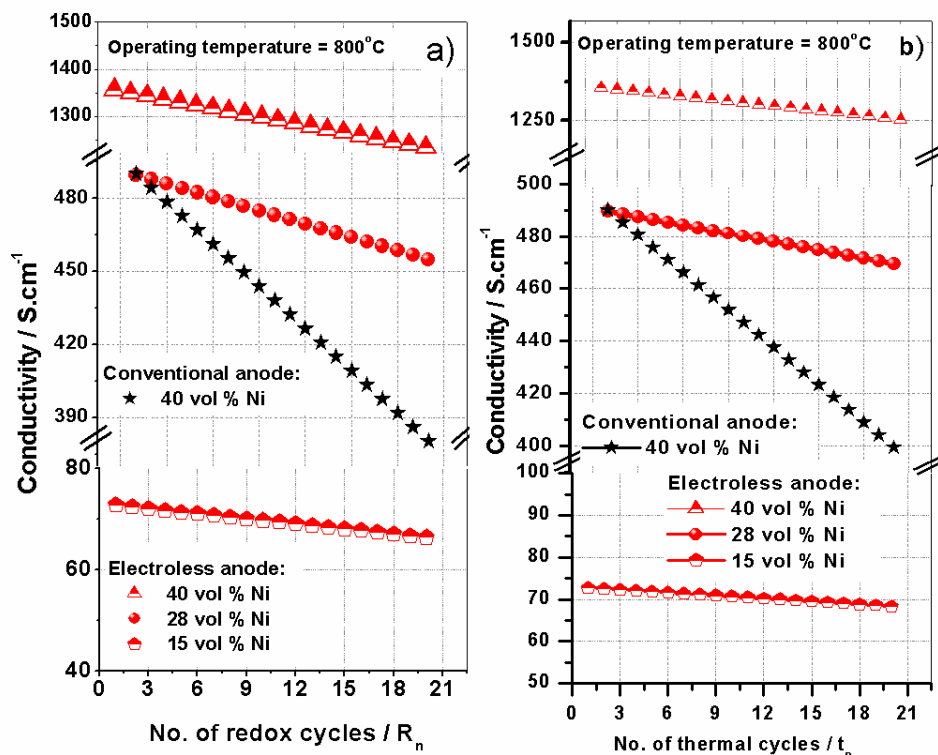


Figure 5. 39: Variation of electrical conductivity of electroless and conventional anode towards: a) redox cycling and b) thermal cycling

Such growth of Ni is also believed to restrict the YSZ network and overall porosity within the matrix by forming continuous metallic chain around the core thereby decreasing the overall electronic conductivity and TPB within the cermet matrix. However, electroless anode with 28 vol% of Ni having highest TPB length in the series (Figure 5.37) shows least electrical conductivity degradation (~7 % after 20 redox cycles) as shown in Figure 5.40 and Table 5.12. Owing to the presence of larger TPB length in the electroless anode with 28 vol % Ni, the associated conductivity degradation is found to be least compared to the batches with 15 vol % (~ 9 % / 20 redox cycles) and 40 vol % (~ 9 %/20 redox cycles). In contrast, absence of patterned intra-anode TPB for the conventional cermets results in ~ 23 % degradation in conductance in 20 redox cycle.

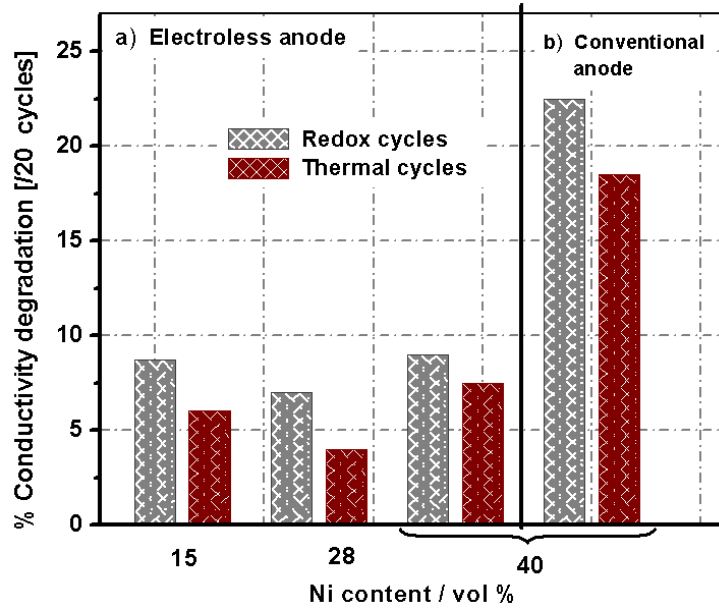


Figure 5. 40: Effect of redox and thermal cycles on degradation rates of electrical conductivity for: a) electroless and b) conventional cermet

The negligible degradation rate for electroless anodes is primarily because of less Ni content and ordered microstructure with interconnection among both Ni and YSZ phases.

Table 5.12: Conductivity degradation rates of SOFC anodes upon redox and thermal cycling

Anode preparation technique	Ni content (vol %)	Conductivity degradation rate (% per 20 cycles)	
		Redox cycle	Thermal cycle
Electroless	15	8.7	6.01
	28	7.01	4.0
	40	9.0	7.5
Conventional solid state	40	22.5	18.5

Thermal cycling of electroless anode cermets shows similar effects of conductivity degradation in Figure 5.39b as discussed above for redox cycling of fabricated anodes. However, from Figure 5.40 and Table 5.12, it is observed that thermal cycling imposes lesser degradation of electrical conductivity [4 % for electroless anode with 28 vol % Ni] compared to redox coupled thermal cycling [7.01 % for the

Chapter – 5.5

similar batch]. In contrast to redox cycles, repeated thermal cycling restricts the possibility for repeated expansion of NiO during oxidation followed its subsequent reduction to metallic Ni. This lowers the extent of TPB reduction and lowering of electrical conductivity. However, repeated temperature variations affect the overall electrical path within the matrix similar to that of phonon scattering and localized joule heating (I^2R) and thereby raising resistance in the electronic path. Such phenomena results into Ni coarsening and reduction in the overall conductivity during temperature variation.

The aforementioned observations regarding durability of anodes w.r.t electrical conduction and can be correlated with effect of redox cycling on intra-anode TPB length as show in Figure 5.41. Negligible change (0.7 % /20 redox cycles) in the intra-anode TPB length is observed for electroless anode after 20 redox cycles (Figure 5.41).

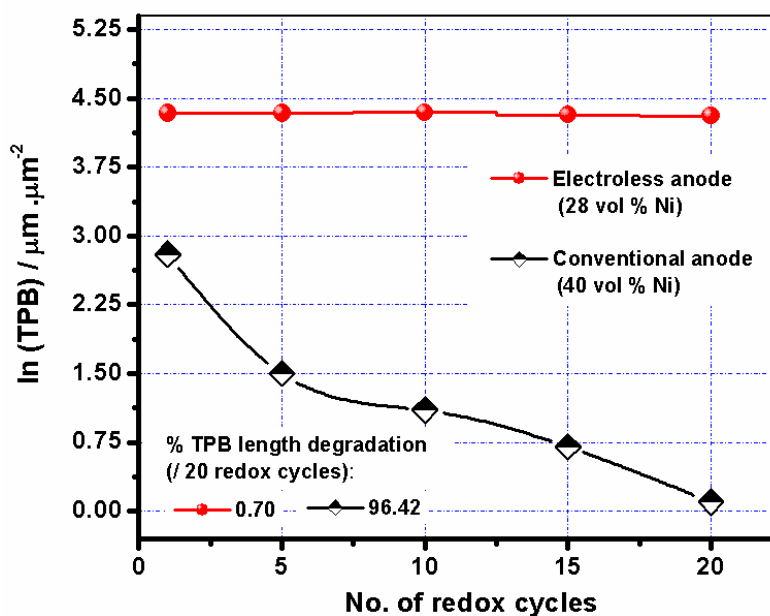


Figure 5.41: Effect of redox cycling on degradation rates of TPB lengths for electroless and conventional cermet

The smaller size of Ni particulate in electroless anode attributes towards the lower degradation rate. In contrast, dispersed Ni and YSZ phases in the conventional anode with higher size of Ni particulate cause rapid Ni grain growth during redox

cycling. This microstructural change causes reduction in surface area of Ni available for effective charge transfer reaction.²¹ Ni coarsening also hampers the fuel percolation through the pores and causes ~ 97% degradation in TPB length in conventional cermets after 20 redox cycles. Therefore, electroless anode with lower Ni content (28-32 vol %) is superior in terms of enhanced redox tolerance having comparable electrical conductivity to the conventional cermet which contain relatively higher Ni content (40 – 60 vol %). The presence of dual TPB sites in the electroless cermet helps in the improvement of the electrochemical activity. In addition, optimized discrete deposition of fine Ni particulates onto core YSZ increases the overall anode surface area and thereby the catalytic activity of electroless anode towards fuel oxidation is enhanced. Therefore, usage of lower Ni content (i.e. higher YSZ content) in electroless anode helps in the retention of core-shell microstructure intact which restricts the overall Ni ripening and hence enhances the redox tolerance.

5.5.3.2. Correlation of dual TPB with electrochemical performance of SOFC

The discussions of the aforementioned sections clearly emphasize on the functionality of the developed electroless anode with unique core (YSZ)-shell (Ni). Formation and optimization of pattern intra-anode TPB allows significant enhancement in the electrochemical activity of SOFCs fabricated with such novel electroless anode. A comparative electrochemical performances of single cell fabricated with either conventional and electroless anode is shown in [Figure 5.42](#). Single cells with electroless anode containing 32 vol % Ni show higher current density of ~ 2.5 Acm⁻² ([Figure 5.42](#)) at 800°C and 0.7 V compared to those with conventional anodes having 40 vol% Ni (~ 1.7 Acm⁻², 800°C and 0.7 V). Therefore, the present investigation intend to report a SOFC anode prepared through electroless technique with a unique microstructure that exhibits better redox resistance than that of the conventional anode.

Chapter – 5.5

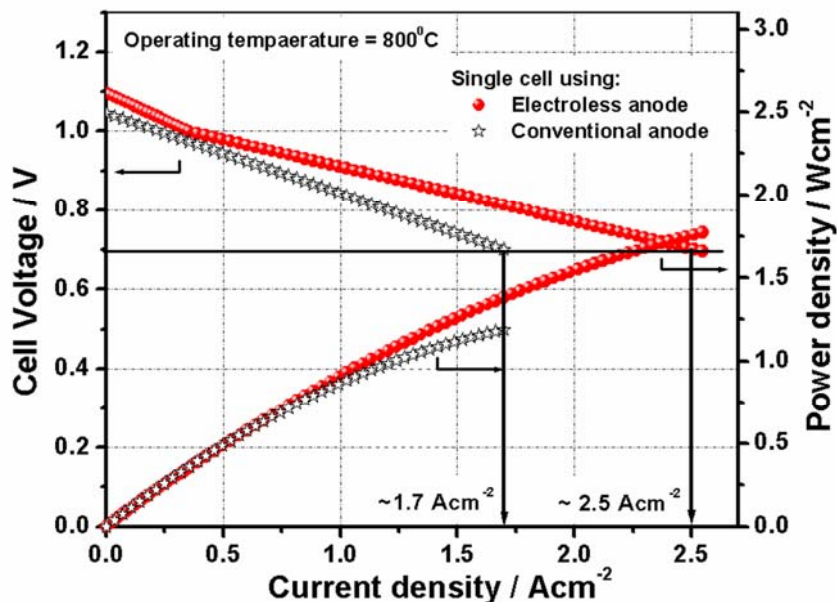


Figure 5.42: Comparative electrochemical performances of single cell with anodes prepared by electroless and conventional technique

Furthermore, power density of single cell (1.75 Wcm^{-2}) fabricated with such electroless anode is also found to be higher compared to the conventional anode-supported cell (1.19 Wcm^{-2}). The presence of intra-anode TPB in electroless cermet helps in the progression of anodic electrochemical activity from interior to the anode/electrolyte interface, thereby adding functionality to the novel cermet.

5.5.4. Summary

A mathematical model has been proposed for the determination of intra-anode TPB of electroless anode. The proposed model has been validated successfully for the electroless cermet and the conventional anodes. Redox tolerant and thermally cyclable electroless cermets having core (YSZ) – Ni (shell) microstructure enables significantly higher conductivity at much lower Ni content (28 vol %). Co-existence of patterned intra-anode and conventional TPBs with increased catalytic activity of fine Ni particulates is responsible for the enhancement of electrochemical performance (2.5 Acm^{-2} at 800°C) for such cells.

Appendix - 2

Table 5.13: List of symbols used in Chapter – 5. 5

Symbols	Word Meaning	Unit
v	Number of closely contacted Ni with YSZ	--
l	Specified sample length	μm
χ_v	Length of each v^{th} contact	μm
τ	Number of core-shell particles under consideration	--
α	Summation of all contact lengths	μm
Γ	Triple phase boundary length	Length unit, μm
Γ_{ind}	TPB length independent of sample sectional length	μm
ξ_{ind}	Contact surface area independent of sample sectional length	μm^2
Γ_{dep}	TPB length dependent of sample sectional length	$\mu\text{m} \cdot \mu\text{m}^{-2}$
ξ_{dep}	Contact surface area dependent of sample sectional length	$\mu\text{m}^2 \cdot \mu\text{m}^{-4}$
A	Total contact lengths per unit sectional length	μm
N	Number of active contact interfaces per unit sectional length	μm^{-1}
T	Number of core-shell particles per unit sectional length	μm^{-1}
d_{ysz}	Average particle size of YSZ particulate	μm
d_{Ni}	Average particle size of Ni	μm
β	Size factor ratio	Dimensionless

*5.6. Structure-Property
Correlation of Tape Cast
Electroless Anode and its
Application in Planar
Anode-supported SOFC*

Chapter – 5.6

Chapter – 5.6

The basic reaction of solid oxide fuel cell (SOFC) involves electrochemical combination of reactants at the 'triple phase boundary (TPB)' of anode-electrolyte and electrolyte-cathode interface. In case of planar anode-supported fuel cells, the electrochemical performance of the cell is principally governed by the properties of anode viz. a) thickness, b) electronic conductivity, c) sufficient interconnected porosity d) electrocatalytic activity etc. of the anode.²²⁻²⁴ Control of the anode microstructure through appropriate processing techniques can play a major role towards its activity in the single cell.

Designing and controlling the anode microstructure is therefore important to satisfy the basic requirements of extending TPB and appropriate gas diffusion paths.²⁵⁻²⁶ In addition to the aforementioned functions, microstructural tuning of anode also renders significant role in minimising the overpotential losses that is built up in a fuel cell during operation under load condition. In fuel cells, useful voltage loss takes place through various means viz. ohmic, concentration/diffusion and activation polarizations.¹⁵ Activation polarization is mainly due to the voltage loss arising out of energy barrier for the fuel oxidation and oxidant reduction at the respective electrodes. Ohmic polarization incorporates resistances from electrolyte, electrodes and electrode-electrolyte interfaces. Finally, the concentration polarization is associated with transport of gaseous species [oxidant and fuel] through porous electrodes. Therefore, an efficient SOFC requires minimization of above mentioned polarization losses.

Irrespective of the conventional preparation techniques e.g. solid state mixing,¹⁶ co-precipitation,²⁷ liquid dispersion,²⁸ heat decomposable aqueous salt solution routes²⁹ etc, the primary requirements of anode¹⁵ required to fulfil SOFC application is satisfied upon using ~ 40-50 vol % of Ni in the cermet.³⁰⁻³³

According to the discussion in Chapter 3, usage of such high content of Ni has been found to impose numerous problems as: a) redox intolerance of anode, b) thermal

Chapter – 5.6

incompatibility with adjacent electrolyte (CTEs of Ni and YSZ are $16.9 \times 10^{-6} \text{ K}^{-1}$ and $10.8 \times 10^{-6} \text{ K}^{-1}$ respectively), c) enhanced Ni coarsening, d) fast degradation of anode which poisons the function of the single cell. ³²⁻³³

It has been experimentally established in section 5.4 that, Ni-YSZ anodes prepared through ‘electroless technique’ having unique ‘core-shell’ microstructure is at par concerning electrical conductivity at even lower Ni content (28 vol %) compared to the cermets synthesized by other conventional techniques (40 vol % Ni). Owing to such reduction in Ni content and unique microstructure comprising of dual TPB zones (Chapter 5.5), numerous shortcomings could be surmounted. A detailed discussion regarding the superiority of bulk electroless Ni-YSZ fabricated by uniaxial pressing has been presented in Chapters 5.4 and 5.5. In the present section, efforts are given to study the structure-property correlation of electroless anode prepared by ‘tape casting and lamination’ technique. Functionality of such novel anodes towards SOFC application are also intended to be presented in terms of performance evaluation of the fabricated single cells, endurance study etc. Intra-correlative assessments among cell performance with other physical properties viz. pore-size distributions, microstructural details, thermal expansion, polarization behaviour etc are also aimed to be scientifically correlated under this investigation.

5.6.1. Optimization of grain and ambipolar resistances of SOFC anode

The performance of SOFC is highly dependent on the characteristics of anode and the associated anodic reactions. It is therefore important to optimize the conductivity and microstructure of anode where surface reactions occur. The total anode resistance (R_{Anode}) can be represented as the contribution of several factors as given in Eq. 5.44.

$$R_{\text{Anode}} = R_g + R_{\text{gas}} + R_{\text{reaction}} + R_{\text{amb}} \quad (5.44)$$

where, R_g , R_{gas} and R_{reaction} are the corresponding resistances offered by grains of the anode, gas transportation and anodic electrochemical reactions respectively. ‘ R_{amb} ’

refers to the resistance in electrical conduction offered due to ambipolar behaviour of SOFC anode cermets. The charge transfer in anode can be represented as two interpenetrating sections of metallic (Ni) electron conductors and ionic (O^{2-} in YSZ) conductors.³⁴ The total ambipolar conductivity is normally being calculated using percolation theory.³⁵

Minimization of anode grain resistance (R_g) depends on appropriate sintering of the cermets. Although a high sintering temperature results in denser anodes with properly sintered grains and therefore the temperature for anode sintering should be optimized in order to maximize the active reaction surface. Figure 5.43 shows that electrical conductivity of Ni-YSZ cermet prepared by either electroless or conventional technique increases steadily with sintering temperature from 1300°C upto 1400°C. However, sintering temperature above 1400°C does not contribute significantly to the enhancement of conductivity.

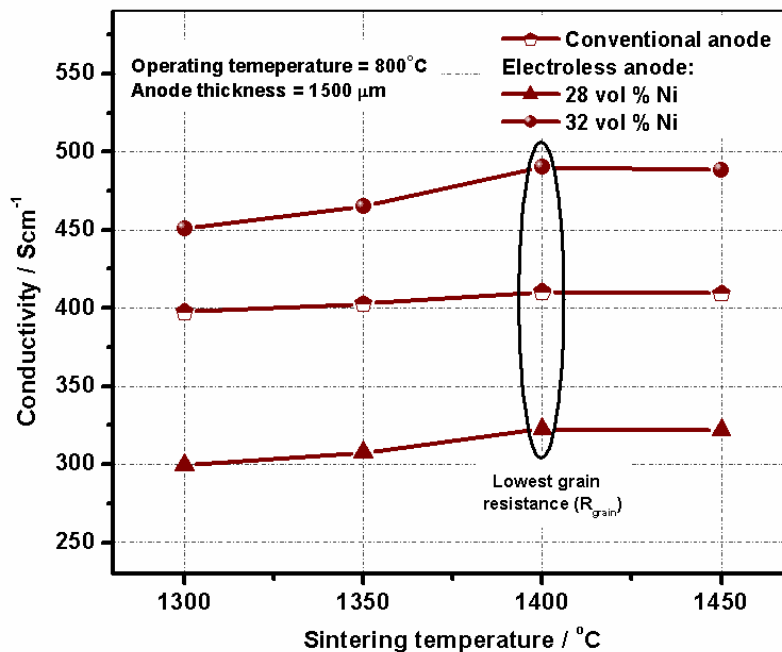


Figure 5.43: Electrical conductivity of anode samples at different sintering temperatures

Chapter – 5.6

On the contrary, there is every possibility that at a higher sintering temperature; the active anode surface will be reduced due to excessive sintering of the grains in the anode microstructure. The overall porosity of the anode gets reduced upon over sintering thereby limiting the triple phase boundary which in turn restricts the electrochemical activity of SOFC. Therefore, resistance being offered by the sintered anode grains can be significantly reduced by limiting the sintering temperature to 1400°C at which maximum conductivity is attained.

Conductivity percolation plots for tape cast anodes prepared by conventional and electroless technique as a function of Ni content is shown in Figure 5.44.

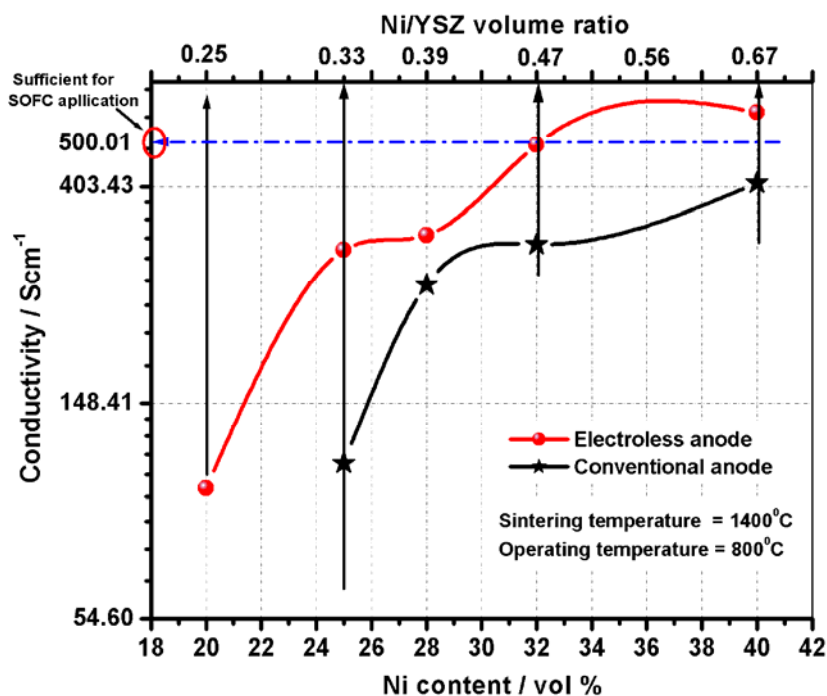


Figure 5.44: Conductivity percolation plots of tape cast anode samples prepared by conventional and electroless technique as a function of Ni content

The transition from ionic (governed predominantly by YSZ phase) to electronic conductivity is initiated at a considerably low Ni content (~ 20 vol %) in electroless cermet, whereas, the percolation necessitates more than 25 vol % Ni for the conventional anodes. The unique core (YSZ)-shell (Ni) microstructure of electroless

cermet enables easy interconnectivity among Ni, YSZ and pore phases throughout the matrix. This helps in imparting the contribution of both Ni and YSZ phase to the overall electrical conductivity at low metallic content and thereby reduce the resistance offered from ambipolar nature of anode (R_{amb}). On the other hand, dispersed distribution of metallic (Ni) and ceramic (YSZ) phases in conventional anode requires higher Ni content (≥ 40 vol %) to satisfy the overall electrical conductivity required for SOFC application. Upon subsequent increase in the volume percentage of Ni, the metallic conductivity predominates over the ambipolar conductivity. It appears that in conventional anode, YSZ phase happens to be disconnected at a Ni/YSZ ratio greater than 0.67 (40:60, according to the theory of ambipolar conductivity) and the contribution of R_{amb} towards the overall anode resistance is found to be insignificant. From the [Figure 5.44](#), it is observed that the electroless anode cermet requires a volumetric fraction of Ni/YSZ of ~ 0.47 for minimizing the ambipolar conductivity and hence the overall electronic conduction shoots up at that particular volume fraction of Ni content when compared with the conventional cermets. From the figure it could be noted that electroless anode necessitates 28-32 vol % Ni to satisfy the electrical conductivity criteria required for SOFC application which is at par with the conduction of conventional anode comprising of ~ 40 vol % Ni. Therefore, in order to substantially reduce the overall anode resistance (R_{Anode}) and enhance the overall electrochemical performance of the anode, attempt has been made to use electroless anode in combination with conventional cermet in varied configurations discussed in the subsequent sections.

5.6.2. Influence of anode configuration on electrical conductivity and correlation with porosity

The advantage of anode-supported cells is the relatively lower contribution of ohmic and activation polarization compare to either electrolyte or cathode

Chapter – 5.6

supported cells. This is due to easy conductive path and higher exchange current density found at low current for such anode-supported cells. ³⁶⁻⁴⁰ Therefore, optimization of electrical conductivity with negligible resistance (R_{Anode}) of anode is one of the crucial factors for governing the performance of SOFC. The principle objective of the present work is to resolve the inadequacies of conventional anode by means of incorporation of an anode prepared by a novel electroless technique.

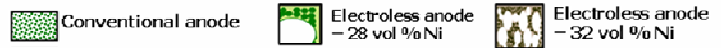
A number of varied configurations of anodes are fabricated in combination with the electroless and conventional Ni-YSZ cermet. Green tapes of electroless anode with varied thickness (25-80 μm) are laminated in combination with conventional anode tapes (80 μm) in four different anode configurations as given in [Table 5.14](#). While the tape thickness of 25 μm are used for fabrication of anode active layer (AAL), the tapes of higher green thicknesses are fabricated for the use as intermediate layers. The configurations (as given in [Table 5.14](#)) as fabricated under this present investigation comprises of:

- a) total anode structural support using conventional cermet having a tape thickness of 80 μm – ‘Configuration – I’
- b) total anode structural support using electroless cermet (28 or 32 vol % Ni) having a tape thickness of 80 μm – ‘Configuration – II’
- c) bilayer anode structure (BLA-series) fabricated by combining conventional NiO-YSZ with electroless Ni-YSZ (28 or 32 vol % Ni) having similar tape thickness of 80 μm and trilayer anode (TLA) structure composed of conventional anode as the structural support and electroless anode (both 32 and 28 vol % Ni) of optimized thicknesses – ‘Configuration – III’
- d) bilayer AAL with reduced electroless (28 or 32 vol % Ni) tape thickness of 25 μm function as active layer (AAL) laminated onto conventional cermet having a tape thickness of 80 μm – ‘Configuration – IV’.

The thickness of electroless anode layers having different Ni content is varied in specific ranges in different configurations as given in Table 5.14 in order to study its effect on electrical conductivity, cell performance and other related properties.

Table 5.14: Fabricated anode cermets having variable configurations

Anode composition		Ni content of conventional anode (vol %)	Ni content of electroless anode (vol %)	Thickness of conventional anode after sintering ($\pm 10 \mu\text{m}$)	Thickness of electroless anode after sintering ($\pm 10 \mu\text{m}$)	Sample ID	Anode Configuration
I Conventional anode		40	--	1250	--	CA-1	
			--	1500	--	CA-2	
II Electroless anode		--	28	--	1250	28 EL-1	
				--	1500	28 EL-2	
			32	--	1250	32 EL-1	
				--	1500	32 EL-2	
III Conventional anode / Electroless anode (thick)	Bilayer anode (BLA-series)	40	28	1450	50	28 BLA-1	
				1380	120	28 BLA-2	
		40	32	1250	250	28 BLA-3	
				1450	50	32 BLA-1	
	Trilayer anode (TLA)	40	28 + 32	180	120	32 BLA-2	
				1250	250	32 BLA-3	
				1400	50 μ each	TLA	
IV Conventional anode / Electroless anode (thin)	Anode support with electroless functional/active Layer (AAL)	40	28	1485	15	28 AAL-1	
				1460	40	28 AAL-2	
				1410	90	28 AAL-3	
				1360	140	28 AAL-4	
		40	32	1485	15	32 AAL-1	
				1460	40	32 AAL-2	
				1410	90	32 AAL-3	
				1360	140	32 AAL-4	



5.6.2.1. Configurations -I & II : Conventional and Electroless cermets as anode support

Based on the discussions of section 5.6.1, electrical conductivity values are reported for the anodes sintered at the optimized temperature of 1400°C. Temperature dependent electrical conductivity of tape cast anodes of Configurations -I and II are presented in Figure 5.45. It can be observed from the above figure that, irrespective of preparation technique and Ni content, all the

Chapter – 5.6

anode samples exhibit similar trend of increasing electrical conductivity with reducing temperature. Significantly higher electrical conduction of 380-535 S.cm⁻¹ at 800°C is obtained for electroless cermet (28 EL and 32 EL) at lower Ni content (28-32 vol %) (Figure 5.45 b) compared to the conventional anode cermet (Figure 5.45 a). Similar electrical conductivity (430 S.cm⁻¹ at 800°C) is obtained for the conventional anode having 40 vol% of Ni content. The activation energy barrier (E_a) for electrical conduction could be easily determined from 'Arrhenius Equation' which exhibits inverse dependence of the electrical conductivity of Ni-YSZ anode on temperature (discussed in section 5.4.2.2).

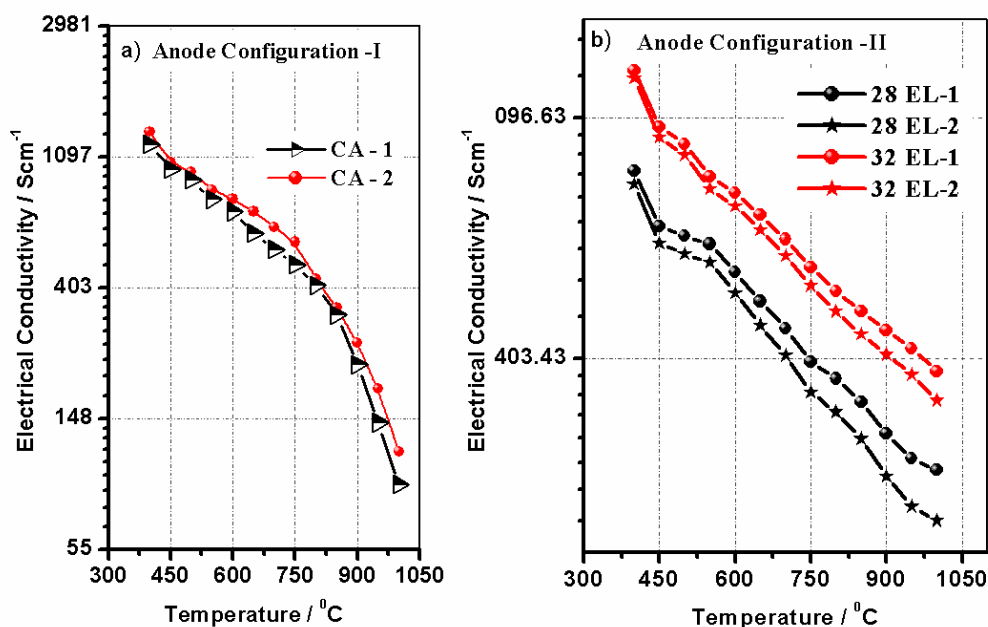


Figure 5.45: Temperature dependent electrical conductivities for anodes of Configuration -I and Configuration-II

The extent of variation of activation energies with fabricated anode configurations is given in Table 5.15. Owing to the unique microstructure of electroless cermet, the energy barrier for electrical conduction is found to be much lower for Configuration - II, as evident from the activation energies (Table 5.15) which is nearly half (~ 15 kJ.mol⁻¹) as compared to the CA-series (~ 30 kJ.mol⁻¹). The higher activation energy for electrical conduction in the conventional matrix is due to the

random distribution of phases and significantly higher metallic content, essential for transition of ionic conduction to electronic conduction as required for SOFC application. This causes higher degree of change in electrical conductivity with change in the temperature.

Table 5.15: Variation of activation energies for electrical conduction with variable anode configurations

Anode Configuration		Anode ID	Activation energies (E_a) for electrical conduction (kJ.mol^{-1})
Configuration –I [Conventional anode]		CA-1	29.55
		CA-2	31.96
Configuration –II [Electroless anode]		28 EL-1	14.62
		28 EL-2	16.38
		32 EL-1	14.21
		32 EL-2	15.19
Configuration –III [Conventional anode / Electroless anode]	BLA-series	28 BLA-1	26.36
		28 BLA-2	23.98
		28 BLA-3	23.06
		32 BLA-1	24.85
		32 BLA-2	22.65
		32 BLA-3	21.69
	TLA	TLA	25.61
Configuration –IV [Conventional anode / Electroless AAL]		28 AAL-1	30.78
		28 AAL-2	25.89
		28 AAL-3	23.422
		28 AAL-4	22.64
		32 AAL-1	28.78
		32 AAL-2	24.39
		32 AAL-3	22.06
		32 AAL-4	21.25

Therefore, generation of unique core-shell structure with optimization of phase distribution in electroless cermet containing much lower Ni content is found to lower the activation barrier of temperature dependent electronic conductivity. Furthermore, as expected from the relation between conductivity and sample depth, the electrical conductivity is found to enhance with reducing the anode thickness from 1500 μm to 1250 μm . However, electrical conduction for anodes of *Configuration-I* is found to be least affected with such thickness variation. The

Chapter – 5.6

energy barrier for conduction is significantly higher ($\sim 30 \text{ kJ.mol}^{-1}$) due to the random distribution of phases in such conventional matrix which surpasses the effect of thickness variation.

5.6.2.2. Configuration-III and IV: Layered anodes with incorporation of electroless cermet

Significant enhancement in the electrical conductivity is observed upon employing electroless anode in conjunction with conventional anode support in the form of layered anode structure as *Configuration – III and IV*. Electrical conductivity of such layered anode as a function of temperature is given in [Figure 5.46](#) and [5.47](#).

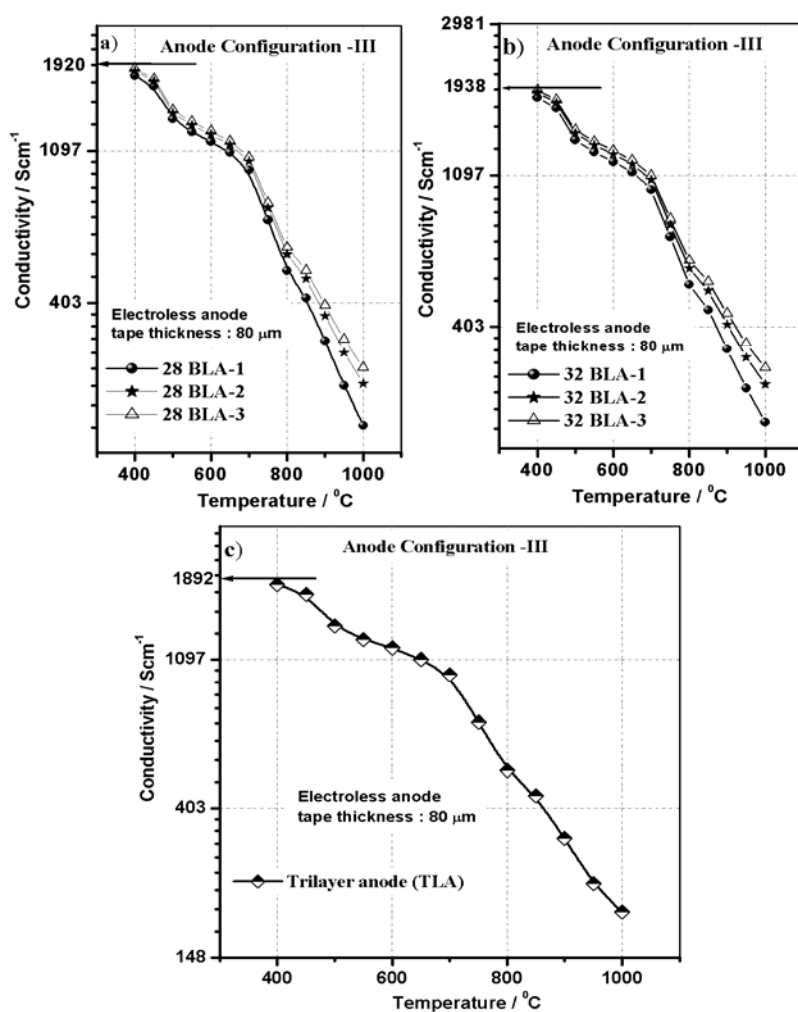


Figure 5.46: Temperature dependent electrical conductivities for anodes of *Configuration –III*

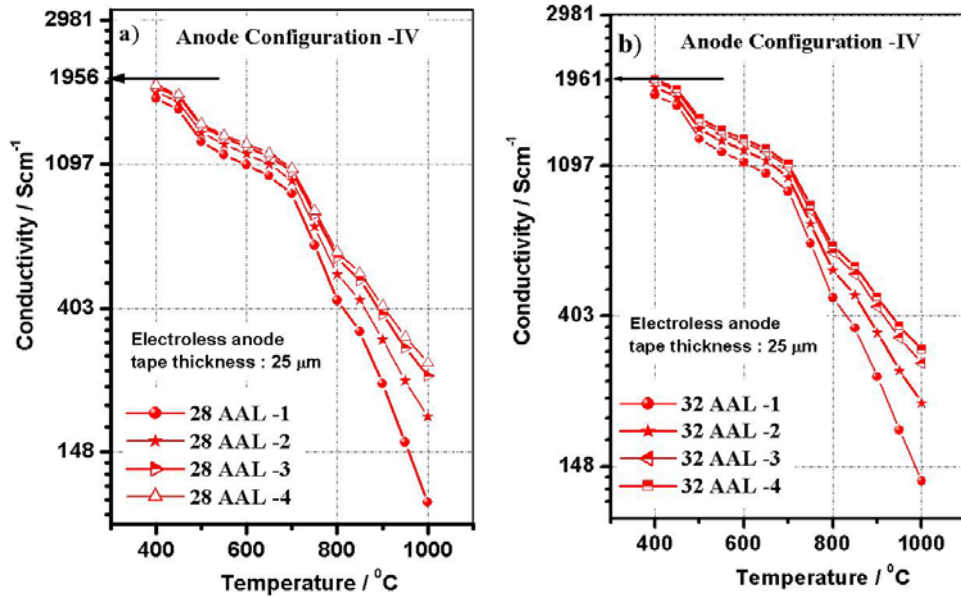


Figure 5.47: Temperature dependent electrical conductivities for anodes of Configuration -IV

The related microstructures of the layered anode with variation in thickness of electroless cermet are also shown in Figure 5.48 a and 5.48 b. It can be observed that, irrespective of the Ni content in electroless cermet, the bilayer anodes having electroless AAL (Configuration-IV) show better electrical conduction. The comparative order of electrical conduction exhibited by such layered anodes is given as:

$$\text{Conductivity trend : } 32/28 \text{ AAL} - 4 > 32/28 \text{ BAL} - 3 > 32/28 \text{ AAL} - 3 > 32/28 \text{ BAL} - 2 > 32/28 \text{ AAL} - 2 > 32/28 \text{ BAL} - 1 > 32/28 \text{ AAL} - 1$$

Incorporation of electroless anode either in the form of layered anode or in the form of an active layer increases the overall electrical conduction in the cermet. However, irrespective of the Ni content in electroless cermet, the bilayer anodes having electroless AAL (Configuration-IV) show better electrical conduction. This may be explained on the basis that, thinner electroless AAL offer least resistance for percolation of charge carriers throughout the matrix. The electrical conductivity of 28 AAL-4 and 32 AAL-4 (Figures 5.47 a and b) anodes having 140 μm electroless AAL is found to exhibit highest electrical conductivity (597 and 644 Scm^{-1} at 800°C) compared to the conduction of layered anode of 28 BAL- 3 and 32 BAL-3

Chapter – 5.6

(Figures 5.46 a and b) having 250 μm electroless layer (584 and 628 Scm^{-1} at 800°C).

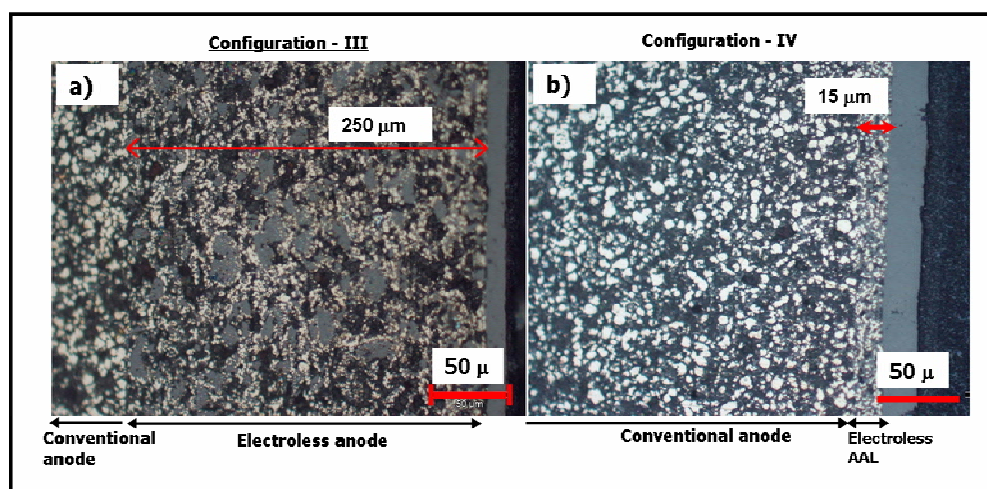


Figure 5.48: Optical microstructures for layered anodes of: a) Configuration- III and b) Configuration -IV

It can be observed from Table 5.15 that, incorporation of electroless layer in either Configuration – III or IV, is responsible for reduction in activation energy barrier for electrical conduction compared to conventional anode support of (Configuration – I). Such enhancement in electrical conductivity with reduction in activation energy for the anode cermet clearly emphasizes the functionality of unique microstructure of the electroless cermet. This is supported by the fact that, the conductivity trend in either Configuration – III or IV, is found to get enhanced with the increase in thickness of electroless layer. However, as layered anode having 140 μm electroless AAL (Configuration–IV) could surpass the conduction of 250 μm electroless layer in Configuration - III, further increment of AAL thickness is evaded.

The influence of Ni content and thickness of electroless cermet on the conductivity of layered anode can be further explained from the conductivity of trilayer structure (TLA) [Figure 5.46 c]. The TLA structure is composed of 50 μm thick electroless (32 vol % Ni) anode as the intermediate layer sandwiched between

conventional and a top electroless anode layer (28 vol % Ni) of similar thickness. The electrical conductivity and the associated activation energy (Table 5.15) of such TLA is found to intermediate to the energy barrier exhibit by 32 BLA-1 and 28 BLA - 1 (Figure 5.46). Placement of relatively denser electroless anode having lower Ni content (28 vol % Ni) as the third layer is believed to interfere in the electronic conduction path and enhance the activation energy (25.6 kJ.mol⁻¹) marginally compared to 32 BLA-1 (24.8 kJ. mol⁻¹).

5.6.2.3. Correlation of electrical conduction with anode porosity

The conductivity trends of fabricated anodes as discussed above can be correlated with porosity variation of anodes as shown in Figure 5.49. The values of the porosity in Figure 5.49 are derived out of the pore size distribution graphs which follows ‘Gaussian type distribution’.

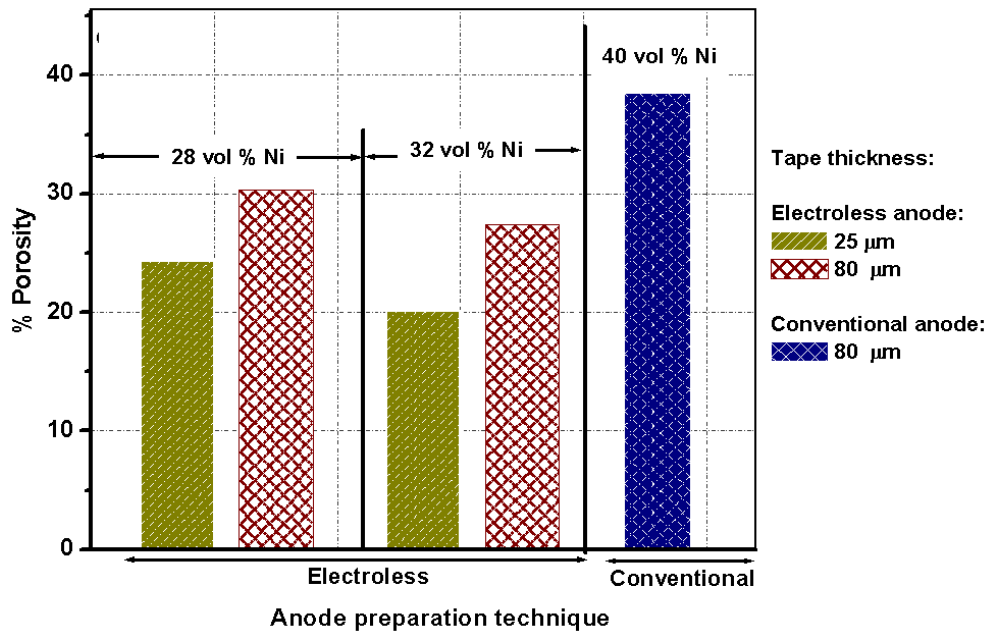


Figure 5.49: Variation in open porosity of SOFC anode prepared through electroless and conventional technique

It is evident from the figure that, the porosity of electroless anode having 80 μm green tape thickness lies in the range of 27 % to 30 % (for 32 and 28 vol % of Ni). However, electroless anodes with thinner green tape thickness of 25 μm are

Chapter – 5.6

found to be relatively more dense having porosity in the range of 20 - 24 % (32 and 28 vol % of Ni). In comparison to the electroless cermets, the conventional anode having 80 μm green tape thickness is found to be more porous (~ 40 %).

In the present context, as given in [Table 5. 14](#), anodes of Configuration - III are fabricated upon combining the former thick electroless layers (tape thickness: 80 μm) with conventional cermet (tape thickness: 80 μm). In similar fashion, anodes of Configuration –IV are fabricated upon combining the thin electroless layers (tape thickness: 25 μm) with conventional cermet (tape thickness: 80 μm). Therefore, blending of anode cermets with gradation in microstructure, Ni content, porosity etc in layered anode offers improvement in electrical conduction properties. This gradation in microstructure in turn helps in the catalytic oxidation of the fuel fed at the base conventional support followed by effective electrochemical reaction at the electroless anode layers.

5.6.2.4. *Electrical conductivity variation with redox cycling of SOFC anode having variable configurations*

As discussed in section 5.6.2.2, the highest conducting tape cast anodes is found to be the layered cermets of *Configuration-IV* (28 IV-4 and 32 IV-4). [Figure 5.50](#) demonstrates the comparative redox tolerance of such superior anodes with conventional anodes of *Configuration-I*. The effect of repeated oxidation and reduction cycles on the fabricated anodes are also assorted in [Table 5.16](#) in terms of percentage conductivity variation. It can be observed from [Figure 5.50](#) and [Table 5.16](#) that, incorporation of electroless layer significantly enhances the redox tolerance of the bilayer anode. The functionality of electroless cermet governs the overall conduction path of the bilayer cermet. The extent of conductivity degradation is found to be least for the anodes of *Configuration-II* compared to either *Configuration –III or IV*. Combining electroless cermet with conventional

anode tends to reduce the rate of conductivity degradation compared to the degradation shown by anodes of Configuration -I as observed from Table 5.16.

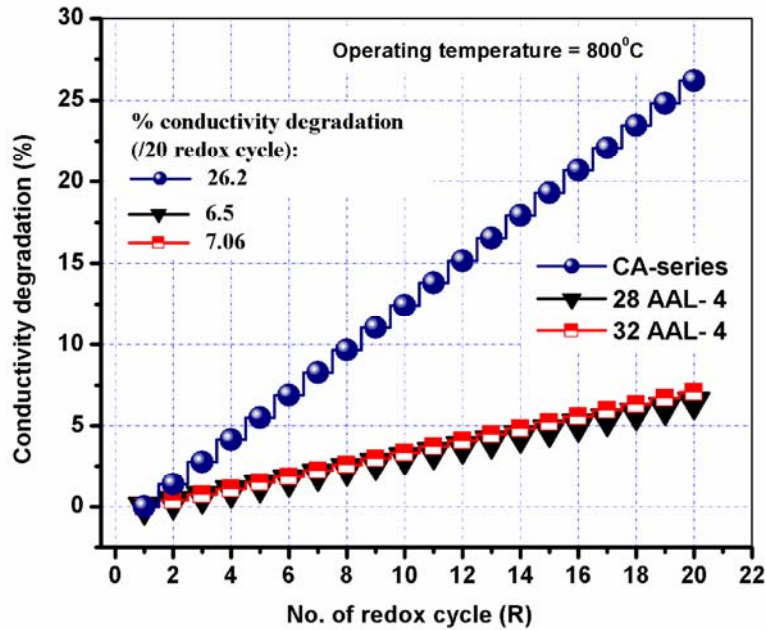


Figure 5.50: Effect of redox cycling on electrical conductivity of: a) conventional anode (CA-series) and b) layered anode with electroless AAL [28 AAL-4 and 32 AAL-4]

Table 5.16: Comparative electrical conductivity degradation of varied anode configurations

Anode Configurations	Anode ID	% Conductivity variation (/20 redox cycles)
Configuration -I	CA-series	26.2
Configuration -II	28 EL-series	4.04
	32 EL- series	6.02
Configuration -III	28 BLA-1	6.89
	28 BLA-2	6.81
	28 BLA-3	6.62
	32 BLA-1	7.30
	32 BLA-2	7.21
	32 BLA-3	7.11
	TLA	6.98
Configuration -IV	28 AAL-1	6.90
	28 AAL-2	6.80
	28 AAL-3	6.64
	28 AAL-4	6.5
	32 AAL-1	7.32
	32 AAL-2	7.20
	32 AAL-3	7.12
	32 AAL-4	7.06

Chapter – 5.6

It is believed that, repeated redox cycling accelerates the rate of Ni coarsening due to the combined effect of phonon scattering and localized joule heating. This causes overall drop in the electrical conduction as shown in [Figure 5.50](#). Conventional anode with ~ 40 vol % Ni exhibit highest conductivity degradation of ~ 26 % after 20 redox cycles ([Figure 5.50](#)). Higher Ni content dispersed in the matrix of conventional cermet primarily causes rapid grain growth and reduces the effective surface area available for catalytic activity and charge transfer reactions. Such irreversible grain growth form Ni islands throughout the conventional anode thereby restricts the contribution of YSZ grains towards overall conductivity. Response of electrical conduction of anodes towards redox cycling is solely governed by the processing technique which leads to the variability in microstructural pattern. In contrast, conductivity degradation is found to reduce drastically upon incorporating electroless layer ([Figure 5.50](#)). Anode samples of 28 AAL-4 and 32 AAL- 4 exhibit only 6.5 and 7 % conductivity degradation after 20 redox cycles. Such reduced rate is mainly because of less Ni content and ordered microstructure with numerous interconnecting paths among Ni and YSZ phases. The rate of volume change upon repeated redox process is less for such electroless cermet having smaller Ni particulate size. In addition, due to easily available conductive path in the electroless matrix, charge carriers preferably follows its least resistive paths and thereby Ni coarsening is least affected compared to the dispersed microstructure of conventional anode. The slight enhancement in the conductivity degradation of layered anodes having 32 vol % Ni (electroless cermet) viz. 32 BAL or 32 AAL-series is due to the presence of higher Ni content in the electroless matrix. However, owing to the increment in electrical conductivity of such 32 AAL- and 32 BAL-series, such degradation rate is found to be negligible. Therefore, highly conductive electroless anode with low Ni content and unique microstructure is superior in terms of increased redox tolerance compared to conventional SOFC anodes

5.6.2.5. Role of moist fuel in electrical conduction of SOFC anode

The aforementioned discussions have clearly highlighted certain factors on which the electrical conduction of SOFC anode is rely on, a) operating temperature, b) Ni: YSZ content, c) porosity , d) thickness of anode cermet, e) microstructural distribution, f) rate of transformation of NiO to Ni during reduction, g) variation in operation environment viz. oxidative or reductive etc. Primarily SOFC anode is responsible for oxidation of fuel (hydrogen, CO etc). Hence, the factors influencing the fuel oxidation are also expected to affect the electrical conduction mechanism of the concerned anode. Subsequent to the densification of anode in oxidative environment, the formed NiO is entailed to get reduced to Ni. Such redox couple reaction involving reduction of NiO to Ni and oxidation of hydrogen is found to be accelerated in the presence of oxygen containing species.¹⁵ The electrical conduction of the developed anodes is also found to be influenced by the presence of moisture in the fuel. Table 5.17 illustrates the dependence of both electrical conduction and redox tolerance of 28/32 AAL-4 anodes on the presence of moisture in the fuel. Since, 28/32 AAL-4 is found to have maximum electrical conductivity with significant redox tolerance; such anodes are selected for the present experiment.

Table 5.17: Effect of moisture towards electrical conductivity of SOFC anodes

Anode ID	Electrical conductivity (S.cm ⁻¹)		% Conductivity variation (/20 redox cycles)	
	Moist Hydrogen	Dry Hydrogen	Moist Hydrogen	Dry Hydrogen
28 AAL-4	597	474	6.5	9.87
32 AAL-4	644	530.3	7.06	13.4

It is vivid from the table that, irrespective of Ni content, anode cermets exhibit significantly lesser conductivity in dry hydrogen. Consequently, the cermets undergo fast degradation in absence of moisture in the fuel. It is established that,

Chapter – 5.6

most of the reduction (NiO to Ni) occurs initially, however, longer time interval is required for the anode conductivity to reach a steady state due to continuing reduction and rearrangement of Ni particles with the progression of reaction. During the reaction, the conductivity usually reaches a maximum very quickly, and then cascade slowly till the achievement of steady state.¹⁶ The maxima occurs when adequate NiO is reduced to form a conducting Ni-Ni matrix, and falls off during redox cycling due to loss of Ni particle contact. Presence of oxygen species in the fuel accelerates the rate of hydrogen oxidation through subsequent reaction sequence of: a) moisture decomposition into oxygen adsorbed on Ni and hydrogen, b) propagation of charge transfer reaction involving oxidation of fuel and subsequent reduction of NiO to Ni. In absence of such oxygen containing species, the charge propagation forms the prime rate determining step which limits the conduction of charge and thereby limits the overall electrical conduction as could be observed from [Table 5.17](#). In the similar means, cyclic reduction and oxidation in absence of moisture imposes significant barrier towards the redox reactions. The anode cermet experiences significant energy barrier for propagation of charge and thereby degrades at a much faster rate. The presence of a definite ratio of moisture in the hydrogen fuel leads a dramatic decrease in the value of anodic overpotential⁴¹⁻⁴² and hence, presence of moisture enables significant role towards the functioning of Ni-YSZ anode for SOFC application.

5.6.3. Electrochemical performance evaluation of SOFC fabricated with assorted anode configuration

The present section is based on the experimental evaluation of the performances of planar solid oxide single cells fabricated with varied anode configurations as tabulated earlier in [Table 5.14](#). The various factors related to the fabrication of the anode and its associated properties affecting the overall

performance of cells are studied in details. As SOFC is an example of an open system, therefore, apart from the combination of three major components viz. anode, cathode and electrolyte, gaseous reactants (fuel and oxidant) play an important role in the overall performance of SOFC. Apart from optimization of microstructural distribution, studies relating to the flow pattern of gaseous reactants followed during electrical conduction, electrochemical activity etc is also imperative for understanding of SOFC performance.

5.6.3.1. Variable modes of gas transport employed in electrical and electrochemical processes

The isothermal transport of gaseous reactants through porous electrodes is governed by fundamental diffusion equations as given below: ⁴³

$$J = -D_{eff} \nabla n + X \delta J - X \gamma \left(\frac{n B_0}{\mu} \right) \nabla p \quad (5.45)$$

where, J, D_{eff} , n, X, B_0 , p, μ and γ are flux of concerned gas, effective diffusivity (applicable for mixture of gasses also), concentration, mole fraction, permeability, total pressure, viscosity and fraction of diffusivity in a mixture of gasses respectively.

The effective binary diffusion coefficient [D_{eff}] for electrodes is the key factor which determines the nature of gaseous flow and correlates with the microstructure which may or may not be position variant. The equation relating the diffusion coefficient with electrode thickness is given as: ⁴³

$$D_{a(eff)} = \frac{D_a V_{v-a}}{\tau_a} = \frac{D_a l_a}{\left(\frac{\tau_a l_a}{V_{v-a}} \right)_{eff}} \quad \& \quad D_{c(eff)} = \frac{D_c V_{v-c}}{\tau_c} = \frac{D_c l_c}{\left(\frac{\tau_c l_c}{V_{v-c}} \right)_{eff}} \quad (5.46)$$

where, $D_{a/c(eff)}$, $D_{a/c}$, V_v , $\tau_{a/c}$, $l_{a/c}$ are effective binary diffusion coefficients of anode or cathode, binary diffusion coefficient for gaseous mixtures at anode/cathode,

Chapter – 5.6

volume fraction of anode/cathode, anode/cathode tortuosity and length of electrodes respectively.

During electrochemical reactions, the process of charge transfer occurs at a certain thickness of electrode from electrolyte/electrode interface. It is found that over this region, contributions of both the electronic and ionic current exits as a function of position. Outside this region, the current is electronic in electrodes and ionic in electrolyte. Owing to this, it could be established that, the flow pattern of gasses follows non-linearity (with rapid flow) at electrode-electrolyte interface and is microstructure variant as shown in [Figure 5.51 a](#).

In anode-supported cells, length of anode (l_a) is significantly higher in comparison to the length of cathode (l_c) [$l_c \lll l_a$], therefore, such non-linearity is evident at only anode side where, l_a signifies the electro catalytic active region, which may not necessarily correspond to the entire anode thickness. It could be observed from [Figure 5.51a](#) that, the flow pattern of fuel is converging towards the interface of anode and electrolyte at which the electrochemical reaction is primarily operative. Therefore, compared to unilayerd anode, employing multilayered anode with gradation in thickness, microstructure, porosity, phase constituents with limited electrochemical active zone is expected to be more effective for cell performance with better durability.

In contrast, electronic conduction of anode is a bulk phenomenon and is confined to the entire conduction path which regulates the flow path of electrons. In this case, effective diffusion of gas entirely depends on the specific thickness of anode and also on the easiest path for the electronic flow. Hence, unlike the electrochemical reactions, electronic conduction seeks linear flow of gasses ([Figure 5.51 b](#)), owing to which reducing thickness of electrodes is found to enhance the magnitude of electrical conduction (sections 5.6.2.1 and 5.6.2.2) as shown in schematic of [Figure 5.51 b, I-II](#). In addition for the anodes having variable electrode thicknesses, electrical conductivity is primarily governed by the microstructural

distribution which dictates the path of overall electrical conduction. Therefore, in case of multilayer anode, conductivity is found to increase with thickness of concerned anode layer whose microstructure favors the conduction path (Figure 5.51 b, III-IV) which is already discussed in section 5.6.2.

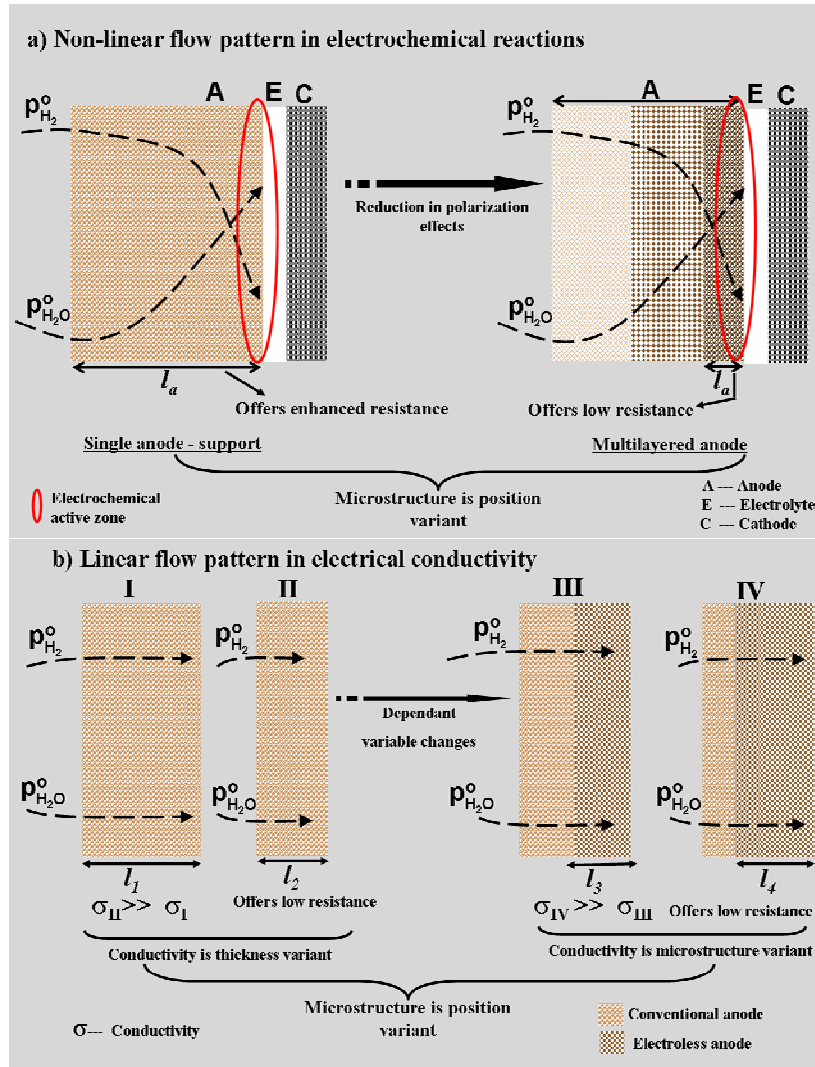


Figure 5.51: Comparative flow pattern of gasses for a) electrochemical reaction and b) electrical conductivity

5.6.3.2. Configuration – I & II: - Conventional and electroless cermet as anode-support

In Configuration-I, total anode-support is made of Ni-YSZ anode prepared by conventional solid state mixing containing 40 vol % Ni. The structure of cell in

Chapter – 5.6

Configuration-I is: Ni-YSZ anode (conventional technique) / YSZ electrolyte / $\text{La}_{0.65}\text{Sr}_{0.3}\text{MnO}_3$ (LSM)-YSZ cathode active layer (CAL)/ LSM cathode layer (CL) (Figure 5.52 a) and The for *Configuration -II* is: Ni-YSZ anode (electroless technique) / YSZ electrolyte / $\text{La}_{0.65}\text{Sr}_{0.3}\text{MnO}_3$ (LSM)-YSZ cathode active layer (CAL)/ LSM cathode layer (CL) (Figure 5.52 b). Since Ni plays a major role for catalytic oxidation of hydrogen, the overall electrochemical activity of anode depends on the extent of reduction from NiO to metallic Ni.

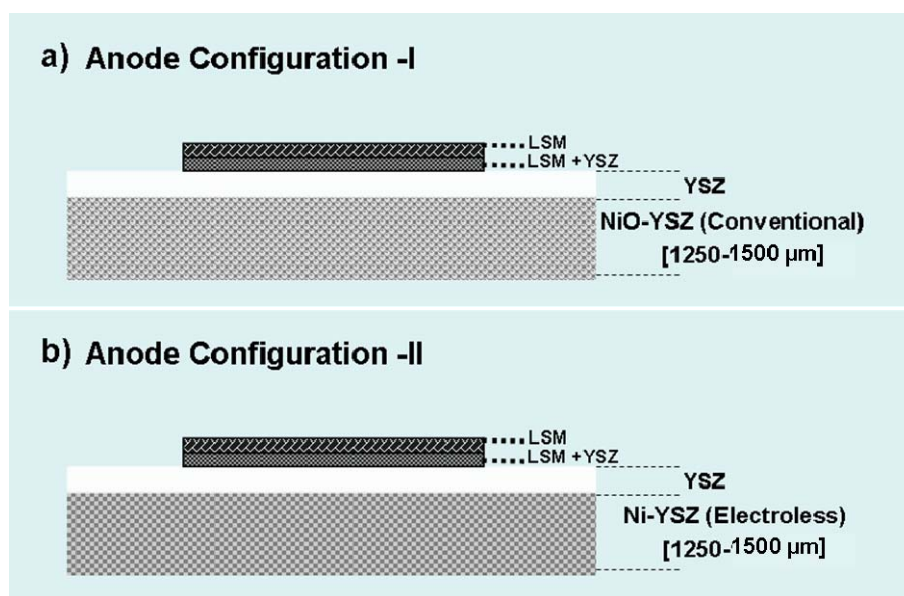


Figure 5.52: Schematic of single cell fabricated with anodes of:
a) Configuration- I and b) Configuration -II

Depending upon characteristics of anode, reduction of NiO during electrochemical testing follows two distinct regions: a) non-equilibrium and b) equilibrium region. Owing to the presence of unique patterned core (YSZ)-shell (Ni) structure of electroless anode, the NiO reduction mechanism could schematically be represented as shown in Figure 5.53. Non-equilibrium region refers to the dynamic state in which the reduction of NiO follows a two step kinetic process. The former step involves reaction between NiO and hydrogen atoms adsorbed on NiO. This step is dependent on the partial pressure of hydrogen and is governed by the

thickness of the anode-support. The second step of the reaction proceeds at the interface between NiO and hydrogen atoms adsorbed on Ni already reduced in the first step. The later reaction is independent of hydrogen partial pressure and is governed by the extent of cermet sintering. However, it is experimentally observed that, after a certain time period, the extent of NiO reduction to Ni reached saturation. Beyond this limit, known as the ‘equilibrium region’ (static state), no further improvement in cell performance is observed.

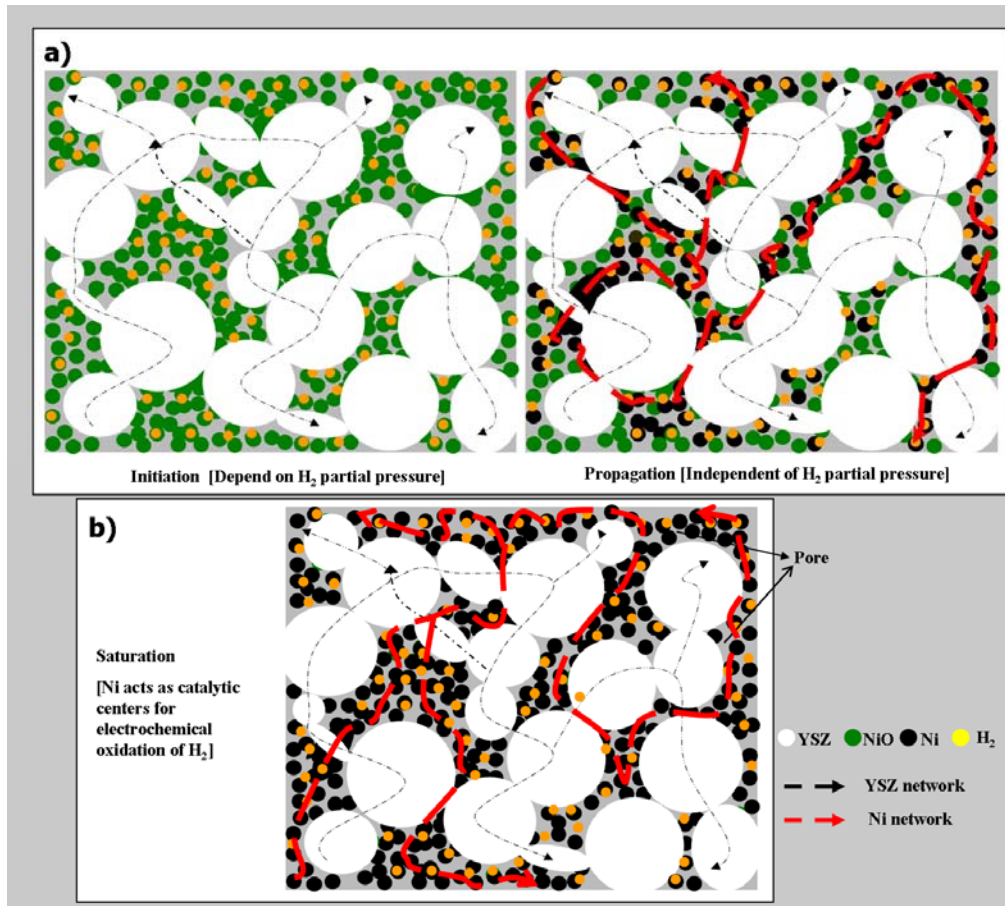


Figure 5.53: Schematic of NiO reduction mechanism in electroless anode cermet following two distinct steps as a) non-equilibrium and b) equilibrium region

With the intention to study the effect of sintering temperature for the formation of proper metal (Ni)-oxide (NiO) interface, the half cells [Anode/electrolyte] are sintered in the temperature range of 1300 -1400°C at an

Chapter – 5.6

interval of 50°C. However, it is observed that the electrochemical performances of single cells with half cells sintered at 1300°C are much lower due to which their results are not included during the discussion. This may be because of the ineffective sintering of YSZ electrolyte layer. Formation of proper metal-oxide interface is found to take place in the sintering temperature range of 1350 -1400°C. The effect of NiO reduction to metallic Ni and sintering temperature of half cells on electrochemical performance of single cells is shown in Tables 5.18 - 5.21. The tables also demonstrate the dependence of cell performance and rate of NiO reduction on the variation of thickness of anode support. The equilibration time of reduction for such anode-support is found to be lesser for anodes of CA-series in comparison to the cell fabricated with anodes of either 32 EL or 28 EL- series.

Table 5.18: Effect of NiO reduction time and sintering temperature on performance of single cells fabricated with anodes of Configuration - I [Anode thickness: 1250 μm]

Sintering temperature of the half cells (°C)		1350					1400				
NiO reduction time (h)		0.5	3	5	20	72	0.5	3	5	20	72
Current density (A.cm ⁻²) at 0.7 V	800°C	0.75	0.98	1.30	1.30	1.30	0.89	1.1	1.7	1.7	1.81
	750°C	0.58	0.75	1.01	1.01	1.01	0.75	0.96	1.25	1.25	1.34
	700°C	0.25	0.48	0.5	0.5	0.5	0.43	0.67	0.90	0.90	1.1

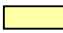
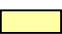
 Equilibrium region

Table 5.19: Effect of NiO reduction time and sintering temperature on performance of single cells fabricated with anodes of Configuration - I [Anode thickness: 1500 μm]

Sintering temperature of the half cells (°C)		1350					1400				
NiO reduction time (h)		0.5	3	6	15	72	0.5	3	6	15	72
Current density (A.cm ⁻²) at 0.7 V	800°C	0.75	0.98	1.30	1.30	1.30	0.89	1.1	1.7	1.7	1.7
	750°C	0.58	0.75	1.01	1.01	1.01	0.75	0.96	1.25	1.25	1.25
	700°C	0.25	0.48	0.5	0.5	0.5	0.43	0.67	0.90	0.90	0.90

 Equilibrium region

Single cells with anodes of CA-series achieve the reduction equilibration at ~ 5-6 h in comparison to 28 EL- (equilibration time ~ 7-10 h) or 32 EL-series (equilibration

time ~ 6-9 h). This could be explained on the basis of microstructural variation of the cermets prepared by two techniques.

Table 5.20: Effect of NiO reduction time and sintering temperature on performance of single cells fabricated with anodes of Configuration - II [Anode thickness: 1250 μm]

Sintering temperature of the half cells (°C)		1350					1400					
		0.5	3	7	15	72	0.5	3	7	15	72	
28 EL-1	NiO reduction time (h)	0.5	3	7	15	72	0.5	3	7	15	72	
	Current density (A.cm ⁻²) at 0.7 V	800°C	0.54	0.78	1.35	1.35	1.35	0.82	0.92	1.43	1.43	1.43
		750°C	0.37	0.59	0.92	0.92	0.92	0.55	0.86	0.99	0.99	0.99
		700°C	0.24	0.37	0.43	0.43	0.43	0.34	0.40	0.46	0.46	0.46
32 EL-1	NiO reduction time (h)	0.5	6	12	20	72	0.5	6	12	20	72	
	Current density (A.cm ⁻²) at 0.7 V	800°C	1.1	1.99	1.99	1.99	1.99	1.5	2.5	2.5	2.5	2.5
		750°C	0.79	1.16	1.16	1.16	1.16	0.96	1.27	1.27	1.27	1.27
		700°C	0.59	0.7	0.7	0.7	0.7	0.73	0.79	0.79	0.79	0.79

Equilibrium region

Table 5.21: Effect of NiO reduction time and sintering temperature on performance of single cells fabricated with anodes of Configuration - II [Anode thickness: 1500 μm]

Sintering temperature of the half cells (°C)		1350					1400					
		0.5	3	6	10	72	0.5	3	6	10	72	
28 EL-2	NiO reduction time (h)	0.5	3	6	10	72	0.5	3	6	10	72	
	Current density (A.cm ⁻²) at 0.7 V	800°C	0.42	0.65	0.90	1.0	1.0	0.7	0.88	0.95	1.32	1.32
		750°C	0.25	0.33	0.47	0.53	0.53	0.45	0.59	0.66	0.75	0.75
		700°C	0.14	0.25	0.29	0.30	0.30	0.28	0.36	0.38	0.40	0.40
32 EL-2	NiO reduction time (h)	0.5	6	9	10	72	0.5	6	9	10	72	
	Current density (A.cm ⁻²) at 0.7 V	800°C	0.95	1.01	1.46	1.46	1.46	1.2	1.4	1.98	1.98	1.98
		750°C	0.61	0.81	1.01	1.01	1.01	0.67	0.89	1.23	1.23	1.23
		700°C	0.48	0.61	0.51	0.51	0.51	0.53	0.65	0.69	0.69	0.69

Equilibrium region

Owing to the non-patterned dispersed distribution of Ni and YSZ in the matrix of conventional anode, the reduction of NiO fails to follow a regular ordered path. The

Chapter – 5.6

overall reduction of NiO to Ni therefore achieves saturation quickly irrespective of operating temperature because the rate limiting steps of the reduction process is invariant of cermet microstructure. Higher porosity in the conventional cermets also facilitates the reduction process. In contrast, the novelty of anode, prepared by electroless technique, is imbued in its unique core (YSZ) – shell (Ni) microstructure. Processing parameters, as optimized during synthesis of Ni-YSZ cermet, enable the deposition of Ni-particulates in a discrete pattern. Such unique structure facilitates the extension of TPB of the cermet matrix which comprises of YSZ-core, discrete Ni-shell around it and the associated porosity. Deposition of metallic Ni around YSZ core is made in such a way that both YSZ and Ni phases are in intra and inter-phase contact throughout the anode matrix. Such interconnecting patterned network between YSZ-YSZ, Ni-Ni and YSZ-Ni with the associated pores helps in the enhancement of TPB length and ensure the availability of O^{2-} ions (through YSZ), electrons (through Ni) and H_2 (through pores) throughout the anode. Therefore, the reduction of NiO also follows an ordered path and the equilibration time period is shifted towards higher magnitude as given in [Tables 5.20 and 5.21](#). However, compared to the anode configuration of 28 EL-series, single cells with 32 EL-series anodes are equilibrated early. The rate of NiO reduction reaction is therefore accelerated by employing anodes of 32 EL-series having 32 vol% of Ni, owing to which the equilibration time range is reduced to 6-9 h compared to 7-10 h time required by cell with 28 EL-series anodes.

Another interesting feature can be noted from the tables that, irrespective of half cell sintering temperature and variation in anode configuration, NiO reduction equilibration is achieved at a much faster rate for thinner anode-support of thickness 1250 μm . In comparison, 1500 μm thick anode-support requires longer time (~ 9-10 h for 28/32 EL-2 series and 6h for CA- 2 series) to reach the reduction saturation limit which indicates relatively slower rate of NiO reduction. Thinner anode-support helps in easy hydrogen diffusion and tends to accelerate

the partial pressure dependent reduction reaction between NiO and hydrogen atoms adsorbed on NiO which is the first step of the reduction process.

Though metal-oxide interface was properly formed at 1350°C, higher electrochemical performances were observed for the cells with half cells sintered at 1400°C. This is primarily because of higher degree of YSZ electrolyte densification at 1400°C. From the tables, it is also observed that, the electrochemical performance of single cell is almost constant after equilibration to 72 h which indicates the steady state reduction of NiO. The single cell performances fabricated with anodes of Configuration-I and II sintered at 1400°C are shown in Figures 5.54, 5.55 and 5.56.

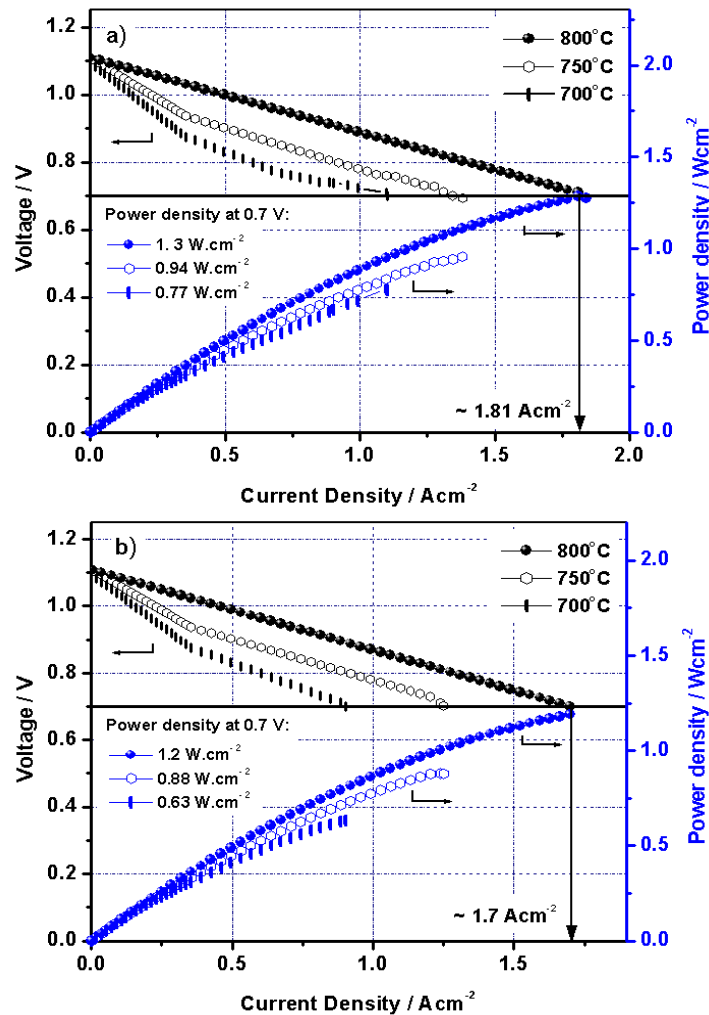


Figure 5.54: Electrochemical performance of SOFC with half cell sintered at 1400°C fabricated with anodes of configuration: a) CA-1 and b) CA-2

Chapter – 5.6

Single cell with 1500 μm thick conventional anode-support showed a current density of $\sim 1.7 \text{ Acm}^{-2}$ [power density $\sim 1.19 \text{ Wcm}^{-2}$] at 800°C and 0.7 V with hydrogen as fuel and oxygen as oxidant (Figure 5.54 b). In contrast, electroless anode-support with 32 vol % Ni (32 EL-2) exceeds the cell performance of CA-2 (current density of $\sim 1.98 \text{ Acm}^{-2}$, power density $\sim 1.4 \text{ Wcm}^{-2}$) under similar experimental conditions (Figure 5.56 b).

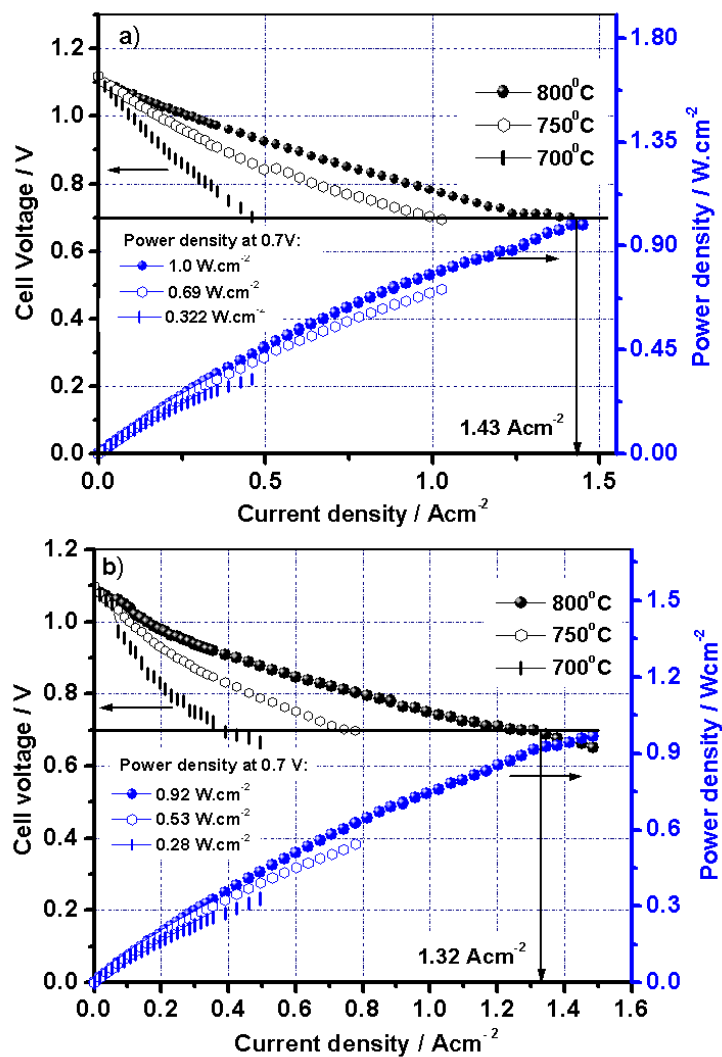


Figure 5.55: Electrochemical performance of SOFC with half cell sintered at 1400°C fabricated with anodes of configuration: a) 28 EL-1 and b) 28 EL-2

In comparison, higher current density of $\sim 2.5 \text{ Acm}^{-2}$ with a power density of $\sim 1.75 \text{ Wcm}^{-2}$ (at 0.7 V and 800°C) is obtained from cells having 1250 μm thick anode-support (32 EL-1) under similar experimental conditions (Figure 5.55 a). The

performances of single cell fabricated with 28 EL-series shown in Figure 5.55 are found to marginally lower than CA-series anodes.

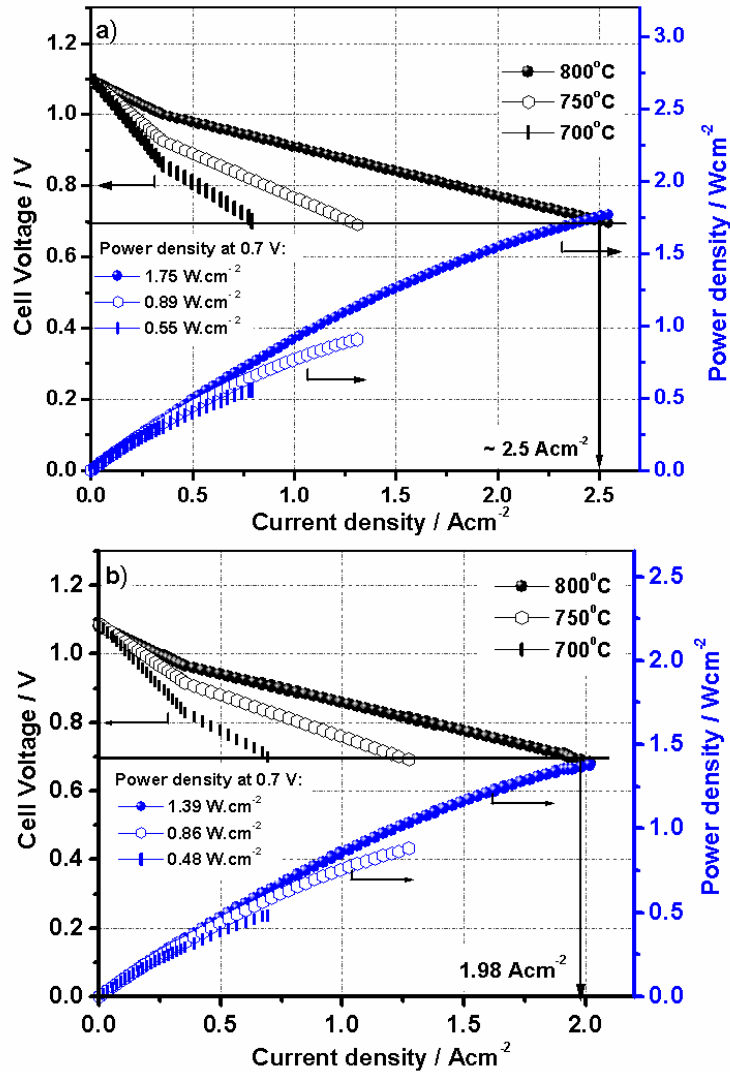


Figure 5.56: Electrochemical performance of SOFC with half cell sintered at 1400°C fabricated with anodes of configuration: a) 32 EL-1 and b) 32 EL-2

The comparative magnitudes of current densities shown in Figures 5.54, 5.55 and 5.56 clearly demonstrate that optimized processing during electroless technique enables the electroless anodes having significantly lower Ni content (28 vol % Ni) to be at equivalence with the conventional cermet that requires ~ 40 vol % Ni for the overall electrochemical performance of the cell. The single cell performances as obtained experimentally could be correlated with the microstructural distribution

Chapter – 5.6

as shown in Figure 5.57. A typical optical micrograph of the cross-section of the cell of Configuration-II (Figure 5.57a) shows retention of unique core (YSZ) - shell (Ni) microstructure in the anode-support prepared through electroless technique. Optimization of process parameters during electroless technique enables controlled deposition of finer Ni particulates onto YSZ surface which is reflected in the micrograph. The corresponding elemental line mapping for nickel and zirconium of such sample is shown in Figure 5.57 b.

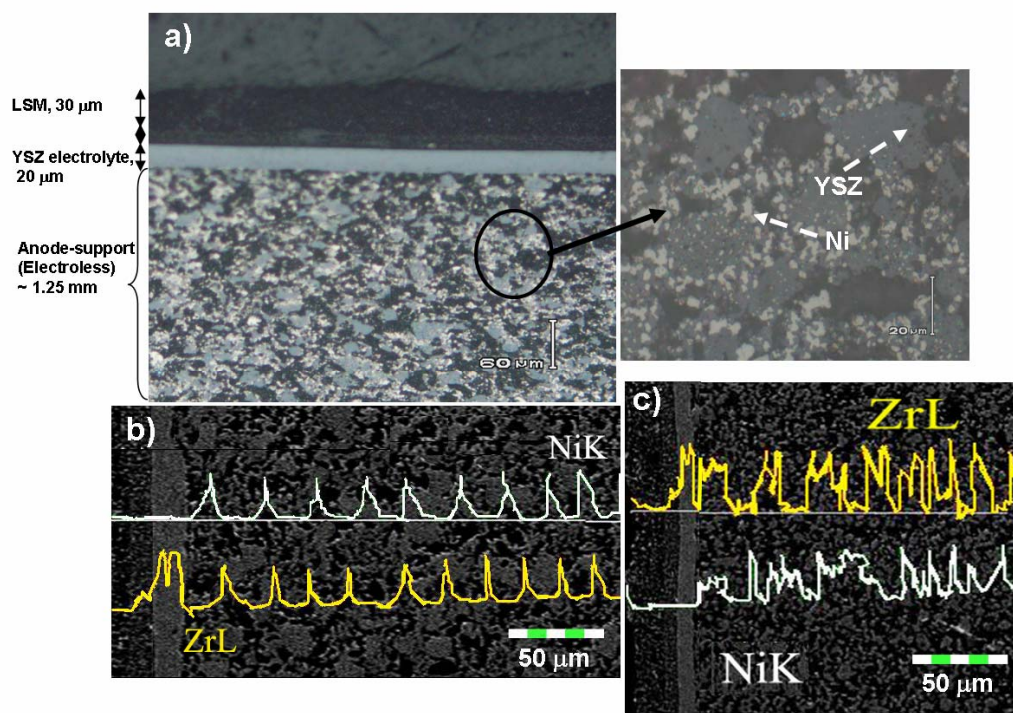


Figure 5.57: a) Optical micrograph [with higher magnification of anode in right side] of single cell fabricated with anodes of EL-2 series, b) corresponding line mapping of single cell after electrochemical measurement with electroless Ni-YSZ as anode- support (EL-2-series-Configuration-II) and c) line mapping of single cell fabricated with anodes of CA-series

It is revealed from the figure that, the concentration of fine Ni particulates at the shell position is higher. In contrast, the YSZ concentration is found to be higher at the core position of the Ni-YSZ cermet prepared by electroless technique. This

corresponds to the periodic crest-hub type distribution of elemental 'Ni' and 'Zr' at the shell and core position respectively. Such core-shell microstructure helps in maintaining electrical interconnection through Ni – Ni nanoparticulates chains in the electroless cermet. However, the non-periodic distribution of elemental 'Ni' and 'Zr' in the matrix of conventional anode support (Figure 5.57c), elucidate the disperse distribution of the constituent phases within the cermet anode. Owing to such dispersed allocation of phases, the conventional cermet lacks the presence of dual TPB zones which limits the overall electrocatalytic activity of such cermets (40 vol % Ni) and thereby results in significantly lower performance of the concerned SOFCs.

5.6.3.3. Configuration – III: Functionality of electroless Ni-YSZ as layered anode

A novel approach of fabricating SOFC anode comprising graded compositions in constituent phases having layer wise microstructural variation is endeavored in the present section. According to the prior arts, layered anode investigated by the other group of researchers^{26, 44-47} is devoid of microstructural variation as the entire anode layers are being synthesized using a single technique. Therefore, the variation of the constituent phases and the microstructural control thereof, is necessary to be adjusted precisely so that the electrical, electrochemical and catalytic properties of anode are not affected. The fabricated layered anode as reported in the present section comprises of electroless Ni-YSZ anode in conjugation with conventional anode for better electrochemical activity, thermal compatibility and cell performance. The present work describes the development of functional layered anode (*Configuration-III*) having variation in porosity, Ni content, layer thickness, Ni / YSZ and pore phase distribution through the entire regime of anode composite. Conventional NiO-YSZ tapes (~ 40 vol % Ni) with higher porosity are used towards the fuel inlet for better gas diffusion and current collection. Electroless anode tape(s) with much lower Ni content (~ 32 vol %) and

Chapter – 5.6

porosity compared to the conventional cermet is placed onto the base support structure. Finally, the third layer(s) of electroless anode having still lower Ni content (~ 28 vol %) and porosity is placed adjacent to the YSZ electrolyte to fabricate the half cell with a trilayered anode (TLA). Similarly, half cells having bilayered anode (BLA) are fabricated using conventional NiO-YSZ with 40 % of Ni as the base support and electroless Ni-YSZ with either 28 or 32 vol % Ni as electrochemically active layer. Schematic of *Configuration-III* in Figure 5.58 shows that, the conventional anode with higher Ni content (40 vol %), having high porosity is placed towards the fuel inlet side as the support structure and electroless anode (having 28 and 32 vol % of Ni) with smaller pores and lesser porosity is placed adjacent to the electrolyte. The thickness of electroless anode layers having different Ni content was varied in the range of 50 - 250 μm to study its effect on the cell performance. A detail of the fabricated anodes of Configuration-III is given in Table 5.14.

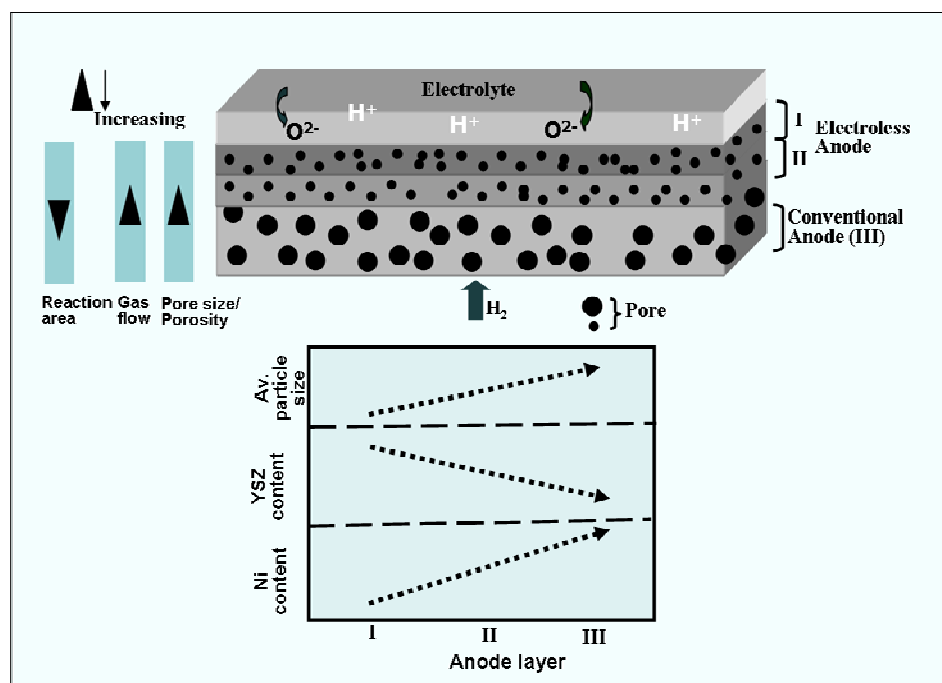


Figure 5.58: Schematic representation of layered anode configuration (Configuration-III) with gradation in physical properties

5.6.3.3.1. Functionality of electroless cermet in bilayered anode (BLA-series)

The sintered temperature of half cells (anode/electrolyte) has been optimized at 1400°C in the earlier sections based on the highest performance of the fabricated single cells. Therefore, in the consequent sections, performances of single cells with half cells sintered at 1400°C are only represented. The performances of single cells having such bilayered anode configuration with varied Ni content (28 BLA-3 and 32 BLA-3) are shown in Figure 5.59 and 5.60.

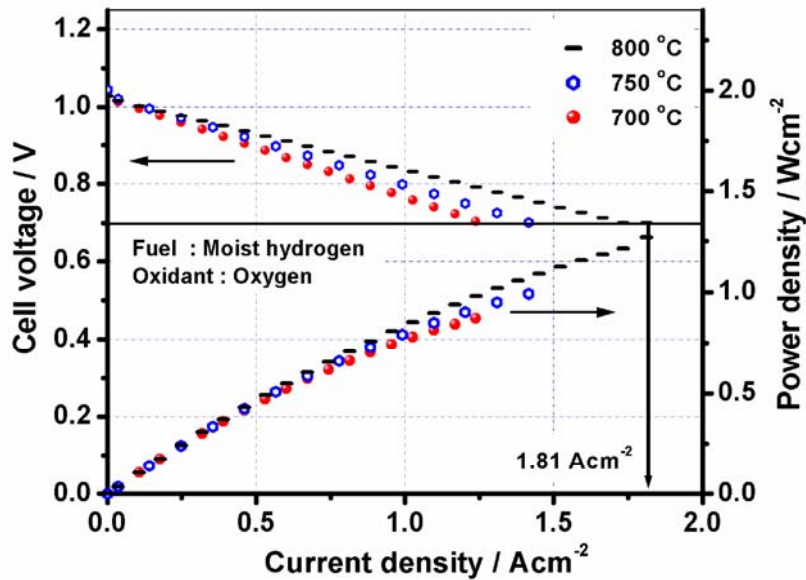


Figure 5.59: Electrochemical performance of single cell fabricated with anode of 28 BLA-3

It can be observed that, single cells with anodes of 28 BLA-3 configurations containing only 28 vol % Ni exhibits a current density of ~ 1.8 Acm⁻² at 800°C, 0.7 V and is found to be marginally better compared to that of the cells having CA-2 anodes. However, a significant enhancement in cell performance of ~ 2.57 Acm⁻² at 800°C, 0.7 V is observed upon increasing Ni content of electroless anode to 32 vol % [32 BLA-3] as shown in Figure 5.60. Owing to the presence of higher porosity in conventional anode support placed at the fuel inlet side, gas transportation is facilitated. Therefore, in such layered anode structure, conventional anode having

Chapter – 5.6

40 vol % of Ni primarily performs the function of effective gas distribution and current collection.

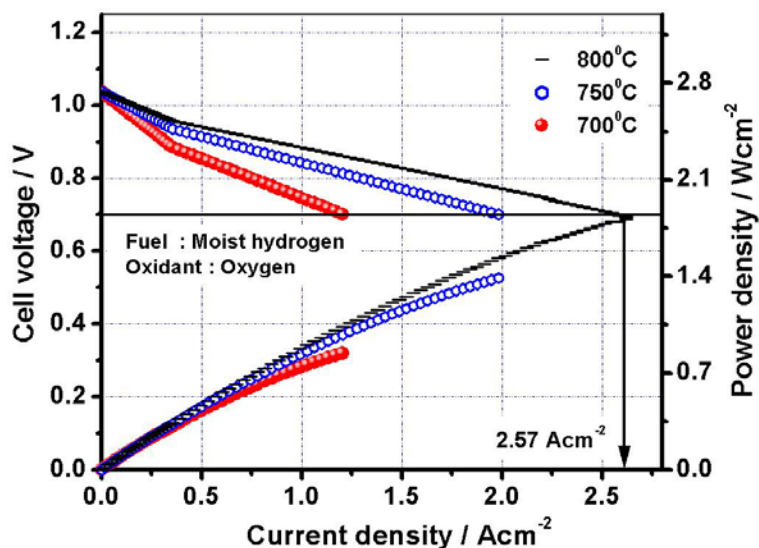


Figure 5.60: Electrochemical performance of single cell fabricated with anode of 32 BLA-3.

Optimized processing technique during electroless deposition of Ni generates core (YSZ) - shell (Ni) microstructure as shown in the Ni mapping of Figure 5.61a.

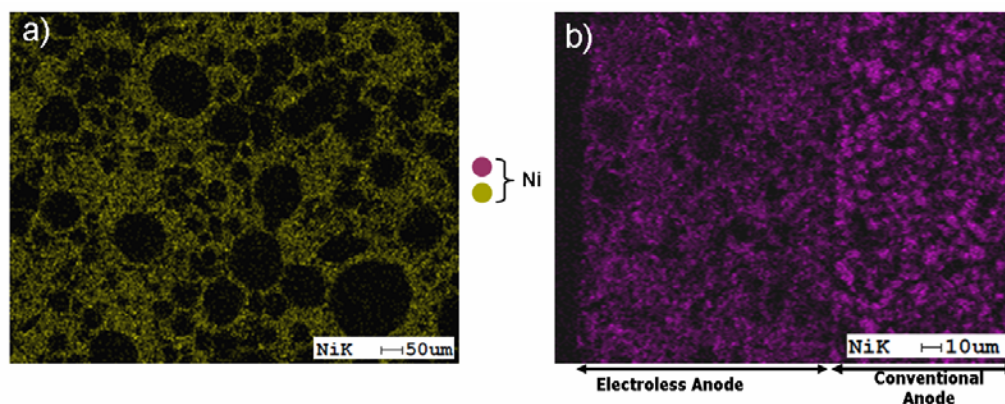


Figure 5.61: Elemental Ni mapping of a) anode prepared by electroless technique and b) layered anode configuration (BLA-series, cross sectional view)

This unique microstructure enables the interconnection among Ni, YSZ and pores throughout the matrix and thereby ensures easy transportation of electrons (through Ni-Ni continuity), O^{2-} ion (through YSZ-YSZ continuity) and gases (through interconnected pores) respectively. Due to such unique microstructure, active TPB

sites are produced in-situ within the anode cermet and are known as intra-anode TPBs. Patterned intra-anode TPB of electroless cermet accelerates the progression of charge transfer reaction ($O_{ad,YSZ}^{2-}$ to $O_{ad,Ni}^{2-}$) from anode-electrolyte interface to the bulk anode and hence makes the layer electrochemically active. The difference in Ni content from the fuel inlet (conventional anode) to the anode/electrolyte interface (electroless anode) is clearly visible from the intensity variation in the Ni mapping of [Figure 5.61 b](#). Therefore, use of conventional anode in conjunction with electroless cermet in such layered structure helps in engineering the microstructures across the anode. This would fulfill the requirements of effective gas transport as well as electrochemical activity over the entire anode surface. Optimization of the electroless layer thickness is a crucial parameter and is expected to enhance the cell performance with effective fuel diffusion followed by the electrochemical charge transfer reaction.

Variation of cell performance as a function of thicknesses and Ni-content of electroless cermet in BLA-series is shown in [Figure 5.62](#). It is observed that for a particular thickness of the electroless anode layer, cell performance increases with increase in Ni content from 28 to 32 vol %. This can be attributed to the fact that usage of higher Ni content provides better electronic conductive path through the matrix and increases the rate of electrochemical activity at the anode/electrolyte interface. However, increasing Ni content beyond a critical limit is expected to create thermal incompatibility with the adjacent YSZ electrolyte and also facilitates the Ni coarsening at high temperature operation of the cell. [Figure 5.62](#) also shows that performance of the single cell increases with reduction in electroless anode layer thickness from 250 μm to 50 μm for the electroless layer having a definite vol % of Ni. In the BLA structure, electroless cermet is responsible for the progression of electrochemical anodic reactions. The charge transfer of oxide ion (O^{2-}) from YSZ to Ni surface occurs instantaneously at the anode/electrolyte interface through surface adsorption mechanism. Presence of patterned intra anode TPBs along with

Chapter – 5.6

the conventional one in the electroless cermet helps in the extension of charge transfer reaction from anode-electrolyte interface to the bulk anode.

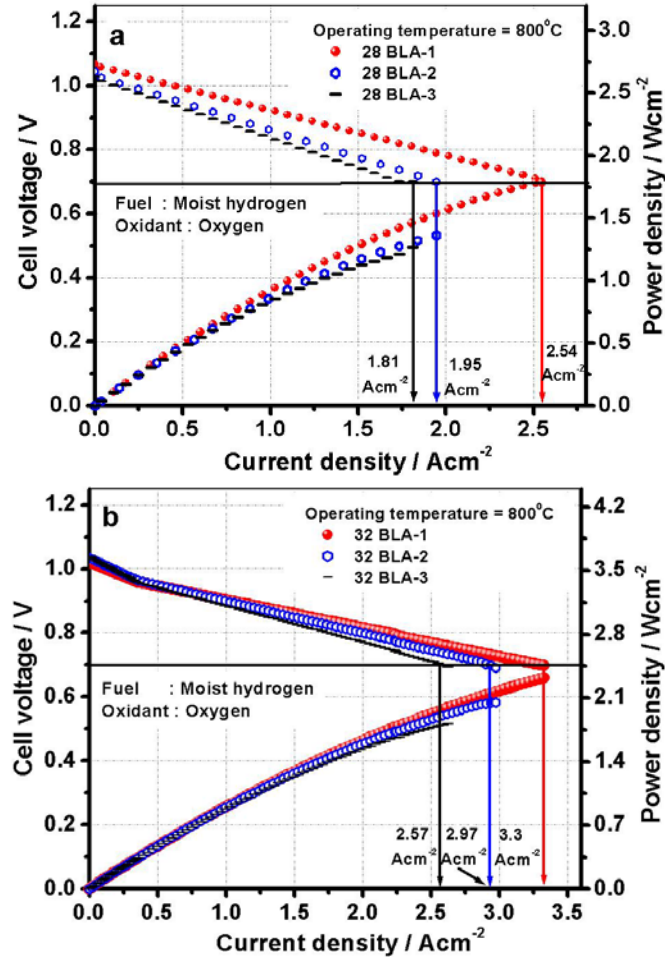


Figure 5.62: Electrochemical performances of single cells (measured at 800°C) as a function of electroless anode layer thickness with anodes of configuration a) 28 BLA-series and b) 32 BLA-series.

In accordance with the kinetic theory, the rate of charge transfer reaction accelerates with the reduction in anode layer thickness. Thus, upon decreasing the electroless anode thickness from 250 to 50 μm , electrochemical performance of the cell (at 800°C and 0.7 V) increases from 1.81 Acm^{-2} (28 BLA-3) to 2.54 Acm^{-2} (28 BLA-1) in the case of 28-BLA series (Figure 5.62 a). Similarly, for 32-BLA series, reduction in the thickness of electroless layer enhances the single cell performance from 2.57 A cm^{-2} (32 BLA-3) to 3.3 Acm^{-2} (32 BLA-1) under similar experimental

condition (Figure 5.62 b). The rate of formation and consumption of $O_{ad, Ni} / O_{ad, YSZ}$ and $H_{ad, Ni} / H_{ad, YSZ}$ species during electrochemical reaction at anode/YSZ interface is maintained at equilibrium upon reducing the thickness of electroless layer. Therefore, the interfacial concentration polarization of BLA-series reduces with enhanced cell performances at an optimum thickness of 50 μm . However, if the thickness of the electroless layer is further reduced, the electrochemical zone becomes ineffective in providing active Ni sites for effective reaction of $O_{ad, Ni} / O_{ad, YSZ}$ species and thereby resists the charge transfer reaction.

5.6.3.3.2. Functionality of electroless cermet in trilayered anode (TLA-series)

Functionality of BLA structure is discussed in details in the above section. In the present section, efforts are made regarding the sequential incorporation of 50 μm electroless layers of 28 BLA-1, 32 BLA-1 and conventional anode-support to fabricate a functional trilayered anode (TLA) with layer-wise variation in properties (Table 5.14, Figure 5.58). In the TLA structure, Ni content is reduced linearly from 40 vol % at fuel inlet side to 28 vol % at the electrolyte side. Electrochemical performance of single cell fabricated with TLA exhibits highest current density of 3.5 Acm^{-2} among Configuration –III at 800°C and 0.7 V as shown in Figure 5.63 a.

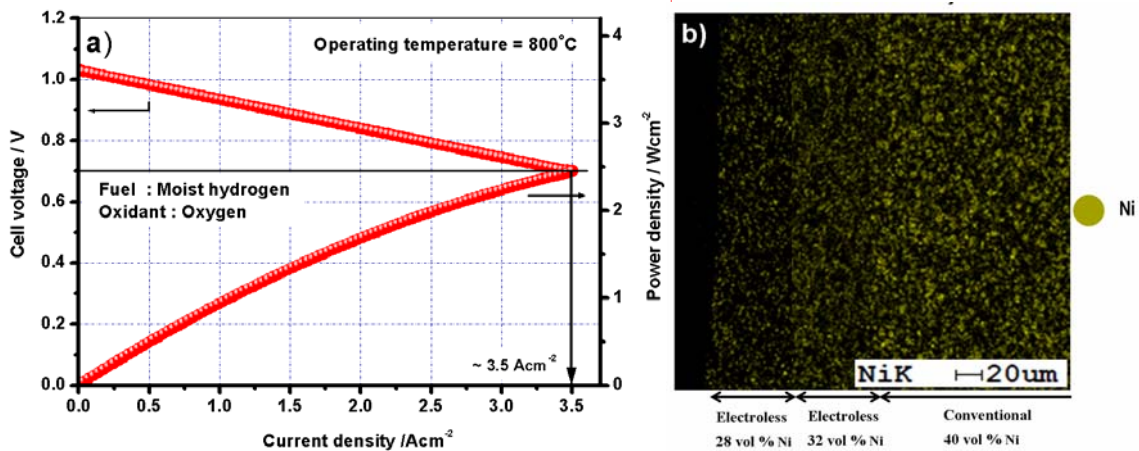


Figure 5.63: a) Electrochemical performance of single cell (measured at 800°C) using functional trilayer anode (TLA) along with b) FESEM micrograph for Ni mapping of TLA

Chapter – 5.6

5.6.3.3. Correlation between NiO reduction process with varied configurations of layered anode

Dependence of NiO reduction time on layered anode configuration is presented in Table 5.22. It has been discussed in the above section that, for cells with anodes of 28/32 BLA-series, electrochemical performances steadily increase with reduction in thickness of electroless layer from 250 to 50 μm which can also be noticed from Table 5.22.

Table 5.22: Effect of NiO reduction time on performance of single cells fabricated with anodes of Configuration - III

NiO reduction time (h)			0.5	6	7	15	72
Current density at 800°C, 0.7V	28 BLA-series	28 BLA-1	1.8	2.54	2.54	2.54	2.54
		28 BLA-2	1.21	1.45	1.91	1.91	1.91
		28 BLA-3	1.01	1.34	1.85	1.85	1.85
NiO reduction time (h)			0.5	5	6	40	72
Current density at 800°C, 0.7V	32 BLA-series	32 BLA-1	2.2	3.3	3.3	3.3	3.3
		32 BLA-2	2.12	2.57	2.97	2.97	2.97
		32 BLA-3	1.99	2.17	2.57	2.57	2.57
NiO reduction time (h)			0.5	5	10	30	72
Current density at 800°C, 0.7V	TLA		2.1	3.5	3.5	3.5	3.5

 Equilibrium region

It can be observed from the table that, rate of equilibration of NiO reduction is achieved faster for single cells having 32 BLA-series anodes compared to 28 BLA-series. This could be accounted due to the enhanced electrochemical activity of 32 BLA-series towards fuel oxidation having higher electrical conduction and dual inter-and intra-anode TPB length. In addition, irrespective of the Ni content of electroless cermet, single cells with electroless layer thickness of 50 μm (28/32 BLA-1 series) is found to equilibrate at a faster rate (5 h for 32 BLA-1 and 6h for 28 BLA-1). This signifies that, decreasing the thickness of electrochemical active zone (electroless anode) from 250 to 50 μm accelerates the rate of fuel diffusion thereby propagating the associated processes viz. dissociation, adsorption, charge transfer

reaction etc. However, an optimized thickness of electroless layer i.e 50 μm is important, further reduction of which tends to restrict the aforesaid reaction sequences and affect the overall cell performance.

Graded trilayer anode (TLA) is found to have the maximum influence of 50 μm electroless layer having 32 vol% of Ni regarding the equilibration time required for NiO reduction (5 h for single cells with TLA). Maximum performance of 3.5 Acm^{-2} is obtained for cells with such TLA anode. Therefore, it could be said that upon employing gradation in properties for the fabrication of multilayered anode, augmentation in performance is obtained along with superior properties with respect to electrical conduction, thermal compatibility etc.

5.6.3.4. Configuration –IV: Electroless cermet as anode active layer (AAL)

The comparative performances of SOFC fabricated with anodes of *Configuration – I, II and III* clearly exhibit the functionality of electroless Ni-YSZ cermet towards the overall electrochemical activity. Electroless cermet is found to be more effective when employed in conjugation with conventional cermet as the anode support structure. Significant enhancement in performance is obtained from the cells fabricated with multilayered anodes. In similar sequence, efforts are exerted to study the functionality of such developed electroless cermet as anode active layer (AAL) in *Configuration-IV*. In order to improve cell performance, incorporation of thin anode functional/active layers (AFL/AAL) between the anode and electrolyte is a standard practice.⁴⁵ Such active layers produces an extended TPB length at the interface causing effective electrochemical reactions and hence, enhancement in performance of the cell.⁴⁴ The microstructural phase distribution of Ni and YSZ in such active layer needs to be homogenous and the contacts between Ni/YSZ should be made coherent to facilitate the electrochemical oxidation of fuel. In order to achieve the homogenous microstructure with a

Chapter – 5.6

continuum between Ni-Ni, YSZ-YSZ and the interconnected pores, the AAL needs to be processed precisely. The basic differences between the anode support and active layer are in the grain sizes, the interconnectivity of the constituent phases, interfacial contact lengths and percentage porosity of the contributing components. Such differences in the conventional anode support and the active layer may also affect the overall charge transfer reaction occurring at the anode active layer / electrolyte interfaces and distributed to the bulk anode through extended TPB.

Figure 5.64 shows the single cells of *Configuration-IV* that incorporates Ni-YSZ cermet prepared by electroless method as an anode active layer (AAL). The structure of cell in *Configuration-IV* is: Conventional NiO-YSZ anode (~ 40 vol % Ni) / Ni-YSZ (Electroless technique) as AAL (28 or 32 vol % Ni) / YSZ / CAL/CL.

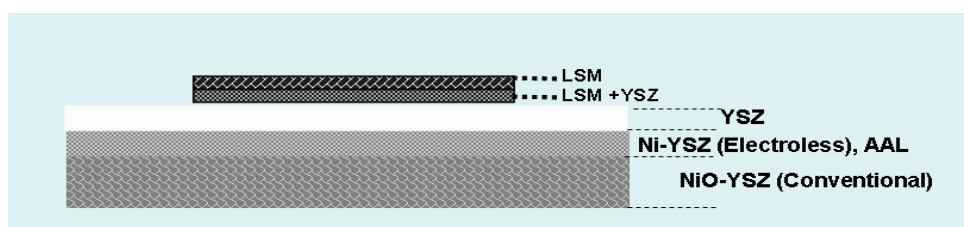


Figure 5.64: Schematic of single cells fabricated with anodes of: *Configuration - IV*

The thickness of AAL is varied sequentially from 140 μm to 15 μm to study its effect on electrochemical performance of single cell. Similar to the above sections, the results of electrochemical studies of single cell fabricated with anodes of *Configuration-IV* are presented for the half cells sintered at 1400°C. The dependence of cell performance (at 800°C, 0.7 V) as a function of AAL thickness and NiO reduction time is shown in Table 5.23. It is evident from Table 5.23 that, irrespective of AAL thickness, current density increases steadily till NiO reduction equilibration is reached. After the saturation limit, the cell performance remains constant. It is found that the equilibrium time for NiO reduction depends on the thickness of AAL layer and Ni content of the electroless cermet. The equilibrium

time for NiO reduction require ~ 6h for cells with 28 AAL-4 anodes, whereas 5h are found to be sufficient for 32 AAL-4.

Table 5.23: Effect of NiO reduction time and AAL thickness on the performance of SOFC fabricated with anodes of Configuration – IV at 800°C

NiO reduction time (h)			0.5	3	5	6	15	30	72
Current density at 800°C, 0.7V	28 AAL-series	28 AAL-1	2.1	3.2	3.2	3.2	3.2	3.2	3.2
		28 AAL-2	1.87	2.75	2.75	2.75	2.75	2.75	2.75
		28 AAL-3	1.34	1.85	2.63	2.63	2.63	2.63	2.63
		28 AAL-4	0.98	1.12	1.31	2.52	2.52	2.52	2.52
NiO reduction time (h)			0.5	3	5	6	15	30	72
Current density at 800°C, 0.7V	32 AAL-series	32 AAL-1	2.7	3.7	3.7	3.7	3.7	3.7	3.7
		32 AAL-2	2.45	3.32	3.53	3.53	3.53	3.53	3.53
		32 AAL-3	2.2	3.12	3.43	3.43	3.43	3.43	3.43
		32 AAL-4	1.99	2.43	3.3	3.3	3.3	3.3	3.3

Equilibrium region

The plausible discussions regarding the superiority of electroless cermet containing 32 vol % Ni towards fast equilibration for NiO reduction in *Configurations – II or III* is already depicted in earlier sections. Similar rationale is factual for the present configuration too. However, a deviation could be noted for the cells fabricated with 28/32 AAL- 1 to 3, where equilibration time interval is similar irrespective of the variation in Ni content in the electroless cermet. This could be explained on the basis that, owing to the patterned core (YSZ)-shell (Ni) microstructure of the electroless cermet, the reduction of NiO also tends to follow an ordered path and forms the primary rate determining step. Such rate determining step is found to be independent of Ni content upon reducing the thickness of AAL beyond 140 μm or ≤ 40 μm, and necessitates 3h for reduction saturation time. In general, the formulation of AAL layer is made such that its porosity becomes less than the anode-support. The relatively denser AAL accelerates charge transfer reaction at the TPB after the electrochemical oxidation of fuel. The diffusion controlled NiO reduction reaction and electrocatalytic

Chapter – 5.6

oxidation of hydrogen becomes faster at conventional anode-support having sufficient porosity and higher Ni content. However, effective charge transfer reaction preferably occurs at the juncture of anode-electrolyte interface and it prefers thinner AAL. Thus, in this investigation, the optimum thickness of AAL is found to be $\leq 40 \mu\text{m}$ which is also evident from the correlation of the NiO reduction process with the cell performances.

Figure 5.65 and 5.66 shows the I-V characteristics of cells fabricated with 28 and 32 AAL-series anodes.

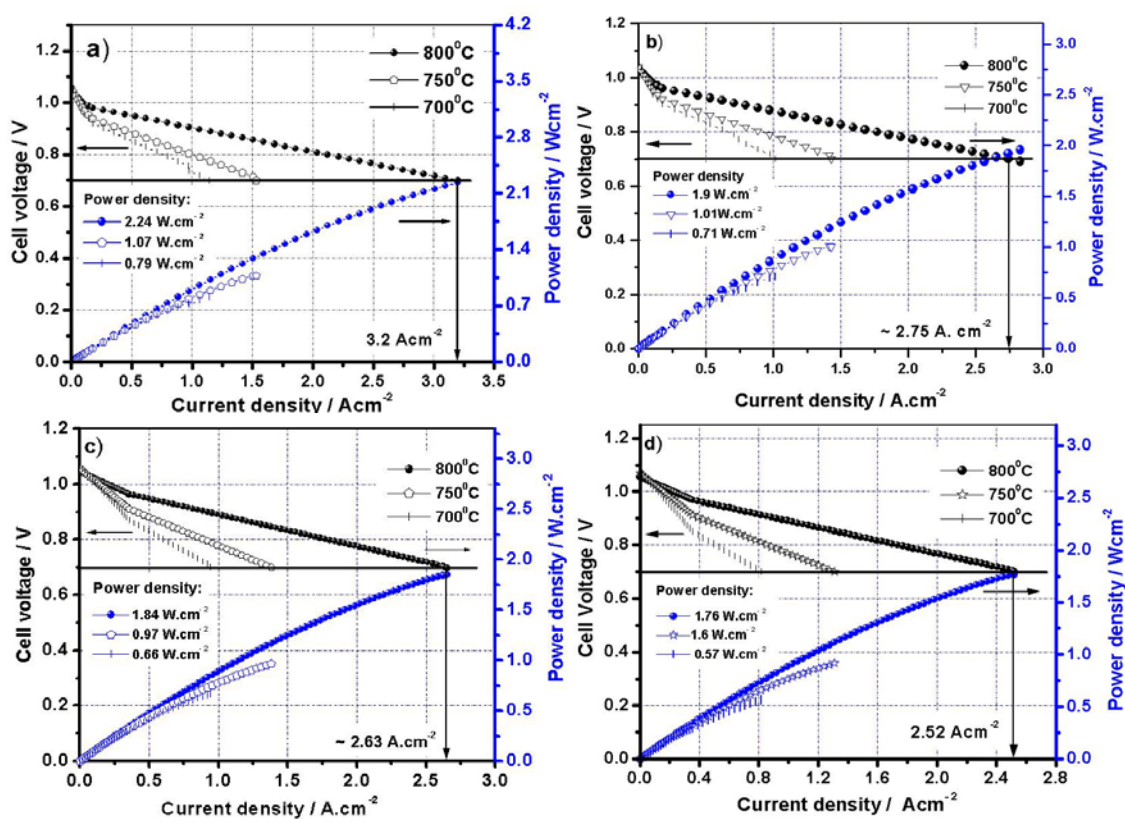


Figure 5.65: Temperature dependent electrochemical performances of single cells fabricated with anodes of Configuration-IV viz. a) 28 AAL-1, b) 28 AAL-2, c) 28 AAL-3 and d) 28 AAL-4

From the figure, it is observed that irrespective of the operating temperature, cell performance increases steadily as the AAL thickness decreases. The current density increases from 2.52 Acm^{-2} to 3.2 Acm^{-2} with corresponding power density of 1.8

Wcm^{-2} to 2.17 Wcm^{-2} at 800°C and 0.7 V (with H_2 as fuel and O_2 as oxidant) for cells with 28 AAL- 4 to 28 AAL-1 (Figure 5.65).

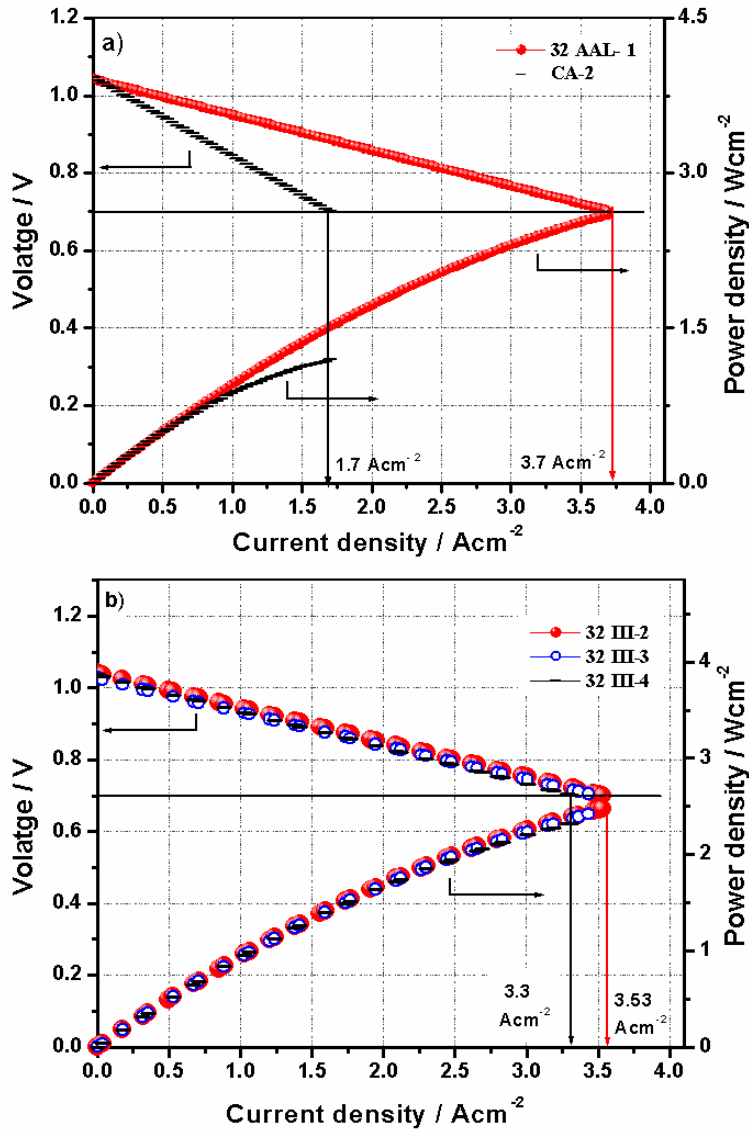


Figure 5.66: Comparative electrochemical performances of single cells at 800°C with anode configurations of a) CA-2 with 32 AAL-1 and b) 32 AAL-2, 32 AAL-3 and 32 AAL-4

The performance of SOFC is found to enhance by ~ 2 folds (3.7 Acm^{-2} at 800°C and 0.7 V) by employing 32 AAL-1 anode (Figure 5.66 a) compared to the cells fabricated with CA-series anodes (1.7 Acm^{-2} at 800°C and 0.7 V). Similar to the trend obtained for cells with 28 AAL-series (Figure 5.65), the performance of the

Chapter – 5.6

cells are found to decrease from 3.7 to 3.3 Acm^{-2} at 800°C and 0.7 V upon increasing the AAL thickness in 32 AAL-series from 15 to 140 μm (Figure 5.66 b). This can be explained in the same way that diffusion controlled reduction reaction and electrocatalytic oxidation of fuel proceeds faster in the porous conventional anode-support (~ 40 vol% Ni) rather than the less porous AAL prepared by electroless technique. The optimum thickness of AAL is found to be $\leq 40 \mu\text{m}$ for effective charge transfer reaction as given in Eq. 1:



where, ' $\text{O}_{\text{ad, YSZ/Ni}}$ ' denotes adsorbed oxygen species on YSZ or Ni surface and ' $\text{O}_{\text{ad, YSZ/Ni}}^{2-}$ ' denotes formation of oxide ion on YSZ and Ni surfaces respectively.

It is quite obvious that thinner the AAL, better is the charge transfer reaction at the anode-electrolyte interface. Higher cell performance with thinner electroless AAL ascertains that during electrochemical reactions, the process of charge transfer occurs at a certain thickness of electrode from electrolyte/electrode interface. Over this region, contributions of both electronic and ionic current exits as a function of position. Outside this range, the current is electronic in electrodes and ionic in electrolyte. Owing to such facts, it has been already established in section 5.6.3.1 (Figure 5.51) that, the variation / flow pattern of gasses follows non-linearity (with rapid flow) at electrode/ electrolyte interface and is microstructure variant. However, below a certain critical AAL thickness, the charge transfer becomes ineffective because of less availability of $\text{O}_{\text{ad, Ni}}^{2-}$ species adjacent to the electrolyte layer to take up the charge from $\text{O}_{\text{ad, YSZ}}^{2-}$. It is observed that, single cells with 15 μm AAL shows highest current density of $\sim 3.7 \text{Acm}^{-2}$ (corresponding power density of $\sim 2.6 \text{Wcm}^{-2}$) at 800°C and 0.7 V with hydrogen as fuel and oxygen as the oxidant. In contrast, single cell fabricated with conventional NiO-YSZ anode-support without AAL exhibits much lower current density of $\sim 1.7 \text{Acm}^{-2}$ as reported in earlier section. After initiation of fuel (H_2) oxidation at conventional anode site through simultaneous adsorption-dissociation reaction, further charge transfer reactions

tend to operate from electroless anode / electrolyte interface. In AAL prepared by electroless technique unique core (YSZ) -shell (Ni) microstructure is found to generate dual triple phase boundary (TPB) in the anode interior (intra-anode) and anode/ electrolyte junction. The electrochemical reaction is therefore progressive in the bulk anode preferentially through intra-anode TPB because Ni, YSZ and pores are patterned and interlinked in relatively dense electroless cermet matrix.

The optical micrograph of the coupon cell having anode active layer (AAL) prepared by electroless technique (*Configuration-IV*) and its corresponding line mapping is shown in [Figure 5.67 a](#) and [b](#) respectively.

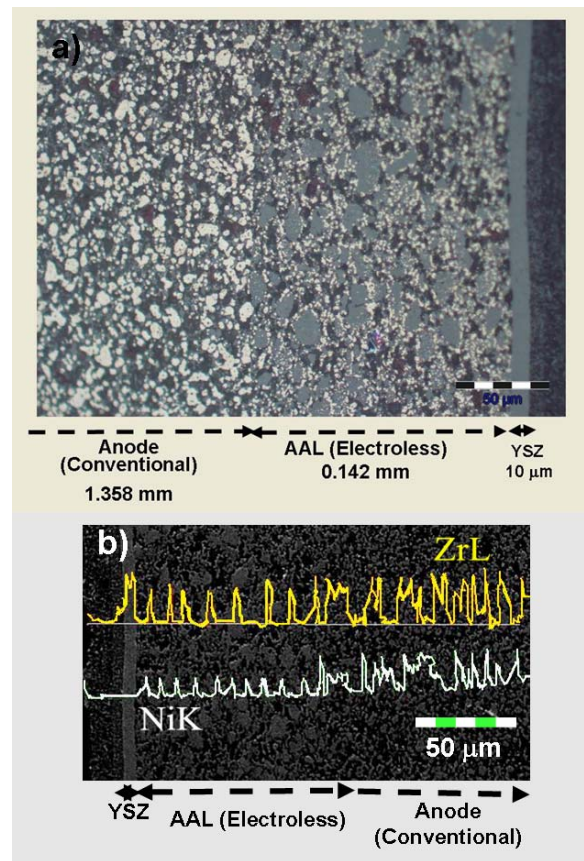


Figure 5.67: a) Optical micrograph and b) corresponding line mapping of single cell fabricated with anodes of Configuration –IV

The figure clearly reveals the difference in microstructure of Ni-YSZ cermet anode prepared by two different processing techniques. Dispersed distribution of Ni and

Chapter – 5.6

YSZ phases in the matrix of conventional anode cermet is clearly observed from the elemental line mapping of 'Ni' and 'Zr', which shows a non periodic distribution in the support structure. As manifested earlier, AAL prepared through electroless technique also maintains the crest-hub type distribution of 'Ni' and 'Zr' as found in the anode-support in [Figure 5.57 b](#). The unique microstructure with discrete Ni particulates around YSZ core either in the anode-support or in the AAL significantly enhances the triple phase boundary lengths. This, in turn, helps in the fuel oxidation and favors the electrochemical reactions at the anode-electrolyte interfaces.

The systematic study of electrochemical performances of SOFC fabricated with variable anodes demonstrates that incorporation of electroless active layers enhances the electrochemical performance of single cells (*Configuration-IV*) compared to the cells having thicker electroless multilayers (*Configuration-III*). It is also found that in contrast to the order of electrical conductivity of anodes of either *Configuration- III or IV* as discussed in sections 5.6.1 and 5.6.2, maximum performance is obtained from cells with thinnest electroless anodes (as layered or active layer). Electrical conduction of cermets is a bulk phenomenon which is based on the charge propagation through a conducting path that follows a linear flow of reactant gasses. In this case, effective diffusion of the gas entirely depends on the specific thickness of anode which favors the electronic flow. Though increase in electroless AAL thickness from 15 to 140 μm manifests linear enhancement of the bulk electrical conductivity of the layered cermet, thinnest electroless layers are found to superior for electrochemical activity. Such experimental study also validates the mode of gas transport as reported in section 5.6.3.1.

5.6.3.5. Effect of pore-size distribution of anodes on cell performance

The present research work employs anodes of four different configurations, the details of which are presented in [Table 5.14](#). Detailed electrochemical

performances of single cells fabricated with variable anode compositions have been already discussed in details in the above sections. The difference in anode configurations is based on the gradation of a number of physical properties viz. a) constituent phases, b) microstructural pattern, c) triple phase boundary, d) pore-size distribution etc as shown in the schematic of Figure 5.68.

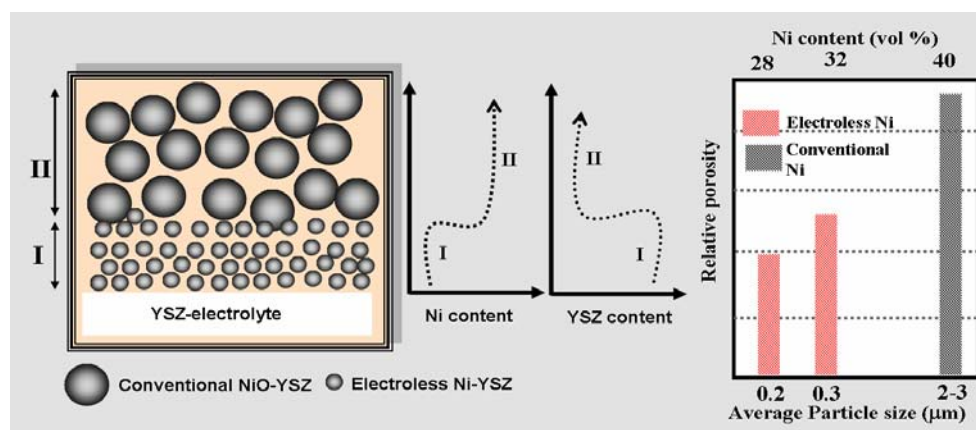


Figure 5.68: Schematic of a layered anode (Configuration – III and IV) with gradation in properties

Apart from the very last factor, influence of all other aspects has been already presented. The present section tends to deal with the variation of pore-size distribution of the anodes and correlate them with electrochemical activity of the fabricated single cells. Figure 5.69 and Figure 5.70 shows the Gaussian type pore-size distribution of anodes of Configuration – I and II. As shown in Figure 5.69, the conventional anode (CA-anodes) exhibits multimodal pore size distribution with peak pore diameters varying in the range of $\sim 1.5 - 8.4 \mu\text{m}$. The figure also illustrates the variation in distribution of pores before and after reduction of the anode cermets. The pattern of distribution is found to be identical in the sintered and reduced state with a more uniformity in the later condition. On the contrary, irrespective of the Ni content, electroless anodes exhibits narrow unimodal pore-size distribution prior and later to reduction (Figure 5.70). Anodes of 28 EL-series shows pore size in the range of $0.85\text{-}0.9 \mu\text{m}$ (Figure 5.70 a), whereas higher peak

Chapter – 5.6

pore diameter of 2.02-2.14 μm is displayed by 32 EL-anodes (Figure 5.70 b), both before and after reduction.

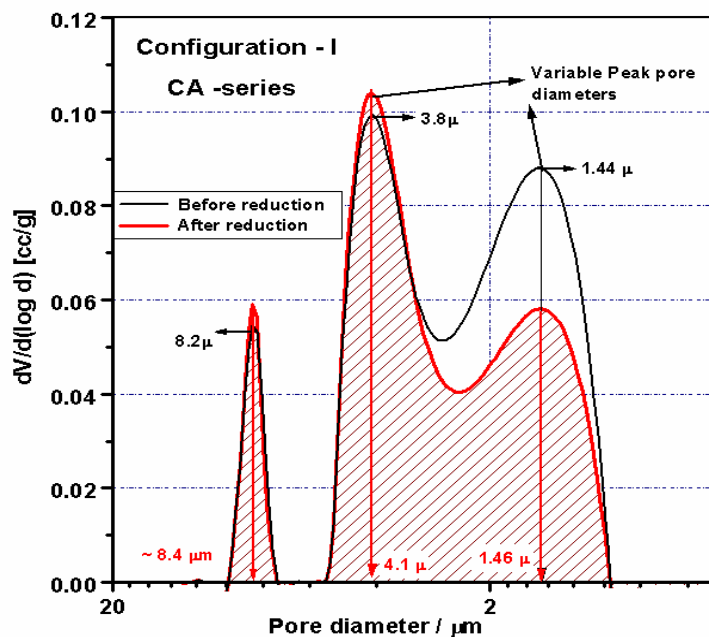


Figure 5.69: Gaussian type pore size distribution plots of anode cermet of Configuration -I

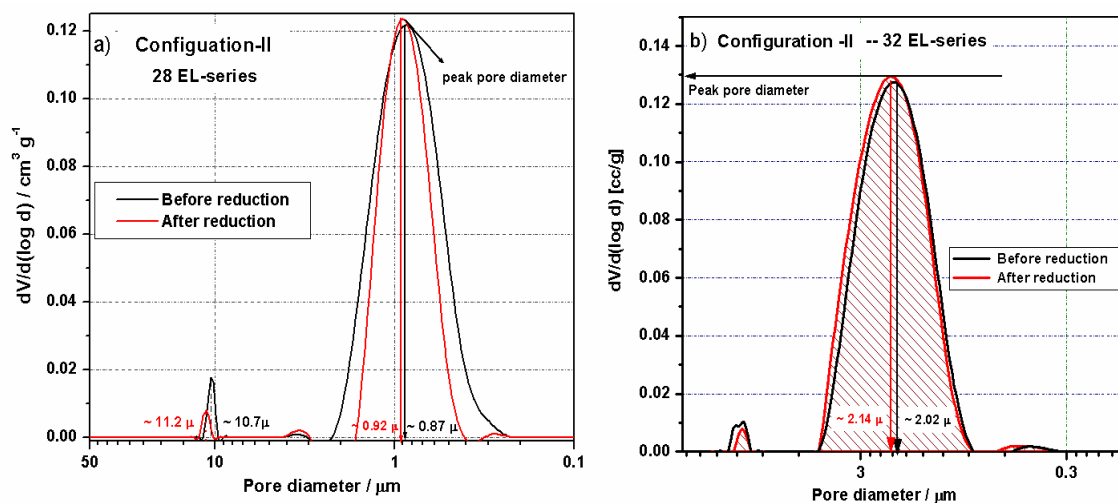


Figure 5.70: Gaussian type pore size distribution plots of anode cermet of Configuration -II having IDs of: a) 28 EL-series and b) 32 EL-series

The enhanced porosity and pore-size of 32 EL-series is the direct outcome of higher Ni content in the cermet anode. Owing to the presence of higher Ni content in 32 EL-series, the extent of oxygen loss from NiO (sintered cermet) during

subsequent reduction is higher which help in the enhancement of porosity along with the larger pore diameters. Wider pore distribution of CA-series (*Configuration-I*) helps in easy gas diffusion through the anode thereby accelerating the fuel percolation and is subsequently followed by the catalytic oxidation. Large pores with multimodal distribution in conventional anode ([Figure 5.69](#)) also results in restricting the extended interfacial contacts required for the necessary electrochemical reactions. On the other hand, electroless anode (*Configuration –II*) shows narrow and unimodal distribution ([Figure 5.70 a and b](#)). Negligible open pores are found in the region of larger pore diameter for such cermets. Pore-size distribution with relatively low peak pore diameter ensures better capillary action for fuel fed across the anode and enhances the electrochemical reaction. For *Configuration-II*, the steady electrochemical reaction is guided not only by smaller percentage of overall Ni content but also by the smaller pore diameters. The gas diffusion process in the anode of *Configuration-II* therefore becomes the rate determining step and hence the limiting factor in obtaining significant high cell performance.

The conjugation of electroless anodes with conventional cermet in the layered anodes of *Configuration –III* can be visualized from the pore-size distribution plots presented in [Figure 5.71](#). The variation in porosity in such layered anode is also visualized from the cross-sectional micrograph of a cell ([Figure 5.72](#)) operated at 800°C. The binerized image clearly shows the extent of porosity in the conventional and electroless cermet. The functionality of such developed layered anode is evident from the pore size distribution of the corresponding anode structure as shown in [Figure 5.71](#). The peak pore diameters of reduced TLA are found to be at 8.94, 5.8 and 2.14 μm respectively. It can be observed from [Figure 5.69, 5.70 and 5.71](#), that larger pores in the range of 5-9 μm correspond to the conventional anode and unimodal distribution of pores with peak pore diameter of 2.14 μm is identified pore size of the electroless cermet. The combined effect of

Chapter – 5.6

these larger and smaller pores is therefore expected to perform the dual function of fuel transportation and electrochemical anodic reactions.

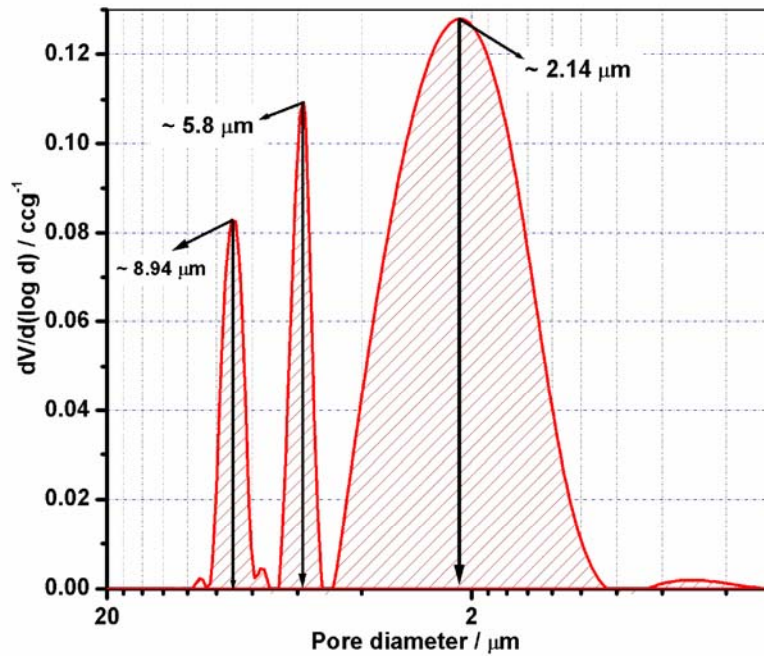


Figure 5.71: Gaussian type pore size distribution plots of anode of Configuration -III

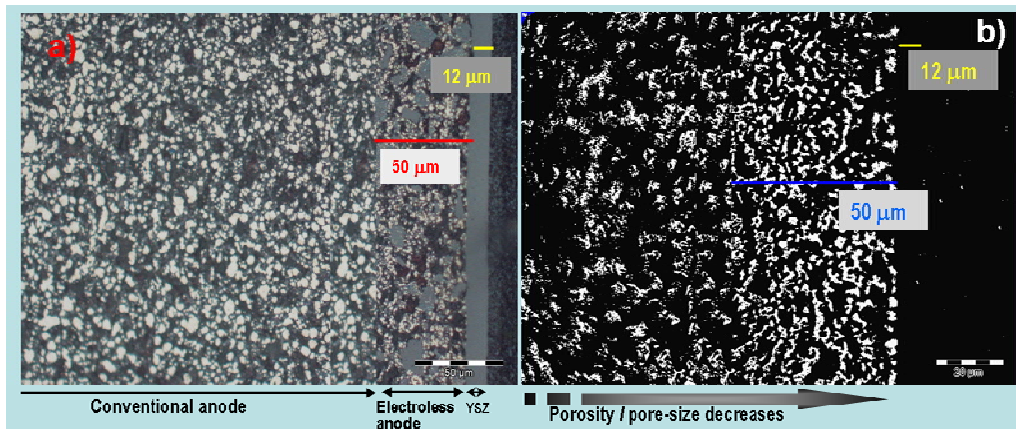


Figure 5.72: a)Optical microstructure and b) binerized image (at higher magnification) of single cell with anode of BLA- series after electrochemical measurement

Therefore, combination of electroless and conventional cermet in the anode of Configuration -III fulfils the requirement of both gas transportation and electrochemical activity and hence enhances the cell performance.

The performance evaluation of single cells as discussed in section 5.6.3 demonstrates that, electroless anode exhibits its utmost superiority in the form of a thin anode active layer (*Configuration -IV*). Distribution of pores in the anodes of *Configuration -IV* is shown in [Figure 5.73](#).

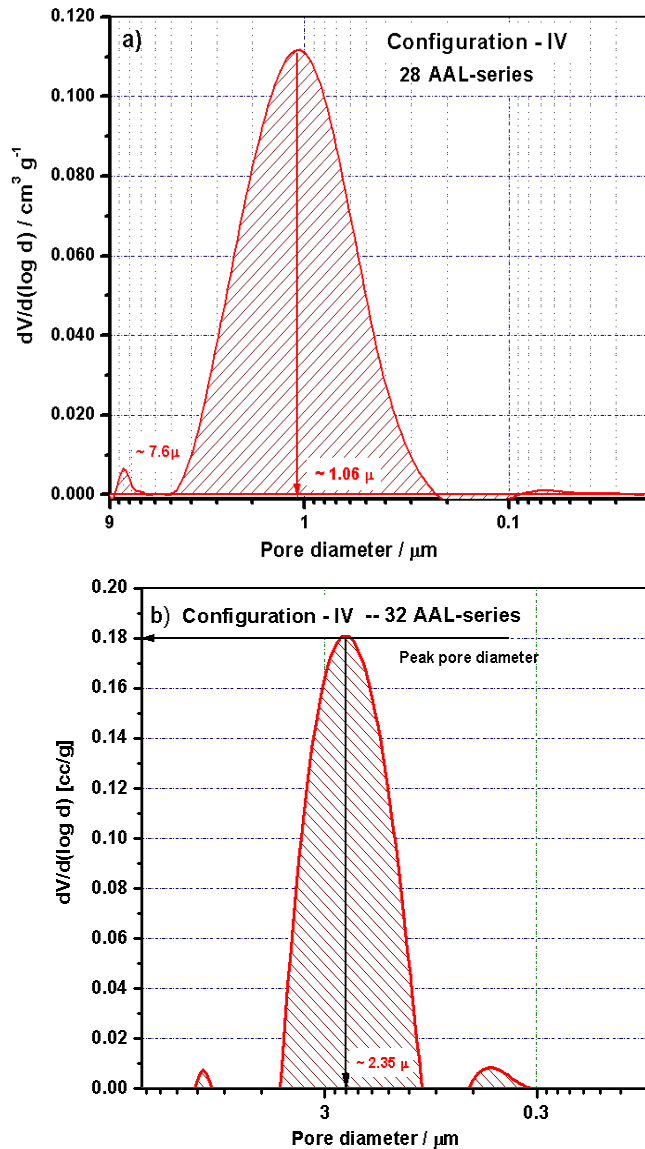


Figure 5.73: Gaussian type pore size distribution plots of anode of Configuration – IV that corresponds to a) 28 AAL-series and b) 32 AAL-series.

The reduced anode cermet of 28 AAL-series ([Figure 5.73 a](#)) are found to bear the pores in the range of 1- 1.15 μm with median and peak pore diameters at $\sim 1.38 \mu\text{m}$ and $\sim 1 \mu\text{m}$. However, the cermet of 32 AAL-series exhibit peak pore diameter

Chapter – 5.6

in at 2.35 μm (Figure 5.73 b). It could be noted from Figures 5.71 and 5.73, that though both Configuration – III and IV corresponds to layered anodes, however, variation in the properties of electroless cermet eg. tape thickness, overall anode thickness, densification etc differentiates the nature of pore-size distribution plots. In contrast to the multimodal distribution of Configuration –III, broad unimodal pattern is observed for anodes of Configuration –IV. The influence of electroless active layer in the anodes of Configuration –IV can be identified from the peak pore diameters which are found to be in the close proximity with the peak diameters of 28 EL-and 32 EL-anodes of Configuration – II (Figure 5.70). The larger median and peak pore diameters of the conventional anode-support help in better gas diffusion. In contrast, the smaller pore diameter of AAL ensures more capillary action for the fuel fed at the anode. The smaller pores in AAL ensures steady electrochemical reaction at the TPB after effective dissociation of hydrogen at the conventional anode-support. Such pore size distribution is expected to be the key factor for getting such high performance for the cells with Configuration-IV.

5.6.3.6. Correlation between anode configuration and area specific resistance (ASR) of the single cell

The area specific resistances (ASR) of single cells are calculated from the slope of the linear portion of I-V curve. In the present investigation, the cell is comprised of varied anode configurations as given in Table 5.14. Thus, the equation comprising of the contributions from all the components towards cell ASR (R) can be written as:

$$R = R_{\text{electrolyte}} + R_{\text{anode}} + (R_{\text{cathode}} + R_{\text{CAL}}) + R_{\text{contact}} \quad (5.48)$$

where, ' $R_{\text{electrolyte}}$, R_{anode} , R_{cathode} , R_{CAL} and R_{contact} ' are contributions of resistances from electrolyte, anode layer, cathode layer, cathode active layer(CAL) and interfacial contacts respectively.

In the present research work, the variable parameter is the configurations of anode, the other parameters of Eq. 5.48 being constant. Therefore, the above equation can be simplified as:

$$R = R_{anode}(\text{variable configurations}) + R_{constant} \quad (5.49)$$

where, 'R_{constant}' is the ASR contribution from other sources as mentioned in Eq.5.48.

Using Table 5.14, Eq. 5.49 can be modified based on the variable configurations of anode and written as:

$$\begin{aligned}
 R_{CON-I} &= \rho_{CA(1/2)} l_{CA(1/2)} + R_{cons \tan t} \Rightarrow \text{Configurat ion - I} \\
 R_{CON-II} &= \rho_{28 EL(1/2)} l_{28 EL(1/2)} + R_{cons \tan t} \Rightarrow \text{for Configurat ion - II} \\
 R_{CON-II} &= \rho_{32 EL(1/2)} l_{32 EL(1/2)} + R_{cons \tan t} \\
 R_{CON-III} &= \rho_{28 BLA(1/2/3)} l_{28 BLA(1/2/3)} + R_{cons \tan t} \\
 R_{CON-III} &= \rho_{32 BLA(1/2/3)} l_{32 BLA(1/2/3)} + R_{cons \tan t} \Rightarrow \text{for Configuration -III} \\
 R_{CON-III} &= \rho_{TLA} l_{TLA} + R_{cons \tan t} \\
 R_{CON-IV} &= \rho_{28 AAL(1/2/3/4)} l_{28 AAL(1/2/4)} + R_{cons \tan t} \Rightarrow \text{Configurat ion - IV} \\
 R_{CON-IV} &= \rho_{32 AAL(1/2/3/4)} l_{32 AA L(1/2/3/4)} + R_{cons \tan t}
 \end{aligned}
 \tag{5.50}$$

where, ρ and l are the resistivity per unit area and thickness of concerned layers corresponding to variable configurations respectively. 1/2/3 designates the anode configurations as listed in Table 5.14.

Figure 5.74 shows the trend of cell ASR variation fabricated with anodes of Configuration - I and II. In this connection it can be said that, since the contribution of other components towards the overall cell ASR is constant, the observed variation is the outcome of variable configurations of anode as also mathematically shown by Eq. 5.50. It is observed from the cells with Configuration-I and II that, for either conventional or electroless anode support, the magnitude of ASR increases

Chapter – 5.6

marginally with increase in cell thickness (Figure 5.74). The thinner anode-support (1250 μm) shows ASR of 276 $\text{m}\Omega\text{-cm}^2$, 139 $\text{m}\Omega\text{-cm}^2$ and 188 $\text{m}\Omega\text{-cm}^2$ for 28 EL -1, 32 EL -1 and CA-1 respectively.

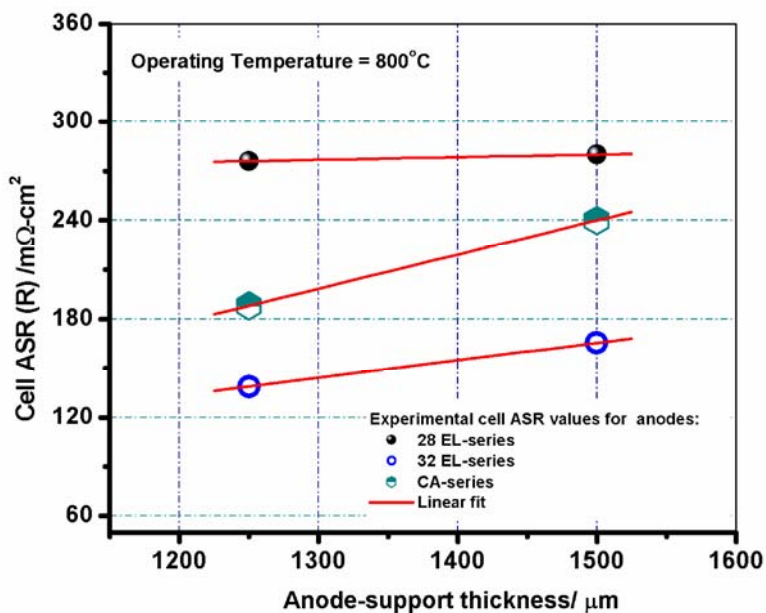


Figure 5.74: Dependence of measured cell ASR as a function of thickness and Ni content for anode-support of Configuration –I and II

In contrast, the thicker one (1.5mm) gives a value of 280 $\text{m}\Omega\text{-cm}^2$, 165 $\text{m}\Omega\text{-cm}^2$ and 240 $\text{m}\Omega\text{-cm}^2$ for 32 EL -1, 28 EL-1 and CA-1 configurations respectively. These experimental trends of ASR variation validate the order of electrochemical performances of single cell fabricated with such anodes as discussed in sections 5.6.3.2 to 5.6.3.4. The associated ASR of the highest performing cells with 32 EL-series anodes are found to be least compared to the cells having 28 EL-and CA-series anodes.

Dependence of area specific resistance (ASR) of the single cell on layered anode of Configuration- III is represented in Figure 5.75. Because of the superior electrochemical activity, cells fabricated with anode configuration of 32 BLA series are found to exhibit least ASR values in the BLA-series. Single cells with 32 BLA-series is found to exhibit significant low ohmic ASR in the range of 88-116 $\text{m}\Omega\text{-cm}^2$

in comparison to the cells fabricated with 28 BLA-series ($141\text{-}186\text{ m}\Omega\cdot\text{cm}^2$) at 800°C . Comparison among Figures 5.74 and 5.75 establishes the fact that bilayer anode with effective fuel oxidation (through conventional anode) and electrochemical reactions (through electroless anode) reduces the overall ohmic polarization of the cell. Reduction in electroless anode thickness from 250 to $50\text{ }\mu\text{m}$ effectively accelerate the charge transfer rate of $\text{O}^{2-}_{\text{ad,YSZ}}$ to $\text{O}^{2-}_{\text{ad,Ni}}$ thereby causing a further reduction in ohmic ASR from $116\text{ m}\Omega\cdot\text{cm}^2$ (32 BLA-3) to $88\text{ m}\Omega\cdot\text{cm}^2$ (32 BLA-1) at 800°C .

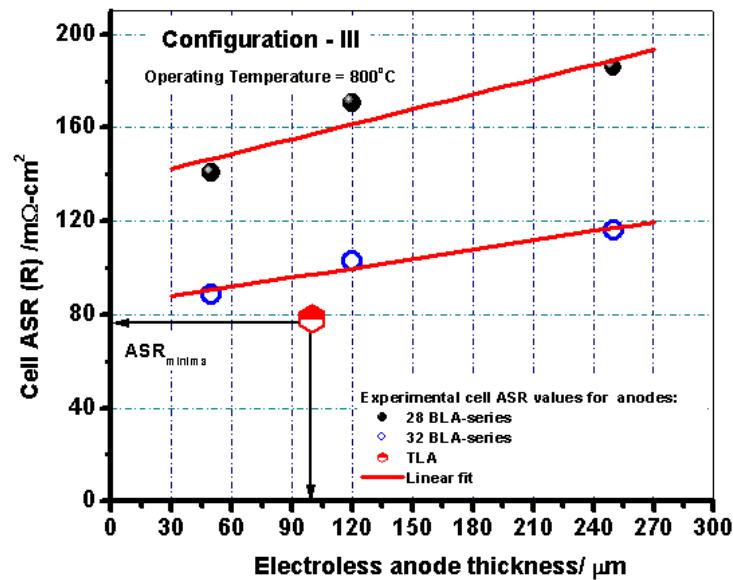


Figure 5.75: Variation of the measured cell ASR for layered anodes of Configuration -III

Similar reducing trend is observed for cells fabricated with 28 BLA-3 to 1series. A sharp decrease of $\sim 63\%$ in ASR is observed from single cells upon incorporating layered anode of 32 BLA-1 and $\sim 24\%$ increment is found in the ASR value with the variation of the electroless layer thickness from 50 to $250\text{ }\mu\text{m}$ (Figure 5.75). Ohmic polarization is found to further reduce by $\sim 12\%$ for cells fabricated with TLA compared to 32 BLA-1. Combination of electroless layers having 32 and 28 vol % Ni accounts for the acceleration of electrochemical reaction and decrease the rate of Ni coarsening at the anode/electrolyte interface.

Chapter – 5.6

Consequently, due to systematic variation of Ni content, porosity and microstructure, the cell ASR is found to be reduced to $\sim 78 \text{ m}\Omega\cdot\text{cm}^2$ at 800°C for single cells fabricated with TLA (Figure 5.75).

The functionality of electroless as anode active layer is further established from the reduced ASR values of single cells having anodes of Configuration –IV given in Figure 5.76. Similar to the trend exhibited by cell with BLA-series, the ASR value increases with increase in AAL thickness for single cells of Configuration-IV, (Figure 5.76). Therefore, cells with AAL thickness of 140, 90, 40 & 15 μm show ASR values of 123, 116, 103 and 94 $\text{m}\Omega\cdot\text{cm}^2$ for 28 AAL-series and 100, 92, 83 and 70 $\text{m}\Omega\cdot\text{cm}^2$ for 32 AAL-series at 800°C respectively.

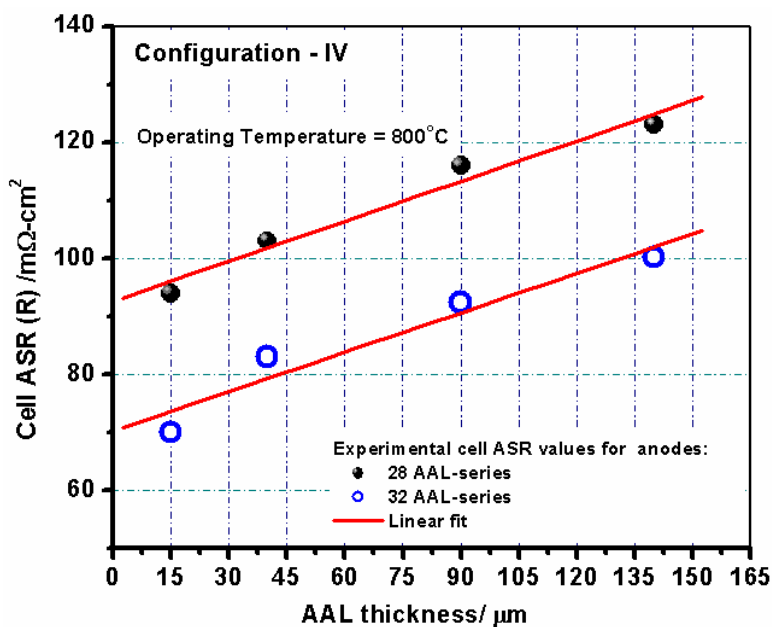


Figure 5.76: Measured cell area specific resistance (ASR) at 800°C as a function of thickness for electroless AAL and Ni content of Configuration –IV

Increase of AAL thickness decreases the effective charge transfer rate of $\text{O}_{\text{ad,YSZ}}^{2-}$ to $\text{O}_{\text{ad,Ni}}^{2-}$ (as given in reaction 5.47) at the AAL-electrolyte interface thereby causing a higher ASR. As expected, least ASR is observed for the cells with 32 AAL-series which shows a maximum performance of 3.7 Acm^{-2} at 800°C . According to the Eq.

5.50, the intercept of the Figures 5.74-5.76 corresponds to the ASR (R_{constant}) contribution from other sources viz. electrolyte, cathode etc.

The role of electroless cermet towards the area specific resistance of single cell can be arbitrated from the comparative plot of Figure 5.77.

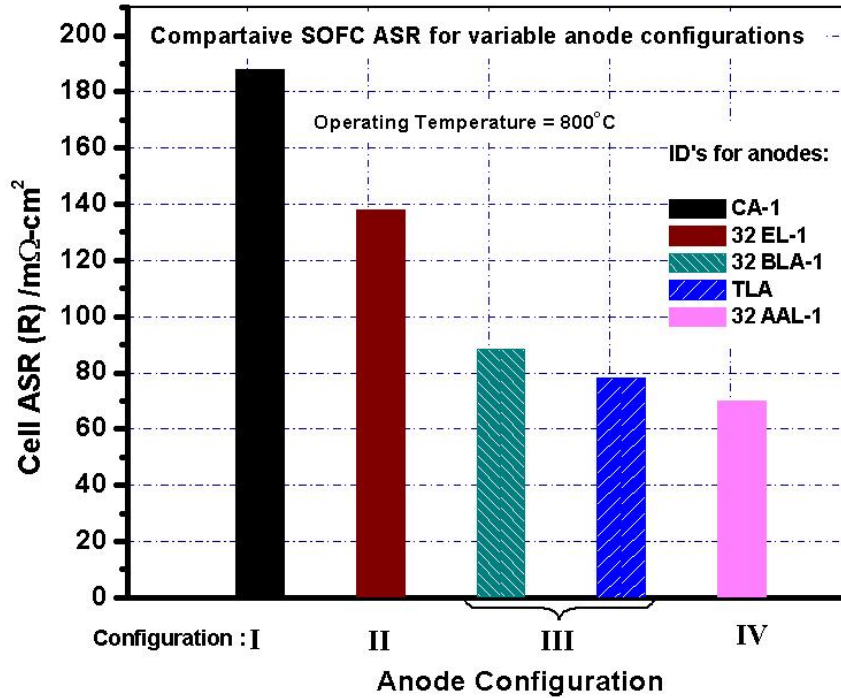


Figure 5.77: Comparative area specific resistance (ASR) at 800°C for single cell fabricated with anodes of various configurations

It can be observed from the above figure that, electroless cermet is more functional when used as layered anode (either thick or AAL) in Configuration –III or IV in conjunction with conventional anode support. The above figure shows steady reduction in the magnitude of cell ASR upon replacement of uni-layer anode support (conventional or electroless) to multilayer anode. Activity of single cell is accelerated more than ~ 2 folds with reduced ohmic polarization through the usage of electroless cermet as active layer. Therefore, among the four configurations 32 AAL-1 turn out to be the optimized anode composition with highest cell performance and minimum area specific resistance.

Chapter – 5.6

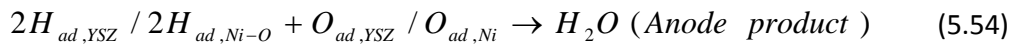
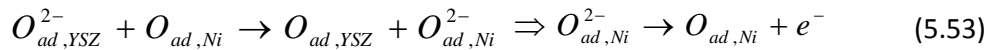
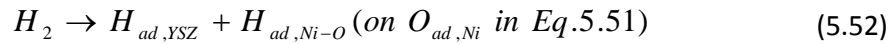
5.6.3.7. Role of moist fuel in anodic electrochemical reactions

The electrochemical behaviour of hydrogen oxidation is significantly influenced by the presence of water or oxygen containing molecules in the fuel. The kinetics of hydrogen oxidation is known to be related with the oxygen activity on Ni surface.¹⁵

Moisture from the fuel undergoes dissociative decomposition to produce oxygen species which readily get adsorbed on Ni surface.



According to the mechanism, both YSZ and Ni contribute towards dissociative H₂ adsorption (Eq. 5.52) at anode. This is followed by charge transfer reaction of adsorbed O²⁻ ion from YSZ to Ni species at active anode (Eq. 5.53) and thereby water is formed as the final by product by releasing electrons to the external circuit.



The decomposition of moisture therefore initiates the reaction path through bulk anode and propagates it towards the electro – active zone at the anode/electrolyte interface. This active zone contributes in the charge transfer reaction and finally forms product at the anode outlet. The content of moisture in the fuel has already been optimized to ~ 3 %, exceeding of which tends to enhance the interfacial resistance thereby reducing the overall cell performance.^{41, 42, 48} An experimental outcome is presented in this section regarding the role of reactant gasses towards the cell performance. For the aforementioned study, specific single cells (CA-1, 32 EL-1, 32 BLA-1, TLA and 32 AAL -1) are selected based on the highest performance in the concerned anode configurations as given in Table 5.14. Four different

experiments based on the variation of composition of reactant gasses on cell performances with varied anode configurations presented in Tables 5.24 to 5.26.

Table 5.24: Effect of moisture in fuel on the performance of single cell fabricated with anodes of Configuration- I and II

Anode Configuration	Exp. No.	Gas Compositions	Gas flow rates (SCCM)					
			20	50	100	150	200	250
			Current density (Acm ⁻²) at 800°C, 0.7					
Configuration –I CA-1	I	O ₂ - 200 SCCM [Fixed] + H ₂ [Moist, variable flow]	1.2	1.34	1.48	1.78	1.81	1.81
	II	O ₂ 200 SCCM [Fixed] + H ₂ [Dry, variable flow]	0.87	0.94	0.99	1.00	1.01	1.01
	III	H ₂ [Moist, 200 SCCM, fixed] + O ₂ [variable flow]	1.79	1.79	1.81	1.80	1.81	1.81
	IV	H ₂ [Dry, 200 SCCM, Fixed]+O ₂ [variable flow]	0.98	0.99	1.01	1.01	1.01	1.01
Configuration -II 32 EL-1	I	O ₂ - 200 SCCM [Fixed] + H ₂ [Moist, variable flow]	1.87	1.98	2.01	2.47	2.5	2.5
	II	O ₂ - 200 SCCM [Fixed] + H ₂ [Dry, variable flow]	1.33	1.41	1.56	1.63	1.64	1.64
	III	H ₂ [Moist, 200 SCCM, Fixed]+O ₂ [variable flow]	2.49	2.49	2.5	2.5	2.5	2.5
	IV	H ₂ [Dry, 200 SCCM, Fixed]+O ₂ [variable flow]	1.63	1.63	1.63	1.64	1.64	1.64

Significant performance variation

It is observed from Tables 5.24 to 5.26 that, irrespective of anode configuration, similar trend is observed in cell performance for all four experiments (I to IV). From experiment-I, it can be observed that systematic increase in the flow rate of fuel from 20 to 200 SCCM linearly enhance the electrochemical performance of the cell. However, increasing the fuel flow rate beyond 200 SCCM does not contribute towards further enhancement of cell performance, owing to which the optimum flow is fixed at 200 SCCM. At lower fuel content, the saturated moisture uptake of

Chapter – 5.6

fuel also happens to be less, due to which the number of oxygen species required for effective adsorption of entire catalytic Ni-sites is insufficient.

Table 5.25: Effect of moisture in fuel on the performance of single cell fabricated with anodes of Configuration- III

Anode Configuration	Exp. No.	Gas Compositions	Gas flow rates (SCCM)					
			20	50	100	150	200	250
			Current density (Acm ⁻²) at 800°C, 0.7					
Configuration –III 32 BLA-1	I	O ₂ - 200 SCCM [Fixed] + H ₂ [Moist, variable flow]	2.5	2.7	3.0	3.28	3.3	3.3
	II	O ₂ 200 SCCM [Fixed] + H ₂ [Dry, variable flow]	2.34	2.35	2.37	2.38	2.4	2.4
	III	H ₂ [Moist, 200 SCCM, fixed] + O ₂ [variable flow]	3.28	3.28	3.29	3.3	3.3	3.3
	IV	H ₂ [Dry, 200 SCCM, Fixed]+O ₂ [variable flow]	2.38	2.4	2.39	2.4	2.4	2.4
Configuration –III TLA	I	O ₂ - 200 SCCM [Fixed] + H ₂ [Moist, variable flow]	2.9	3.2	3.32	3.45	3.5	3.5
	II	O ₂ - 200 SCCM [Fixed] + H ₂ [Dry, variable flow]	2.43	2.56	2.57	2.65	2.71	2.71
	III	H ₂ [Moist, 200 SCCM, Fixed]+O ₂ [variable flow]	3.4	3.48	3.5	3.5	3.5	3.5
	IV	H ₂ [Dry, 200 SCCM, Fixed]+O ₂ [variable flow]	2.67	2.68	2.70	2.71	2.71	2.71

Significant performance variation

As the flow rate is enhanced, the availability of such adsorbates (O²⁻) is increased which accelerates charge transfer reaction in Eq. 5.53 towards the forward direction. However, upon increasing the fuel flow rate beyond saturation (highest current density in respective configurations) would simply provide excess O²⁻ species without significant performance enhancement. The extent of performance increment is however observed to be marginal upon using dry H₂ as the fuel (experiment II) in which the initiation reaction (Eq. 5.51, 5.52) is absent. Therefore,

dry hydrogen tends to lower the overall cell performance due to the enhancement in associated interfacial resistance. ⁴⁸

Table 5.26: Effect of moisture in fuel on the performance of single cell fabricated with anodes of Configuration- IV

Anode Configuration	Exp. No.	Gas Compositions	Gas flow rates (SCCM)					
			20	50	100	150	200	250
Configuration –IV 32 AAL-1	I	O ₂ - 200 SCCM [Fixed] + H ₂ [Moist, variable flow]	3.1	3.3	3.48	3.67	3.7	3.7
	II	O ₂ 200 SCCM [Fixed] + H ₂ [Dry, variable flow]	2.4	2.65	2.78	3.0	3.03	3.03
	III	H ₂ [Moist, 200 SCCM, fixed] + O ₂ [variable flow]	3.67	3.68	3.7	3.7	3.7	3.7
	IV	H ₂ [Dry, 200 SCCM, Fixed]+O ₂ [variable flow]	3.03	3.03	3.03	3.03	3.03	3.03

Significant performance variation

In contrast, variation in O₂ flow rate is found to have negligible contribution to the overall performance of single cell as observed in either of the experiments III and IV. Therefore, moisture content in the fuel is found to impart significant role towards the oxidation of H₂ and electrochemical activity of the single cell.

5.6.3.8. Dependence of cell performance on type of oxidant

It has been observed during the course of experiments that, in spite of employing optimized anode configuration in selected fuel environment at anode compartment, cell performance tends to reduce drastically on variation of oxidant. SOFC being an example of open system, it is primarily governed by the concentration of reactant gasses (fuel and oxidant) expressed in the form of partial pressure terms as: $V(I) = V^{\circ} + \frac{RT}{4F} \ln(p_{O_2}^{\circ}) + \frac{RT}{2F} \ln(p_{H_2}^{\circ}) - \frac{RT}{2F} \ln(p_{H_2O}^{\circ})$ (5.55) where, V(I), V^o, p^o, R and T are experimental voltage under load, standard Nernst potential, partial pressures of concerned gasses outside anode or cathode compartment, universal gas constant and operating temperature of the cell

Chapter – 5.6

respectively. Therefore, it could be said from Eq. 5.55, that the electrochemical reaction is linearly proportional to the partial pressure of oxygen [$V(I) \propto p_{O_2}^0$] gas used as oxidant at the cathode side.

The electrochemical performances of single cells fabricated with all experimental anode configurations in the oxidant environment of both ‘oxygen and air’ are compared in [Table 5.27](#).

Table 5.27: Effect of oxidant variation on the performances of single cell fabricated with varied anode configurations

Anode Configurations	Anode ID	Type of oxidant	
		Oxygen	Air
		Electrochemical performance at 800°C, 0.7 V (A.cm ⁻²)	
Configuration -I	CA-1	1.81	1.01
	CA-2	1.7	0.88
Configuration -II	28 EL-1	1.43	0.85
	28 EL-2	1.32	0.78
	32 EL- 1	2.5	1.09
	32 EL-2	1.98	0.99
Configuration -III	28 BLA-1	2.54	1.12
	28 BLA-2	1.95	1.02
	28 BLA-3	1.81	0.89
	32 BLA-1	3.3	2.02
	32 BLA-2	2.97	1.61
	32 BLA-3	2.57	1.39
	TLA	3.5	2.12
Configuration –IV	28 AAL-1	3.2	2.2
	28 AAL-2	2.75	1.51
	28 AAL-3	2.63	1.34
	28 AAL-4	2.52	1.13
	32 AAL-1	3.7	2.8
	32 AAL-2	3.53	2.34
	32 AAL-3	3.43	2.15
	32 AAL-4	3.3	2.04

The respective trends of performances with variation in anode configuration can also be observed from [Figure 5.78](#). It can be observed that, irrespective of anode configurations, significant deterioration in cell performance is obtained with air as oxidant. Such observation is based on the factors effecting

oxidant reduction reaction at cathode and the associated polarization generated through the reactions.

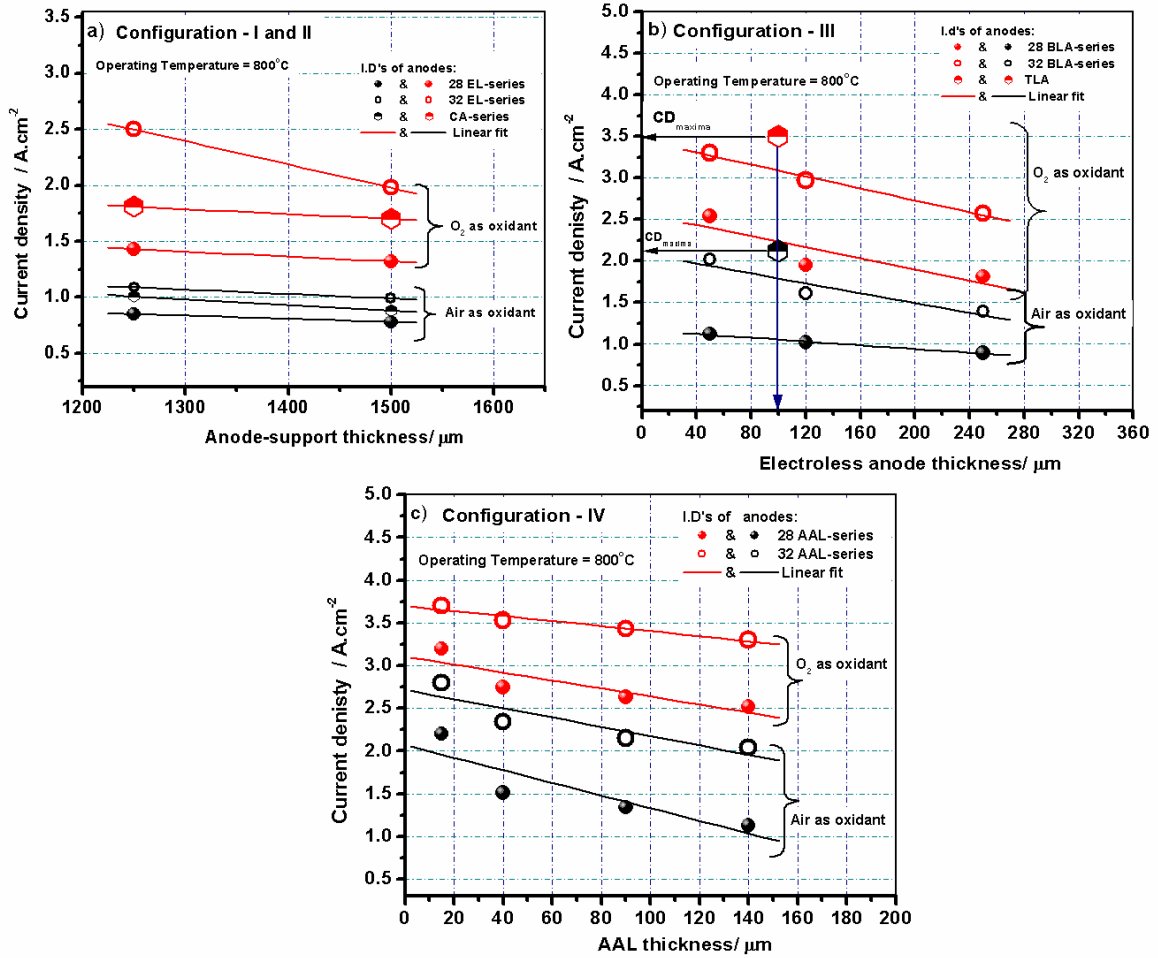
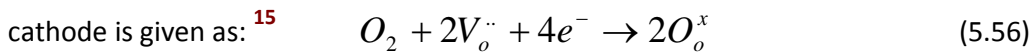


Figure 5.78: Correlation among type of oxidants and performances of single cell fabricated with varied anode configurations

The overall reaction for the oxygen reduction reaction (ORR) at SOFC cathode is given as:



The reaction given in Eq. 5.56 is made up of a series of bulk and surface processes.

The mechanistic contribution to cathode polarization losses ($R_{Cathode}$) can be written as:

$$R_{Cathode} = R_{Gas\ diffusion} + R_{Surface\ adsorption / diffusion} + R_{Charge\ transfer} + R_{ohmic} \quad (5.57)$$

where, 'R' terms refers to the various polarization factors offered towards overall cathode polarization. Each of these factors is a subsequent product of microstructure and material kinetic properties as mentioned below:

Chapter – 5.6

1. $R_{\text{Gas Diffusion}}$ and R_{Ohmic} are functions of:
 - a) Microstructure -- porosity & phase fraction, tortuosity, connectivity etc.
 - b) Conductance- solid phase conductivity or gas phase diffusivity
2. $R_{\text{Surface Adsorption/Diffusion}}$ are functions of:
 - a) Microstructure-- surface area/volume
 - b) Reaction kinetics - surface coverage, surface diffusivity
3. $R_{\text{Charge Transfer}}$ is function of:
 - a) Microstructure -- L_{TPB} , surface area/volume etc
 - b) Reaction kinetics -- Oxygen reduction rate (ORR)

Eq. 5.56 can be modified as: ¹⁵

$$\begin{aligned}
 V(I) - V^{\circ} &= \frac{RT}{4F} \ln(p_{O_2}^{\circ}) + \frac{RT}{2F} \ln(p_{H_2}^{\circ}) - \frac{RT}{2F} \ln(p_{H_2O}^{\circ}) \\
 &= R_{\text{Cathode}} + R_{\text{Anode}} + R_{\text{Electrolyte}} + R_{\text{Other factors}} = \eta \\
 &= R_{\text{Cathode}} + R_K
 \end{aligned} \tag{5.58}$$

where, η is the overall cell polarization and R_k is the resultant polarization contributed from all other terms except cathode.

Therefore, upon combing Eqs. 5.57 and 5.58, we can have:

$$\begin{aligned}
 R_{\text{Cathode}} &= \left[\frac{RT}{4F} \ln(p_{O_2}^{\circ}) + \frac{RT}{2F} \ln(p_{H_2}^{\circ}) - \frac{RT}{2F} \ln(p_{H_2O}^{\circ}) \right] - R_k \\
 \Rightarrow R_{\text{Cathode}} &\propto p_{O_2}^{\circ}
 \end{aligned} \tag{5.59}$$

Eq. 5.59 clearly describes the linear correlation of cathode polarization with partial pressure of oxygen. Therefore, reduction in electrochemical performance of the single cells with air is mainly because of reduced oxygen reaction rate (ORR) at the cathode compartment due to the reduced partial pressure of oxygen.⁵⁰ Enhanced anodic electrochemical activity for the single cells having BAL or AAL-series anode though accelerates the overall performance, but higher cathodic polarization generated upon using air as the oxidant contributes significantly towards diminishing the activity of the single cell.

5.6.3.9. Endurance analysis of fabricated SOFC's

SOFC is believed to be technologically viable provided it is capable of withstanding environmental fluctuations viz. repeated redox cycling, long term sustainability under load etc. In the present research work, efforts are made to study the endurance of single cells against a constant load of 0.5, 0.75 and 1.0 A.cm⁻² for a considerable time period of ~ 2000 h. Figure 5.79 shows the rate of change of cell voltage (at 800°C) as a function of operation time for cells having different configurations at a constant load of 0.5 A.cm⁻².

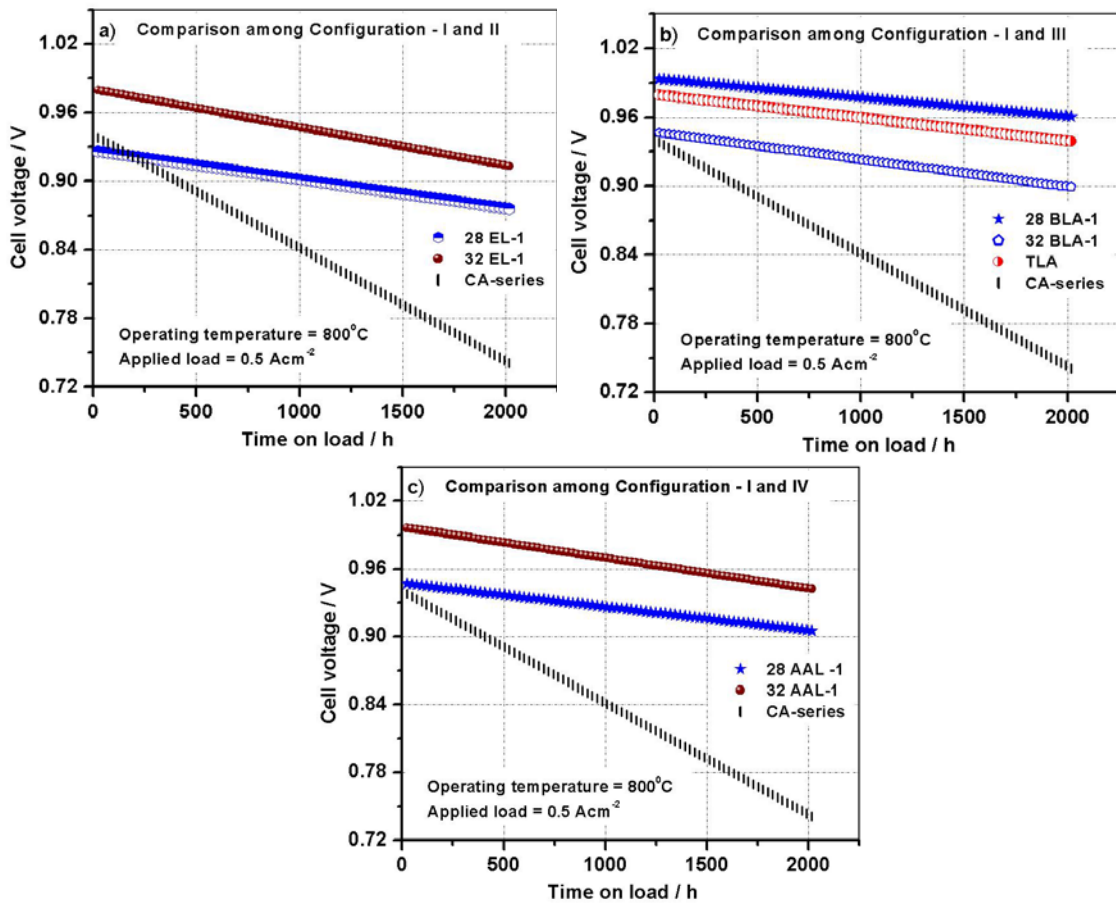


Figure 5.79: Comparative endurance test on single cells with a load of 0.5 A.cm⁻² among: a) Configuration – I and II, b) Configuration – I and III and c) Configuration – I and IV

The figure represents a comparative trend in voltage reduction of cells fabricated with anodes of Configuration-I with that of Configuration –II-IV in order to exhibit

Chapter – 5.6

the functionality of electroless anodes towards long term endurance of single cells. It is evident from Figure 5.79 that, usage of electroless cermet in the form of either anode-support or layer structure tend to reduce the rate of voltage deterioration significantly. It can be observed from the graph that, upon application of electronic load in the circuit, cell voltage drops significantly in the initial time period of 1000 h. In the subsequent time period (1000 -2000 h), the deterioration rate is found to be comparatively lesser. The rate of degradation is significantly higher for cells with CA-series ($194.6\text{m}\Omega\text{-cm}^2\text{kh}^{-1}$) as given in Table 5.28.

Table 5.28: Comparative endurance test of single cell fabricated with varied anode configurations

Anode Configurations	Anode ID	Degradation rate at 0.5 A.cm^{-2} ($\text{m}\Omega\text{-cm}^2\text{kh}^{-1}$)
Configuration -I	CA-1	194.58
Configuration -II	28 EL-1	49.44
	32 EL- 1	65.84
Configuration -III	28 BLA-1	32.4
	32 BLA-1	46.74
	TLA	39.86
Configuration -IV	28 AAL-1	42.16
	32 AAL-1	53.38

In contrast, for cells fabricated with 28/32 EL-series, the magnitude of degradation is found to be in the range of 49 to 66 $\text{m}\Omega\text{-cm}^2\text{kh}^{-1}$. Furthermore, incorporation of electroless cermet as layer structure still reduces the deterioration rate to 32 to 47 $\text{m}\Omega\text{-cm}^2\text{kh}^{-1}$ for 28/32 BLA-1, 39.86 $\text{m}\Omega\text{-cm}^2\text{kh}^{-1}$ for TLA and 42-53 $\text{m}\Omega\text{-cm}^2\text{kh}^{-1}$ for 28/32 AAL-1 anodes. This drop is found to be more pronounced as the applied load is increased from 0.5 Acm^{-2} to 1.0 Acm^{-2} . Percentage degradation rates are determined from the durability curve using standard method of calculating the absolute voltage drop and normalizing the same to 1000 h.⁵¹ Figures 5.80-5.82 shows such degradation plot of the fabricated cells against applied loads of 0.5 to

1.0 A.cm⁻² upto 2000 h of continuous operation. Degradation of single cells is found to be correlated with the anode configuration.

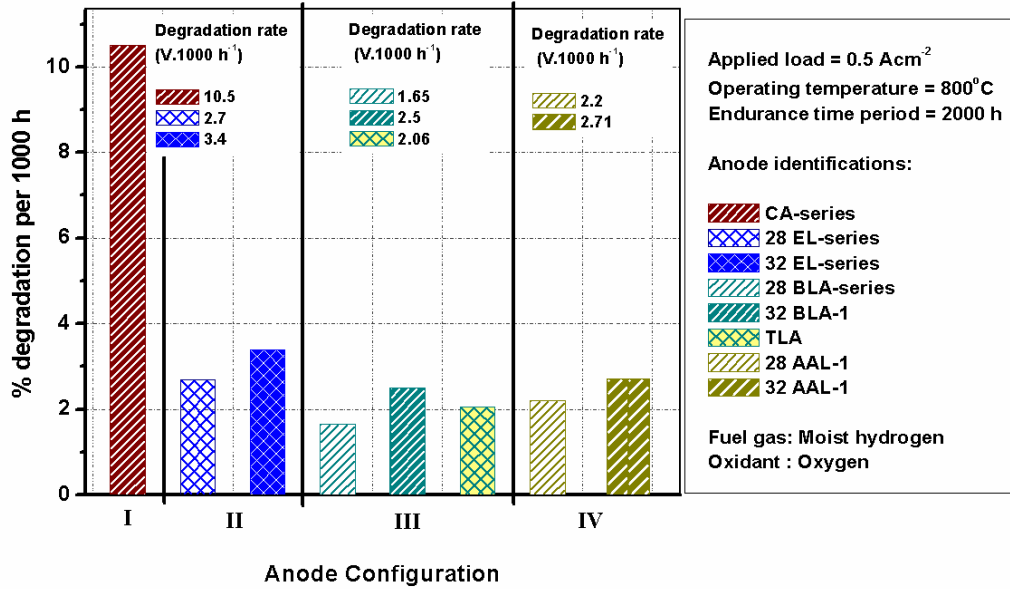


Figure 5.80: Degradation rates determined from durability test on single cell with varied anode configurations subjected to an electronic load of 0.5 Acm⁻²

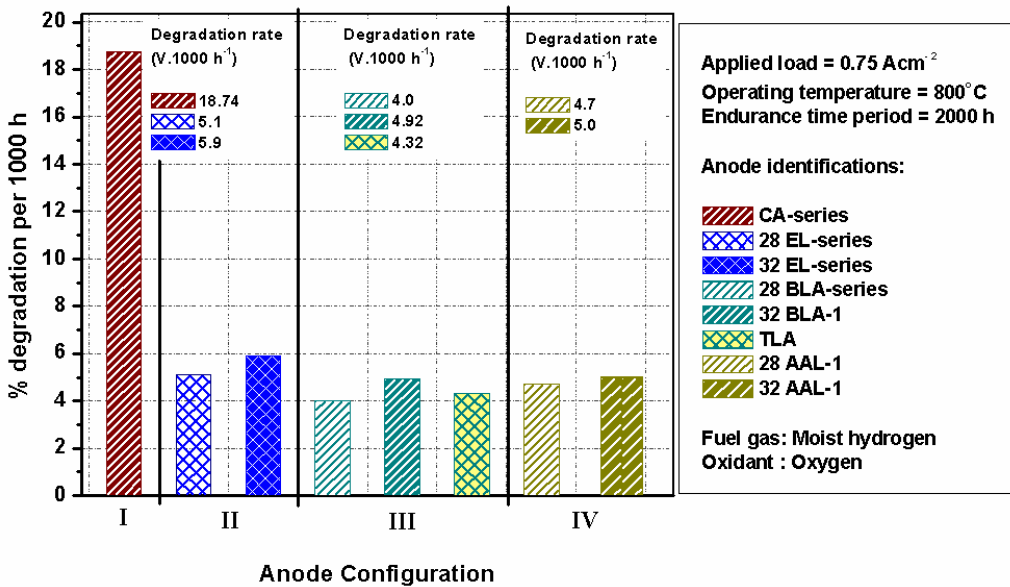


Figure 5.81: Degradation rates determined from durability test on single cell with varied anode configurations subjected to an electronic load of 0.75 Acm⁻²

Comparative study of Figures 5.80-5.82 reveals that, irrespective of the magnitude of applied load, highest degradation is found with the cells fabricated with

Chapter – 5.6

conventional anode cermets (CA-1) [$\sim 26\%$ voltage drop per 1000 h at 1.0 A.cm^{-2} load].

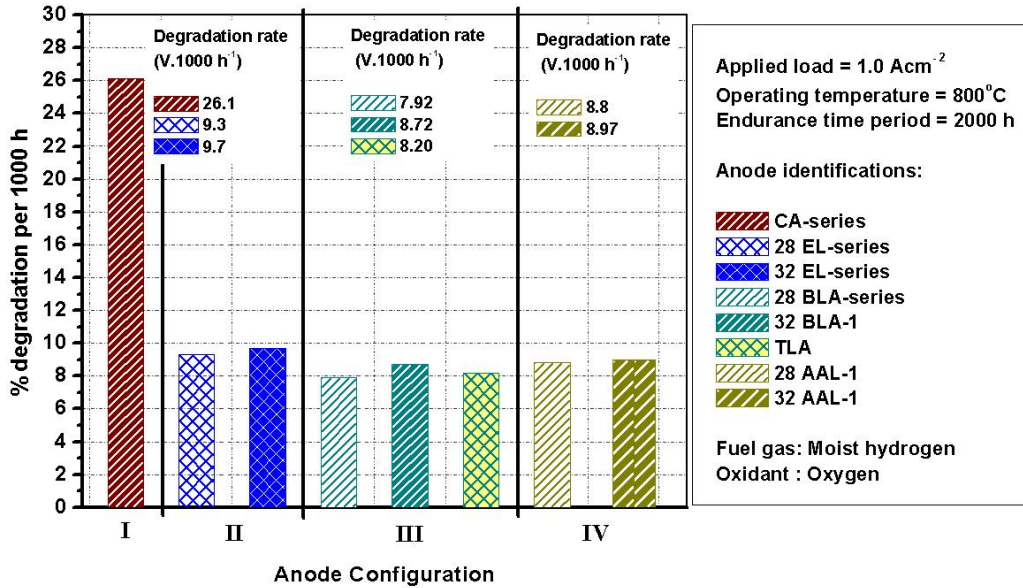


Figure 5.82: Degradation rates determined from durability test on single cell with varied anode configurations subjected to an electronic load of 1.0 A.cm^{-2}

As the load increased from 0.5 to 1.0 A.cm^{-2} , the degradation rate also increases. However, the incremental trend of degradation is dependent on the functionality of anode employed.

Irrespective of designated configurations; incorporation of electroless anode is always found to reduce the rate of cell degradation during long term testing for ~ 2000 h. Compared to cells with CA-series anode which yield ~ 10.5 to 26% degradation per 1000 h, cells with 28 EL-1 results in only 2.7 - 9.3% and 32 EL-1 shows 3.4 - 9.7% voltage drop per 1000 h in *Configuration-I* at a load of 0.5 - 1.0 A.cm^{-2} . Long term endurance tests of cells with TLA (*Configuration-III*) exhibits a reduced voltage degradation rate of $\sim 2.06 - 8.2\%$ per 1000 h which is intermediate of the rate as shown by cells fabricated with either 28 EL-1 or 32 EL-1 anodes at similar load conditions. Similar to the above observations, significant reduction in cell deterioration (2.2 - 8.8% per 1000 h for 28 AAL-1 and 2.71 - 8.97%

per 1000 h for 32 AAL-1) is observed upon employing electroless cermet as AAL. Degradation of the electrochemical performance of single cell is expected to be primarily associated with increase in ohmic resistances in bulk layers and interfaces, coarsening in various layers and other associated reactions at anode-electrolyte interfaces.^{15, 51} With increase in applied load across the cell, local joule heating or resistive heating is expected to get enhanced and in turn influence the extent of Ni coarsening. The rate of Ni-coarsening is higher for the cells with conventional anode-support having higher Ni content with dispersed distribution of Ni and YSZ phases. In contrast, owing to the formation of unique core-shell microstructure in the matrix of electroless anode, innumerable Ni-Ni and YSZ-YSZ interconnected networks are produced. Continuous application of electronic load (0.5 to 1.0 Acm^{-2}) though initiates significant joule heating; the resultant effect is quashed through such numerous paths and thereby the overall deterioration rate is reduced. In addition, the presence of lower Ni content (28-32 vol %) in electroless contributes towards lowering the magnitude of Ni coarsening and cell degradation compared to the conventional matrix (40 vol % Ni). The influence of anode microstructure on the rate of degradation of single cell is presented in [Figure 5.83](#). Ni coarsening is clearly visualized from the binerized optical image of the conventional cermet after an operation of 2000 h ([Figure 5.83 c, d](#)). The Ni-particulates with fairly large content and particle size undergoes rapid coarsening in the form of clusters or islands of Ni in the matrix. These sinteractive metallic clusters show higher tendency to coalesce into bigger particles not only reduce the catalytic activity of Ni but also hamper the electrochemical charge transfer reaction. However, tendency of Ni particle agglomeration is found to be lesser in the electroless anode matrix ([Figure 5.83 e, f](#)). The formation of patterned core (YSZ) - shell (Ni) structure increases the energy barrier required for the rearrangement of metallic phases in the matrix during cohesion of Ni particulates. The size and distribution of Ni phases of electroless anode is therefore observed to

Chapter – 5.6

remain almost unchanged during a reasonable period of operation of 2000 h (Figure 5.83 e and f).

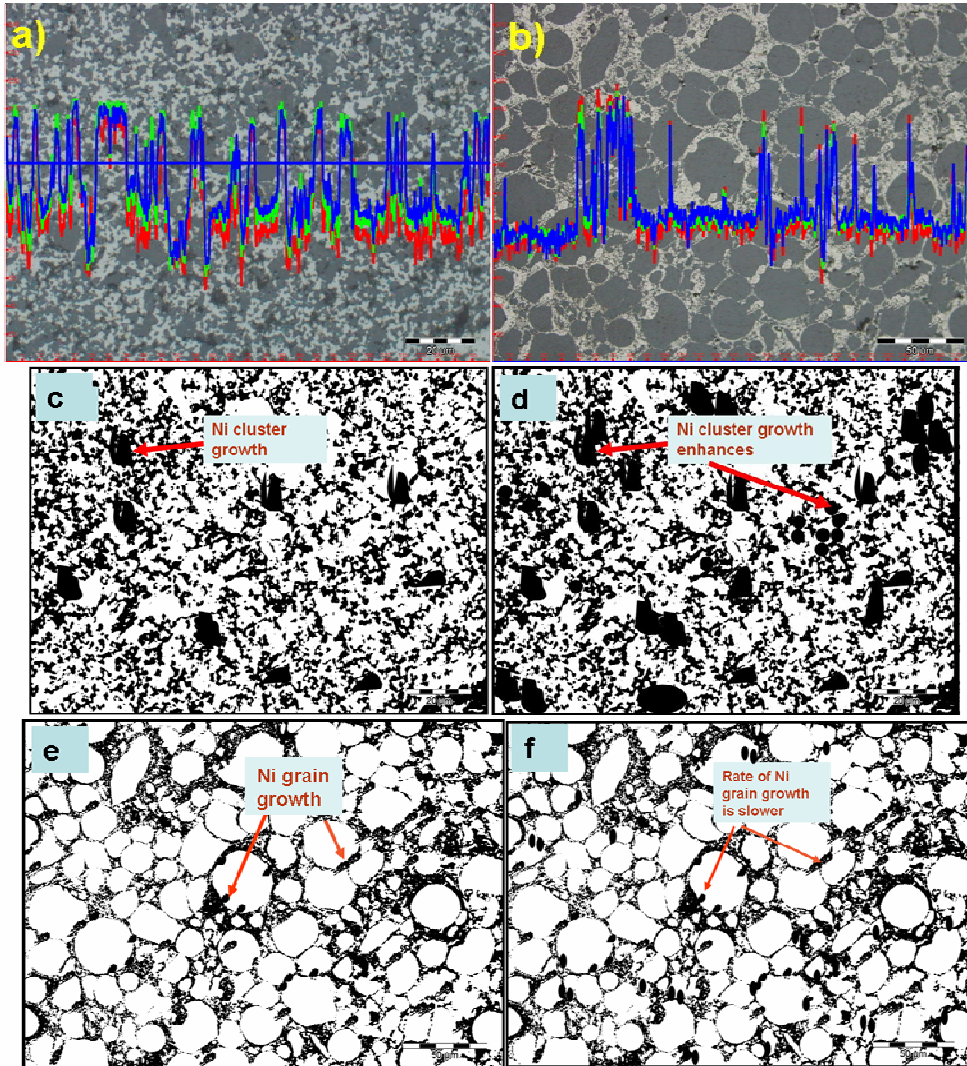


Figure 5.83: Optical microstructure and intensity profile for phases of: a) conventional anode, b) electroless anode after endurance test of single cell, [c) and d)] are binerized images of conventional anode and [e) and f)] are binerized images of electroless anode subjected to electronic load of 0.5 and 1.0 Acm^{-2} respectively

In addition, the intensity profile in the optical images of Figure 5.83 a and b determines the specific regions of the sample where Ni-coarsening is operative. The regions of Ni-coarsening show multiple intensified peaks in the microstructure.

Therefore, single cell with layered anode having electroless layer in vicinity of electrolyte is superior in terms of higher performance along with reduced degradation. It can be said that for the layered anode structure of *Configuration – III and IV*, performance deterioration is truly governed by the degree of degradation exhibited at the electro active anode layer present adjacent to the electrolyte. Therefore, such layered anode having electroless layer in vicinity of electrolyte exhibit high electrochemical performance with reduced microstructural deterioration.

5.6.3.9.1. Role of moisture content in the fuel towards the endurance of SOFC

The role of moisture in the fuel is an essence for electrochemical anodic reactions which has been studied and discussed in section 5.6.3.7. In light of this experiment, efforts are exerted to study the consequences of load application to the fabricated single cells in dry hydrogen as the fuel. The comparative study of the endurance of single cells in presence/absence of moisture content in the fuel is given in [Table 5.29](#). It can be observed from the table that, irrespective of the magnitude of applied load, the extent of degradation is significantly rapid for the single cells operated in dry hydrogen as the fuel. Upon subsequent enhancement of electronic load from 0.5 to 1.0 Acm⁻², cells fabricated with CA-series exhibit degradation rate of 10 to 26 % per 1000 h in moist hydrogen and oxygen environment, whereas the degree of deterioration increased to 37- 84 % per 1000 h using dry hydrogen and oxygen gasses respectively. Compared to ~ 3 times increment in the rate of degradation showed by cells fabricated with CA-1, incorporating of electroless cermet in *Configuration – II, III and IV* is found to reduce the degradation rate to ~ 1.5 times upon changing from moist to dry fuel. The electrochemical activity of a single cell is limited by the polarization/resistances contributed through the cell components according to Eq. 5.58 modified to:

$$\begin{aligned} \eta &= R_{Cathode} + R_{Anode} + R_{Electrolyte} + R_{Other\ factors} \\ &= R_{Anode} + R_K \end{aligned} \quad (5.60)$$

Chapter – 5.6

Table 5.29: Effect of moisture content in the fuel on the endurance test of single cell fabricated with varied anode configurations

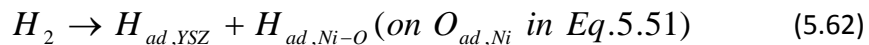
Anode Configurations	Anode ID	% Degradation per 1000 h					
		Moist fuel			Dry fuel		
		Applied load (A.cm ⁻²)			Applied load (A.cm ⁻²)		
		0.5	0.75	1.0	0.5	0.75	1.0
Configuration -I	CA-1	10.5	18.74	26.1	33.6	59.97	83.52
Configuration -II	28 EL-1	2.7	5.1	9.3	4.45	8.42	15.35
	32 EL-1	3.4	5.9	9.7	5.61	9.74	16.01
Configuration -III	28 BLA-1	1.65	4.0	7.92	2.73	6.6	13.07
	32 BLA-1	2.5	4.92	8.72	4.13	8.12	14.39
	TLA	2.06	4.32	8.20	3.39	7.13	13.53
Configuration -IV	28 AAL-1	2.2	4.7	8.8	3.63	7.76	14.52
	32 AAL-1	7.71	5.0	8.97	12.72	8.25	14.80

where, η is the overall cell polarization and R_{κ} is the resultant polarization contributed from all other terms except anode.

The resistance offered by anode could also be identified in the form of various factors as mentioned below:

$$R_{Anode} = R_{Gas\ diffusion} + R_{Surface\ adsorption} + R_{Charge\ transfer\ reaction} + R_{Amb} + R_{ohmic} \quad (5.61)$$

where, R terms refer to the various polarization factors offered towards overall anode polarization. Presence of oxygen containing species in the fuel gas is found to initiate the anodic reactions through diffusion, surface adsorption, charge transfer and redox mechanisms as already discussed using Eq. 5.51 – 5.54 in section 5.6.3.7.¹⁵ The primary governing steps involve dissociation and adsorption of 'O_{ad}' species onto metallic surface as:



The aforementioned governing reactions are absent by using dry hydrogen as fuel. Consequently the resistive factors viz. ' $R_{\text{surface adsorption}}, R_{\text{charge transfer}}, R_{\text{ohmic}}$ ' is increased with the enhancement of R_{Anode} (Eq. 5.61). The electrochemical reaction sequences are altered which contributes in enhancing the energy barrier for fuel oxidation and subsequent anodic reactions. Owing to such features, irrespective of anode employed, the performance of single cell reduces significantly by using dry hydrogen as fuel as also evident from [Table 5.29](#). However, due to the added functionalities of electroless cermet (*Configuration – II to IV*), the influence of dry fuel towards the degradation of single cell is lower compared to the conventional anode cermets (*Configuration - I*).

5.6.4. Thermal characterizations of the fabricated anodes

The comprehensive experimental studies discussed in aforementioned sections clearly demonstrate the applicability of electroless anode for SOFC applications based on the requirement. In addition to the major advantages, superiority of electroless cermet can also be accounted in terms of thermal compatibility which is mentioned in the present section.

Comparisons of coefficients of thermal expansion (CTE) are given in [Figure 5.84](#). CTE of electroless anode of *Configuration-II* ($11.5 \times 10^{-6} \text{ }^{\circ}\text{C}^{-1}$) is found to be close to that of YSZ electrolyte ($10.85 \times 10^{-6} \text{ }^{\circ}\text{C}^{-1}$) compared to the conventional anode (*Configuration-I*) with higher CTE ($13 \times 10^{-6} \text{ }^{\circ}\text{C}^{-1}$). The layered anodes of *Configuration-III and IV* are found to exhibit CTE values similar to the electroless anode compatible with the CTE of YSZ electrolyte. This indicates significant contribution of electroless cermet towards the thermal expansion behavior of anodes of both *Configuration-III and IV*. Dependence of the trend of CTE variation with anode configurations is given in [Table 5.30](#). It can be observed from the table that, owing to the presence of lower Ni content (28-32 vol %) and patterned microstructural arrangement in the cermet of electroless anode, the CTE values of

Chapter – 5.6

Configuration-II are lower in comparison to the values of *Configuration -I*. As expected from the linear relation among CTE magnitude and Ni content of the cermet, the extent of thermal expansion is higher for 32 BLA-series compared to 28 BLA- anodes.

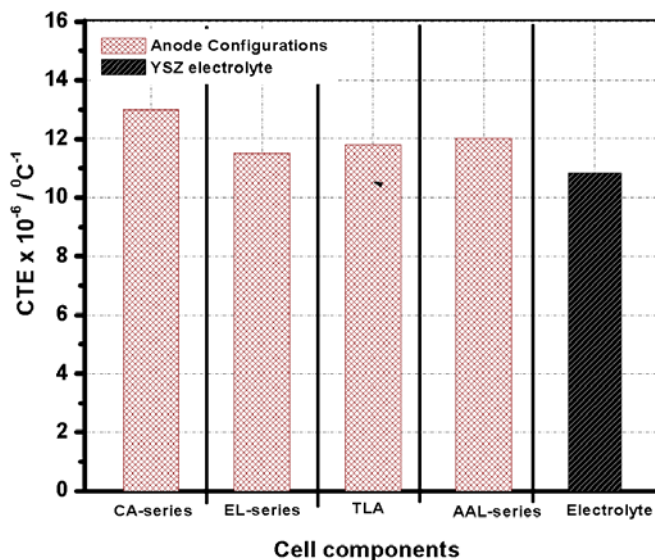


Figure 5.84: Comparative coefficients of thermal expansion of YSZ electrolyte with fabricated anode configurations

Anode Configurations	Anode ID	CTE (x 10 ⁻⁶) °C ⁻¹	Average CTE (x 10 ⁻⁶) °C ⁻¹
Configuration -I	CA-1	13.0	13
	CA-2	13.01	
Configuration -II	28 EL-1	11.0	11.5
	28 EL-2	11.4	
	32 EL- 1	11.7	
	32 EL-2	11.9	
Configuration -III	28 BLA-1	11.54	11.8
	28 BLA-2	11.44	
	28 BLA-3	11.35	
	32 BLA-1	12.74	
	32 BLA-2	12.34	
	32 BLA-3	11.65	
	TLA	11.45	
Configuration -IV	28 AAL-1	11.86	12.0
	28 AAL-2	11.78	
	28 AAL-3	11.68	
	28 AAL-4	11.59	
	32 AAL-1	12.98	
	32 AAL-2	12.58	
	32 AAL-3	11.89	
	32 AAL-4	11.69	

However, combined matrix effect in TLA series reduces the thermal expansion behavior of the composite anode regardless of the presence of both 32 and 28 vol % Ni in the electroless Ni-YSZ cermet. The functionality of electroless cermet is clearly visualized by its influence exerted in the graded anodes of *Configuration- III and IV* towards significant reduction in the magnitude of coefficient of thermal expansion. Therefore, incorporation of electroless cermet either as the layered anode or active layer (AAL) contributes towards the enhancement in the performance of single cell with reduced degradation and compatible thermal expansion.

5.6.5. Polarization effects in anode-supported SOFC and its dependence on anode configuration

An electrochemical phenomenon is an inherent / intrinsic property of an open SOFC system which involves certain fundamental mechanisms of: gas diffusion, adsorption, surface diffusion, charge transfer and associated electron transfer reactions. A schematic of electrochemical processes at the anode/electrolyte interface is shown in [Figure 5.85](#).

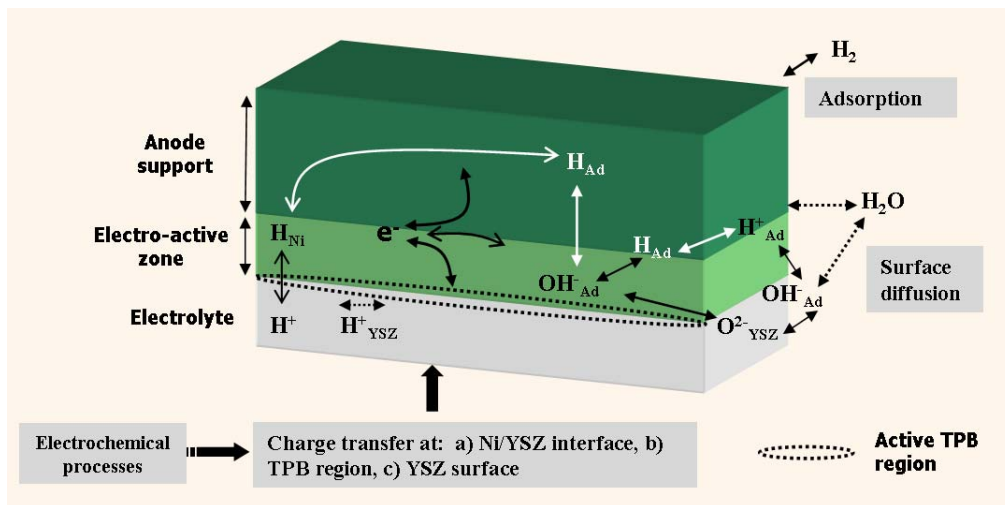


Figure 5.85: Schematic of fundamental electrochemical processes at anode/electrolyte interface of a planar anode-supported SOFC

Chapter – 5.6

It can be observed from the generalized schematic that, irrespective of anode materials and configurations, existence of electro active zone is always operative and functional preferentially at the interface of anode and electrolyte. The purpose of gradation in anode structure based on constituent phases, thickness, microstructure, etc is essential for diminishing the polarization losses. Such resistances/ polarizations are generated during the fundamental reaction mechanisms as mentioned above and results in reducing the performance of SOFC which is judged on its extent of load (electronic current) bearing capacity (Voltage vs. current plot).

According to the prior arts, the voltage (V) vs. current density (I) plot for anode-supported SOFC's can be alienated into three portions ⁶² viz. a) initial 'concave-up' curvature ($d^2V/dI^2 \geq 0$) at low current may account for the participation of activation polarization, b) intermediate straight portion ($d^2V/dI^2 = 0$) is ohmic contribution in which both activation and concentration may take part depending upon the cell configuration and c) 'convex-up' non-linear trend ($d^2V/dI^2 \leq 0$) at higher current is attributed to concentration polarization.

The main purpose of the present section is to identify and determine the polarization factors and their correlation with various anode configurations. There could be certain specific boundary conditions to be considered prior to the determination of polarization factors as:

- a) The theoretical determination of polarization factors through experimental calculations is concentrated within the ohmic range in which correlation of voltage (V) and current density (I) is linear [$dV / dI = f(R)$] as illustrated in [Figure 5.86](#). The supplementary non-linear dependence among V vs I, in either lower or higher current density range (schematic of [Figure 5.86](#)) is not considered in the present context.
- b) For anode-supported SOFC's, the value of exchange current density is significantly higher. Consequently, the activation polarization exhibit

essentially an ohmic behavior over a wide range of current density and therefore, the corresponding charge transfer resistance evolve as a part of ohmic contribution.⁵³

- c) In view of the fact that, while the charge transfer reactions are diffusion driven process, mass transport effects are intrinsically involved. Therefore, in addition to charge transfer polarization, the concerned ohmic part also incorporates significant contribution from concentration polarization. The resistances offered through ohmic mechanism (linear V vs. I plot) is combined effect of both activation and concentration polarization as:

$$R_{\text{ohmic}} = R_{\text{Charge transfer}} + R_{\text{Concentration}} \quad (5.63)$$

where, 'R' denotes the polarization factors.

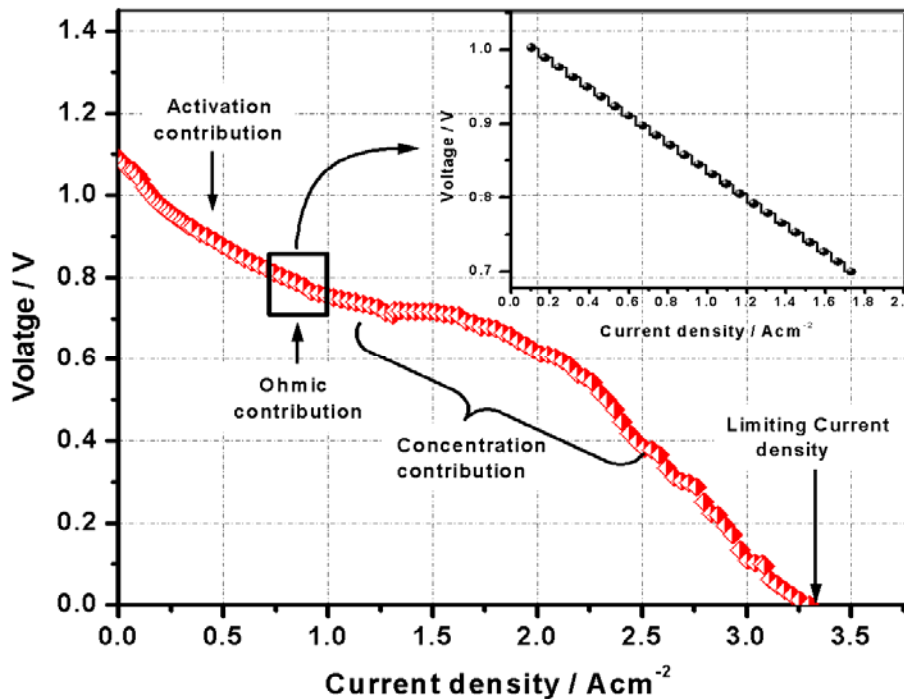


Figure 5.86: Trend of V vs I curve exhibiting contributions from various polarization factors and its extrapolation to obtain limiting current density³⁶

The combined linear and non-linear reliance between V vs. I is a direct consequence of certain major phenomena e.g. adsorption, charge transfer and conduction process. However, it could be experimentally observed from cell

Chapter – 5.6

performance plots in sections 5.6.3.2 to 5.6.3.4 that the extent of non-linearity at the low and high current densities is found to be negligible for the anode-supported cells. The extent of non-linearity is even lower for cells fabricated with anodes of *Configuration –III and IV* (layered anodes with incorporation of electroless cermet as anode layer or active layer). Therefore, the polarization effects on such cells are calculated based on the contributions of various overpotentials in the linear variation of V-I plot. The voltage under load [V (I)] for the cell reaction, $2H_2 (Anode) + O_2 (Cathode) = 2H_2O (Anode)$ is given as:¹⁵

$$V(I) = V^{\circ} + \frac{RT}{4F} \ln(p_{O_2}^{\circ}) + \frac{RT}{2F} \ln(p_{H_2}^{\circ}) - \frac{RT}{2F} \ln(p_{H_2O}^{\circ}) \quad (5.64)$$

where, V° , p° , R and T are standard Nernst potential, partial pressures of concerned gasses outside anode or cathode compartment, universal gas constant and operating temperature of the cell respectively. Incorporating the interfacial partial pressures fluxes and the fundamental equations governing the isothermal transport of mixture of gases through porous electrodes as predicted by Douglas and Mason^{43, 52}, Eq 5.64 could be modified as:

$$V(I) = V^{\circ} - IR_i + \frac{RT}{4F} \ln \left[p_{O_2}^{\circ} - \left(\frac{p - p_{O_2}^{\circ}}{p} \right) \left\langle \frac{RT}{4FD_c} \left(\frac{\tau_c l_c}{V_{v-c}} \right)_{eff} \right\rangle I \right] \quad (5.65)$$

$$+ \frac{RT}{2F} \ln \left(p_{H_2}^{\circ} - \left\langle \frac{RT}{2FD_a} \left(\frac{\tau_a l_a}{V_{v-a}} \right)_{eff} \right\rangle I \right) - \frac{RT}{2F} \ln \left(p_{H_2O}^{\circ} + \left\langle \frac{RT}{2FD_a} \left(\frac{\tau_a l_a}{V_{v-a}} \right)_{eff} \right\rangle I \right)$$

where, R_i , p , τ_a , τ_c , l_a , l_c , $V_{v(a)}$, $V_{v(c)}$ and D_a , D_c are the associated cell resistance, interfacial partial pressure of concerned gasses, tortuosity factor, thickness, volume fraction of porosity and binary diffusion coefficients of anode and cathode respectively. The current density dependent area specific resistance (R_{slope}) of the cell is determined as:

$$R_{slope} = -\frac{dV(I)}{dI}$$

$$= R_i + \frac{RT}{4F} \left[\frac{\left(\frac{p - p_{O_2}^{\circ}}{p} \right) \left\langle \frac{RT}{4FD_c} \left(\frac{\tau_c l_c}{V_{v-c}} \right)_{eff} \right\rangle + 2 \left\langle \frac{RT}{2FD_a} \left(\frac{\tau_a l_a}{V_{v-a}} \right)_{eff} \right\rangle + 2 \left\langle \frac{RT}{2FD_a} \left(\frac{\tau_a l_a}{V_{v-a}} \right)_{eff} \right\rangle}{p_{O_2(c)} + p_{H_2(a)} + p_{H_2O(a)}} \right] \quad (5.66)$$

$$= R_{CT-oh} + R_{Cone-oh}$$

In Eq. 5.66, R_{CT-oh} and $R_{Conc.-oh}$ denote the resistances offered due to charge transfer and concentration polarization.

In the present section, both the polarization factors related to linear dependence of voltage vs. current density is considered. From theoretical aspect, concentration polarization appears when electrode reaction is hindered by mass transport phenomenon which is primarily a diffusion controlled process. The parameter that governs the diffusion rate is the limiting current density (I_{lim}). ' I_{lim} ' signifies the maximum current density that can be employed to obtain a desired electrode reaction without interference from concentration overpotentials i.e prior to the discharge of reactants. ⁵³

Representing Eq. 5.66 in terms of limiting current density:

$$\begin{aligned}
 R_{slope} &= R_{CT-oh} + R_{Conc.-oh} \\
 &= R_{CT-oh} + \frac{RT}{4F} \left[\frac{1}{(I_{lim-C} - I)} + \frac{2}{(I_{lim-A} - I)} + \frac{2}{\left(\frac{p_{H_2O}^o}{p_{H_2}^o} \times I_{lim-A} + I \right)} \right] \quad (5.67)
 \end{aligned}$$

where, ' I_{lim-A} and I_{lim-C} ' are anode and cathode limiting current density.

In anode supported cells, $I_c \ll I_a$, therefore, the term related to I_{lim-C} can be neglected and Eq. 5.67 can be rewritten as:

$$R_{slope} = R_{CT-oh} + \frac{RT}{2F} \left[\frac{1}{(I_{lim-A} - I)} + \frac{1}{\left(\frac{p_{H_2O}^o}{p_{H_2}^o} \times I_{lim-A} + I \right)} \right] \quad (5.68)$$

Eq. 5.68 correlates the ohmic contribution of activation and concentration polarizations with ASR (R_{slope}) determined from the slope of ohmic portion of 'Voltage vs Current density' plot as shown in the schematic of [Figure 5.86](#). Limiting current density (I_{lim-A}) is obtained by extrapolating the 'V vs I' curve to V= 0 ([Figure 5.86](#)).

Functionality of electroless cermet can be accounted from [Figure 5.87](#), in which the cells fabricated with electroless anode (32 vol %, 32 EL-series) exhibit

Chapter – 5.6

lower magnitude of polarizations with enhanced cell performance. Formation of unique core-shell microstructure with extended intra-anode TPB enables lower energy barrier for reaction initiation for the cells with 32 EL-anodes. The calculated limiting current density (i_{lim}) for 32 EL-series is found to be the highest (5 to 6.25 Acm^{-2}) among *Configuration –I and II* as given in [Table 5.31](#). Such high limiting current density denotes better electrical conduction in the cermet and hence least concentration polarization in the cells of *Configuration –I and II*. In spite of dual TPB in the anode interior and interface, the calculated overpotential values for 28 EL-series cermet is found to be higher compared to the CA-series ([Figure 5.87](#)).

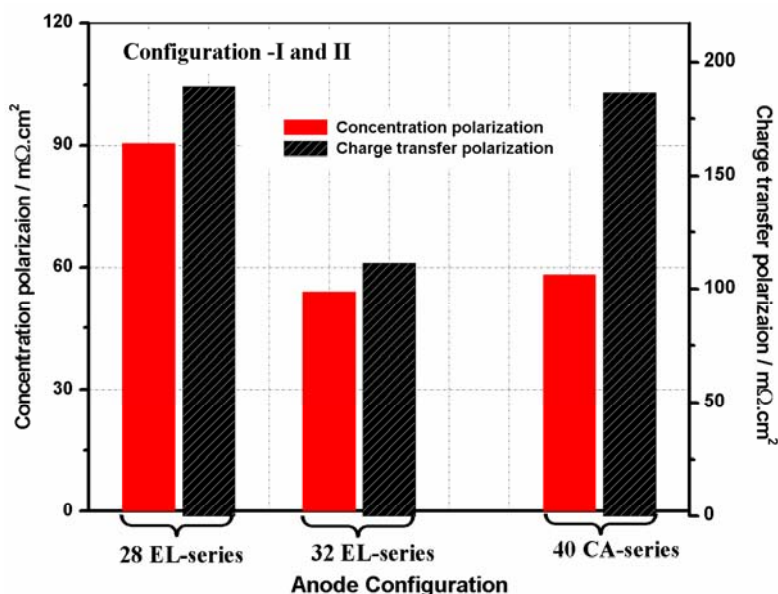


Figure 5.87: Variation of concentration and charge transfer polarization of single cell fabricated with anodes of *Configuration – I and II*

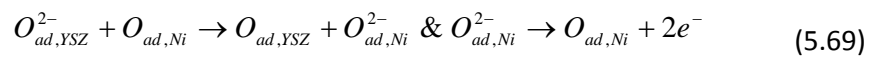
While, the higher charge transfer resistance of 28 EL-series is primarily due to the lesser TPBs available in the anode-electrolyte interface and intra-anode sites, the higher concentration polarization is attributed to the lower limiting current (3.3 - 3.5 $A.cm^{-2}$ in [Table 5.31](#)). This may be explained because of the lower Ni content in such cermet configuration. From [Figure 5.88 a](#) and [b](#), it can be observed that introduction of electroless cermet as layered anode/ AAL significantly reduces the overpotential losses of the cells. It is found that the polarization losses for cells with

32 BLA or 32 AAL- configurations are significantly lesser compared to 28 BLA or 28 AAL-series.

Table 5.31: Variation of cell performance and limiting current density with variable anode configurations

Anode Configurations	Anode ID	Current density at 800°C, 0.7 V (A.cm ⁻²)	Limiting current density, I _{lim} (A.cm ⁻²)
Configuration -I	CA-1	1.801	4.5
	CA-2	1.7	4.25
Configuration -II	28 EL-1	1.43	3.56
	28 EL-2	1.32	3.3
	32 EL- 1	2.5	6.25
	32 EL-2	1.98	4.95
Configuration -III	28 BLA-1	2.54	6.35
	28 BLA-2	1.95	4.88
	28 BLA-3	1.81	4.53
	32 BLA-1	3.3	8.25
	32 BLA-2	2.97	7.4
	32 BLA-3	2.57	6.43
	TLA	3.5	8.71
Configuration –IV	28 AAL-1	3.2	8.0
	28 AAL-2	2.75	6.9
	28 AAL-3	2.63	6.58
	28 AAL-4	2.52	6.3
	32 AAL-1	3.7	9.25
	32 AAL-2	3.53	8.83
	32 AAL-3	3.43	8.6
	32 AAL-4	3.31	8.28

For cells with *Configuration – III*, it is observed that with increasing electroless layer thickness from 50 to 250 μm, polarization values are increased ([Figure 5.88 a](#)). Because of the microstructural variation in conventional and electroless cermet, the flow paths of the electrons are expected to be different. Presence of dual TPB though assists in the acceleration of charge transfer reaction, microstructural variation in the layered anode, generates ‘intra-anodic stratum’ which interferes with the electronic motion during charge transfer reactions:



At lower thickness of electroless layer, the intra-anodic stratum is least and is overshadowed by the overall microstructure of the conventional anode. A direct

Chapter – 5.6

consequence of the formation of such intra-anodic stratum can be observed from the highest performance and least polarizations of single cells with TLA among Configuration –III.

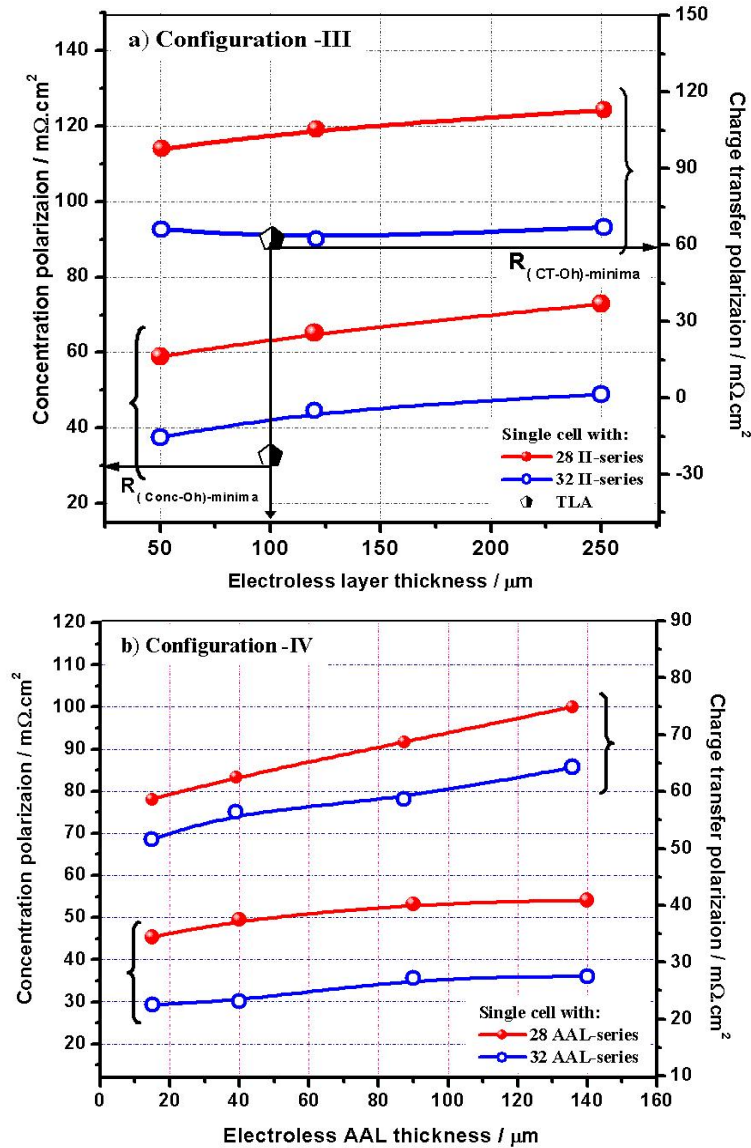


Figure 5.88: Variation of concentration and charge transfer polarization of single cell fabricated with anodes of a) Configuration – III and b) Configuration- IV

From Table 5.31, it is observed that such cells having TLA exhibits both highest current density of 2.5 Acm^{-2} and limiting current density of 8.71 Acm^{-2} among the series. The magnitude of polarization factors are also found to be less for cells with TLA compared to cell having 28/32 BLA-series (Figure 5.88 a). In TLA- composition,

the intermediate electroless layer of 32 vol % Ni accounts for the acceleration of anodic electrochemical reactions thereby reducing the resistance offered by charge transfer. The rate of consumption of the reactant species to form products is also increased that limits the concentration resistance of the single cell. Owing to the presence of lower Ni content (28 vol %) at the anode/electrolyte interface having unique core-shell microstructure, the anode deterioration is reduced significantly with enhanced magnitude of limiting current density. Therefore, among *Configuration-III*, cells with TLA are effective in enhancing the performance with least contribution of polarization effects. Similar trend of escalating either concentration or charge transfer polarization values is observed with increasing thickness of electroless AAL from 15 to 140 μm in *Configuration-IV* (Figure 8.88 b). However, it could be noted that, incorporation of electroless cermet as AAL is found to be more beneficial in terms of reduced polarization compared to layered anodes of *Configuration -III* (Figure 8.88 and Table 5.31). Therefore, the functionality of electroless cermet in *Configuration-IV* is superior in terms of charge transfer reaction as well as higher limiting current of 9.25 Acm^{-2} . The functionality of optimized electroless AAL (15 μm) in *Configuration -IV* favors low concentration polarization and hence enhance the electrochemical performance to 3.7 Acm^{-2} at 800°C and 0.7 V.

Impedance spectra of Figure 8.89 show the influence of anode configuration on the temperature dependent cell polarization. Irrespective of the anode configuration, with increasing operating temperature from $700\text{-}800^\circ\text{C}$, the arcs are found to be depressed showing lower cell polarization resistances $[\text{Re}(Z)]$. This could be explained on the basis that, the rate of electrochemical reaction is accelerated with raise in temperature which in turn reduces the energy barrier for the corresponding rate determined steps which is represented by each arc. It could also be noticed that, at 800°C , the system experiences minimum resistance which is illustrated by coalescence of three arcs into a single one. The vivid transformation

Chapter – 5.6

of the nature of impedance plots from Figure 8.89a to Figure 8.89d could be accounted specifically for the variation of anode configuration, since; the other components of the single cell are kept identical.

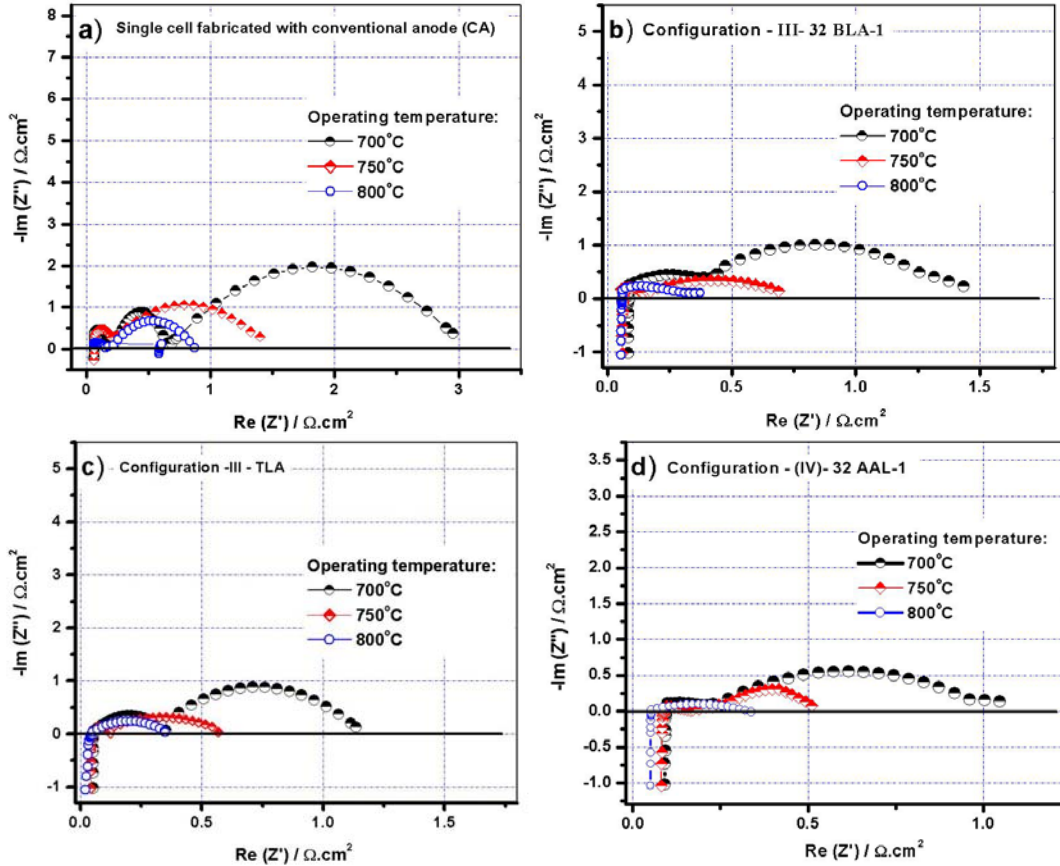


Figure 5.89: Influence of anode configuration a) Configuration -I, b) Configuration - III- 32 BLA-1, c) Configuration-III- TLA and d) Configuration -IV on electrochemical impedance spectra of SOFC

Cells with conventional anodes (*Configuration -I*) show the overall cell polarization of $\sim 0.9 \Omega\text{-cm}^2$ at 800°C (Figure 8.89a), which is substantially reduced to $\sim 0.4 \Omega\text{-cm}^2$ (32 BLA-1), $0.35 \Omega\text{-cm}^2$ (TLA) (*Configuration -III*) and $\sim 0.3 \Omega\text{-cm}^2$ (*Configuration -IV*, 32 AAL-1) for layered anodes having gradation in microstructures (Figure 8.89 b-d). Formation of extended dual TPBs within electroless anode and anode/electrolyte interface accelerates the rate of electrochemical reaction for cells with anodes of *Configuration-III and IV*. The resistances offered by the associated processes are therefore reduced which

results in the reduction of cell polarization by ~ 3 folds for the cells with layered anode. Compared to anodes of 32 BLA-1, the polarization of single cells fabricated with TLA is found to be less. This may be resulted due to the gradation in physical properties of the trilayerd anode which helps in reducing the resistances offered by various factors as mentioned in section 5.6.3.6. The prime difference between [Figures 8.89 b and 8.89 c](#) lies in the characteristics of skinniness of the electroless layer and the resistance offered by the virtue of intra anodic stratum as discussed above. Thin electroless AAL having dense microstructure and higher charge conduction posses better electro catalytic activity at the anode/electrolyte interface and thereby causes lesser charge transfer polarization. Additionally, due to thinner dimension of electroless AAL in *Configuration –IV*, the gas diffusion in the porous conventional anode layer becomes more feasible which enumerate lower concentration polarization. Anode of such configuration also helps in lowering the resistance of electronic flow path by minimizing the intra anodic stratum. Consequently the cell with 32 AAL-1 exhibits least polarizations as observed from the impedance spectra. Therefore, incorporation of electroless in conjugation with conventional anode tends to significantly enhance the electrochemical performance of single cell with reduced polarization losses.

5.6.6. Summary

In summary, the functionality of electroless Ni-YSZ anode cermet is examined in terms of its application in anode-supported configuration of solid oxide fuel cells. In this connection, four types of anodes are fabricated namely, a) *Configuration –I*, conventional anode with variable thickness (1250, 1500 μm) acts as the support structure, b) *Configuration –II*, electroless cermet with variable Ni content (28 -32 vol %) and variable thickness (1250, 1500 μm) acts as the anode support, c) *Configuration –III*- layered anode structure: electroless cermet is employed in conjugation with conventional anode support. Thickness (50-250 μm)

Chapter – 5. 6

and Ni content (28, 32 vol %) of electroless cermet is varied, d) *Configuration –IV*-layered anode structure: electroless cermet acts as anode active layer (AAL) along with conventional anode support. Thickness (15-140 μm) and Ni content (28, 32 vol %) of electroless cermet is varied. The tape thickness of electroless anode ranges from 0.08 μm in *Configuration –III* to 0.025 μm in *Configuration –IV*. Systematic studies are carried out to characterize all such anodes through electrical, optical, thermal, densification etc measurements. Electrical measurements ascertain the functionality for anodes of *Configuration –IV* which exhibit highest electrical conduction in comparison with the samples from other series. Among the anodes of *Configuration –IV*, the samples with 140 μm electroless layer are found to exhibit maximum electrical conduction, which directly clarifies dependence of conductivity on microstructural distribution of constituent phases. Electroless anodes with unique core (YSZ)-shell (Ni) structure enables easy interconnecting paths among Ni, YSZ and pore phases, thereby enhancing the conductivity with least degradation (~ 6.5 % per 20 redox cycles for *Configuration –IV*) with subsequent redox cycles. Dispersed microstructure of conventional matrix causes significant deterioration in electrical conductivity of ~ 26 % per 20 redox cycles for *Configuration –I*.

Electrochemical performances of single cells fabricated with variable anode configurations are studied sequentially with respect to: a) thickness of anode-support (in *Configuration –I and II*), b) thickness of electroless layer (in *Configuration –III and IV*) and c) NiO reduction kinetics. The experimental findings also support the aforementioned superiority of electroless layer as AAL (*Configuration –IV*), which exhibit the maximum performances (3.7 Acm^{-2} at 800°C and 0.7 V) of single cell. However, in contrast to the observations from conductivity measurements, cells with 15 μm electroless AAL are found to exhibit the highest electrochemical performance. Such distinction is found to originate from the variation in flow-pattern of the reactant gasses followed during charge conduction

Chapter – 5. 6

and electro anodic reactions. The experimental upshot of electrochemical reactions are correlated with: a) optical microstructures, b) elemental mapping, c) NiO reduction equilibrium, d) pore-size distribution in anodes, e) effect of moisture in the fuel, f) variation in oxidant type etc. The influence of polarization/ resistive factors is also studied in terms of both mathematic approach and electrochemical impedance measurements.

Therefore, the developed layered anode with gradation in physical properties and electroless Ni-YSZ as the active layer could act as a potential high performance anode and possibly could emerge as an alternate anode for solid oxide fuel cell (SOFC) application.

Appendix - 3

Table 5.32: List of symbols used in Chapter – 5.6		
Symbols	Word Meaning	Unit
R_{Anode}	Total anode resistance	$\text{m}\Omega.\text{cm}^2$
R_g	Resistance offered by anode grains	$\text{m}\Omega.\text{cm}^2$
R_{gas}	Resistance offered by gas transportation	$\text{m}\Omega.\text{cm}^2$
R_{reaction}	Resistance offered by anodic electrochemical reactions	$\text{m}\Omega.\text{cm}^2$
R_{amb}	Ambipolar resistance	$\text{m}\Omega.\text{cm}^2$
$V(I)$	Voltage under load	V
I	Current density	$\text{A}.\text{cm}^{-2}$
V^0	Standard Nernst potential	V
p^0	Partial pressures of concerned gasses outside anode or cathode compartment	atm or Pa
R	Universal gas constant	$\text{J}.\text{mol}^{-1}.\text{deg}^{-1}$
T	Operating temperature	$^{\circ}\text{K}$
F	Faraday's constant	$\text{C}.\text{mol}^{-1}$
R_i	Associated cell resistances	$\text{m}\Omega.\text{cm}^2$
p	Interfacial partial pressure of the concerned gasses	atm or Pa
τ_a	Anode tortuosity factor	Dimensionless
τ_c	Cathode tortuosity factor	Dimensionless
l_a	Thickness of anode electrode	mm or μm
l_c	Thickness of cathode electrode	mm or μm
V_{v-a}	Volume fraction for anode porosity	Dimensionless
V_{v-c}	Volume fraction for cathode porosity	Dimensionless
D_a	Binary diffusion coefficient for anode	$\text{mm}^2.\text{sec}^{-1}$ or $\text{cm}^2.\text{sec}^{-1}$
D_c	Binary diffusion coefficient for cathode	$\text{mm}^2.\text{sec}^{-1}$ or $\text{cm}^2.\text{sec}^{-1}$
$R_{\text{CT-Oh}}$	Charge transfer polarization	$\text{m}\Omega.\text{cm}^2$
$R_{\text{Conc.-Oh}}$	Concentration polarization	$\text{m}\Omega.\text{cm}^2$
R_{slope}	Area specific resistance of the I-V plot of SOFC	$\text{m}\Omega.\text{cm}^2$
I_{lim}	Limiting current density	$\text{A}.\text{cm}^{-2}$
J	Flux of gasses	Flow /area
D_{eff}	Effective diffusivity	$\text{m}^2.\text{sec}^{-1}$
n	Concentration	$\text{mol}.\text{L}^{-1}$
X	Mole fraction	Dimensionless
B_0	Permeability	$\text{Henries}.\text{m}^{-1}$
μ	Viscosity	$\text{Pa}.\text{s}$
γ	Diffusivity	$\text{m}^2.\text{sec}^{-1}$

5.7. References

1. McCabe, Smith and Harriott, Unit Operations of Chemical Engineering. McGraw-Hill Book Co., Singapore. 5th Edition, p. 980-982 (1993).
2. J. P. Lorimer, T. J. Mason, *Chemical Society Review*. **16**, 239-274 (1987).
3. S. V. Ley, C. M. R. Low, Ultrasound in synthesis; Springer, NewYork (1989).
4. K. S. Suslick, *Scientific American*. **260**, 62-68 (1989).
5. G.E. Boyd, A.W. Adamson, L. S. Myers, Jr. *Journal of American Chemical Society*. **69**, 2836-2848 (1947).
6. Duong D. Do, Adsorption Analysis: Equilibria and Kinetics, Imperial College Press, p. 562 (1998).
7. D.M. Ruthven, Principles of Adsorption and Adsorption Process, p. 199, 200 (1984).
8. Josef Toth, Adsorption: Theory, Modeling and Analysis, Surfactant Science Series, Vol. 107, p. 356 (2002).
9. W. Zhu, Advance Inductively Coupled Plasma – Mass Spectrometry Analysis of Rare Earth Elements, Environmental Applications, p. 65 (1999).
10. S.S.E.H. Elnashaie and S.S. Elshishini, Modelling, Simulation and Optimization of Industrial Fixed Bed Catalytic Reactions, Topics in Chemical Engineering, Vol.7, p.146, 153 (1993).
11. A. Leusch, B. Volesky, *Journal of Biotechnology*. **43**, 1-10 (1995).
12. B. Wehrli, S. Ibric, W. Stumm, *Colloids Surface*. **511**, 77-88 (1990).
13. K. Kesenci, R. Say, A. Denizli, *European Polymer Journal*. **38**, 1443-1448 (2002).
14. J. H. Lee, H. Moon, H. W. Lee, J. Kim, J. D. Kim, K. H. Yoon, *Solid State Ionics*. **148**, 15-26 (2002).
15. N.Q. Minh, T. Takahashi, *Science and Technology of Ceramic Fuel Cells*, Elsevier, New York, USA, p. 147-164, 203-204, 207 (1995).

Chapter – 5.6

16. D.W. Dees, T.D. Claar, T.E. Easler, D.C. Fee, F.C. Mrazek, *Journal of the Electrochemical Society*. **134**, 2141–2146 (1987).
17. Horst Scholze, *Glass: Nature, Structure and Properties*, Springer-Verlag, Science (1991).
18. J. W. Kim, A. V. Virkar, K. Z. Fung, K. Mehta, S. C. Singhal, *Journal of the Electrochemical Society*. **146**, 69-78 (1999).
19. H. Itoh, T. Yamamoto, M. Mori, T. Horita, N. Sakai, H. Yokokawa and M. Dokia, *Journal of the Electrochemical Society*. **144**, 641-646 (1997).
20. S.P. Jian, in *Science and Technology of Zirconia V*, S. P. S. Badwal, M. J. Bannister and R. H. J. Hannink (Eds.), Technomic Publishing Company, Lancaster, PA, , p. 819 (1993).
21. S.W. Baek and J. Bae, *International Journal of Hydrogen Energy*. **36**, 689-705 (2011).
22. D. J. L. Brett, A. Atkinson, N. P. Brandon and S. J. Skinner, *Chemical Society Reviews*. **37**, 1568 -1578 (2008).
23. P. Holtappels, U. Vogt and T. Graule, *Advanced Engineering Materials*. **7**, 292-302 (2005).
24. A. Weber and E. I. Tiffée, *Journal of Power Sources*. **127**, 273-283 (2004).
25. H. Koide, Y. Someya, T. Yoshida and T. Maruyama, *Solid State Ionics*. **132**, 253-260 (2000).
26. A. C. Muller, D. Herbstritt and E. I. Tiffée, *Solid State Ionics*. **152-153**, 537-542 (2002).
27. N. M. Sammes, M. Brown, I. W. M. Brown, *Journal of Material Science*. **31**, 6069-6072 (1996).
28. T. Kawada, N. Sakai, H. Yokokawa, M. Dokia, M. Mori, I. Iwata, *Solid State Ionics*. **40**, 402- 406 (1990).
29. S.K. Pratihari, R.N. Basu, S. Mazumdar, H.S. Maiti, *Proceedings of the Solid Oxide Fuel Cells (SOFC VI)*, PV. 99-19, Electrochemical Society, p. 513 (1999).

Chapter – 5.6

30. G. Maggio, I. Ielo, V. Antonucci, N. Giordan, et al, (Eds.), SOFC II, p. 611, The Commission of the European Communities, Luxembourg, (1991).
31. T. Iwata, *Journal of the Electrochemical Society*. **143**, 1521-1525 (1996).
32. S. C. Singhal and K. Kendall, High temperature solid oxide fuel cells: fundamentals, design and applications. U. K, Elsevier (2003).
33. R. N. Basu, In: Basu S, editor. Recent trends in fuel cell science and technology: materials for solid oxide fuel cell. New Delhi/New York: Anamaya Publisher/Springer, p. 284 (2006).
34. I. Bredikhin, V. Sinitsyn, A. Aronin, I. Kuritsyna, S. Bredikhin, *Electrochemical Society Transactions*. **7**, 1533-1540 (2007).
35. Z. Wu and M. Liu, *Solid State Ionics*. **93**, 65-84 (1997).
36. J. S. Newman and C. Tobias. *Journal of the Electrochemical Society*. **109**, 1183-1191 (1962).
37. T. Kenjo, S. Osawa and K. Fujikawa, *Journal of the Electrochemical Society*. **138**, 349-355 (1991).
38. T. Kenjo and M. Nishiya, *Solid State Ionics*. **57**, 295-302 (1992).
39. H. Deng, M. Zhou and B. Abeles, *Solid State Ionics*. **74**, 75- 84 (1994).
40. C.W. Tanner, K. Z. Fung and A. V. Virkar, *Journal of the Electrochemical Society*. **144**, 21-30 (1997).
41. D. W. Dees, U. Balachandran, S.E. Dorris, J.J. Heiberger, C. C. MacPheeters and J. J. Picciolo, *in the Proceedings of 1st International symposium of the Solid Oxide Fuel Cells*, Hollywood, FL, S.C. Singhal (Eds), Electrochemical Society, Pennigton, NJ, p. 317 (1989).
42. D. W. Dees, U. Balachandran, S. E. Dorris, J. J. Heiberger, C. C. MacPheeters and J. J. Picciolo, *in the Proceedings of symposium on Solid Oxide Fuel Cells*, San Francisco, CA, R.E.White and A. J. Appleby (Eds.), Electrochemical Society, Pennigton, NJ, p. 130 (1989).

Chapter – 5.6

43. E. A. Mason and A. P. Malinauskas, *Gas transport in Porous Media: The Dusty Gas Model*, Elsevier, Amsterdam (1983).
44. M. Cassidy, G. Lindsay, K. Kendall. Proc. 1st Eur. SOFC Forum, p. 205– 221 (1994).
45. Z. R. Wang, J. Q. Qian, S. R. Wang, J. D. Cao and T. L. Wen. *Solid State Ionics*. **179**, 1593–1596 (2008).
46. M. Taillades, P. Batocchi, A. Essoumhi, G. Taillades, D. Jones and J. Roziere. *Electrochemical Society Transactions, The Electrochemical Society*. **25**, 2193-2200 (2009).
47. K. Jonoa, S. Suda and M. Hattori. *Electrochemical Society Transactions, The Electrochemical Society*. **7**, 1541-1546 (2007).
48. M. Nagata and H. Iwahara, *Journal of Applied Electrochemistry*. **23**, 275-278 (1993).
49. Eric D. Wachsman and Eric N. Armstrong, *Electrochemical Society Transactions, The Electrochemical Society*. **35**, 1955-1963 (2011).
50. Xingbao Zhua, Zhe Lü, BoWeia, Kongfa Chena, Mingliang Liu, Xiqiang Huang and Wenhui Su, *Journal of Power Sources*. **190**, 326-330 (2009).
51. L.G. J. de Haart, J. Mougín, O. Posdziech, J. Kiviaho, and N. H. Menzler, *Fuel Cells*. **9**, 794–804 (2009).
52. A. McDougall, *Fuel Cells*, MacMillan Press, London (1976).
53. O. Yamamoto, Y. Takeda, N. Imanashi and Y. Sakaki, in the proceedings of the 3rd International Symposium on Solid Oxide Fuel Cells. S.C. Singhal and H. Iwahara, Editors, PV 93-4. The Electrochemical Society Proceedings Series, Pennington, NJ, p.205 (1993).

~

C *HAPTER-6*

Conclusions

&

Future

Outlook

Chapter – 6

CONCLUSIONS

This Chapter intends to highlight the summary of research work performed and presented in a comprehensive manner in previous Chapters. Along with the conclusive statements, significance of the undertaken effort towards the practical application is also aimed to be emphasized.

The concept of ‘electroless technique’ for the synthesis of nickel (Ni) - 8 mol % yttria stabilized zirconia (YSZ) is introduced through the research review. Ni-YSZ cermet is a widely used anode material for solid oxide fuel cell (SOFC) application. However, a number of inadequacies are experienced using such anode which in turn limits the operational era of SOFCs. The intention of the reported investigation is to wipe out the limitations of such Ni-YSZ anode by engaging a novel optimized electroless technique meant for its preparation.

The research outcomes can be broadly classified into two major areas such as:

- 1) Optimization of electroless technique for the generation of functional Ni-YSZ cermet having unique and beneficial features. The developed composite fabricated through uniaxial pressing is characterized through numerous means to demonstrate and evaluate the associated properties.
- 2) Application and evaluation of the developed electroless cermet in planar anode-supported SOFCs.

The major outcomes under aforementioned classifications are presented below in a concise manner.

Development of Anode Cermet by Electroless Technique

Electroless technique comprises of two major steps namely: a) initial sensitization of precursor YSZ particulates involves physically adsorption of active

Chapter – 6

Pd⁰ species on their surface and b) in-situ reduction of Ni from Ni²⁺ solution and its subsequent deposition onto the sensitized YSZ powders. The technique is primarily governed by the effectivity of YSZ sensitization. Based on the present investigation, YSZ sensitization is carried out through two processes viz., a) Ball milling technique and b) High energy ultrasonification.

The composite cermets are fabricated through a) uniaxial pressing and b) tape casting followed by lamination. The prior technique is used for generalized characterization of anodes and the latter technique is used for the corresponding application in single cell fabrication.

Synthesis of electroless Ni-YSZ anode using ball milling sensitization:

1. The prime advantage of such ball milling technique lies in the up scalability and cost effectiveness.
2. The YSZ sensitization is initiated by pouring the required amount of the processed YSZ powders. Such powders are obtained by heat treating the as-received YSZ powder ($d_{50} \sim 0.2 \mu\text{m}$) at 900°C followed by grinding so as to increase the d_{50} value to $\sim 27 \mu\text{m}$. The powders are then poured into polypropylene jar containing redox mixture of palladium chloride and stannous chloride. The jar is then subjected to ball mill using zirconia balls as the milling media for 15 in the range of rotating speed of 25 – 65 rpm.
3. Based on the concept of ball milling theory and experimental adsorption capacity of YSZ, the milling speed is optimized as 45 rpm.
4. Electroless technique with optimized sensitization at 45 rpm tend to generate unique 'core (YSZ) - shell (Ni)' microstructure with discrete distribution of Ni particulates onto YSZ core. Such microstructure enables interconnection among Ni, YSZ and pore phases throughout the cermet matrix. In contrast, dispersed distribution of constituent phases is generated by conventional solid state technique.

5. However, in case of YSZ sensitization carried out at other milling speeds eg. 25 or 65 rpm degenerate shells are produced owing to ineffective sensitization.
6. The most important consequence of electroless technique (via ball mill sensitization) is the significant reduction of upper percolation threshold (corresponding to a conductivity value of 500 Scm^{-1}) of electrical conduction. The threshold is achieved at $\sim 33 \text{ vol\%}$ of Ni in case of the anodes prepared through electroless deposition with YSZ sensitized at an optimum milling speed of 45 rpm. However, the required electrical conductivity value of the anode is found to be fulfilled at 40 vol\% of Ni content when prepared by solid state technique.
7. Owing to the retention of continuous metallic network in the matrix of electroless cermet due to the formation of core-shell microstructure, the onset of electrical conductivity percolation of electroless anode starts at $\sim 10 \text{ vol \%}$ of Ni compared to $> 25 \text{ vol \%}$ Ni required by the conventional cermets.
8. The electrical conduction between 500 and 1000°C is highest for the electroless Ni-YSZ cermet prepared from YSZ sensitized at optimum milling speed of 45 rpm.
9. The activation energy for electrical conduction is found to be the lowest (30.7 kJ.mol^{-1}) for electroless cermet at an optimum milling speed of 45 rpm. This clearly indicates the presence of metallic network continuum throughout the anode matrix. At 45 rpm, the frequency factor of Arrhenius equation is found to be the highest ($\sim 13 \text{ Scm}^{-1}$). The frequency factor is proportional to the number of reaction sites for adsorption of Pd^0 onto YSZ followed by in-situ reduction of Ni^{2+} to Ni^0 during electroless deposition.
10. Finally, the superiority of the developed electroless anode through ball mill sensitization is established over conventional cermet anode which is primarily governed by process optimization during preparation of anodes applicable to SOFC.

Chapter – 6

Synthesis of electroless Ni-YSZ anode using high energy ultrasonic sensitization:

1. The high energy ultrasonification helps in the generation of very high temperatures and pressures at the localized position. This helps in stabilizing the reduced state of the metal (Pd^0) quite effectively compared to the sensitization technique by ball milling.
2. Such power ultrasound assisted Pd^0 adsorption onto YSZ particulates is primarily governed by two major kinetic processes viz., a) external mass transfer and b) intraparticle mass transfer.
3. The entire adsorption regime can be alienated into two portions e.g., a) non-transient adsorption equilibrium (governed by external mass transfer) and b) transient adsorption equilibrium (governed by intra-particle mass transfer).
4. A typical kinetic model comprising of a number of associated parameters is successfully derived based on certain rudimentary assumptions. A correlation among physical adsorption (through Vander Wall interactive forces), mass transport effects, surface and molecular diffusion involving bulk and pore, equilibrium adsorption capacity etc is successfully endeavoured.
5. The developed theoretical model is validated using certain experimental parameters viz. a) particle size of YSZ, b) effect of sonochemical agitation frequency, c) application of external mass transfer phenomena, d) application of intra-particle mass transfer phenomena and e) effectiveness factor for adsorption mechanism etc.
6. Experimental correlation among the above experimental factors with kinetic model establishes the optimized agitation frequency to be 16 kHz which results in effective YSZ sensitization.
7. Such transient equilibrated sensitization process helps to encapsulate YSZ with freshly adsorbed Pd^0 which is evident from the positive value of effectiveness factor of the proposed kinetic model.

8. Systematic studies are performed using ultrasonic assisted electroless anodes synthesized in variable transient equilibration time interval with respect to the characterizations of a) electrical, b) densification, c) microstructural and d) thermal behaviour.
9. Compared to ball mill assisted electroless cermets (33 vol % Ni), the upper percolation threshold for electrical conduction of ultrasonic assisted (at transient equilibration) electroless anodes is reduced to ~ 28 vol% of Ni.
10. Consequently, the activation energy barrier for electronic conduction is significantly less ($\sim 17 \text{ kJmol}^{-1}$) for such ultrasonic assisted (at transient equilibration) electroless anodes.
11. The attainment of transient equilibrium leads to the formation of prominent core-shell structure which makes the electronic path continuous in the cermets thereby increasing the conductivity at lower activation energy.
12. The major superiority of electroless cermet is the usage of lower Ni content (28 vol %) for achieving sufficient electrical conduction. The transient equilibrated electroless anode having only 28 vol % is found to be thermally compatible ($11.40 \times 10^{-6} \text{ K}^{-1}$) with adjacent YSZ electrolyte ($10.85 \times 10^{-6} \text{ K}^{-1}$) which fulfils the primary criteria of an anode to be applicable for SOFC.
13. The superior properties of electroless anode are the direct outcome of the formation of unique microstructure. Such interconnection between YSZ/YSZ, Ni/Ni and YSZ/Ni with the associated pores helps in the formation of patterned intra-anode TPB [Ni/YSZ/fuel (through pores)] within the anode.
14. In contrast to the conventional anodes having conventional TPB (site for electrochemical reactions), electroless anodes are composed of dual TPB sites namely, a) intra-anode (within anode) and b) inter-anode (at anode/electrolyte interface).
15. A mathematical model is proposed for determining intra-anode TPB length for electroless cermets and is experimentally validated as a function of Ni content.

Chapter – 6

16. Experimental studies clearly exhibits that the magnitude of intra-anode TPB length for electroless anode is highest in the Ni content regime of 28-32 vol %.
17. Electroless anode with 28 vol% of Ni having highest TPB length is found to show least electrical conductivity degradation (~ 7 % after 20 redox cycles). In contrast, absence of patterned intra-anode TPB for the conventional cermets results in ~ 23 % degradation in conductance in 20 redox cycle.
18. Experimental studies also demonstrate negligible change (0.7 % /20 redox cycles) in the intra-anode TPB length for electroless anode after 20 redox cycles.
19. Excessive Ni coarsening in the conventional cermet hampers the fuel percolation through the pores and causes ~ 97% degradation in TPB length after 20 redox cycles.
20. Therefore, superior ultrasonification technique enables effective sensitization of YSZ and generates unique microstructure. The related experiments among the physical properties of anode cermets establish the functionality of electroless cermet which is capable of eliminating the drawbacks of Ni-YSZ synthesized through other conventional techniques.

Performance Evaluation of SOFC using Electroless Ni-YSZ

1. Planar SOFCs are fabricated by means of tape casting, lamination and screen printing.
2. The associated resistances of tape-cast electroless anode offered by grains and ambipolar behaviour are found to be least compared to the conventional cermets.
3. The transition from ionic (governed predominantly by YSZ phase) to electronic conductivity is initiated at a considerably low Ni content (~ 20 vol %) in

electroless cermet, whereas, the percolation necessitates more than 25 vol % Ni for the conventional anodes.

4. Electroless anode necessitates 28-32 vol % Ni to satisfy the electrical conductivity criteria required for SOFC application which is at par with the conduction of conventional anode comprising of ~ 40 vol % Ni.
5. Magnitude of anode grain resistance depends on the sintering temperature of anode which is optimized at 1400°C.
6. The functionality of electroless anode is experimentally studied upon fabricating four different types of anode configurations as:
 - a) Total anode structural support using conventional cermet having a tape thickness of 80 μm – ‘Configuration – I’ [CA-1 (anode thickness = 1250 μm) and CA-2 (anode thickness = 1500 μm)]
 - b) Total anode structural support using electroless cermet having a tape thickness of 80 μm and Ni content of 28/32 vol % – ‘Configuration – II’ [28/32 EL-1 (anode thickness = 1250 μm) and 28/32 CA-2 (anode thickness = 1500 μm)]
 - c) Bilayer anode structure (BLA-series) fabricated by combining conventional NiO-YSZ with electroless Ni-YSZ (28 or 32 vol % Ni) having similar tape thickness of 80 μm [28/32 BLA-1/2/3 where 1 = 50 μm , 2 = 120 μm and 3 = 250 μm of electroless layer]. Trilayer anode (TLA) structure composed of conventional anode as the structural support and electroless anode (both 32 and 28 vol % Ni) of 50 μm thicknesses each – ‘Configuration – III’]
 - d) Bilayer AAL with reduced electroless (28 or 32 vol % Ni) tape thickness of 25 μm function as active layer (AAL) laminated onto conventional cermet having a tape thickness of 80 μm – ‘Configuration – IV’ [28/32 BLA-1/2/3/4 where 1 = 15 μm , 2 = 40 μm , 3 = 90 μm and 4 = 140 μm of electroless layer].

Chapter – 6

7. Among the aforementioned four configurations, highest electrical conductivity is obtained from anodes of 28 / 32 AAL- 4 (597 and 644 Scm^{-1} at 800°C) among the respective series.
8. The functionality of layered anode (Configuration–III and IV) is the outcome of the gradation in physical properties viz. compositions of constituent phases, porosity, microstructure, TPB length etc.
9. Tape-cast electroless anodes with unique core (YSZ)-shell (Ni) structure enables easy interconnecting paths among Ni, YSZ and pore phases, thereby enhancing the conductivity with least degradation (~ 6.5 % per 20 redox cycles for Configuration -IV) with subsequent redox cycles. In contrast, dispersed microstructure of conventional matrix causes significant deterioration in electrical conductivity of ~ 26 % per 20 redox cycles for Configuration–I.
10. Electrochemical performances of single cells fabricated with variable anode configurations are studied sequentially with respect to a) thickness of anode-support (in Configuration–I and II), b) thickness of electroless layer (in Configuration –III and IV) and c) NiO reduction kinetics.
11. The experimental findings support the aforementioned superiority of electroless layer as AAL (Configuration-IV), which exhibit the maximum performances (3.7 Acm^{-2} at 800° C and 0.7 V) of single cell.
12. In contrast to the observations from conductivity measurements, cells with 15 μm electroless AAL are found to exhibit the highest electrochemical performance. Such distinction is found to originate from the variation in flow-pattern of the reactant gasses followed during charge conduction and electro anodic reactions.
13. The experimental upshot of electrochemical reactions are correlated with a) optical microstructures, b) elemental mapping, c) NiO reduction equilibrium, d) pore-size distribution in anodes, e) effect of moisture in the fuel, f) variation in oxidant type etc.

14. The influence of polarization/resistive factors is also studied in terms of both mathematic approach and electrochemical impedance measurements.

Therefore, the developed layered anode with gradation in physical properties and electroless Ni-YSZ as the active layer could act as a potential high performance anode and possibly could emerge as an alternate anode for solid oxide fuel cell (SOFC) application. The anode cermet prepared through novel electroless technique is established to bear the functionalities, owing to which innumerable shortcomings could be efficiently wiped out.

FUTURE OUTLOOK

Solid oxide fuel cells offer valuable contribution to future power generation facilities. They improve the flexibility and increase the options for many applications, such as distributed power, vehicle propulsion, and portable devices. Their main property is the high electrical efficiency compared to other energy conversion devices. Both the low temperature and the high temperature fuel cells have their advantages and disadvantages depending on the application. In real scenario, there is no such device as the ideal fuel cell for any applications. The best suited fuel cell depends on the requirements of the application. Not only the fuel cell itself but the entire system has to be under investigation when customising fuel cells for specific purposes.

In this context, the Ni-YSZ anode prepared through novel electroless technique is capable of diminishing a number of shortcomings associated with conventional anode cermets. Affirmative impact could be drawn out from higher volume efficient FC stacks fabricated using such functional electroless anodes. According to the outcomes of present research, electroless cermets bear the competence of multi-configurational application in the form of: a) anode-support structure, b) multilayered anode, c) anode active layer etc. which unlock its horizon for large scale application. Additionally, for further reduction in the deterioration of the cell performance, gradation could be implanted within electroless layers in terms of porosity, Ni content etc. to make it applicable for anode-support structure in multilayer configuration.

Electroless technique may also be implemented for synthesizing other cermet composites e.g. Ni-CGO, Ni-TiO₂-ZrO₂, Ni-YDC (yttria doped ceria) etc which are capable of functioning with numerous fuel gases e.g. methane, syngas, carbon monoxide etc. Through the optimized electroless processing technique, tailoring of

Chapter – 6

microstructure is expected to be feasible for such newer anodes which would help to enhance the associated endurance of multi dimensional fuel cells.

Therefore, further research and development regarding the present electroless process could illuminate the fuel cell exploration. In future these new generation SOFCs compete when capital costs can be reduced due to technological advancement and increases in production volumes. Such clean energy conversion system is expected to prevail over and furnish the 'Earth' a newer start.

~

*Reprint of
Publications*



Available online at www.sciencedirect.com

SciVerse ScienceDirect

journal homepage: www.elsevier.com/locate/ijhe

Engineered anode structure for enhanced electrochemical performance of anode-supported planar solid oxide fuel cell

Madhumita Mukhopadhyay, Jayanta Mukhopadhyay, Abhijit Das Sharma, Rajendra N. Basu*

Fuel Cell and Battery Division, CSIR - Central Glass and Ceramic Research Institute, Kolkata 700 032, India

ARTICLE INFO

Article history:

Received 30 August 2011

Received in revised form

14 October 2011

Accepted 17 October 2011

Available online 12 November 2011

Keywords:

Layered SOFC anode

Core-shell electroless anode

Pore-size distribution

High cell performance

Cell polarization

Cell degradation

ABSTRACT

A novel approach of fabricating SOFC anode comprising graded compositions in constituent phases having layer wise microstructural variation is reported. Such anode encompasses conventional NiO–YSZ (40 vol% Ni) with higher porosity at the fuel inlet side and Ni–YSZ electroless cermet (28–32 vol% Ni) with less porosity toward the electrolyte. Microstructures and thicknesses of the bilayer anodes (BLA) are varied sequentially from 50 to 250 μm for better thermal compatibility and cell performance. Significant augmentation in performance (3.5 A cm^{-2} at 800°C , 0.7 V) is obtained with engineered trilayer anode (TLA) having conventional anode support in conjunction with layers of electroless cermet each of $50 \mu\text{m}$ having 28 and 32 vol% Ni. Engineered TLA accounts for substantial reduction both in cell polarization (ohmic ASR: $78 \text{ m}\Omega \text{ cm}^2$ versus $2835 \text{ m}\Omega \text{ cm}^2$; cell impedance: $0.35 \Omega \text{ cm}^2$ versus $0.9 \Omega \text{ cm}^2$) and degradation rate ($76 \mu\text{V h}^{-1}$ versus $219 \mu\text{V h}^{-1}$) compared to cells fabricated with conventional cermet.

Copyright © 2011, Hydrogen Energy Publications, LLC. Published by Elsevier Ltd. All rights reserved.

1. Introduction

Performance of anode-supported planar SOFC is mainly dependent on thickness, electronic conductivity, interconnected porosity and electrocatalytic activity of the anode [1–4]. Control of the anode microstructure through appropriate processing techniques can play a major role toward its functional activity in a single cell. Concentration and activation polarization resistances of the cell are highly related with such porous anode. Designing and controlling the anode microstructure is therefore important to satisfy the basic requirements of extending triple phase boundary (TPB) and appropriate gas diffusion paths [5,6]. One of the major challenges of SOFC is the long term stability of anode during high temperature operation. Conventional nickel

(Ni) - 8 mol% yttria stabilized zirconia (YSZ) anode is susceptible to long term degradation which can be ascribed due to the agglomeration of Ni particles at high operating temperature ($800\text{--}1000^\circ\text{C}$) [7]. It is believed that ohmic losses occurring across the electrical contacts or polarization losses at the TPB increases the local temperature and causes agglomeration of Ni phases [7]. Werber [8] reported that, insufficient removal of water vapor that formed during electrochemical reaction during high temperature operation of single cell also resulted in Ni oxidation and caused Ni agglomeration. In addition, such conventional anode cermet suffers from thermal incompatibility with other cell components due to the presence of higher Ni content (~ 40 vol% Ni) [9–12]. An electroless technique for the preparation of Ni–YSZ anode has been reported in our earlier

* Corresponding author. Tel.: +91 33 2473 3469x3507; fax: +91 33 2473 0957.

E-mail addresses: rnbasu@cgcri.res.in, rajenbasu54@gmail.com (R.N. Basu).

0360-3199/\$ – see front matter Copyright © 2011, Hydrogen Energy Publications, LLC. Published by Elsevier Ltd. All rights reserved.
doi:10.1016/j.ijhydene.2011.10.077

publications which requires only ~28 vol% of Ni for satisfying the required electrical conductivity for SOFC operation [13–17]. The electroless anode thus developed has a core (YSZ)–shell (Ni) microstructure. Such unique microstructure enables interconnecting network of Ni, YSZ and pores throughout the cermet matrix. Under the optimized condition, fine Ni-particulates are produced in-situ in the electroless bath and deposited on YSZ in a discrete manner so as to generate a patterned intra-anode TPB network within the cermet anode [17].

In order to improve cell performance, incorporation of thin anode functional/active layer (AFL/AAL) between the anode and electrolyte is a standard practice [18]. Such active layers produce an extended TPB length at the interface causing effective electrochemical reactions and hence, enhancement in performance of the cell [19,20]. The microstructural phase distribution of Ni and YSZ in such active layer needs to be homogenous and the contacts between Ni/YSZ should be made coherent to facilitate the electrochemical oxidation of fuel. In order to achieve the homogenous microstructure with a continuum between Ni–Ni, YSZ–YSZ and the interconnected pores, the AAL needs to be processed precisely. The basic differences between the anode support and active layer are in the grain sizes, the interconnectivity, interfacial contact lengths and percentage porosity of the contributing components. Such differences in the conventional anode support and the active layer may also affect the overall charge transfer reaction occurring at the anode active layer/electrolyte interfaces and distributed to the bulk anode through extended TPB. An alternate approach is to use a layered anode structure with variation in Ni content, porosity and particle size of the constituent phases [6,21–23]. Owing to the presence of higher interfacial contacts between Ni/YSZ/pore at anode–electrolyte junction, the smaller pores effectively enhance the rate of charge transfer reaction. This reaction is extended toward the bulk anode through the available TPB sites. In layered anode, while the smaller pores at the anode/electrolyte interface offer large resistance to the gas diffusion in a thick anode, the larger pores at the anode support helps in easy percolation of the fuel. Similarly, the Ni content needs to be higher at the fuel inlet for higher catalytic activity. The reduction of Ni content along the thicknesses of the anode layers reduces the thermal mismatch at the anode/electrolyte interface. The layered anode investigated by other group of researchers [20–23] is devoid of microstructural variation as all the layers are being synthesized using a single technique. Therefore, the variation of the constituent phases and the microstructural control thereof, is necessary to be adjusted precisely so that the electrical, electrochemical and catalytic properties of anode are not affected [24].

In the present investigation, anode-supported planar SOFC having an engineered layered anode structure is fabricated. The layer anode comprises of electroless Ni–YSZ anode in conjugation with conventional anode for better electrochemical activity, thermal compatibility and cell performance. The present work describes the development of functional layered anode having variation in porosity, Ni content, layer thickness, Ni/YSZ and pore phase distribution through the entire regime of anode composite. The influence

of variation in anode porosity on the overall cell performance is studied in detail. Attempt has also been made to correlate ohmic area specific resistance (ASR) and impedance spectra of single cell with layered anode configuration. Long term performance of single cells having varied anode configurations are also investigated along with the rate of cell degradation.

2. Experimental

SOFC anode powders were prepared by two techniques viz. a) conventional solid state route (NiO–YSZ) and b) electroless technique (Ni–YSZ). Ni–YSZ anode powders prepared by electroless technique involve an initial sensitization of YSZ precursor by the adsorption of metallic Pd⁰ species. Pd⁰ was produced in-situ in the redox bath of Pd²⁺ and Sn²⁺. Adsorbed Pd⁰ onto YSZ act as the catalytic sites for the reduction of Ni²⁺ to Ni in the electroless bath containing nickel nitrate salt solution and sensitized YSZ. The reduction of Ni²⁺ to Ni⁰ was carried out by addition of hydrazine hydrate as a reducing agent. Optimized processing conditions help in the discrete deposition of fine Ni-particulates onto YSZ. The detailed process is described in our earlier publications [13,14]. For single cell fabrication, simple and up-scalable processing techniques viz. tape casting and screen printing were used [25,26]. Under the present investigation, three different categories of single cells having distinguished anode configurations were fabricated and are summarized in Table 1. Conventional NiO–YSZ tapes (~40 vol% Ni) with higher porosity were used toward the fuel inlet for better gas diffusion and current collection. Electroless anode tape(s) with much lower Ni content (~32 vol%) and porosity compared to the conventional cermet was placed onto the base support structure. Finally, the third layer(s) of electroless anode having still lower Ni content (~28 vol%) and porosity was placed adjacent to the YSZ electrolyte to fabricate the half cell with a trilayered anode (TLA). Similarly, half cells having bilayered anode (BLA) were fabricated using conventional NiO–YSZ with 40% of Ni as the base support and electroless Ni–YSZ with either 28 or 32 vol% Ni as electrochemically active layer. The thickness of electroless anode layers having different Ni content was varied in the range of 50–250 μm to study its effect on the cell performance. Pore-size distribution of the reduced anodes (800 °C for 10 h at Ar: H₂ – 80:20) of various configurations was determined by mercury porosimetry (Quantachrome Poremaster 60, Florida, USA). Fabrication of single cells involved an initial tape casting of anodes [conventional/electroless] of various thickness and 20 μm thin layer of YSZ electrolyte. The tapes of conventional anode (40 vol% Ni) and two different types of electroless Ni–YSZ (28 and 32 vol% Ni) anodes were cast separately using graphite based porosifier. This was followed by room temperature lamination of the anode tapes together with the electrolyte tape on top to have different configurations of half cells (green monoliths) as shown in the schematic of Table 1. The green laminated blocks were co-sintered at around 1400 °C for 4–6 h with an intermediate binder burnout step at 1000 °C for 4 h (with a very slow heating rate of 1 °C/min to remove

the organics completely) so as to obtain the sintered half cell. The sintered half cells were then screen printed with lanthanum strontium manganite (LSM) – YSZ (50:50) as cathode active layer and LSM as cathode. The prepared blocks were then co-sintered at 1150 °C for 2 h to obtain the single cell [25–28]. Single cells (~16 mm diameter), thus fabricated, were tested for electrochemical performance evaluation. The compartment sealing was carried out using high temperature glass sealants after melting at ~1000 °C. The whole assembly was then brought down to 800 °C and the electrochemical activity was measured with hydrogen as fuel and oxygen/air as the oxidant in the temperature range of 700–800 °C under applied electronic loads (Amrel, USA). Long term electrochemical performances of single cells were evaluated upto 2000 h using hydrogen (with 3% moisture) as fuel and oxygen as oxidant in the temperature range of 700–800 °C. The electrochemical impedance spectroscopy (EIS) measurements of the anode-supported single cells having conventional and optimized layered anode configuration were carried out using an Impedance Analyzer [Solartron S1 1287] with an applied AC voltage of 100 mV in the temperature range of 700–800 °C in an increment of 50 °C. The spectrum was captured for the full range of the frequency; ($10^{-1} \leq f \leq 10^6$ Hz). The electrochemical performances were correlated with the microstructures using a high resolution optical microscope (Olympus GX 71, Japan) and field emission scanning electron microscope [FESEM] (Gemini Supra 35, Zeiss). Coefficient of thermal expansion (CTE) was measured in an inert atmosphere of argon using a high temperature dilatometer (NETZSCH, Model DIL 402 C).

3. Results & discussion


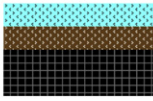
3.1. Functionality of electroless Ni–YSZ in bilayered anode (BLA)

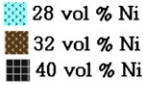
3.1.1. Introducing electroless cermet in bilayer anode (BLA) configuration

Incorporation of anode active layers (5–15 μm) between electrolyte and conventional anode support is a common practice to enhance the rate of electrochemical reaction [18,29,30]. Usually, conventional solid state mixing (of NiO and YSZ) is followed to prepare both the anode support and AAL. Hence, a dispersed distribution of Ni and YSZ phases is reported throughout the anode matrix by the other group of researchers. Marginal enhancement in cell performance is obtained upon using such conventional AAL compared to that with only conventional anode support without such active layers [18,25,29]. Relatively denser microstructure of conventional AAL with finer grains of Ni and YSZ phases tend to accelerate the anodic electrochemical reaction at the conventional TPBs adjacent to the AAL/electrolyte interface and accounts for such performance increment [18,19].

In the present investigation, efforts have been made to replace such conventional AAL by layered anode structure with layer wise variation in contents of the constituent phases viz. Ni, YSZ and pores. A comprehensive detail of anode configurations fabricated in the present study is given in Table 1. Schematic in Fig. 1 shows that, the conventional anode with higher Ni content (40 vol%), having high porosity is placed toward the fuel inlet side as the support structure and

Table 1 – Different anode configurations in the fabricated cells.

Anode composition	Ni content (vol %)		Thickness of electroless anode layer (μm)	Sample ID	Anode Configuration
	Conventional anode	Electroless anode			
Conventional anode	40	---	---	CA	 Conventional Anode support
Conventional anode / Electroless anode (28 or 32 vol % Ni)	40	28	250	28 BLA -3	} Electroless layer Conventional Anode support OR Electroless layer Conventional Anode support
			120	28 BLA -2	
			50	28 BLA -1	
	40	32	250	32BLA -3	
			120	32 BLA -2	
			50	32BLA -1	
Conventional anode / Electroless anode (32 vol % Ni) / Electroless anode (28 vol % Ni)	40	32 and 28	50 [each Electroless layer]	TLA	 Electroless layer Conventional Anode support



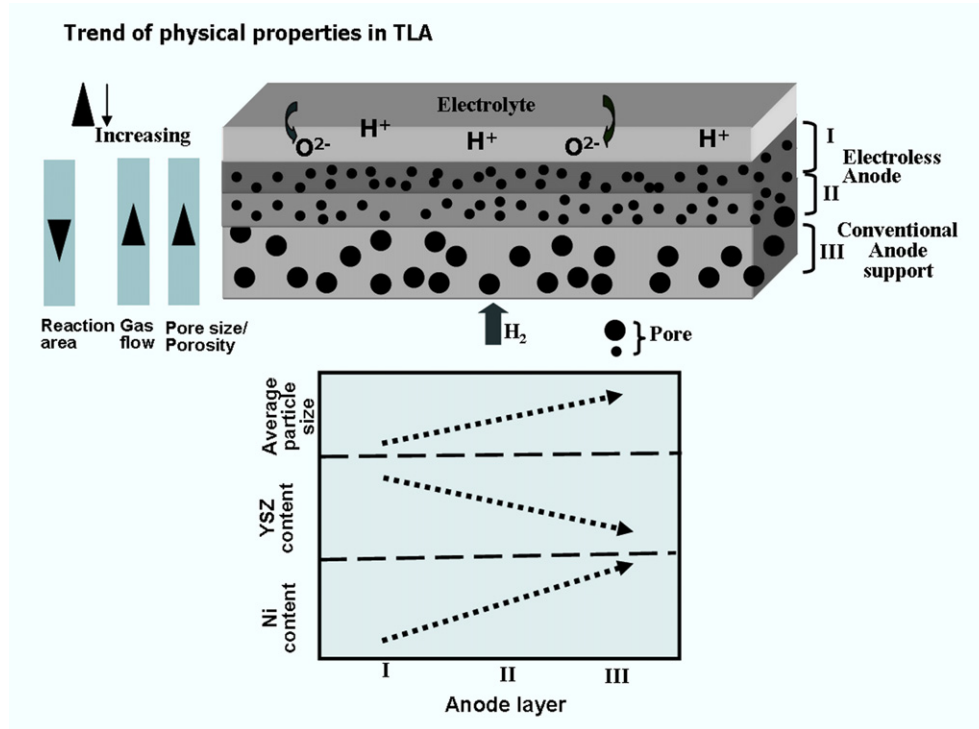


Fig. 1 – Schematic representation of trilayered anode (TLA) configuration with gradation in physical properties.

electroless anode (having 28 and 32 vol% of Ni) with smaller pores and lesser porosity is placed adjacent to the electrolyte.

The performances of single cells having such bilayered anode configuration with varied Ni content (28 BLA-3 and 32

BLA-3) are shown in Fig. 2a and b. It can be observed that, single cells with anodes of 28 BLA-3 configurations containing only 28 vol% Ni exhibits a current density of $\sim 1.8 \text{ A cm}^{-2}$ at 800°C , 0.7 V and is found to be marginally better compared to

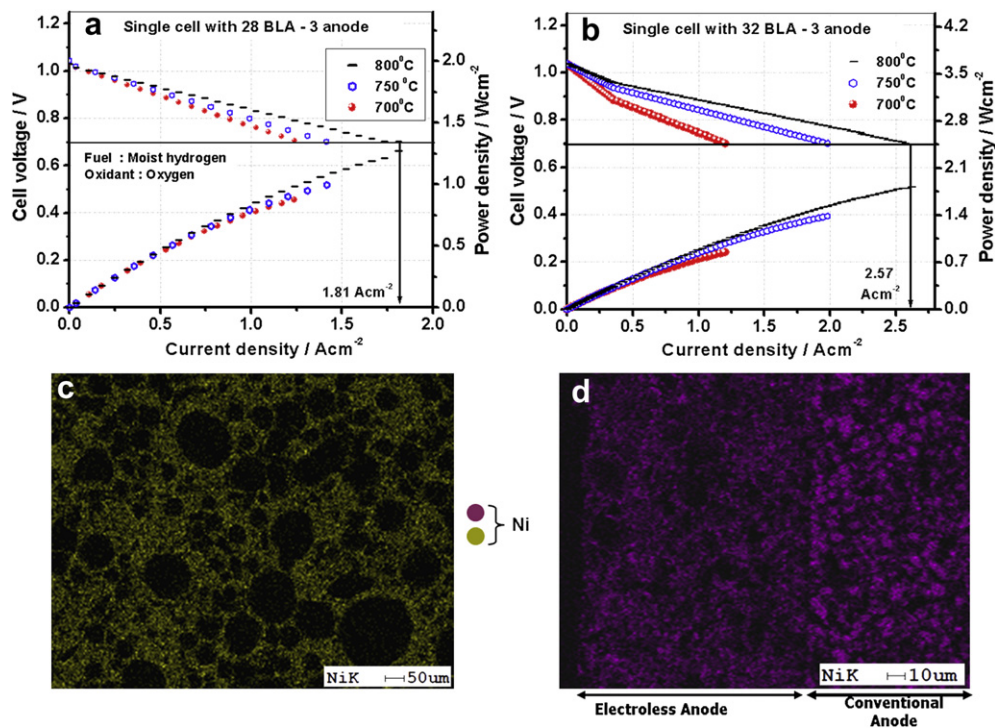


Fig. 2 – Electrochemical performances of single cell fabricated with anode of: a) 28 BLA-3 and b) 32 BLA-3 configurations; elemental Ni mapping of, c) electroless anode and d) BLA-series (cross-sectional view).

that of the cells having conventional anodes (CA configuration). However, a significant enhancement in cell performance of $\sim 2.57 \text{ A cm}^{-2}$ at 800°C , 0.7 V is observed upon increasing Ni content of electroless anode to 32 vol% [32 BLA-3] as shown in Fig. 2b. It is worth mentioning here that the thickness of electroless anode layers in both the cases is $\sim 250 \mu\text{m}$ which is about 25 times higher than a typical conventional AAL thickness ($\sim 10\text{--}15 \mu\text{m}$).

Owing to the presence of higher porosity in conventional anode support placed at the fuel inlet side, gas transportation is facilitated. Therefore, in such layered anode structure, conventional anode having 40 vol% of Ni primarily performs the function of effective gas distribution and current collection. Optimized processing technique during electroless deposition of Ni generates core (YSZ)–shell (Ni) microstructure as shown in the Ni mapping of Fig. 2c. This unique microstructure enables the interconnection among Ni, YSZ and pores throughout the matrix and thereby ensures easy transportation of electrons (through Ni–Ni continuity), O^{2-} ion (through YSZ–YSZ continuity) and gases (through interconnected pores) respectively. Due to such unique microstructure, active TPB sites are produced in-situ within the anode cermet and are known as intra-anode TPBs [17]. Patterned intra-anode TPB of electroless cermet accelerates the progression of charge transfer reaction ($\text{O}_{\text{ad,YSZ}}^{2-}$ to $\text{O}_{\text{ad,Ni}}^{2-}$) from anode–electrolyte interface to the bulk anode and hence makes the layer electrochemically active [17].

The difference in Ni content from the fuel inlet (conventional anode) to the anode/electrolyte interface (electroless anode) is clearly visible from the intensity variation in the Ni mapping of Fig. 2d. Therefore, use of conventional anode in conjugation with electroless cermet in such layered structure helps in engineering the microstructures across the anode. This would fulfill the requirements of effective gas transport as well as electrochemical activity over the entire anode surface. Optimization of the electroless layer thickness is a crucial parameter and is expected to enhance the cell performance with effective fuel diffusion followed by the electrochemical charge transfer reaction and is discussed in the subsequent sections.

3.1.2. Effect of thickness variation and pore-size distribution of electroless anode on cell performance

Variation of cell performance as a function of thicknesses and Ni content of electroless cermet in BLA-series is shown in Fig. 3. It is observed that for a particular thickness of the electroless anode layer, cell performance increases with increase in Ni content from 28 to 32 vol%. This can be attributed to the fact that usage of higher Ni content provides better electronic conductive path through the matrix and increases the rate of electrochemical activity at the anode/electrolyte interface. However, increasing Ni content beyond a critical limit is expected to create thermal incompatibility with the adjacent YSZ electrolyte and also facilitates the Ni coarsening at high temperature operation of the cell.

Fig. 3 also shows that performance of the single cell increases with reduction in electroless anode layer thickness from $250 \mu\text{m}$ to $50 \mu\text{m}$ for the electroless layer with a definite vol% of Ni. In the bilayer anode structure, electroless cermet is responsible for the progression of electrochemical anodic

reactions. The electrochemical oxidation of the fuel (H_2) is primarily governed by three major processes viz. gas diffusion, adsorption of electroactive reactant species and charge transfer reaction. All the aforementioned steps are dependant on the concentration of the available catalytic Ni sites which act as the primary adsorbent [17,28,31]. The charge transfer of oxide ion (O^{2-}) from YSZ to Ni surface occurs instantaneously at the anode/electrolyte interface through surface adsorption mechanism. Presence of patterned intra-anode TPBs along with the conventional one in the electroless cermet helps in the extension of charge transfer reaction from anode–electrolyte interface to the bulk anode [17]. In accordance with the kinetic theory, the rate of charge transfer reaction accelerates with the reduction in anode layer thickness. Thus, upon decreasing the electroless anode thickness from 250 to $50 \mu\text{m}$, electrochemical performance of the cell (at 800°C and 0.7 V) increases from 1.81 A cm^{-2} (28 BLA-3) to 2.54 A cm^{-2} (28 BLA-1) in the case of 28-BLA series. Similarly, for 32-BLA series, reduction in the thickness of electroless layer enhances the single cell performance from 2.57 A cm^{-2} (32 BLA-3) to 3.3 A cm^{-2} (32 BLA-1) under similar experimental condition. The rate of formation and consumption of $\text{O}_{\text{ad,Ni}}/\text{O}_{\text{ad,YSZ}}$ and $\text{H}_{\text{ad,Ni}}/\text{H}_{\text{ad,YSZ}}$ species during electrochemical reaction at anode/YSZ interface is maintained at equilibrium upon reducing the thickness of electroless layer. From the

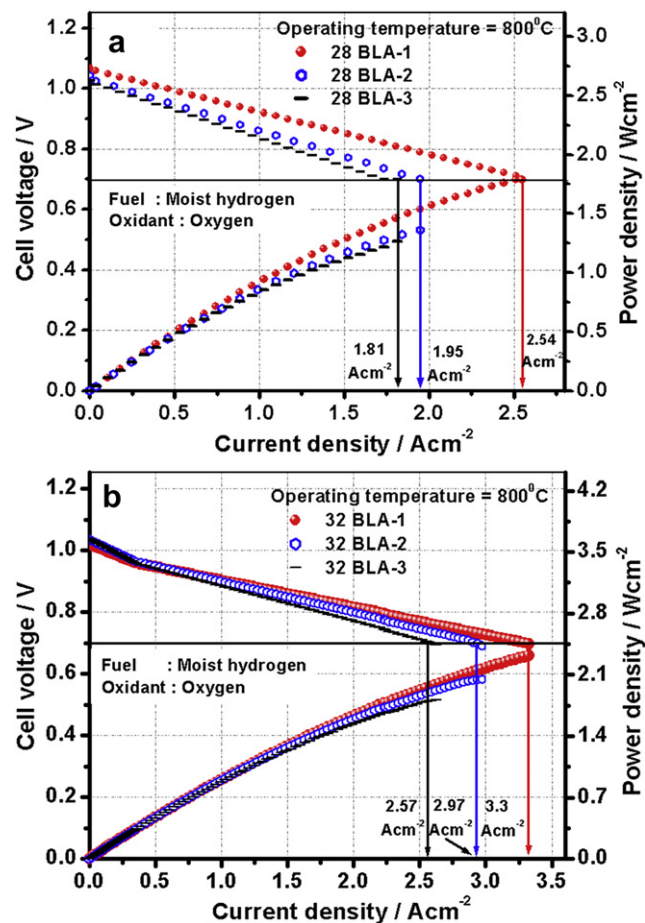


Fig. 3 – Electrochemical performances of single cells as a function of electroless anode layer thickness with anodes of configuration: a) 28 BLA and b) 32 BLA.

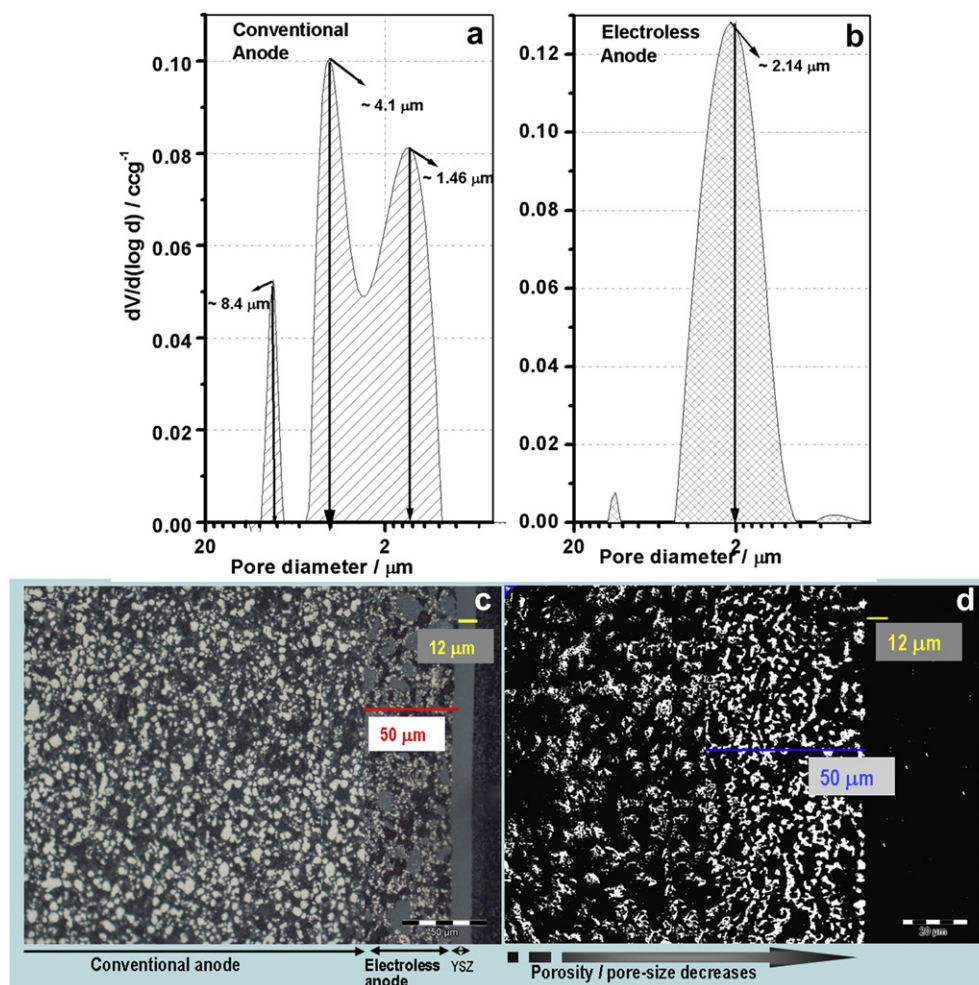


Fig. 4 – Pore-size distribution of Ni–YSZ anode cermets prepared by: a) conventional and b) electroless technique; c) Optical microstructure and d) binarized image (at higher magnification) of single cell with anode of BLA-1 after electrochemical measurement.

electrochemical reaction mechanisms [31], it is understood that an optimum concentration of Ni sites is essential for anodic electrochemical reactions. Though reduction in electroless layer thickness in BLA configuration helps in improving the overall electrochemical activity, the optimum thickness of electroless layer under this present investigation is found to be 50 μm . Therefore, the interfacial concentration polarization of BLA-series reduces with enhanced cell performances at an optimum thickness of 50 μm . However, if the thickness of the electroless layer is further reduced, the electrochemical zone becomes ineffective in providing active Ni sites for effective reaction of $\text{O}_{\text{ad,Ni}}/\text{O}_{\text{ad,YSZ}}$ species and thereby resists the charge transfer reaction.

The contribution of bilayer anode structure toward the enhancement of cell performance can also be correlated with the pore-size distribution of the respective anodes (Fig. 4). As shown in Fig. 4a, the conventional anode exhibits multimodal pore-size distribution with peak pore diameters varying in the range of ~ 1.5 – 8.4 μm . Such wider pore distribution helps in easy gas diffusion through the anode thereby accelerating the fuel percolation and is subsequently followed by the catalytic oxidation. Large pores with multimodal distribution in

conventional anode (Fig. 4a) also result in restricting the extended interfacial contacts required for the necessary electrochemical reactions. On the other hand, electroless anode shows narrow unimodal distribution with peak pore diameter of ~ 2.14 μm (Fig. 4b). Negligible open pores are found in the region of larger pore diameter for such cermets. Such distribution with relatively low peak pore diameter ensures better capillary action for fuel fed across the anode and enhances the electrochemical reaction [28]. The variation in porosity in such layered anode is also visualized from the cross-sectional micrograph of a cell (Fig. 4c and d) operated at 800 $^{\circ}\text{C}$. Therefore, combination of electroless and conventional cermet in the bilayer anode fulfills the requirement of both gas transportation and electrochemical activity and hence enhances the cell performance.

3.2. Functionality of electroless Ni–YSZ in trilayered anode (TLA)

Functionality of bilayer anode structure is discussed in details in the above sections. Tailoring of electroless layer thickness shows that, cells with anodes of either 28 BLA-1 and 32 BLA-1

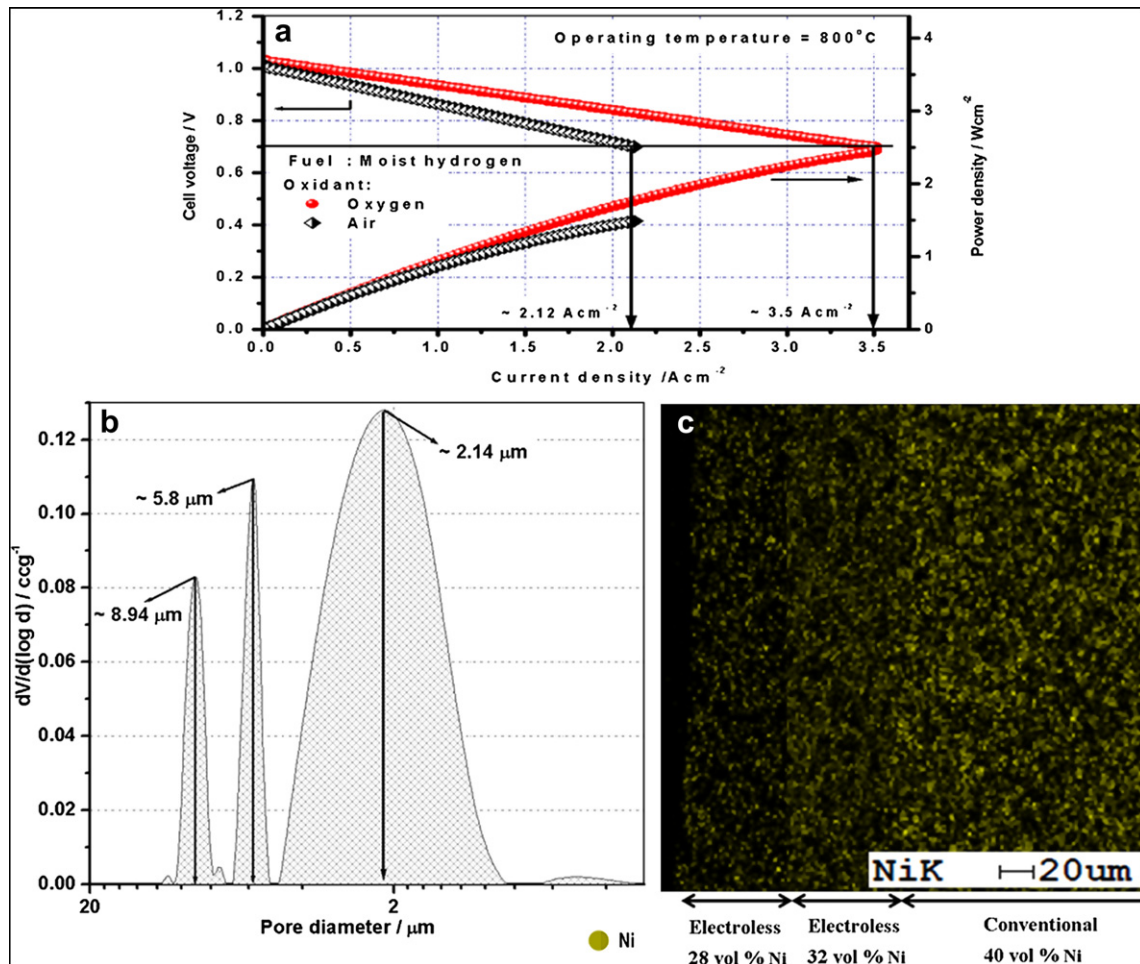


Fig. 5 – a) Electrochemical performances of single cell fabricated with functional trilayer anode (TLA) using oxygen and air as oxidant, b) pore-size distribution of TLA and c) FESEM micrograph for Ni mapping of TLA.

(with 50 μm electroless layer) shows highest performance of 2.54 and 3.3 A cm⁻² at 800 °C and 0.7 V respectively. In the present investigation, efforts are made regarding the sequential incorporation of 50 μm electroless layers of 28 BLA-1, 32 BLA-1 and conventional anode support to fabricate a functional trilayered anode (TLA) with layer wise variation in properties (Table 1, Fig. 1). In the TLA structure, Ni content is reduced linearly from 40 vol% at fuel inlet side to 28 vol% at the electrolyte side. Electrochemical performance of single cell fabricated with TLA exhibits highest current density of 3.5 A cm⁻² at 800 °C and 0.7 V as shown in Fig. 5a. The electrochemical performance of the cell with TLA is found to be 2.12 A cm⁻² compared to 0.88 A cm⁻² for the cells with CA at 800 °C using air as an oxidant. Single cells having TLA maintains thermal compatibility with the YSZ electrolyte because of the presence of lower Ni content (28 vol%) adjacent to the electrolyte layer. In addition, presence of lower Ni at the anode/electrolyte interface is also found to be effective in propagating the anodic reaction with reduced coarsening rate. The functionality of such developed multilayer anode is also evident from the pore-size distribution of the corresponding anode structure as shown in Fig. 5b. The peak pore diameters of TLA are found to be at 8.94, 5.8 and 2.14 μm respectively. It

can be observed from Fig. 5b, Fig. 4a and b, that larger pores in the range of 5–9 μm correspond to the conventional anode and unimodal distribution of pores with peak pore diameter of 2.14 μm is identified pore-size of the electroless cermet. The combined effect of these larger and smaller pores is therefore expected to perform the dual function of fuel transportation and electrochemical anodic reactions. Fig. 5c shows the FESEM microstructure for elemental Ni mapping of the fabricated TLA. Variation in Ni content is clearly visualized from the intensity of Ni mapping in the concerned anode zones. The CTE of the composite anode having the TLA configuration (CTE = 11.10 × 10⁻⁶ K⁻¹) is found to be lower than BLA configuration (28 BLA-3) having CTE value of 11.43 × 10⁻⁶ K⁻¹. Therefore, layered anode of TLA configuration is thermally compatible with the YSZ electrolyte (CTE = 10.8 × 10⁻⁶ K⁻¹).

3.3. Effect of anode configuration on cell polarizations

Dependence of ohmic polarization i.e. area specific resistance (ASR) of the single cell on anode configuration is represented in Fig. 6. The ASR of single cells is calculated from the linear portion of slope of the current–voltage (*I*–*V*) curve. Because of the superior electrochemical activity, cells fabricated with

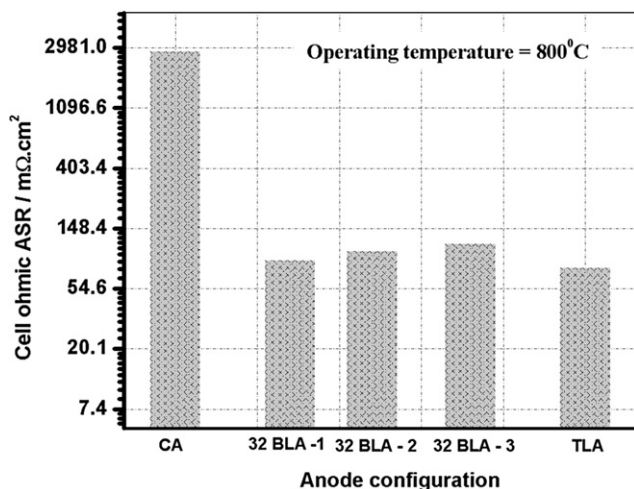


Fig. 6 – Variation in measured cell ohmic ASR values as a function of anode configuration.

anode configuration of 32 BLA-series are investigated for ASR comparison. Single cells with 32 BLA-series is found to exhibit significant low ohmic ASR in the range of ~ 116 – 88 mΩ cm² in comparison to the cells fabricated with CA (~ 2835 mΩ cm²) at 800 °C. This establishes the fact that bilayer anode with effective fuel oxidation (through conventional anode) and electrochemical reactions (through electroless anode) reduces the overall ohmic polarization of the cell. Reduction in electroless anode thickness from 250 to 50 μm effectively accelerate the charge transfer rate of $O_{ad,YSZ}^{2-}$ to $O_{ad,Ni}^{2-}$ thereby causing a further reduction in ohmic ASR from 116 (32 BLA-3) to 88 (32 BLA-1) mΩ cm² at 800 °C. A sharp decrease of $\sim 97\%$ in ASR is observed from single cells upon incorporating layered anode of 32 BLA-1 and $\sim 25\%$ increment is found in the ASR value with the variation of the electroless layer thickness from 50 to 250 μm. Such correlation among ASR (R_{cell}) values and thickness of electroless layer is also justified mathematically from Eq. (1).

$$R_{cell} = \rho_{BLA} l_{BLA} + R_{constant} \quad (1)$$

where, $R_{constant} = R_{electrolyte} + (R_{cathode} + R_{CAL}) + R_{contact}$ and ' ρ and l ' are the resistivity per unit area and thickness of

concerned layers corresponding to variable configurations respectively.

The Eq. (1) implies that R_{cell} decreases upon reduction in l_{BLA} which in turn correlates the enhancement in the cell performance with reduction in electroless layers thickness in BLA configuration as also observed experimentally (Figs. 3 and 6). Ohmic polarization is found to further reduce by $\sim 12\%$ for cells fabricated with TLA compared to 32 BLA-1. Combination of electroless layers having 32 and 28 vol% Ni accounts for the acceleration of electrochemical reaction and decrease the rate of Ni coarsening at the anode/electrolyte interface. Consequently, due to systematic variation of Ni content, porosity and microstructure, the cell ASR is found to be reduced to ~ 78 mΩ cm² at 800 °C for single cells fabricated with TLA.

Apart from the ohmic cell ASR, the temperature dependant overall cell polarization for the optimized anode formulation i.e. TLA obtained from the electrochemical impedance spectra (EIS) is given in Fig. 7 along with the polarization of single cell fabricated with CA. Irrespective of the anode configuration, with increase in operating temperature from 700 to 800 °C, the arcs are found to be depressed showing lower cell polarization resistances. This could be explained on the basis that, the rate of electrochemical reaction is accelerated with rise in temperature which in turn reduces the energy barrier for the corresponding rate determined steps which is represented by each arc. It could also be noticed that, at 800 °C, the system experiences minimum resistance which is illustrated by coalescence of three arcs into a single one. The vivid transformation of the nature of impedance plots from Fig. 7a to b could be accounted specifically for the variation of anode configuration, since; the other components of the single cell are kept identical. Cells with conventional anodes show the overall cell polarization of ~ 0.9 Ω cm² at 800 °C (Fig. 7a), which is substantially reduced to ~ 0.35 Ω cm² for cells with TLA. Formation of extended TPBs [17] within electroless anode and anode/electrolyte interface accelerates the rate of electrochemical reaction for cells with anodes of TLA configuration.

3.4. Effect of anode configuration on cell degradation

Fig. 8a and b shows the results of electrochemical endurance test on single cells having different anode configurations (CA,

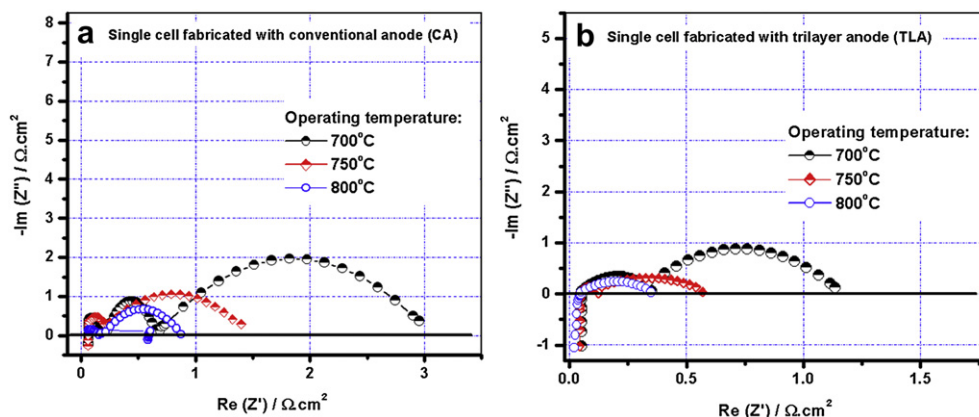


Fig. 7 – Temperature dependent impedance spectra of single cell fabricated with: a) CA and b) TLA.

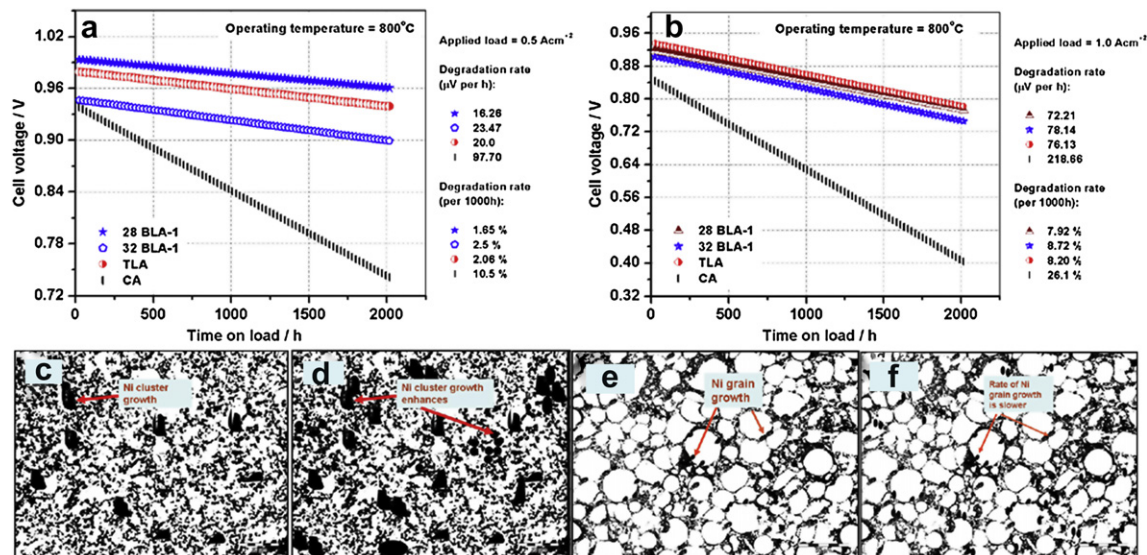


Fig. 8 – Comparative endurance test of single cell with conventional and multilayered anodes for 2000 h with experimental degradation rate at: a) 0.5 A cm⁻² & b) 1.0 A cm⁻² and respective binerized images of conventional anodes (c and d) and electroless cermet (e and f).

28 BLA-1, 32 BLA-1 and TLA) carried out at 800 °C for a period of 2000 h under a constant load of 0.5 A cm⁻² and 1.0 A cm⁻². It is evident from the figure that, among all, the cells with 28 BLA-1 exhibits the least degradation rate ($\sim 16 \mu\text{V h}^{-1}$ and $\sim 72 \mu\text{V h}^{-1}$ at 0.5 and 1.0 A cm⁻² which corresponds to 1.65% and 7.92% 1000 h⁻¹). However, single cell with 32 BLA-1 show slightly higher degradation rates of $\sim 23.5 \mu\text{V h}^{-1}$ (2.5% 1000 h⁻¹) and $\sim 78 \mu\text{V h}^{-1}$ (8.72% 1000 h⁻¹) under similar experimental conditions. This can be attributed due to the increased joule heating within the electroless anode upon using higher Ni content (32 vol%) for such cells [17]. However, cells with TLA exhibit a degradation rate of $\sim 20 \mu\text{V h}^{-1}$ and $\sim 76 \mu\text{V h}^{-1}$ which corresponds to $\sim 2.06\%$ and 8.20% 1000 h⁻¹ under similar experimental conditions. As the single cell with TLA is configured with the combination of 32 BLA-1 and 28 BLA-1 onto the conventional anode support, the cell degradation is also found to be intermediate between 32 BLA-1 and 28 BLA-1 (Fig. 8a and b). In contrast, significant performance deterioration of $\sim 98 \mu\text{V h}^{-1}$ (10.5% 1000 h⁻¹) and $\sim 219 \mu\text{V h}^{-1}$ (26.1% 1000 h⁻¹) is observed (Fig. 8a and b) for the cells fabricated with CA at 0.5 and 1.0 A cm⁻². As expected, irrespective of anode configurations usage of higher electronic load (1.0 A cm⁻²) results in higher cell deterioration observed from Fig. 8. However, the rate of cell deterioration is found to reduce substantially upon incorporation of electroless anode in multilayer configuration. Ni coarsening is clearly visualized in the binerized optical image of the conventional cermet after an operation of 2000 h (Fig. 8c and d). The Ni-particulates with fairly large content and particle size undergoes rapid coarsening in the form of clusters or islands of Ni in the matrix. These sinteractive metallic clusters show higher tendency to coalesce into bigger particles not only reduce the catalytic activity of Ni but also hamper the electrochemical charge transfer reaction [32]. Increase in electronic load from 0.5 to 1.0 A cm⁻² is found to enhance the rate of coarsening as observed from Fig. 8d, owing to which the degradation rate is

accelerated. However, tendency of Ni particle agglomeration is found to be lesser in the electroless anode matrix (Fig. 8e,f). The formation of patterned core (YSZ)–shell (Ni) structure increases the energy barrier required for the rearrangement of metallic phases in the matrix during cohesion of Ni-particulates. The size and distribution of Ni phases of electroless anode is therefore observed to remain almost unchanged during a reasonable period of operation of 2000 h and an increased load of 1.0 A cm⁻² (Fig. 8f). Negligible enhancement in Ni coarsening is found in such functional cermet after increasing load from 0.5 to 1.0 A cm⁻². Thus, for the cell with either BLA or TLA structure, performance deterioration is truly governed by the degree of degradation exhibited at the anode layer present adjacent to the electrolyte. The reported SOFC with novel functional anodes in the present investigation are found to be superior in terms of high performance, reduced polarization losses, enhanced endurance etc [20,23,33,34]. Therefore, single cell with layered anode having electroless layer in vicinity of electrolyte exhibit high electrochemical performance and could emerge as a potential high performance SOFC anode.

4. Conclusions

The present investigation is based on the development of high performance SOFC fabricated with layered anodes with variation in constituent phases, microstructure and porosity. Cells with bilayer anodes (BLA) are fabricated in combination with conventional NiO–YSZ (40 vol% Ni) at the fuel inlet and electroless Ni–YSZ cermet (28 or 32 vol% Ni) adjacent to the YSZ electrolyte. Single cells with 32 BLA-series showed superiority over 28 BLA-series in terms of electrochemical performance. It is observed that, cells fabricated with 32 BLA having an electroless layer thickness of 50 μm shows highest performance of 3.3 A cm⁻² at 800 °C and 0.7 V. Functionality of

electroless anode lies in the formation of core (YSZ)–shell (Ni) microstructure which enables patterned interconnection among Ni, YSZ and pores throughout the matrix. Functional trilayered (TLA) anode is fabricated with layer wise variation of constituent phases (Ni, YSZ and pores), porosity and microstructure. In such configuration, conventional anode forms the basic support structure onto which electroless cermet with 32 vol% of Ni (intermediate layer – 50 μm) and 28 vol% Ni (adjacent to electrolyte – 50 μm) are laminated successively. A current density as high as 3.5 A cm^{-2} (800 °C and 0.7 V) is obtained from such cells with TLA configuration with lowest ohmic cell ASR of $\sim 78 \Omega \text{cm}^2$. Substantial reduction in overall cell polarizations measured from EIS at 800 °C are found with TLA configuration ($\sim 0.35 \Omega \text{cm}^2$) compared to the conventional anode ($\sim 0.9 \Omega \text{cm}^2$). Such TLA is found to reduce the cell degradation rate to $\sim 20 \mu\text{V h}^{-1}$ and $\sim 76 \mu\text{V h}^{-1}$ compared to the cells with conventional anode support ($\sim 98 \mu\text{V h}^{-1}$ and $\sim 219 \mu\text{V h}^{-1}$) at 0.5 and 1.0 A cm^{-2} for 2000 h respectively. The significant functional influence of electroless cermet in TLA structure is also supported by thermal compatibility (CTE = $11.10 \times 10^{-6} \text{K}^{-1}$) with the adjacent electrolyte (CTE = $10.8 \times 10^{-6} \text{K}^{-1}$). Hence, the developed layered anode with gradation in physical properties could act as a potential high performance SOFC anode.

Acknowledgments

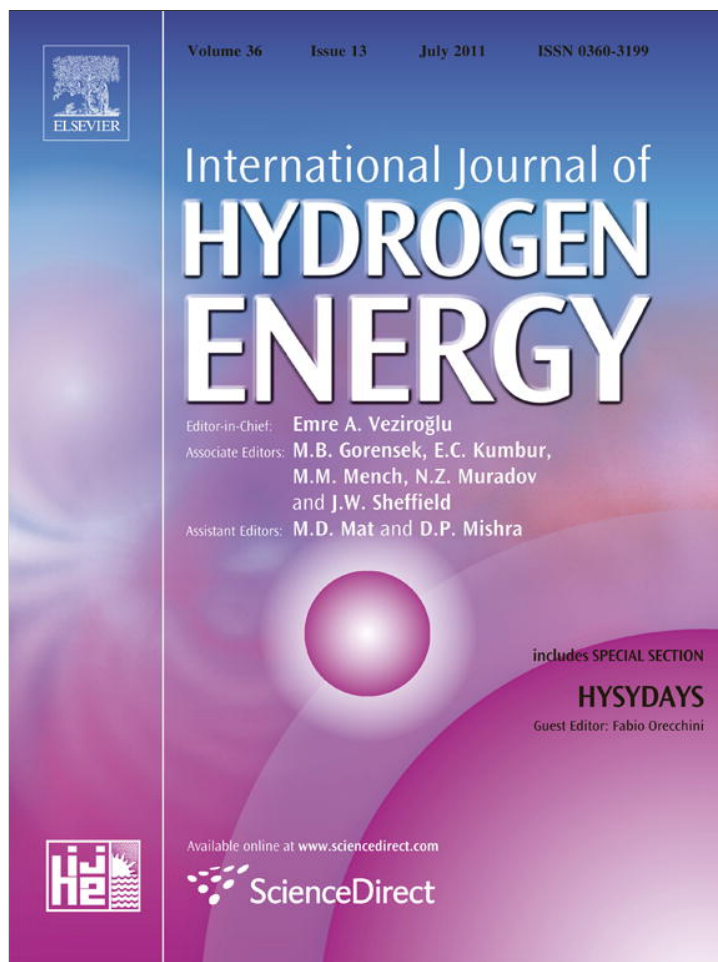
The authors acknowledge Director, CSIR-CGRI for his kind permission to publish the work. One of the authors (MM) is thankful to Council of Scientific and Industrial Research (CSIR), India for providing senior research fellowship.

REFERENCES

- [1] Brett DJL, Atkinson A, Brandon NP, Skinner SJ. Intermediate temperature solid oxide fuel cells. *Chemical Society Reviews* 2008;37:1568–78.
- [2] Holtappels P, Vogt U, Graule T. Ceramic materials for advanced solid oxide fuel cells. *Advanced Engineering Materials* 2005;7:292–302.
- [3] Weber A, Tiffée EI. Materials and concepts for solid oxide fuel cells (SOFCs) in stationary and mobile applications. *Journal of Power Sources* 2004;127:273–83.
- [4] Telebi T, Sarrafi MH, Haji M, Raissi B, Maghsoudipour A. Investigation on microstructures of NiO–YSZ composites and Ni–YSZ cermet for SOFCs. *International Journal of Hydrogen Energy* 2010;35:9440–7.
- [5] Koide H, Someya Y, Yoshida T, Maruyama T. Properties of Ni/YSZ cermet as anode for SOFC. *Solid State Ionics* 2000;132:253–60.
- [6] Muller AC, Herbstritt D, Tiffée EI. Development of a multilayer anode for solid oxide fuel cells. *Solid State Ionics* 2002;152–153:537–42.
- [7] Minh NQ, Takahashi T. *Science and technology of ceramic fuel cells*. New York: USA Elsevier; 1995.
- [8] Werber T. Joining of Ni powder grains by thermal oxidation. *Solid State Ionics* 1990;42:205–11.
- [9] Maggio G, Ielo I, Antonucci V, Giordan N. In: Grosz F, Zegers P, Singhal SC, Yamamoto O, editors. *SOFC II*. Luxembourg: The Commission of the European Communities; 1991. p. 611–20.
- [10] Iwata T. Characterization of Ni–YSZ anode degradation for substrate-type solid oxide fuel cells. *Journal of Electrochem. Soc.* 1996;143:1521–5.
- [11] Singhal SC, Kendall K. *High temperature solid oxide fuel cells: fundamentals, design and applications*. UK: Elsevier; 2003.
- [12] Basu RN. In: Basu S, editor. *Recent trends in fuel cell science and technology: materials for solid oxide fuel cell*. New Delhi/New York: Anamaya Publisher/Springer; 2006. p. 284.
- [13] Mukhopadhyay J, Banerjee M, Das Sharma A, Basu RN, Maiti HS. Development of functional SOFC anode. *ECS Transactions* 2007;7(1):1563–72. The Electrochemical Society.
- [14] Mukhopadhyay J, Banerjee M, Basu RN. Influence of sorption kinetics for zirconia sensitization in solid oxide fuel cell functional anode prepared by electroless technique. *Journal of Power Sources* 2008;175:749–59.
- [15] Mukhopadhyay M, Mukhopadhyay J, Das Sharma A, Basu RN. Ball mill assisted synthesis of Ni–YSZ cermet anode by electroless technique and their characterization. *Material Science & Engineering B* 2009;163:120–7.
- [16] Pratihari SK, Das Sharma A, Basu RN, Maiti HS. Preparation of nickel coated YSZ powder for application as an anode for solid oxide fuel cells. *Journal of Power Sources* 2004;129:138–42.
- [17] Mukhopadhyay M, Mukhopadhyay J, Das Sharma A, Basu RN. In-situ patterned intra-anode triple phase boundary in SOFC electroless anode: an enhancement of electrochemical performance. *International Journal of Hydrogen Energy* 2011;36:7677–82.
- [18] Hassan Ahmed AE, Menzler Norbert H, Blass Günter, Ali Mostapha E, Buchkremer Hans P, Stöver D. Development of an optimized anode functional layer for solid oxide fuel cell applications. *Advanced Engineering Materials* 2002;4:125–9.
- [19] Wang ZR, Qian JQ, Wang SR, Cao JD, Wen TL. Improvement of anode-supported solid oxide fuel cells. *Solid State Ionics* 2008;179:1593–6.
- [20] Wang Zhenhua, Zhang Naiqing, Qiao Jinshuo, Sun Kening, Xu Ping. Improved SOFC performance with continuously graded anode functional layer. *Electrochemical Communications* 2009;11:1120–3.
- [21] Cassidy M, Lindsay G, Kendall K. In: *Proc. 1st Eur. SOFC Forum*; 1994. p. 205–21.
- [22] Taillades M, Batocchi P, Essoumhi A, Taillades G, Jones D, Roziere J. Development of multilayer anodes for proton-conducting solid oxide fuel cells. *ECS Transactions* 2009;25(2):2193–200 [The Electrochemical Society].
- [23] Jonoa K, Suda S, Hattori M. Effect of graded porous structure on Ni–YSZ anode performance. *ECS Transactions* 2007;7(1):1541–6. The Electrochemical Society.
- [24] Chen-Xin Li, Chang-Jiu Li. Guo Lie-Jin. Effect of composition of NiO/YSZ anode on the polarization characteristics of SOFC fabricated by atmospheric plasma spraying. *International Journal of Hydrogen Energy* 2010;35:2964–9.
- [25] Basu RN, Das Sharma A, Dutta A, Mukhopadhyay J. Processing of high-performance anode-supported planar solid oxide fuel cell. *International Journal of Hydrogen Energy* 2008;33:5748–54.
- [26] Dutta A, Mukhopadhyay J, Basu RN. Combustion synthesis and characterization of LSCF-based materials as cathode of intermediate temperature solid oxide fuel cells. *J. European Ceramic Society* 2009;29:2003–11.
- [27] Mukhopadhyay M, Mukhopadhyay J, Das Sharma A, Basu RN. Use of electroless anode active layer in anode-supported planar SOFC. *Electrochem. Soc. Transaction* 2009;25:2267–74. The Electrochemical Society.

- [28] Mukhopadhyay M, Mukhopadhyay J, Das Sharma A, Basu RN. High performance planar solid oxide fuel cell fabricated with Ni–Yttria stabilized zirconia anode prepared by electroless technique. *International Journal of Applied Ceramic Technology*. in press. [DOI: 10.1111/j.1744–7402.2011.02646.x].
- [29] Basu RN, Günter Blass, Buchkremer Hans P, Stöver D, Tietz F, Wessel E, et al. Simplified processing of anode-supported thin film planar solid oxide fuel cells. *Journal of European Ceramic Society* 2005;25:463–71.
- [30] Moon H, Kim SD, Park EW, Hyun SH, Kim HS. Characteristics of SOFC single cells with anode active layer via tape casting and co-firing. *International Journal of Hydrogen Energy* 2008; 33:2826–33.
- [31] Mukhopadhyay M, Mukhopadhyay J, Das Sharma A, Basu RN. *ECS Transactions* 2011;35:1293–302. The Electrochemical Society.
- [32] Baek S-W, Bae J. Anodic behavior of $8Y_2O_3-ZrO_2/NiO$ cermet using an anode-supported electrode. *International Journal of Hydrogen Energy* 2011;36:689–705.
- [33] Feng Zhao, Virkar AV. Dependence of polarization in anode-supported solid oxide fuel cells on various cell parameters. *Journal of Power Sources* 2005;141:79–95.
- [34] Leng YJ, Chan SH, Khor KA, Jiang SP. Performance evaluation of anode-supported solid oxide fuel cells with thin film YSZ electrolyte. *International Journal of Hydrogen Energy* 2004; 29:1025–33.

Provided for non-commercial research and education use.
Not for reproduction, distribution or commercial use.

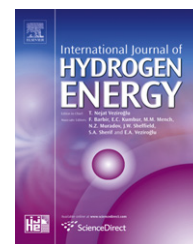


This article appeared in a journal published by Elsevier. The attached copy is furnished to the author for internal non-commercial research and education use, including for instruction at the authors institution and sharing with colleagues.

Other uses, including reproduction and distribution, or selling or licensing copies, or posting to personal, institutional or third party websites are prohibited.

In most cases authors are permitted to post their version of the article (e.g. in Word or Tex form) to their personal website or institutional repository. Authors requiring further information regarding Elsevier's archiving and manuscript policies are encouraged to visit:

<http://www.elsevier.com/copyright>

Available at www.sciencedirect.comjournal homepage: www.elsevier.com/locate/he

Technical Communication

In-situ patterned intra-anode triple phase boundary in SOFC electroless anode: An enhancement of electrochemical performance

Madhumita Mukhopadhyay, Jayanta Mukhopadhyay, Abhijit Das Sharma, Rajendra N. Basu*

Fuel Cell and Battery Division, Central Glass and Ceramic Research Institute, CSIR, Kolkata 700 032, India.

ARTICLE INFO

Article history:

Received 24 February 2011

Received in revised form

16 March 2011

Accepted 19 March 2011

Available online 19 April 2011

Keywords:

Electroless anode

Anode-supported-SOFC

Intra-anode TPB

Modeling

Electrochemical performance

ABSTRACT

Co-existence of intra-anode and conventional triple phase boundary (TPB) is reported for the first time in core (YSZ)–shell (Ni) electroless anode cermet. A mathematical model is proposed for determination of intra-anode TPB length and has been validated experimentally. Retention of longer intra-anode TPB even after repeated redox cycling is responsible for relatively lower conductivity degradation of such cermets. Existence of intra-anode TPB in electroless anode results in significant improvement of electrochemical performance. Single cells with electroless anode exhibit a current density of 2.5 A cm^{-2} compared to cells with conventional anode (1.7 A cm^{-2}) at $800 \text{ }^\circ\text{C}$, 0.7 V .

Copyright © 2011, Hydrogen Energy Publications, LLC. Published by Elsevier Ltd. All rights reserved.

1. Introduction

The basic reaction of solid oxide fuel cell (SOFC) involves electrochemical combination of reactants at the TPB of anode–electrolyte and electrolyte–cathode interfaces. Apart from high electronic conductivity, interconnected porosity of anode is responsible for effective fuel diffusion [1–4]. Nickel (Ni)-8 mol% yttria stabilized zirconia (YSZ) anode with unique core (YSZ)–shell (Ni) microstructure is prepared by our group through electroless technique [5,6]. Electroless anode has an advantage of using lower Ni content [28 vol%] compared to conventional anode [40–45 vol%] without compromising the

required electrical conductivity for SOFC application. Higher Ni content in conventional anode causes Ni coarsening during high temperature operation [7–11]. In order to solve these problems, optimization of microstructure has been proposed by Itoh et al. [12]. Optimized in-situ deposition of Ni around YSZ core by electroless technique [5] ensures intra (Ni/Ni, YSZ/YSZ and connected pore) and inter (Ni/YSZ/pore) phase contact of YSZ, Ni and pores throughout the matrix (Fig. 1). Such interconnection between YSZ/YSZ, Ni/Ni and YSZ/Ni with the associated pores helps in the formation of patterned intra-anode TPB [Ni/YSZ/fuel (through pores)] within the anode. As shown in Fig. 1, co-existence of intra-anode and

* Corresponding author. Tel.: +91 33 2473 3469x3507; fax: +91 33 2473 0957.

E-mail address: rnbasu@cgcri.res.in (R.N. Basu).

0360-3199/\$ – see front matter Copyright © 2011, Hydrogen Energy Publications, LLC. Published by Elsevier Ltd. All rights reserved.
doi:10.1016/j.ijhydene.2011.03.114

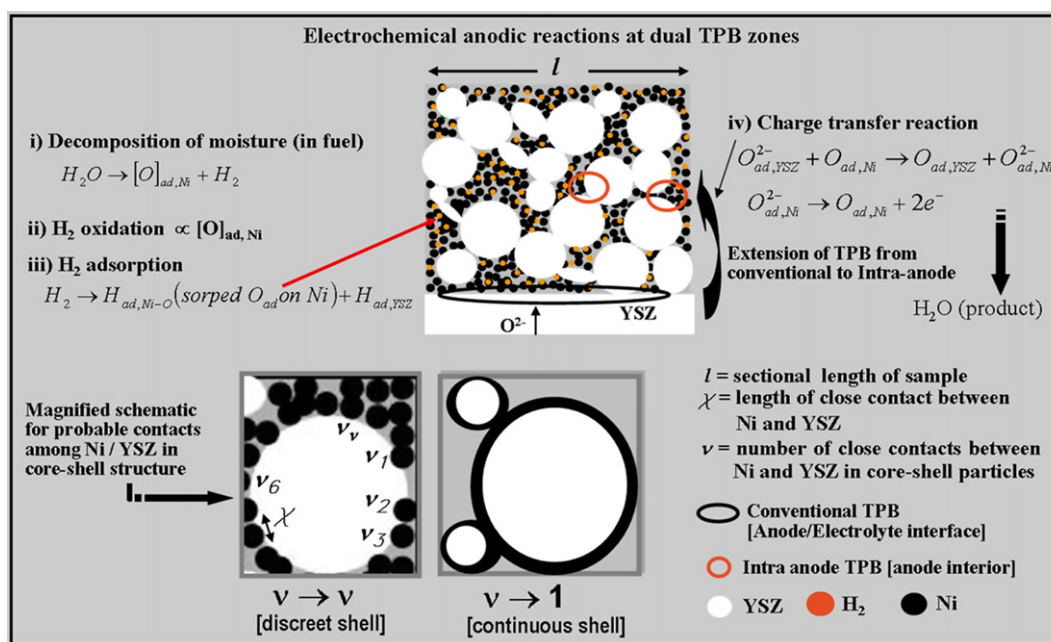


Fig. 1 – Schematic of anodic electrochemical reactions at dual TPB zones of Ni–YSZ electroless anode.

conventional [anode/electrolyte/pores – exterior to anode] TPB sites helps in the enhancement of overall TPB length of the single cell. Therefore, percolation of O^{2-} ions (through YSZ), electrons (through Ni) and H_2 (through interconnected pores) also follows a patterned network throughout the electroless cermet. In present investigation, a mathematical model is proposed for determining intra-anode TPB length for electroless cermets and is experimentally validated as a function of Ni content. Intra-anode TPB lengths of electroless anodes are measured and correlated with degradation in conductivity during repeated redox cycles. The presence of lower Ni content in electroless anode with relatively smaller particulate size may restrict the rate of Ni coarsening during high temperature SOFC operation. Therefore, electroless anode is expected to be superior for reduced degradation of electrical and electrochemical properties upon redox cycling due to retention in longer TPB lengths. To the best of our knowledge, formation of patterned intra-anode TPB by electroless technique and the associated improvement of electrical and electrochemical properties have not been reported elsewhere.

2. Experimental

Synthesis of Ni–YSZ cermet by electroless technique was reported in our earlier communication [5]. Electroless technique involves an initial sensitization of YSZ precursor by adsorption of Pd^0 species (in ppm level) produced in-situ in the redox bath containing Pd^{2+} and Sn^{2+} . Adsorbed Pd^0 acts as the catalytic sites for reduction of Ni^{2+} to Ni in the electroless bath. The reduction of Ni^{2+} to Ni^0 is carried out using hydrazine hydrate as a reducing agent. Optimization of the processing parameters attributed to the discreet and patterned deposition of Ni particulates onto sensitized YSZ [5]. Electroless [15–40 vol% Ni] and conventional [40 vol% Ni] anode powders were compacted

uniaxially at 170 MPa. The green compacts were air sintered at 1400 °C for 6 h and were finally reduced at 800 °C for 10 h in an atmosphere of Ar:H₂ (80:20). Electrical conductivity measurements of the reduced anodes were carried out by 4-probe technique in the temperature range of 500–1000 °C at an interval of 50 °C. The anode cermets were subjected to repeated oxidation to NiO–YSZ at 1000 °C and re-reduction (at 800 °C) in the same atmosphere of Ar:H₂. The effect of 20 such redox cycles on degradation of electrical conductivities of anode cermets was examined and correlated with the experimental intra-anode TPB lengths. FESEM (Gemini, Zeiss) images of reduced anodes were analyzed through image analysis (Olympus, Germany) to determine the intra-anode TPB length. Fabrication of single cells involves an initial tape casting of anodes with a thin layer of YSZ electrolyte [13,14]. This was followed by their room temperature lamination and co-sintering at around 1400 °C to form the half cells. The sintered half cells were screen printed with lanthanum strontium manganite (LSM) as cathode and LSM–YSZ (50:50) as cathode active layer. The prepared block upon co-sintering at 1150 °C formed the single cell. Use of tape casting and co firing for IT-SOFC fabrication is also practiced by others [15]. Coupon cells (~16 mm diameter) thus fabricated was tested for electrochemical performance evaluation using hydrogen as fuel and oxygen as oxidant in the temperature range of 700–800 °C under applied electronic loads (Amrel, USA).

3. Modeling of intra-anode TPB length

A mathematical model is proposed for determining intra-anode TPB length of SOFC cermet anode. The mechanism for electrocatalytic oxidation of fuel involves an initiation of charge transfer reaction from $O_{ad,YSZ}^{2-}$ to $O_{ad,Ni}^{2-}$ at conventional TPB which exists at the anode–electrolyte interface [3]. This charge

transfer is progressive in the bulk anode preferentially through intra-anode TPB because Ni, YSZ and pores are patterned and interlinked in a definite pattern in the electroless cermet matrix. Fig. 1 describes the anodic electrochemical reactions at dual TPB zones [conventional and intra-anode] of electroless anode.

In the proposed model, ν defines the number of closely contacted Ni with YSZ within a specified length (l) of sample and χ_ν denotes the length of each ν^{th} contact. In addition, τ denotes the number of core-shell particles under consideration. At the contact points, pores also co-exist with Ni and YSZ phases and thereby ensure the availability of electrons, O^{2-} ions and fuel at intra-anode TPB sites.

Summation of all contact lengths [α] can be written as:

$$\alpha = \left(\sum_1^\nu \chi_\nu \right) \quad (1)$$

TPB length [Γ] can be expressed as:

$$\Gamma \propto \alpha \nu \tau \Rightarrow \Gamma = k \alpha \nu \tau \quad (2)$$

where, k is proportionality constant.

Though, TPB exists in 3D contour, TPB length, a uni-dimensional parameter, is modeled based on two-dimensional cross-sections.

Considering circular geometry of 2D plane, TPB length can be written as:

$$\Gamma_{\text{ind}} = \pi \alpha \tau, \text{ valid for continuous Ni shell } [\nu \rightarrow 1, \text{ Fig. 1}] \quad (3)$$

where, Γ_{ind} defines TPB length in ‘ μm ’ independent of sample sectional length (l).

Generation of continuous Ni shell as shown in Fig. 1 (Eq. (3)) is ineffective for maximization of TPB, as it decreases the number of contact points. In addition, formation of continuous Ni shell also restricts the YSZ contribution for the functionality of such anode cermet.

Maximizing the number of contacts at, $\nu \rightarrow \nu$ (highest limit, Fig. 1), which signifies discrete deposition of Ni particulates around YSZ core, Γ_{ind} is written as:

$$\Gamma_{\text{ind}} = \pi \alpha \nu \tau \quad (4)$$

Similarly, contacted surface area (ξ) expressed in ‘ μm^2 ’ of TPB independent of l can be written as:

$$\xi_{\text{ind}} = \pi \left(\frac{\alpha^2}{4} \right) \nu_{xy}^2 \tau_{xy}^2 \text{ at } \nu \rightarrow \nu (\text{highest limit}) \quad (5)$$

Equations governing Γ_{dep} [expressed in $\mu\text{m} \mu\text{m}^{-2}$] and ξ_{dep} [expressed in $\mu\text{m}^2 \mu\text{m}^{-4}$] dependent of l are given as:

$$\Gamma_{\text{dep}} = \pi \left(\frac{\alpha}{l} \right) \left(\frac{\nu}{l} \right) \left(\frac{\tau}{l} \right) \text{ and } \xi_{\text{dep}} = \pi \left(\frac{\alpha}{2l} \right)^2 \left(\frac{\nu}{l} \right)^2 \left(\frac{\tau}{l} \right)^2 \quad (6)$$

$$\therefore \Gamma_{\text{dep}} = \pi \text{ANT} \text{ and } \xi_{\text{dep}} = \pi \left(\frac{A^2}{4} \right) N^2 T^2$$

where A, N and T are total contact lengths, number of active contact interfaces and number of core-shell particles per unit sectional length respectively.

There could be two boundary conditions for the developed model:

- a) Limiting range of ν varies from unity to infinity [ν_1^2]. At highest limiting range [$\nu \rightarrow \infty$], both TPB and surface area are enhanced as evident from Eqs. (4)–(6):

$$\Gamma \propto \nu \text{ or } N \text{ and } \xi \propto \nu^2 \text{ or } N^2$$

This signifies that optimized Ni deposition around YSZ core during electroless technique increases the number of active contact points enhancing both intra-anode TPB and surface area.

- b) The size factor ratio (β) is defined as $\beta = d_{\text{YSZ}}/d_{\text{Ni}} \approx 10^n$, where d_{YSZ} and d_{Ni} are the average particle size of YSZ and Ni particulates, respectively. For measurable intra-anode TPB in electroless anode, β should vary at least an order of 10. Theoretically, with increase in β , ν increases but τ (number of core-shell particulates) decreases. Therefore, an optimization between the size ratio of YSZ and Ni particles is necessary for enhancing the TPB. Average particle sizes of Ni and YSZ of electroless anode are $\sim 70 \text{ nm}$ and $\sim 30 \mu\text{m}$, respectively. Therefore, β vary in the range of 10^2 – 10^3 and thereby satisfy the required boundary condition. Average particle sizes of Ni and YSZ phases of the conventional cermet are almost in the same order of magnitude. In addition, due to disperse Ni and YSZ distribution in the microstructure of conventional cermets, [$\tau \rightarrow 0$ & $\nu \rightarrow \text{undefined} \Rightarrow \Gamma \approx 0$] patterned intra-anode TPBs are not observed. Therefore, existence of dual TPB zones is not feasible in the matrix of conventional anode.

4. Results & discussion

Intra-anode TPB dependent on sample sectional length is calculated from Eq. (6). As already mentioned, the values of interfacial contact points (ν) and their respective lengths (χ_ν) are obtained by image analysis. TPB length of electroless anode in different sections (l_1, l_2, l_3) (Fig. 2a, c-1) of the sample, each having a length of $\sim 43 \mu\text{m}$ has been investigated. The respective TPB zones are identified upon mapping the locations of Zr and Ni phases as shown in Fig. 2a. The experimental TPB lengths of core-shell electroless anode are calculated with negligible error percentage ($\sim 0.08\%$). This attributes toward the uniform distribution of intra-anode TPB length throughout the cermet matrix. Though patterned intra-anode TPB is absent in conventional cermet, TPB lengths are measured considering probable contacts of Ni with YSZ through elemental mapping (Fig. 2b). However, experimental calculations clearly depict that only 3% probability (as shown in Fig. 2 c-2) exists for the presence of intra-anode TPB sites in the conventional anodes. The processing conditions for synthesizing the conventional anode by mechanical mixing generate inhomogeneous distribution of Ni, YSZ and pores. Therefore, it cannot ensure the uniform three phases contact throughout the matrix. This inhomogeneous distribution does not lead to patterned intra-anode TPBs within the conventional anode which is also supported experimentally by the model. It is observed from Fig. 3a that, TPB length of electroless anode increases with increase in Ni content and reaches a maximum of $\sim 77 \mu\text{m} \mu\text{m}^{-2}$ in the range of 28–32 vol% of Ni in the cermet matrix. At lower Ni content of this threshold, active Ni–YSZ interfaces are found to be of smaller interfacial length which results in lower TPB. On the other hand, as

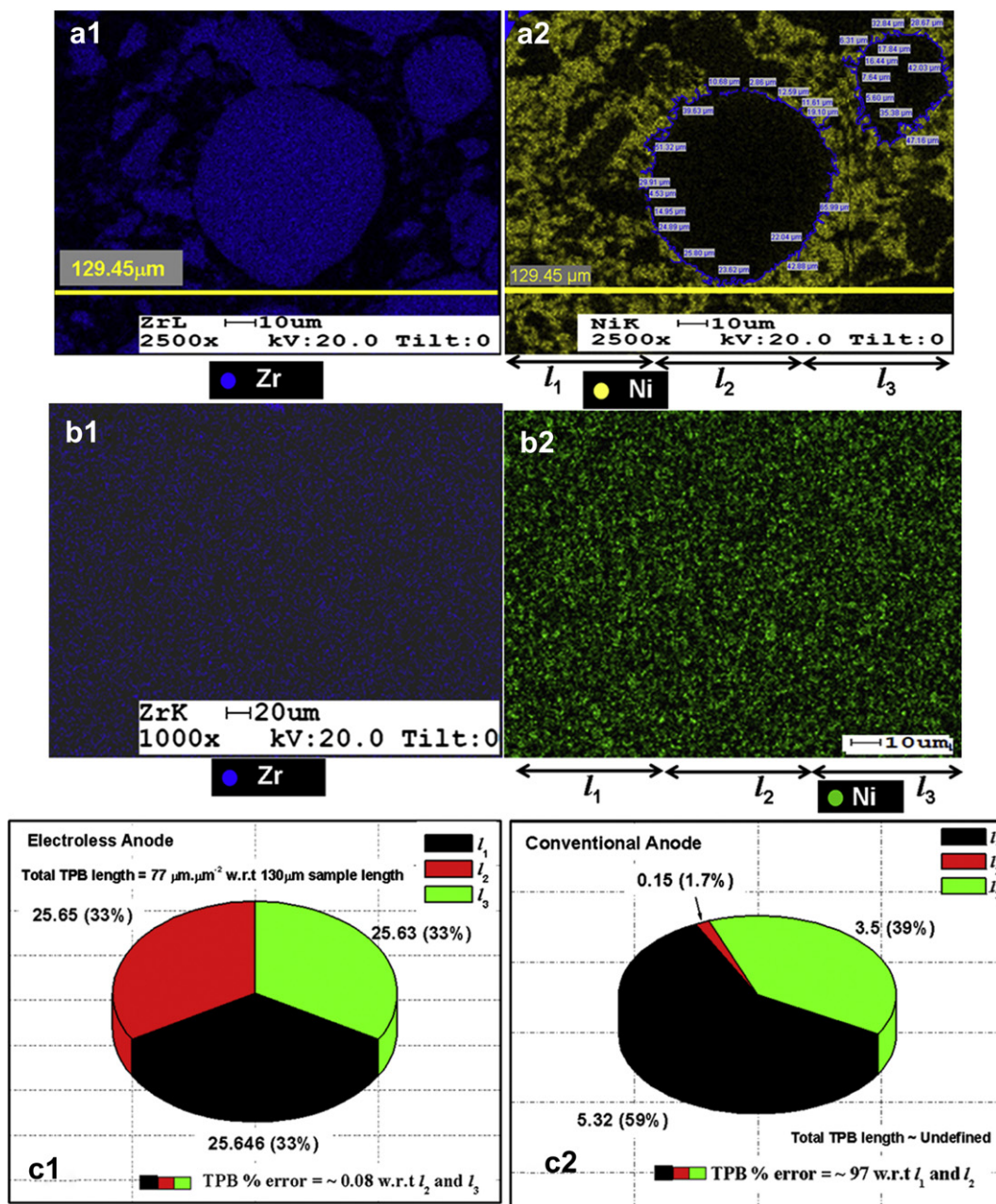


Fig. 2 – (a-1) Zr and (a-2) Ni mapping of electroless anode, (b-1) Zr and (b-2) Ni mapping of conventional anode and sectional TPB length distribution for: (c-1) electroless and (c-2) conventional anode cermet.

evident from Fig. 3a, the increment of shell thickness is found to be significant with increase in Ni content (>32 vol%) thereby reducing the intra-anode TPB length.

As described earlier, the reduced Ni–YSZ cermets prepared by both techniques are allowed to undergo redox cycling. It can be observed from Fig. 3b that before redox cycling, electrical conductivity (~500 S cm⁻¹) of electroless anode with only 28 vol% Ni is equivalent to the conductivity value of conventional cermet having much higher Ni content (40 vol%). This can be attributed to the formation of unique core (YSZ) – shell (Ni) microstructure in the electroless matrix. The optimized deposition of discreet Ni particulates enables continuous network of both metallic (Ni) and ceramic (YSZ) phases throughout the

cermet thereby results in higher electrical conduction at much lower Ni content. At high operating temperature of 800 °C, it is believed that Ni coarsens not only because of phonon scattering, but also due to localized joule heating (I^2R). This causes overall reduction in electrical conductivity of the anode upon repeated redox cycling as is observed in Fig. 3b. However, electroless anode with 28 vol% of Ni having highest TPB length in the series (Fig. 3a) shows least electrical conductivity degradation (~7% after 20 cycles). The negligible degradation rate for electroless anodes is primarily because of less Ni content and ordered microstructure with interconnection among both Ni and YSZ phases. This also accounts for negligible change in the intra-anode TPB length of electroless anode

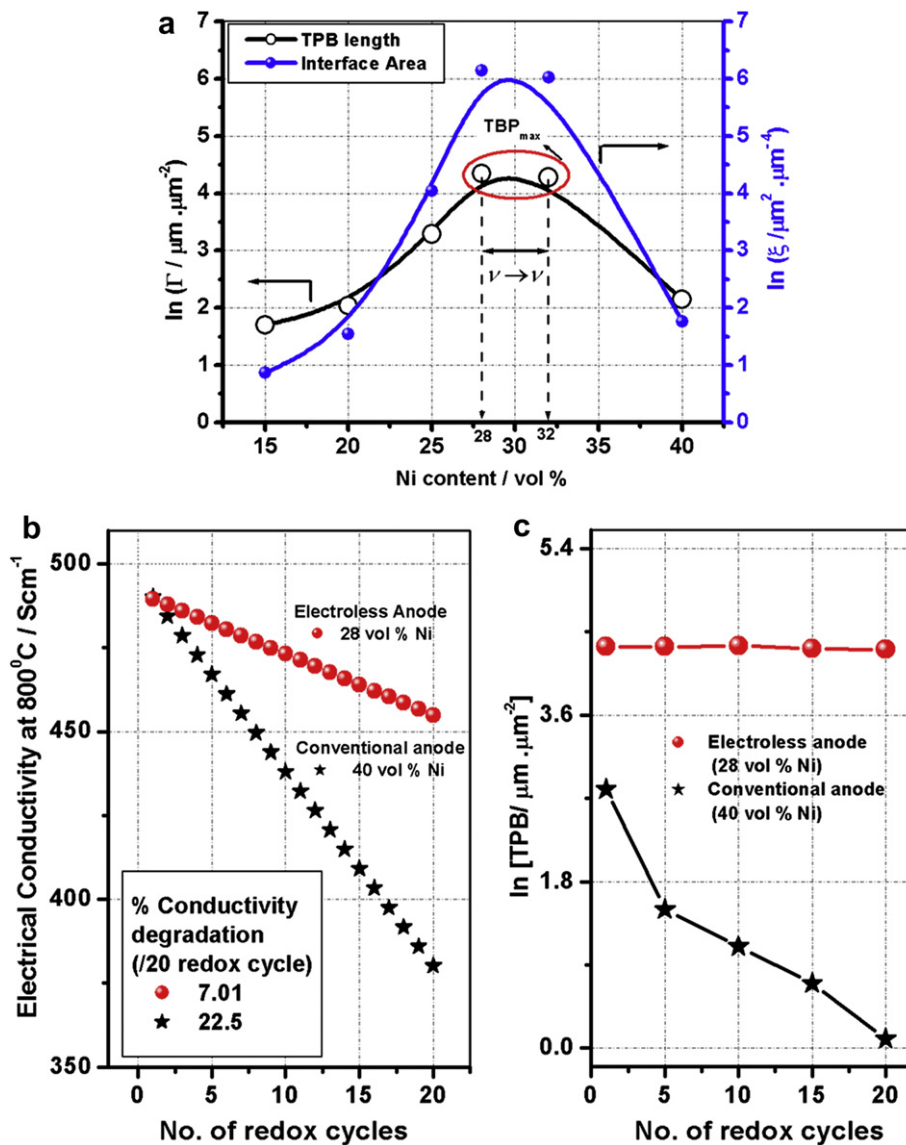


Fig. 3 – (a) Variation of intra-anode TPB length and surface area of electroless anode as a function of Ni content, effect of redox cycling on degradation of (b) electrical conductivity and (c) TPB length of electroless and conventional anode cermets.

after 20 redox cycles (Fig. 3c). The smaller size of Ni particulate in electroless anode attributes toward the lower degradation rate. In contrast, dispersed Ni and YSZ phases in the conventional anode with higher size of Ni particulate cause rapid Ni grain growth during redox cycling. This microstructural change causes reduction in surface area of Ni available for effective charge transfer reaction [16]. Ni coarsening also hampers the fuel percolation through the pores and causes ~23% electrical conductivity degradation in conventional cermets after 20 cycles. Therefore, electroless anode with lower Ni content (28–32 vol%) is superior in terms of enhanced redox tolerance having comparable electrical conductivity to the conventional cermet which contains relatively higher Ni content (40–60 vol %). The presence of dual TPB sites in the electroless cermet helps in enhancing the electrochemical activity. In addition, optimized discreet deposition of fine Ni particulates onto core YSZ increases the overall anode surface area and thereby the catalytic activity of electroless anode toward fuel oxidation is

enhanced. Therefore, usage of lower Ni content (i.e. higher YSZ content) in electroless anode helps in the retention of core-shell microstructure intact which enhances the redox tolerance. On the otherhand, owing to the formation of unique microstructure with enhanced TPB length and increased anode catalytic activity, the electrochemical performance of cells fabricated with such electroless cermet is found to be considerably high. Single cells with electroless anode containing 32 vol% Ni show higher current density of ~2.5 A cm⁻² (Fig. 4) at 800 °C and 0.7 V compared to those with conventional anodes having 40 vol% Ni (~1.7 A cm⁻², 800 °C and 0.7 V). Therefore, the present investigation intend to report a SOFC anode prepared through electroless technique with a unique microstructure that exhibits better redox resistance than that of the conventional anode. Furthermore, power density of single cell (1.75 W cm⁻²) fabricated with such electroless anode is also found to be higher compared to the conventional anode-supported cell (1.19 W cm⁻²).

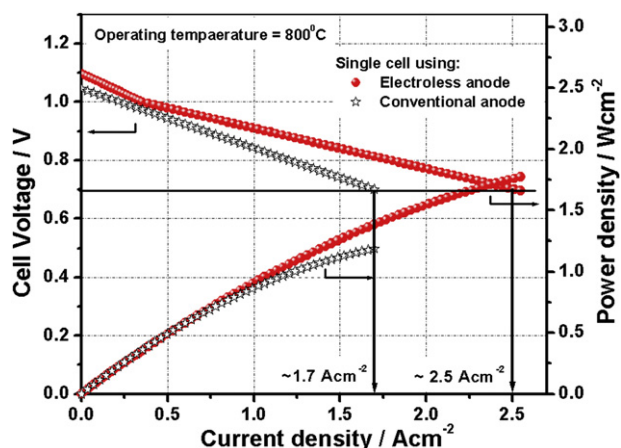


Fig. 4 – Comparative electrochemical performances of single cell with anodes prepared by electroless and conventional technique.

In summary, the attempt for validation of the proposed mathematical model for determination of intra-anode TPB length of electroless anode is successfully done by us. Such redox tolerant electroless cermet with core (YSZ)–Ni (shell) microstructure enables significantly higher electrical conductivity at much lower Ni content (28 vol%). Co-existence of patterned intra-anode and conventional TPBs with increased catalytic activity of fine Ni particulates is responsible for the enhancement of electrochemical performance (2.5 A cm^{-2} at 800°C) for such cells.

Acknowledgment

The authors acknowledge Director, CGCRI for his permission to publish the work. One of the authors (MM) is thankful to CSIR for providing senior research fellowship.

REFERENCES

- [1] Singhal SC, Kendall K. High temperature solid oxide fuel cells: fundamentals, design and applications. UK: Elsevier; 2003.
- [2] Basu RN. In: Basu S, editor. Recent trends in fuel cell science and technology: materials for solid oxide fuel cell. New Delhi/New York: Anamaya Publisher/Springer; 2006. p. 284.
- [3] Minh NQ, Takahashi T. Science and technology of ceramic fuel cells. New York, USA: Elsevier; 1995. 203–204, 207147–164.
- [4] Telebi T, Sarrafi MH, Haji M, Raissi B, Maghsoudipour A. Investigation on microstructures of NiO–YSZ composites and Ni–YSZ cermet for SOFCs. *Int J Hydrogen Energy* 2010;35: 9440–7.
- [5] Mukhopadhyay J, Banerjee M, Basu RN. Influence of sorption kinetics for zirconia sensitization in solid oxide fuel cell functional anode prepared by electroless technique. *J Power Sources* 2008;175:749–59.
- [6] Pratihari SK, DasSharma A, Basu RN, Maiti HS. Preparation of nickel coated YSZ powder for application as an anode for solid oxide fuel cells. *J Power Sources* 2004;129:138–42.
- [7] Dees DE, Claar TD, Easler TE. Conductivity of porous Ni/ZrO₂–Y₂O₃ cermets. *J Electrochem Soc* 1987;134:2141–6.
- [8] Iwata T. Characterization of Ni–YSZ anode degradation for substrate – type solid oxide fuel cells. *J Electrochem Soc* 1996;143:1521–5.
- [9] Klemenso T, Chung C, Larson PH, Mogensen MJ. The mechanism behind redox instability of anodes in high-temperature SOFC. *Electrochem Soc* 2005;152:A2186–92.
- [10] Fouquet D, Muller AC, Webber A, Ivers-Tiffée E. Kinetics of oxidation and reduction of Ni/YSZ cermets. *Ionics* 2003;9: 103–8.
- [11] Stathis G, Simwonis D, Tietz F, Moropoulou A, Naoumides A. Oxidation and resulting mechanical properties of Ni/8 Y₂O₃ stabilized zirconia anode substrate for solid oxide fuel cells. *J Mater Res* 2002;17:951–8.
- [12] Itoh H, Yamamoto T, Mori M, Horita T, Sakai N, Yokokawa H, et al. Configurational and electrical behavior of Ni–YSZ cermet with novel microstructure for solid oxide fuel cell anodes. *J Electrochem Soc* 1997;144:641–6.
- [13] Basu RN, Das Sharma A, Dutta A, Mukhopadhyay J. Processing of high-performance anode-supported planar solid oxide fuel cell. *Int J Hydrogen Energy* 2008;33:5748–54.
- [14] Mukhopadhyay M, Mukhopadhyay J, Das Sharma A, Basu RN. Use of electroless anode active layer in anode-supported planar SOFC. *Electrochem Soc Trans* 2009;25:2267–74 [The Electrochemical Society].
- [15] Moon H, Kim SD, Hyun SH, Kim HS. Development of IT-SOFC unit cells with anode-supported thin electrolytes via tape casting and co-firing. *Int J Hydrogen Energy* 2008;33: 1758–68.
- [16] Baek SW, Bae J. Anodic behavior of 8Y₂O₃–ZrO₂/NiO cermet using an anode-supported electrode. *Int J Hydrogen Energy* 2011;36:689–705.

International Journal of
**Applied
Ceramic
TECHNOLOGY**

Ceramic Product Development and Commercialization

High Performance Planar Solid Oxide Fuel Cell Fabricated with Ni–Yttria Stabilized Zirconia Anode Prepared by Electroless Technique

**Madhumita Mukhopadhyay, Jayanta Mukhopadhyay, Abhijit Das Sharma, and
Rajendra N. Basu***

*Fuel Cell and Battery Division, Central Glass & Ceramic Research Institute, Council of Scientific &
Industrial Research (CSIR), Kolkata 700 032, India*

Nickel (Ni)–8 mol% yttria stabilized zirconia (YSZ) cermet prepared through novel electroless technique is used as solid oxide fuel cell anode. The developed anode (28 vol% Ni) is used in two different configurations, viz. anode support and anode active layer (AAL). Highest electrochemical performance of 3.2 A/cm^2 with lowest cell area specific resistance ($\sim 94 \text{ m}\Omega \text{ cm}^2$) at 800°C is obtained from anode-supported single cell having an optimized $15 \mu\text{m}$ electroless AAL. Electrochemical performances are correlated with anode pore-size distributions. Such high performance cells also exhibit significant low degradation rate ($\sim 2\% \text{ 1000 h}^{-1}$ at a load 0.5 A/cm^2) during long-term testing.

Introduction

Nickel–8 mol% yttria stabilized zirconia (Ni–YSZ) is the most widely accepted anode material in solid oxide fuel cell (SOFC). In order to meet the requirements of SOFC, the anode material should fulfill certain important criteria. The anode should have enough elec-

tronic conductivity, matching thermal expansion coefficient with other cell components, sufficient interconnected porosity, electrocatalytic activity, and so forth. These factors play a major role in determining the overall performance of the cell.^{1–3} Metallic Ni has good catalytic activity toward oxidation of hydrogen, which acts as a fuel in SOFC. However, Ni has the problem of thermal incompatibility with other cell components due to its high coefficient of thermal expansion (CTE).⁴ In order to solve this problem, YSZ is added to metallic Ni

*rnbasu@cgcric.res.in; rajenbasu54@gmail.com
© 2011 The American Ceramic Society

to form the cermet anode. Another purpose of adding YSZ is to retain the anode microstructure without significant Ni coarsening during high temperature operation (750–800°C). In addition, YSZ also imparts ionic conduction for the generation of significant mixed conductivities (ionic and electronic) in the cermet matrix.⁵ Over the decades, various preparation techniques such as mixed oxide,⁶ coprecipitation,⁷ slurry coating, liquid dispersion,⁸ and heat decomposable aqueous salt solution routes⁹ are used to prepare Ni–YSZ cermet matrix. In all such preparation routes, Ni and YSZ phases are distributed in a dispersed manner. In general, 40 vol% of Ni and 60 vol% of YSZ are needed to satisfy the required level of electronic conductivity during SOFC operation.^{10,11} As mentioned above, such high Ni content poses thermal incompatibility problem with adjacent YSZ electrolyte (CTEs of Ni and YSZ are 16.9×10^{-6} and $10.8 \times 10^{-6} \text{ K}^{-1}$ respectively).

In fuel cells, useful voltage loss takes place through various means, viz. ohmic, concentration/diffusion, and activation polarizations.⁵ Ohmic polarization incorporates resistances from electrolyte, electrodes, and electrode–electrolyte interfaces. The concentration polarization is associated with the transport of gaseous species (oxidant and fuel) through porous electrodes. Finally, activation polarization is mainly due to the voltage loss arising out of oxidant reduction and fuel oxidation at the respective electrodes. Therefore, an efficient SOFC requires minimization of above-mentioned polarization losses. According to the prior arts, presence of higher Ni content in the anode cermet enhances the cell polarizations due to higher rate of Ni coarsening. This results in significant performance degradation at high operating temperature.¹² The aforesaid problems are expected to be resolved when Ni–YSZ anode is prepared by a novel electroless technique as already reported by our group.^{9,13,14} Ni–YSZ anode prepared by electroless technique involves an initial sensitization of YSZ precursor by adsorption of *in situ* produced Pd⁰ species. Pd⁰ centers act as the catalytic sites, which help in the reduction of Ni²⁺ to Ni in the electroless bath containing Ni salt solution and the sensitized YSZ mass. The reduction of Ni²⁺ to metallic Ni (Ni⁰) is carried out using hydrazine hydrate.¹⁴ Optimized processing conditions thereby help in discrete deposition of finer Ni particulates onto YSZ core. The anode prepared by such electroless technique requires only ~28 vol% Ni to satisfy the required electronic conductivity. The unique core–shell microstructure of such anode with

discrete Ni particles around the YSZ core helps in maintaining continuous Ni–Ni network throughout the matrix. Formation of such unique microstructure is expected to enhance the triple-phase boundary (TPB) length for fuel oxidation. In the present investigation, such Ni–YSZ cermet prepared through electroless technique is used in two different configurations: (a) as the total anode support and (b) as anode active layer (AAL). In the first configuration, Ni–YSZ anode with 28 vol% Ni constitutes the support structure. In the second configuration, conventional anode (NiO–YSZ) with ~40 vol% Ni is used as the main support structure; whereas, the Ni–YSZ prepared by electroless technique (28 vol% Ni) is used as an AAL. The conventional anode is placed toward the fuel side and AAL is placed adjacent to the electrolyte layer. While the conventional anode helps in providing the basic mechanical support with catalytic oxidation of the fuel, Ni–YSZ anode prepared through electroless technique is expected to enhance the electrochemical activity by reducing the charge transfer polarization losses. The thickness of anode support as well as AAL prepared by electroless technique is varied sequentially and optimized primarily based on the electrochemical performance of the single cell. To the best of our knowledge, fabrication of single cells using such anode for high performance SOFC is unique and reported for the first time by our group. Various factors affecting electrochemical activity, viz. sintering temperature of half cell, type of oxidant at cathode, thickness of structural support, and AAL, are thoroughly investigated. An attempt has been made to correlate the reduction process of NiO to metallic Ni in the anodes with the corresponding cell performances for both configurations. The pore-size distributions of anode cermet of both the configurations are correlated with the corresponding electrochemical performances. Prolonged operation of such cells is carried out for a considerable time period of 2000 h and the corresponding degradation rates are also studied.

Experimental Procedure

The electroless technique involve Ni deposition onto sensitized YSZ powder (particulates). YSZ (TZ-8Y, Tosoh, Tokyo, Japan) precursor powders were sensitized under a high energy ultrasonification in a redox system of Pd²⁺ and Sn²⁺. The redox couple of Pd²⁺ and Sn²⁺ generate Pd⁰ during

high energy ultrasonification. In electroless bath, Pd⁰ acts as the catalytic sites for reduction of Ni²⁺ to metallic Ni (Ni⁰). Excess Pd²⁺ in the sensitized mass was washed thoroughly with water until the subsequent chemical analysis ensured the absence of Pd²⁺ ions. The adsorbed Pd⁰ concentration onto YSZ is significantly small (in the order of ppm) and acts just as the catalytic sites for the reduction of Ni²⁺ to metallic Ni⁰ in the electroless bath through dropwise addition of hydrazine hydrate. The detailed synthesis process for such Ni-YSZ powder prepared through electroless method was reported in our previous communications.^{13,14}

Single Cell Fabrication

Anode-supported single cells of two different configurations were fabricated. In *Configuration 1*, total anode support was made of Ni-YSZ anode prepared by electroless method containing 28 vol% Ni. The structure of cell in *Configuration 1* is Ni-YSZ anode (electroless technique)/YSZ electrolyte/La_{0.65}Sr_{0.3}MnO₃ (LSM)-YSZ cathode active layer (CAL)/LSM cathode layer (CL) (Fig. 1a). Figure 1b shows the single cells of *Configuration 2* that incorporates Ni-YSZ cermet prepared by electroless method as an AAL. The structure of cell in *Configuration 2* is conventional NiO-YSZ anode (~40 vol% Ni)/Ni-YSZ (electroless technique) as AAL (28 vol%)/YSZ/CAL/CL. Fabrication of SOFC single cells involved two major steps. The first step was the fabrication of half cells that involve casting of anode and electrolyte slurries into tapes followed by

room-temperature lamination and cosintering in the temperature range of 1300–1400°C. In the second step, flat half cells were screen printed successively with CAL and CL and were co-fired at above 1000°C in air for 2–4 h to form the single cells. While LSM and YSZ were taken in 1:1 ratio (by weight) and was used for CAL, the CL contained only LSM. Typically, the thicknesses of LSM-YSZ-based CAL- and LSM-based CL were maintained in the range of 10–15 and 50–60 μm, respectively. The detailed cell fabrication procedure was described in our earlier publications.^{15,16} The cells were fabricated with variation of thickness of the anode support as well as AAL prepared by electroless technique in order to study its effect on the single cell performance. In *Configuration 1*, thickness of the anode support was varied from 1.25 to 1.5 mm; whereas, in *Configuration 2*, thickness of AAL was varied between 140 and 15 μm.

Electrochemical Characterization

Electrochemical performance evaluation was carried out with coupon cells (diameter ~16 mm) of both the configurations using hydrogen as fuel at anode and oxygen/air as the oxidant at cathode. During testing, flow rates of both oxidant and fuel gases (100 sccm each) were maintained with the help of electronic mass flow controllers (MKS Instruments, Andover, MA). The current density as a function of cell voltage was evaluated across the cell under different loads applied by electronic load bank (Amrel, San Diego, CA). The *I*-*V* characteristics of the cells were measured in the temperature

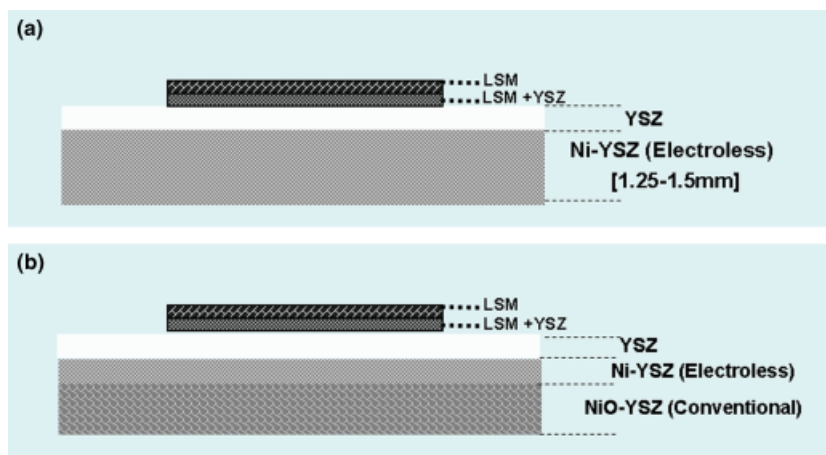


Fig. 1. Solid oxide fuel cell configuration with Ni-YSZ prepared through electroless technique: (a) as total anode support and (b) as anode active layer (AAL).

range of 700–800°C. The single cell performances were correlated with the extent of NiO reduction to metallic Ni as a function sintering temperature.

Pore-Size Distribution

The pore-size distribution of the sintered and reduced tape cast anode cermets of both the configurations were measured using mercury porosimetry (Quantachrome Poremaster 60, Version 7.01, Quantachrome Instruments, Boynton Beach, FL) and were correlated with the cell performances.

Microstructural Characterizations

The polished cross sections of single cells of both the configurations were observed using a high resolution optical microscope (Olympus GX 71, Olympus, Tokyo, Japan). For elemental detection, representative line scanning of such samples was carried out under high resolution field emission microscope (Gemini Supra 35, Zeiss, Jena, Germany).

Long Term Electrochemical Performance Study

Long term electrochemical testing was carried out using single cell of *Configuration 2* with optimum AAL thickness in order to study the degradation rate for 2000 h. For comparison, similar test was conducted on single cell with only conventional anode support. Endurance test on such cells was performed at 800°C using constant current load of 0.5, 0.75, and 1.0 A/cm² using humidified H₂ as the fuel and oxygen as oxidant.

Results and Discussion

Correlation Between NiO Reduction Processes with Cell Performance

Configuration 1—Anode Support Prepared by Electroless Technique: Ni–YSZ anode prepared by electroless technique was used as the structural support in *Configuration 1* as shown in Fig. 1a. Because Ni plays a major role for catalytic oxidation of hydrogen, the overall electrochemical activity of anode depends on the extent of reduction from NiO to metallic Ni. Depending upon characteristics of electroless cermet, reduction of NiO during electrochemical testing follows two distinct regions: (a) nonequilibrium and (b) equilibrium region. Nonequilibrium region refers to the dynamic state in

which the reduction of NiO follows a two-step kinetic process. The former step involves reaction between NiO and hydrogen atoms adsorbed on NiO. This step is dependent on the partial pressure of hydrogen and is governed by the thickness of the anode support. The second step of the reaction proceeds at the interface between NiO and hydrogen atoms adsorbed on Ni already reduced in the first step. The later reaction is independent of hydrogen partial pressure and is governed by the extent of cermet sintering. However, it is experimentally observed that after a certain time period, the extent of NiO reduction to Ni reached saturation. Beyond this limit, known as the equilibrium region (static state), no further improvement in cell performance is observed. The novelty of anode, prepared by electroless technique, is imbibed in its unique core (YSZ)–shell (Ni) microstructure. Processing parameters, as optimized during synthesis of Ni–YSZ cermet, enable the deposition of Ni particulates in a discreet pattern.¹⁴ Such unique structure facilitates the extension of TPB of the cermet matrix that comprises of YSZ core, discrete Ni shell around it, and the associated porosity. Deposition of metallic Ni around YSZ core was made in such a way that both YSZ and Ni phases were in intra- and interphase contact throughout the anode matrix. Such interconnecting engineered network between YSZ–YSZ, Ni–Ni, and YSZ–Ni with the associated pores helps in the enhancement of TPB length and ensure the availability of O²⁻ ions (through YSZ), electrons (through Ni), and H₂ (through pores) throughout the anode.

To study the effect of sintering temperature for the formation of proper metal (Ni)–oxide (NiO) interface, the half cells (anode/electrolyte) were sintered in the temperature range of 1300–1400°C at an interval of 50°C. It was observed that the electrochemical performances of single cells with half cells sintered at 1300°C were much lower (results not shown). This may be because of the ineffective sintering of YSZ electrolyte layer. Formation of proper metal–oxide interface was found to take place in the sintering temperature range of 1350–1400°C. The effect of NiO reduction to metallic Ni and sintering temperature of half cells on electrochemical performance of single cells is shown in Tables I and II. From the tables it can be observed that, irrespective of half cell sintering temperature, NiO reduction equilibration was achieved at a much faster rate for thinner anode support of thickness ~1.25 mm. The equilibration time of reduction for such anode support is found to be ~7 h. In comparison, 1.5 mm thick anode support

Table I. Effect of NiO Reduction Time and Sintering Temperature on Electrochemical Performance of Single Cells of Configuration 1 (Anode Thickness: 1.5 mm)

Sintering temperature of the half cells (°C)		1350					1400				
NiO reduction time (h)		0.5	3	6	10	72	0.5	3	6	10	72
Current density (A/cm ²) at 0.7 V	800°C	0.42	0.65	0.90	1.0	1.0	0.7	0.88	0.95	1.32	1.32
	750°C	0.25	0.33	0.47	0.53	0.53	0.45	0.59	0.66	0.75	0.75
	700°C	0.14	0.25	0.29	0.3	0.3	0.28	0.36	0.38	0.4	0.4

■, equilibrium region.

prepared by electroless technique requires ~10 h to reach the reduction saturation limit that indicates relatively slower rate of NiO reduction. Thinner anode support helps in easy hydrogen diffusion and tends to accelerate the partial pressure dependent reduction reaction between NiO and hydrogen atoms adsorbed on NiO (first step of the reduction process).

Although metal–oxide interface was properly formed at 1350°C, higher electrochemical performances were observed for the cells with half cells sintered at 1400°C. This is primarily because of higher degree of YSZ electrolyte densification at 1400°C. From Table I, it is also observed that, the electrochemical performance of single cell is almost constant from 10 to 72 h, which indicates the steady state reduction of NiO. Single cell with 1.5 mm thick anode support showed a current density of ~1.32 A/cm² (power density ~0.92 W/cm²) at 800°C and 0.7 V with hydrogen as fuel and oxygen as oxidant (Fig. 2a). In comparison, higher current density of ~1.43 A/cm² with a power density of ~1.0 W/cm² (at 0.7 V and 800°C) was obtained from cells having 1.25 mm thick anode support under similar experimental conditions (Fig. 2b). It may be noted that when air was used as the oxidant, irrespective of the half cell sintering temperature, electrochemical performance drops. Thus, current densities of ~0.78 and ~0.85 A/cm² were obtained for the cells with 1.5 mm thick and 1.25 mm thick

anode support, respectively, with air as the oxidant. Reduction in electrochemical performance of the single cells with air is mainly because of reduced oxygen reaction rate (ORR) at the cathode compartment due to the reduced partial pressure of oxygen.¹⁷

Configuration 2—AAL Prepared by Electroless Technique: In Configuration 2, electroless cermet containing 28 vol% Ni was used as an AAL with conventional NiO–YSZ (40 vol% Ni and 60 vol% YSZ) anode support (Fig. 1b). In the present investigation, thickness of AAL was varied sequentially from 140 down to 15 μm to study its effect on electrochemical performance of single cell. The results of electrochemical studies of single cell with Configuration 2 were presented for the half cells sintered at 1400°C.

The dependence of cell performance (at 800°C, 0.7 V) as a function of AAL thickness and NiO reduction time is shown in Table III. It is evident from Table III that irrespective of AAL thickness, current density increases steadily till NiO reduction equilibration is reached. After the saturation limit, the cell performance remains constant. It is found that the equilibrium time for NiO reduction depends on the thickness of AAL layer. The equilibrium time for NiO reduction require ~6 h for 140 μm AAL; whereas, it decreases to ~3 h for AAL thickness of ≤40 μm. In general, the formulation of AAL layer was made such that its porosity

Table II. Effect of NiO Reduction Time and Sintering Temperature on Electrochemical Performance of Single Cells of Configuration 1 (Anode Thickness: 1.25 mm)

Sintering temperature of the half cells (°C)		1350					1400				
NiO reduction time (h)		0.5	3	7	15	72	0.5	3	7	15	72
Current density (A/cm ²) at 0.7 V	800°C	0.54	0.78	1.35	1.35	1.35	0.82	0.92	1.43	1.43	1.43
	750°C	0.37	0.59	0.92	0.92	0.92	0.55	0.86	0.99	0.99	0.99
	700°C	0.24	0.37	0.43	0.43	0.43	0.34	0.40	0.46	0.46	0.46

■, equilibrium region.

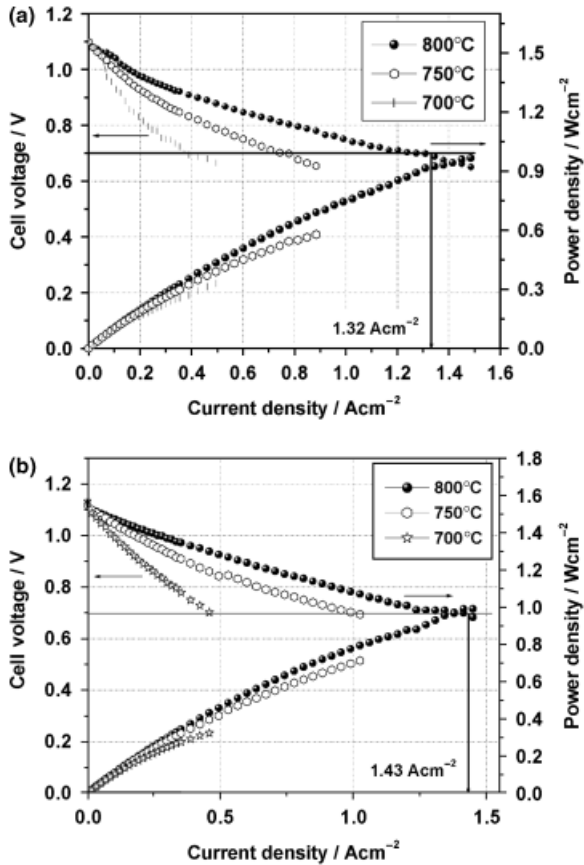
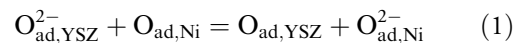


Fig. 2. Electrochemical performance of SOFC with half cell sintered at 1400°C having anode (prepared through electroless technique) thickness of (a) 1.5 mm and (b) 1.25 mm.

becomes less than the anode support. The relatively denser AAL accelerates charge transfer reaction at the TPB length after the electrochemical oxidation of fuel.

The diffusion controlled NiO reduction reaction and electrocatalytic oxidation of hydrogen becomes faster at conventional anode support having sufficient porosity and higher Ni content. However, effective charge transfer reaction preferably occurs at the juncture of anode–electrolyte interface and it prefers thinner AAL. Thus, in this investigation, the optimum thickness of AAL is found to be $\leq 40 \mu\text{m}$, which is evident from the correlation of the NiO reduction process with the cell performances.

Figure 3 shows the I – V characteristics of cells having AAL thicknesses of 140 and 15 μm . From the figure, it is observed that irrespective of the operating temperature, cell performance increases steadily as the AAL thickness decreases. The performances of single cell with different AAL thickness (140, 90, 40, and 15 μm) are presented in Table III. The current density increases from 2.52 to 3.2 A/cm² with corresponding power density of 1.8–2.17 W/cm² at 800°C and 0.7 V (with H₂ as fuel and O₂ as oxidant) with decrease of the AAL thickness from 140 to 15 μm . This can be explained in the same way that diffusion controlled reduction reaction and electrocatalytic oxidation of fuel proceeds faster in the porous conventional anode support ($\sim 40 \text{ vol}\%$ Ni) rather than the less porous AAL prepared by electroless technique. The optimum thickness of AAL is found to be $\leq 40 \mu\text{m}$ for effective charge transfer reaction as given in Eq. (1)



where $\text{O}_{\text{ad,YSZ/Ni}}$ denotes adsorbed oxygen species on YSZ or Ni surface and $\text{O}_{\text{ad,YSZ/Ni}}^{2-}$ denotes formation of oxide ion on YSZ and Ni surfaces.

Table III. Effect of NiO Reduction Time and AAL Thickness on the Performance of SOFC of Configuration 2 at 800°C

Thickness of AAL (μm)	NiO reduction time (h)						
	0.5	3	5	6	15	30	72
	Current density (A/cm ²) at 0.7 V						
140	0.98	1.12	1.31	2.52	2.52	2.52	2.52
90	1.34	1.85	2.63	2.63	2.63	2.63	2.63
40	1.87	2.75	2.75	2.75	2.75	2.75	2.75
15	2.1	3.2	3.2	3.2	3.2	3.2	3.2

■, equilibrium region.

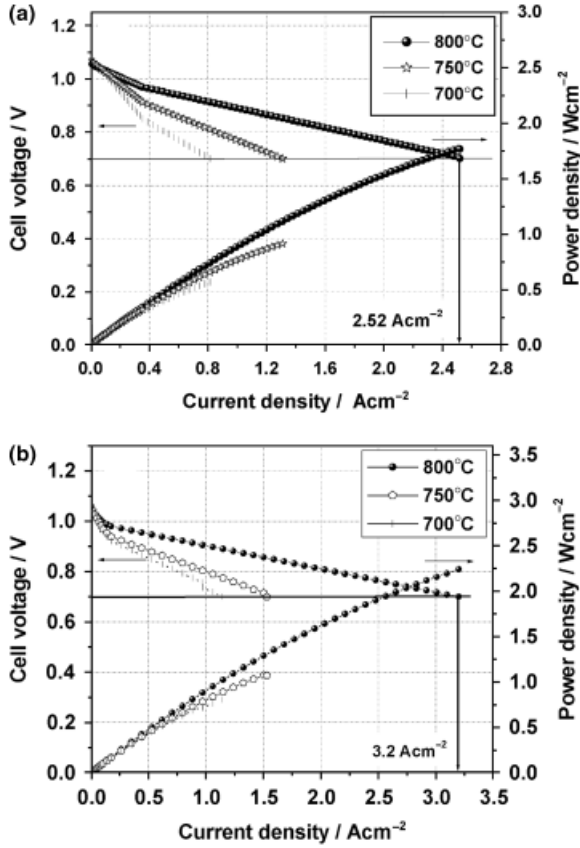


Fig. 3. Electrochemical performance of SOFC with AAL thickness of (a) 140 μm and (b) 15 μm .

It is quite obvious that thinner the AAL, better is the charge transfer reaction at the anode–electrolyte interface. However, below a certain critical AAL thickness, the charge transfer becomes ineffective because of less availability of $\text{O}_{\text{ad},\text{Ni}}^{2-}$ species adjacent to the electrolyte layer to take up the charge from $\text{O}_{\text{ad},\text{YSZ}}^{2-}$. It is observed that single cells with 15 μm AAL show highest current density of $\sim 3.2 \text{ A/cm}^2$ (power density of $\sim 2.3 \text{ W/cm}^2$) at 800°C and 0.7 V with hydrogen as fuel and oxygen as the oxidant. In contrast, single cell fabricated with conventional NiO–YSZ anode support without AAL exhibits much lower current density of $\sim 1.7 \text{ A/cm}^2$ as reported in our previous communication.¹⁵ In AAL prepared by electroless technique, unique core (YSZ)–shell (Ni) microstructure is expected to increase the TPB (because of controlled deposition of discrete Ni around the YSZ core) that helps in enhancing the electrochemical performance of such cells.

Correlation Between Cell Configuration and Area Specific Resistance (ASR) of the Cell

The ASR of single cells are calculated from the slope of the linear portion of I – V curve. In the present investigation, the cell is comprised of five distinct layers. Thus, contributions from all components toward cell ASR (R) can be written as

$$R = R_{\text{electrolyte}} + (R_{\text{anode}} + R_{\text{AAL}}) + (R_{\text{cathode}} + R_{\text{CAL}}) + R_{\text{contact}} \quad (2)$$

where $R_{\text{electrolyte}}$, R_{anode} , R_{AAL} , R_{cathode} , R_{CAL} , and R_{contact} are contributions of resistances from electrolyte, anode layer, AAL, CL, CAL, and interfacial contacts, respectively.

Because the only varied parameter in the present investigation is the thickness of anode and AAL, Eq. (2) can be written as

$$R = \rho_{\text{anode}} l_{\text{anode}} + R_{\text{constant}} \text{ for Configuration 1} \quad (3)$$

$$R = \rho_{\text{AAL}} l_{\text{AAL}} + R_{\text{constant}} \text{ for Configuration 2}$$

where ρ_{anode} , ρ_{AAL} , l_{anode} , and l_{AAL} are resistivity per unit area and thickness of anode and AAL, respectively. R_{constant} is the ASR contribution from other sources as mentioned in Eq. (2).

It is observed from the cells with *Configuration 1* that ASR increases marginally with increase in cell thickness. Thus, the thinner anode support (1.25 mm) shows ASR of $276 \text{ m}\Omega \text{ cm}^2$; whereas, the thicker one (1.5 mm) gives a value of $280 \text{ m}\Omega \text{ cm}^2$. Similarly, for single cells of *Configuration 2*, the ASR value increases with increase in AAL thickness (Fig. 4). Therefore, cells with AAL thickness of 140, 90, 40, and 15 μm show ASR values of 123, 116, 103, and 94 $\text{m}\Omega \text{ cm}^2$, respectively. Increase of AAL thickness decreases the effective charge transfer rate of $\text{O}_{\text{ad},\text{YSZ}}^{2-}$ to $\text{O}_{\text{ad},\text{Ni}}^{2-}$ (as given in reaction 1) at the AAL–electrolyte interface, thereby causing a higher ASR. In comparison, single cell with conventional NiO–YSZ anode support shows higher ASR of $\sim 2850 \text{ m}\Omega \text{ cm}^2$ at 800°C.¹⁸ The plot of measured ASR (R) of single cells with half cell sintered at 1400°C as a function of AAL thickness in *Configuration 2* is observed to be linear from Fig. 4. The intercept of the figure corresponds to the ASR (R_{constant}) contribution from other sources, viz. electrolyte, cathode, and so forth. Therefore, incorporation of Ni–YSZ cermet prepared through electroless

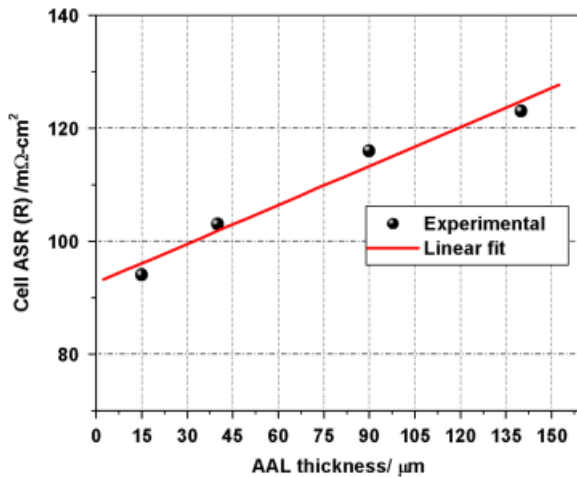


Fig. 4. Measured cell area specific resistance (ASR) at 800°C as a function of thickness for AAL prepared by electroless technique.

technique in the form of AAL is found to be more effective (with higher electrochemical performance) than that of the total structural support.

Microstructural Features

A typical optical micrograph of the cross-section of coupon cell of *Configuration 1* is shown in Fig. 5a. The figure shows retention of unique core (YSZ)–shell (Ni) microstructure in the anode support prepared through electroless technique. Optimization of process parameters during electroless technique enables controlled deposition of finer Ni particulates onto YSZ surface, which is reflected in the micrograph. The corresponding elemental line mapping for nickel and zirconium of such sample is shown in Fig. 5b. It is revealed from the figure that the concentration of fine Ni particulates at the shell position is higher. In contrast, the YSZ concentration is found to be higher at the core position of the Ni–YSZ cermet prepared by electroless technique. This corresponds to the periodic crest-hub type distribution of elemental “Ni” and “Zr” at the shell and core position, respectively. Such core–shell microstructure helps in maintaining electrical interconnection through Ni–Ni nanoparticulate chains in the electroless cermet.

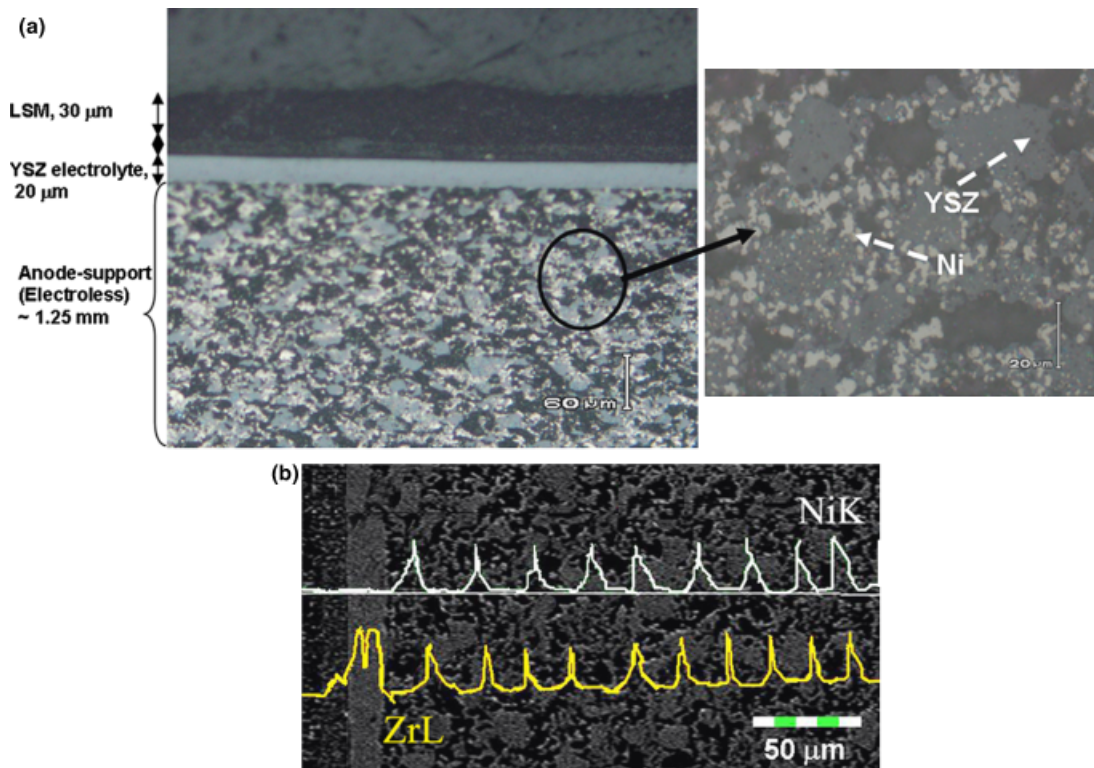


Fig. 5. (a) Optical micrograph (with higher magnification of anode in right side) and (b) corresponding line mapping of single cell with Ni–YSZ as anode support prepared through electroless technique after electrochemical measurement.

The optical micrograph of the coupon cell having AAL prepared by electroless technique (*Configuration 2*) and its corresponding line mapping is shown in Figs. 6a and b, respectively. The figure clearly reveals the difference in microstructure of Ni-YSZ cermet anode prepared by two different processing techniques. Dispersed distribution of Ni and YSZ phases in the matrix of conventional anode cermet is clearly observed from the elemental line mapping of “Ni” and “Zr,” which shows a nonperiodic distribution in the support structure. AAL prepared through electroless technique still maintain the crest-hub type distribution of “Ni” and “Zr” (Fig. 6b) as also found in the anode support (Fig. 5b). The unique microstructure with discrete Ni particulates around YSZ core either in the anode support or in the AAL is expected to enhance the triple phase boundary lengths. This, in turn, helps in

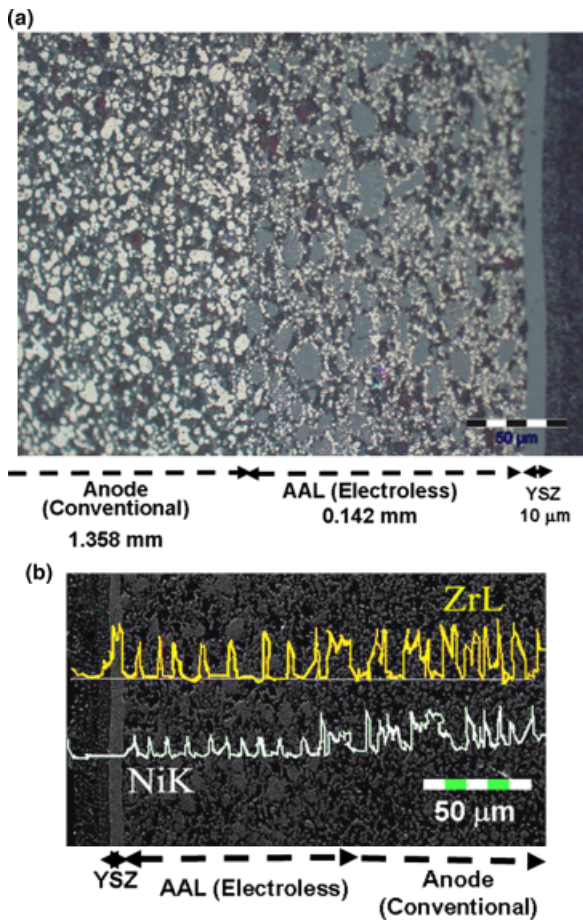


Fig. 6. (a) Optical microstructure and (b) line mapping of SOFC after electrochemical measurement having anode active layer prepared through electroless technique.

the fuel oxidation and favors the electrochemical reactions at the anode–electrolyte interfaces.

Effect of Pore-Size Distribution of Anode on Cell Performance

Figure 7 shows the pore-size distribution of anodes of both configurations measured before and after reduction. Figure 7a shows a narrow unimodal pore-size distribution of 1.25 mm anode support prepared through electroless technique (*Configuration 1*) with pore-size in the range of 0.85–0.9 μm both before and after reduction. The median pore diameter for *Configuration 1* (Fig. 7a) was found to be ~0.96 μm; whereas, the peak pore diameter was found to be ~0.92 μm for the reduced samples. In comparison, Fig. 7b shows wider

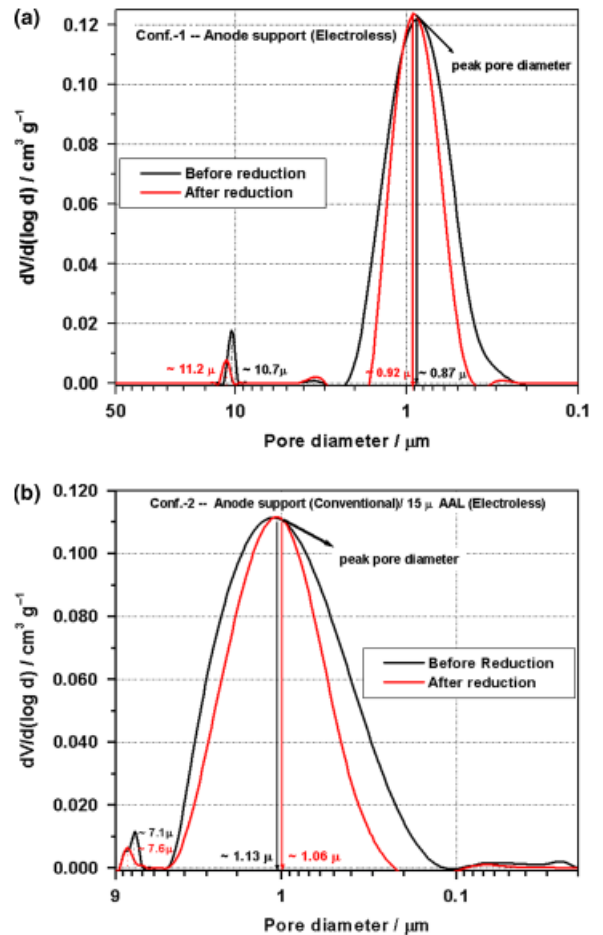


Fig. 7. Pore-size distribution of the anode cermets sintered at 1400°C of (a) Configuration 1 and (b) Configuration 2.

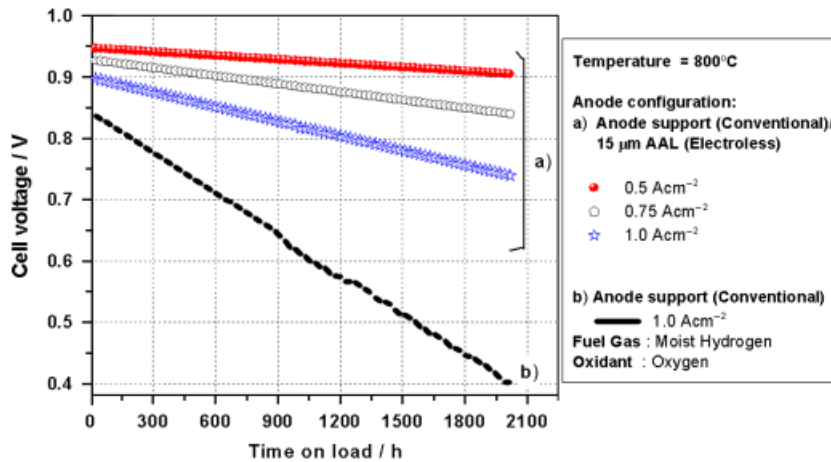


Fig. 8. Endurance test on single cell with anode configurations: (a) conventional anode support/15 μm AAL and (b) conventional anode support.

pore-size distribution of anode cermet containing AAL of $\sim 15 \mu\text{m}$ thickness prepared through electroless technique (*Configuration 2*). Such reduced anode cermets were found to have pores in the range of 1–1.15 μm with median and peak pore diameters at ~ 1.38 and $\sim 1 \mu\text{m}$, respectively. For both the configurations, it is observed that median pore diameter reduces after reduction of anode structure, which is indicative of more uniformity of the pore-size distribution. In *Configuration 2*, the effect of porosity is primarily observed because of conventional anode support where the effect of thin AAL ($\sim 15 \mu\text{m}$) is found to be negligible. The larger median and peak pore diameters of the conventional anode support help in better gas diffusion. In contrast, the smaller pore diameter of AAL ensures more capillary action for the fuel fed at the anode. The smaller pores in AAL ensure steady electrochemical reaction at the TPB after effective dissociation of hydrogen at the conventional anode support. Such pore-size distribution is expected to be the key factor for getting such high performance for the cells with *Configuration 2*. For *Configuration 1*, the steady electrochemical reaction is guided not only by smaller percentage of overall Ni content but also by the smaller pore diameters. The gas diffusion process in the anode of *Configuration 1* becomes the rate determining step and hence the limiting factor in obtaining significant high cell performance.

Endurance Test of SOFC

The single cells fabricated with anode support with AAL prepared by electroless technique (*Configuration 2*)

and conventional NiO–YSZ was subjected to constant electronic load for considerable time period (2000 h) to study the rate of performance degradation. Figure 8 shows the rate of change of cell voltage (at 800°C) as a function of operation time under three different loads (0.5, 0.75 and 1.0 A/cm^2) for cells having different configurations. Upon application of electronic load in the circuit, cell voltage drops significantly in the initial time period of 1000 h. This drop is found to be more pronounced as the applied load is increased from 0.5 to 1.0 A/cm^2 . Degradation rates were determined from the durability curve using standard method of calculating the absolute voltage drop and normalizing the same to 1000 h.¹⁹ Figure 9 shows such degradation plot against applied loads up to 2000 h of continuous operation. It is observed from the figure that irrespective of the applied load, the cell degradation is more pronounced for the initial 1000 h of operation. As the load increased from 0.5 to 1.0 A/cm^2 , the degradation rate increased from 42 to $79 \text{ m}\Omega \text{ cm}^2/\text{kh}$, respectively. The cell degradation behavior is expected to be primarily associated with increase in ohmic resistances in bulk layers and interfaces, coarsening in various layers, and other associated reactions at anode–electrolyte interfaces.^{5,19} With increase in applied load across the cell, local joule heating or resistive heating is expected to get enhanced. Over 2000 h of cell operation, the degradation rates of the cell are found to be 42, 58, and $79 \text{ m}\Omega \text{ cm}^2/\text{kh}$ at the corresponding applied load of 0.5, 0.75 and 1.0 A/cm^2 , respectively. Table IV shows the degradation at these applied loads corresponds to 2.2, 4.7% and 8.8% voltage degradation per 1000 h of operation. In comparison,

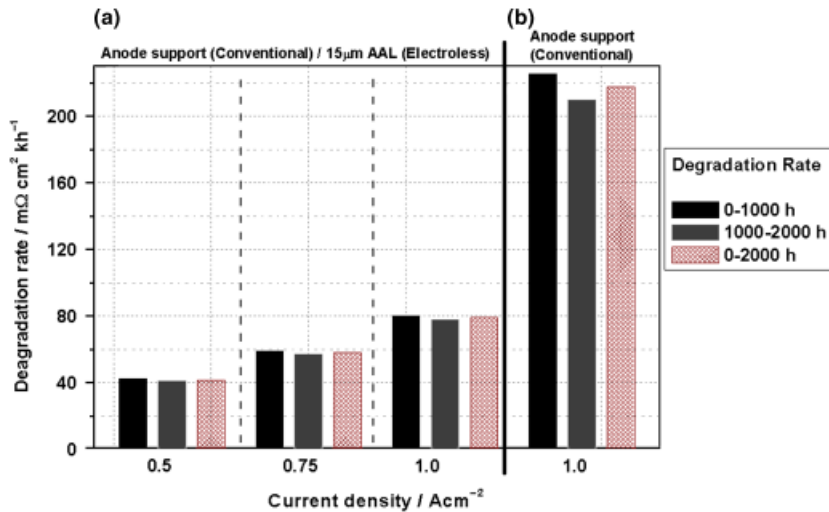


Fig. 9. Degradation rates determined from durability test on single cell with anode configurations: (a) conventional anode support/15 μm AAL (electroless technique) and (b) conventional anode.

for the single cells with conventional anode support such degradation rate is found to be ~26% at an applied circuit load of 1.0 A/cm² (Table IV). The reason for such difference could be due to increased local resistive heating and enhanced Ni coarsening in the presence of a constant load of ~1.0 A/cm². The rate of Ni coarsening is higher for the cells with conventional anode support having higher Ni content with dispersed distribution of Ni and YSZ phases.

Conclusions

Anode cermet powder synthesized by electroless technique containing 28 vol% Ni is successfully used for the fabrication of single cells in two different configurations as (a) structural support and (b) AAL using

simple tape casting and lamination techniques. Unique core (YSZ)–shell (Ni) microstructure is obtained through electroless technique during the optimized deposition of discrete Ni particulates onto sensitized YSZ. Such microstructure is believed to enhance the TPB (both at the anode–electrolyte interface and within the anode) compared with the conventional anode cermet. These features add functionality and enable the anode support prepared through electroless technique containing only 28 vol% of Ni to be electrochemically active at par with the conventional cermet having ~40 vol% Ni. However, incorporation of Ni–YSZ as AAL prepared through electroless technique dramatically increases the electrochemical performance of the developed single cells. It is further observed that the cell performance increases with decreasing thickness of the Ni–YSZ cermet prepared through electroless technique in both the configurations. The electrochemical activity of cell depends on the extent of reduction from NiO to metallic Ni of anode. Lowering in anode thickness from 1.5 to 1.25 mm decreases the NiO reduction saturation time period from ~10 to ~7 h. However, in *Configuration 2*, sequential reduction in AAL thickness from 140 to 15 μm further enhances the NiO reduction process and subsequently reduces the reduction equilibration time to ~3 h. It is experimentally determined that, for effective charge transfer reaction, thickness of AAL layer should either be equal to or less than 40 μm. Single cell containing ~15 μm AAL sintered at 1400°C shows highest performance of ~3.2 A/cm² at 0.7 V and 800°C.

Table IV. Comparative Single Cell Degradation Rates Using Different Anode Configurations

Anode configuration	Applied load (A/cm ²)	% Degradation w.r.t. voltage per 1000 h
Conventional anode/ 15 μm AAL (by electroless technique) (Fig. 9a)	0.5	2.2
	0.75	4.7
	1.0	8.8
Conventional anode support (Fig. 9b)	1.0	26.1

Therefore, AAL thickness is optimized to 15 μm for the most effective charge transfer reaction with maximum electrochemical performance among the series. The microstructural studies exhibit retention of core (YSZ)–shell (Ni) structure of the anode prepared through electroless technique in single cells. Such unique microstructure helps in maintaining interconnection among Ni particulates as well as between adjacent YSZ particles. The degradation of single cell with 15 μm AAL is found to be 42, 58, and 79 $\text{m}\Omega\text{cm}^2/\text{kh}$ over a time period of 2000 h of operation (at the corresponding load of 0.5, 0.75, and 1.0 A/cm^2). Corresponding degradation rates are calculated to be 2.2%, 4.7% and 8.8% voltage degradation per 1000 h in comparison with $\sim 26\%$ degradation for the cell with conventional anode support. It is observed from pore-size distribution that the diffusion of the fuel fed at the anode is primarily governed by the conventional anode support having wider pore-size distribution; whereas, the smaller pore diameter of the AAL prepared by electroless technique having narrower pore-size distribution ensures more capillary action. Therefore, high electrochemical performance is obtained for the cells with conventional anode support with a critical AAL thickness.

Acknowledgments

The authors acknowledge the director of CGCRI for his kind permission to publish the work. M. M. is thankful to Council of Scientific and Industrial Research (CSIR), India, for providing senior research fellowship.

References

1. D. J. L. Brett, A. Atkinson, N. P. Brandon, and S. J. Skinner, "Intermediate Temperature Solid Oxide Fuel Cells," *Chem. Soc. Rev.*, 37 1568–1578 (2008).
2. P. Holtappels, U. Vogt, and T. Graule, "Ceramic Materials for Advanced Solid Oxide Fuel Cells," *Adv. Eng. Mater.*, 7 292–302 (2005).
3. A. Weber and E. Ivers-Tiffée, "Materials and Concepts for Solid Oxide Fuel Cells (SOFCs) in Stationary and Mobile Applications," *J. Power Sources*, 127 273–283 (2004).
4. A. Tsoga, A. Naoumidis, and P. Nikolopoulos, "Wettability and Interfacial Reactions in the Systems Ni/YSZ and Ni/Ti–TiO₂/YSZ," *Acta Mater.*, 44 3679–3692 (1996).
5. N. Q. Minh and T. Takahashi, *Science and Technology of Ceramic Fuel Cells*, Elsevier, New York, 1995.
6. D. E. Dees, et al., "Conductivity of Porous Ni/ZrO₂–Y₂O₃ Cermet," *J. Electrochem. Soc.*, 134 2141–2146 (1987).
7. N. M. Sammes, M. Brown, and I. W. M. Brown, "Synthesis and Properties of Dense Nickel and Cobalt Zirconia Cermet Anodes for Solid Oxide Fuel Cells," *J. Mater. Sci.*, 31 6069–6072 (1996).
8. T. Kawada, N. Sakai, and H. Yokokawa, "Structure and Polarization Characteristics of Solid Oxide Fuel Cell Anodes," *Solid State Ionics*, 40 [1] 402–406 (1990).
9. S. K. Pratihari, R. N. Basu, S. Mazumdar, and H. S. Maiti, "Electrical Conductivity and Microstructure of Ni–YSZ Anode Prepared by Liquid Dispersion Method," *Proceedings of the Solid Oxide Fuel Cells (SOFC VI)*, Electrochemical Society, 1999.
10. S. C. Singhal and K. Kendall, *High Temperature Solid Oxide Fuel Cells: Fundamentals, Design and Applications*, Elsevier, U.K., 2003.
11. R. N. Basu, *Materials for Solid Oxide Fuel Cells in Recent Trends in Fuel Cell Science and Technology*, ed., S. Basu. Anamaya Publishers/Springer, New Delhi, India/New York, 2006.
12. T. Iwata, "Characterization of Ni–YSZ Anode Degradation for Substrate-Type Solid Oxide Fuel Cells," *J. Electrochem. Soc.*, 143 1521–1525 (1996).
13. J. Mukhopadhyay, M. Banerjee, A. Das Sharma, R. N. Basu, and H. S. Maiti, "Development of Functional SOFC Anode," *Electrochem. Soc. Trans.*, 7 [1] 1563–1572 (2007).
14. J. Mukhopadhyay, M. Banerjee, and R. N. Basu, "Influence of Sorption Kinetics for Zirconia Sensitization in Solid Oxide Fuel Cell Functional Anode Prepared by Electroless Technique," *J. Power Sources*, 175 749–759 (2008).
15. R. N. Basu, A. Das Sharma, A. Dutta, and J. Mukhopadhyay, "Processing of High Performance Anode-Supported Planar Solid Oxide Fuel Cell," *Int. J. Hydrogen Energy*, 33 [20] 5748–5754 (2008).
16. M. Mukhopadhyay, J. Mukhopadhyay, A. Das Sharma, and R. N. Basu, "Use of Electroless Anode Active Layer in Anode-Supported Planar SOFC," *Electrochem. Soc. Trans.*, 25 [2] 2267–2274 (2009).
17. X. Zhua, et al., "Enhanced Performance of Solid Oxide Fuel Cells with Ni/CeO₂ Modified La_{0.75}Ce_{0.25}Cr_{0.5}Mn_{0.5}O_{3–d} Anodes," *J. Power Sources*, 190 [2] 326–330 (2009).
18. A. Dutta, J. Mukhopadhyay, and R. N. Basu, "Combustion Synthesis and Characterization of LSCF-Based Materials as Cathode of Intermediate Temperature Solid Oxide Fuel Cells," *J. Eur. Ceram. Soc.*, 29 2003–2011 (2009).
19. L. G. J. de Haart, J. Mougou, O. Posdziech, J. Kiviahio, and N. H. Menzler, "Stack Degradation in Dependence of Operation Parameters; the Real SOFC Sensitivity Analysis," *Fuel Cells*, 9 [6] 794–804 (2009).

Multilayered SOFC Anode Structure with Electroless Ni-YSZ for Enhancement of Cell Performance

Madhumita Mukhopadhyay, J. Mukhopadhyay, A. Das. Sharma and R. N. Basu

Fuel Cell & Battery Division, Central Glass & Ceramic Research Institute, CSIR
Kolkata 700 032, India

High performance SOFC is fabricated using multilayer anode support with graded porosity. The graded anode fulfills the requirement of proper fuel oxidation at anode, effective electrochemical reaction at anode/electrolyte interface, thermal compatibility among cell components and long term stability. In such multilayer anode, conventional cermet (40 vol% Ni) helps in proper fuel diffusion and catalytic oxidation. Novel electroless anode (28-32 vol% Ni) is employed adjacent to YSZ electrolyte for effective electrochemical activity and thermal compatibility. Because of the presence of unique core (YSZ)-shell (Ni) microstructure, electroless anode is found to extend the anodic electrochemical reaction from electrolyte/anode interface to the bulk. Significant performance enhancement with current density of $\sim 3.3 \text{ A cm}^{-2}$ is observed for single cells fabricated with multilayer anode at 800°C , 0.7V. The multilayer anode is found to reduce the cell degradation from $\sim 11\%$ (conventional anode) to $\sim 1.6\%$ /1000 h during long term performance (~ 2000 h).

Introduction

Solid oxide fuel cell (SOFC) has attracted global attention and emerged as a potential source of alternate energy. It is a promising technology as a cogeneration system because of its high efficiency and low gas emissions. Although electrical efficiency of 45-50% is reported in literatures (1), technological viability depends on the degree of efficiency obtained under practical environmental conditions. The electrolyte supported SOFC practiced in past, operates at $\sim 1000^\circ\text{C}$. The modern approach of lowering the operation temperature to $600\text{-}800^\circ\text{C}$ reduces the SOFC system costing by broadening the choice of compatible materials (2). In this context, the anode-supported cell designs with thinner electrolyte offer an easier method of lowering SOFC operating temperature with low ohmic losses (3-4). However, at intermediate temperature, the interfacial resistance of the anode-supported SOFC becomes dominant. Therefore, the quality of anode has a pronounced effect on the performance of anode-supported cell. Besides high efficiency and power output, long term stability is one of the challenging aspects of modern anode-supported SOFCs. The widely used SOFC anode [nickel-8 mol% yttria stabilized zirconia (Ni-YSZ)] is susceptible to long term degradation. This can be ascribed due to the agglomeration of Ni particles at high operating temperature ($800\text{-}1000^\circ\text{C}$) and thermal incompatibility with electrolyte due to the presence of higher (~ 40 vol%) Ni content (5-7). The multilayered anode structure is therefore proposed to prevent degradation and increase performance. Such anode structure is fabricated preferably with variable Ni-

content and porosity (8). Smaller pores in the anode cermet are expected to provide large interfacial area per unit volume and therefore contribute towards enhanced triple phase boundary (TPB). However, these smaller pores offer relatively large resistance to gas diffusion in a thicker anode. In contrast, large pores are effective in facilitating gas diffusion, but the effective interfacial areas are reduced. For effective gas diffusion at the anode with enhanced electrochemical reaction at anode/electrolyte interface, microstructure of the bulk anode and interface should have variation in porosity and Ni content. Therefore, multilayered anode cermet of aforesaid configuration is expected to fulfill the aforesaid criteria for fabrication of high performance cells.

An electroless technique for the preparation of Ni-YSZ anode with ~ 28 vol% Ni is reported in our earlier communications for satisfying the required electrical conductivity in SOFC operational condition (9-10). The electroless anode is developed with core (YSZ) - shell (Ni) microstructure. Such unique microstructure enables interconnecting network of Ni, YSZ and pores throughout the cermet matrix. Fine Ni particulates are produced in-situ in the electroless bath and deposited on YSZ. The optimum reaction condition for electroless deposition generates patterned intra-anode TPB network within the anode cermet. In the present investigation, electroless cermet is used in combination with conventional (11-12) NiO-YSZ to fabricate the multilayer anode structure. Electroless anode (28-32 vol% Ni) with smaller pores and lower porosity is used adjacent to the YSZ electrolyte. This facilitates better thermal compatibility, low polarization losses and higher electrochemical activity. However, conventional anode (~ 40 vol% Ni) with larger pores and higher porosity is used towards the fuel side for better gas diffusion and effective catalytic oxidation. Multilayer anode is fabricated with variation in electroless anode thickness to study its effect on the cell performance. The effect of multilayer anode configuration is studied for its thermal compatibility with YSZ electrolyte. Single cells fabricated with multilayer anode are tested electrochemically for performance evaluation and comparison of performances based on different configurations between conventional and electroless cermet. Prolonged operation of single cells is carried out for a reasonable time period of 2000 h and the corresponding degradation rates are also investigated and compared with the cells prepared with conventional anode.

Experimental

Two different processing techniques viz. a) conventional and b) electroless are employed for the preparation of NiO/Ni-YSZ anode powders. The synthesis procedures are already described in our earlier communications (9-10, 13-14). The synthesized electroless (28-32 vol% Ni) and conventional (40 vol% Ni) anode powders are tape casted into green tapes and are laminated together at room temperature to form multilayer anode. In addition, green (unfired) block of conventional and electroless anode are also prepared by similar casting and lamination. The fabricated green anodes are air sintered at 1400^oC and are finally reduced at 800^oC for 10 h in an atmosphere of Ar: H₂ (80:20). The coefficient of thermal expansions (CTE) of the reduced samples is measured by a high temperature dilatometer (NETZSCH, Model DIL 402C) under argon atmosphere. Pore distribution of the fabricated anodes is determined by mercury porosimetry (Quantachrome Poremaster 60, Florida, USA).

Fabrication of half cells involves an initial tape casting of anode (both conventional and electroless) with variable porosity as described above with a thin layer of YSZ

electrolyte. This is followed by room temperature lamination and co-sintering at 1400°C to form the corresponding half cells with multilayer anode structure (conventional anode/electroless anode/YSZ electrolyte) with graded porosity. The sintered half cells are screen printed with cathode (CL-LSM) and cathode active layer (CAL-LSM+YSZ) followed by co-sintering at 1100°C to form the single cell (13-15). The thickness of electroless anode layer is varied in the order of 250 to 50 μm to study the effect on various single cell properties. For comparison, single cells with conventional anode cermets (without any gradation in porosity in anode) are also fabricated. The coupon cells (~ 16 mm diameter) thus fabricated is subjected to electrochemical measurement using hydrogen as fuel and oxygen as the oxidant in the temperature range of 700-800°C. The detail of measurement set up is also described in our earlier communications (13-15). The dependence of cell performance on fuel and oxidant flow rates is also investigated. Long term electrochemical testing of single cells of both the configurations (with and with out multilayer anode support) is carried out for ~ 2000 h to study the respective degradation rates. The observed electrochemical activity of the aforesaid cells are correlated with the microstructures obtained by using high resolution microscope (Olympus GX 71, Japan) and field emission scanning electron microscope (FESEM) [Gemini Supra 35, Zeiss], respectively.

Results and Discussion

Dependence of Electrochemical Performance on Anode Configuration

The schematic of multilayer anode is shown in Fig. 1. It can be seen from the figure that, conventional anode with 40 vol % Ni, having higher porosity is placed towards the fuel inlet side. However, electroless anode (28-32 vol % Ni) with relatively smaller Ni particulates and lower porosity is laminated adjacent to the YSZ electrolyte. Therefore, the characteristics of each component in the multilayered anode prepared by two different techniques differ widely in terms of particle size, porosity and Ni content. Single cell with novel electroless anode (32 vol % Ni) shows higher performance of 1.98 Acm⁻² in contrast to the cell fabricated with conventional anode (1.7 Acm⁻²) with 40 vol% Ni at 800°C, 0.7 V (Fig. 2). Optimized processing conditions during electroless technique generates core (YSZ) - shell (Ni) microstructure as observed from the Ni mapping in Fig. 2b. Such unique microstructure forms continuous network of Ni, YSZ and pores throughout the cermet and thereby ensures easy percolation of electron, O²⁻ ion and fuel in the matrix. In addition, such microstructure has an added advantage of generating

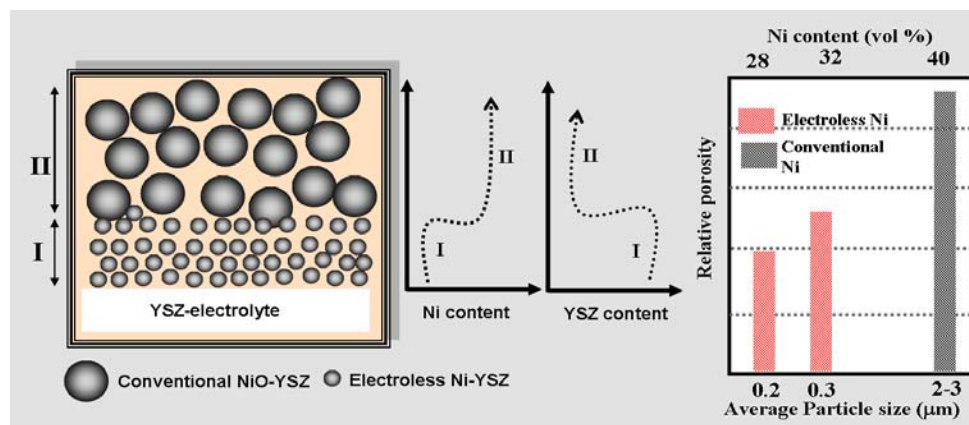


Figure 1. Schematic of a multilayered anode with graded properties.

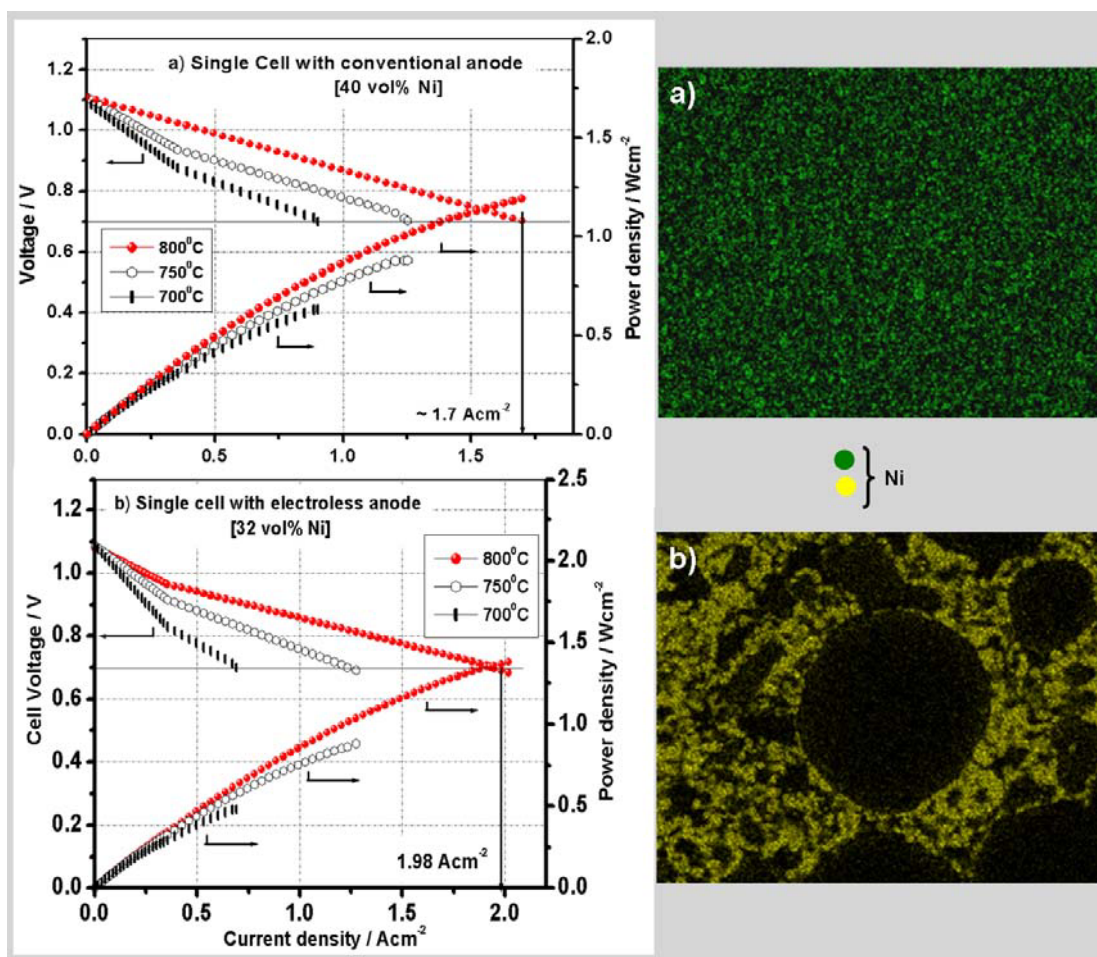


Figure 2. Electrochemical performance of single cell fabricated with: a) conventional and b) electroless anode with the corresponding Ni-mapping.

patterned intra-anode TPB sites within the anode in order to facilitate the anodic electrochemical reactions. The electrocatalytic activity of fine Ni particulates of electroless anode is higher compared to the dispersed bulk/cluster Ni (Fig. 2a) of the conventional cermet. These superiorities of electroless anode result in higher electrochemical performance of single cell at much lower Ni content.

Incorporation of multilayer anode increases the cell performance to $\sim 2.54 \text{ Acm}^{-2}$ at 800°C and 0.7 V (Fig. 3). In the multilayered anode, conventional cermet with higher porosity and pore-size helps in easy fuel diffusion. In addition, higher Ni-content (40 vol% Ni) with relatively large particle size maintains good electrical contact with the current collector. The higher Ni content also facilitates the effective fuel oxidation. The conventional porous layer therefore acts as the gas distributor, current collector and catalyst layer. On the other hand, the electroless anode ($\sim 28 \text{ vol\% Ni}$) with lesser porosity placed adjacent to YSZ electrolyte is the electrochemically active layer. Patterned intra-anode TPB of electroless anode accelerates the progression of charge transfer reaction ($\text{O}^{2-}_{\text{ad,YSZ}}$ to $\text{O}^{2-}_{\text{ad,Ni}}$) from conventional TPB (anode/electrolyte interface) to the bulk anode. The polarization resistance generated during electrocatalytic reactions therefore get reduced upon using electroless anode at YSZ interface. The comparative ohmic area specific resistance calculated from the linear part of the I-V plot

shows significant reduction ($141 \text{ m}\Omega\cdot\text{cm}^2$) compared to the cells with conventional anode ($2850 \text{ m}\Omega\cdot\text{cm}^2$). The difference in Ni content of electroless and conventional anode is observed from the intensity variation in the Ni mapping of Fig.3.

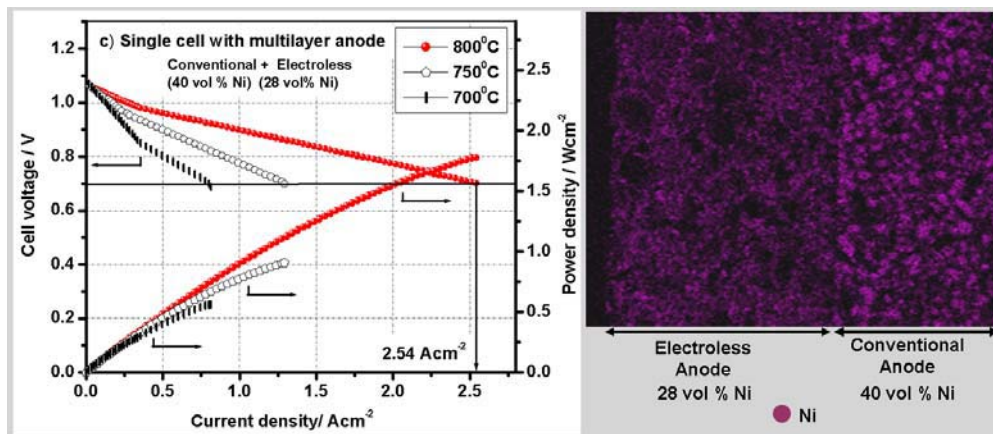


Figure 3. Electrochemical performance of single cell fabricated with multilayered anode with the corresponding Ni-mapping.

In addition, it is observed from Fig.4 that, coefficient of thermal expansion (CTE) of electroless anode ($11.5 \times 10^{-6} \text{ } ^\circ\text{C}^{-1}$) is found to be close to that of YSZ electrolyte ($10.85 \times 10^{-6} \text{ } ^\circ\text{C}^{-1}$) in comparison to conventional anode with higher CTE ($13 \times 10^{-6} \text{ } ^\circ\text{C}^{-1}$). The multilayer anode is found to exhibit CTE value similar to the electroless anode. This indicates significant contribution of electroless cermet towards the thermal expansion behaviour of multilayer anode. Therefore, multilayer cermet acts as the effective anode with compatible CTE which prevents interfacial delamination and consists of extended TPB for enhanced electrochemical reaction.

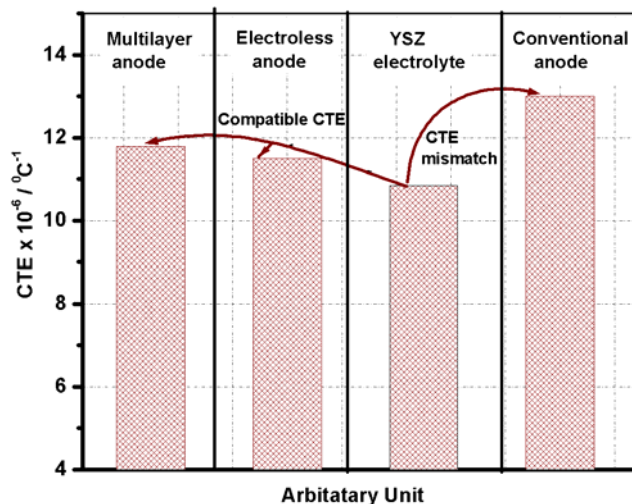
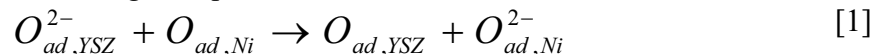


Figure 4. Comparative CTEs of electrolyte with electroless, conventional and multilayer anodes.

Tailoring Electroless Anode Thickness and Correlation with Pore-size Distribution

The dependence of single cell performance with multilayer anode on the thickness of electroless cermet (32 vol% of Ni) is shown in Fig. 5. It is observed from the figure that performance of the single cell varies linearly with reduction of electroless anode

thickness. In the multilayer anode structure, electroless cermet is responsible for the progression of electrochemical anodic reactions. The charge transfer of oxide ion (O^{2-}) from YSZ to Ni surface occurs instantaneously at the anode-electrolyte interface through adsorption mechanism according to Eq.1.



Presence of dual TPB zones (intra-anode and conventional anode) in the electroless cermet help in the enhancement charge transfer reaction from anode-electrolyte interface to the bulk anode. According to the usual kinetic theory, the rate of charge transfer reaction accelerates with the reduction in layer thickness. Upon decreasing the electroless

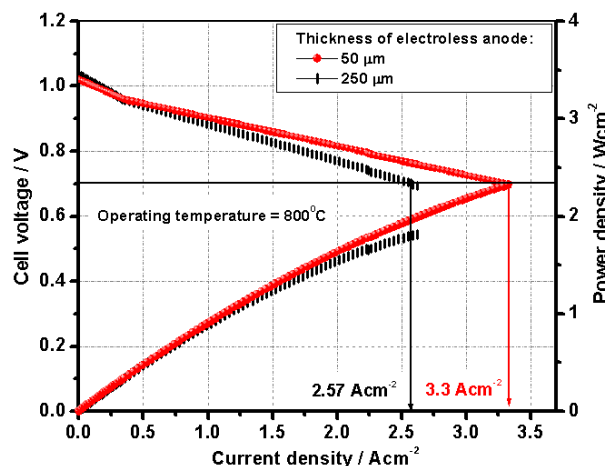


Figure 5. Comparative electrochemical performance of single cell with variation of electroless anode thickness (50-250 μm) of the multilayer anode.

anode thickness from 250 to 50 μm , ohmic polarization loss decreases (130 to 101 $\text{m}\Omega\cdot\text{cm}^2$). This results in increasing the cell performance from 2.57 Acm^{-2} (250 μm) to 3.3 Acm^{-2} (50 μm) at 800 $^{\circ}\text{C}$ and 0.7 V. However, reducing the electroless anode thickness beyond a critical range induces resistance for the above reaction. This is due to the fact that, very thin electrochemical zone adjacent to the electrolyte is ineffective in providing enough active Ni sites for effective adsorption of the transferred O^{2-} ions from YSZ layer.

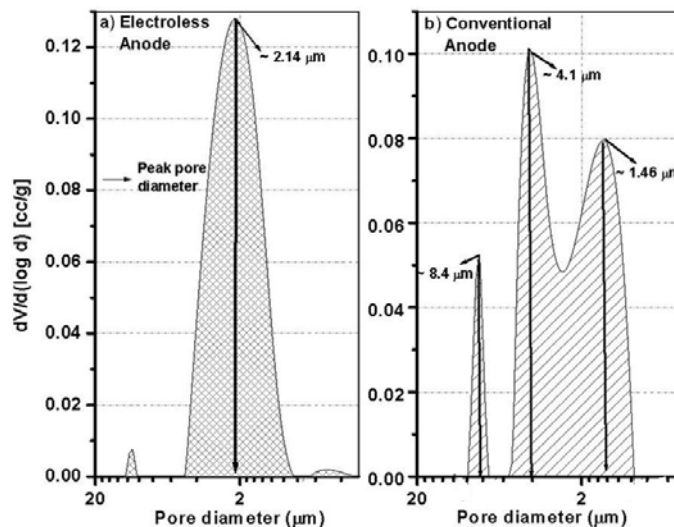


Figure 6. Pore-size distributions of a) electroless and b) conventional anodes.

The contribution of multilayer anode towards cell performance can be correlated with the pore-size distribution of the respective anodes (Fig. 6). The unimodal narrow pore size distribution of electroless anode (Fig. 6a) with relatively less peak pore diameter (2.14 μm) ensures better capillary action for the fuel fed. Such distribution is effective for enhancement of electrochemical reaction at TPB but ineffective for sufficient gas diffusion through the anode. In contrast, the multimodal pore-size distribution of conventional anode with larger pore size (1.5 - 8.4 μm) facilitates gas diffusion through it. However, large variable pores of the conventional anode restrict the interfacial area. Therefore, combination of electroless and conventional cermet in the multilayer anode fulfils the requirement of both gas transportation and electrochemical activity thereby enhancing the cell performance with least polarization losses.

Role of Fuel in Anodic Electrochemical Reactions

The electrochemical behaviour of hydrogen oxidation is significantly influenced by the presence of water in the fuel. For the aforesaid study, single cells fabricated with multilayer anode having 50 μm thick electroless layer is selected. The kinetics of hydrogen oxidation is known to be related with the oxygen activity on Ni surface (16).

TABLE I. Effect of gas composition on the performance of single cell fabricated with multilayer anode

Experiment Number	Gas compositions	Gas flow rates (SCCM)				
		20	50	100	150	200
		Current density (Acm^{-2}) at 800 ^o C and 0.7 V				
I	O ₂ - 200 SCCM+ H ₂ [Moist, flow Changed]	2.5	2.7	3.0	3.28	3.3
II	O ₂ - 200 SCCM+ H ₂ [Dry, flow Changed]	2.34	2.35	2.37	2.38	2.4
III	H ₂ [Moist, 200 SCCM]+ O ₂ [flow Changed]	3.3	3.282	3.3	3.29	3.3
IV	H ₂ [Dry, 200 SCCM]+ O ₂ [flow Changed]	2.38	2.4	2.39	2.4	2.4

■ Significant performance variation

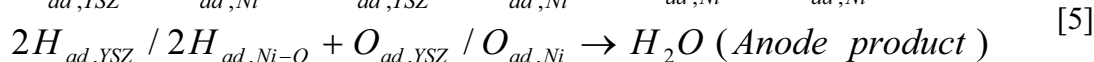
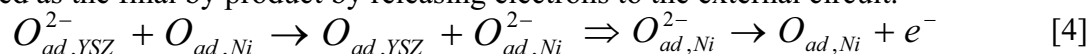
Moisture from the fuel undergoes dissociative decomposition to produce oxygen species which readily get adsorbed on Ni surface.



According to the mechanism, both YSZ and Ni contributes towards dissociative H₂adsorption (Eq.3) at anode. This is followed by charge transfer reaction of adsorbed



O²⁻ ion from YSZ to Ni species at active electroless anode (Eq.4) and thereby water is formed as the final by product by releasing electrons to the external circuit.



The decomposition of moisture therefore initiates the reaction path through bulk anode and propagates it towards the electroless layer. This active layer contributes in the charge

transfer reaction and finally forms product at the anode outlet. From experiment-I (as shown in Table I), it can be observed that at a lower flow rate of the fuel, the required moisture content is significantly low. The number of oxygen species required for effective adsorption of entire catalytic Ni-sites is insufficient. As the flow rate is enhanced, the availability of such adsorbates (O^{2-}) is increased which accelerates reaction in Eq.1 towards the forward direction. However, upon increasing the fuel flow rate beyond saturation (highest current density of 3.3 Acm^{-2}) would simply provide excess O^{2-} species without significant performance enhancement. The extent of performance increment is however observed to be marginal upon using dry H_2 as the fuel (Exp. II) in which the initiation reaction (Eq.1) is absent. In contrast, variation in O_2 flow rate is found to have negligible contribution to the overall performance of single cell as observed in either of the exps. III and IV. Therefore, moisture content in the fuel is found to impart significant role towards the oxidation of H_2 and electrochemical activity of the single cell.

Correlation of Microstructural Changes upon Long Term Electrochemical Study

Significant performance deterioration of $\sim 10.5 \%$ per 1000h is observed for single cells with conventional anode at a constant load of 0.5 Acm^{-2} after a considerable time period of $\sim 2000\text{h}$ (Table II). In contrast, incorporation of multilayered anode reduces the cell

TABLE II. Comparative cell degradation rate using different anode configuration

Anode configuration	Ni-content in electroless anode	% degradation w.r.t voltage per 1000 h (Applied load - 0.5 Acm^{-2})
Conventional anode (40 vol % Ni)/ 50 μm electroless anode	28	1.65
	32	2.5
Conventional anode (40 vol % Ni)	-	10.5

degradation to 1.65 - 2.5 % per 1000 h at a similar load. It is also observed from Table II that increase of Ni-content (28 to 32 vol %) in the electroless cermet enhance the cell degradation rate marginally. This can be attributed due to the increased joule heating within the anode upon using higher Ni-content. Performance degradation can be correlated with microstructural changes during long term study. Increased Ni coarsening after 2000 h operation is clearly visualized in the conventional cermet (Fig. 7a). The Ni-particulates with fairly high particle size undergoes fast sintering/coarsening thereby forming clusters or islands of Ni in the matrix. These sinteractive metallic clusters shows higher tendency to coalesce into bigger particles thereby reducing the catalytic activity of Ni required for electrochemical fuel oxidation. However, tendency for the increase in Ni particle diameter which is the index of cohesion is relatively less in the electroless matrix. The formation of unique core (YSZ) – shell (Ni) structure increases the activation energy required for the rearrangement of metallic phases in the matrix during cohesion of Ni and YSZ particulates. The size and distribution of Ni phases of electroless anode is therefore, observed to remain almost constant during long term operation (Fig. 7b). In a multilayer anode structure, deterioration in cell performance is truly governed by the degree of degradation exhibited by the anode layer present adjacent to the electrolyte. This can be ascribed due to dependence of cell performance on the electrochemical activity of the

interfacial anode. Hence, due to the reduced coarsening of the electroless anode, the electrochemical activity of the cell suffers little variation. The binarized images in Fig. 7 clarify the degree of anode coarsening of either technique. In addition, the intensity profile in the optical images of Fig. 7 determines the specific regions of the sample where Ni-coarsening is operative. The regions of Ni-coarsening show multiple intensified peaks

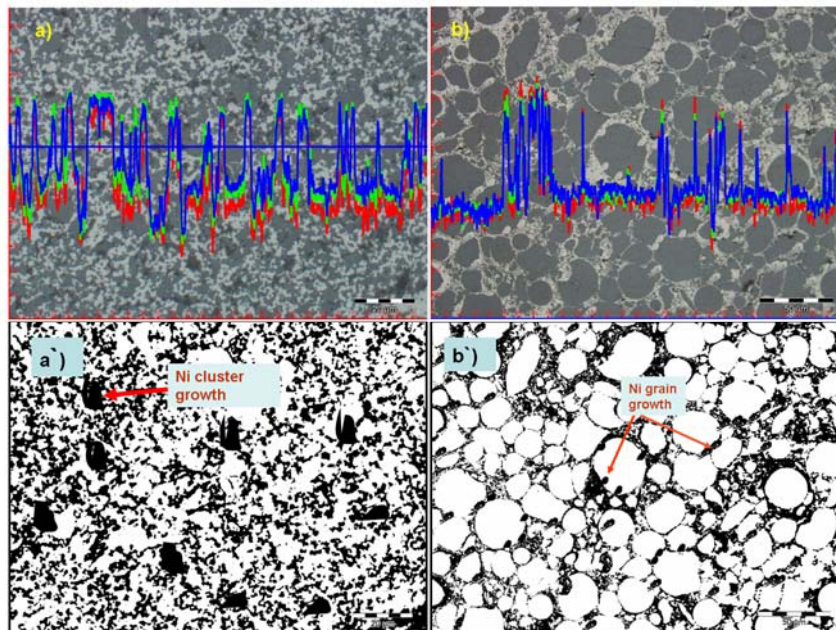


Figure 7. Optical microstructure and intensity profile for phases of a) electroless and b) conventional anode after endurance test of single cell. [a') and b') are binarized image].

in the microstructure. Therefore, single cell with multilayer anode having electroless layer in vicinity of electrolyte is superior in terms of higher performance along with reduced degradation.

Conclusions

SOFC anode prepared by novel electroless technique consists of fine catalytic Ni particulates with unique core (YSZ)-shell (Ni) microstructure. Such anode is found to exhibit significant electrochemical activity and thereby accelerates the rate of cell performance in SOFC. Incorporation of multilayer anode consisting of conventional anode (at the fuel side) and electroless anode (at the electrolyte junction) has been observed to increase the cell performance significantly. Conventional anode (40 vol% Ni) with multimodal size distribution helps in easy fuel transportation. In addition, due to the presence of higher Ni content, rate of catalytic fuel oxidation is increased by the conventional anode. In contrast, electroless anode (28-32 vol% Ni) with unimodal pore-size distribution and smaller pores is found to extend the charge transfer reaction from YSZ/anode interface to the bulk anode through enhanced interfacial area. By the virtue of using significantly less Ni-content (28 vol%), electroless anode is thermally compatible with the adjacent YSZ electrolyte with matching CTE. Therefore, upon using multilayered anode, the rate of fuel oxidation as well as charge transfer reactions are accelerated. It has been experimentally studied that, saturated moisture in the fuel imparts significant role towards H₂ oxidation and overall electrochemical activity of single cell. Single cell with such multilayered anode results in reasonable higher current density of

3.3 Acm⁻² (at 800⁰C, 0.7V) with low degradation of 1.7-2.5 % per 1000 h during long term study of ~ 2000h.

Acknowledgments

The authors acknowledge Director, CGCRI for his kind permission to publish the work. One of the authors (MM) is thankful to Council of Scientific & Industrial Research (CSIR) for providing senior research fellowship.

References

1. Y. Someya, H. Koide, M. Ando, T.Yoshida, in: Proc. 4th Int Symp. on Solid Oxide Fuel Cells, Vol. 86, (1995).
2. K. Yamahara, T.Z. Sholklapper, C.P. Jacobson, S.J. Visco, L.C. De Jonghe, *Solid State Ionics*, **176**, 1359 (2005)
3. S.D. Kim, S.H. Hyun, J. Moon, J. H. Kim, R.H. Song, *J. Power Sources*, **139**, 67 (2005)
4. J. Will, A. Mitterdorfer, C. Kleinlogel, D. Perednis, L.J. Gauckler, *Solid State Ionics*, **131**, 79 (2000).
5. G. Maggio, I. Ielo, V. Antonucci, N. Giordan, et al, (Eds.), SOFC II, p. 611, The Commission of the European Communities, Luxembourg,(1991).
6. T. Iwata, *J. Electrochem. Soc.* **143**, 1521 (1996).
7. T. Weber, *Solid State Ionics*, **42**, 205– 221 (1990).
8. M. Cassidy, G. Lindsay, K. Kendall, Proc. 1st Eur. SOFC Forum, 1994, pp. 205– 221.
9. J. Mukhopadhyay, M. Banerjee, A. Das Sharma, R.N. Basu, and H.S. Maiti, *Electrochem. Soc. Transaction.* **7[1]**, 1563-1572 (2007). The Electrochemical Society, Pennington, USA.
10. J. Mukhopadhyay, M. Banerjee, and R. N. Basu, *J. of Power Sources.* **175**, 749– 759 (2008)
11. S.C Singhal, and K. Kendall, High Temperature Solid Oxide Fuel Cells: Fundamentals, Design and Applications. Elsevier, U. K. Editor. 2003.
12. R.N. Basu, Materials for Solid Oxide Fuel Cells in Recent Trends in Fuel Cell Science and Technology. Edited by S. Basu, Jointly published by Anamaya Publishers, New Delhi (India) and Springer, p. 284, New York -USA, (2006)
13. R.N. Basu, A. Das Sharma, A. Dutta and J. Mukhopadhyay, *International Journal of Hydrogen Energy*, **33[20]**, 5748-5754 (2008).
14. R.N. Basu, A. Das Sharma, A. Dutta, J. Mukhopadhyay and H.S. Maiti, *Electrochem. Soc. Transaction*, **7[1]**, 227-234 (2007). The Electrochemical Society.
15. Madhumita Mukhopadhyay, J. Mukhopadhyay, A. Das Sharma, R.N. Basu, *Electrochem. Soc. Transaction.* **25[2]**, 2267-2274 (2009). The Electrochemical Society.
16. N.Q. Minh, T. Takahashi, Science and Technology of Ceramic Fuel Cells, Elsevier, New York, USA, 1995, pp. 147-164.

Use of Electroless Anode Active Layer in Anode-Supported Planar SOFC

Madhumita Mukhopadhyay, J. Mukhopadhyay A. Das Sharma and R. N. Basu

Fuel Cell & Battery Division, Central Glass & Ceramic Research Institute
CSIR, Kolkata - 700032, India

In SOFC, a novel Ni-YSZ cermet developed through electroless technique is used as an anode as well as anode active layer (AAL). In the present investigation, thickness of such AAL (varied in the range 15 – 140 μm) is optimized sequentially for fabricating high performance single cell. The fabrication technique involves tape casting followed by room temperature lamination to form the half cells. Effect of sintering temperature of half cells on the electrochemical performance has been carried out in the range of 1300 $^{\circ}\text{C}$ to 1400 $^{\circ}\text{C}$. A typical I-V characteristics of coupon cell (active area of $\sim 0.3 \text{ cm}^2$) sintered at 1400 $^{\circ}\text{C}$ with an optimum AAL thickness show current density of $\sim 3 \text{ A/cm}^2$ and power density of $\sim 2 \text{ W/cm}^2$ at 0.7 V and 800 $^{\circ}\text{C}$. Electrochemical performances of single cells using only electroless anode are also evaluated for comparison. Microstructures of these single cells are correlated with the electrochemical performances.

Introduction

In an anode supported planar SOFC, catalytic activity of anode plays a major role in determining the overall performance of the cell (1-3). Nickel-8 mol% yttria stabilized zirconia (Ni-YSZ) cermet is the most widely used anode material. Ni in the anode cermet not only acts as a good catalyst for hydrogen (fuel) oxidation but also has high electronic conductivity. On the other hand, Ni has thermal incompatibility and low wettability problem with YSZ electrolyte (4). The Ni-YSZ cermet is generally prepared by various techniques, e.g., mixed oxide (5), co-precipitation (6), slurry coating (7), liquid dispersion (8, 9), and heat decomposable aqueous salt solution routes (10). In all these preparation techniques, Ni is uniformly distributed in YSZ matrix. Irrespective of the preparation techniques, the anode cermet require $\sim 40 \text{ vol } \%$ of Ni in order to have sufficient electrical conductivity to be used in SOFC. Such a high Ni content ($\text{CTE} = 16.9 \times 10^{-6} \text{ K}^{-1}$) poses the problems of thermal incompatibility with adjacent YSZ electrolyte ($\text{CTE} = 10.8 \times 10^{-6} \text{ K}^{-1}$). Apart from the thermal mismatch problem, high Ni content increases coarsening phenomena significantly at SOFC operating temperature ($> 700^{\circ}\text{C}$) resulting in the performance degradation (11, 12). An electroless preparation of Ni-YSZ anode cermet, as reported by our group (13, 14), is expected to solve the above said problems. Due to the unique core (YSZ) - shell (Ni) microstructure of the resultant cermet, continuous Ni-Ni network in the matrix is attained at a Ni content of only $\sim 28 \text{ vol } \%$ (14) that gives the required electrical conductivity. The presence of lower Ni content in such anode cermet, not only reduces the thermal mismatch of the anode with adjacent cell components but also the Ni coarsening problem during long term operation is expected to be minimized. In the present investigation, planar anode-supported SOFC single cells

have been fabricated using such electroless Ni-YSZ anode through simplified processing techniques such as tape casting and screen printing. The electroless anode cermet has been used as total anode support as well as anode active layer (AAL). The unique core-shell microstructure (14) of the Ni-YSZ anode prepared through such electroless technique is expected to enhance the triple phase boundary length (tpb) for fuel oxidation and therefore interfacial polarization losses are expected to be minimized. In addition, in the electroless AAL, the presence of finer Ni around YSZ core could enhance the overall electrocatalytic activity for the necessary electrochemical oxidation of the fuel. During cell fabrication, conventional anode (NiO-YSZ) containing higher Ni content (~ 40 vol %) is used towards the fuel side for better fuel oxidation. However, electroless Ni-YSZ with low Ni content (~ 28 vol %) is used towards the electrolyte for better thermal compatibility, low polarization losses and higher electrochemical activity. The thickness of the AAL has been varied and optimized based on the electrochemical performance of the single cell. For comparison, single cells with electroless Ni-YSZ as total structural support with varied thickness has also been fabricated and are characterized through microstructural and electrochemical performance studies.

Experimental

Fabrication of SOFC single cell involves two major steps; a) tape casting using the slurries of anode and electrolyte in the form of tapes followed by their room temperature lamination to form the half cells [NiO-YSZ (anode-support)/Ni-YSZ (electroless)-AAL/YSZ] and b) screen printing of cathode active layer (CAL) and cathode layer (CL) on the fired half cells followed by cathode sintering to finally form SOFC single cells (15,16). A schematic of the fabrication technique is shown in Fig. 1. The anode material is processed through two different techniques, a) conventional solid state synthesis and b) electroless technique. In the former case NiO (Inco, Canada) and YSZ (TZ-8Y, Tosoh Corporation, Japan) powders are mixed in 60: 40 mass ratios along with organic binder, plasticizer and porosifier in specific proportions in a ball mill to form NiO-YSZ slurry (16). The details for the synthesis of Ni-YSZ anode cermet by electroless technique have been discussed in our previous communications (13,14). Optimized processing conditions during synthesis generate unique core-shell (YSZ as core and finer Ni particulates as shell) microstructure which is responsible for high electronic conduction at much lower Ni content compared to the solid state route (14). Electroless Ni-YSZ powder thus obtained is mixed with non-aqueous solvent media, plasticizer and porosifier in a ball mill in a similar manner as stated before to form the slurry. Slurry of YSZ powder is also prepared in the same manner as described above (16).

Sr-doped lanthanum manganite, $\text{La}_{0.65}\text{Sr}_{0.3}\text{MnO}_{3.8}$ (LSM) along with YSZ (1:1) is used for cathode active layer (CAL) while cathode layer (CL) contains only LSM. The cathode material is prepared by combustion synthesis technique as described in our earlier communication (16). Viscous pastes of both CAL and CL are prepared by mixing the powders with a tarpenol based organic vehicle.

Casting the slurries of the anode and electrolyte component is carried out by a laboratory tape casting machine (EPH, USA). In the first step, several sheets of conventional NiO-YSZ are laminated along with thin (15-140 μm) sheets of electroless Ni-YSZ together with YSZ sheet on top using a press under a predetermined uniaxial

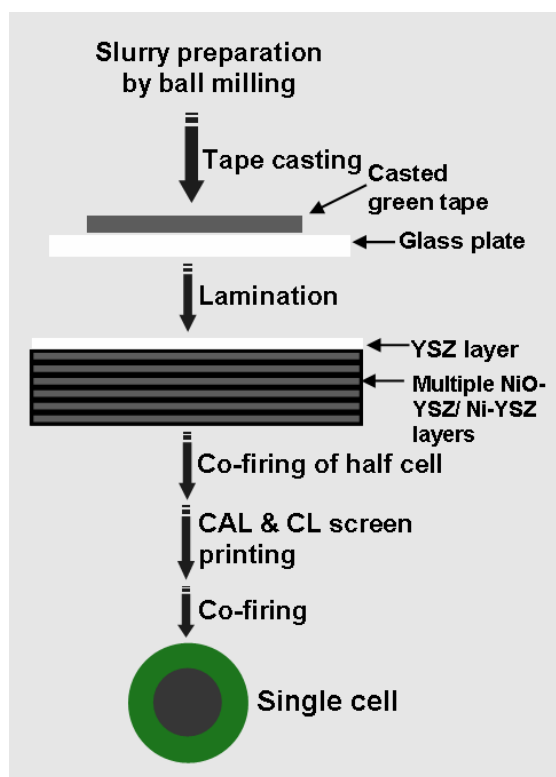


Figure 1. Schematic for the fabrication of anode supported SOFC.

pressure. The half cell monolith thus obtained is co-fired in the temperature range of 1300-1400⁰ C for 2 hrs. The flat half cells are then screen printed successively with LSM-YSZ cathode active layer (CAL) and LSM cathode layers (CL) respectively. Prior to screen-printing, the half cells are thoroughly cleaned under acetone in an ultrasonic bath followed by oven drying. A 10–15 μm thin layer of CAL is first screen printed on the YSZ surface of the half cell and a relatively thick film (50 – 60 μm) of CL is then screen printed over the dried CAL. After proper drying, the bi-layer consisting of CAL and CL (on the top of half cell) is co-fired above 1000⁰C in air for 2–4 h to complete the single cell fabrication process. Single coupon cells (~ 16mm diameter and 1.5 mm thick) fabricated by the aforesaid technique are used for electrochemical measurement using a vertical split type furnace (ATS Corporation, USA) with hydrogen as fuel fed at anode and oxygen as the oxidant fed at the cathode through electronic mass flow controllers (MKS Instruments, USA). The current density as function of cell voltage is evaluated across the cell under different loads and the corresponding measurements is carried in the range of 700-800⁰C. The polished cross sections of the single cells are observed with a high resolution microscope (Olympus GX 71, Japan). The aforesaid experiments are also carried out with the single cells where Ni-YSZ electroless cermet containing 28 vol% of Ni is used as a total anode support. The configuration of such single cells is: Ni-YSZ electroless anode/YSZ/CAL/CL.

In the present investigation Ni-YSZ anode prepared by electroless technique has been used in two different configurations for the fabrication of SOFC namely:

- Configuration 1: As total structural support (shown in Fig. 2a)
- Configuration 2: As anode active layer (shown in Fig. 2b)

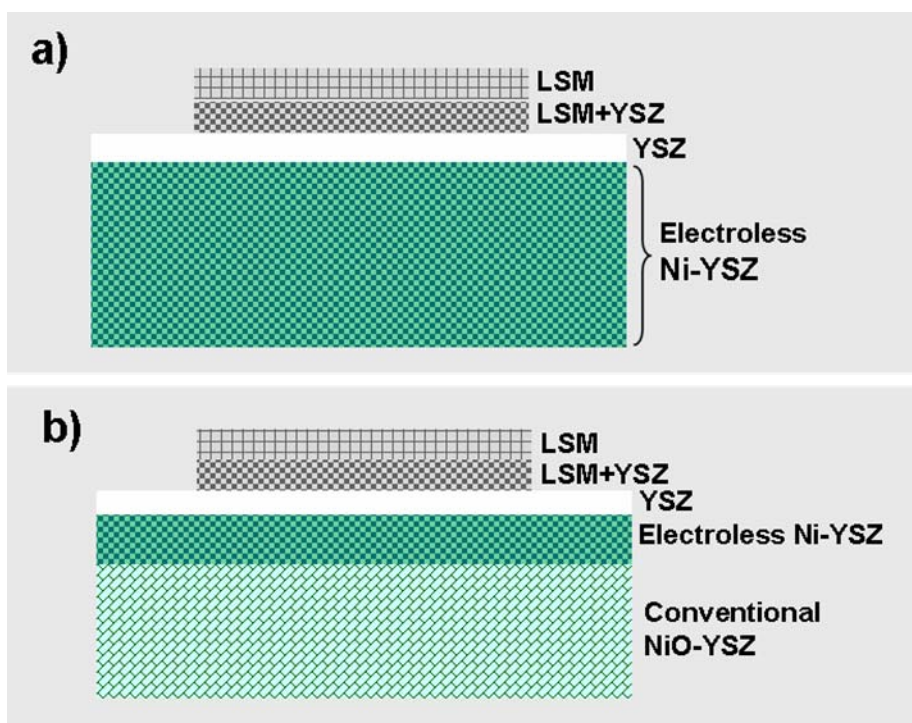


Figure 2. SOFC with electroless Ni-YSZ: a) as total anode support and b) as anode active layer (AAL).

Results and Discussion

Electroless Ni-YSZ as Anode Support

In configuration 1, the electroless anode cermet is used as the total anode monolith as shown schematically in Fig. 2a. Figs. 3 and 4 show the electrochemical performance of SOFC with varied thicknesses of anode (1.5 and 1.25 mm respectively) at different temperatures. In each case, the corresponding half cells were sintered at two different sintering temperatures (1350°C and 1400°C).

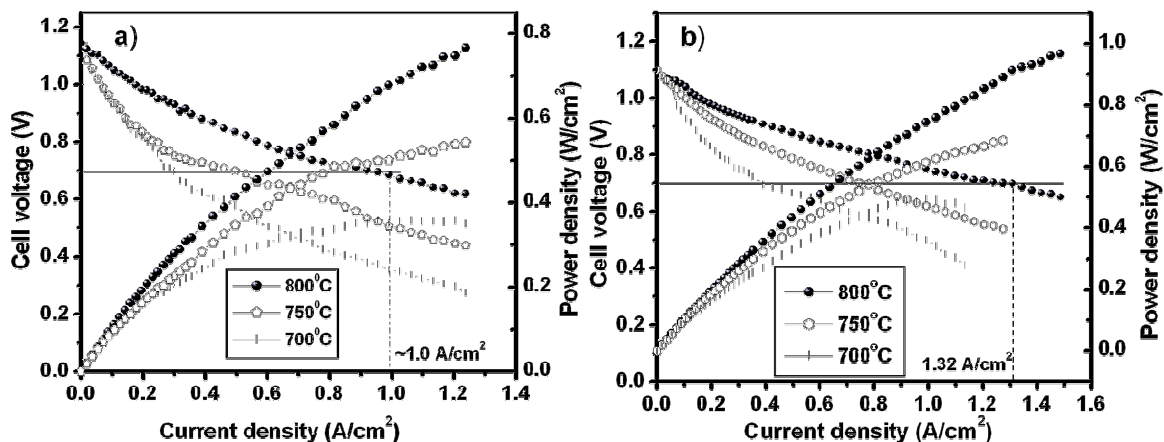


Figure 3. Electrochemical performance of SOFC with anode thickness of 1.5 mm: Half cell sintered at a) 1350°C and b) 1400°C.

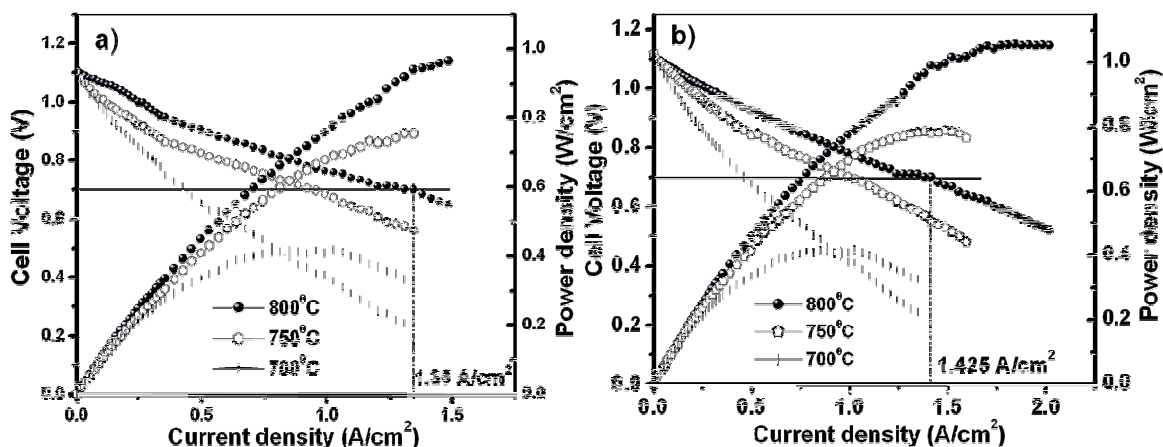


Figure 4. Electrochemical performance of SOFC with anode thickness of 1.25 mm: Half cell sintered at a) 1350⁰C and b) 1400⁰C.

As already mentioned, such electroless anode cermet contain only ~ 28 vol% of Ni. Both the figures show that irrespective of the anode thickness, a sintering temperature (1400⁰C) of the half cell gives better performance. From the figures it can also be seen that, thinner the anode support (1.25 mm) better is the electrochemical performance. During fuel cell operation, fuel diffusion through the porous anode, electrocatalytic oxidation of the fuel followed by release of the electrons and subsequent interfacial reaction with oxide ion are the key steps for effective reactivity of an anode. It is believed that the diffusion polarization will be less if the thickness of the anode support is less; however, an optimum thickness of anode layer is necessary for the effective electrocatalytic oxidation reaction of the fuel. Thus, the highest current density of ~1.4 A/cm² with a power density of ~ 1.0 W/cm² (at 0.7 V and 800⁰C) is obtained for the single cell of such configuration having 1.25 mm thick anode – support and the half cell sintered at 1400⁰C. The electrochemical performances of the single cells with half cells sintered at 1300⁰C are found to be much lower (results not shown).

A typical optical microphotograph of the cross section of coupon cell after electrochemical measurement is shown in Fig.5. The figure shows the retention of unique

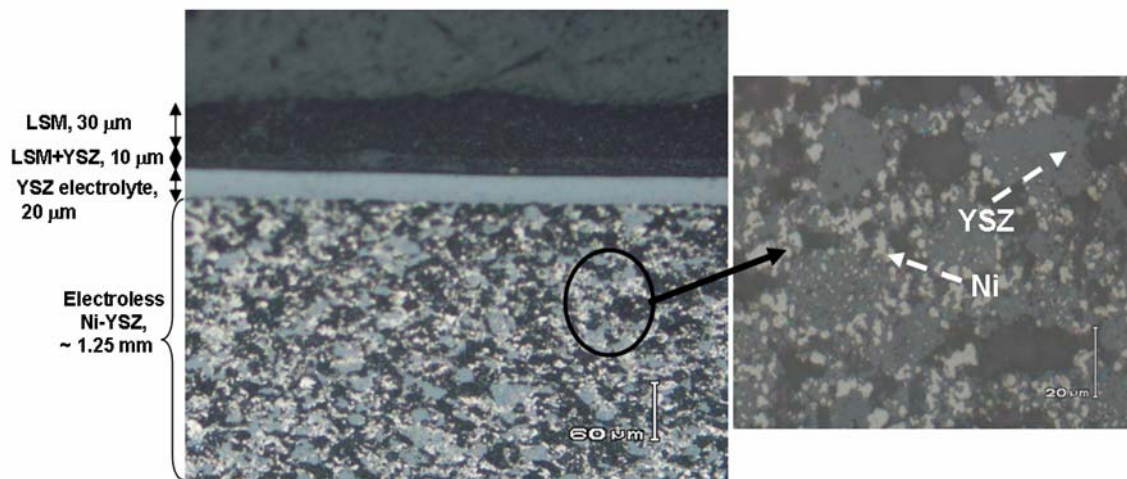


Figure 5. Optical microstructure of SOFC with electroless Ni-YSZ as anode-support after electrochemical measurement. (Enlarged microstructure of electroless Ni-YSZ anode is also shown).

core (YSZ) - shell (Ni) microstructure of the electroless anode support (shown in enlarged view). Optimization of process parameters during electroless technique (14) enables the deposition of finer Ni particulates onto YSZ as can be seen from the figure. This, in turn, helps in maintaining interconnection among Ni as well as YSZ particulates throughout the cermet and thereby expected to minimize the polarization losses and enhance the triple phase boundary for fuel oxidation.

Electroless Ni-YSZ as AAL

In configuration 2, the electroless anode cermet is used as the AAL as shown schematically in Fig. 2b. In this configuration, conventional NiO-YSZ forms the base layer onto which electroless Ni-YSZ that acts as AAL is laminated. The base layer of anode support consists of ~ 40 vol % Ni whereas only ~ 28 vol % of Ni is present in the anode active layer. Reduction of Ni content adjacent to electrolyte increases thermal compatibility. The thickness of AAL has been varied from 15 – 140 μm to study its effect on the electrochemical performance. As mentioned above, the electrochemical performance of cells having configuration 1 was found to be highest when the corresponding half cells were sintered at 1400^oC. Therefore, for the electrochemical studies of SOFC with configuration 2, the half cells were sintered at this optimized sintering temperature (1400^oC). Fig. 6 shows the electrochemical performance of coupon cells with varied AAL thickness. The figure reveals that incorporation of AAL into the anode support increases the performance to a significant extent. In the AAL layer, YSZ core is covered with fine discrete Ni particulates which effectively increase the triple phase boundary. The AAL is formulated in such a fashion that overall porosity is also reduced in comparison with the underlying anode-support and thereby enhances contact of metallic Ni. This helps in releasing the electrons after the electrochemical oxidation of the fuel at the triple phase boundary and enhances the overall charge transfer mechanism (17). Reduction in the AAL thickness also helps in reducing the overpotential at the anode-electrolyte interfaces and thereby enhances the overall electrochemical performances of the single cell. An optimum thickness of AAL is necessary so that electrocatalytic activity for fuel oxidation is effectively operative and contribution towards the overall electronic and ionic conductivity is significant. From Fig. 6, it can be observed that single cell with thin electroless AAL of ~ 15 μm shows the highest electrochemical performance of ~ 3.1 A/cm² with a power density of 2.17 W/cm² at 0.7 V and 800^oC.

A typical cross section of coupon cell having electroless AAL is shown in Fig. 7. The figure clearly reveals the difference in microstructure of Ni-YSZ cermet anode produced by two different processing techniques. Conventional anode cermet produces dispersed Ni and YSZ phases distributed throughout the matrix whereas finer Ni shells with YSZ particulates in the core is the unique characteristics of the electroless synthesized cermet used as the anode active layer.

Conclusions

Electroless Ni-YSZ anode has been used in two different configurations for fabrication of SOFC through simple processing techniques. Irrespective of the single cell configuration, electroless anode cermet uses only ~ 28 vol% of Ni, whereas the conventional cermet uses ~ 40 vol% of Ni. Electroless Ni-YSZ anode when used as the

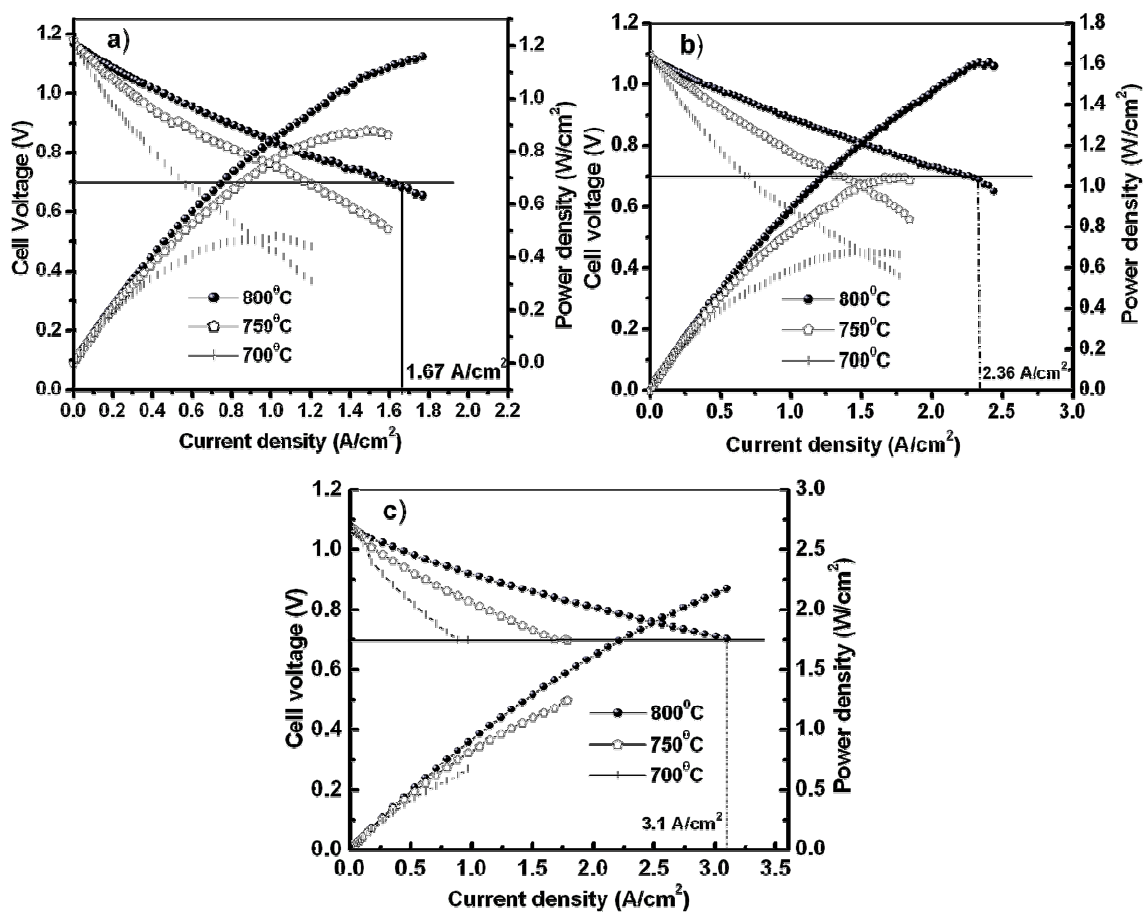


Figure 6. Electrochemical performance of SOFC with AAL thickness of: a) 140 μm , b) 90 μm and c) 15 μm .

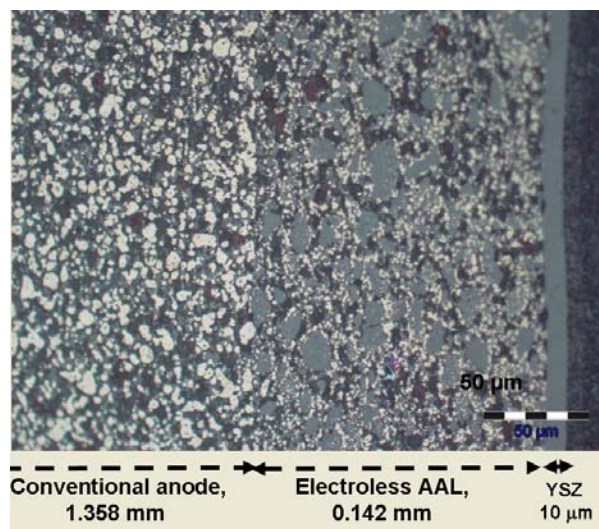


Figure 7. Optical microstructure of coupon cell after electrochemical measurement having electroless anode active layer.

anode support in the single cell configuration of Electroless Ni-YSZ/YSZ/CAL/CL gave the highest performance of $\sim 1.43 \text{ A/cm}^2$ at 0.7V and 800°C with the anode support of 1.25 mm. However, introducing the electroless Ni-YSZ as anode active layer (AAL) onto the conventional anode cermet with cell configuration, conventional NiO-YSZ/

electroless Ni-YSZ (AAL)/YSZ/CAL/CL], the electrochemical performance increases significantly. It is observed that reduction in thickness of AAL increases the single cell performance and cells with $\sim 15 \mu\text{m}$ thin AAL gives the maximum performance of $\sim 3.1 \text{ A/cm}^2$ at 0.7V and 800°C . The unique core-shell microstructure of electroless Ni-YSZ is responsible not only for high electronic conductivity at lower Ni content but is also expected to enhance the triple phase boundary length at anode - electrolyte interface. The respective microstructural characterizations of the single cells show the retention of such core-shell structure in the sintered cermets.

Acknowledgments

The authors acknowledge Director, CGCRI for his kind permission to present the work. Financial support from Council of Scientific & Industrial Research (CSIR), Government of India, under NMITLI project is gratefully acknowledged. One of the authors (mm) is thankful to Council of Scientific and Industrial Research (CSIR) for providing research fellowship.

References

1. D. J. L. Brett, A. Atkinson, N. P. Brandon and S. J. Skinner, *Chem. Soc. Rev.*, **37**, 1568 (2008).
2. P. Holtappels, U. Vogt and T. Graule, *Adv. Eng. Mater.*, **7**, 292 (2005).
3. A. Weber and E. Ivers-Tiffée, *Journal of Power Sources*, **127**, 273 (2004).
4. A. Tsoga, A. Naoumidis and P. Nikolopoulos, *Acta Materiala*, **44**, 3679 (1996).
5. D. E. Dees, T. D. Claar, T. E. Easler, et.al, *J. Electrochem. Soc.*, **134**, 2141 (1987).
6. N. M. Sammes, M. Brown, I. W. M. Brown, *J. Mater. Sci.*, **31**, 6069 (1996).
7. J. Macek, M. Marinsek, 2nd European SOFC Forum, Proceedings vol.1, p. 341, Oslo, (1996).
8. T. Kawada, N. Sakai, H. Yokokawa, *Solid State Ionics*, **40 (1)**, 402 (1990).
9. S. K. Pratihari, R. N. Basu, H. S. Maiti, *Trans. Indian Ceram. Soc.*, **56**, 85 (1997).
10. S. K. Pratihari, R. N. Basu, S. Mazumdar, H. S. Maiti, *SOFC-VI*, **99-19**, p. 513, Electrochemical Society, Pennington, NJ, (1999).
11. G. Maggio, I. Ielo, V. Antonucci, N. Giordan, et al, *SOFC-II*, p. 611, The Commission of the European Communities, Luxembourg, (1991).
12. T. Iwata, *J. Electrochem. Soc.*, **143**, 1521 (1996).
13. J. Mukhopadhyay, M. Banerjee, A. Das Sharma, R. N. Basu, and H. S. Maiti, *Electrochem. Soc. Transactions*, **7[1]**, 1563-1572 (2007).
14. J. Mukhopadhyay, M. Banerjee, and R. N. Basu, *J. of Power Sources*, **175**, 749 (2008).
15. R. N. Basu, A. Das Sharma, A. Dutta, J. Mukhopadhyay and H. S. Maiti, *Electrochem. Soc. Transactions*, **7[1]**, 227-234 (2007).
16. R. N. Basu, A. Das Sharma, A. Dutta and J. Mukhopadhyay, *International Journal of Hydrogen Energy*, **33[20]**, 5748-5754 (2008).
17. N. Q. Minh, T. Takahashi, *Science and Technology of Ceramic Fuel Cells*, Elsevier, New York, USA, (1995).

Provided for non-commercial research and education use.
Not for reproduction, distribution or commercial use.



This article appeared in a journal published by Elsevier. The attached copy is furnished to the author for internal non-commercial research and education use, including for instruction at the authors institution and sharing with colleagues.

Other uses, including reproduction and distribution, or selling or licensing copies, or posting to personal, institutional or third party websites are prohibited.

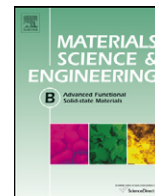
In most cases authors are permitted to post their version of the article (e.g. in Word or Tex form) to their personal website or institutional repository. Authors requiring further information regarding Elsevier's archiving and manuscript policies are encouraged to visit:

<http://www.elsevier.com/copyright>



Contents lists available at ScienceDirect

Materials Science and Engineering B

journal homepage: www.elsevier.com/locate/mseb

Ball mill assisted synthesis of Ni–YSZ cermet anode by electroless technique and their characterization

Madhumita Mukhopadhyay, Jayanta Mukhopadhyay, Abhijit Das Sharma, Rajendra N. Basu*

Fuel Cell and Battery Division, Central Glass & Ceramic Research Institute, Council of Scientific & Industrial Research (CSIR), Kolkata 700 032, West Bengal, India

ARTICLE INFO

Article history:

Received 20 January 2009

Received in revised form 3 April 2009

Accepted 24 May 2009

Keywords:

Solid oxide fuel cell

Anode

Cermet

Ball milling

Electroless

Core-shell

ABSTRACT

Ni–YSZ composite cermet used as the anode material for solid oxide fuel cell is prepared by electroless technique involving an important sensitization process of YSZ. In the present investigation, the sensitization process of YSZ is carried out through cost-effective controlled ball milling. The effect of milling speed on electrical, thermal and microstructural properties of such anodes is investigated and optimized at 45 rpm. Microstructural analysis of the synthesized Ni–YSZ cermets prepared under the optimized milling conditions showed a core-shell microstructure with YSZ as core and fine metallic Ni particulates as the shell. The interconnected metallic Ni creates a conductive pathway at room temperature. Such type of unique core-shell anode cermet, results in higher electrical conductivity ($\sigma_{800^\circ\text{C}} \sim 500 \text{ S/cm}$) at much lower Ni content ($\sim 33 \text{ vol\%}$) compared to conventional anode cermet with thermal expansion coefficient ($\sim 11.48 \times 10^{-6} \text{ K}^{-1}$) compatible to other cell components.

© 2009 Elsevier B.V. All rights reserved.

1. Introduction

For anode-supported planar solid oxide fuel cell (SOFC), the most widely used anode material is nickel–8 mol% yttria stabilized zirconia (Ni–YSZ) cermet. Electrochemical oxidation of fuels mainly depends on the catalytic activity and total electrical conductivity of the anode. Thermal compatibility of the anode with the other cell component is an important parameter. Conventionally, a minimum of 40 vol% of Ni is used in the cermet anode in order to obtain the required electrical conductivity during the SOFC operation at an intermediate temperature range of 700–800 °C [1–3]. As metallic Ni has very high coefficient of thermal expansion (CTE) of $\sim 16.9 \times 10^{-6} \text{ K}^{-1}$, higher amount of Ni in the cermet would lead to higher mismatch of CTE with the adjoining YSZ electrolyte (CTE $\sim 10.8 \times 10^{-6} \text{ K}^{-1}$). Along with the difficulty of thermal mismatching with other cell components, another major drawback associated with a relatively high Ni content in the cermet matrix is the coarsening of the nickel after long-term SOFC operation. In order to overcome these problems associated with the conventionally prepared anodes [4,5] a novel electroless technique to synthesize such cermet has been used earlier by our group [6–8] so that the electrical conductivity percolation threshold [9] in the cermet is significantly lowered down with respect to total Ni content without compromising the overall electrical properties of the anode as required for the SOFC application. The cermet anode (Ni–YSZ)

prepared by the electroless technique consists of a core-shell structure with YSZ as core and fine Ni particulates as shell [7,8]. The functionality in the cermet is attained by the enhancement of Ni–Ni chain formation and the flow path of electrons is made continuous through this Ni–Ni shell with a consequent increase in electrical conductivity at a much lower vol% of Ni compared to anodes prepared by conventional method. The electroless deposition of metallic Ni particulates onto YSZ precursor is a two step process: (i) sensitization of YSZ powders and (ii) controlled deposition of metallic nickel particulates onto sensitized YSZ. Among these two steps, sensitization process is the key step for the generation of core-shell structure that involves adsorption of metallic palladium (Pd^0) produced by an in situ reaction of stannous chloride (SnCl_2) and palladium chloride (PdCl_2).

Detailed study of the sorption kinetics which controls the sensitization process reveals the importance of equilibration time which is primarily based on (a) the external mass transfer of sorbate species from the bulk solution to the surface of sorbents, (b) the intraparticle mass transfer of sorbet (Pd^0) species from the surface of sorbent (YSZ) to the pores and vice versa and (c) the chemical reaction on the surface of sorbents [6,8,10]. In our earlier studies, we have established that high power ultrasound is one of the effective processes for such sensitization [6,8]. However, the limiting factor for sensitization through such ultrasonication is to handle large volume of precursor powders in a single run. The excessive heat generated during sonifications leads to ineffective YSZ sensitization by enhancing the Pd^0 desorption rate. In the present study an attempt has been made to use the conventional ball milling technique for sensitization of

* Corresponding author. Tel.: +91 33 2473 3469; fax: +91 33 2473 0957.
E-mail addresses: rnbasu@cgcri.res.in, rajenbasu@yahoo.ca (R.N. Basu).

YSZ powders so as to make the process cost effective and up scalable.

Various milling parameters, viz. rotating speed (rpm), milling time and volume ratio with respect to constituents have been systematically varied to study their effects on the extent of YSZ sensitization and the properties of the corresponding Ni–YSZ cermet anodes obtained by subsequent electroless Ni deposition. The thermal, microstructural and electrical characterizations of the Ni–YSZ cermets thus prepared are studied in detail.

2. Experimental

Preparation of Ni–YSZ powder by electroless technique involves an initial sensitization process of the YSZ particulates followed by an in situ reduction of Ni^{2+} to Ni and its corresponding deposition onto sensitized YSZ. To facilitate effective sensitization, the as-received YSZ powder [TZ-8Y, Tosoh Corporation, Japan ($d_{50} \sim 0.2 \mu\text{m}$)] is heat treated at 900°C followed by dry milling using zirconia grinding media for ~ 10 h so as to increase the d_{50} value to $\sim 27 \mu\text{m}$. For sensitization of YSZ particulates by surface adsorption of metallic palladium (Pd^0), required amount of the processed YSZ powders are added into polypropylene jars containing mixture of palladium chloride [sd fine-chem Limited, India, 99.5%] and stannous chloride [Merck, India, 99.5%] solutions where metallic palladium (Pd^0) is produced in situ through a redox reaction [7,8]. The redox reaction may be given as



The polypropylene jars containing the redox mixture and YSZ powder are then subjected to ball milling using ZrO_2 balls as the milling media for 15 h. During milling, the powder to media ratio is maintained at 0.45 and the rotating speed is varied in the range of 25–65 rpm. For the complete reduction of Pd^{2+} in the sensitized bath, the ratio of $\text{PdCl}_2:\text{SnCl}_2$ is kept at 1:3. Sensitization of the YSZ particulates by a controlled ball milling technique favors the forward rate of the redox reaction given in Eq. (1). However, even if some unreduced Pd^{2+} is present in the medium, it is removed during siphoning of the supernatant liquid and the sensitized mass obtained is washed thoroughly until the subsequent chemical analysis certify the absence of Pd^{2+} ions. Depending on the capacity of the polypropylene jars, 100–1000 g YSZ powder can be processed in a single run. The sensitized YSZ after milling is further equilibrated with the redox mixture for a pre-determined period of time (25–2000 min) in order to have effective adsorption of Pd^0 onto YSZ powder. In order to determine the time dependent concentration of adsorbed Pd^0 on YSZ surface, a certain quantity of aliquot from the supernatant solution of the sensitized bath is collected at a definite interval of time and the remnant concentration of Pd^{2+} in the supernatant solution is measured with the help of an Inductive Coupled Plasma Atomic Emission Spectrophotometer (Kleve, Germany). In the present investigation, the concentration of palladium is expressed in parts (of Pd) per million (ppm) parts of solution. Concentration of the adsorbed Pd^0 is calculated from the difference between the initial Pd^{2+} and remnant Pd^{2+} (in the supernatant liquid) concentration. It has been taken into consideration that the total Pd^0 formed during the sensitization process, is adsorbed on YSZ surface provided it is allowed to attain transient equilibrium. However, a small amount of desorbed Pd^0 during the transient equilibrated sorption process is also considered during the reversible adsorption kinetics. The sensitization technique under transient equilibrium condition of adsorption is characterized in the same way as that reported in our earlier investigation where detailed study of the adsorption kinetic model under power ultrasounds is reported [8]. An electroless bath containing nickel nitrate [sd fine chem. Limited, India, 99.5%] is prepared for the con-

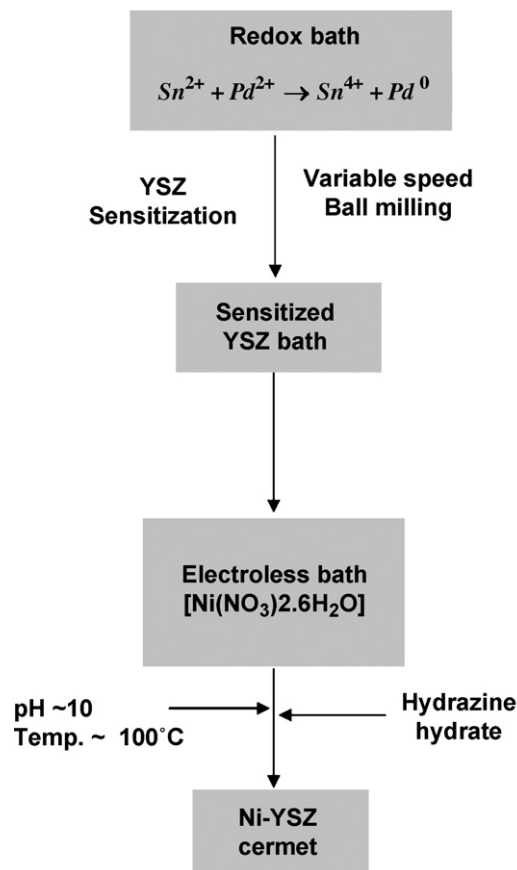


Fig. 1. Process flow chart for ball mill assisted electroless technique.

trolled deposition of Ni particulates onto sensitized YSZ. A process flow chart for the synthesis of Ni–YSZ cermets by electroless technique with YSZ sensitized by ball milling is shown in Fig. 1. The sensitized YSZ particles are poured in the reaction bath containing Ni^{2+} salt solution for electroless deposition. During deposition, a pH value of ~ 10.0 and a bath temperature of $\sim 100^\circ\text{C}$ are maintained. The reduction of Ni^{2+} was carried out by in situ liberation of nascent hydrogen generated by quantified addition of hydrazine hydrate. The nickel concentrations in the cermets are varied in the range between 5 and 40 vol%. In addition to the batches prepared by electroless technique as mentioned above, for comparison, several batches with Ni content between 10 and 40 vol% have also been prepared by conventional solid state technique. For phase identification, the Ni–YSZ cermets are characterized through X-ray diffraction using an X-ray diffractometer (Philips X'pert, PANalytical, Eindhoven, Netherlands) with $\text{Cu K}\alpha$ radiation. Rectangular bars of dimensions $25 \text{ mm} \times 10 \text{ mm} \times 3 \text{ mm}$ are prepared using uniaxial pressing of the powders under a specific pressure of 170 MPa. The green pressed bars are then sintered in air at a temperature of 1400°C for 6 h. The air sintered samples, thus obtained, are reduced under argon and hydrogen mixture (4:1) at 1000°C . The electrical conductivity of the reduced Ni–YSZ cermets is carried out from room temperature up to a maximum 1000°C by the standard 4-probe DC measurement technique using an 8 1/2 digit multimeter (Keithley, Model 2002). The coefficient of thermal expansions of the reduced samples with varying Ni content is measured by a high temperature dilatometer (NETZSCH, Model DIL 402C) under argon atmosphere. The microstructures of polished surfaces of the cermets are examined with the help of a high resolution optical microscope (Olympus, Model GX 71). High resolution field emission microscopy (FESEM) [Gemini Supra 35, Zeiss] for sintered

and reduced Ni–YSZ cermets prepared by electroless technique at optimum milling speed of 45 rpm was performed. Spot energy dispersive X-ray (EDX) as well as the line scanning of such core–shell Ni–YSZ cermet anode was also carried out for estimation of YSZ and Ni in their core and shell positions respectively.

3. Results and discussion

Fig. 2 shows the change in concentration of adsorbed Pd⁰ on YSZ, equilibrated in the redox mixture for different time interval, as a function of milling speed (rpm). It is observed that irrespective of the equilibration time, the amount of Pd⁰ adsorption increases with increase in milling speed upto a maxima (corresponding to 45 rpm) and then decreases with further increase in the milling speed. Pd⁰ adsorption on YSZ is an example of reversible physisorption [8]. The extent of Pd⁰ adsorption is ineffective with milling speed of less than 45 rpm whereas for a higher rpm, the desorption rate starts dominating due to self-nucleation among sorbet species which is evident also from Fig. 2. Thus, it is clear from Fig. 2 that the amount of Pd⁰ adsorption on YSZ from the sensitized bath is found to be optimum at a milling speed corresponding to 45 rpm, equilibrated for about 2000 min. YSZ sensitization at such optimum milling condition promotes in situ Ni²⁺ reduction during the subsequent electroless Ni deposition. Beyond this equilibrium time of adsorption, the desorption rate starts predominating resulting in slight decrease in adsorbed Pd⁰ concentration which is also evident from Fig. 2.

Optimization of milling speed for sensitization of YSZ particulates is based on the classical theory of the milling [11]. The energy input to the ball mill increase with increase in the speed of rotation. The power to the mill is transmitted from the shell lines to the first layer of grinding media and then to subsequent layers. There is some power loss between the layers due to slippage of the media. A schematic of the ball milling is shown in Fig. 3. The rpm of the mill (n) can be expressed in terms of angle of the particle inside the container (α) and radius of the container ($r=0.05$ m) as

$$n = \sqrt{\left(\frac{g}{4\pi^2}\right) \left(\frac{\cos \alpha}{r}\right)} \quad (2)$$

At $\alpha=0$ (~135 rpm), critical speed of milling is achieved where grinding of the YSZ particulates is expected to be maximum. At $\alpha=45^\circ$ (~113 rpm), mixing and grinding are equally poised, still excessive grinding may lead to fragmentation of the treated

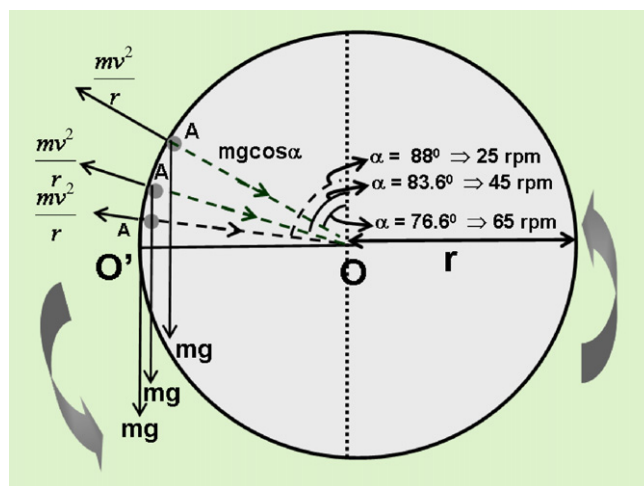


Fig. 3. Schematic for the balance of force during ball milling.

YSZ particulates ($d_{50} \sim 27 \mu\text{m}$) which results in no significant Pd⁰ adsorption. Therefore, in this present investigation the experimental rpm is chosen where the impact of grinding becomes $\leq 1/4$ th of the total grinding and mixing energy. This leads to experimental milling speeds to be ≤ 56 rpm. At milling speed of 25 rpm ($\alpha = 88^\circ$) mixing predominates with hardly any formation of Pd⁰ and subsequent adsorption onto YSZ (Fig. 2). At higher rpm of 65 ($\alpha = 76.6^\circ$), grinding becomes predominating which may lead to fragmentation of YSZ particles and therefore YSZ absorption capacity decreases (Fig. 2). Therefore, an intermediate rpm of 45 is found to be most suitable for mixing as well as optimum impact of grinding which results in favorable forward redox reaction (Eq. (1)) followed by subsequent adsorption of Pd⁰ onto YSZ. This is also evident from Fig. 2 where maximum adsorption capacity of YSZ is found to be at milling speed of 45 rpm (q_t at equilibration time is ~ 83 ppm).

Fig. 4 compares the X-ray diffractograms of the sintered and reduced anode cermets containing 35 vol% Ni, prepared by electroless technique with YSZ sensitized under milling speeds of 25, 45 and 65 rpm. These diffractograms of the electroless samples are compared with that of the Ni–YSZ cermet (having same vol% of Ni) prepared by conventional solid state technique. It is evident that only metallic Ni and YSZ phases, without any impurity phase, are developed in both the cases and are comparable with each other so far as the phase formation is concerned. However, the ratio of the

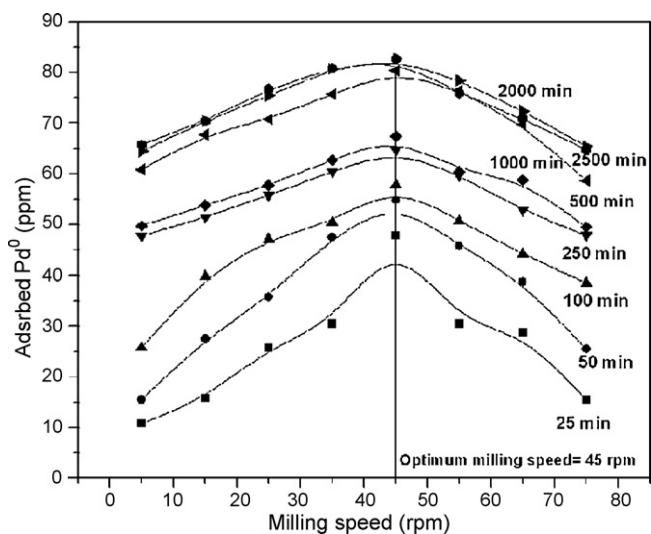


Fig. 2. Dependence of adsorption capacity on milling speed.

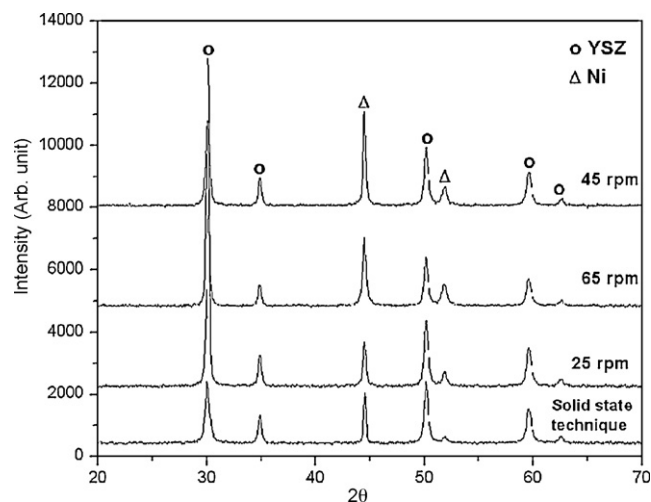


Fig. 4. XRD pattern of anodes prepared by ball mill assisted electroless and conventional solid state techniques.

Table 1
 I_{Ni}/I_{YSZ} of X-ray diffraction for electroless and conventional anodes.

Type of sample	Milling speed during YSZ sensitization (rpm)	I_{Ni}/I_{YSZ}
As-synthesized Ni–YSZ powder prepared by electroless technique	25	0.474
	45	0.866
	65	0.651
Ni–YSZ cermet anode prepared by solid state technique	–	0.814

relative intensities of metallic Ni and YSZ (I_{Ni}/I_{YSZ}) for the samples prepared under different conditions shows some interesting feature. The I_{Ni}/I_{YSZ} values, as calculated from Fig. 4, corresponding to the major peaks for both the batches are presented in Table 1. It is interesting to note that the value of I_{Ni}/I_{YSZ} for the powder prepared by electroless technique with YSZ sensitized at an optimum milling speed of 45 rpm is more than the intensity ratio (I_{Ni}/I_{YSZ}) of the conventionally prepared cermet. A plausible explanation for this is shown schematically in Fig. 5. As Ni forms shell around YSZ core, the relative intensity ratio of Ni is found to be higher compared to that of the uniformly dispersed Ni and YSZ cermet in conventional anode resulting in higher values of I_{Ni}/I_{YSZ} for such core–shell cermet. It is believed that because of the electroless deposition of the fine Ni particulates around YSZ sensitized at an optimum milling speed of 45 rpm, the relative intensity of YSZ becomes weak and therefore I_{Ni}/I_{YSZ} is found to be high (Fig. 5a). Due to effective YSZ sensitization at 45 rpm, formation of Ni shell around the YSZ core is uniform. This uniformity in Ni shell results in higher intensity of Ni in X-ray diffraction pattern and thereby resulting in highest I_{Ni}/I_{YSZ} value for such core–shell anode. On the other hand, a lower value of I_{Ni}/I_{YSZ} for conventionally prepared cermet indicates relatively uniform scattering from both the dispersed Ni and YSZ phases (Fig. 5b). I_{Ni}/I_{YSZ} values for electroless anode powders prepared with YSZ sensitized at 25 and 65 rpm are even lower than the intensity ratio of conventional anode due to the insufficient YSZ sensitization as observed by the lower Pd⁰ adsorption onto YSZ at different equilibration time interval (Fig. 2).

The values of sintered and reduced densities of the electroless samples prepared from YSZ precursor sensitized at different milling speeds with their respective Ni content are listed in Table 2. For comparison, the values for the samples prepared by conventional solid state technique are also given. It is observed that the electroless samples prepared with YSZ sensitized at an optimum milling speed of 45 rpm are less dense and consequently more porous than

the samples prepared through solid state technique. At the optimum milling speed of 45 rpm as obtained under our experimental condition, sensitization of YSZ becomes most effective. On the other hand, at the milling speed of either 25 or 65 rpm, due to ineffective adsorption (for 25 rpm) or reversible desorption (for 65 rpm) of Pd⁰ onto sensitized YSZ surface, the catalytic sites which are required for the in situ reduction of Ni²⁺ in the electroless bath become insufficient. In the absence of sufficient active Pd⁰ sites, quantitative addition of reducing agent in the electroless bath generates excess free Ni in the matrix. These free Ni particulates are not associated with the shell formation around the YSZ core. Under the sintering conditions of the present investigation (in air at 1400 °C), these uncovered YSZ particles are likely to be more sinterable resulting in a higher effective density value for electroless samples prepared from sensitized YSZ at both 25 and 65 rpm. Thus, it is believed that YSZ sensitization at an optimum milling speed of 45 rpm results in the formation of core–shell structure with controlled Ni deposition. During sintering in air, Ni is converted into NiO that also covers the YSZ grains. So during sintering, direct contact between the YSZ grains are limited in such core–shell anode. As the sinterability of NiO is less than that of the YSZ, the densification of such core–shell NiO–YSZ is also found to be less than the conventional anode samples where the NiO is dispersed in YSZ.

This lower density during sintering in the electroless anode samples is also reflected in the reduced cermets. Moreover, oxygen loss during subsequent reduction of NiO to metallic Ni increases porosity of the anodes in the reduced state. On the other hand, the fully dispersed Ni particulates in the cermet matrix of conventionally prepared anodes results in relatively higher density and hence lower porosity.

Dependence of electrical conductivities measured at 800 °C as a function of the total Ni content in the cermet anodes prepared by electroless technique at three different milling speeds of 25, 45 and 65 rpm is shown in Fig. 6. For comparison, anode cermet prepared by conventional solid state technique is also included in the figure. It is interesting to note that it could be possible to bring

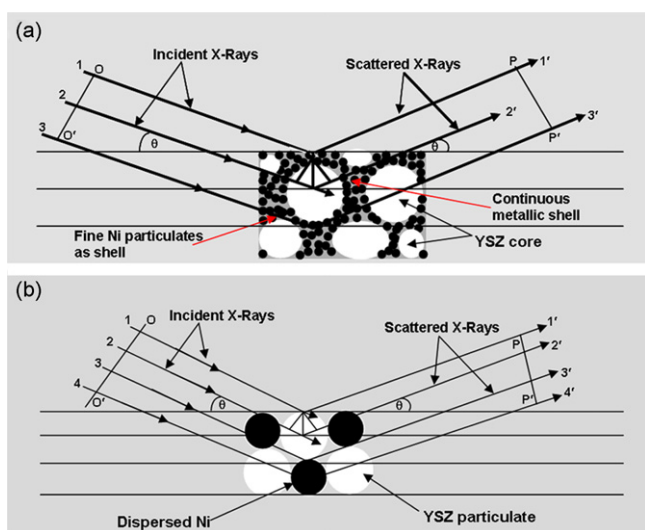


Fig. 5. Schematic of X-ray diffractions from Ni–YSZ cermet anodes prepared by: (a) ball mill assisted electroless and (b) conventional solid state technique.

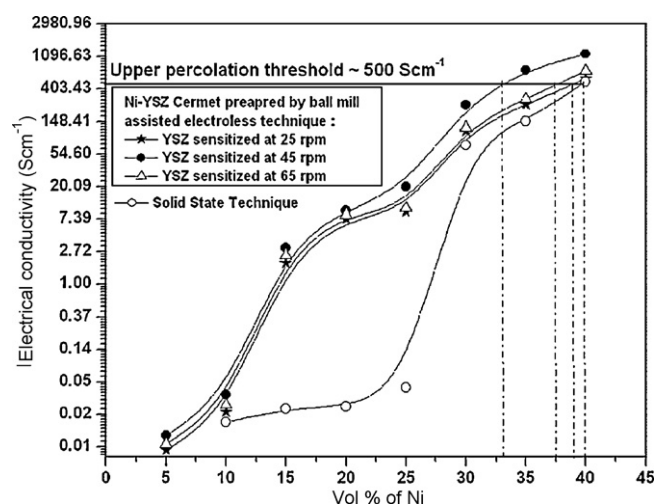


Fig. 6. Comparison of electrical conductivities of Ni–YSZ prepared by different technique.

Table 2
Density values of anode cermet prepared by electroless and conventional solid state technique.

Ni content (vol%)	Electroless technique						Solid state technique	
	Sintered density (g/cm ³)			Reduced density (g/cm ³)			Sintered density (g/cm ³)	Reduced density (g/cm ³)
	25 rpm	45 rpm	65 rpm	25 rpm	45 rpm	65 rpm		
5	6.30	6.24	6.27	5.82	5.57	5.71	–	–
10	6.07	6.02	6.05	5.67	5.37	5.58	6.09	5.53
15	6.01	5.86	5.98	5.45	5.25	5.35	6.08	5.43
20	5.99	5.79	5.84	5.04	4.89	4.95	6.02	4.99
25	5.82	5.58	5.68	5.00	4.80	4.85	5.99	4.82
30	5.73	5.49	5.57	4.87	4.68	4.72	5.97	4.69
35	5.62	5.40	5.49	4.69	4.50	4.58	5.67	4.53
40	5.70	5.67	5.69	4.57	4.49	4.50	5.77	4.51

down the upper percolation threshold for the total electrical conductivity to ~33 vol% of Ni in case of the anodes prepared through electroless deposition with YSZ sensitized at an optimum milling speed of 45 rpm in comparison to batches milled at other speeds. The total electrical conductivity value of the anode is required to be sufficiently high (~500 S/cm) for SOFC application which entirely depends on the presence of the Ni in the cermet matrix. The required electrical conductivity value of the anode is found to be at 40 vol% of Ni content when prepared by solid state technique (Fig. 6). Therefore, a decrease of ~7 vol% of Ni in the cermet matrix of the electroless anode samples prepared at a milling speed of 45 rpm is observed without compromising the total electrical conductivity. Minimization of Ni coarsening during high temperature operation of SOFC may be controlled using such electroless anode due to lesser Ni content in the cermet matrix. In addition, the thermal compatibility of anode with the other cell components may also improve because of relatively lesser CTE value of the anode cermet having lower Ni content. It is observed that irrespective of the milling speeds used for YSZ sensitization, the onset of electrical conductivity percolation starts ~10 vol% of Ni in the anode cermets prepared by electroless technique. Continuous metallic network is retained in the matrix due to the formation of core-shell microstructure in the anode cermet. The flow path of the electrons is thus made continuous through the Ni-Ni shell with a consequent increase in electrical conductivity at a much lower Ni content. However, in contrast, for the cermets prepared by conventional technique, the onset of increase in electrical conductivity starts from ~25 vol% Ni onwards. The presence of randomly dispersed Ni in the conventional anode results in the requirement of a higher Ni content for the onset of electrical conductivity percolation.

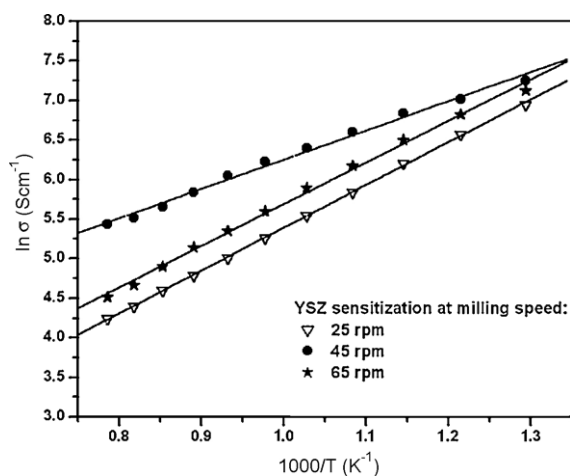


Fig. 7. Temperature dependent electrical conductivities of cermet anodes (33 vol% Ni) prepared by ball mill assisted electroless technique.

Table 3
Variation of frequency factor with milling speed during YSZ sensitization for electroless anodes.

Milling speed during YSZ sensitization (rpm)	Frequency factor "A" in S/cm
25	0.986
45	12.894
65	1.537

As shown in Fig. 7, the temperature dependant electrical conductivity of Ni-YSZ cermets prepared by electroless technique follow a metallic behavior. It must be mentioned here that though the conductivity in these cermets is predominantly metallic in nature, the overall conductivities are the manifestation of total ceramic and metallic components in the cermet matrix and is highly dependent on the processing condition of the materials. The temperature dependence of electrical conductivity plots (Fig. 7) shows Arrhenius type behavior for the cermets prepared with sensitized YSZ at three different milling speeds (25, 45 and 65 rpm). It is evident that the electrical conduction at different temperatures is highest for the electroless Ni-YSZ cermets prepared from YSZ sensitized at optimum milling speed of 45 rpm. The frequency factor 'A' of the Arrhenius equation [$\sigma = A \exp(-E_a/RT)$], are obtained from the intercept of Fig. 7. Variation of 'A' as a function of milling speed is given in Table 3. The frequency factor 'A' which is proportional to the number of reaction sites for adsorption of Pd⁰ onto YSZ followed by reduction of Ni²⁺ to Ni⁰ during electroless deposition are found to be maximum at the optimum milling speed of 45 rpm. Therefore, it is clear that 45 rpm is the optimum milling speed that facilitates proper YSZ sensitization by surface adsorption of active Pd⁰ sites (~83 ppm adsorbed Pd⁰ in Fig. 2). Table 4 shows the dependence of activation energies as a function of milling speed. Activation energies are calculated from the corresponding slopes of Fig. 7. The lowest activation energy at an optimum milling speed of 45 rpm clearly indicates the presence of continuous metallic network throughout the anode matrix.

As expected, CTE values of the electroless Ni-YSZ cermet prepared with sensitized YSZ at optimum milling speed of 45 rpm corresponding to 33 vol% of Ni content is found to be less ($11.48 \times 10^{-6} \text{ K}^{-1}$) than that of the conventional solid state anode ($12.79 \times 10^{-6} \text{ K}^{-1}$) and becomes closer to that of YSZ electrolyte

Table 4
Variation of activation energies with milling speed during YSZ sensitization for electroless anodes.

Milling speed during YSZ sensitization (rpm)	Activation energy (E _a) for electrical conductivity (Ni-YSZ cermet) in kJ/mol
25	44.93
45	30.71
65	43.72

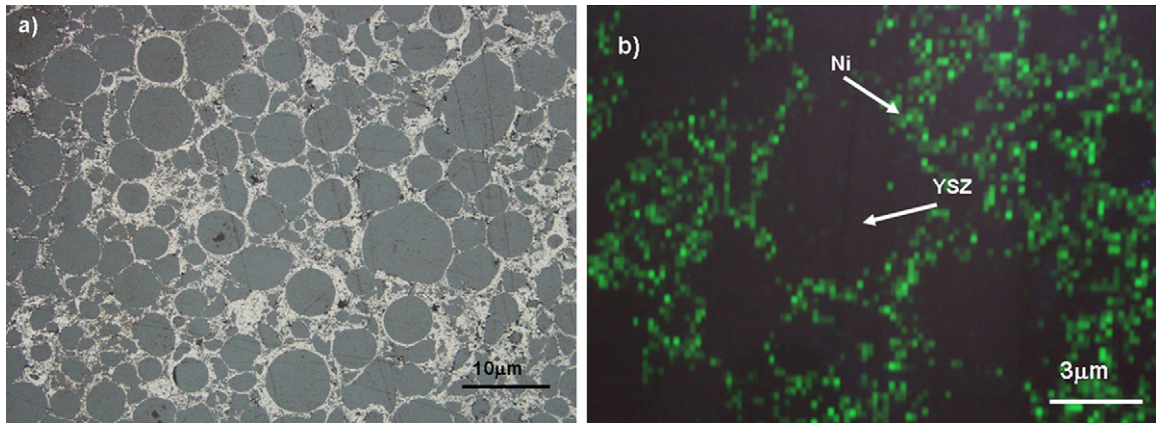


Fig. 8. (a) Optical micrograph of polished Ni-YSZ surface (33 vol% Ni) prepared by electroless technique and (b) corresponding Ni-mapping of the selected area.

($10.85 \times 10^{-6} \text{ K}^{-1}$). Thus the anode prepared by such electroless technique is thermally more compatible to the other cell components.

Fig. 8 shows optical microscopy of Ni-YSZ cermet with 33 vol% of Ni content prepared by such electroless technique with sensitized YSZ under optimized milling speed of 45 rpm reveals the core-shell microstructure with fine metallic Ni particulates in the grain boundary region and YSZ in the core region (Fig. 8a). Elemental Ni mapping also supports the formation of discrete metallic Ni

shell around YSZ core for the electroless Ni-YSZ cermets prepared under the optimum conditions (Fig. 8b). The high resolution of field emission scanning electron microscope (FESEM) image of sintered and reduced Ni-YSZ cermet prepared by such electroless technique at an optimum milling speed (45 rpm) is shown in Fig. 9. The line mapping of the selected area for such electroless anode is shown in the figure by the individual color code. This clearly indicates the presence of metallic Ni in the shell and YSZ in the core. This is also supported by elemental Ni mapping shown in Fig. 8b. From

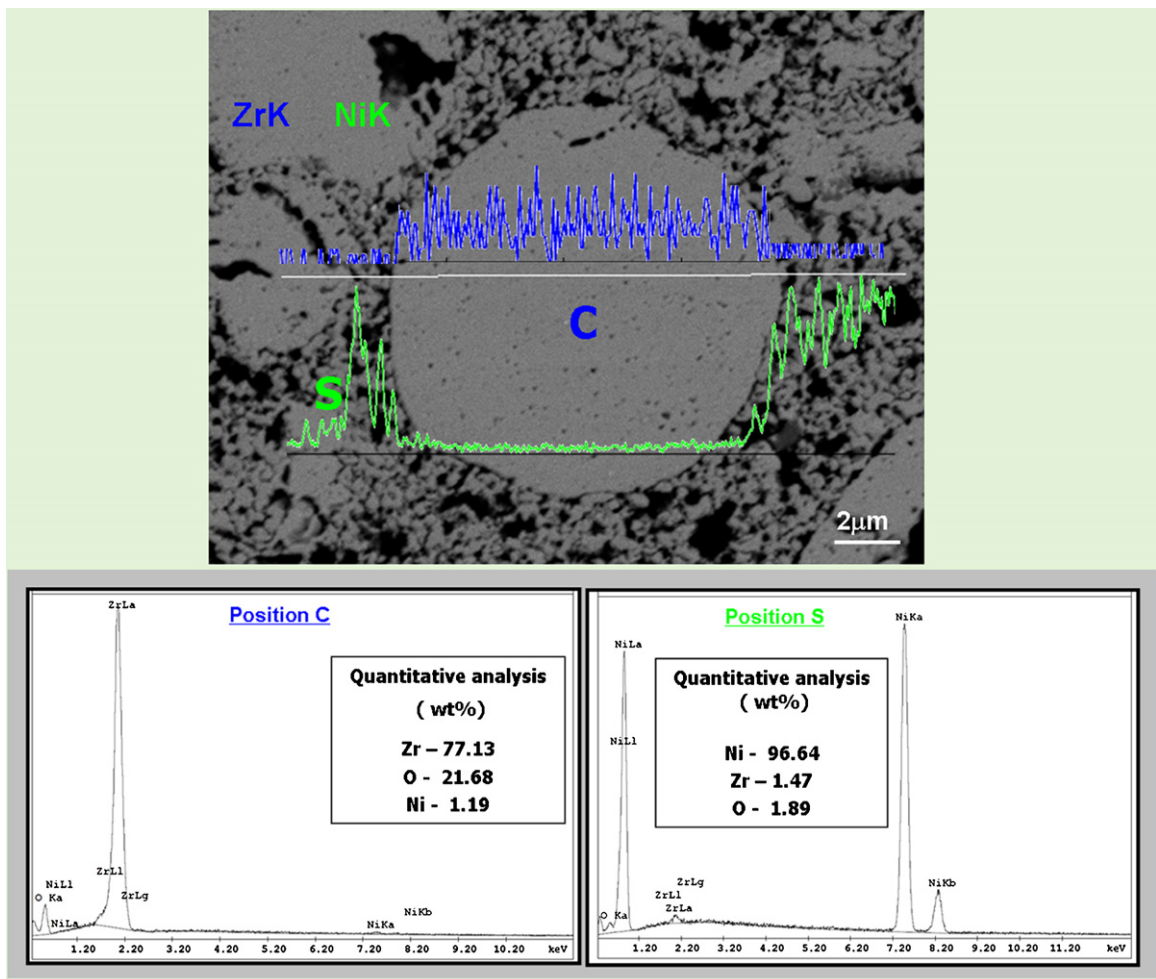


Fig. 9. FESEM image of electroless Ni-YSZ along with quantitative spot EDX and the corresponding line mapping.

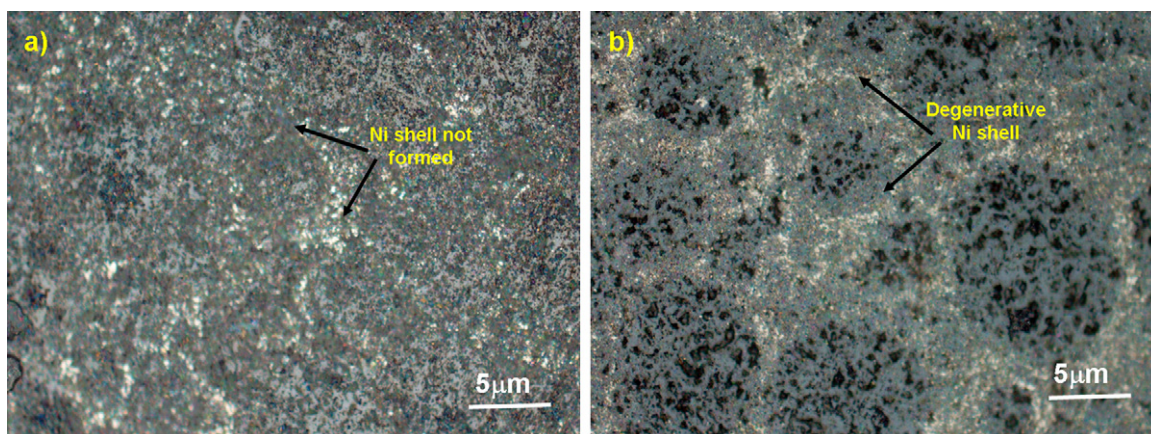


Fig. 10. Optical micrograph of electroless Ni-YSZ cermet with YSZ sensitized at: (a) 25 rpm and (b) 65 rpm.

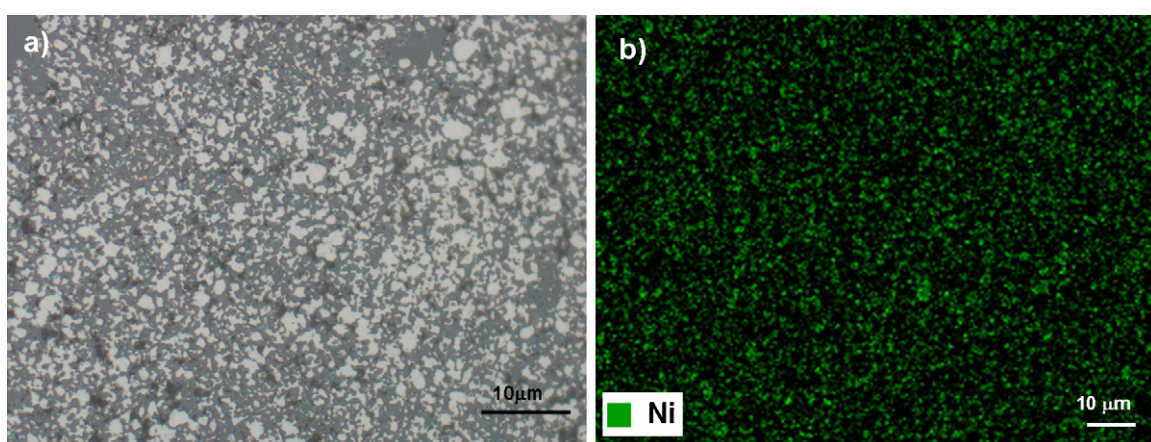


Fig. 11. (a) Optical micrograph of the polished Ni-YSZ surface (40 vol% Ni) prepared by conventional solid state technique and (b) corresponding Ni mapping of the selected area.

quantitative spot EDX (Fig. 9), it can be concluded that the core (position C) contains ~98 wt% zirconia while the shell (position S) contains ~97 wt% of Ni in the reduced electroless Ni-YSZ cermets. Fig. 10 shows the optical micrographs of Ni-YSZ cermet prepared with YSZ sensitized at 25 rpm (Fig. 10a) and 65 rpm (Fig. 10b). From the micrographs, it is observed that in both the cases, the Ni shell is either not formed due to ineffective sensitization of YSZ or degenerated due to excessive fragmentation of YSZ particulates because of high grinding impact.

From Fig. 11, completely different microstructure is observed in case of conventionally prepared cermet having 40 vol% Ni where a dispersed metallic nickel in the YSZ matrix is observed (Fig. 11a). Elemental mapping of the conventional cermets (Fig. 11b) supports the existence of randomly dispersed Ni compared to the core shell microstructure of the anode cermet prepared by electroless technique. The particle size of Ni for the sintered and reduced electroless Ni-YSZ cermets is found to be finer than that of the Ni particles in conventional anode. From the Ni mapping of the electroless anode, it is observed that the size of electroless Ni is ~0.2–0.3 μm (Fig. 8b). From the mapping of the conventional anode (Fig. 11b), the size range of Ni is found to be >1 μm. This is reflected in the XRD pattern (Fig. 4) of the samples and the Ni peak broadening in the electroless samples may be attributed for finer sizes of the Ni particulates.

Therefore, experimental results obtained from the adsorption capacity of YSZ (Fig. 2), activation energies from the Arrhenius plot and the optical micrographs of the electroless anodes prepared

under different milling speed for sensitization of YSZ are correlated with the theoretical explanation of milling. Milling speed of 45 rpm for zirconia sensitization is found to be optimum for preparation of Ni-YSZ electroless anode cermet.

4. Conclusions

During synthesis of Ni-YSZ cermet anode by electroless technique, sensitization process of the YSZ powder at an optimum milling speed of 45 rpm has a significant role in the formation of metallic Ni shell as fine particulates around YSZ core thereby maintaining continuous metallic pathway throughout the cermet. The adsorbed Pd⁰ formed by the sensitization process acts as catalytic centers for in situ reduction of Ni²⁺ to Ni and its consequent controlled deposition onto YSZ in the electroless bath. The upper electrical conductivity percolation threshold is brought down to ~33 vol% of Ni in case of the anodes prepared through electroless with YSZ sensitized at an optimum milling speed of 45 rpm compared to ~40 vol% Ni in the conventionally prepared anodes. The temperature dependence of electrical conductivity plots show that irrespective of preparation technique, electrical conduction is metallic in nature and is highest for the electroless Ni-YSZ cermets prepared from sensitized YSZ at an optimum milling speed of 45 rpm wherein the activation energy is found to be lowest. Optical micrographs of electroless anodes show that at 45 rpm milling speed during YSZ sensitization, proper Ni shell

onto YSZ core is formed with fine Ni particulates having continuous metallic network throughout the matrix. Formation of this unique microstructure is also supported by elemental Ni mapping. CTE value of $\sim 11.48 \times 10^{-6} \text{ K}^{-1}$ of such anode prepared by electroless technique is also found to be relatively closer to the other cell components, especially, to that of YSZ electrolytes. Compared to these anodes, conventionally prepared anodes show presence of randomly dispersed Ni in the cermets. Therefore, it may be concluded that Ni–YSZ cermet anode prepared by electroless technique at optimized milling parameters is superior to the conventional Ni–YSZ with respect to their electrical and thermal properties for the application as SOFC anode.

Acknowledgements

The authors acknowledge Director, CGCRI for his kind permission to present the work. One of the authors (M.M.) is thankful to Council of Scientific and Industrial Research (CSIR) for providing Junior Research Fellowship.

References

- [1] N.Q. Minh, T. Takahashi, Science and Technology of Ceramic Fuel Cells, Elsevier, New York, USA, 1995.
- [2] S.C. Singhal, K. Kendall, High Temperature Solid Oxide Fuel Cells: Fundamentals, Design and Applications, Elsevier, U.K. Editor, 2003.
- [3] R.N. Basu, in: S. Basu (Ed.), Materials for Solid Oxide Fuel Cells in Recent Trends in Fuel Cell Science and Technology, Jointly published by Anamaya Publishers, New Delhi (India) and Springer, New York, USA, 2006, 284.
- [4] T. Iwata, J. Electrochem. Soc. 143 (1996) 1521–1525.
- [5] J. Mizusaki, S. Tsuchiya, K. Waragai, J. Am. Ceram. Soc. 79 (1996) 109–113.
- [6] J. Mukhopadhyay, M. Banerjee, A. Das Sharma, R.N. Basu, H.S. Maiti, Electrochem. Soc. Trans. 7 (1) (2007) 1563–1572 (The Electrochemical Society).
- [7] S.K. Pratihari, A. Das Sharma, R.N. Basu, H.S. Maiti, J. Power Sources 129 (2004) 138–142.
- [8] J. Mukhopadhyay, M. Banerjee, R.N. Basu, J. Power Sources 175 (2008) 749–759.
- [9] D.E. Dees, T.D. Claar, T.E. Easler, et al., J. Electrochem. Soc. 134 (1987) 2141.
- [10] G.E. Boyd Jr., A.W. Adamson, L.S. Myers, J. Am. Chem. Soc. 69 (1947) 2836–2848.
- [11] McCabe, Smith, Harriott, Unit Operations of Chemical Engineering, fifth ed., McGraw-Hill Book Co., Singapore, 1993, p. 980–982.

Influence of sorption kinetics for zirconia sensitization in solid oxide fuel cell functional anode prepared by electroless technique

Jayanta Mukhopadhyay, Madhumita Banerjee, Rajendra N. Basu*

Fuel Cell & Battery Division, Central Glass & Ceramic Research Institute, Kolkata 700032, India

Received 18 June 2007; accepted 21 September 2007

Available online 9 October 2007

Abstract

For preparation of solid oxide fuel cell functional anode (Ni-YSZ) by electroless deposition technique, surface adsorption of metallic palladium (Pd^0) on zirconia is the most important step during the sensitization process. For the sensitization process, the initial reaction kinetics are based on external mass transfer followed by intra-particle mass transfer phenomena. A kinetic model for the reversible sorption of Pd^0 on zirconia is developed that incorporates an effectiveness factor (η) which estimates the extent of intra-particle mass transfer. Based on the proposed model, an expression for Pd^0 uptake at equilibrium (p), an important property of YSZ, is developed. The theoretical kinetic model proposed is verified with experimental parameters like electrical properties of these functional anodes prepared under various sensitization conditions, e.g., agitation frequencies, equilibration time etc. Due to intra-particle mass transfer, the concentration gradient of Pd^0 from the surface of YSZ to bulk is minimized which favours uniform deposition of Ni on YSZ. Consequently, during subsequent electroless deposition of metallic Ni, the concentration gradient of the same is reduced from the bulk to the YSZ surface and results in enhanced functionality in the cermet anode. The validation is correlated with the electrical properties and surface morphologies of these functional cermets.

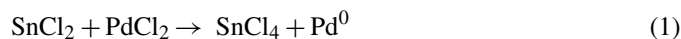
© 2007 Elsevier B.V. All rights reserved.

Keywords: Solid oxide fuel cell; Functional anode; Electroless deposition; Sorption kinetics

1. Introduction

For the anode-supported solid oxide fuel cell (SOFC), the most important cell component is the anode support. Apart from high electronic conductivity, anode should have sufficient interconnected porosity for proper percolation of the fuel and also to provide the effective number of electrocatalytic sites for oxidation of the fuel [1–3]. A functional anode with core–shell microstructures can reduce the Ni-content in the cermet even up to ~25 vol.% compared with 40 vol.% in conventionally prepared nickel–yttria stabilized zirconia (Ni–YSZ) cermet [4]. It is expected that these improved properties may help in reducing the mismatch of coefficient of thermal expansion between Ni and YSZ and may also solve the Ni coarsening problem during long-term SOFC operation [4–6]. The functional anode prepared

by electroless technique involves an initial sensitization process which is the surface adsorption of metallic palladium (Pd^0) on YSZ under high energy ultrasonication. Power ultrasound has been found to have a profound influence on chemical reactions conducted in liquid phase, irrespective of whether they are homogeneous or heterogeneous in nature, and can cause a number of chemical effects [7–9]. This high-energy sonochemical reaction is used for sensitization of zirconia by surface adsorption of Pd^0 that forms instantaneously in the redox sensitization bath as follows:



Pd^0 adsorption on YSZ powder is an example of physisorption because metallic palladium is held by Van der Waals interaction with the YSZ precursor powder. Therefore, Pd^0 adsorption kinetics mainly involve two processes: (i) the external mass transfer of Pd^0 species from the bulk solution to the surface of YSZ and (ii) the intra-particle mass transfer of Pd^0 in the pores and on the YSZ surface [10]. An apparent kinetics

* Corresponding author. Tel.: +91 33 2473 3469/96x3507; fax: +91 33 2473 0957.

E-mail addresses: rnbasu@cgcric.res.in, rajnbasu@yahoo.ca (R.N. Basu).

takes into account the effects of both the chemical and physical rate processes and various physical process parameters, such as: (i) flow conditions, (ii) intensity of mixing and (iii) heat and mass transfer in the system, which can influence the kinetic rate [11–14].

The development of reversible sorption kinetics of the sensitization process is essential for understanding the basic mechanisms of surface adsorption of Pd⁰ on YSZ particulates that govern the formation of core–shell structure in the functional cermet. The understanding of this physisorption process is mandatory for effective formation of the Ni shell around the YSZ core that enhances the functionality by increasing the overall triple-phase boundary length required for electrocatalytic oxidation of the fuel. This is reflected in the attainment of a transient equilibrium during the sensitization process. Various sensitization conditions, e.g., agitation frequencies, equilibration time etc will have a pronounced effect on the overall electrical properties of these functional anodes.

In the present investigation, a reversible kinetic model for the adsorption process during sensitization of YSZ is proposed and validated with relevant experimental evidence. In the present context, an effectiveness factor (η) has been introduced to estimate the effect of intra-particle mass transfer. This modification simplifies the evaluation of intra-particle mass transfer by avoiding consideration of the distribution of solute concentration in the pores of YSZ adsorbent.

2. Proposed kinetic model

2.1. Adsorption kinetics of Pd⁰ on YSZ particulates

The adsorption process is mainly governed by the intra-particle mass transfer phenomena because the effect of external mass transfer can be eliminated by intensive agitation as will be shown in the subsequent sections. Intra-particle mass transfer involves not only surface and molecular diffusion but also diffusion in the pores of the particle. These effects can be expressed by an effectiveness factor (η) which can be defined as:

$$\eta = \frac{r_p}{r_s} \quad (2)$$

where r_s and r_p are the actual adsorption rate and the same evaluated at the outer surface condition, respectively [15].

2.2. Derivation of expression for r_s

YSZ sensitization process can be represented by the following equation:



where YSZ–Pd⁰ represents weak Van der Waals interaction between YSZ and Pd⁰.

Applying the mass action law to the reaction given in Eq. (3), the rate of formation of YSZ–Pd⁰ is given as

$$r_s = \frac{d[\text{YSZ-Pd}^0]}{dt} = k_1 e^{-E_1/RT} [\text{Pd}^0][\text{YSZ}] - k_2 e^{-E_2/RT} [\text{YSZ-Pd}^0] \quad (4)$$

Since the unoccupied surface active sites of YSZ are equal to the difference between the total active sites (YSZ_t) and the occupied surface active sites (YSZ–Pd⁰), Eq. (4) can be written as

$$r_s = \frac{d[\text{YSZ-Pd}^0]}{dt} = k_1 e^{-E_1/RT} [\text{Pd}^0][\text{YSZ}_t - \text{YSZ-Pd}^0] - k_2 e^{-E_2/RT} [\text{YSZ-Pd}^0] \quad (5)$$

where [] denote the concentration (ppm) of the involved species, YSZ the adsorbent, Pd⁰ the adsorbate, R the universal gas constant, T the experimental absolute temperature and k_1 , k_2 and E_1 , E_2 are the frequency (or pre-exponential) factors and activation energies for the forward and backward reactions, respectively, which are involved in the rate equation proposed by transition state theory.

Thus, Eq. (5) can also be written as

$$r_s = \frac{d[\text{YSZ-Pd}^0]}{dt} = k'_{\text{ads}} [\text{Pd}^0][\text{YSZ}_t - \text{YSZ-Pd}^0] - k'_{\text{des}} [\text{YSZ-Pd}^0] \quad (6)$$

where $k'_{\text{ads}} = k_1 e^{-E_1/RT}$ (ppm⁻¹ min⁻¹) and $k'_{\text{des}} = k_2 e^{-E_2/RT}$ (min⁻¹)

Eq. (6) could be further simplified as

$$p = [\text{YSZ-Pd}^0], \quad p_m = [\text{YSZ}_t], \quad q = [\text{Pd}^0]$$

$$r_s = k'_{\text{ads}} q(p_m - p) - k'_{\text{des}} p \quad (7)$$

Eq. (2) can now be written as

$$r_p = \eta r_s = \eta [k'_{\text{ads}} q(p_m - p) - k'_{\text{des}} p] \quad (8)$$

2.3. External mass transfer model

The external mass transfer model describes the change in adsorbate concentration with time. It can be expressed as

$$-\frac{dq}{dt} = k_f a_m (q - q_i) \quad (9)$$

where k_f is the mass transfer coefficient between the bulk solution and sorbent surface (cm min⁻¹), a_m the volumetric specific area of the adsorbent (cm² cm⁻³), q and q_i are the sorbate concentrations (ppm) in the bulk solution and at the surface of YSZ, respectively.

Assuming the YSZ particles to be spherical [16], an equation for volumetric specific area (a_m) can be written as

$$a_m = \frac{6m}{d_p \rho_p (1 - \varepsilon_p)} = \frac{6m}{d_p \rho_b} \quad (10)$$

where m , d_p , ρ_p , ρ_b , ε_p are the concentration (g cm⁻³), the average size (μm), theoretical density (g cm⁻³), bulk density (g cm⁻³) and porosity of YSZ, respectively.

When external mass transfer is the controlling step, the surface concentration of metallic palladium (sorbate) is approximately constant. Taking the overall mass conservation into

consideration, the bulk concentration can be written as

$$q = q_0 - \frac{pM}{v} \tag{11}$$

where q_0 , p , M and v are the initial concentration of Pd^{2+} (ppm) used (in the form of PdCl_2 solution), the Pd^0 uptake at equilibrium (ppm g^{-1}), the mass quantity of YSZ powder (g) and the water volume (ml) in the sensitized bath, respectively.

Substituting q , from Eq. (11) to Eq (9) gives:

$$\frac{dp}{dt} = \frac{vk_{\text{f}}a_{\text{m}}(q - q_{\text{t}})}{M} \tag{12}$$

Using Eqs. (12) and (6), the expression for maximum adsorption capacity can be written as

$$p = \frac{B/C - \sqrt{(B/C)^2 - (4A/C)} - \left\{ (B/C) + \sqrt{(B/C)^2 - (4A/C)} \right\} \exp \left(2.303 \eta t C \sqrt{(B/C)^2 - (4A/C)} \right)}{2 \left[\exp \left(2.303 \eta t C \sqrt{(B/C)^2 - (4A/C)} \right) - 1 \right]} \tag{19}$$

$$r_{\text{s}} = \frac{d[\text{YSZ-Pd}^0]}{dt} = \frac{dp}{dt} = k'_{\text{ads}}q_{\text{t}}(p_{\text{m}} - p) - k'_{\text{des}}p = \frac{vk_{\text{f}}a_{\text{m}}(q - q_{\text{t}})}{M}$$

$$\Rightarrow q_{\text{t}} = \frac{vk_{\text{f}}a_{\text{m}}q/M + k'_{\text{des}}p}{k'_{\text{ads}}(p_{\text{m}} - p) + k_{\text{f}}a_{\text{m}}v/M} \tag{13}$$

When the external mass transfer is the controlling step, i.e. $k_{\text{f}}a_{\text{m}}v/M \ll k'_{\text{ads}}(p_{\text{m}} - p)$ and $k_{\text{f}}a_{\text{m}}$ has a small value, Eq. (13) can be modified as

$$q_{\text{t}} = \frac{k'_{\text{des}}p}{k'_{\text{ads}}(p_{\text{m}} - p)} \tag{14}$$

Assuming the sorption isotherm to follow the Langmuir equation, expression for the Pd^0 uptake at equilibrium (p in ppm g^{-1}) can be written as

$$p = \frac{K_1 p_{\text{m}} q_{\text{s}}}{1 + K_1 q_{\text{s}}} \tag{15}$$

where K_1 is the equilibrium constant (ppm^{-1}), p_{m} the maximum sorption capacity of the sorbent (ppm g^{-1}) and q_{s} is the total Pd^0 concentration in solution (ppm).

Substituting Eq. (15) into Eq. (14) yields:

$$q_{\text{t}} = \frac{k'_{\text{des}} K_1 q_{\text{s}}}{k'_{\text{ads}}}$$

Given that $K_1 = k'_{\text{ads}}/k'_{\text{des}}$, the above equation can be written as

$$q_{\text{t}} = q_{\text{s}} \tag{16}$$

It is to be noted that Eq. (16) is applicable only at maximum adsorption capacity when it is considered that the total Pd^0 formed gets adsorbed on the sensitized YSZ surface.

As q_{t} is related to the equilibrium concentration, which is independent of time, Eq. (9) can be integrated with the following

boundary conditions: at $t=0$, $q = q_0$ (considering total reduction of Pd^{2+} to Pd^0); and at $t = t$, $q = q$:

$$\ln \frac{q_0 - q_{\text{t}}}{q - q_{\text{t}}} = k_{\text{f}}a_{\text{m}}t \tag{17}$$

2.4. Model solution of proposed adsorption kinetics

From Eqs. (8) and (11),

$$r_{\text{p}} = \eta r_{\text{s}} = \eta \left[k'_{\text{ads}} \left(q_0 - \frac{pM}{v} \right) (p_{\text{m}} - p) - k'_{\text{des}} p \right]$$

$$\Rightarrow \frac{dp}{dt} = \eta \left[k'_{\text{ads}} \left(q_0 - \frac{pM}{v} \right) (p_{\text{m}} - p) - k'_{\text{des}} p \right] \tag{18}$$

Integrating Eq. (18), the expression for Pd^0 uptake at equilibrium (p) can be written as

where:

$$A = k'_{\text{ads}} p_{\text{m}} q_0 \tag{20}$$

$$B = - \left(\frac{k'_{\text{ads}} p_{\text{m}} M}{v} + k'_{\text{ads}} q_0 + k'_{\text{des}} \right) \tag{21}$$

$$C = \frac{k'_{\text{ads}} M}{v} \tag{22}$$

3. Experimental

The above proposed kinetic model is validated by the following experiments.

3.1. Particle-size distribution of YSZ adsorbent

Experiments were performed using two types of YSZ powder namely: (i) TZ-8Y, from Tosho Corporation, Japan ($d_{50} \sim 0.2 \mu\text{m}$ and henceforth referred to as YSZ-Tosho), (ii) FYT from Unitech Corporation, UK ($d_{50} \sim 3 \mu\text{m}$ and henceforth referred to as YSZ-Unitech). YSZ-Tosho was further processed to increase the d_{50} value to $\sim 27 \mu\text{m}$. In the present context, three different size fractions of YSZ powders were used to investigate the effect of particle size on the sorption kinetics of metallic palladium (Pd^0), which is the rate-controlling step for electroless deposition. Fig. 1 shows an inverse linear relationship between bulk density and particle size of the adsorbent (YSZ powders), from which it is clear that the bulk density decreases with increase in particle size of the YSZ powder.

3.2. Sorption kinetics with variable agitation frequencies

An adsorption study of Pd^0 on YSZ was carried out with the help of a high-energy ultrasonifier (BRANSON, SONIFIER 450) with an adjustable agitation frequency. While starting the process, the required amount of YSZ powder was added to a

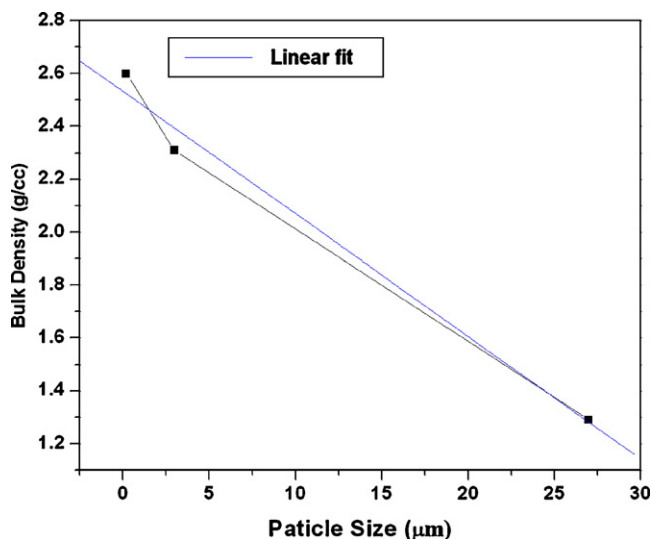


Fig. 1. Variation of bulk densities with particle size of YSZ powder.

redox bath that contained 0.001(M) palladium chloride solution and 0.265(M) stannous chloride solution. Metallic palladium (Pd^0), produced in situ (reaction given in Eq. (1)), was adsorbed on the YSZ surface upon placing the redox bath under a high energy ultrasonifer for 20 min at room temperature and in the agitation frequency range of 10–16 kHz. The sensitized bath was then kept for attaining equilibrium for effective adsorption of Pd^0 and complete precipitation of sensitized YSZ powder. In order to determine the adsorbed concentration of Pd^0 (q_t) on the YSZ surface, a certain aliquot from the supernatant solution of the sensitized bath was collected at a definite time interval and the residual concentration of Pd^{2+} in the supernatant solution was measured with the help of an inductive coupled plasma atomic emission spectrophotometer (Spectro Analysis Instrument, Kleve, Germany). The concentration of the adsorbed Pd^0 is calculated from the difference between the initial Pd^{2+} and the residual Pd^{2+} (in the supernatant liquid) concentration.

Adsorption being reversible in nature, simultaneous adsorption and desorption occur at the adsorbent surface and is generally known as sorption. The equilibration time is one of the crucial factors and is unique for a particular sorbent species. It is considered that the total Pd^0 formed during the sensitization process is adsorbed on the YSZ surface provided the sorbent is allowed to attain the transient equilibrium. However, the small amount of Pd^0 desorbed during the equilibrium sorption process is also taken into consideration during the reversible sorption kinetics.

3.3. Electroless deposition of Ni on to sensitized YSZ at different equilibration time intervals

The YSZ particulates sensitized at different time intervals of equilibration process were subjected to an electroless bath [4,5,17]. The flow chart of the process is shown in Fig. 2. The reaction bath is kept constant at ammoniacal pH and a temperature 80–90 °C. The reduction of Ni^{2+} from nickel nitrate solution was carried out by in situ liberation of the nascent hydrogen generated from a quantified addition of hydrazinehydrate.

3.4. Conductivity measurements of Ni–YSZ cermets

As-synthesized Ni–YSZ powders, prepared by electroless deposition on YSZ equilibrated in the sensitization baths for different periods of time, were mixed with 1.5 wt.% polyvinyl butyral (PVB) binder and pressed uniaxially in the form of green compacts of dimension 25 mm × 10 mm × 3 mm under a specific pressure of 170 MPa. The green compacts were sintered in air at a temperature of 1400 °C for 6 h. The sintered samples were then reduced at 1000 °C under a gaseous flow of argon and hydrogen (4:1) for 10 h and thus Ni–YSZ cermet bulk samples were produced. Conductivities of the reduced Ni–YSZ samples as a function of temperature were measured using standard 4-probe dc measurement technique using a 81/2 digit multimeter (Keithley, Model 2002). The corresponding conductivity values in various temperatures were then calculated using the formula:

$$\sigma = \frac{L}{Rbt} \quad (23)$$

where σ is the conductivity, R the 4-probe resistance of the samples measured, L the length between the two voltage probes, b the breadth and t is the sample thickness.

3.5. Surface morphologies of Ni–YSZ cermets at different equilibration time intervals

The highly polished microstructures of the Ni–YSZ functional cermets prepared with sensitized YSZ at different equilibration times of the adsorption regimes were observed with a high resolution optical microscope (Olympus GX 71, Japan). The microstructures of conventionally prepared Ni–YSZ cermets were also studied with the same microscope.

4. Results and discussion

4.1. Effect of particle size of YSZ on sorption kinetics

Kinetic experiments to study the effect of particle size of sorbent were carried out at the highest sonochemical agitation frequency of 16 kHz. It has been already mentioned that in the present context three different particle sizes of YSZ powder (0.2 μm, 27 μm of YSZ-Tosho and 3 μm of YSZ-Unitec) were used to study the size effect on the adsorption kinetics of Pd^0 on YSZ powder. The volumetric specific areas of the YSZ powders of varying particle size (0.2 μm and 27 μm of YSZ-Tosho and 3 μm of YSZ-Unitec) were determined from Eq. (10) and are summarized in Table 1. It is observed that with increase in particle size of adsorbent, the value of the bulk density decreases and thereby decreases the volumetric specific area, which is evident from Eq. (10).

Table 1
Determination of volumetric specific area of precursor YSZ powders ($m = 0.0267 \text{ g cm}^{-3}$)

Particle size (d_p) (μm)	0.2	3	27
Bulk density (ρ_b) (g cm^{-3})	2.6	2.3	1.3
Volumetric specific area (a_m) ($\text{cm}^2 \text{ cm}^{-3}$)	3081	231	46

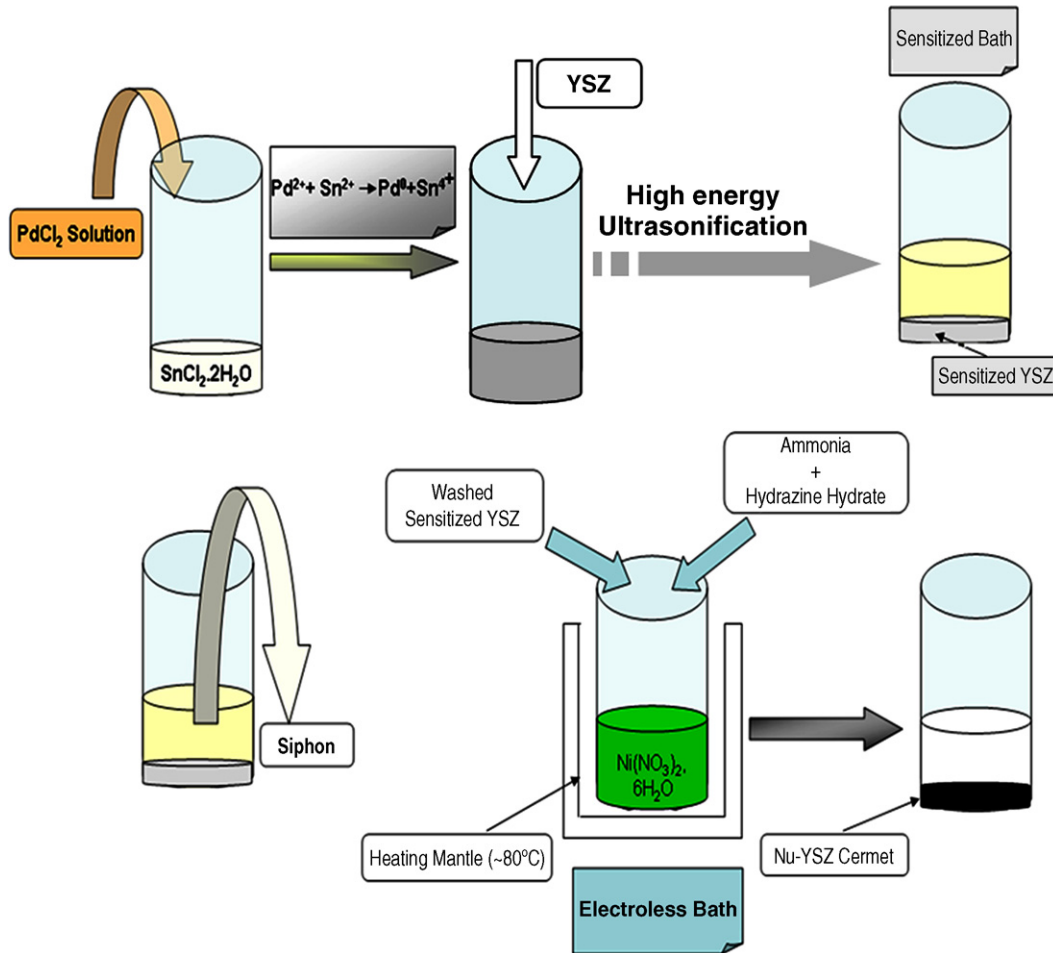


Fig. 2. Process flow chart for preparation of functional SOFC cermet.

Fig. 3 shows the dependence of the adsorption capacity (q_t) of YSZ with variation of time and establishes the particle size dependent equilibrium adsorption capacity (q_e). It can be concluded that specially treated YSZ-Tosho powder with particle size of $27 \mu\text{m}$ is most effective and optimum for surface

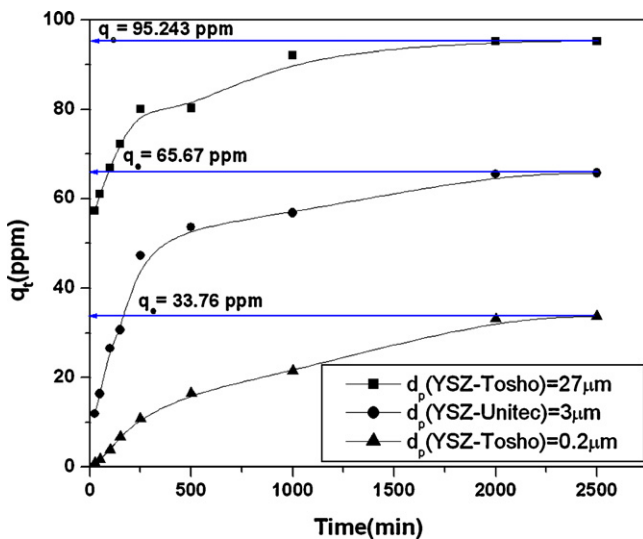


Fig. 3. Effect of particle size on adsorption kinetics ($\nu = 16 \text{ kHz}$).

adsorption of Pd^0 , which is strongly supported from the highest equilibrium Pd^0 concentration value (q_e) of 95.243 ppm. With increase in particle size of the sorbent (from 0.2 to $27 \mu\text{m}$), the uptake of Pd^0 increases. At this optimum size, the extent of physical Van der Waals interaction among the interacting species is expected to be strong enough and this results in better adsorption in comparison to smaller YSZ particle sizes.

4.2. Effect of sonochemical agitation frequency on sorption kinetics

Specially treated YSZ-Tosho powder ($d_p \sim 27 \mu\text{m}$) is most effective and optimum for surface adsorption of Pd^0 , which is strongly supported from the highest equilibrium Pd^0 concentration value (q_e) as discussed in the previous section. Thus, the aforesaid experimental YSZ powder is used to study the effect of varying sonochemical agitation frequencies (10, 12, 14 and 16 kHz). The results in Fig. 4 shows that the sorption of Pd^0 by YSZ-Tosho powder is faster at higher frequency (16 kHz). It can be easily observed from the graph that in all cases, the equilibrium concentration value (q_e) of adsorbed Pd^0 approaches a constant value of 95.243 ppm but the equilibrium state is reached quickly at a relatively higher frequency. An increase in the adsorption rate with increase in agita-

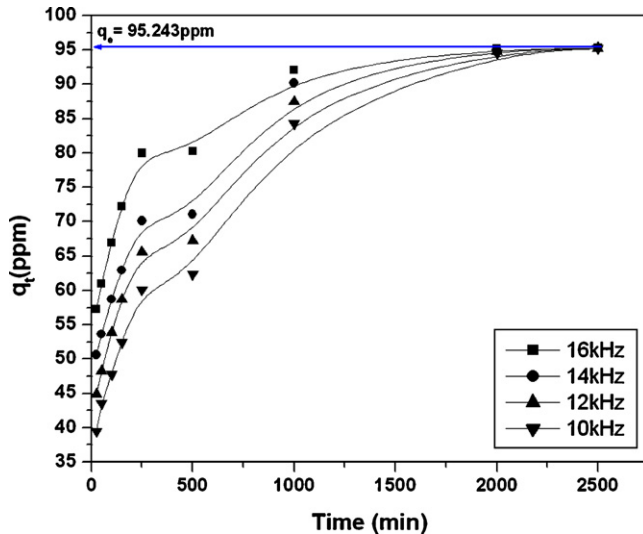


Fig. 4. Effect of agitation frequency on sorption capacity (q_t) of Pd^0 by YSZ-Tosho powder ($d_p \sim 27 \mu\text{m}$).

tion frequency can be explained by an enhanced turbulence in the solution (sensitized bath) which results in a decreased thickness of liquid boundary layer surrounding particles that leads to an increase in external mass transfer coefficient. At highest agitation frequency value of 16 kHz, the boundary layer becomes very thin and approaches a laminar sub-layer. Under these conditions, the external mass transfer resistance and coefficient values are almost constant and thus can be neglected.

4.3. Application of external mass transfer coefficient on sorption kinetics

Adsorption of Pd^0 on YSZ particulate is governed mainly by external mass transfer and intra-particle mass transfer phenomena. From Fig. 4, it is clear that depending on the time, the kinetics for Pd^0 adsorption proceeds at two different rates [18,19]. Initially (up to nearly 500 min), the adsorption proceeds very fast, which is indicated by a much steeper slope in the graph (Fig. 4). The high initial rate of Pd^0 uptake suggests that the adsorption occurs mainly at the sorbent (YSZ) surface and the external mass transfer plays an active role during this period of time. This is followed by a longer period of slower adsorption (plateau region in the graph) up to 2500 min. This behaviour indicates that the mechanism of intra-particle mass transfer (diffusion technique) is also involved in the sorption kinetic model and is represented by the slower adsorption rate, as mentioned above. The variation of external mass transfer governed sorption capacity (q_t) for the initial 250 min is shown in Fig. 5. It is clear that at the beginning of sorption, external mass transfer controls the process and the surface reaction is fast. With time, the driving force for external mass transfer in the pores decreases resulting from a decrease of Pd^0 concentration in the solution and, consequently, the mass transfer of metallic palladium becomes the main resistance. Fig. 5 is valid up to an equilibration time of 250 min where the change of adsorbate concentration with time according to the external mass trans-

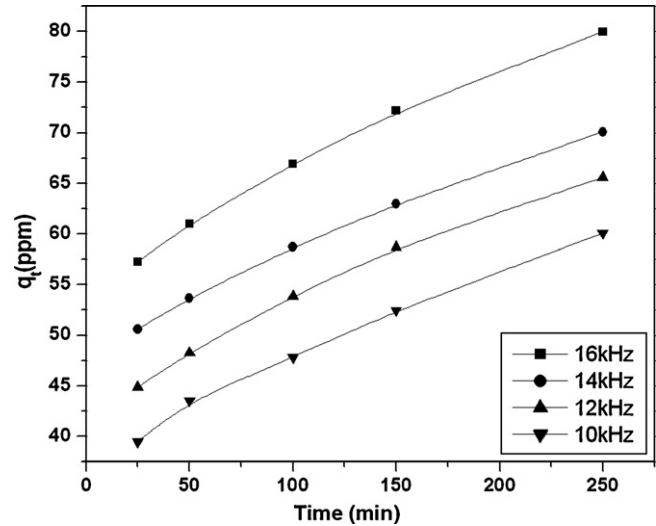


Fig. 5. Effect of agitation frequency on sorption capacity (q_t) of Pd^0 by YSZ-Tosho powder ($d_p \sim 27 \mu\text{m}$) up to experimental time interval.

fer model follows first-order kinetics. An experimental linear fit of the external mass transfer model (Eq. (17)) for Pd^0 adsorption kinetics up to 250 min at different agitation frequencies is shown in Fig. 6. The values of the volumetric external mass transfer coefficient (k_v), which is equal to the product of the external mass transfer coefficient (k_f) and the specific area of the YSZ particle, are obtained from the slopes of Fig. 6 and are tabulated along with the corresponding k_f values in Table 2. It is observed that with increase in agitation frequency, the volumetric mass transfer coefficient increases and, therefore, for a particular YSZ adsorbent with a definite volumetric specific area, the external mass transfer coefficient increase which also supports that the adsorption regime is controlled primarily by external mass transfer.

4.4. Application of intra-particle mass transfer model on sorption kinetics

To obtain the equilibrium constant (K_1) for Pd^0 adsorption on specially-treated YSZ-Tosho ($d_p \sim 27 \mu\text{m}$) for the reaction given in Eq. (3), the Langmuir adsorption isotherm (Eq. (15)) is used and can be linearly expressed as

$$\frac{1}{p} = \frac{1}{p_m} + \frac{1}{K_1 p_m q_s} \quad (24)$$

$$\Rightarrow \frac{q_s}{p} = \frac{q_s}{p_m} + \frac{1}{K_1 p_m} \quad (25)$$

Eq. (25) is used to fit the data in Fig. 4; the results are given in Fig. 7. As the parameters in the Langmuir equation are governed

Table 2

The external and volumetric mass transfer coefficients at different agitation frequency ($d_p \sim 27 \mu\text{m}$ and $a_m = 45.99 \text{ cm}^2 \text{ cm}^{-3}$)

Agitation frequency (kHz)	10	12	14	16
$k_{f \text{ exp}} (\times 10^{-5} \text{ cm min}^{-1})$	2.68	3.31	3.40	5.72
$k_{v \text{ exp}} (\times 10^{-3} \text{ min}^{-1})$	1.23	1.52	1.57	2.63

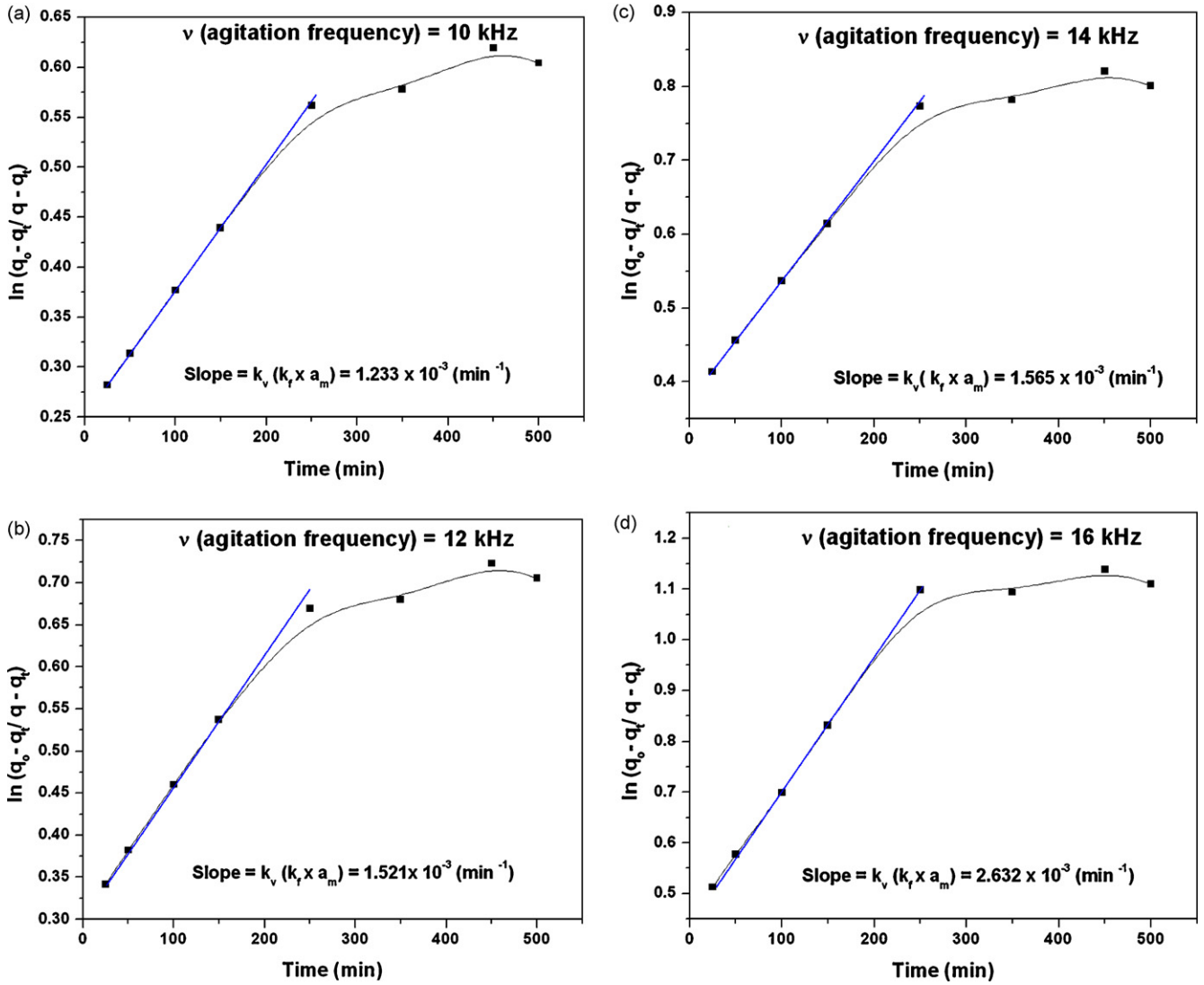


Fig. 6. Variation of $\ln(q_0 - q_t/q - q_t)$ vs. time for Pd^0 adsorption with agitation frequencies (ν) of: (a) 10 kHz, (b) 12 kHz, (c) 14 kHz and (d) 16 kHz.

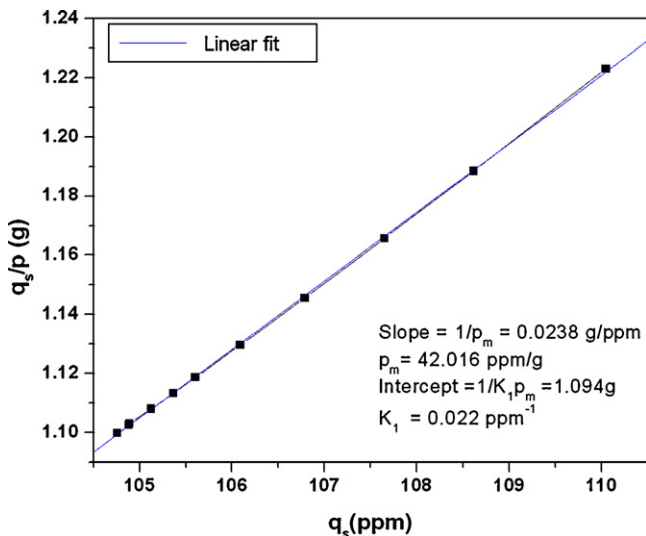


Fig. 7. Linear Variation of q/p vs. q .

by the equilibrium state of a time-dependent reversible process, Eq. (25) can only be applied in the transient equilibrium range (from 1000 to 2500 min) shown in Fig. 4. It can be seen from the linear fit of Fig. 7, that the Langmuir adsorption isotherm is valid in the latter stage of Pd^0 adsorption (Fig. 4), where the kinetics is governed entirely by intra-particle mass transfer phenomena and is responsible for the slower adsorption rate.

4.4.1. Determination of η (effectiveness factor)

For any reversible reaction as given in Eq. (3), the equilibrium constant can be written in terms of the forward and backward rate constants as

$$K_1 = \frac{k'_{\text{ads}}}{k'_{\text{des}}} \quad (26)$$

Therefore, using Eq. (26), Eqs. (20)–(22) can be modified as

$$\frac{B}{C} = - \left(p_m + \frac{q_0 v}{M} + \frac{v}{MK_1} \right) \quad (27)$$

Table 3
Comparative electrical conductivities of SOFC anodes prepared by different techniques

Temperature (°C)	Functional anodes		Conventional
	Transient equilibrated sensitized bath (28 vol.% Ni)	Non-transient equilibrated sensitized bath (37 vol.% Ni)	Solid state (40 vol.% Ni)
Conductivities of Ni–YSZ cermet (S cm ⁻¹)			
1000	264.54	205.82	149.11
800	489.59	486.19	505.73

and

$$\frac{A}{C} = \frac{p_m q_0 v}{M} \quad (28)$$

Considering the average equilibration time at 1750 min (Fig. 3) and $q = q_s$ in Eq. (15), theoretical adsorbate uptake at equilibrium (p) can be calculated from the Langmuir isotherm (Eq. (15)).

Using Eqs. (26)–(28) and the calculated value of p , Eq. (19) can be solved as

$$\eta k'_{\text{ads}} = 7.595 \text{ ml (g min)}^{-1} \quad (29)$$

$$\eta k'_{\text{des}} = 3.45 \times 10^{-4} \text{ min}^{-1} \quad (30)$$

The physical significance of $\eta > 0$ is that diffusional resistances favour the forward reaction rate (adsorption) whereas, $\eta < 0$ promote the desorption rate [15]. Thus, from Eqs. (29) and (30), it can be proposed that the diffusion process (intra-particle mass transfer) not only favours the attainment of an adsorption equilibrium, but at the same time, it favours the adsorption rate. As $k'_{\text{ads}} \gg k'_{\text{des}}$ (evident from Eqs. (29) and (30)) and η has a positive value in the equilibrium region of adsorption kinetics, the same is preferred over the backward desorption kinetics. Consequently, the concentration gradient of Pd⁰ from the YSZ surface to the bulk is minimized and thereby reduces the Ni concentration gradient during subsequent electroless deposition from the bulk to YSZ surface, which, in turn, enhances the functionality of the materials for fuel cell applications.

4.5. Effect of equilibration time on enhancement of functionality

4.5.1. Electrical characterization

Fig. 8 shows the electrical conductivity values at 800 °C of SOFC functional anodes (prepared with transient and non-transient equilibrated sensitized bath) compared with those of the conventionally prepared anodes. The conductivity percolation threshold is brought down to ~28 vol.% Ni in the functional anode prepared with transient equilibrated sensitized bath in comparison with ~40 vol.% Ni for conventionally prepared samples. The functional anodes prepared with non-transient

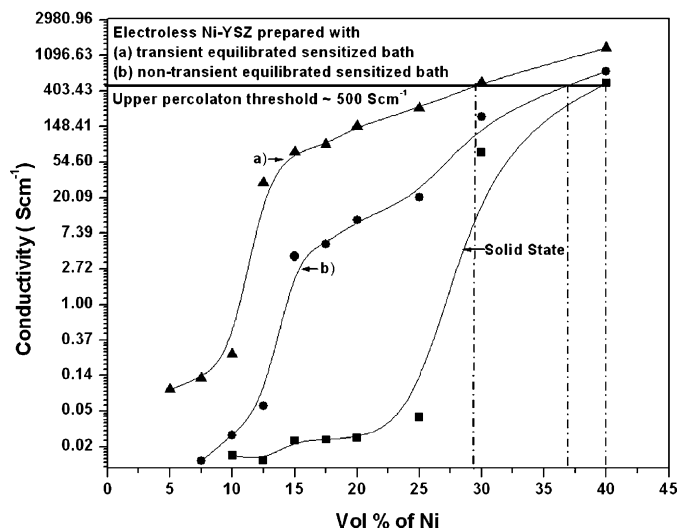


Fig. 8. Comparative electrical conductivities of Ni–YSZ cermet prepared by different techniques.

equilibrated sensitized bath does not show much improvement in lowering the vol.% of Ni in the cermet matrix for attaining the required upper percolation threshold for the electrical conductivity that is required for SOFC applications. The comparative electrical conductivities of functional and conventional anodes are given in Table 3.

Arrhenius plots for the reduced Ni–YSZ samples for functional anodes prepared at transient and non-transient equilibrated state of sensitization are given in Fig. 9 and compared with that obtained from conventional solid-state synthesis. The corresponding activation energies for their conductivities are compared in Table 4. The nature of conduction is predominantly metallic. For the functional anode prepared with transient and non-transient equilibrated sensitized bath, conduction starts from 15 vol.% Ni onwards. For a conventional solid state synthesis, however, reasonable conductivity starts from 30 vol.% Ni. The important role of equilibration time during the sensitization process can be noted from the activation energies given in Table 4. The activation energy values for functional anodes prepared with transient equilibrated sensitized bath are less than those prepared from non-transient equilibrated sensitized bath

Table 4
Activation energies for electrical conductivities

vol.% of Ni content	15	20	25	28	30	37	40
E_{act} (kJ mol ⁻¹), transient equilibrium	23.59	21.76	16.77	16.56	16.44	–	40.09
E_{act} (kJ mol ⁻¹), non-transient equilibrium	38.01	36.24	33.17	–	32.96	32.71	36.09
E_{act} (kJ mol ⁻¹), solid state	–	–	–	–	43.18	–	49.31

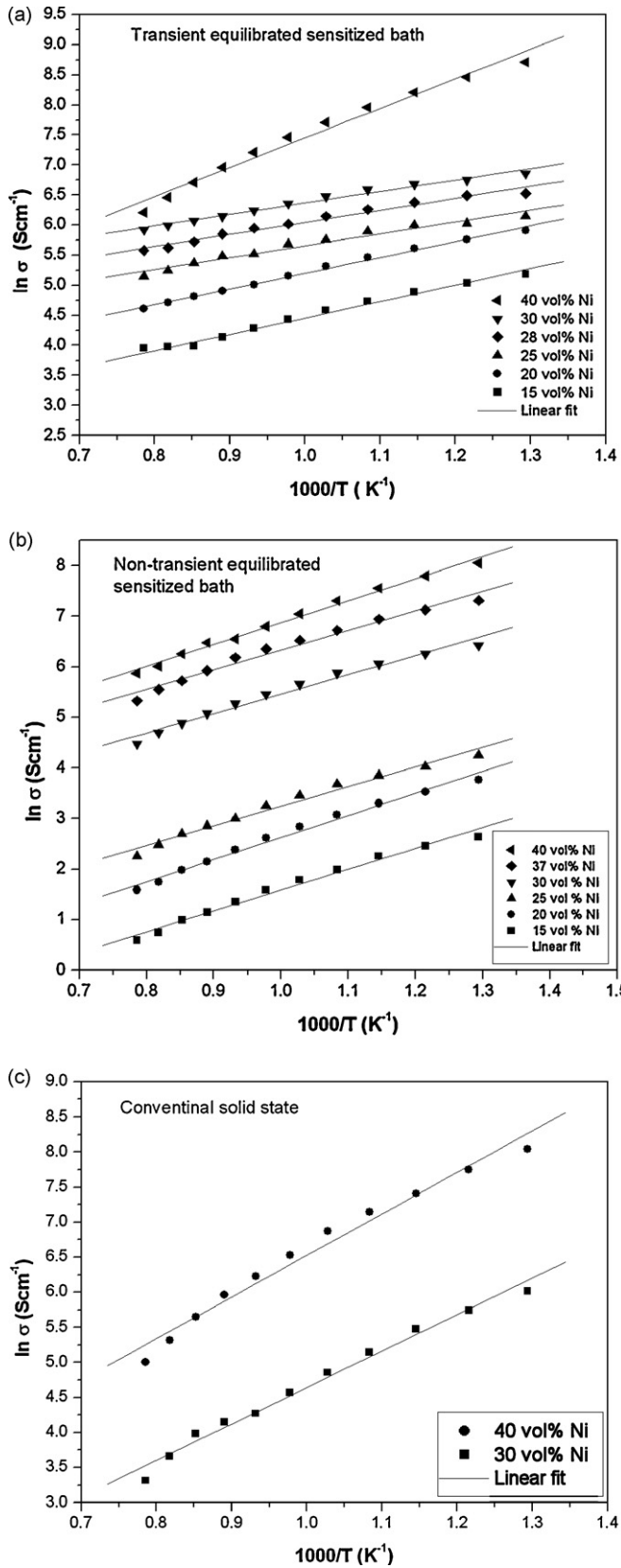


Fig. 9. Arrhenius plots of electrical conductivities as a function of nickel content for: (a) functional anodes prepared with transient equilibrated sensitized bath, (b) functional anode prepared with non-transient equilibrated sensitized bath and (c) conventionally prepared anode.

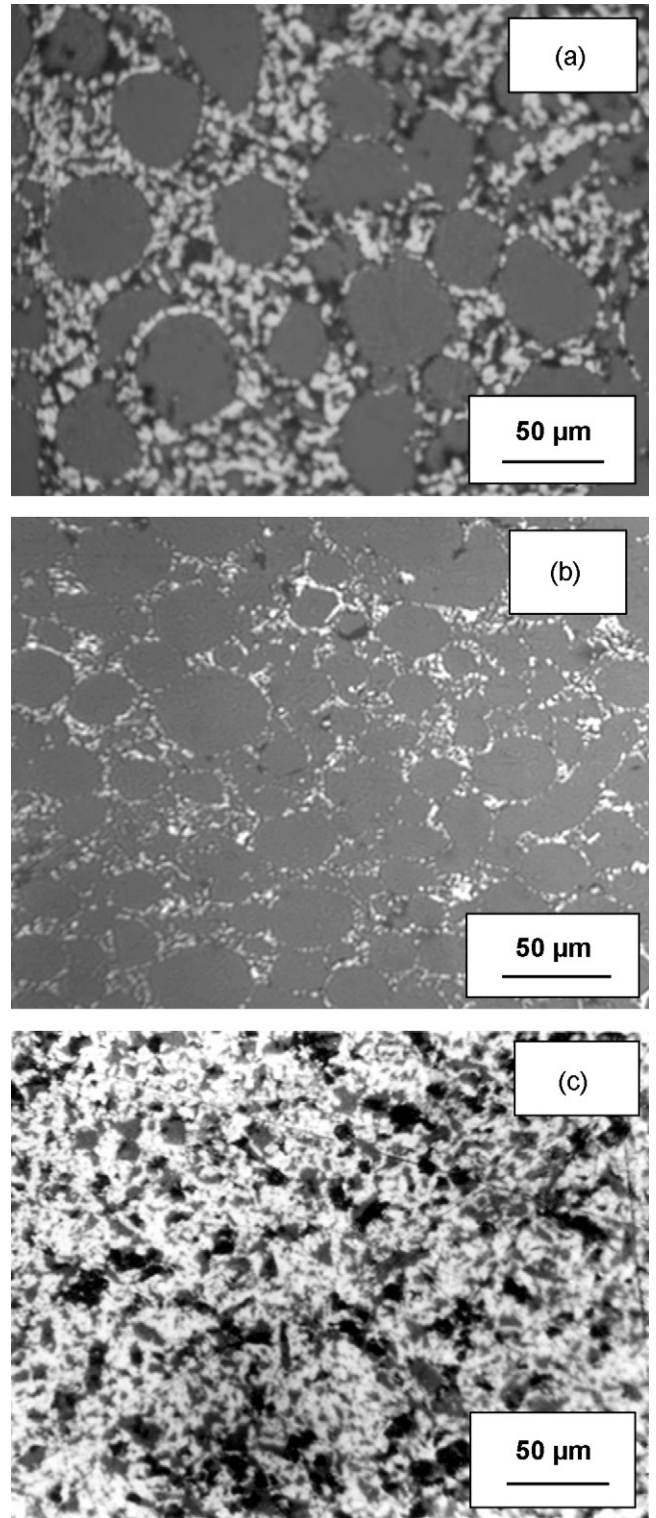


Fig. 10. Optical micrographs of functional Ni-YSZ cermet: (a) transient equilibrium adsorption, (b) non-equilibrium adsorption and (c) optical micrograph of conventionally prepared Ni-YSZ cermet.

up to 30 vol.% of Ni. From this observation, it may be concluded that in the former process, attainment of transient equilibrium leads to the formation of a prominent core–shell structure that makes the electronic path continuous in the cermets and thereby increases the conductivity at lower activation energy in comparison with the functional anodes prepared in a non-transient equilibrated state. By contrast, a reverse trend of activation energies in the functional anodes is observed at 40 vol.% Ni. Formation of a dense core–shell structure at 40 vol.% Ni in the functional anode prepared at a transient equilibrated state results in a higher rate of change of conductivity with temperature. This implies that the transient equilibrated sensitized bath favours the uniform formation of a Ni shell over the YSZ core, which is also supported by the proposed kinetic model.

4.5.2. Surface morphology

Fig. 10 compares the optical micrographs of the functional anodes prepared with transient and non-transient equilibrated sensitized bath with that of a conventionally prepared cermet. The core–shell microstructure is more prominent in Fig. 10a due to better sensitization of the YSZ particulate because of effective surface adsorption in comparison with Fig. 10b. This difference in the microstructure is due to the fact that in the first case, the sensitized bath is allowed to attain a transient equilibrium. This transient equilibrated sensitization process helps to encapsulate YSZ by freshly adsorbed Pd⁰ which is evident from the positive value of the effectiveness factor of the proposed kinetic model. Thus, it is expected that because of the proper shell formation in this case, Ni distribution is more uniform across the thickness of the shell which, in turn, enhances the triple-phase boundary length required for fuel oxidation at the anode side. Compared to this functional anode, the microstructure observed in the case of the conventionally prepared cermet shown in Fig. 10c, is clearly visible as dispersed Ni in the YSZ matrix. Thus high energy sonochemical reaction contributes significantly to the effective surface adsorption of Pd⁰ on zirconia that eventually enhances the functionality of Ni–YSZ cermet.

5. Conclusions

Ni–YSZ functional anode can be prepared by a novel electroless technique in which a sensitization process is the key step and involves surface adsorption of Pd⁰ on to YSZ particulates. A sorption kinetic model with an effectiveness factor (η) is developed. It simplifies evaluation of the intra-particle mass transfer during the surface adsorption of Pd⁰ on 8 mol% yttria stabilized zirconia (YSZ) powder under a high energy sonochemical reaction. Kinetic parameters such as effectiveness factor (η), time-dependent sorption capacity (q_t) and equilibrium sorption capacity (q_e) change with the particle size of the sorbent (YSZ). The reversible sorption kinetic model involves two processes: (i) external mass transfer and (ii) intra-particle mass transfer. The initial adsorption is preferably governed by external mass transfer but intra-particle mass transfer phenomena favour the attainment of an adsorption equilibrium. The external mass transfer coefficient depends on the agitation frequency but at a high value of 16 kHz, the effect of external mass transfer can be

neglected after attaining equilibration. In this particular equilibrium adsorption regime, the sorption kinetics depend solely on intra-particle mass transfer since the sorption of Pd⁰ on the YSZ surface is an example of physical adsorption.

Langmuir isotherm is used to fit the adsorption kinetics in the equilibrium adsorption region, where intra-particle mass transfer plays a major role. The equilibrium constant (K_1) and maximum adsorption capacity (p_m) values are determined from the Langmuir isotherm plot. The effectiveness factor (η) for Pd⁰ adsorption is found to be positive which favours the forward adsorption rate in the equilibrium region where intra-particle mass transfer is the rate-controlling step. For preparation of a functional cermet anode of Ni–YSZ that is applicable for fuel cell anode materials, adsorbed Pd⁰ on zirconia particulate acts as catalytically active sites for the reduction of Ni²⁺ to metallic Ni followed by subsequent formation of the uniform core–shell Ni–YSZ cermet. This is also reflected in the electrical conductivity values of functional anodes. Conductivities with transient equilibrated sensitized YSZ shows a prominence of Ni-shell formation across the YSZ-core and are correlated with optical micrographs. The experimental results validate the proposed sorption kinetic model with a positive effectiveness factor (η).

Supplementary data

Expression for adsorbate uptake at equilibrium.

Acknowledgements

The authors acknowledge the Director of CGCRI for his kind permission to present the work, Dr. Dipali Kundu of CGCRI, Kolkata for extending co-operation for ICP-AES measurements, and Dr. Abhijit Das Sharma, Scientist of Fuel Cell & Battery Division of the Institute for his valuable input. The authors also acknowledge CSIR-NMITLI project for financial support to conduct this research activity.

References

- [1] S.C. Singhal, K. Kendall, High Temperature Solid Oxide Fuel Cells: Fundamentals, Design and Applications, Elsevier, 2003.
- [2] R.N. Basu, S. Basu (Eds.), Materials for Solid Oxide Fuel Cells in Recent Trends in Fuel Cell Science and Technology, Anamaya Publishers, New Delhi, India, and Springer, New York, USA, 2006.
- [3] N.Q. Minh, T. Takahashi, Science and Technology of Ceramic Fuel Cells, Elsevier, New York, USA, 1995, pp. 147–164.
- [4] J. Mukhopadhyay, M. Banerjee, A. Das Sharma, R.N. Basu, H.S. Maiti, Electrochem. Soc. Trans. 7 (1) (2007) 1563–1572, The Electrochemical Society.
- [5] S.K. Pratihari, A. Das Sharma, R.N. Basu, H.S. Maiti, J. Power Sources 129 (2004) 138–142.
- [6] D.E. Dees, T.D. Claar, T.E. Easler, et al., J. Electrochem. Soc. 134 (1987) 2141.
- [7] J.P. Lorimer, T. Mason, J. Chem. Soc. Rev. 16 (1987) 239–274.
- [8] S.V. Ley, C.M.R. Low, Ultrasound in Synthesis, Springer, New York, 1989.
- [9] K.S. Suslick, Scient. Am. 260 (2) (1989) 62–68.
- [10] G.E. Boyd, A.W. Adamson Jr., L.S. Myers, J. Am. Chem. Soc. 69 (1947) 2836–2848.
- [11] D.D. Do, Adsorption Analysis: Equilibria and Kinetics, Imperial College Press, 1998, 562 pp.

- [12] D.M. Ruthven, Principles of Adsorption and Adsorption Process, 1984, pp. 199–200.
- [13] J. Toth, Adsorption: Theory, Modeling and Analysis, Surfactant Science Series, vol. 107, 2002, 356 pp.
- [14] W. Zhu, Advance Inductively Coupled Plasma—Mass Spectrometry Analysis of Rare Earth Elements, Environmental Applications, 1999, 65 pp.
- [15] S.S.E.H. Elnashaie, S.S. Elshishini, Topics in Chemical Engineering, vol. 7, 1993, pp. 146, 153.
- [16] Leusch, B. Volesky, J. Biotechnol. 43 (1995) 1–10.
- [17] S.K. Pratihar, R.N. Basu, A. Das Sharma, H.S. Maiti, A process for preparing nickel yttria stabilized zirconia (Ni-YSZ cermet), Indian Patent (appl. no. 306/DEL/01 dated 27.02.2001).
- [18] B. Wehrli, S. Ibric, W. Stumm, Colloids Surf. 511 (1990) 77–88.
- [19] K. Kesenci, R. Say, A. Denizli, Eur. Polym. J. 38 (2002) 1443–1448.

Development of Functional SOFC Anode

J. Mukhopadhyay, M. Banerjee, A. Das Sharma, R.N. Basu, and H.S. Maiti

Fuel Cell & Battery Section
Central Glass & Ceramic Research Institute, Kolkata - 700032, India

For anode-supported planar SOFC, the most widely accepted anode material is nickel-8mol% yttria stabilized zirconia (Ni-YSZ) cermet. For the required electrical conductivity during intermediate temperature SOFC operation ($\sim 800^{\circ}\text{C}$), conventionally 35-40vol.% Ni is used. Reduction of nickel content not only solves nickel coarsening problem during long-term SOFC operation but also makes thermal expansion coefficient much closer to YSZ. In this investigation, a novel electroless technique is employed to prepare uniform coating of metallic Ni onto YSZ to make core-shell anode cermet structure. Compared to conventionally prepared anodes ($\sim 35\text{vol.}\% \text{ Ni}$), in this functional anode, percolation threshold is lowered down to $\sim 20\text{vol.}\%$ to achieve almost same electrical conductivity ($\sigma_{800^{\circ}\text{C}} \sim 150 \text{ S cm}^{-1}$). However, the properties of these cermets depend strongly on several processing conditions like particle size of YSZ powders, sensitization process, electroless bath composition and deposition temperature. A simple adsorption kinetic model for sensitization process is proposed.

Introduction

For the state-of-the-art anode-supported SOFC, the most important cell component is the anode support. Apart from its high electronic conductivity, the anode should have enough interconnected porosity for proper percolation of the fuel gas and also to provide the effective number of the electrocatalytic sites for the oxidation of the fuel (1-3). The most widely accepted anode material for SOFC is nickel-8mol% yttria-stabilized zirconia (YSZ) composite, commonly known as Ni-YSZ cermet. The purposes of YSZ addition in Ni-YSZ cermet is to reduce the thermal expansion of nickel and thereby make it more compatible with the YSZ electrolyte and also to inhibit coarsening of nickel during prolonged operation at high temperature (4-9). As the thermal expansion coefficient of nickel ($16.9 \times 10^{-6} \text{ K}^{-1}$) is much more than that of YSZ ($10.8 \times 10^{-6} \text{ K}^{-1}$), lowering the amount of nickel will give rise to a cermet with lower thermal expansion and thus will be closer to the coefficient of thermal expansion of YSZ electrolyte. At the same time, the electrical conductivity cannot be compromised as this determines the current-carrying capacity of the anode material. Hence, an optimum nickel concentration has to be selected. Conventionally the amount of Ni in the Ni-YSZ cermet is maintained at 35-40vol.% for achieving a continuous Ni-Ni network (4-6). Apart from higher thermal mismatch, another major drawback of such compositions having significantly high Ni content is the coarsening of nickel particles at higher operating temperature ($> 750^{\circ}\text{C}$) for a long term operation (7-9). So, lowering the volume of Ni in Ni-YSZ cermet is required not only to reduce thermal expansion but also to prohibit Ni coarsening under long term

operation of SOFC. The Ni-YSZ cermet is generally prepared by various techniques, e.g., mixed oxide route (4), co-precipitation route (10), slurry coating route (11), liquid dispersion route (12,13), and heat decomposable aqueous salt solution route (14) where in almost all cases Ni is more or less uniformly distributed in YSZ matrix. In our earlier work, we have already shown that in a novel technique, electroless deposition of Ni onto sensitized YSZ powders significantly lowers the Ni content in the Ni-YSZ cermet without much affecting the essential electronic conductivity in the cermet (15). The expected Ni deposition by this electroless technique onto YSZ particles helps to generate metallic chain during sintering at high temperature followed by subsequent reduction and a core-shell structure is formed with a core made of YSZ and shell made of metallic Ni. Thus the functionality in the cermet is added and the flow path of electrons is made continuous by the Ni-Ni sintered shell rather than the dispersed Ni-YSZ cermet. However, the major factors for this electroless technique are bath composition and temperature, initial particle size and morphology as well as the sensitization process of YSZ powders (16). In this investigation, all these parameters have been studied and optimized. The most critical among the above is the sensitization process where metallic palladium (Pd) is adsorbed onto the YSZ particles by an *in situ* redox reaction of stannous (Sn^{2+}) and palladium (Pd^{2+}) ions. To understand the sensitization process and calculate the minimum residence time required for surface adsorption of metallic Pd on YSZ, a simple kinetic model is also established from the residual Pd^{2+} concentrations supernatant solution of the sensitized bath. However, adsorption is often a time dependent rather than a transient equilibrium process. Its kinetics involves the following three kinds of processes of mass transfer and surface reaction on the adsorbents that take place during adsorption, i) the external mass transfer of metal ions from the bulk solution to the surface of adsorbents, ii) the intraparticle mass transfer of metal ions in the pores and on the surface of adsorbents, and iii) the chemical reaction on the surface of adsorbents (17).

Experimental

For the purpose of electroless deposition of Ni onto YSZ two types of powders are used, a) TZ-8Y, from Tosoh Corp., Japan (d_{50} 0.2-0.3 μm and henceforth referred to as YSZ-T), and b) FYT 1 13.0 – 001H from Unitech Corporation, UK (d_{50} 2-3 μm and henceforth referred to as YSZ-U). YSZ-T is further processed in order to facilitate effective sensitization. Both the powders (processed YSZ-T and YSZ-U) are poured into a redox bath containing 0.001(M) palladium chloride and 0.265(M) stannous chloride. The *in situ* reduction reaction producing metallic palladium (Pd) and its deposition on YSZ powders are facilitated by placing the bath in high energy ultrasonification (BRANSON, SONIFIER, 450, 50/60 Hz) for 15 min. The sensitized bath is then allowed for required equilibration time in order to achieve proper surface adsorption of metallic Pd onto YSZ. For calculating minimum equilibrium time, a certain amount of aliquot from the supernatant solution of the sensitized bath is taken at definite time interval and the remnant concentration of Pd^{2+} in the supernatant solution is measured with the help of an Inductive Coupled Plasma Atomic Emission Spectrophotometer, Spectro Analysis Instrument (Kleve, Germany). This study is carried out for 25vol.% of Ni in Ni-YSZ cermets. The effect of pH on surface adsorption of Pd^0 onto both YSZ-T and YSZ-U is studied in Conductometer, 712, Metrohm Ltd., Switzerland. The kinetic model for surface adsorption of Pd^0 is established and verified with the measurement parameters. After successful evaluation for the required equilibration time for surface adsorption of

metallic Pd, the sensitized YSZ particles are added to an electroless bath containing nickel nitrate with requisite quantity of Ni. The reaction bath is kept constant at ammoniacal pH and temperature 80-90°C. The reduction of the Ni²⁺ from nickel nitrate solution is carried out by *in situ* liberation of the nascent hydrogen generated from the quantified addition of hydrazine hydrate. A typical flow diagram for the electroless process is given in Figure 1.

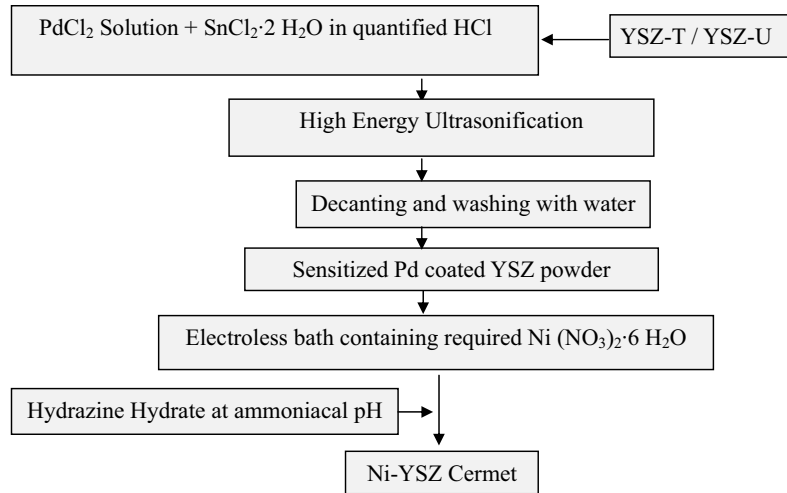


Figure 1. Flow diagram of Ni-YSZ cermet preparation by electroless process.

The Ni-YSZ cermets with Ni content ranging from 10-40vol.%, thus produced are characterized by X-ray diffraction with the help of a Philips X'pert X-ray diffractometer with a Cu-K α radiation. The as-synthesized powders are mixed with 1.5wt.% polyvinyl butyral (PVB) binder and pressed uniaxially in the form of green compacts of dimension 25 mm \times 10 mm \times 3 mm under a specific pressure of 170 MPa. The green compacts are sintered in air at a temperature of 1400°C for 6 h and their sintered densities are measured by Archimedes principle. The sintered samples are then reduced at 1000°C under a gaseous flow of argon and hydrogen (4:1) for 10 h and thus Ni-YSZ cermet bulk samples are produced. A few samples are also prepared by conventional solid state as well by liquid state dispersion technique under the similar conditions for suitable comparison (13,14). Conductivities of the reduced Ni-YSZ samples as a function of temperature are measured using standard 4-probe DC measurement technique. The reducing atmosphere within the furnace is maintained by purging the same gaseous mixture mentioned above. Resistances of the samples are then measured using an eight and half digit multimeter (Keithley, 2002). The corresponding conductivity values in various temperatures are then calculated using the formula:

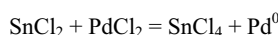
$$\sigma = \frac{L}{Rbt} \quad [1]$$

where σ is the conductivity, R is the 4-probe resistance of the samples measured, L is the length in between the two voltage probes, b is the breadth and t is the sample thickness respectively. The optical micrographs of conventionally prepared sintered reduced samples are compared with those prepared by electroless techniques with the help of high resolution optical microscope (Olympus GX 71, Japan). Functionality of these anodes is correlated with their relevant microstructures and electrical conductivities for attaining the optimized Ni shell onto the core YSZ structures.

Results and Discussion

Kinetic Model for Metallic Pd Adsorption

Pd catalyst required for electroless deposition of Ni onto YSZ, is produced by the redox reaction of stannous chloride and palladium chloride which is shown below:



Parent particle size should not be below a particular value for effective and homogeneous deposition (15). Figure 2 illustrates the variation of the adsorption capacity (q_t) of Pd^0 with time calculated from remnant Pd^{2+} concentration in the supernatant liquid of the sensitized bath. From the Figure 2 it is clear that surface adsorption rates of Pd^0 on YSZ are fast at the beginning and then slowed as the equilibrium is approached.

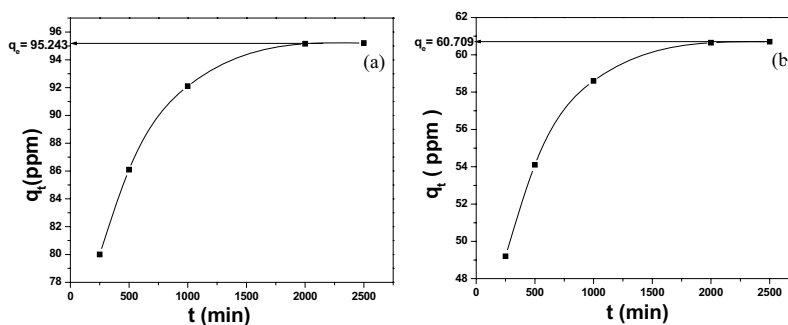


Figure 2. Variation of adsorption capacity (q_t) of Pd^0 on sensitized YSZ: a) YSZ-T and b) YSZ-U.

From the graphs shown above, it is clear that the adsorption equilibrium of Pd^0 is attained near 2000 min. The equilibrium concentration of the adsorbed Pd^0 onto sensitized YSZ varies depending on the nature of the adsorbent, e.g., for YSZ-T the equilibrium concentration (q_e) for adsorbed Pd^0 is ~ 95 ppm but the same for YSZ-U is ~ 61 ppm. However, this seems to be dependent on the initial particle size distribution as well as surface morphology of the starting YSZ powders. It is observed that YSZ-T

having particle size range of $10.25 \mu\text{m} \leq d_{50} \leq 60.5 \mu\text{m}$ are quite effective for surface adsorption of Pd^0 rather than YSZ-U having particle size range of $2.5 \mu\text{m} \leq d_{50} \leq 50 \mu\text{m}$.

It is also observed that pH of the sensitized bath has a pronounced effect on the surface adsorption of Pd^0 onto YSZ absorbents. Though the original pH of the sensitized bath is ~ 2 , it is found that q_e increases with an increase in pH and reaches equilibrium at $\sim \text{pH } 5$. The variation of q_e for Pd^0 for YSZ-T and YSZ-U are shown in Figure 3. As q_e is maximum at $\text{pH} \sim 5$, the kinetic model is calculated and fitted with respect to q_e obtained at $\text{pH } 5$.

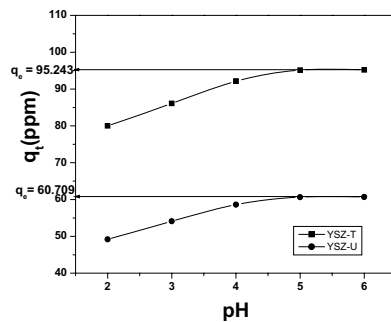


Figure 3. Variation of adsorption capacity (q_t) with pH for YSZ-T and YSZ-U.

The adsorption kinetics of Pd^0 on sensitized YSZ could be well predicted by the pseudo-second order kinetic model given in the following equation:

$$\frac{dq_t}{dt} = k_2 (q_e - q_t)^2 \quad [2]$$

where k_2 is the rate constant of pseudo-second-order rate in ppm min^{-1} , q_e is the adsorption capacity at equilibrium in ppm; and q_t is the adsorption capacity at time t , also in ppm. Separating the variables in the above equation and integrating gives,

$$\frac{t}{q_t} = \frac{1}{k_2 q_e^2} + \frac{1}{q_e} t \quad [3]$$

The equilibrium adsorption capacity q_e and the pseudo second-order rate constant k_2 can be experimentally determined from the slope and the intercept of the plot t/q_t against t . Figure 4 shows the variation of t/q_t with time t . The plots are fitted linearly using Equation [3] and k_2 calculated for YSZ-T and YSZ-U. Kinetic parameters like q_e , k_2 and percentage fit with linearity are given in Table I. Adsorption of Pd^0 in both the cases of YSZ-T and YSZ-U are found to follow the pseudo-second order kinetics with almost same rate constant value but it is quite clear that in the case of YSZ-U, as q_e is much lower than that of YSZ-T, the expected nickel deposition will be much lower in the case of YSZ-U than that of YSZ-T.

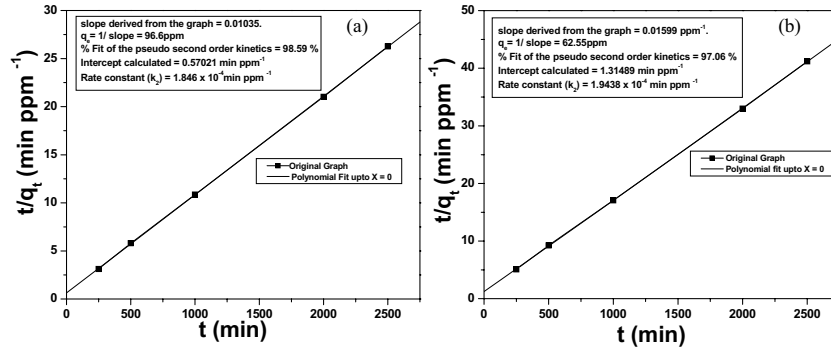


Figure 4. Variation of t/q_t vs. time: (a) YSZ-T and (b) YSZ-U.

TABLE I. Kinetic Parameters for Adsorbed Pd⁰ Onto Sensitized YSZ

Parameters	YSZ-T		YSZ-U	
	Estimated	Theoretical	Estimated	Theoretical
Equilibrium Adsorption Capacity (q_e), ppm	95.243	96.6	60.709	62.55
Pseudo Second-order Rate Constant (k_2), min ppm ⁻¹	1.846×10^{-4}		1.9438×10^{-4}	
% Fit with Linearity	98.59		97.06	

Powder and Bulk Sample Characterization

Figure 5 shows the XRD patterns of as-synthesized powders which indicates the formation of metallic Ni within YSZ matrix in each case irrespective of the starting powders as well as the volume percentage of Ni in the cermet batch. The densities of the NiO-YSZ samples sintered in air at 1400°C for 6 h and the same for their reduced samples are given in Table II. It is observed that with an increase in percentage of Ni content, the densities of NiO-YSZ varies non-linearly, whereas in the case of reduced Ni-YSZ density change follows a linear decreasing trend. Similar trend is also observed by Lee et al. (18). However, more detailed studies are currently being carried out to check the addition of pore former in the cermet matrix.

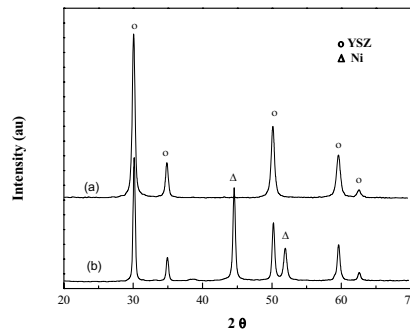


Figure 5. XRD pattern of (a) YSZ-T/YSZ-U and (b) Ni coated YSZ-T /YSZ-U.

TABLE II. Density of Sintered NiO-YSZ and Reduced Ni-YSZ Prepared by Electroless.

Ni Content (vol.%)	Density of NiO-YSZ (g/cc)		Density of Ni-YSZ (g/cc)	
	YSZ-T	YSZ-U	YSZ-T	YSZ-U
10	5.79	5.01	4.92	4.51
15	5.71	4.85	4.77	4.16
20	5.47	4.76	4.54	3.85
25	5.23	4.59	4.22	3.52
30	5.33	5.02	4.21	3.459
40	5.45	5.39	4.08	3.29

Figure 6 shows the comparative electrical conductivities of SOFC anodes prepared by conventional solid state, liquid dispersion method and electroless deposition techniques. The percolation threshold for electrical conductivity for these functional anodes has been brought down to 20vol.% from 30-35vol.% in the case of conventionally prepared SOFC anodes (4).

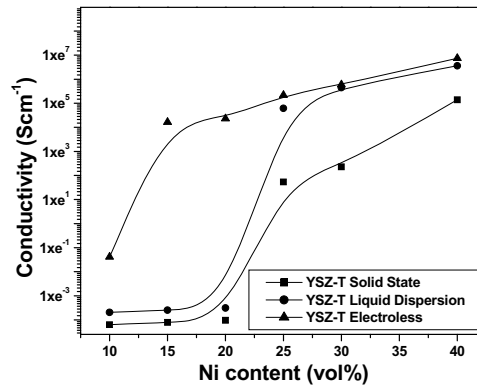


Figure 6. Comparison of electrical conductivity for Ni-YSZ prepared by different techniques.

A comparative electrical conductivity plot at room temperature (RT) and operating temperature (OT) of SOFC (800°C) is given in Figure 7. As expected from the preparation of this functional anode, the as-pressed (green stage) samples are also conducting enough. The Arrhenius plots for the sintered and reduced samples prepared from batches YSZ-T and YSZ-U are shown in Figure 8. The nature of conduction is predominantly dictated by the metallic nature. For YSZ-T, conduction starts from 15vol.% nickel onwards, while for YSZ-U the same requires more than 20vol.% of nickel. These results can be correlated with the kinetic parameters as given in Table I. The

equilibrium concentration (q_e) of adsorbed Pd^0 is much lower in the case of YSZ-U than that of YSZ-T, which ultimately decides the continuous Ni shell formation on YSZ core in electroless technique. This implies the core shell structure is more prominent in YSZ-T rather than in YSZ-U.

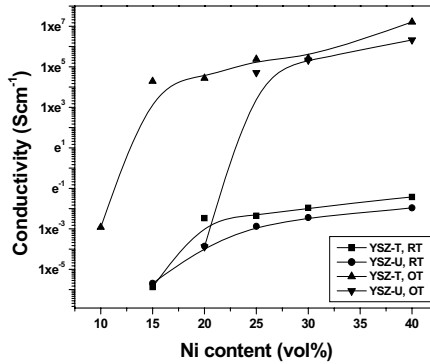


Figure 7. Conductivity plots for YSZ-T and YSZ-U at RT and OT.

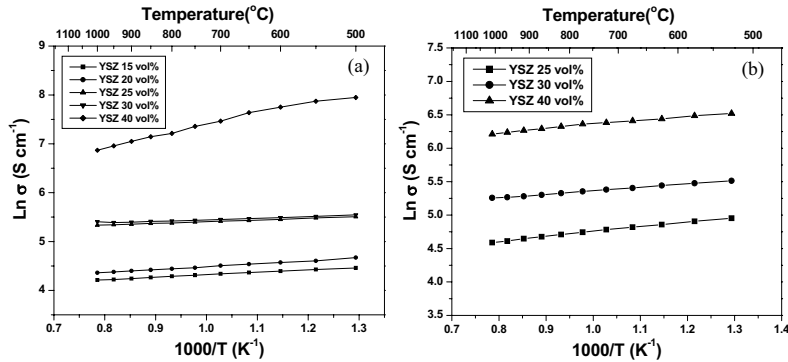


Figure 8. Temperature dependence of electrical conductivity as a function of nickel content: (a) YSZ-T and (b) YSZ-U.

Figure 9 compares the optical micrographs of the two experimental powders containing 25vol.% Ni prepared by electroless technique and 40vol.% of Ni-YSZ prepared by conventional solid state method respectively. Completely distinct microstructures are observed in case of electroless technique that forms core-shell functional anode with higher concentration of metallic Ni in the grain boundary region (white portions in the micrographs) and that of YSZ in the core grain (gray portions in the micrographs). Compared to this functional anode, the microstructure observed in case of the conventionally prepared cermet, is the dispersed Ni in the YSZ matrix rather than any Ni coated YSZ core shell (Fig. 9c).

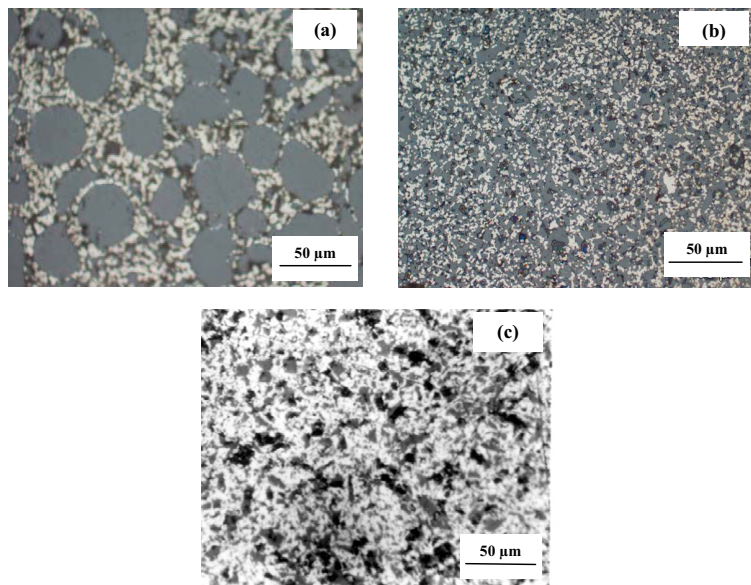


Figure 9. Optical micrographs of a) 25-YSZ-T, b) 25-YSZ-U prepared by electroless, and c) 40-YSZ-T prepared by conventional solid state technique.

Thus the functionality of this cermet anode prepared by this electroless technique is justified which may be quite effective from SOFC application point of view. Due to more prominent core-shell microstructure observed in the case of YSZ-T, the electrical conductivity values are found higher for YSZ-T than that of YSZ-U. The electrical conductivity percolation threshold is found at lower vol.% of Ni for YSZ-T than YSZ-U which also supports the higher extent of Ni deposition onto sensitized YSZ-T. This is also reflected in Pd^0 adsorption kinetics.

Conclusions

Nickel coated YSZ powder can be synthesized by electroless technique without any impurity phase. Initial YSZ particle size distribution is one of the key parameters for surface adsorption of Pd^0 which act as the catalytic sites for Ni deposition. Metallic palladium adsorption kinetics is found to follow pseudo-second order kinetics irrespective of initial YSZ particle size distribution. The samples produced by this technique are electrically conducting even at room temperature. It is observed that the conductivity percolation threshold could be lowered down to even 20vol.% for the functional anode prepared by electroless technique as compared to 35-40vol.% in conventionally prepared anodes by solid state synthesis. The reduction in nickel content will help not only to match coefficient of thermal expansion with YSZ electrolyte but also to prohibit Ni coarsening on long term SOFC operation. Therefore, Ni-YSZ cermets prepared by this

technique could be better alternative SOFC functional anode than those prepared by conventional techniques.

Acknowledgments

The authors acknowledge CSIR-NMITLI program for sponsoring the project and Director, CGCRI for his kind permission to present the work. The authors also acknowledge Dr. D. Kundu of CGCRI, Kolkata for extending co-operation for ICP-AES measurements.

References

1. S.C. Singhal and K.Kendall, *High Temperature Solid Oxide Fuel Cells: Fundamentals, Design and Applications*, Elsevier, U. K. Editor, (2003).
2. S.P.S. Badwal, K. Foger, *Ceram. Int.*, **22**, 257 (1996).
3. N.Q. Minh, T. Takahashi, *Science and Technology of Ceramic Fuel Cells*, Elsevier, New York, USA, (1995).
4. D.E. Dees, T.D. Claar, T.E. Easler, et.al, *J. Electrochem.Soc.* **134**, 2141 (1987).
5. R.N. Basu, *Materials for Solid Oxide Fuel Cells in Recent Trends in Fuel Cell Science and Technology*, p. 284, S. Basu, Editor, Jointly published by Anamaya Publishers, New Delhi (India) and Springer, New York (USA), (2006).
6. J. Mizusaki, S. Tsuchiya, K. Waragai, et.al, *J. Am. Ceram. Soc.*, **79**, 109 (1996).
7. G. Maggio, I. Ielo, V. Antonucci, N. Giordan, et al, (Eds.), *SOFC II*, p. 611, The Commission of the European Communities, Luxembourg (1991).
8. G.E. Pike, C.H. Seager, *J. Appl. Phys.*, **48**, 5152 (1997).
9. T. Iwata, *J. Electrochem. Soc.*, **143**, 1521 (1996).
10. N.M. Sammes, M. Brown, I.W.M. Brown, *J. Mater. Sci.*, **31**, 6069 (1996).
11. J. Macek, M. Marinsek, *2nd European SOFC Forum*, Proceedings vol.1 p. 341, Osolo, (1996).
12. T. Kawada, N. Sakai, H. Yokokawa, *Solid State Ionics*, **40 (1)**, 402 (1990).
13. S.K. Pratihari, R.N. Basu, H.S. Maiti, *Trans. Indian Ceram. Soc.*, **56**, 85 (1997).
14. S.K. Pratihari, R.N. Basu, S. Mazumdar, H.S. Maiti, *Solid Oxide Fuel Cells (SOFC VI)*, PV 99-19, p. 513, The Electrochemical Society (1999).
15. S. K. Pratihari, A. Das Sharma, R.N. Basu, H.S. Maiti, *J. Power Source*, **129**, 138 (2004).
16. G. Wen, Z.X. Guo, C.K.L. Davies, *Scr. Mater.*, **43**, 307 (2000).
17. G.E. Boyd, A.W. Adamson Jr., L.S. Myers, *Am. Chem. Soc.*, **69**, 2836 (1947).
18. J.-H. Lee, H. Moon, H.-W.Lee, J.Kim, et.al, *Solid State Ionics*, **148**, 15 (2002).

Madhumita Mukhopadhyay (Bamerjee)
16.03.2012.